UNIVERSITY OF ICELAND

**Ph.D. Dissertation**
**in Physics**

# Ordering in multistable magnetic nanostructures

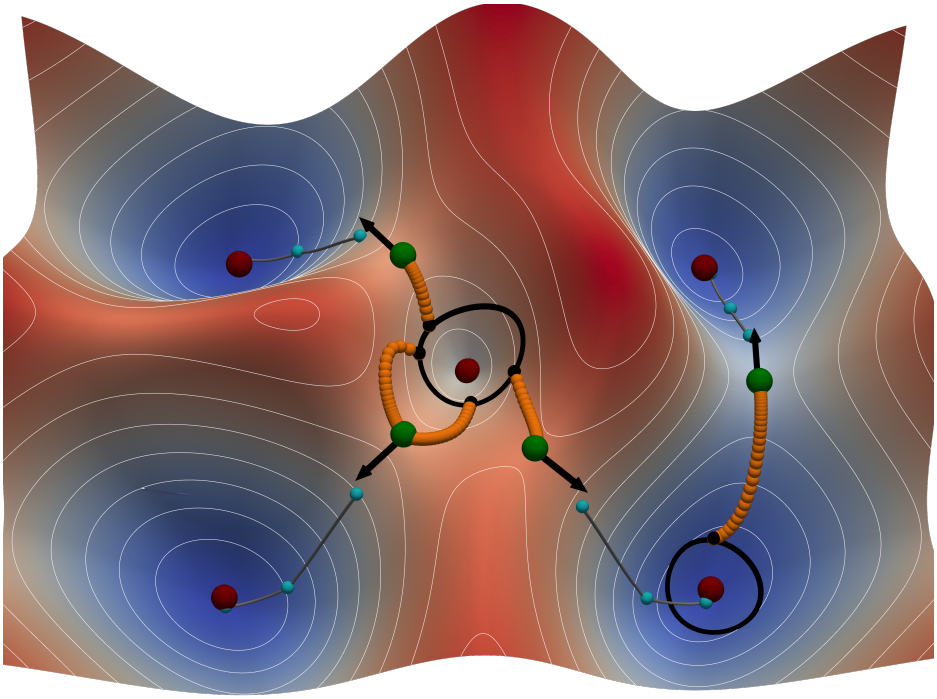

**Hendrik Schrautzer**

November 2025

FACULTY OF FACULTY OF PHYSICAL SCIENCES

# Ordering in multistable magnetic nanostructures

Hendrik Schrautzer

Dissertation submitted in partial fulfillment of a
*Philosophiae Doctor* degree in Physics

Ph.D. Committee
Pavel Bessarab
Snorri Þorgeir Ingvarsson
Hannes Jónsson
Stefan Heinze

Opponents
Vitaliy Lomakin
Denys Makarov

Faculty of Faculty of Physical Sciences
School of Engineering and Natural Sciences
University of Iceland
Reykjavik, November 2025

Ordering in multistable magnetic nanostructures

Dissertation submitted in partial fulfillment of a *Ph.D.* degree in Physics



Faculty of Faculty of Physical Sciences
School of Engineering and Natural Sciences
University of Iceland
Dunhagi 3 IS-107, Reykjavik Iceland

Telephone: 525-4000

Bibliographic information:
Hendrik Schrautzer, 2025, *Ordering in multistable magnetic nanostructures*, Ph.D.Dissertation, Faculty of Faculty of Physical Sciences, University of Iceland, 193 pp.

Author ORCID: 0000-0001-7332-9059
ISBN: 978-9935-9826-7-4

Printing: XXPrinter
Reykjavik, Iceland, November 2025

# Abstract

Magnetic nanosystems hosting co-existing localized magnetic textures beyond skyrmions are of great interest for fundamental science and technological applications, but their characterization is challenging due to the complexity of the energy surface. This energy surface is uniquely determined by the underlying interactions between magnetic moments and can exhibit numerous local minima associated with metastable states. Within harmonic transition state theory or Kramers/Langer theory, the identification of first-order saddle points on this surface is essential for calculating transition rates between metastable states and thus for quantitative assessment of the thermal stability of localized magnetic structures. In this work, a theoretical framework is developed and implemented that enables the systematic identification of first-order saddle points on the energy surface of magnetic systems. In contrast to methods based on finding minimum energy paths, the developed approach does not require prior knowledge of the final state of the transitions. The approach does not rely on phenomenological models and subjective assumptions, thereby opens the door for highly predictive simulations of long time-scale thermal dynamics of multistable magnetic systems and systematic sampling of the energy surface based on recursive traversing between energy minima via saddle points. The methodology is applied to various systems capable of hosting a large diversity of localized magnetic textures including two- and three-dimensional chiral magnets and transition-metal ultrathin film and multilayer systems. In particular, a hierarchy of transition mechanism universal for various topological textures in two-dimensional chiral magnets is discovered and the interplay between the topology of a texture and its thermodynamically accessible collapse paths is investigated. Furthermore, it is demonstrated that long-range dipole-dipole interactions lead to a vastly increasing complexity of transition mechanisms of three-dimensional textures such as chiral bobbers, skyrmion tubes, and globules. In ultrathin transition metal systems, prototypical for applications, the method reveals that higher-order exchange interactions can strongly enhance the lifetime of skyrmions and antiskyrmions. Together with the presented applications, the developed methodology constitutes an important advancement for the theoretical prediction of the long time-scale magnetization dynamics and characterization of the energy surface of complex, technologically relevant magnetic systems.

# Ágrip

Nanóskala segulkerfi sem hýst geta ýmis staðbundin segulmynstur samtímis, t.a.m. skyrmeindir og enn flóknari mynstur, eru áhugaverð fyrir grunnvísindi sem og tækninýjungar, en greining á slíkum kerfym er krefjandi vegna þess hve orkuyfirborð þeirra er flókið. Víxverkuninni milli segulvigranna ákvarðar lögun orkuyfirborðsins og þar geta komið fram fjöldi staðbundinna lágmarka sem samsvara hálfstöðugum ástöndum. Innan kjörsveifilsnálgunar virkjunarástandskenningarinnar sem og Kramers/Langer kenningunni er lykilatriðið að finna fyrsta stigs söðulpunkta til að meta gang og hraða umbreytinga milli ástanda og þar með meta stöðugleika staðbundinna segulmynstra við tiltekið hitastig. Í þessu verkefni er þróuð og innleidd umgjörð til að gera það kleift að finna fyrsta stigs söðulpunkta á orkuyfirborði segulkerfa á kefisbundinn hátt. Ólíkt aðferðum til að finna lágmarksorkuferla, þarf aðferðin sem þróuð er hér ekki upplýsingar um lokaástand umbreytinganna. Aðferðafræðin byggist ekki á fyrirbærafræðilegum líkönum og nálgunum og opnar því möguleikann á því að framkvæma reikninga sem geta spáð fyrir um varmadrifnar umbreytingar á löngum tímaskala í segulklerfum þar sem mörg ástönd eru til staðar. Kerfisbundin greining á orkuyfirborðinu er fengin með því að staðsetja orkulágmörk og tengja þau með leiðum í gegnum fyrsta stigs söðulpunkta. Aðferðinni er beitt á ýmis kerfi sem geta verið í margs konar ástöndum sem samsvara staðbundnum segulmynsttrum, þar með tví- og þrívíð hendin segulkerfi og örþunnar húðir hliðarmálma sem og marglaga kerfi. Til að mynda er fundin stigskipting á hvarfgangi sem á við um margskonar grannfræðileg mynstur sem og ráðandi gangur fyrir eyðingu þeirra. Enn fremur er sýnt fram á að langdræg tvískautsvíxverkun leiðir til mun flóknari hvarfgangs í þrívíðum kerfum, þar með hendnum bobbum, skyrmeindastrengjum og kúlulaga mynstrum. Í örþunnum húðum hliðarmálma, sem eru oft notuð, sýna reikningarnir að hærri gráðu víxlverkun getur aukið líftíma skyrmeinda og andskyrmeinda. Þessi dæmi um notkun aðferðarinnar sýna að hún markar mikilvægt skref í kennilegum spám um langtíma framvindu segulkerfa og greiningu á orkuyfirborði flókinna kerfa sem nýst geta í nýrri tækni.

# Table of Contents

# List of Figures

# List of Publications

## Publications included in this thesis

**Paper I:** **H. Schrautzer**, S. von Malottki, P.F. Bessarab, S. Heinze, 2022, Effects of interlayer exchange on collapse mechanisms and stability of magnetic skyrmions. *Physical Review B*, Vol. 105, Issue 1, pp. 014414. Accessed at `https://journals.aps.org/prb/abstract/10.1103/PhysRevB.105.014414`. Hendrik performed the calculations, analyzed the data, prepared the figures and wrote the article together with all authors.

**Paper II:** **H. Schrautzer**, M. Sallermann, P.F. Bessarab, H. Jónsson, 2025, Identification of mechanisms of magnetic transitions using an efficient method for converging on first-order saddle points. *Physical Review B*, Vol. 112, Issue 10, pp. 104433. Accessed at `https://link.aps.org/doi/10.1103/z673-hhnp`. Hendrik developed the method together with M. Sallermann, implemented and tested the method, performed the simulations and prepared the figures and wrote the article together with all authors.

**Paper III:** **H. Schrautzer**, M.A. Goerzen, B.Beyer, S.Haldar, P.F. Bessarab, S. Heinze, 2025, Impact of higher-order exchange on the lifetime of skyrmions and antiskyrmions. *npj Computational Materials (submitted)*. Accessed at `https://arxiv.org/abs/2511.05278`. Hendrik performed the calculations, prepared the figures, implemented the method together with M. Goerzen and B. Beyer and wrote the article together with all authors.

**Paper IV:** **H. Schrautzer**, T. Drevelow, Hannes Jónsson, P.F. Bessarab, 2025, Network of localized magnetic textures revealed using a saddle-point search framework. Accessed at `https://arxiv.org/abs/2512.07663`. Hendrik developed and implemented the methodology, performed the calculations, analyzed the data together with P.F. Bessarab and wrote the article together with all authors.

## Other publications during the doctorate

**Paper V:** A. Kudlis, M. Kazemi, Y. Zhumagulov, **H. Schrautzer**, A. I. Chernov, P.F. Bessarab, I. V. Iorsh, I. A. Shelykh, 2023, All-optical magnetization control in $CrI_3$ monolayers: A microscopic theory. *Physical Review B*, Vol. 108, Issue 9, pp. 094421. Accessed at https://journals.aps.org/prb/abstract/10.1103/PhysRevB.108.094421.

**Paper VI:** D. Li, S. Haldar, L. Kollwitz, **H. Schrautzer**, M. A. Goerzen, S. Heinze, 2024, Prediction of stable nanoscale skyrmions in monolayer $Fe_5GeTe_2$. *Physical Review B*, Vol. 109, Issue 22, pp. L220404. Accessed at https://journals.aps.org/prb/abstract/10.1103/PhysRevB.109.L220404.

**Paper VII:** L. Kollwitz, M. A. Goerzen, B. Beyer, **H. Schrautzer**, S. Heinze, 2026, Entropy-driven phase transition in a non-collinear antiferromagnet due to higher-order exchange interactions. *npj Spintronics*, Vol. 4, Article number: 2. Accessed at https://www.nature.com/articles/s44306-025-00121-z.

**Paper VIII:** M. A. Goerzen, T. Drevelow, S. Haldar, **H. Schrautzer**, S. Heinze, D. Li, 2025, Lifetime of bimerons and antibimerons in two-dimensional magnets. *Physical Review X (submitted)*. Accessed at https://arxiv.org/abs/2509.09344.

**Paper IX:** S. von Malottki, M. A. Goerzen, **H. Schrautzer**, P. F. Bessarab, S. Heinze, 2025, Eigenmode following for direct entropy calculation and characterization of magnetic systems. *npj Computational Materials (submitted)*. Accessed at https://arxiv.org/abs/2503.12109.

**Paper X:** M. A. Goerzen, T. Drevelow, **H. Schrautzer**, S. Haldar, S. Heinze, D. Li, 2025, Emergence of coexisting topological spin textures in an all-magnetic van der Waals heterostructure. *Physical Review B (submitted)*. Accessed at https://arxiv.org/abs/2408.15974

# Abbreviations and Notations

In this thesis, vector quantities in $\mathbb{R}^2$ or $\mathbb{R}^3$ are denoted as $\vec{x}$, while in $\mathbb{R}^{2N}$ or $\mathbb{R}^{3N}$ they are written as $\boldsymbol{x} = (\vec{x}_1, \ldots, \vec{x}_N)^T$. An overview of the abbreviations used in this thesis can be found below.

**SP** *saddle point*

**SPSF** *saddle point search framework*

**GMMF** *geodesic minimum mode following*

**S-GMMF** *subsystem-based GMMF*

**GNEB** *geodesic nudged elastic band*

**ci-GNEB** *climbing image-GNEB*

**MEP** *minimum energy path*

**HTST** *harmonic transition state theory*

**RQM** *Rayleigh quotient minimization*

**LLG** *Landau-Lifshitz-Gilbert*

**L-BFGS** *limited-memory Broyden-Fletcher-Goldfarb-Shanno*

**DMI** *Dzyaloshinskii-Moriya interaction*

**HOI** *higher-order exchange interactions*

**MAE** *magnetocrystalline anisotropy energy*

**RKKY** *Ruderman–Kittel–Kasuya–Yosida*

**FM** *ferromagnetic*

# Acknowledgements

The past five years during which this thesis was written have been both short and long at the same time – years filled with new experiences and challenges, both professional and personal. I would therefore like to take this opportunity to express my gratitude to all those who accompanied and supported me along the way.

First and foremost, I would like to thank my academic advisor, Pavel Bessarab, for welcoming me into his research group, for granting me access to his expertise, and for the many insightful and respectful discussions we shared. Whether the topic concerned scientific problems, the development of my own ideas, or personal challenges, I could always rely on his openness and support, and I learned a great deal from him. I am also grateful for the opportunities to attend conferences and training events. I would like to express my sincere thanks to Stefan Heinze for always welcoming me in his group at the University of Kiel, for his many years of kind support, and for his scientific advice. During the development of the methodology presented in this thesis, I benefited greatly from the invaluable expertise of Hannes Jónsson. I owe him special thanks – not only for his generous guidance, but also for the warm welcome I received when joining his group in Iceland. My heartfelt thanks also go to Snorri Ingvarsson for his continuous support in administrative matters and for always having a friendly word for me. To my entire doctoral committee – Pavel, Stefan, Hannes, and Snorri – Thank you! I could not have wished for better supervision. I also thank my opponents Prof. Vitaliy Lomakin and Dr. Denys Makarov for the thorough evaluation of my thesis. This thesis was funded by the Icelandic Research Fund (IRF), grant number 239435, for which I am very grateful.

I am also grateful to all my colleagues in Reykjavík, Kiel, and Kalmar for excellent collaboration, mutual support, humor, and simply for making work an enjoyable place to be. You are fantastic: Felix, Moritz G., Moritz S., Mohammad, Tim, Grzegorz, Ólafur, Ivan, Cecilia, Stephan, Vladyslav, Bjarne, Leo, Soum, Rohit, André, and everyone else who shared this journey with me.

I would like to thank my family – Anke, Joachim, Torben, and Merve – for their constant support in my life. You are the best! The same is true for all my friends, including, of course, the Schwammtisch. Without my family and friends, this thesis might never have been completed, and it certainly would not have turned out the way it has. Thank you all! And even though I mention her last, my heartfelt gratitude goes to Doro. Thank you for standing by my side and supporting me.

# 1 Introduction

## 1.1 Motivation and state-of-the-art

Keeping pace with the rapidly growing volume of data, especially since the advent of machine learning, poses a major challenge to modern society [1]. The concept of spintronics [2, 3], which exploits both charge and spin degrees of freedom of electrons, has attracted great attention as a way to overcome the limitations of conventional microprocessors – such as restricted miniaturization and performance bottlenecks caused by heat dissipation and quantum effects [4, 5].

Magnetic skyrmions – topologically nontrivial magnetic textures – have been observed in a broad range of materials, including non-centrosymmetric B20 crystals [6, 7], ultrathin transition-metal films [8, 9, 10] and two-dimensional van der Waals magnets [11, 12, 13]. An exemplary skyrmion in shown in Fig. 1.1. Due to their intriguing physical properties, e.g. meta-stability in a ferromagnetic background or movement via spin-polarized currents [14], their discovery has led to numerous potential applications, including skyrmion-based memory devices [15], transistors [16, 17], diodes [18, 19] and logic gates [20, 21, 22, 23, 24, 25]. Skyrmions have also been proposed for emerging computing paradigms such as neuromorphic [26, 27] and reservoir computing [28], and even as qubits for quantum computing [29, 30, 31].

Beyond skyrmions – a prominent example of topological magnetism – various other localized magnetic textures in two and three dimensions have been discovered in recent years [32]. Systems capable of simultaneously hosting multiple such textures [33, 34, 35, 36, 37] are particularly interesting, as they can exhibit rich phenomena [37] driven by transformations between different magnetic states.

However, the practical use of systems with localized magnetic textures critically depends on the controlled creation and annihilation of these particle-like states. Therefore, a detailed understanding of creation and annihilation mechanisms and thermally activated transitions is necessary. A central challenge is to quantitatively estimate transition rates and identify the mechanisms governing transformations between different metastable magnetic states. The stability of a given magnetic texture depends on the competition between magnetic interactions present in the system, such as the Heisenberg exchange interaction and the *Dzyaloshinskii-Moriya interaction* (DMI) [38, 39], which arises from spin–orbit coupling in systems lacking inversion symmetry, such as surfaces [40]. Furthermore, frustrated exchange interactions – stemming from competing ferromagnetic and antiferromagnetic couplings beyond nearest neighbors – can stabilize isolated skyrmions [41, 42, 43, 44, 45] and antiskyrmions [46] even in the absence of DMI. Recently, *higher-order exchange interactions* (HOI) have gained attention as an additional mechanism influencing skyrmion stability [8, 47, 48, 49].

The transition rates can be computed using *harmonic transition state theory* (HTST) [50,

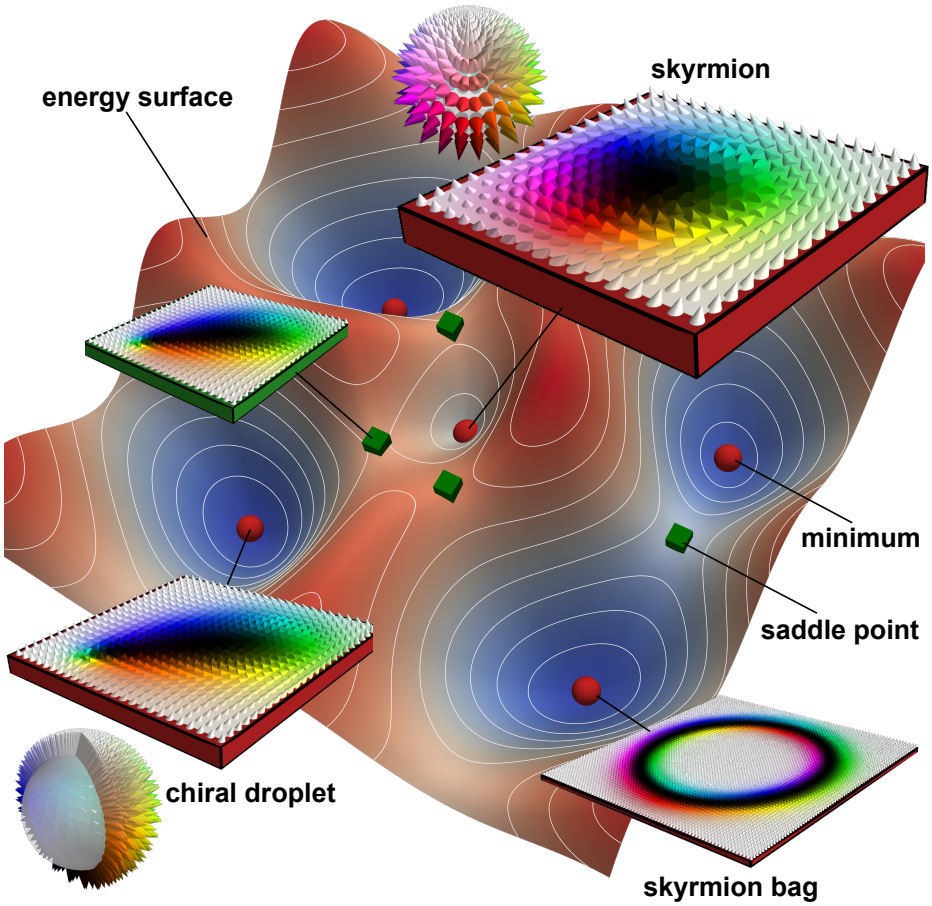


**Figure 1.1.** A sketch of the energy surface of a magnetic system. The minima (red dots) are associated with magnetic textures such as the skyrmion, the chiral droplet, and the skyrmion bag. The SPs (green dots) correspond to transitions between the minima. The topology of a magnetic texture can be visualized by a projection of all magnetic moments onto a sphere, as shown for the Sk and chiral droplet. For the topologically-nontrivial skyrmion, the moments cover the whole sphere, while the topologically-trivial droplet corresponds only to half coverage.

51] or related rate theories such as Kramers/Langer theory [52, 53]. In these frameworks, the stability of magnetic textures is intrinsically linked to the structure of the system's multidimensional energy surface, where each magnetic configuration has a specific energy, defined by the magnetic interactions (see Fig. 1.1). Local minima of this energy surface correspond to metastable states, which are connected via SPs representing transition states.

The transition rate at temperature $T$ follows an Arrhenius law:

$$\nu = \nu_0 \mathrm{e}^{-\beta \Delta E} \ ,$$

where $\beta^{-1} = k_\mathrm{B} T$ with the Boltzmann constant $k_\mathrm{B}$, $\Delta E$ is the energy barrier (energy difference between the SP and the minimum) and $\nu_0$ is the pre-exponential factor containing the dynamic and entropic contributions. Both $\nu_0$ and $\Delta E$ depend heavily on an accurate calculation of the corresponding SP. Consequently, the identification of all SPs neighboring a minimum is crucial for the prediction of the lifetime of a magnetic texture.

The large number of SPs on the high-dimensional energy surface of realistic systems makes their systematic identification challenging. SP search methods are typically divided into double-ended and single-ended approaches. In double-ended problems, both the initial and final states are known, and the SP can be located by identifying the highest-energy point along the MEP connecting the two states [54]. These approaches have proven powerful [55, 10, 56] but they rely on prior knowledge of both metastable states, limiting their ability to reveal unexpected transition pathways or new metastable configurations. In systems hosting multiple textures, this restriction may cause relevant transitions to be overlooked, since the number of metastable states is in general unknown.

To address this, single-ended SP search methods have been developed. These algorithms start from a single known minimum and identify nearby SPs and thereby also potentially unknown adjacent energy minima. Recent advances have applied such approaches to magnetic systems [57, 58, 59, 60]. However, since these methods cannot start directly from the minimum, they rely on carefully prepared initial configurations, and it remains limited understanding of which initialization strategy is most efficient.

Solving this initialization problem is crucial for enabling more complex algorithms that repeatedly perform SP searches. One long-term goal is to perform global searches for (meta)stable states by recursively traversing the energy surface from one minimum to another via SPs. Combined with on-the-fly rate calculations from HTST, this forms the basis of adaptive kinetic Monte Carlo simulations [61, 62], which enable the study of long-timescale dynamics of a magnetic system. SP search methods are also useful in broader contexts, such as global optimization [63], path optimization [64], tunneling calculations in instanton theory [65, 66], and even in radio wave propagation problems [67].

Within this broader context, the motivation for this work arises from the importance of studying kinetic processes and stability mechanisms in realistic magnetic materials hosting multiple localized magnetic textures. To investigate their mutual transformations an efficient and systematic computational framework identifying SPs on the systems energy surface is needed.

## 1.2 Significance, scientific novelty, and general outline of the thesis

This thesis presents a single-ended *saddle point search framework* (SPSF) to globally explore the energy surface of systems hosting localized magnetic textures, identifying metastable states and calculating their transition rates. The developed methodology is applied to quantitatively estimate the lifetime of skyrmions and antiskyrmions in the prototypical materials fcc-Pd/Fe/Ir(111) and fcc-Rh/Fe/Ir(111) including the effect of *higher-order exchange interactions* (HOI) for the first time. Furthermore, the framework is used to study two- and three-dimensional chiral magnets that can host numerous different localized magnetic textures [36, 68]. While these metastable states have been categorized [36] the systematics of their mutual transformations remain largely unknown. Using the developments of this thesis, SPs on the energy surface of chiral magnets are systematically identified.

Fig. 1.2 illustrates a schematic two-dimensional energy surface containing multiple minima and SPs. Traditionally, the *geodesic nudged elastic band* (GNEB) method [54] has been the main tool for locating SPs by calculating the *minimum energy path* (MEP) between two metastable states. The method connects the two minima via a chain of intermediate configurations, so called images, which relax iteratively toward the MEP (see Fig. 1.2b). The SP is then identified as the highest-energy point along this path. The GNEB method has been successfully applied to various double-ended problems [43, 69, 45, 55, 56, 46], such as skyrmion and antiskyrmion collapse into the *ferromagnetic* (FM) state. In this work we applied the GNEB method to calculate the MEP associated to the collapse of metastable skyrmions in magnetic multilayers and studied the effect of the coupling between the layers on their stability.

However, in systems featuring multiple unknown metastable states and transition pathways, the final state of a transition is often not known a priori, limiting the predictive power of GNEB. For example, a skyrmion in a magnetic multilayer can decay into the FM state via sequential collapse of the skyrmions in the individual layers representing various transition mechanisms. Capturing all the associated SPs using the GNEB method becomes significantly more difficult for a growing number of layers. To address such problems, the present work develops a single-ended SP search method that can start from a known minimum and identify connected SPs without prior knowledge of the final states. Specifically, this thesis presents an efficient computational single-ended SPSF for localized magnetic textures, comprising four stages: preprocessing stage, escape stage, convergence stage and postprocessing stage. The SPSF does not require prior knowledge of neighboring minima and is therefore ideally suited to explore transformations in systems with unknown metastable states or unexpected transitions.

A first-order SP is a stationary point where the Hessian of the energy of the system has exactly one negative eigenvalue, indicating one direction along which the energy decreases referred to as unstable mode. In the present work the *geodesic minimum mode following* (GMMF) method was developed exploiting this property by iteratively displacing the magnetic configuration to maximize energy along one direction while minimizing it in all others. The process represents the convergence stage of the SPSF

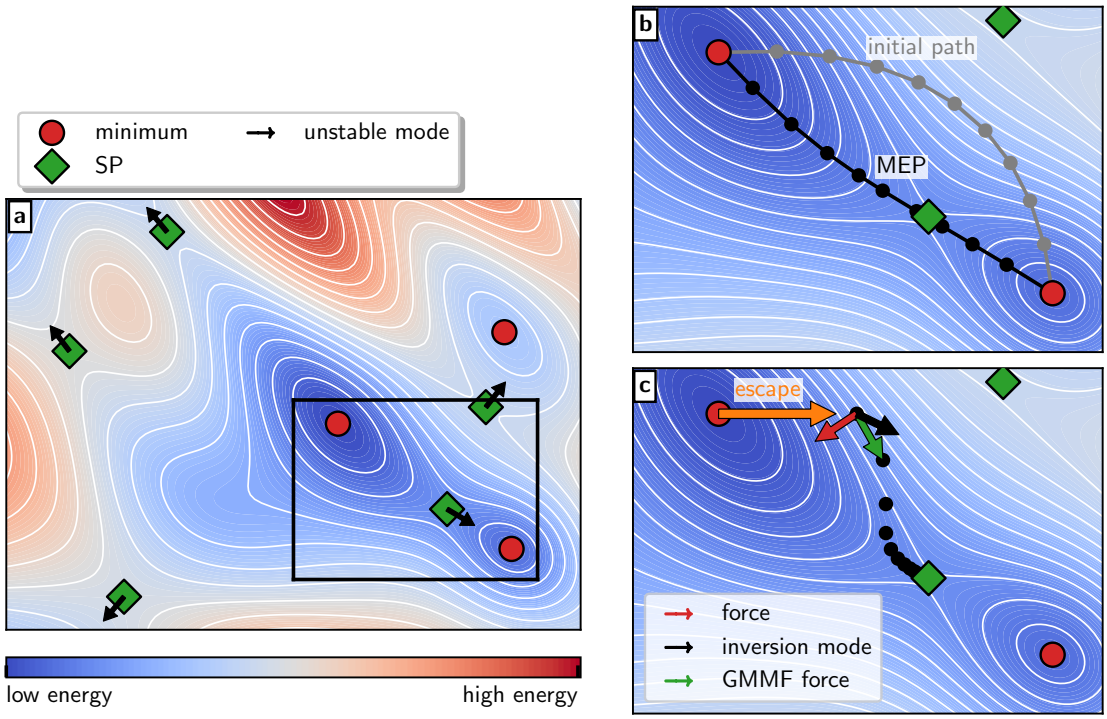


**Figure 1.2.** **a**: Sketch of a two-dimensional energy surface with several minima (red) and SPs (green). The black box marks the part of the surface shown in **b** and **c**. App. A. presents how this and similar two-dimensional surfaces have been generated to visualize the concepts of the developed methodology. **b**: Sketch of the double-ended GNEB method. Two minima are connected by an initial path (gray) which is a series of configurations called images (circles). The GNEB method optimizes this path iteratively converging onto the MEP (black). **c**: Sketch of the single-ended GMMF method. After initial displacement process called escape (orange), the GMMF method iteratively displaces along the modified GMMF force (green) obtained from the force (red) and the minimum mode (black).

and is guided by the GMMF force [57, 58, 59][Paper II]:

$$\boldsymbol{f} = -\boldsymbol{g} + 2(\boldsymbol{g} \cdot \boldsymbol{q})\boldsymbol{q} \ , \tag{1}$$

where $\boldsymbol{g}$ is the energy gradient and $\boldsymbol{q}$ is the inversion mode. Effectively, the component of the conventional force $(-\boldsymbol{g})$ parallel to the inversion mode $\boldsymbol{q}$ is reversed, producing an effective energy climb along $\boldsymbol{q}$, which is ultimately chosen as the eigenvector of the lowest Hessian eigenvalue. Fig. 1.2c illustrates how the GMMF algorithm ascends the energy surface from a point near a minimum to a first-order SP.

A major computational bottleneck in GMMF lies in determining the lowest eigenmodes of the Hessian, which traditionally involves explicit and costly matrix evaluations. To overcome this, this thesis introduces the *Rayleigh quotient minimization* (RQM) method, which efficiently determines minimal Hessian modes without constructing the full matrix, enabling SP searches in large three-dimensional systems, even for long-range dipole–dipole interactions.

A second challenge in single-ended SP searches is the initialization of the algorithm. The GMMF cannot start directly at a minimum, since the surrounding convex region provides little to no guidance toward promising ascending directions on the energy surface. Thus, a procedure called escape from the convex region is needed to generate starting points likely to lead to nearby SPs. The efficiency and completeness of SP discovery depend critically on this escape strategy [70, 71]. Prior approaches often used random displacements or followed low-energy modes of the system [57, 58]. Most likely there is no universal optimal escape technique but for magnetic systems hosting localized magnetic textures this thesis introduces a systematic, symmetry-based escape method. Since many magnetic textures exhibit characteristic symmetries (e.g., axial symmetry of skyrmions), their transformation often involves local symmetry breaking (see SP configuration in Fig. 1.1), suggesting that targeted local perturbations are ideal for initiating searches for relevant SPs.

In summary, this thesis presents the development of the SPSF structured into the following stages:

1. *preprocessing stage*: Determine the symmetry elements and the fundamental domain – a region containing all unique physical information without repetition – of the texture corresponding to the initial energy minimum.

2. *escape stage*: Sample configurations outside the convex region of the minimum by applying deformations in spatially confined subsystems of the magnetic texture centered at various points within the fundamental domain.

3. *convergence stage*: Perform SP searches initialized with the configurations obtained by the escape stage using the efficient GMMF method.

4. *postprocessing stage*: Group identified SPs, verify their connectivity to the initial minimum, and determine adjacent minima.

The developed methodology is applied to address two open questions in the field of topological magnetism:

- HOI, which couple more than two magnetic moments, can play a significant role in both insulating [72, 73] and itinerant electron magnets [74, 75, 76], influence

the magnetic ground state [75] and stabilize complex magnetic textures as observed experimentally [8, 77, 78, 79, 80, 81]. Although HOI have been shown to affect skyrmion stability [8, 47, 48, 49] – e.g., by enhancing energy barriers – no quantitative estimates of skyrmion or antiskyrmion lifetimes in systems including HOI have been reported. In this work, HTST is used to determine entropic, dynamic, and energy barrier contributions to the lifetimes of skyrmions and antiskyrmions in the prototypical materials fcc-Pd/Fe/Ir(111) and fcc-Rh/Fe/Ir(111) including HOI. This is particularly relevant given the current interest in defect-free 2D van der Waals magnets, which often lack DMI due to inversion symmetry but may exhibit strong HOI.

- Chiral magnets, representing a wide range of materials [48, 82, 83, 84, 85, 86, 87], can host numerous metastable, topologically distinct textures [36]. From a topological perspective localized magnetic textures can be sorted into classes, characterized by the topological invariant [88]:

$$Q = \frac{1}{4\pi} \int \left[\vec{m}(\vec{r}) \cdot (\partial_x \vec{m}(\vec{r}) \times \partial_y \vec{m}(\vec{r})\right] \mathrm{d}r^2 \ ,$$

  where $\vec{m}(\vec{r})$ denotes the magnetization. A systematic categorization of metastable configurations in chiral magnets showed that localized textures are composed of combinations of just three fundamental features: closed contours which form skyrmion bags [89, 35, 90, 91], chiral kinks [36] and tails [68]. However, the mutual transformations between them are less understood despite their relevance for technological applications. Mathematically it is always possible to continuously transform the magnetization between two textures of the same class, which is called a homotopy [37] – in fact there is an infinite number of such homotopies. A continuous transformation between magnetic textures with a different topological charge $Q$ inevitably leads to the formation of discontinuities of the magnetization [35]. It is an open question if always at least one of the homotopies corresponds to an MEP passing through a first order SP. The SPSF is used here to explore the energy surfaces of chiral magnets and to classify transformations between metastable states by systematically identifying the corresponding SPs.

This thesis is structured as follows: The remainder of Chap. 1 reviews the atomistic and continuum models of magnetism, the characterization of topological textures, and the principles of HTST and existing methods to identify first-order SPs for magnetic systems. Finally, it briefly presents the application of the GNEB method to multilayer skyrmions (Paper I) and thereby motivates the development of a systematic single-ended SP search method. Chap. 2 presents the developments of the SPSF (Paper IV) and the GMMF method (Paper II), while Chap. 3 summarizes the applications featuring two- and three-dimensional chiral magnets (Paper II, Paper IV), ultrathin transition-metal films with HOI (Paper III) and magnetic multilayers (Paper I). The conclusion highlights the main findings and outlines future research directions.

## 1.3 Modeling thermally activated transitions in magnetic systems

### 1.3.1 Energy model

The magnetic systems investigated in this work include two- and three-dimensional isotropic chiral magnets (Paper II and IV) as well as ultrathin transition-metal films (Paper I and III). All methodological developments, implementations, and applications in this thesis use an atomistic spin model. A continuous model is employed where analytical expressions are required. Both descriptions are briefly introduced below.

#### Atomistic spin model

An atomistic spin model is employed, in which each atomic site $\vec{r}_i$ is associated with a total magnetic moment represented by a classical vector $\vec{M}_i$. The magnitude of the magnetic moment is typically either assumed to be constant – independent of its orientation – or treated as a fast degree of freedom within the adiabatic approximation. In the latter case, the magnitude $\mu_i = |\vec{M}_i|$, measured in units of the Bohr magneton $\mu_B$, is determined for fixed orientation of the magnetic moments, regarded as a slow variable [92].

The energy $E(\boldsymbol{m})$ of a magnetic configuration $\boldsymbol{m} = (\vec{m}_1, \ldots, \vec{m}_N)$ with $N$ magnetic moments is given by the extended Heisenberg Hamiltonian:

$$E = E_{\text{ex}} + E_{\text{4-spin}} + E_{\text{DMI}} + E_{\text{MAE}} + E_{\text{mag}} + E_{\text{Zee}} \ , \tag{2}$$

where, in the order listed, the contributions correspond to the pairwise exchange and *higher-order exchange interactions* (HOI) (including up to four magnetic moment couplings), the *Dzyaloshinskii-Moriya interaction* (DMI) energy, the *magnetocrystalline anisotropy energy* (MAE), the classical dipole–dipole interaction energy, and the Zeeman energy due to an external magnetic field. The microscopic origin and the respective explicit expressions are given below.

The origin of **Exchange interactions** lies in the quantum mechanical nature of electrons – specifically, the combined effect of the Coulomb interaction and the Pauli exclusion principle for indistinguishable fermions [93]. For a wide range of magnetic materials a classical treatment is justified [94, 95], where the spin operators are replaced by normalized vectors $\vec{m}_i = \langle \hat{\vec{S}}_i \rangle / S_i$, allowing the exchange energy to be described by a classical vector field within the atomistic spin model.

In reality, the short-ranged direct exchange mechanism, as originally formulated by Heisenberg [96], is often not the physical origin of collective magnetic order as the distance between the magnetic ions is too large to produce significant orbital overlap [93]. Instead, in metals the exchange interaction can be mediated indirectly through itinerant electrons – giving rise to the *Ruderman–Kittel–Kasuya–Yosida* (RKKY) interaction [97, 98, 99]. The RKKY coupling oscillates in sign and decays with interatomic distance, leading to competing ferromagnetic and antiferromagnetic alignments. In insulators non-magnetic ions like oxygen can mediate a coupling called superexchange [100] between the magnetic ions.

Despite their different microscopic origins, these mechanism yield an effective Hamiltonian in the Heisenberg form

$$E_{\text{ex}} = -\frac{1}{2}\sum_{n}\sum_{\langle i,j\rangle_n} J_n \vec{m}_i \cdot \vec{m}_j \ , \tag{3}$$

where the outer sum runs over atomic neighbor shells $n = 1, 2, \ldots$ and the inner sum includes all sites $i, j$ separated by the distance corresponding to the $n$-th neighbor shell. Importantly, competing ferromagnetic ($J_n > 0$) and antiferromagnetic ($J_n < 0$) exchange interactions from different shells yield frustration effects favoring non-collinear magnetic textures such as skyrmions [41, 43, 10].

The Heisenberg model [Eq. (3)] is best realized in magnetic insulators and magnetic metals, where the magnetism arises due to localized moments. However, there are materials where **Higher-order exchange interactions** (HOI), coupling more than two magnetic moments, are important to describe the magnetic ground-state of the system [75].

In order to describe such multi-spin interaction, a Hubbard model is appropriate accounting for electrons hopping between atomic sites with on-site Coulomb repulsion $U$. In the limit of large $U/t$, where $t$ is the hopping amplitude, a second-order perturbative expansion in $U/t$ yields an effective Heisenberg coupling [101, 102]. Going beyond, a fourth order expansion in the hopping interaction strength of a multi-band Hubbard model yields correction terms to the effective Heisenberg model capturing HOI [103]

$$E_{\text{4-spin}} = -\sum_{ijkl} C_{ijkl}(\vec{m}_i \cdot \vec{m}_j)(\vec{m}_k \cdot \vec{m}_l) \ , \tag{4}$$

coupling up to four different magnetic moments $\vec{m}_i$ (4-spin) of the system. However, if $i = k$ and $j = l$, effectively only two lattice sites (2-site) are contributing to the so called biquadratic or 4-spin-2-site interaction. Similar 4-spin-3-site and 4-spin-4-site terms have been discussed [103]. These distinguished terms – restricted to the shortest distances between magnetic moments – will be referred to as the biquadratic energy [100, 104, 105]

$$E_{\text{biquad}} = -\sum_{ij} B_1(\vec{m}_i \cdot \vec{m}_j)^2 \ , \tag{5}$$

with interaction parameter $B_1$, the 3-site energy [103]

$$E_{\text{3-site}} = -2\sum_{ijk} Y_1(\vec{m}_i \cdot \vec{m}_j)(\vec{m}_i \cdot \vec{m}_k) \ , \tag{6}$$

with parameter $Y_1$ and the 4-site energy [103, 47, 106]

$$E_{\text{4-site}} = -\sum_{ijkl} K_1\big[(\vec{m}_i \cdot \vec{m}_j)(\vec{m}_k \cdot \vec{m}_l) + (\vec{m}_i \cdot \vec{m}_l)(\vec{m}_j \cdot \vec{m}_k) - (\vec{m}_i \cdot \vec{m}_k)(\vec{m}_j \cdot \vec{m}_l)\big] \ , \tag{7}$$

with parameter $K_1$.

In systems without inversion symmetry, spin-orbit coupling gives rise to an antisymmetric exchange term known as the **Dzyaloshinskii-Moriya interaction** (DMI) [38,

39]. The DMI favors a fixed sense of rotation between neighboring magnetic moments and thereby introduces chirality into the magnetic structure. In its general form, the DMI contribution to the atomistic Hamiltonian in Eq. (2) can be written as

$$E_{\mathrm{DMI}} = -\frac{1}{2}\sum_{n}\sum_{\langle i,j\rangle_n} D_n \vec{d}_{ij}\cdot(\vec{m}_i \times \vec{m}_j) \ , \tag{8}$$

where $D_n$ is the DMI parameter per pair of magnetic moments for the $n$-th neighbor shell depending on the strength of the spin-orbit coupling and the unit vector $\vec{d}_{ij}$ is determined by the symmetry of the crystal environment:

$$\vec{d}_{ij} = R_\beta \frac{\vec{r}_{ij}}{|\vec{r}_{ij}|} \ , \tag{9}$$

where the matrix $R_\beta \in \mathbb{R}^{3\times3}$ describes the right handed rotation by an angle $\beta$ around the $z$-axis. In bulk non-centrosymmetric materials with B20 symmetry, the lack of inversion symmetry leads to Bloch-type DMI [7, 82, 84] with $\vec{d}_{ij}$ aligned parallel to the connection line $\vec{r}_{ij} = \vec{r}_j - \vec{r}_i$ of the interacting sites, which corresponds to $\beta = 0$. On the other hand interfacial DMI can arise if the inversion symmetry is broken due to an interface of the magnetic film with a substrate [107]. An indirect exchange mechanism between two magnetic moments mediated by a nonmagnetic atom with large spin orbit can be derived with an additional term in the RKKY interaction [108]. This leads to $\beta = \pi/2$ and consequently $\vec{d}_{ij}$ is oriented perpendicular to $\vec{r}_{ij} = \vec{r}_j - \vec{r}_i$ within the plane of the magnetic film and produces Néel-type chiral modulations [9, 85, 109].

The **magnetocrystalline anisotropy energy** (MAE) originates from the coupling between the electronic spin and the crystal lattice via spin–orbit interaction. It breaks the rotational symmetry of the magnetic Hamiltonian and defines energetically preferred orientations (easy axes) of the magnetic moments with respect to the crystallographic directions. The magnitude and sign of the MAE determine whether the magnetization favors alignment along a particular axis (uniaxial anisotropy) or within a specific plane (planar anisotropy). For a uniaxial system, the anisotropy energy can be expressed as

$$E_{\mathrm{MAE}} = -K_{\mathrm{u}} \sum_i (\vec{m}_i \cdot \vec{n})^2 \tag{10}$$

where $K$ is the anisotropy constant and $\vec{n}$ denotes the unit vector along the easy axis. A positive $K$ corresponds to an out-of-plane easy axis (perpendicular anisotropy), whereas negative $K$ indicates that the magnetization prefers to lie within the plane. Microscopically, the MAE results from second-order perturbations of the spin–orbit coupling [110] and can be evaluated from first principles using, for instance, the magnetic force theorem to compute total energy differences between constrained magnetization directions [111].

The classical **dipole-dipole interaction** can be an important energy correction term leading to anisotropy effects. In ultrathin transition-metal films this can often effectively be included in a thereby reduced uniaxial anisotropy constant in Eq. (10) [112, 113]. However, in three-dimensional systems magnetostatic interactions become increasingly important (cf. Sec. 3.2). Their explicit contribution to Eq. (2) reads

$$E_{\mathrm{mag}} = -\frac{\mu_0 \mu^2}{4\pi} \sum_{i<j} \frac{3(\vec{m}_i \cdot \vec{r}_{ij})(\vec{m}_j \cdot \vec{r}_{ij})}{r_{ij}^5} - \frac{\vec{m}_i \cdot \vec{m}_j}{r_{ij}^3} \ , \tag{11}$$

where $\mu_0$ is the vacuum permeability and $\vec{r}_{ij}$ connects the sites $i$ and $j$. For the materials investigated in this work all the atoms carry the same magnetic moment such that the index of $\mu = \mu_i$ can be suppressed. Note, evaluating Eq. (11) is of complexity $\mathcal{O}(N^2)$ due to the double sum over all magnetic moments and thus not feasible for large systems. Therefore, Eq. (11) is treated as a convolution and expressed as a product of Fourier transforms, which can be computed via a fast Fourier transform algorithm [114, 115]. This leaves computational complexity of $\mathcal{O}(N \log N)$.

The **Zeeman interaction** describes the coupling of the magnetic moments to an external magnetic field $\vec{B}$ and the corresponding energy reads:

$$E_{\text{Zee}} = -\mu \sum_{i=1}^{N} \vec{B} \cdot \vec{m}_i \ . \tag{12}$$

An applied field is often used as control parameter to manipulate magnetic textures [56], affect dynamic magnetic processes [116] or tune the energy surface [9].

### Derivatives of the energy in the lattice model

The algorithms developed in the context of this work require calculating the gradient and the Hessian of the energy. The derivative of Eq. (2) with respect to the cartesian components of the magnetic moment $\vec{m}_i$ is given by

$$\begin{aligned} \vec{\nabla}_i^T E = &- \sum_n \sum_{\langle k,j \rangle_n} \delta_{ki} J_n \vec{m}_j - 4 \sum_{jkl} C_{ijkl} \left( \vec{m}_k \cdot \vec{m}_l \right) \vec{m}_j \\ &- \sum_n \sum_{\langle k,j \rangle_n} \delta_{ki} D_n (\vec{m}_j \times \vec{d}_{kj}) - K_{\text{u}} \sum_{i=1}^{N} 2(\vec{m}_i \cdot \vec{n}) \vec{n} \\ &- \frac{\mu_0 \mu}{4\pi} \sum_{\substack{j=1 \\ j \neq i}}^{N} \left( \frac{3(\vec{m}_j \cdot \vec{r}_{ij}) \vec{r}_{ij}}{r_{ij}^5} - \frac{\vec{m}_j}{r_{ij}^3} \right) - \mu \vec{B} \ . \end{aligned} \tag{13}$$

where $\vec{\nabla}_i = (\partial_{m_i^x}, \partial_{m_i^y}, \partial_{m_i^z})$. Thus, the derivative of Eq. (2) with respect to all magnetic moments reads

$$\boldsymbol{\nabla} E = (\vec{\nabla}_1 E, \ldots, \vec{\nabla}_N E)^T \ , \tag{14}$$

with $\boldsymbol{\nabla} E \in \mathbb{R}^{3N}$. The 3 by 3 blocks of the matrix of second derivatives with respect to the magnetic moments $\vec{m}_i$ and $\vec{m}_j$ are calculated via

$$(\boldsymbol{\nabla}\boldsymbol{\nabla}^T E)_{ij} = \begin{pmatrix} \frac{\partial^2 E}{\partial m_i^x \partial m_j^x} & \frac{\partial^2 E}{\partial m_i^y \partial m_j^x} & \frac{\partial^2 E}{\partial m_i^z \partial m_j^x} \\ \frac{\partial^2 E}{\partial m_i^x \partial m_j^y} & \frac{\partial^2 E}{\partial m_i^y \partial m_j^y} & \frac{\partial^2 E}{\partial m_i^z \partial m_j^y} \\ \frac{\partial^2 E}{\partial m_i^x \partial m_j^z} & \frac{\partial^2 E}{\partial m_i^y \partial m_j^z} & \frac{\partial^2 E}{\partial m_i^z \partial m_j^z} \end{pmatrix} \ , \tag{15}$$

with $\boldsymbol{\nabla}\boldsymbol{\nabla}^T E \in \mathbb{R}^{3N \times 3N}$ and explicitly the derivative of Eq. (13) with respect to $\vec{m}_j$ reads [117]:

$$\begin{aligned} (\boldsymbol{\nabla}\boldsymbol{\nabla}^T E)_{ij} = &- J_{ij} \mathbb{1} + \vec{\nabla}_i \vec{\nabla}_j^T E_{\text{4-spin}} \\ &- D_{ij} \sum_{k=1}^{3} (\vec{d}_{ij} \times \hat{e}_k) \hat{e}_k^T - K_{\text{u}} \delta_{ij} \vec{n} \vec{n}^T \\ &+ \vec{\nabla}_i \vec{\nabla}_j^T E_{\text{mag}} \ , \end{aligned} \tag{16}$$

where $\mathbb{1} \in \mathbb{R}^{3\times3}$ and $\hat{e}_k \in \mathbb{R}^3$ denote the unit matrix and the $k$-th unit vector of $\mathbb{R}^3$. The interaction parameters $J_{ij}$ and $D_{ij}$ correspond to $J_n$ and $D_n$ for the sites $i$ and $j$ being in $n$-th nearest neighbor distance to each other. The second derivative of the magnetostatic interaction energy will be addressed via finite difference calculations of the respective gradients in this work and is part of Paper II (see Sec. 2.3.2). The derivation of the second-order derivatives of the HOI energy is part of Paper III and is presented in Sec. 3.3. Note to obtain the true physical Hessian and energy gradient from these derivatives, the curvature of the configuration space has to be considered (Sec. 1.3.2).

#### Continuous-theory model of the magnetization

The discrete nature of Eq. (2) limits the possibility to obtain analytical results. Most of the theory developed for chiral magnets is based on continuous-theory for the magnetization $\vec{m} = \vec{m}(\vec{r})$ with $\vec{m}(\vec{r}_i) = \vec{m}_i$ and $|\vec{m}(\vec{r})| = 1$. The corresponding energy functional for a two-dimensional system is then:

$$\mathcal{E} = \int \left[\frac{\mathcal{J}}{2}|\vec{\nabla}\vec{m}|^2 + \mathcal{D}\left(R_\beta\vec{m}\cdot\vec{\nabla}\times R_\beta\vec{m}\right) - M_S(\vec{B}\cdot\vec{m} - B)\right]\mathrm{d}r^2 + \mathcal{E}^{\mathrm{FM}}\,, \tag{17}$$

where $M_S$ is the saturation magnetization and $\mathcal{J}$ and $\mathcal{D}$ are the continuous-theory exchange and DMI parameter, respectively. The energy of the FM state is denoted by $\mathcal{E}^{\mathrm{FM}}$.

The continuous-theory Hamiltonian can be derived starting from the lattice Hamiltonian [cf. Eq. (2)] using a series expansion [118] and the parameters $J_n$ and $D_n$ can be defined such that both descriptions are equivalent in the continuum limit, which is shown in App. 4. To improve the correspondence between both descriptions below the continuum limit, up to the fourth-order terms are considered in the series expansion of Eq. (2) [119, 120]. All parameters can be expressed in units of the continuous-theory exchange parameter $\mathcal{J}$, of the equilibrium period of chiral modulations at the ground state $L_D = 2\pi\mathcal{J}/\mathcal{D}$ and of the saturation field $B_D = \mathcal{D}^2/(M_S\mathcal{J})$, where $\mathcal{D}$ is the continuous-theory DMI parameter. The magnetic field is then given in units of the saturation field $B = hB_D$.

### 1.3.2 Configuration space of magnetic states

The configuration space of a system comprising $N$ magnetic moments is given by the direct product of $N$ two-dimensional spheres, $S^2$, corresponding to the orientation $\vec{m}_i$ of each magnetic moment:

$$\mathcal{R} = \bigotimes_N S^2 \subset \mathbb{R}^{3N}, \tag{18}$$

resulting in a total of $2N$ degrees of freedom (see Fig. 1.3). Hence, it can be seen as a $2N$-dimensional Riemannian submanifold $\mathcal{R}$ embedded in $\mathbb{R}^{3N}$. The tangent space $\mathcal{T}_{\boldsymbol{m}}$ for a given magnetic configuration $\boldsymbol{m} = (\vec{m}_1, \ldots, \vec{m}_N)$ is, intuitively speaking, represented by $N$ two-dimensional planes tangent to the individual magnetic moments [121] (see Fig. 1.3b) A local tangent space basis can be constructed using $\vec{\xi}_i = \vec{k}_i/|\vec{k}_i|$ and $\vec{\eta}_i =$

$\vec{\xi} \times \vec{m}_i$ as basis vectors for the $i$th magnetic moment $\vec{m}_i$ with:

$$\vec{k}_i = \begin{cases} (1-(m_i^x)^2, -m_i^y m_i^x, -m_i^z m_i^x)^T, & |m_i^z| \geq 0.5 \\ (-m_i^z m_i^x, -m_i^z m_i^y, 1-(m_i^z)^2)^T, & |m_i^z| < 0.5 \ . \end{cases} \tag{19}$$

Using these basis vectors a projection matrix $U \in \mathbb{R}^{3N \times 2N}$ from the embedding space to the tangent space is given by direct sum [122]

$$U = \bigoplus_{i=1}^{N} U_i \tag{20}$$

over the projection matrices $U_i = (\vec{\xi}_i, \vec{\eta}_i) \in \mathbb{R}^{3\times 2}$ (see Fig. 1.3a) of the individual magnetic moments.

The energy gradient $\boldsymbol{g}(\boldsymbol{m}) = (\vec{g}_1, \ldots, \vec{g}_N)$ at some configuration $\boldsymbol{m}$ must be defined in the tangent space $\mathcal{T}_{\boldsymbol{m}}$, which can be achieved by eliminating the $N$ superfluous degrees of freedom from the derivative of the energy [Eq. (14)]:

$$\vec{g}_i = \vec{\nabla}_i E - (\vec{\nabla}_i E \cdot \vec{m}_i)\vec{m}_i \ . \tag{21}$$

Note, that $\boldsymbol{g}(\boldsymbol{m}) \in \mathbb{R}^{3N}$ is represented in embedding space basis but by construction lies in the tangent space of the configuration. A representation in the local tangent space basis can be obtained via $U^T \boldsymbol{\nabla} E(\boldsymbol{m}) \in \mathbb{R}^{2N}$.

Furthermore, the matrix of second derivatives [Eq. (15)] of the energy with respect to the components of the magnetic moments is defined in $3N$ dimensional embedding space. To obtain the physical relevant representation $2N$ dimensional representation of the Hessian matrix, adhering to the curvature of the configuration space, the projection operator approach is used [123, 57, 122]:

$$H = U^T(\boldsymbol{\nabla}\boldsymbol{\nabla}^T E - \mathcal{L})U, \tag{22}$$

where $\mathcal{L}$ is the shape operator, accounting for the curvature of the configuration space. In the context of this work, eigenvalues $\lambda_i$ and eigenvectors $\boldsymbol{v}_i^{2N}$ always refer to the $2N$ eigenpairs of the Hessian matrix $H$. Furthermore, it will be always assumed they are sorted with increasing eigenvalue $\lambda_1 \leq \lambda_2 \leq \ldots \lambda_{2N}$ and the embedding space representation of the eigenvectors is denoted as:

$$\boldsymbol{v}_i = U\boldsymbol{v}_i^{2N}. \tag{23}$$

The Hamiltonian is a continuous smooth real-valued function on $\mathcal{R}$. For any optimization method on such a manifold the concepts of retraction (moving on the manifold along geodesics) and parallel transport [124] (translation of geometrical data on a manifold) are of crucial importance and are implemented for magnetic systems via rotations [121] (see Fig. 1.3b). Specifically, retracting a magnetic moment $\vec{m}_i$ along the direction $\vec{\chi}_i \in \mathcal{T}_{\vec{m}_i}$ to its updated position $\vec{m}_i'$ and transporting a vector $\vec{a} \in \mathcal{T}_{\vec{m}_i}$ to the tangent space of the rotated magnetic moment $\vec{a}' \in \mathcal{T}_{\vec{m}_i'}$ reads

$$\vec{m}_i' = D_{\vec{\chi}_i}(\epsilon)\vec{m}_i \tag{24}$$

$$\vec{a}_i' = D_{\vec{\chi}_i}(\epsilon)\vec{a}_i \ , \tag{25}$$

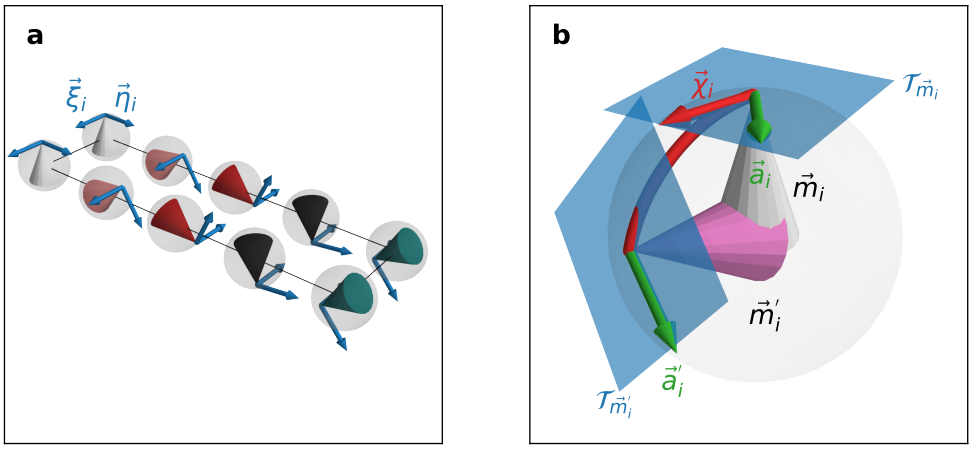


**Figure 1.3.** Visualization of the concepts of configuration space (gray spheres) for a system with magnetic moments $\vec{m}_i$ (cones), tangent space (blue planes), retraction along a geodesic defined by a vector $\vec{\chi}_i \in \mathcal{T}_{\vec{m}_i}$ (red) and parallel transport (green) of a vector $\vec{a}_i$ from the tangent space $\mathcal{T}_{\vec{m}_i}$ to $\vec{a}'$ in the tangent space $\mathcal{T}_{\vec{m}'_i}$ of the rotated moment $\vec{m}'_i$ . Part **b** schematically depicts the situation for an individual magnetic moment and **a** shows a system of ten magnetic moments and the basis vectors $\vec{\eta}_i$, $\vec{\xi}_i$ of the local tangent space representation.

where $D_{\vec{\chi}_i}(\epsilon)$ is a $3 \times 3$ matrix given by Rodriguez formula [125]

$$D_{\vec{\chi}_i} = \mathbb{1} + \sin\epsilon_i K_{\vec{\chi}_i} + (1 - \cos\epsilon_i) K^2_{\vec{\chi}_i} \ , \tag{26}$$

describing a rotation around the axis $\vec{k}_i = \vec{m}_i \times \vec{\chi}_i / |\vec{\chi}_i|$ about the angle $\epsilon_i = \epsilon |\vec{\chi}_i|$. The matrix $K_{\vec{\chi}_i}$ is denotes as:

$$K_{\vec{\chi}_i} = \begin{pmatrix} 0 & -k_i^z & k_i^y \\ k_i^z & 0 & -k_i^x \\ -k_i^y & k_i^x & 0 \end{pmatrix} \ . \tag{27}$$

The retraction and parallel transport for a magnetic configuration in $\mathcal{R}$ can be described by the direct sum of the rotation matrices for the individual magnetic moments:

$$\mathcal{D}_{\boldsymbol{\chi}}(\epsilon) = \bigoplus_{i=1}^{N} D_{\vec{\chi}_i}(\epsilon) \ . \tag{28}$$

It is crucial for every optimization problem to take into account the geometry of the respective manifold. In particular, the GMMF (cf. Sec. 2.3.1) and RQM (cf. Sec. 2.3.2) algorithms developed in Paper II require the implementation of retraction and parallel transport on the manifold $\mathcal{R}$ and on the Grassmann manifold, respectively.

### 1.3.3 Characterization of localized magnetic textures

#### Topology

The topology of magnetic textures is associated to important physical phenomena, such as the topological Hall effect [126] and the skyrmion Hall effect [127]. Topology, in a mathematical sense, concerns the properties of smooth fields that remain unchanged under continuous transformations – bending or stretching without cutting or gluing. In

magnetic systems, the term topology arises because certain configurations cannot be transformed into others (for example, a skyrmion cannot be unwound into a uniform FM state) without passing through a discontinuous magnetic configuration. In the continuous magnetization theory, the high-dimensional configuration space [Eq. (18)] is approximated by the space of continuous mappings of $\vec{m} : \mathbb{R}^2 \to S^2$. Importantly, we require the magnetization to be uniform at infinity, usually the FM state with

$$\lim_{|\vec{r}|\to\infty} \vec{m}(\vec{r}) = \hat{e}_z \ . \tag{29}$$

Consequently, the points of $\mathbb{R}^2$ at infinity map to a single point – practically e.g. by sterographic projection – which makes the domain $\mathbb{R}^2$ compact and homeomorphic to $S^2$. The space of all configurations, expressed by the mappings $S^2 \to S^2$, can then be classified using the homotopy group $\pi_2(S^2) = \mathbb{Z}$. Each configuration belongs to a homotopy class labeled by an integer $Q \in \mathbb{Z}$ referred to as topological charge [88][1]:

$$Q = \frac{1}{4\pi} \int_{\mathbb{R}^2} \vec{m}(\vec{r}) \cdot \left( \frac{\partial \vec{m}(\vec{r})}{\partial x} \times \frac{\partial \vec{m}(\vec{r})}{\partial y} \right) \mathrm{d}r^2 \ . \tag{30}$$

It is always possible to find a continuous transformation between two magnetic textures from the same class and such transformation is referred to as homotopy [37]. However, two configurations with different $Q$ cannot be continuously transformed into each other without introducing a discontinuity in the magnetization (e.g. a Bloch point) [35]. To obtain a representation of the topological charge which can be interpreted intuitively the magnetization can be written in spherical coordinates

$$\vec{m}(\vec{r}) = (\sin\Theta\cos\Phi, \sin\Theta, \sin\Phi, \cos\Theta)^T \tag{31}$$

for all points $\vec{r} \in \Pi$, where $\Pi$ is the whole plane $\mathbb{R}^2$ minus tiny disks around cores defined by $\vec{m}(\vec{r}) = -\hat{e}_z$. Assume that the areas magnetized antiparallel to the background are isolated such that disjoint curves $\gamma_k$ can be drawn around them and define a vector field $\vec{A}(\vec{r}) = (1 - \cos\Theta)\vec{\nabla}_{\vec{r}}\Phi$, where $\nabla_{\vec{r}} = (\partial_x, \partial_y, \partial_z)$. Then after standard vector-calculus and Stokes theorem $Q$ reads:

$$Q = \frac{1}{4\pi} \int_{\Pi} (\vec{\nabla}_{\vec{r}} \times \vec{A}) \cdot \hat{e}_z \, \mathrm{d}r^2 = \frac{1}{4\pi} \oint_{\partial\Pi} \vec{A} \, \mathrm{d}\vec{l} \tag{32}$$

The boundary $\partial\Pi$ can be split into an outer loop $\gamma_\infty$ and closed curves $\gamma_k$. Note, the surface normal $\hat{e}_z$ in Eq. (32) fixes the orientation of $\gamma_\infty$ (counter-clockwise) and the curves $\gamma_k$ (clockwise) such that the interior of $\Pi$ is always on the left as one traverses

[1]The integration domain is $\mathbb{R}^2$ since the region at infinity is not contributing $\partial_\alpha \vec{m}(\vec{r}) \to 0$ for $|\vec{r}| \to \infty$ and $\alpha = \{x, y\}$ due to the boundary condition in Eq. (29).

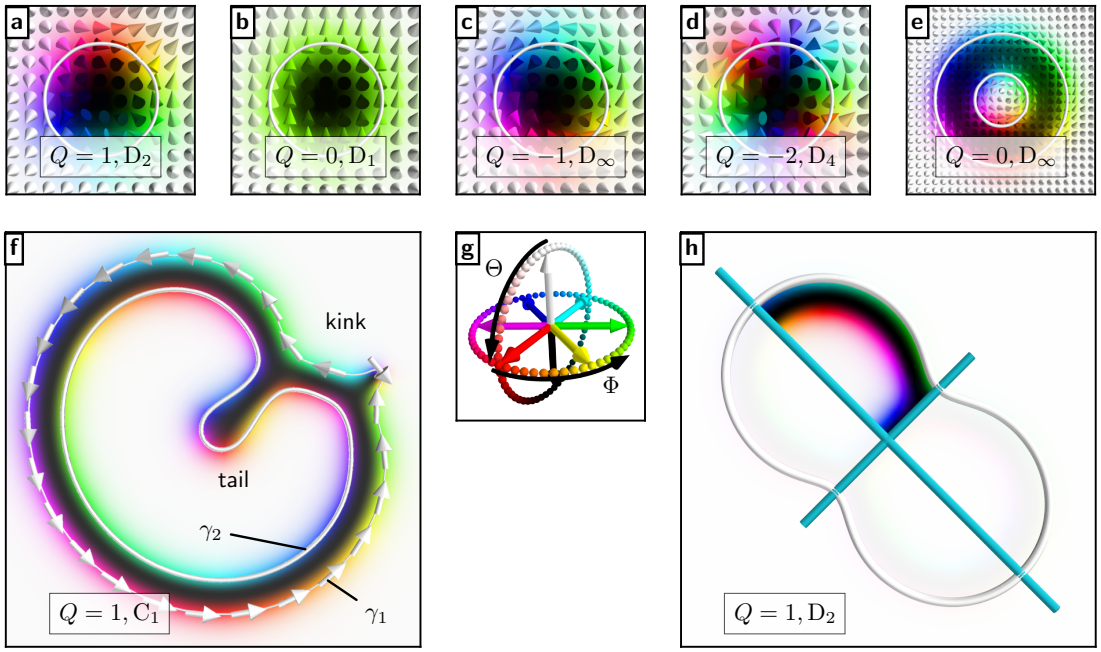


**Figure 1.4.** **a-e**: Configurations obtained using $\Phi = \Omega\varphi + \pi/2$ and $\Theta(\rho)$ in Eq. (31) on a square lattice. The white curves represent the contours $\gamma_k$. **g**: The hue-saturation-lightness color scheme used for visualizing magnetic textures. The azimuthal angle is represented by the hue, the lightness encodes the polar angle of the magnetic moments for a fixed saturation of $1.0$. **f**: Exemplary magnetic texture exhibiting a chiral kink on the contour $\gamma_1$ and a tail on the inner contour $\gamma_2$. **h**: Mirror axes (cyan) for a skyrmion bag texture comprising two inner contours. The fundamental domain is highlighted, while the remaining parts of the texture are grayed out. The textures in **f** and **h** correspond to metastable states in a two-dimensional chiral magnet for $L_D = 40$ and $h = 0.623$ (see Eq. (17)). For all shown textures $Q$ denotes the topological charge and $\mathrm{C}_n$ and $\mathrm{D}_n$ indicates the respective symmetry group.

along the boundary. Consequently, one can write

$$Q = \frac{1}{4\pi}\left[\oint_{\gamma_\infty}^{\mathrm{CCW}} (1-\cos\Theta)\vec{\nabla}_{\vec{r}}\Phi \,\mathrm{d}\vec{l} - \sum_k \oint_{\gamma_k}^{\mathrm{CW}} (1-\cos\Theta)\vec{\nabla}_{\vec{r}}\Phi \,\mathrm{d}\vec{l}\right] \tag{33}$$

$$= \frac{1}{4\pi}\sum_k \oint_{\gamma_k}^{\mathrm{CCW}} (1-\cos\Theta)\vec{\nabla}_{\vec{r}} \,\mathrm{d}\vec{l} \tag{34}$$

$$= \sum_k \Omega_k \ , \tag{35}$$

where the curve $\gamma_\infty$ is not contributing due to $1-\cos\Theta \to 0$ for $|\vec{r}| \to \infty$ and the winding number $\Omega_k$ was defined for each contour [37]:

$$\Omega_k = \frac{1}{2\pi}\oint_{\gamma_k}^{\mathrm{CCW}} \vec{\nabla}\Phi \,\mathrm{d}\vec{l} \ . \tag{36}$$

Note, the polar angle was evaluated to $\Theta \to \pi$ yielding $1-\cos\Theta \to 2$ by taking $\gamma_k$ to be an infinitesimal loop around the $k$-th core. For practical purposes the value of polar angle on the contour can be chosen arbitrary as long as $0 < \Theta < \pi$ [37] and for the remainder of this work the contours are chosen as curves in real space where the magnetization is in-plane ($\Theta = \pi/2$)[2]. The topological invariant $Q$ can now be calculated intuitively by counting how many times $\Omega_k$ the azimuthal magnetization wraps around the $k$-th core along the contours $\gamma_k$ of a localized texture.

Figs. 1.4a-e shows configurations obtained using polar coordinates $(\rho, \varphi)$ for $\mathbb{R}^2$, $\Theta = \Theta(\rho)$ and $\Phi(\varphi) = \Omega\varphi + \eta$, where $\eta$ is the helicity corresponding either Bloch-type ($\eta = \pi/2$) or Néel-type ($\eta = 0$) textures. For the simple cases shown in Fig. 1.4a-d the topological charge corresponds to the winding number of a single contour curve $\gamma_1$ ($Q = \Omega_1$). Fig. 1.4e shows a texture with two contours – one entirely embedded within the other. Naturally the winding number of this inner contour carries the opposite sign as the winding number of the outer contour line yielding a total charge of $Q = 0$.

In practice, computing the topological charge on discrete lattices involves summing over spherical triangles spanned by the magnetic moments $\vec{m}_i$, $\vec{m}_j$ and $\vec{m}_k$ localized at the vertices of triangles $t$ [128]:

$$Q \approx \frac{1}{4\pi}\sum_t 2\arctan\left[\frac{\chi_{ijk}}{1+\vec{m}_i\cdot\vec{m}_j+\vec{m}_j\cdot\vec{m}_k+\vec{m}_k\cdot\vec{m}_i}\right] \ , \tag{37}$$

where

$$\chi_{ijk} = \vec{m}_i\cdot(\vec{m}_j\times\vec{m}_k) \tag{38}$$

denotes the scalar spin chirality [129, 130], a local measure for noncoplanarity of magnetic moments.

[2]Mathematically, when moving the boundary to from $\Theta = \pi$ to $\Theta = \pi/2$ one must add and area integral over the annulus between the two loops which then carries $\Omega_k/2$.

### Features of localized magnetic textures

In a physical sense, one is first and foremost interested in magnetic textures which correspond to (local) minima on the energy surface as those are associated with metastable states. In general [32] and in chiral magnets specifically a wide variety of magnetic textures can emerge as metastable states [36]. In two-dimensional chiral magnets any isolated texture can be described in terms of three fundamental building blocks:

- **Closed contours**: Real space curves $\gamma \in \mathbb{R}^2$ separating domains of magnetic moments with $\Theta < \pi/2$ from regions with $\Theta > \pi/2$. The DMI defines the chirality of the system and thus determines the sense of rotation of the magnetization along the contours. The outermost contour defines the boundary of a localized texture.
- **Chiral kinks**: Localized twist of the magnetization along the contour exhibiting a rotational sense opposite to the systems chirality.
- **Tails**: Local deformations of a countour that modify the shape but not alter the sense of the rotation of the magnetization along the contour.

Note, in Sec. 3.2 localized magnetic textures in three-dimensional chiral magnets are discussed, where the real space contour curves are replaced by contour surfaces embedded in three dimensions. Closed contours can be nested within each other forming so-called skyrmion bags [89, 90, 91] (cf. Fig. 1.4e). Chiral kinks occur due the DMI favoring a specific sense of rotation. If a texture features regions of different senses of rotation of the magnetization along a contour, the region of disfavored chirality shrinks and forms a localized chiral kink [36]. For the energy model of chiral magnets used in this work each chiral kink adds one winding to the host contour line (positive chiral kink). Thus, it increases the total topological charge of the system by one. Note, for models with strong easy-axis anisotropy also negative chiral kinks can exist [36]. The tail feature affects the geometric shape of the texture but does not modify its topological charge [68].

Fig. 1.4f shows an exemplary texture comprising all three features: two closed contours $\gamma_1$ and $\gamma_2$, a chiral kink attached to the outermost contour $\gamma_1$ and a tail deformation of the contour $\gamma_2$. This texture corresponds to a minimum of Eq. (2) for a magnetic field of $h = 0.623$ and $L_D = 40$.

### Symmetries of magnetic textures

The topological charge $Q$ of a texture along is insufficient to uniquely characterize a magnetic texture. Different textures may share the same topological charge but exhibit a different shape and distinct symmetry (cf. Figs. 1.4f,h). Moreover the dynamical behavior of an isolated magnetic texture is directly influenced by its symmetry [131].

Consider a localized magnetic texture characterized by magnetic moments $\vec{m}_i = \vec{m}(\vec{r}_i)$ at lattice sites $\vec{r}_i$ with its center $\vec{c}$ [132, 133, 134, 135]:

$$\vec{c} = \frac{\sum\limits_{i\in\mathcal{I}} \vec{r}_i(m_i^z - 1)}{\sum\limits_{i\in\mathcal{I}} m_i^z - 1} \ . \tag{39}$$

The symmetry operations of such a texture corresponds to elements of spin point groups [136, 137, 138, 139]. These elements, denoted by $[\mathcal{M}||\mathcal{N}]$, act in a combined

way on the space of the spatial coordinates ($\mathcal{M}$) and on the space of magnetic moments ($\mathcal{N}$) [139]:

$$[\mathcal{M}||\mathcal{N}]\vec{m}(\vec{r}_i) = \mathcal{M}\vec{m}(\mathcal{N}^{-1}(\vec{r}_i - \vec{c}) + \vec{c}) \ . \tag{40}$$

In this work, $n$-fold rotations of both the spatial coordinates and the orientation of the magnetic moments are considered, expressed by elements $[R_{2\pi/n}||R_{2\pi/n}]$ [140, 141]:

$$\vec{m}'(\vec{r}) = R_{2\pi/n}\vec{m}\left(R_{-2\pi/n}(\vec{r}_i - \vec{c}) + \vec{c}\right) \ . \tag{41}$$

In addition to rotations mirror operation elements $[R_{\pi-2\beta}P||P]$ are considered [140]:

$$\vec{m}'(\vec{r}_i) = R_{\pi-2\beta}P\vec{m}(P(\vec{r}_i - \vec{c}) + \vec{c}) \ , \tag{42}$$

where $P = 2\vec{p}\cdot\vec{p}^T - \mathbb{1}$ denotes the reflection on an axis with direction $\vec{p}$ in the plane of a two-dimensional system. The additional rotation in the space of the magnetic moments accounts for the helicity of the magnetic texture related to the angle $\beta$ of the DMI vector [cf. Eq. (8)].

Magnetic textures invariant under Eq. (41) correspond to a spin point group denoted by $C_n$, where $C_1$ describes the identity (cf. Fig. 1.4f). A texture exhibiting $n$-fold rotations and $n$-mirrors according to Eq. (42) is assigned the group $D_n$ with examples shown in Figs. 1.4a,b,d,h. For axial symmetric configurations (see Figs. 1.4c,e) the infinite group $C_\infty$ or $D_\infty$ is assigned. Note, that the Hamiltonian in Eq. (17) is invariant translations combined with these $n$-fold rotations and mirrors.

In the context of this project, the rotational and mirror symmetry elements are used to define the fundamental domain, which is the part of the texture with non-repeating physical information. For the texture displayed in Fig. 1.4h this domain corresponds to one of the quarters divided by the mirror axes. One of the key ideas of the SP searches developed in this project was to define localized excitations of a magnetic state within its fundamental domain to locally break the symmetry of the texture and introduce a tendency towards various SPs (see Secs. 2.1,2.2). An algorithm was developed in Paper IV identifying the symmetries and thereby the fundamental domain of a given two-dimensional magnetic textures.

### 1.3.4 Harmonic Transition State Theory

Using magnetic textures in technological applications, e.g. data processing and storage units [142], requires a quantitative estimation of their lifetime with respect to thermally activated transitions. Furthermore, in magnetic systems capable of hosting multiple structures simultaneously [33, 34, 35, 36, 37], which hold great promise for technological applications, it is an important question how the system traverses between these multiple states over long timescales due to thermal activation.

In this work, *harmonic transition state theory* (HTST) [50, 51] is applied to magnetic systems [143] to approach these questions. Consider a system with $N$ magnetic moments, which is adequately described by the $2N$ dimensional energy surface defined by the atomistic Hamiltonian[3], and assume that it is in some state $A$ associated with

[3]The length constraint of the magnetic moments corresponds to the Born-Oppenheimer (adiabatic) approximation often included in the assumptions of transition state theory in a chemistry context.

a local energy minimum $E_A$ of Eq. (2) corresponding to a magnetic texture. Thermodynamically this state is described by an ensemble $\Omega_A$ of configurations. At finite temperature $T > 0$ there is the chance that the system undergoes a thermally activated transition into some other state associated to an energy minimum $B$. The lifetime of the state around $A$ is given by:

$$\tau_A^{-1} = \sum_{\substack{B \\ B \neq A}} \nu^{A \to B} \ , \tag{43}$$

where $\nu^{A \to B}$ is the rate of the $A \to B$ transition. Note, generally $\nu^{A \to B}$ is the sum of the rates of all reaction mechanisms connecting $A$ and $B$. To calculate the individual transition rates $\nu^{A \to B}$, the key idea is to define a $2N - 1$ dimensional dividing surface on the energy surface that represents a bottleneck for going from the initial state to a final state and represents the boundary between both states. This bottleneck can be due to an energy barrier or and/or due to an entropy barrier. Adding an infinitesimal thickness $\sigma$ to the dividing surface gives the so-called transition state, indicated by the symbol ‡. The foundations of *Transition State Theory* are the following [144, 145, 146]:

1. The dynamics of the system can be treated classically and quantum effects can be neglected.

2. The system is in thermodynamic equilibrium with a heat bath and the population of the ensemble associated to the initial state corresponds to a Boltzmann distribution – a transition is assumed to be a rare event[4].

3. If a trajectory heading away from the initial state reaches the transition state, it will lead directly to the final state. Recrossings of the transition state are neglected and thus the transition rate $\nu^{A \to B}$ is an overestimate. Therefore, the choice of the dividing surface which gives the smallest rate estimate corresponds to the optimal transition state [147].

Considering the ensemble of the transition state $\Omega_\ddagger$ to be the outer boundary part included in the ensemble of the initial state, the rate is given by the probability of finding the system at the transition state and the flux out of the initial state through the dividing surface. For magnetic systems one can write [122, 146, 143]:

$$\nu^{A \to B} = \frac{\int\limits_{\Omega_\ddagger} \mathrm{e}^{-\beta E(\boldsymbol{m})} v_\perp(\boldsymbol{m}) h(v_\perp(\boldsymbol{m})) \mathrm{d}\boldsymbol{m}}{\int\limits_{\Omega_A} \mathrm{e}^{-\beta E(\boldsymbol{m})} \mathrm{d}\boldsymbol{m}} \ , \tag{44}$$

where $\beta = 1/(k_\mathrm{B}T)$, and $h$ is the Heavyside step function counting only trajectories leaving the initial state. In contrast to atomic systems, where the full phase space includes both particle positions and canonical momenta, magnetic systems are described solely by the orientations of magnetic moments constrained to unit length. The dynamics of these moments are governed by the *Landau-Lifshitz-Gilbert* (LLG) equation [148, 149], which is first order in time and does not contain a kinetic energy term. Consequently, no conjugate momenta exist for the spin degrees of freedom, and the statistical weight of a microstate depends only on the configurational energy $E(\boldsymbol{m})$. The partition

[4] As a rule of thumb this is satisfied if the free energy barrier is larger than $5k_\mathrm{B}T$ [144].

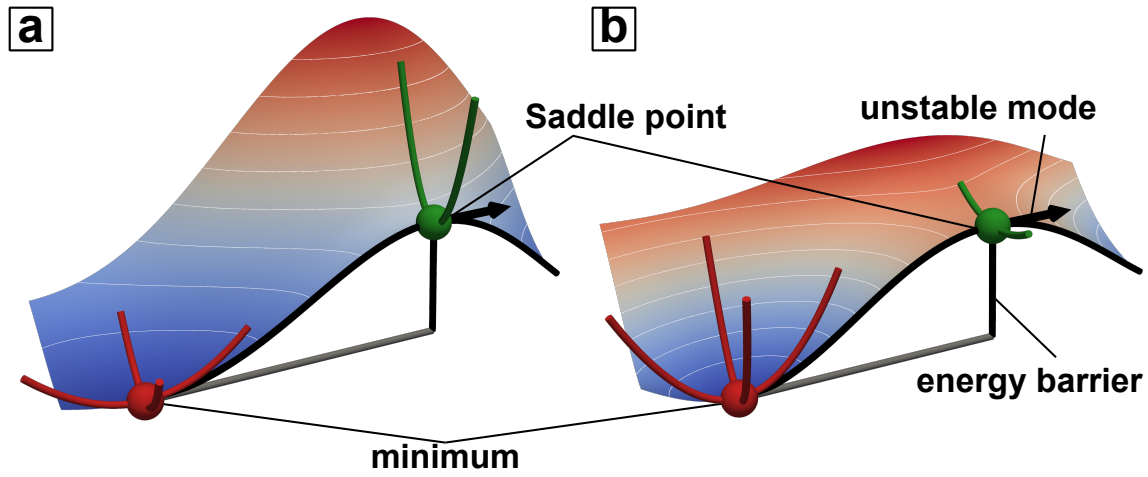


**Figure 1.5.** Schematic two-dimensional energy surfaces with low curvature at the minimum (red) and large curvature at the SP (green) in **a** and vice versa in **b**.

function of a magnetic system therefore reduces to an integral over spin orientations, $\int \exp[-\beta E(\boldsymbol{m})]\mathrm{d}\boldsymbol{m}$, as given in Eq. (44). The flux term $v_\perp(\boldsymbol{m})$ represents the component of the spin dynamics normal to the dividing surface, determined directly from the deterministic LLG equation. It plays the same role as the momentum component perpendicular to the surface in conventional TST but arises dynamically rather than statistically.

In the harmonic approximation of TST (HTST) a specific dividing surface is chosen as a hyperplane going through a first order SP on the energy ridge separating the initial from the final state [143, 122] and with a normal vector parallel to the unstable mode of the SP. Geometrically, the perpendicular hypersurface in the vicinity of the SP is approximated with a plane. The energy is expanded quadratically around the minimum with energy $E_A$ and the SP with energy $E_{\mathrm{SP}}$ with respect to a small deviation $\delta\boldsymbol{m}$ of the magnetization [146]

$$E(\boldsymbol{m}_{A/\mathrm{SP}} + \delta\boldsymbol{m}) = E_{A/\mathrm{SP}} + \frac{1}{2}\sum_{i=1}^{2N}\sum_{i'=1}^{2N} q_i q_{i'} (\boldsymbol{v}^{2N}_{A/\mathrm{SP},i})^T H_{A/\mathrm{SP}} \boldsymbol{v}^{2N}_{A/\mathrm{SP},i} \tag{45}$$

$$= E_{A/\mathrm{SP}} + \frac{1}{2}\sum_{i=1}^{2N} \lambda_i^{A/\mathrm{SP}} q_i^2 \ , \tag{46}$$

where the eigenvectors $\boldsymbol{v}^{2N}_{A/\mathrm{SP},i} \in \mathbb{R}$ of the constrained Hessian $H^{2N}_{A/\mathrm{SP}}$ are used as local basis vectors of the energy surface with coordinates $q_i$. The orthogonality of this chosen basis allows to write the expansion in the form of Eq. (46) with the eigenvalues $\lambda_i^{A/\mathrm{SP}}$ of the Hessian reflecting the curvature of the energy surface at the stationary points as sketched in Fig. 1.5. Inserting Eq. (46) in Eq. (44) leads to a factorization of the integrals into a product of the contributions of the individual eigenmodes of the Hessian. Note, since the transition state is defined as a hyperplane with infinitesimal thickness orthogonal to the unstable mode, the integration of the partition function of the SP excludes the unstable mode. Linearising the equations of motion with respect to a small deviation $\delta\boldsymbol{m}$ within the dividing surface to determine the velocity and some

algebra [143, 69, 122, 146] yields in summary an Arrhenius law:

$$\nu^{A\to B} = \nu_0^{A\to B} \mathrm{e}^{-\beta\Delta E} \ , \tag{47}$$

where $\Delta E = E_{\mathrm{SP}} - E_A$ is the energy barrier and $\nu_0$ is the pre-exponential factor accounting for entropic and dynamic contributions $\Lambda$ to the rate:

$$\nu_0^{A\to B} = \frac{\Lambda}{2\pi}\frac{V^{\mathrm{SP}}}{V^{\mathrm{A}}}\left(\frac{2\pi}{\beta}\right)^{\frac{Z^A - Z^{\mathrm{SP}}}{2}} \sqrt{\frac{\prod\limits_{i=1+Z^A}^{2N}\lambda_i^A}{\prod\limits_{i=2+Z^{\mathrm{SP}}}^{2N}\lambda_i^{\mathrm{SP}}}} \ . \tag{48}$$

Importantly, the harmonic approximation can be insufficient for certain eigenmodes, e.g. excitations along translational or rotational degrees of freedom of a magnetic texture barely cost energy, and those are often better treated in Goldstone mode approximation [55, 69, 46, 146] assigning a zero mode volume $V_A$ or $V_{\mathrm{SP}}$ to the contribution of $Z^A$ and $Z^{\mathrm{SP}}$ zero modes at the minimum and the SP, respectively. The respective eigenmodes are excluded from the above products of eigenvalues. The dynamical factor $\Lambda$ describes the flux of trajectories through the dividing surface and is given by [122, 146]

$$\Lambda = \gamma\sqrt{(A\boldsymbol{v}_{\mathrm{SP},1}^{2N})^T H_{\mathrm{SP}} A\boldsymbol{v}_{\mathrm{SP},1}^{2N}} \ , \tag{49}$$

where $\boldsymbol{v}_{\mathrm{SP},i}^{2N}$ is the eigenvector of the unstable mode of the SP and $A \in \mathbb{R}^{2N\times 2N}$ is a block diagonal matrix with:

$$(A)_{ii'} = \frac{\delta_{ii'}}{\mu_i}\begin{pmatrix} 0 & -1 \\ 1 & 0 \end{pmatrix} \ . \tag{50}$$

The pre-exponential factor is proportional to the entropy barrier of the transition [150] and the relevant entropies of the minimum and SP depend on the Hessian eigenvalues reflecting the curvature of the energy surface. The effect of these curvature values $\lambda_i^{\mathrm{A/SP}}$ on the lifetime of a metastable state is schematically illustrated in Fig. 1.5, where two-dimensional energy surfaces are shown with identical energy barriers, but different shape of the energy surface around the critical points. A flat minimum combined with a sharply curved energy surface at the SP corresponds large entropy barrier and yields a small $\nu_0^{A\to B}$, leading to a longer lifetime in such a situation (Fig. 1.5a). Conversely, a sharply curved energy surface at the minimum and a less curved energy surface at the SP increase $\nu_0$, reducing the lifetime of the metastable state (Fig. 1.5a).

HTST is a statistical approach effectively taking into account all trajectories of the system undergoing a thermally activated transition from one metastable state to another. It takes only the corresponding configuration of the minimum and the associated first-order SP on the energy surface as input to compute the rate of the respective transition. Thereby, the identification of all relevant SPs connected to a given energy minimum is crucial to correctly estimate the lifetime of a state. In particular, the low-energy SPs corresponding to the thermodynamically most likely transitions are important.

### 1.3.5 Identification of first order SPs

This section outlines the concept of methods for identifying SPs that connect minima on the energy surface. It is useful to begin by introducing some terminology characterizing geometric properties of energy surfaces. Recall that the eigenvalues of the Hessian of the energy of the system reflect the curvature of the energy surface along the directions of the respective eigenvectors. Minima and first-order SP are stationary points on the energy surface. While a minimum is embedded within a *convex region*[5], a region characterized by exclusively non-negative eigenvalues ($\lambda_1 \geq 0$), an SP is a point with just one negative eigenvalue ($\lambda_1 < 0 \leq \lambda_2$), the unstable mode. Two minima are connected, if a *steepest descent path* exists, obtained by following the energy gradient downhill from both sides of a first-order SP with respect to its unstable mode (see Fig. 1.6a). In this work a steepest descent path is used synonymously with the *minimum energy path* (MEP) [151][6]. The point of highest energy on the MEP is a first-order SP. Geometrically an SP is part of a valley, which can be defined by the line on the energy surface, where the eigenvector of the lowest Hessian eigenvalue aligns with the energy gradient ($|\boldsymbol{g} \cdot \boldsymbol{v}_1|/|\boldsymbol{g}| = 1$) while there is at most one negative eigenvalue ($\lambda_1 \leq 0 < \lambda_2$) [154, 71]. Note, such a valley does not necessarily connect the SP all the way down to the minimum and may at some point transform into a ridge [155, 156, 157, 158, 159, 160], which is characterized by alignment of the gradient and the minimum mode and two negative eigenvalues: $\lambda_1 \leq \lambda_2 < 0 < \lambda_3$. A third category of points on the energy surface correspond to $2N-1$-dimensional perpendicular hypersurfaces where the gradient is perpendicular to the minimum mode ($\boldsymbol{g} \cdot \boldsymbol{v}_1 = 0$) [71]. Examples of valleys, ridges and perpendicular hypersurface are shown in Fig. 1.6b,c for a schematic two-dimensional surface.

Existing methods that aim to identify first-order SPs on the system's energy surface can be divided into two classes:

- Double-ended methods: If an SP between two specific minima is sought, the *geodesic nudged elastic band* (GNEB) method [54] and its variants are applied. It calculates an interpolation of the MEP connecting the two minima and subsequently determines the SP as point of highest energy on the path.
- Single-ended methods: If a single energy minimum is given and the connected SPs shall be identified – possibly without knowing the final states of the respective transitions – variants of the *geodesic minimum mode following* (GMMF) method [57, 58, 59] are used. Initialized at a certain point on the energy surface these single-ended methods climb upwards in energy along the minimum mode and apply relaxation along all perpendicular degrees of freedom to ultimately reach SPs.

In both methods the word *geodesic* refers to the length constraint of the magnetic

[5]Note, a minimum is always surrounded by a convex region while a convex region does not necessarily contain a minimum [71] (cf. Fig. 1.6a)

[6]Note, sometimes the MEP is characterized by the property that the energy increases in all directions perpendicular to the path [152]. This is however, not equivalent with a steepest descent path as it implies that the MEP lies within a region where at most one Hessian eigenvalue is negative. It is not always possible to connect an SP and a minimum by a continuous curve that runs exclusively through a region with at most one negative eigenvalue and thus the MEP within this narrow definition might not exist [153].

configuration space (cf. Sec. 1.3.2).

In the following the concept of the well-established GNEB method will be presented briefly, supported by the simple schematic two-dimensional energy surface shown in Fig. 1.6b. The GNEB algorithm [54] performs the following tasks, where steps 2-4 are repeated until convergence:

1. Generate an initial path connecting the two minima on the energy surface. A path is a series of images $\boldsymbol{m}^\nu$, which are replicas of the system interpolating between the configurations of the end points. Usually a geodesic interpolation between the initial and the final state is chosen as the initial path.

2. For each image $\boldsymbol{m}^\nu$ obtain the local tangent $\boldsymbol{\tau}^\nu$ of the path by considering the directions in configuration space connecting the image with its neighbors $\boldsymbol{m}^{\nu-1}$ and $\boldsymbol{m}^{\nu+1}$ [161, 145]. Project the tangent vector to the tangent space of the image such that $\boldsymbol{\tau}^\nu \in \mathcal{T}_{\boldsymbol{m}^\nu}$ [54].

3. Compute the force contribution perpendicular to the tangent of the path:

$$\boldsymbol{f}^\nu_{\text{ortho}} = -\boldsymbol{g}(\boldsymbol{m}^\nu) + (\boldsymbol{g}(\boldsymbol{m}^\nu) \cdot \boldsymbol{\tau}^{\boldsymbol{\nu}})\boldsymbol{\tau}^{\boldsymbol{\nu}} \ , \tag{51}$$

   where $\boldsymbol{g}(\boldsymbol{m}^\nu) \in \mathcal{T}_{\boldsymbol{m}^\nu}$ is the energy gradient (cf. Eq. 21). Secondly, compute a spring force parallel to the tangent direction:

$$\boldsymbol{f}^\nu_{\text{spring}} = -\kappa[d(\boldsymbol{m}^{\nu+1}, \boldsymbol{m}^\nu) - d(\boldsymbol{m}^\nu, \boldsymbol{m}^{\nu-1})]\boldsymbol{\tau}^\nu \ , \tag{52}$$

   where $\kappa$ is the spring force parameter and $d(\boldsymbol{m}^\nu, \boldsymbol{m}^{\nu\pm1})$ denotes the geodesic distance between adjacent images [54].

4. Displace each image $\boldsymbol{m}^\nu$ along the GNEB force $\boldsymbol{f}^\nu_{\text{GNEB}} = \boldsymbol{f}^\nu_{\text{ortho}} + \boldsymbol{f}^\nu_{\text{spring}}$ within a numerical optimization scheme [54]. Effectively, the orthogonal force minimizes the energy of the path along all degrees of freedom except the tangent direction of the path while the spring force maintains an equal distribution of images along the path.

When the GNEB force drops below a pre-defined threshold, this algorithm is considered converged. Effectively, the GNEB method relaxes an initial path between two energy minima like a rubber band into a nearby MEP. However, the SP is not necessarily contained in the images of this interpolation. Thus, in a secondary optimization, the *climbing image-GNEB* (ci-GNEB) obtains the SP by allowing the image of the highest energy along the path to climb in energy by replacing the spring force for this *climbing image* with an inverted force projected to the tangent of the path [54].

If the initial and final state of a transition are known in beforehand the GNEB method has been successfully applied to identify SPs associated to transformations of localized magnetic textures in various two- and three-dimensional magnetic systems [34, 43, 69, 45, 55, 56, 46]. One example of such an application is briefly discussed below. In Paper I the GNEB method was used to study the effects of interlayer exchange coupling on the mechanisms of skyrmions collapsing into the *ferromagnetic* (FM) state in systems comprising several magnetic layers, each hosting a conventional two-dimensional skyrmion. Fig. 1.7a shows the energy along the MEP associated to the collapse of a

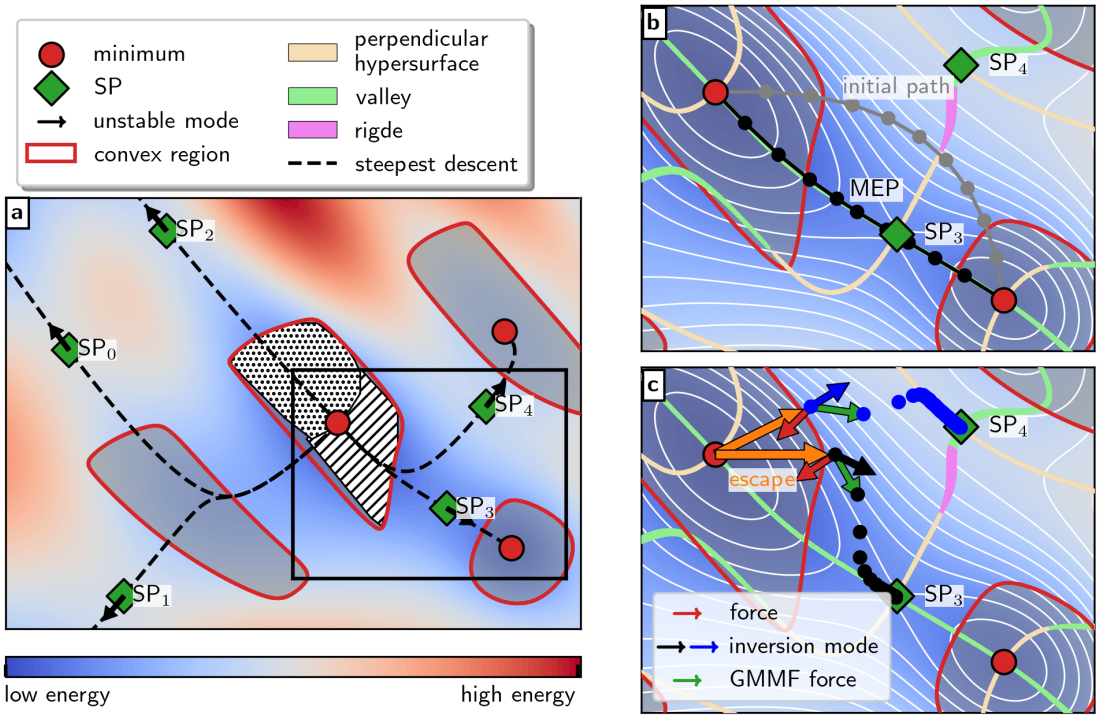


**Figure 1.6.** **a**: Schematic two-dimensional energy surface with three minima (red) and five SPs (green). The black box marks the part of the surface shown in **b** and **c**. Steepest descent paths are marked by dashed black lines. Convex regions are surrounded by red lines. In **b**,**c** also perpendicular hypersurfaces (wheat), valleys (light green) and ridges (violet) are shown. **b**: Sketch of the double-ended GNEB method. Two minima are connected by an initial path (gray) which is a series of images (circles). The GNEB method optimizes this path iteratively converging onto the MEP (black). **c**: Sketch of the single-ended GMMF method. After initialization, referred to as escape attempts (orange), the GMMF method iteratively displaces along the GMMF force (green, cf. Eq. (53)) obtained from the force (red) and the inversion mode (black and blue). Within the central convex region in **a** two regions are hatched. The dotted region (stripe patterned region) corresponds to initial points for which the GMMF method converges onto $SP_2$ ($SP_3$), respectively.

bilayer skyrmion (Figs. 1.7i) for $J^{\perp} = 20$ meV, where $J^{\perp}$ denotes the nearest neighbor interlayer exchange coupling parameter.

In this regime of strongly coupled layers, the skyrmions in the two layers disappear simultaneously via the so-called radial collapse mechanism, which describes radially-symmetric shrinking of a skyrmion followed by its annihilation into the *ferromagnetic* (FM) background via a Bloch point (cf. Fig. 1.7ii). The associated energy barrier corresponds to twice the energy barrier of the skyrmion collapse in the respective monolayer system. This MEP was obtained by applying the GNEB to an initial path generated as the geodesic interpolation between the initial and the final state, which corresponds to a uniform rotation of each magnetic moment from the bilayer skyrmion configuration into the FM configuration.

However, the predictive power of the GNEB method is limited in situations where several transition pathways are possible between two metastable states or where the final state of a transitions is unknown. As an example for the former situation consider a bilayer skyrmion collapse in the low interlayer exchange coupling regime. The black curve in Fig. 1.7b shows the energy along the MEP obtained by applying the GNEB method to the geodesic initial path for $J^{\perp} = 0.15$ meV[7]. Here, the bilayer skyrmion collapse proceeds via sequentially disappearing skyrmions in the individual layers, both via a radial mechanism (cf. Fig. 1.7iv). However, $\mathrm{SP}_{\mathrm{rad}}$, associated to the radial collapse of the first skyrmion that disappears, does not correspond to the lowest-energy SP connected to the minimum of the bilayer skyrmion for $J^{\perp} = 0.15$ meV. It is obtained, because the MEP describing the radial-symmetric shrinking of the skyrmion is similar to the geodesic initial path and the GNEB converges on a local MEP depending on the initial guess for the path. If random noise is applied to each image of this local MEP and if the GNEB starts from this path, it converges onto a different MEP describing an asymmetric Chimera collapse mechanism [10, 56] of the skyrmion (cf. Fig. 1.7v). The energy along this MEP is shown in red in Fig. 1.7b and $\mathrm{SP}_{\mathrm{chim}}$ corresponds to a slightly lower energy barrier than $\mathrm{SP}_{\mathrm{rad}}$ [8]. Thus, in situations where multiple SPs are expected to be relevant for a given energy minimum it is more systematic to apply a single-ended methodology without defining the final states of the transitions in beforehand. This is particularly significant if the number metastable states and thus also the number of transition mechanisms increases, e.g. for more magnetic layers included in the model (Paper I).

Situations such as the one described above motivate the development of single-ended SP search methods. In Fig. 1.6a an energy surface with a central minimum and five surrounding SPs is shown. A single-ended SP search method aims to identify, in the best case all, SPs connected to the minimum.Loosely speaking, one tries to climb the energy surface around the minimum along different directions to find distinct SPs. The GMMF algorithm is suitable for this task and displaces a configuration along the

[7]Note, as this MEP exhibits an intermediate minimum corresponding to one FM layer and one layer hosting a skyrmion, the two parts of the MEP are determined by two separate GNEB calculations [54], each identifiyng one of the two SPs.

[8]In Paper I this is related to the reduced interlayer exchange energy costs of $\mathrm{SP}_{\mathrm{chim}}$ compared to $\mathrm{SP}_{\mathrm{rad}}$.

GMMF force (cf. Refs. [57, 58, 59] and Paper II)

$$\boldsymbol{f} = -\boldsymbol{g} + 2(\boldsymbol{g} \cdot \boldsymbol{q})\boldsymbol{q} \ , \tag{53}$$

which inverts the component of the force along the inversion mode $\boldsymbol{q}$. As a result, the energy is minimized along all degrees of freedom except in the direction of the inversion mode, along which it is maximized. Repeated application of these displacements drives the system toward a first-order SP. In the vicinity of the SP, the inversion mode is always chosen as the minimum mode ($\boldsymbol{q} = \boldsymbol{v}_1$), consistent with the fact that an SP represents a local maximum along a valley. Note however, Paper II and Paper IV demonstrate situations in which it is advantageous to temporarily select $\boldsymbol{q} = \boldsymbol{v}_2$ for a number of iterations – an aspect that has received little attention so far.

A key aspect for the practical application of the GMMF algorithm is its initialization procedure, which provides a set of configurations around the energy minimum enabling the method to reach many distinct SPs. In Fig. 1.6a two regions within the convex region are highlighted with different hatches. If the GMMF algorithm is initialized with a point in the dotted domain it converges onto $\mathrm{SP}_2$, while it converges to $\mathrm{SP}_3$ for the striped region. Therefore, initializing the GMMF method close to the minimum within the convex region yields only two of five possible SPs. In general, the convex region embedding the initial minimum provides only little guidance for identifying different ascending directions leading to distinct SPs on the energy surface as[162].

The goal of the initialization of GMMF, referred to as escape-stage, is to prepare the ground for the GMMF algorithm by displacing the minimum configuration to a point outside the convex region where at least one Hessian eigenvalue is negative. By generating a diverse set of such escape points close to the $2N-1$-dimensional boundary of the convex region one increases the variety of SPs that be reached in the subsequent convergence-stage (GMMF). Therefore, the realization of the escape-stage is crucial for the development of single-ended SP searches and despite its seemingly straightforward purpose it possesses significant practical challenges, particularly in high-dimensional systems. Paper IV presents the development of a systematic escape-stage suitable for localized magnetic textures.

Two exemplary GMMF attempts are shown in black and blue in Fig. 1.6c, initialized at two different points outside the convex region. While the black painted attempt climbs the energy surface and enters the region containing the valley leading to $\mathrm{SP}_3$, the blue attempt climbs in energy and then reaches the vicinity of a perpendicular hypersurface where $\boldsymbol{g} \cdot \boldsymbol{v}_1 = 0$. The GMMF force in Eq. (53) then equals the conventional force and the algorithm performs an energy minimization along all degrees of freedom. This can either leads to a sideways motion to $\mathrm{SP}_4$ in this case. Note that if a perpendicular hypersurface is met in the vicinity of a convex region it is likely that the GMMF method fails by re-entrance into a convex region.

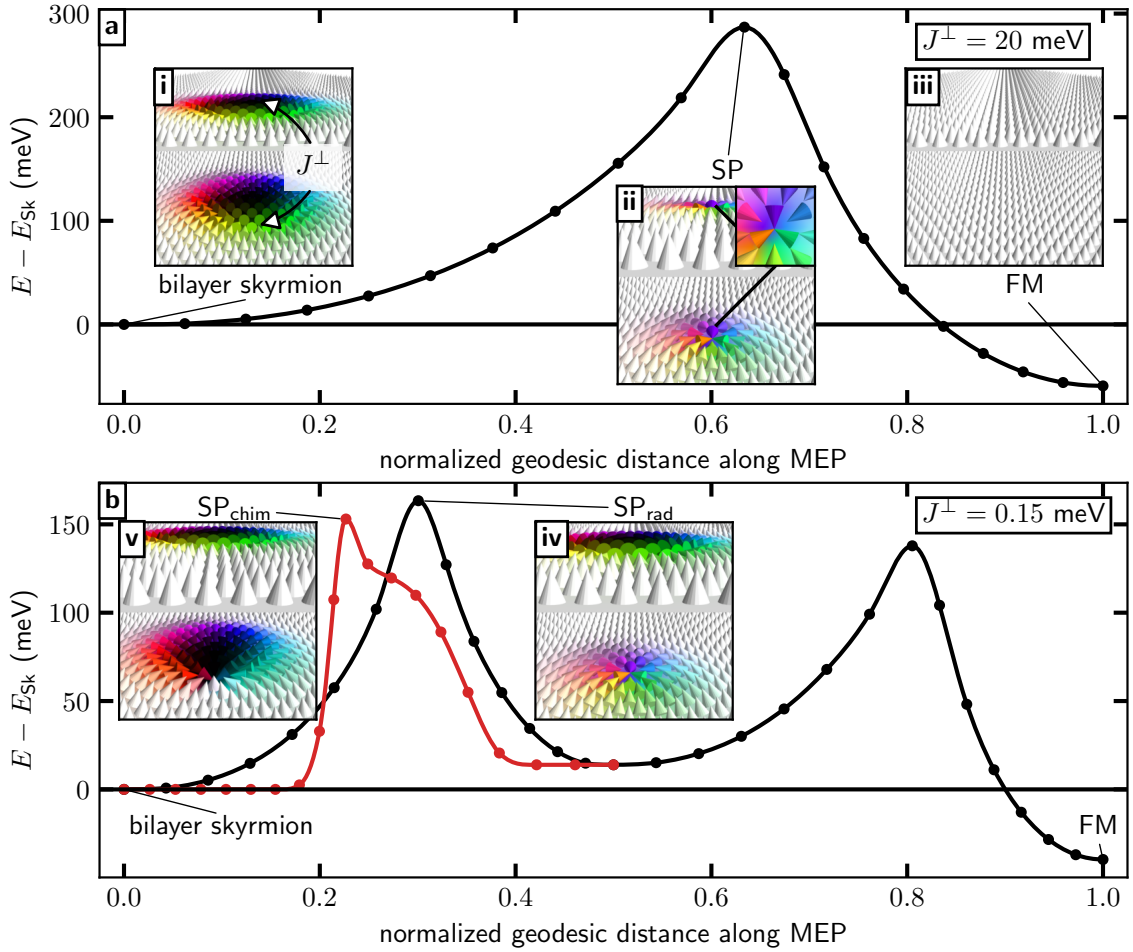


**Figure 1.7.** Energy relative to the energy of the skyrmion ($E_{\mathrm{Sk}}$) along the MEPs of skyrmion collapses for two values of the nearest neighbor interlayer exchange coupling, $J^\perp = 20$ meV in **a** and $J^\perp = 0.15$ meV in **b**, for a bilayer system based on the intralayer parameters of the magnetic layer of fcc-Pd/Fe/Ir(111) [43]. The geodesic distance along the MEP is normalized such that the bilayer skyrmion (**i**) corresponds to zero and the FM (**iii**) to one. Panel **a** shows a simultaneous collapse via the SP shown in **ii** and panel **b** shows two sequential collapse mechanisms of the skyrmions in the individual layers. The MEP associated to the lowest energy barrier is shown in red and corresponds to $\mathrm{SP}_{\mathrm{chim}}$ (**v**). This plot was generated for this thesis based on the data obtained in Paper I.

# 2 Methodological Developments

The identification of first-order SPs on the energy surface is paramount for systems hosting localized magnetic textures to assess their mutual transformations and estimate their lifetime by means of *harmonic transition state theory* (HTST) (cf. Sec. 1.3.4). This section presents an automated framework for single-ended SP searches systematically identifying them on the systems energy surface, which is designed to be executed repeatedly for a wide range of different metastable states, allowing seamless integration into global optimization methods and methods for evaluating long-timescale dynamics. The *saddle point search framework* (SPSF) is structured into stages (preprocessing, escape, convergence and postprocessing stage) (Fig. 2.1a) starting always with a configuration corresponding to a (local) energy minimum. Here, a comprehensive overview is provided discussing the key concepts but sparing out the details which can be found in Paper II and Paper. IV. As SP searches are computationally heavy, their development tries to fulfill the following objectives pareto-optimal: find a maximum number of distinct SPs, minimize the overall number of SP search attempts.

An application of the SPSF aims to identify the SPs representing the transition mechanisms of a given metastable state, which is in this work associated to a localized magnetic texture. The symmetry elements of this texture, which are calculated during preprocessing, define the fundamental domain – the smallest region containing unique physical information without repetition. The escape strategy is then determined by sampling points in the fundamental domain corresponding to centers of elliptical subsystems of the texture and generating diverse displacements acting on these subsystems. Thereby a sampling of points outside the convex region is generated, each yielding at least one negative eigenvalue of the Hessian (see Fig. 2.1c). The *geodesic minimum mode following* (GMMF) algorithm in the subsequent convergence stage then climbs in energy along the direction of the corresponding eigenvectors while minimizing the energy along all perpendicular degrees of freedom (Fig. 2.1d). The bottleneck of this approach is the repeated calculation of the minimal Hessian eigenmodes. In this work these are determined efficiently using the developed *Rayleigh quotient minimization* (RQM) algorithm enabling application to systems with many magnetic moments and dense Hessians. The successful attempts of the convergence stage correspond to various SPs. However, inevitably SPs are revisited (cf. Fig.2.1d) or SPs are obtained that essentially represent the same magnetic configuration, differing only by translations and/or global rotations. During postprocessing the redundant exemplars are filtered from the set of SPs using machine-learning cluster-techniques. From each cluster a single representative SP is drawn and the calculation of steepest descent paths reveals the connectivity to the initial minimum (Fig. 2.1e). Furthermore, also the adjacent energy minima are revealed representing other, possibly unknown, metastable states. The SPs obtained represent the transition mechanisms toward these adjacent states. If an SP is identified, which is not connected to the initial minimum, it is nev-

ertheless stored as it holds valuable information about other transitions on the energy surface. As depicted in Fig. 2.1a the individual escape and convergence attempts are independent of each other and are executed in parallel yielding a significant boost in the wall time of batches of SP searches.

## 2.1 Preprocessing stage

Each application of the SPSF is initialized with an energy minimum configuration that may include one or more localized magnetic textures (see Fig. 2.2a). During preprocessing the fundamental domain of each of these textures is calculated, which is determined by the symmetry elements of the corresponding texture (cf. Fig. 2.3f). Therefore, the preprocessing stage executes two tasks: the recognition and separation of the localized textures contained in the initial configuration and the computation of the symmetry operations under which each texture remains invariant. The first step is realized by calculating contours $\gamma_i$ associated to in-plane oriented magnetic moments (Fig. 2.2b), grouping them via density-based clustering algorithms [163, 164] (Fig. 2.2c) and defining a magnetic texture through the magnetic moments $\vec{m}_i$ at the lattice sites $\vec{r}_i$ which are located within an outer closed contour of a texture. This is presented in detail in Paper IV.

In Paper IV an algorithm was developed to calculate the symmetry elements of a spin point group $C_n$ or $D_n$ associated to a magnetic texture in a two-dimensional system. First, it is tested whether an $n$-fold rotation [Eq. (41)] of the texture around its center $\vec{c}$ [Eq. (39)] constitutes a symmetry operation. Practically the sites $\vec{r}_i$ and the magnetic moments $\vec{m}_i = \vec{m}(\vec{r}_i)$ of the texture are transformed using Eq. (41) and the rotated configuration is compared to the initial texture by calculating the geodesic distance [54] between both. If this distance is small the corresponding rotation operation is considered as a symmetry. For the exemplary texture in Fig. 2.2d a two-fold ($n = 2$) rotational symmetry was determined. Subsequently, a sector is defined which represents $1/n$-th of the texture (cf. red sector in Fig. 2.2). A transformation is applied to this sector that effectively stretches it around $\vec{c}$ with the result shown in Fig. 2.2e. This sector exhibits no rotational symmetry elements but either exactly one or no mirror symmetry elements. The candidate direction of a reflection axis can be computed via $\vec{p} = \vec{f}_2 - \vec{f}_1$, where $\vec{f}_1$ and $\vec{f}_2$ are fix-points of the mirror symmetry. Since Eq. (42) leaves the $z$-component of the magnetic moments invariant, e.g. Eq. 39 can be evaluated with regard to the magnetic moments and sites of the transformed sector to compute $\vec{f}_1$. For $\vec{f}_2$ the second moment of the distribution of the $z$-component of the magnetic moments of the sector is chosen as described in Paper IV. The candidate reflection axis $\vec{p}$ computed for the transformed sector correspond to $\vec{p}_1, \ldots, \vec{p}_n$ mirrors of the original texture shown in Fig. 2.2f, which can be obtained by reversing the transformation from the red sector in Fig. 2.2d to Fig. 2.2e. Finally a reflection operation [Eq. (42)] with respect to one of the axes $\vec{p}_i$ is applied to the texture to evaluate whether the operation constitutes a symmetry.

Paper IV explains how to obtain the fundamental domain for textures with symmetries corresponding to different spin point groups $C_n$ and $D_n$. For the example shown in Fig. 2.2f the fundamental domain corresponds to those magnetic moments $\vec{m}_i$ of the

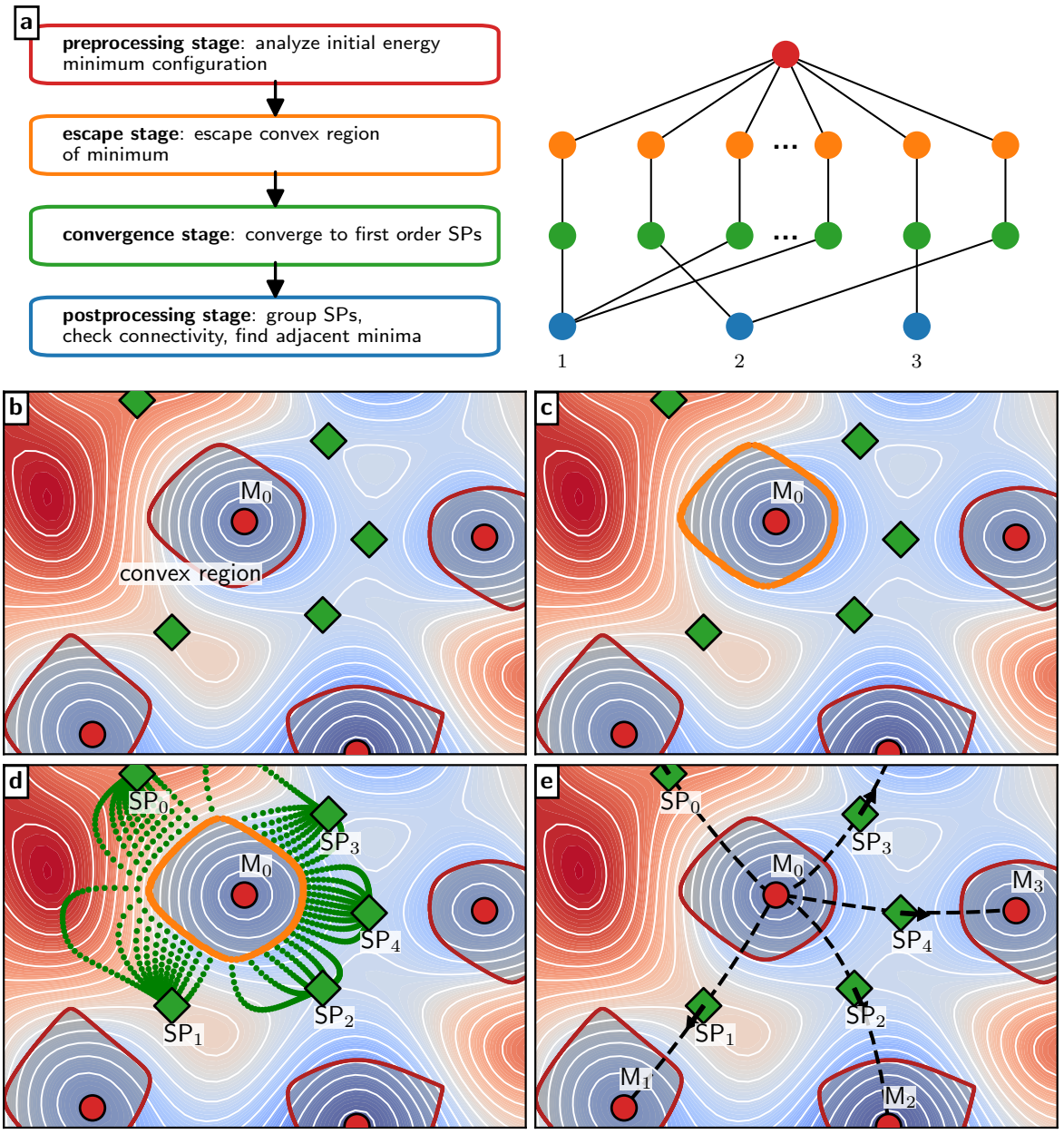


**Figure 2.1.** **a**: The SPSF is structured into stages. During preprocessing the initial energy minimum configuration $M_0$ (**b**) is analyzed to obtain information used in the subsequent escape stage (**c**), which creates a sampling of configurations (orange) near the boundary of the convex region surrounding the minimum. The convergence stage (**d**) aims to converge onto first order SPs (green) and the postprocessing stage (**e**) checks their connectivity to the initial minimum by calculating steepest descent paths (dashed black lines) and calculates the adjacent minima by displacement along the unstable mode (black arrows) and a subsequent energy minimization.

texture for which the angle of $\vec{r}_i$ with respect to the $x$-axis is larger than the angle of $\vec{p}_1$ but smaller than the angle of $\vec{p}_2$ to the $x$-axis. The above algorithm is presented in detail alongside with its mathematical description in Paper IV.

## 2.2 Escape stage

As described in Sec. 1.3.5 the GMMF method used in the convergence stage of the SPSF should not be initialized from within the convex region of a local minimum. The nontrivial task of the escape stage is to generate starting configurations for the convergence stage by sampling a diverse set of points outside the convex region of the initial minimum. The escape stage is a crucial part of the SPSF [63, 71], and its strategy must be chosen carefully so as to maximize the completeness of SP sampling. This section presents the escape stage proposed in this work.

The escape strategy relies on generating low-energy excitations within subsystems of a given localized texture. Each subsystem is defined as an elliptical region centered within the texture's fundamental domain. A set of subsystems is constructed by sampling the ellipse center, the lengths of the semi-axes, and the orientation of the major axis. This sampling ensures that physically nonequivalent regions of the texture are systematically explored. Note that some ellipses may extend beyond the fundamental domain. Importantly, at least one subsystem is chosen to encompass the entire texture, ensuring that deformations affecting the full texture are adequately captured. Fig. 2.3a shows a skyrmion bag state featuring two inner contours with a symmetry associated to $D_2$. Exemplary elliptical subsystems are centered within the fundamental domain, which may reach out to other parts of the texture.

The central idea is to iteratively displace the magnetic moments $\boldsymbol{m}^s$ within these subsystems along a diverse set of excitations. In principle, any displacement within the tangent space $\mathcal{T}_{\boldsymbol{m}^s}$ of the subsystem is admissible. However, there are several advantages to defining these displacements along the eigenvectors $\boldsymbol{v}_i^s$ of the subsystem Hessian $H^s$ that are associated with low-curvature directions. On the one hand, these eigenvectors lie in the tangent space of the subsystem by construction and form an orthogonal set, thereby reducing the likelihood that different displacement directions drive the system toward the same SP. On the other hand, eigenvectors corresponding to the lowest eigenvalues of $H^s$ naturally represent low-energy excitations of the subsystem. The partial Hessian $H^s$ is obtained by calculating the rows and columns of the full Hessian $H$ [cf. Eq. (22)] that correspond to the magnetic moments belonging to the subsystem. Examples of subsystem Hessian eigenvectors are shown in the lower right insets of Figs. 2.3b-d.

Thereby, during the escape stage a total of $N_{\text{esc}} = N_p \cdot N_E \cdot N_v \cdot 2$ escape trajectories are computed. These are generated by sampling $N_p$ points within the fundamental domain of the texture, defining $N_E$ elliptical subsystems for each point, and selecting $N_v$ subsystem eigenmodes, each of which is followed in both directions of the corresponding eigenvector. In practice, each escape trajectory is built iteratively. At every iteration, the magnetic moments within the subsystem are first displaced by a small step using the retraction defined in Eq. (24). The remaining degrees of freedom in the system are then relaxed using the *limited-memory Broyden-Fletcher-Goldfarb-Shanno* (L-BFGS)

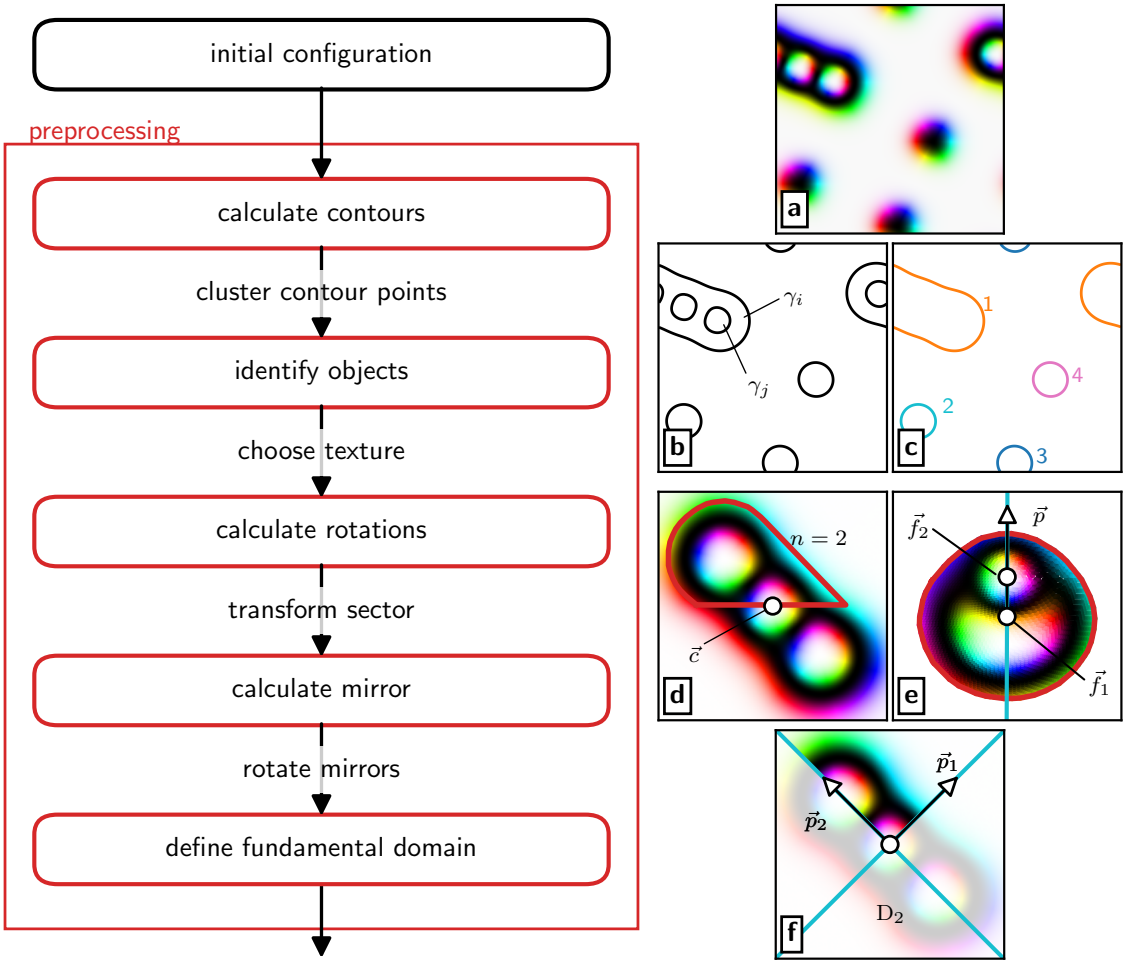


**Figure 2.2.** Flow of the preprocessing state through an exemplary application of the SPSF to the metastable magnetic state in part **a** obtained for a square lattice chiral magnetic with $L_D = 64a$, a magnetic field of $h = 0.65$ and DMI vector associated to $\beta = 30°$. The result of calculating the $m_z = 0$ contours is shown in **b**. Nested contours (e.g. $\gamma_j$) are excluded an the remaining contours are grouped sing a density-based spatial clustering each defining the outer boundary of a texture (**c**). **d**: Texture selected from **a** centered at the fix-point $\vec{c}$. A two-fold rotational symmetry is obtained and one of the domains is highlighted by a red surrounding. **e**: Selected sector in **d** transformed as described in the main text. The candidate reflection axis is calculated using two fix-points of Eq. $(42)$ $\vec{f}_1$ and $\vec{f}_2$. **f**: The obtained reflection axis yields $n = 2$ mirror axis $\vec{p}_n$. Thus, the texture corresponds to the symmetry group $\mathrm{D}_2$. The fundamental domain of the texture is highlighted and the remaining parts of the texture are grayed out. A similar version of this figure can be found in Paper IV.

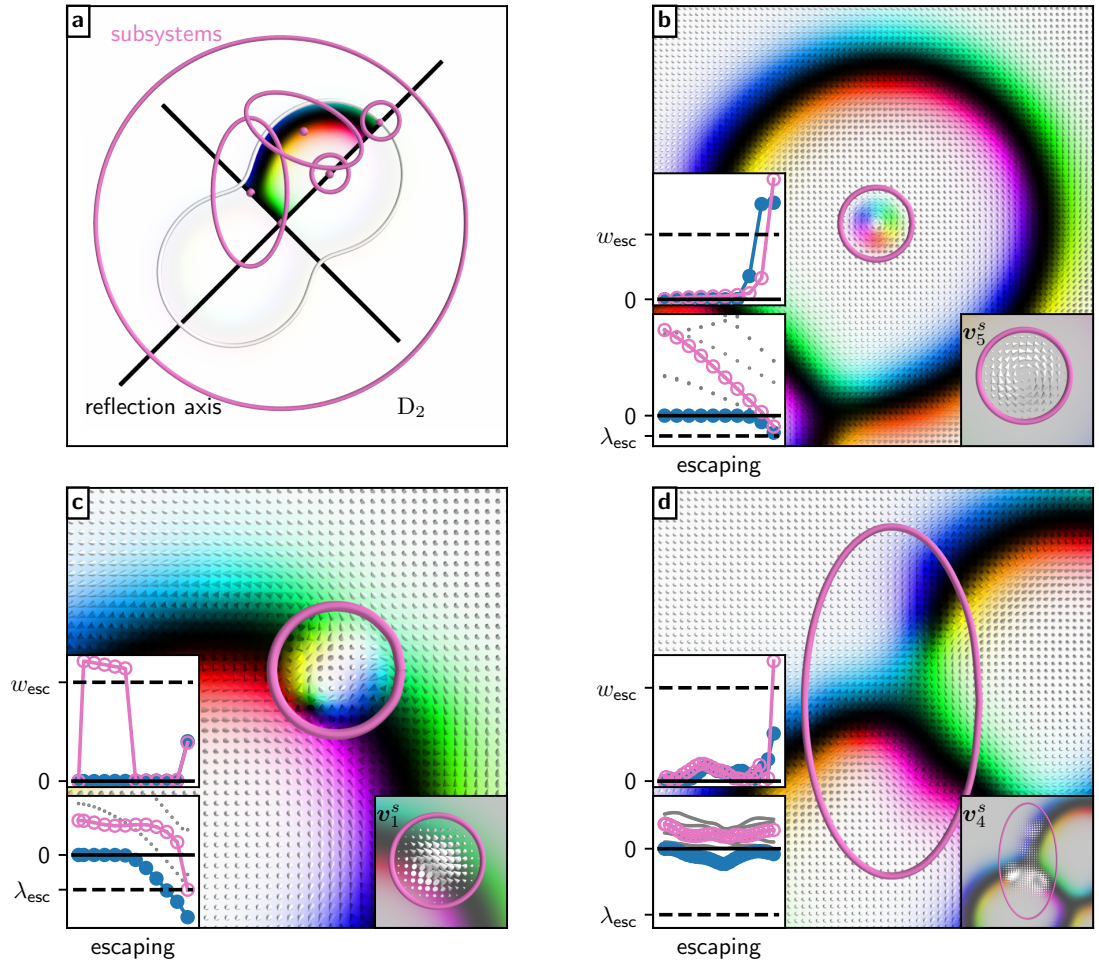


**Figure 2.3.** **a**: Metastable double-bag configuration with symmetry $D_2$ in a square lattice chiral magnet for a magnetic field of $h = 0.623$ and $L_D = 2\pi\mathcal{J}/\mathcal{D} = 24a$, where $\mathcal{J}$ and $\mathcal{D}$ are the continuous-theory exchange interaction and DMI parameter, respectively [cf. Eq. 17]. The fundamental domain is highlighted while the rest of the texture is grayed out. Examples of elliptical subsystems with centers in the fundamental domain are shown. For three of the subsystems **b**-**d** present the final configurations of exemplary escape attempts following certain subsystem eigenmodes ($\boldsymbol{v}_{S,5}$ (**b**), $\boldsymbol{v}_{S,1}$ (**c**), $\boldsymbol{v}_{S,4}$ (**d**)). The insets show the quantities of the subsystem (pink) and the full system (blue) relevant for the evaluation of the escape criterion (Eqs. (54),(55),(56)), here $w_{esc} = 0.25$ and $\lambda_{esc} = -0.1\mathcal{J}$.) during the escape process. The lower inset shows the eigenvalue of the followed subsystem eigenmode (open pink circles), the other subsystem eigenvalues (gray points) and the lowest eigenvalue of the full system Hessian (filled blue circles). Similarly the upper inset shows the alignment between the gradient and the minimum mode in the full system (blue) and in the subsystem (pink), respectively.

algorithm [165]. This relaxation, performed while keeping the subsystem configuration fixed, ensures a smooth magnetization profile across the subsystem boundary and avoids the emergence of artificial boundary artifacts. Furthermore, this guarantees that the full magnetic texture can adapt to the local perturbation introduced in the subsystem relaxing along all degrees of freedom associated to changes of the magnetization outside the subsystem. After the relaxation step, the subsystem eigenmode is recalculated and used as input for the next iteration.

Implementing an escape-stage strategy requires defining an escape criterion that evaluates whether the iterative displacements during an escape attempt are sufficient to proceed with the GMMF algorithm in the convergence stage. Starting from a minimum – where the energy surface exhibits strictly positive curvature – the lowest Hessian eigenvalue will eventually pass through zero and become negative, indicating that an inflection point has been crossed and the convex region has been left.

However, using only the condition $\lambda_1 < 0$ as the escape criterion entails the risk of re-entering the convex region during the subsequent convergence stage. This may occur because the GMMF force [cf. Eq. (53)] effectively reduces to an energy minimization if the alignment between the energy gradient $\boldsymbol{g}$ [cf. Eq. (21)] and the minimum mode $\boldsymbol{v}_1$ is weak. To avoid this issue, the following combined escape criterion is imposed:

$$\lambda_1 < 0, \tag{54}$$

$$\frac{|\boldsymbol{v}_1 \cdot \boldsymbol{g}|}{|\boldsymbol{g}|} \geq w_{\text{esc}}, \tag{55}$$

where the parameter $w_{\text{esc}}$ controls the required degree of alignment between the energy gradient and the minimum mode. Note, that this aligment is also a signature of valleys and ridges on the energy surface (cf. Sec. 1.3.5). Alternatively, a single escape condition may be employed:

$$\lambda_1 \leq \lambda_{\text{esc}}, \tag{56}$$

where the threshold $\lambda_{\text{esc}} < 0$ specifies how far the system must move beyond the convex region. This threshold is particularly important in high-dimensional systems, where configurations may possess zero modes for which excitations correspond to overcoming very small – but still finite – energy barriers. During the escape stage, such modes can acquire small negative eigenvalues, signaling proximity to an SP associated, for example, with a skyrmion translation [69, 55]. An appropriately chosen escape threshold filters out these uninteresting SPs efficiently.

However, controlling Eqs. (54),(55),(56) during the escape stage would require repeated calculations of the minimal eigenmodes of the full system Hessian. This is unnecessarily costly in terms of computational efficiency, since only the magnetic moments in a subsystem change significantly during the escape. In practice, it is sufficient to apply Eqs. (54), (55), or Eq. (56) to the subsystem. Mathematically, the partial Hessian $H^s$ is a compression of the full Hessian $H$. Cauchy's interlacing eigenvalue theorem [166] relates the eigenvalues $\lambda_\alpha^s$ of the subsystem Hessian to the eigenvalues $\lambda_\alpha$ of the full system, implying

$$\lambda_1 \leq \lambda_1^s \, . \tag{57}$$

Thus, checking $\lambda_1^s \leq \lambda_{\text{esc}}$ or $\lambda_1^s < 0$ provides a conservative and computationally efficient approximation for the corresponding full-system criteria in Eqs. (54) and (56). After a few iterations of the escape stage – during which the magnetic texture is perturbed only within the chosen subsystem – it is observed that the minimum mode of the full system becomes strongly localized in the same region. Its components outside the subsystem remain negligible, and the resulting eigenvector closely matches the minimum mode obtained from the subsystem calculation. Therefore, in practice, the alignment condition $|\boldsymbol{v}_1^s \cdot \boldsymbol{g}^s|/|\boldsymbol{g}^s| \geq w_{\text{esc}}$ is evaluated to test the escape criterion in Eq. (55), where $\boldsymbol{g}^s$ and $\boldsymbol{v}_1^s$ denote the subsystem energy gradient and subsystem minimum mode, respectively.

Consider the escape attempts of the double-bag state, for which the final configurations are shown in Fig. 2.1b–d. In Fig. 2.1b, the system is excited within a circular subsystem located inside one of the inner contours. During the escape process, the eigenvalue associated with the chosen subsystem eigenvector ($\boldsymbol{v}_{S,5}$) decreases and ultimately becomes the lowest eigenvalue of the subsystem, while the lowest eigenvalue of the full system remains smaller throughout. The alignment measures in both the subsystem and the full system exhibit a similar trend and increase sharply at the same point, indicating a successful escape according to Eqs. (54) and (55).

In the escape attempt shown in Fig. 2.1c, the subsystem is circular and located at the outer contour of the double-bag state, and the chosen eigenmode is $\boldsymbol{v}_1^s$. Here, the alignment between the subsystem gradient and minimum mode exceeds $w_{\text{esc}}$ already at the beginning of the escape process. However, since all subsystem eigenvalues are still positive at that time, Eq. (54) is not satisfied and the algorithm proceeds. Eventually, the eigenvalue corresponding to the followed eigenmode decreases sharply and becomes more negative than the escape threshold $\lambda_{\text{esc}}$, thereby fulfilling Eq. (56).

By contrast, for the elliptical subsystem and the chosen eigenmode $\boldsymbol{v}_4^s$ shown in Fig. 2.1d, Eq. (56) is never satisfied. Instead, the escape is detected through the alignment measure, which exceeds $w_{\text{esc}}$ [Eq. (55)] while the lowest subsystem eigenvalue is negative.

A detailed description an a flowchart of the escape stage algorithm can be found in Paper IV.

## 2.3 Convergence stage

Initialized with the final configurations of the escape stage, the convergence stage aims to locate first-order SPs by climbing the energy surface along one direction and simultaneously minimizing the energy along the perpendicular degrees of freedom. This is realized by the *geodesic minimum mode following* (GMMF) method, which was developed in Paper II. The GMMF algorithm presents a two-fold nested optimization problem. While the outer part, discussed in Sec. 2.3.1, probes the energy surface to locate first-order SPs, the inner part determines efficiently the minimal Hessian eigenmodes using the *Rayleigh quotient minimization* (RQM) method and is discussed in Sec. 2.3.2.

The applicability of the GMMF method is not limited to localized magnetic textures or two-dimensional systems. Thus, in Sec. 2.3.1 first the general concept of the GMMF

algorithm is presented, followed by the specific application to localized magnetic textures as employed within the SPSF featuring a subsystem-based variant of the GMMF method.

### 2.3.1 The GMMF method

The *geodesic minimum mode following* (GMMF) algorithm is guided by the GMMF force representing the basic idea of the method: transform the problem of locating SPs into the simpler task of gradient-based minimization. In each iteration $k$ of the algorithm a search direction $\boldsymbol{\chi}^k$ is computed, which is based on the GMMF force rewritten here for convenience [cf. Eq. (53)]:

$$\boldsymbol{f}(\boldsymbol{m}^k) = -\boldsymbol{g}^k + 2(\boldsymbol{g}^k \cdot \boldsymbol{q}^k)\boldsymbol{q}^k \ ,$$

where $\boldsymbol{g}^k = \boldsymbol{g}(\boldsymbol{m}^k)$ and $\boldsymbol{q}^k = \boldsymbol{q}(\boldsymbol{m}^k)$ are the energy gradient and the inversion mode at the current configuration $\boldsymbol{m}^k$, respectively. By construction $\boldsymbol{f}(\boldsymbol{k}^k)$ is in the tangent space $\mathcal{T}_{\boldsymbol{m}^k}$. To compute the search direction $\boldsymbol{\chi}^k \in \mathcal{T}_{\boldsymbol{m}^k}$ a quasi-Newton *limited-memory Broyden-Fletcher-Goldfarb-Shanno* (L-BFGS) solver [167] is used, which uses the forces and search directions computed at previous iterations (memory) to approximate an effective second-order derivative. The magnetic configuration is then moved along the search direction taking into account the geometry of the configuration space by using the retraction defined in Eq. (24). Importantly, the L-BFGS solver requires forces and search directions anchored in the tangent space of the configurations of previous iterations. Therefore, these quantities are moved toward the tangent space of the current iterate using the concept of parallel transport as denoted in Eq. (25). This process is repeated until an first-order SP is reached, which is a stationary point ($\boldsymbol{g} = 0$) with one and only one negative Hessian eigenvalue. The convergence criterion thereby reads

$$\max_{i\in\{1,\dots,N\}} |\vec{f}_i| \leq c_{\text{conv}}, \quad \lambda_1 < 0, \quad \text{and} \quad \lambda_2 \geq 0 \ , \tag{58}$$

where $c_{\text{conv}}$ is a small numerical threshold. Satisfying Eq. (58) represents a successful attempt of the convergence stage. However, the inversion mode can become orthogonal to the energy gradient (see perpendicular hypersurfaces in Fig. 1.6). In this case the GMMF force equals the conventional force and the algorithm resembles an energy minimization along all degrees of freedom leading toward a convex region. Such a reentrance into a convex region marks the failure of an convergence attempt and can be identified during the algorithm testing whether the lowest eigenvalue $\lambda_1$ turns positive.

#### Choice of the inversion mode

Since a first-order SP is located within a valley characterized by a single ascending direction along the minimum mode, typically and always toward the end of the GMMF calculation the inversion of the force component is carried along the direction of the minimum mode: $\boldsymbol{q} = \boldsymbol{v}_1$. Thereby, in its final phase the GMMF algorithm climbs in energy along the direction of the unstable mode.

However, during the GMMF optimization situations may appear in which it is beneficial to use $\boldsymbol{q} = \boldsymbol{v}_2$ for limited number of iterations. For example a crossing of the two lowest Hessian eigenvalues can occur. Effectively, this leads to an abrupt change in the GMMF force. Most of the times the method still converges to an SP after such a

crossing. However, repetitive mode-crossing events can occur if the two, almost degenerate, eigenmodes describe completely different changes to the magnetic texture and this can prevent the method from converging. In these cases staying on the previous inversion mode, which then corresponds to the eigenvector $\boldsymbol{v}_2$, removes this unwanted behavior. Afterward, inevitably a second mode-crossing between the two lowest eigenvalues occurs since the GMMF force relaxes the magnetic texture along the $\boldsymbol{v}_1$ degree of freedom. Thus, ultimately the GMMF algorithm always uses $\boldsymbol{q} = \boldsymbol{v}_1$. Examples for such situations can be found in Paper II and Paper IV.

### A subsystem variant of the GMMF method

The performance of the convergence stage of the SPSF can be further improved by applying the GMMF method to the subsystems defined in the escape stage (cf. Sec. 2.2). In this *subsystem-based GMMF* (S-GMMF) approach, only the magnetic configuration within the subsystem is iteratively updated according to Eq. (53), whereas the rest of the system is relaxed after each iteration. The convergence to a subsystem-constrained SP is signaled if Eq. (58) is satisfied for the subsystem quantities, i.e. the maximum component of the GMMF force drops below a threshold $c^s_{\mathrm{conv}}$ while $\lambda^s_1 < 0$ and $\lambda^s_2 \geq 0$. Computing the inversion mode for a subsystem is substantially cheaper than for the full system. At the same time, the subsystem-constrained SP obtained with S-GMMF is often already close to the true SP of the full system, enabling the subsequent full-system GMMF calculation to converge rapidly. This formulation significantly reduces the total computational cost of the convergence stage compared with applying GMMF to the full system immediately after the escape stage. A further advantage of the S-GMMF method is that, by constraining the SP search to the same subsystems used during the escape stage, it strengthens the correspondence between escape-stage excitations and the SPs that are eventually identified. This makes SP sampling more systematic. Each S-GMMF attempt is followed by a full-system GMMF calculation initialized with the final configuration obtained from the S-GMMF run –even in cases where S-GMMF does not produce a subsystem-constrained SP. S-GMMF may fail to converge if the chosen subsystem is too small. In such cases, the method typically relaxes back into a convex region of the subsystem, indicated by $\lambda^s_1 \geq 0$. However, due to Cauchy's interlacing eigenvalue theorem, this does not necessarily imply that the configuration lies in a convex region of the full system. The subsequent full-system GMMF calculation often still converges to an SP.

Fig. 2.4 visualizes the convergence stage calculations corresponding to the escape attempts of the double-bag state shown in Fig. 2.3. Consider in particular the escape attempt displayed in Fig. 2.3c, which serves as the initial configuration for the convergence stage calculation discussed in the following. As shown in Fig. 2.4a, during the S-GMMF phase the lowest subsystem eigenvalue $\lambda^s_1$decreases, while $\lambda^s_2$ becomes positive. Once the GMMF force in the subsystem drops below the convergence threshold $c_{\mathrm{conv}}$ for the configuration illustrated in the inset of Fig. 2.4b – indicating proximity to a subsystem-constrained SP – the full-system GMMF refinement is initiated. This second phase brings the system with high accuracy to the SP shown in Fig. 2.4b, characterized by a single negative eigenvalue $\lambda_1$ and a zero mode $\lambda_2$.

The S-GMMF algorithm may also terminate with a re-entrance into a convex region of the subsystem configuration space, indicated by $\lambda^s_1 \geq 0$. Such a situation arises in

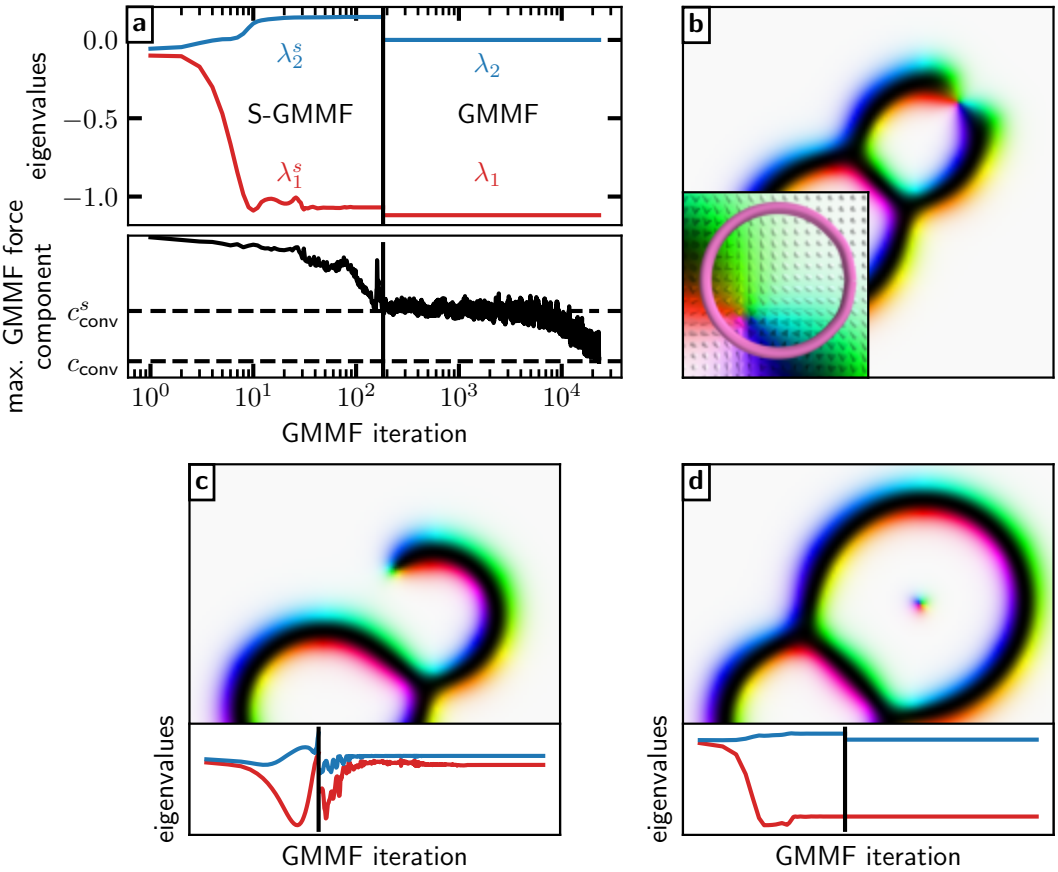


**Figure 2.4.** **a**: The two lowest eigenvalues of the subsystem Hessian (left to the vertical black line) and full system Hessian (right to the black line) during the convergence stage of the subsystem-based SPSF for the concrete example of the escape attempt shown in Fig. 2.3c. The maximum component of the gradient is plotted below. The black line indicates the switch from the subsystem GMMF to the full system GMMF. **b**: SP configuration associated to the final iteration shown in **a**. The inset shows the corresponding configuration at the end of the subsystem GMMF. **c**,**d**: SP configurations obtained in the convergence attempts associated to the escape attempts shown in Figs. 2.3d,b, respectively. A visualization analogue to **a** for these attempts is shown in the insets.

the convergence stage of the escape attempt shown in Fig. 2.3d. The inset of Fig. 2.4c illustrates how both subsystem eigenvalues become positive toward the end of the S-GMMF phase. Importantly, this does not imply that the corresponding configuration has re-entered a convex region on the full-system energy surface, since Cauchy's interlacing theorem guarantees $\lambda_1 \leq \lambda_1^s$. As a result, the full-system GMMF refinement still converges successfully onto the SP displayed in Fig. 2.4c. For completeness, the convergence-stage simulation for the escape attempt shown in Fig. 2.3b is presented in Fig. 2.4d. Notably, all three SPs depicted in Figs. 2.4b–d correspond directly to local transformations of the magnetic texture introduced during the escape stage, underscoring the systematic and targeted nature of the escape strategy.

### 2.3.2 Rayleigh Quotient Minimization

The repeated computation of at least the two[9] lowest eigenvalues $\lambda_\alpha$ and corresponding eigenvectors $\boldsymbol{v}_\alpha$ of the Hessian $H$ represents the bottleneck of the GMMF algorithm. An explicit calculation of $H$ is not feasible for large systems with many magnetic moments or systems with long-range interactions yielding a dense Hessian matrix. In Paper II a method based on the minimization of the generalized Rayleigh quotient is presented, that allows the efficient computation of the minimal modes without explicitly calculating the Hessian matrix.

Consider a magnetic configuration $\boldsymbol{m}$, which can be thought of as the current configuration of the GMMF algorithm, and its associated Hessian $H$. The goal is to determine the two-dimensional subspace of the tangent space of $\boldsymbol{m}$ which corresponds to the two lowest eigenvalues of $H$. This can be achieved by defining the objective using the generalized Rayleigh quotient

$$R(X) = \mathrm{tr}(X^T H X) \ , \tag{59}$$

where $X$ is a $2N \times 2$ matrix with two orthonormal columns. For each distinct matrix $Y \in \mathbb{R}^{2N\times 2}$ with $Y \neq X$ which orthonormal columns span the same subspace as $X$ the Rayleigh quotient yields the same value $R(Y) = R(X)$. Therefore, the Rayleigh quotient is defined on the Grassmann manifold, which parametrizes all two-dimensional subspaces of $\mathcal{T}_{\boldsymbol{m}}$ [124]. The specific subspace containing the two minimal Hessian eigenmodes is spanned by the columns of $X_{\mathrm{min}}$, where $X_{\mathrm{min}}$ yields the minimum of $R$ [121]. In Paper II the *Rayleigh quotient minimization* (RQM) method is presented which finds the solution $X_{\mathrm{min}}$ of this minimization problem using the gradient of the Rayleigh Quotient

$$\nabla R(X) = 2[HX - X(X^T H X)] \tag{60}$$

embedded in an L-BFGS optimization scheme. Note, for the concrete implementation the concepts of retraction and parallel transport have to be applied on the Grassmannian [121].

After $X_{\mathrm{min}}$ has been determined the corresponding eigenvectors are obtained from $\boldsymbol{v}_\alpha = U X_{\mathrm{min}} \tilde{\boldsymbol{v}}_\alpha$ with

$$(X_{\mathrm{min}}^T H X_{\mathrm{min}}) \tilde{\boldsymbol{v}}_\alpha = \lambda_\alpha \tilde{\boldsymbol{v}}_\alpha \ . \tag{61}$$

In summary there are two reasons why the RQM method is ideally suited to be used as the eigensolver within the GMMF algorithm:

- **Optimal initialization**: Between two iterations of the GMMF algorithm the lowest subspace of the Hessian only changes gradually as schematically shown in Fig. 2.5. Thus, the solution for $X_{\mathrm{min}}^k$ of the current GMMF iterate can be used to initialize the RQM method for the next GMMF iteration determining $X_{\mathrm{min}}^{k+1}$ within just a few iterations.

[9] Characterizing a first-order SP requires evaluating $\lambda_1 < 0$ and $\lambda_2 \geq 0$. Furthermore, mode-crossings can only be identified and taken care of if the two lowest modes are computed (cf. Sec. 2.3.1).

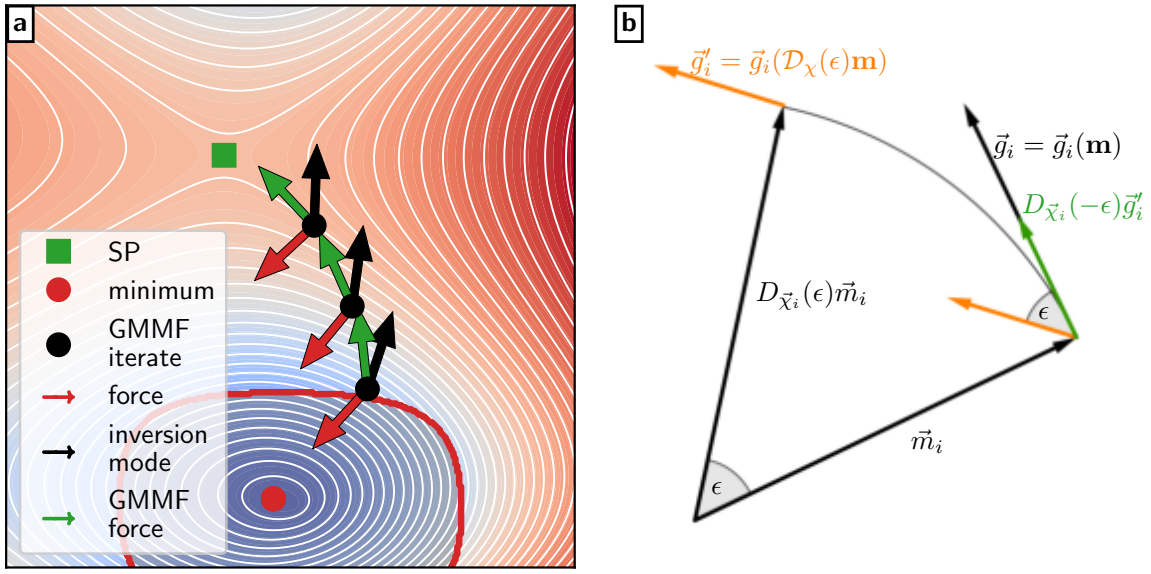


**Figure 2.5.** **a**: Schematic two-dimensional energy surface with one minimum (red) and one SP (green). An GMMF calculation is launched close to the boundary of the convex region (red). The force (red), the GMMF force (green) and the inversion mode (black) are shown by the arrows attached to the points (black) during the GMMF algorithm. **b**: Illustration of the quantities involved in calculating the action of the Hessian in finite-difference approximation for a single magnetic moment $\vec{m}_i$ with a displacement parameter $\epsilon$. The finite-difference along a direction $\vec{\chi}_i$ is computed by calculating the gradient $\vec{g}_i$ (black) at $\vec{m}_i$ and the gradient $\vec{g}_i'$ (orange) at a rotated (retracted) magnetic moment $D_{\vec{\chi}_i}(\epsilon)\vec{m}_i$. Parallel transport ($D_{\vec{\chi}_i}(-\epsilon)\vec{g}_i'$) is applied to ensure both gradients are within the same tangent space to calculate the finite difference.

- **No explicit Hessian needed**: The Rayleigh Quotient Eq. (59) as well as its gradient [Eq. (60)] only depend on matrix-vector multiplications $H\boldsymbol{x}$, where $\boldsymbol{x}$ is a column of X. Using the finite-difference scheme of the energy gradient explained below, this product can be estimated without the need for an explicit calculation of $H$.

### The action of the Hessian matrix

The product $H\boldsymbol{x}$ can be efficiently calculated using a finite-difference approximation of the energy gradients. The idea is the following: Displace the magnetic configuration $\boldsymbol{m}$ along the direction $\boldsymbol{x}$ by a small step $\epsilon$ and calculate the energy gradient $\boldsymbol{g}(\boldsymbol{m}')$ for the displaced configuration $\boldsymbol{m}'$. Note that these displacements should be defined by retractions representing rotations to take the curvature of the configuration space into account (cf. Sec. 1.3.2). The difference between $\boldsymbol{g}(\boldsymbol{m}')$ and the gradient $\boldsymbol{g}(\boldsymbol{m})$ of the original configuration $\boldsymbol{m}$ yields the curvature information of the energy surface along the direction $\boldsymbol{x}$, which corresponds to the product $H\boldsymbol{x}$.

Practically, these gradients are anchored in the different tangent spaces and the direction $\boldsymbol{x} \in \mathbb{R}^{2N}$ is defined in local tangent space basis $\mathcal{T}_{\boldsymbol{m}}$. To avoid frequent basis changes the direction is represented in embedding space using $\boldsymbol{\chi} = U\boldsymbol{x}$ and the gradient $\boldsymbol{g}(\boldsymbol{m}')$ is parallel transported to $\mathcal{T}_{\boldsymbol{m}}$. A forward finite-difference scheme for a small displacement $\epsilon$ reads [cf. Eq. (25)]:

$$H\boldsymbol{x} \approx U^T \frac{\mathcal{D}_{\vec{\chi}}(-\epsilon)\boldsymbol{g}(\boldsymbol{m}') - \boldsymbol{g}(\boldsymbol{m})}{\epsilon} \,, \tag{62}$$

where $\boldsymbol{m}' = \mathcal{D}_{\boldsymbol{\chi}}(\epsilon)\boldsymbol{m}$ and $U^T$ projects the action of the Hessian to the local basis representation of $\mathcal{T}_{\boldsymbol{m}}$. Fig. 2.5 schematically illustrates this computation for a single magnetic moment.

### Scaling of the computational effort

The computational cost of the RQM method is dominated by evaluating the gradient of the Rayleigh quotient, $\nabla R$. Figure 2.6 shows how the performance of computing Eq. (60) scales with the number $N$ of magnetic moments in a cubic system, both with and without magnetostatic interactions. The scaling behavior reflects the nature of the underlying interactions: in the absence of magnetostatics, the cost increases linearly with system size, $\mathcal{O}(N)$. When magnetostatic interactions are included, the computation scales as $\mathcal{O}(N \log N)$, as expected from the use of FFT-based methods. While the distinction between linear and $\mathcal{O}(N \log N)$ scaling is subtle in the current system size range, the data remain consistent with the expected behavior. Importantly, the RQM algorithm itself does not introduce any additional scaling overhead beyond that associated with computing the system's energy and its gradient. This makes the method well suited for large-scale applications, including systems with long-range interactions.

## 2.4 Postprocessing

Consider again the SPSF application to the double bag state shown in Figs. 2.3,2.4. Upon completion of one run of the SPSF, the SPSF yields a graph as shown in Fig. 2.7

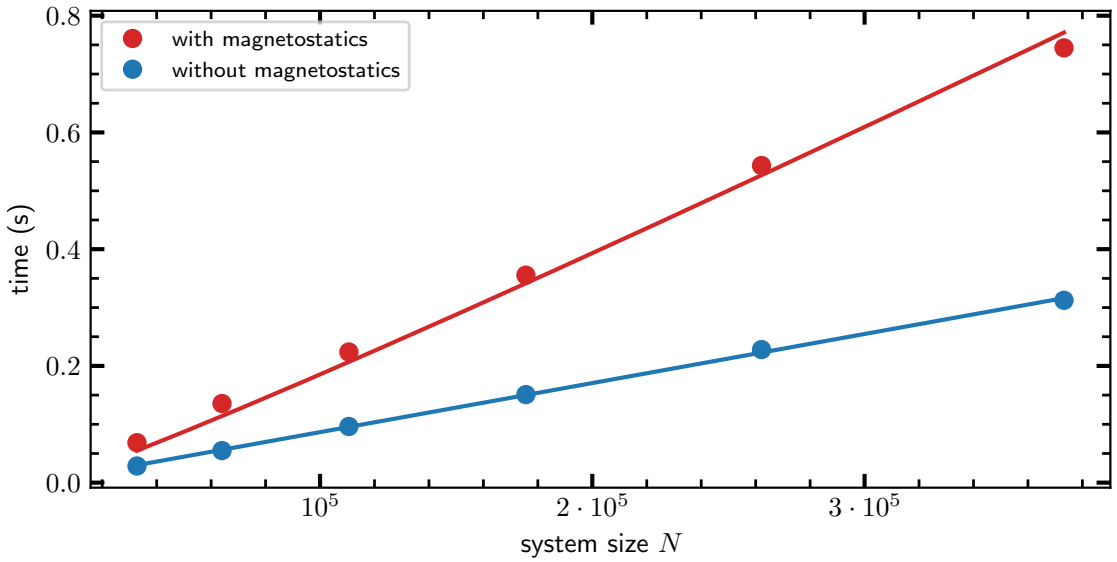


**Figure 2.6.** Mean CPU time required for a single evaluation of the Rayleigh quotient gradient $\nabla R(X)$ [see Eq. (60)] as a function of the number of magnetic moments $N$ in a cubic system with and without magnetostatic interactions, as indicated in the legend. The blue (red) line shows the linear $(N \log N)$ fit. The remaining interaction parameters are nearest neighbor exchange $J_1 = 1$ meV, Bloch-type nearest neighbor DMI $D_1 = 0.45$ meV and an applied field of $B = 2.8$ T. Figure modified from Paper II with permission from APS.

providing information about the SPs representing transition mechanisms (green) and adjacent energy minima (red). To extract the information for this final result of the SPSF postprocessing is needed as described in the following.

Different SP searches may converge to SPs that correspond to essentially the same magnetic configuration, differing only by a translation or a global rotation of the texture. As a result, the list of SPs obtained during the convergence stage can contain considerable redundancy. The purpose of the postprocessing stage is to eliminate this redundancy, producing a unique set of distinct saddle points, and to embed these SPs within a state network by identifying their adjacent energy minima.

The first task is approached by cluster algorithms like affinity propagation [168] or k-means [169] from the field of unsupervised learning as implemented in modern machine learning libraries [170] (see Paper II). Secondly, from each of the groups containing equivalent SPs one representative is selected to compute the connectivity. This SP is displaced slightly forward and backward along the eigenvector of its unstable mode and a Heun solver is used to calculate steepest descent paths revealing two energy minima. If one of the minima is the initial minimum the SPSF was applied to, the corresponding SP is considered as *connected*. The unconnected SPs are nevertheless stored since they represent information about metastable states and transitions important for later runs of the SPSF applied to different minima.

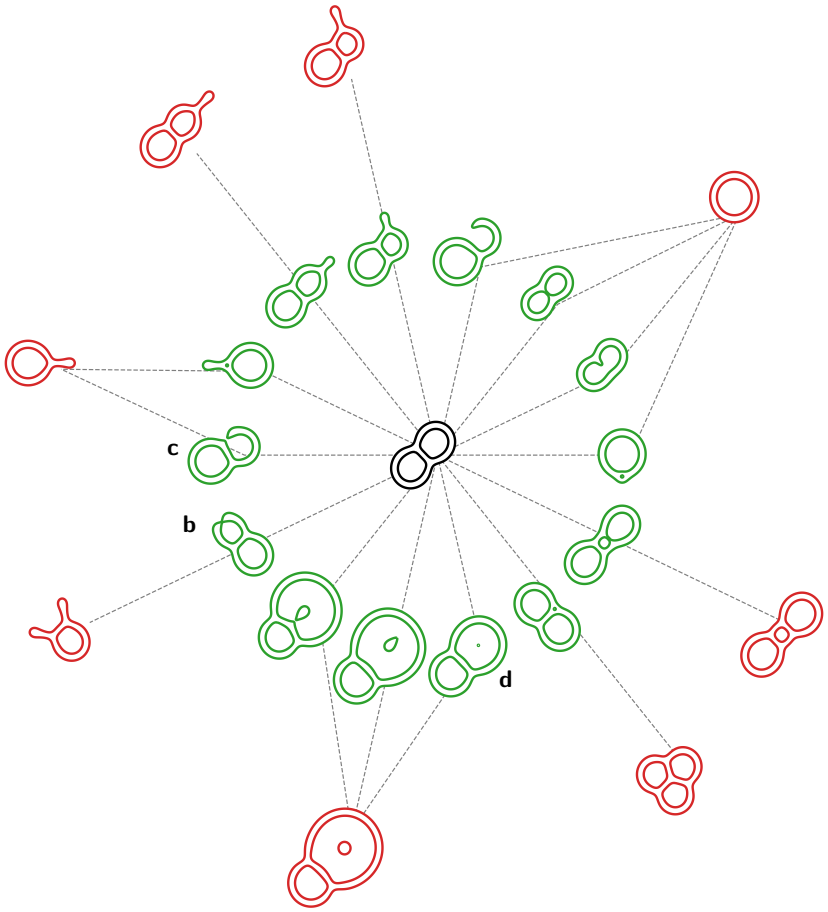


**Figure 2.7.** Schematic graph visualization of the result of an application of the SPSF to the double-bag state (black) represented by its $m_z = 0$ contour curves. The identified SPs are shown in green whereas the revealed adjacent energy minima are shown in red. The specific SPs shown in Figs. 2.4b,c,d are highlighted.

# 3 Applications

This section presents the key results of the application of the developed *saddle point search framework* (SPSF) to chiral magnets (Paper II and Paper IV) and ultrathin transition-metal films (Paper III).

In Sec. 3.1 the rich energy surface of two-dimensional chiral magnets is systematically explored using the SPSF. Sec. 3.2 demonstrates the application of the developed methodology to three-dimensional chiral magnets featuring long-range dipole-dipole interactions. Finally, Sec. 3.3 discusses the effect of *higher-order exchange interactions* (HOI) on the lifetimes of skyrmion and antiskyrmions in the materials fcc-Pd/Fe/Ir(111) and fcc-Pd/Fe/Rh(111). In Paper I the double-ended GNEB method was applied to skyrmions in systems comprising several magnetic layers. The corresponding main results are presented in Sec. 3.4.

## 3.1 Transformations between topological magnetic textures in two-dimensional chiral magnets.

In this section, the developed *saddle point search framework* (SPSF) is applied to a two-dimensional square-lattice chiral magnet that includes exchange interactions, DMI, and an external magnetic field $\vec{B} = B\hat{z}$ perpendicular to the film surface [cf. Eq. (2)], as presented in Paper IV. In the continuum limit, this system is described by Eq. (17). To improve the correspondence between the lattice Hamiltonian and continuous-theory – while simultaneously avoiding higher-order spatial derivatives of the magnetization – the parameters of Eq. (2) are chosen such that the higher-order terms vanish [171, 172], as detailed in App. B. All model interaction parameters can be expressed in terms of the continuous-theory exchange parameter $\mathcal{J}$, the equilibrium period of chiral modulations at the ground state $L_D = 2\pi\mathcal{J}/\mathcal{D}$ and the saturation field $B_D = \mathcal{D}^2/(M_S\mathcal{J})$, where $\mathcal{D}$ is the continuous-theory DMI parameter. For a square lattice with lattice constant $a$, this yields the following expressions for the bilinear interactions:

- Exchange: $J_1 = \frac{4}{3}\mathcal{J}$, $J_2 = 0$ and $J_3 = -\frac{1}{12}\mathcal{J}$.
- DMI: $D_1 = \frac{8\pi}{3L_D}a\mathcal{J}$, $D_2 = 0$ and $D_3 = -\frac{2\pi}{3L_D}a\mathcal{J}$.

The magnetic field $B = hB_D$ is chosen by the dimensionless parameter $h$ and the magnetic moment $\mu$ relates to the saturation magnetization by $\mu = M_S a^2$.

Magnetic textures emerging as metastable states for the above model can take a wide variety of forms. Nevertheless, any isolated texture can be described in terms of three fundamental building blocks: closed contours, chiral kinks and tails (cf. Sec. 1.3.3). Various combinations of these elementary building blocks yield a surprisingly large diversity of configurations that can be obtained [35, 36, 68]. Whether a given con-

figuration corresponds to a true energy minimum ultimately depends on the specific parameters of the Hamiltonian. Unless stated otherwise, in this section the external magnetic field is set to $h = 0.623$, for which closed contours, chiral kinks and tails can be present as components of meta-stable textures [173] and the $L_D$-parameter is set to $L_D = 40a$.

Figs. 3.1a-d present exemplary SPSF runs each initialized with one of the following four metastable configurations: a chiral droplet (Fig. 3.1a), a skyrmion bag (Fig. 3.1b), a bag with two inner contours (Fig. 3.1c), and a chiral droplet featuring an additional tail (Fig. 3.1d). These configurations are shown in the center of Figs. 3.1a-d. The identified SPs (green) and the corresponding adjacent energy minimum configurations (red) are visualized by their respective contours. Each SP corresponds to an edge and each energy minimum to a node. Thereby a region of the energy surface is mapped onto a graph. These graphs, generated using the SPSF, can be linked together to construct a network of metastable states, enabling a global exploration of the energy surface, as demonstrated in Fig. 8 of Paper IV.

In general, all textures can be classified according to their integer topological charge [cf. Eq. (30)], i.e., $Q = -1$, $Q = 0$, $Q = 1$ and $Q = 2$, as illustrated in Fig. 3.1 by the color of the background-circle for each texture. The topology of a given texture is uniquely determined by its combination of closed contours and chiral kinks, as described in Sec. 1.3.3. Transformations associated with an SP between two metastable localized magnetic textures fall into two categories: those that preserve the topological charge (homotopies) and those that change it. Whenever an SP connects two states belonging to different topological classes, a pronounced canting of the magnetic moments necessarily occurs at some point during the transformation. This strong noncoplanarity is tied to large exchange-energy costs and therefore often appears for the highest-energy point along the *minimum energy path* (MEP) – the SP itself. A local measure of this noncoplanarity is the scalar spin chirality [cf. Eq. (38)]. In Fig. 3.1, the location within each SP configuration where the spin chirality reaches its maximum value is marked.

Considering all SPs identified through repeated applications of the SPSF, five distinct categories of SPs can be identified:

- Nucleation of a chiral kink
- Formation of a closed contour via injection of a Bloch point–like defect
- Merging of two contours
- Formation of a tail
- Merging of two contours accompanied by the nucleation of a chiral kink

Examples of SP configurations from each category are shown in Fig. 3.2b-f. When the winding of the magnetization is locally changed along the texture's contour, a chiral kink forms (see Fig. 3.2b). Within this kink, the magnetic moments exhibit a rotation sense opposite to the system's intrinsic chirality. Because the energy model in this section lacks anisotropy, only positive chiral kinks with a contribution of $+1$ to the contour winding number appear in metastable textures [36]. Thus, this SP category entails transformations with $\Delta Q = +1$.

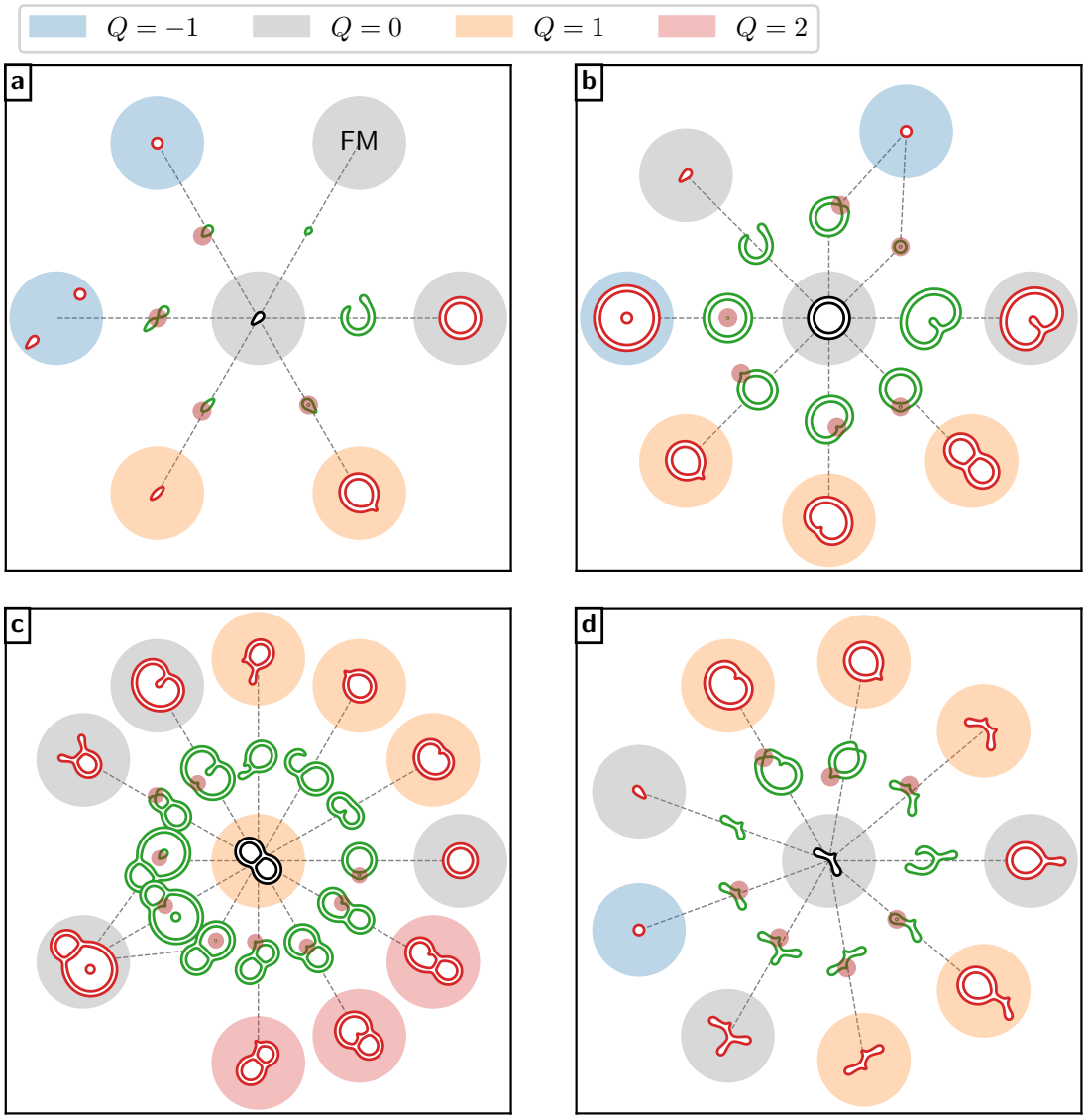


**Figure 3.1.** Schematic graph visualization of results of runs of the SPSF applied to four metastable states in a square lattice chiral magnet with a magnetic field of $h = 0.623$ and $L_D = 40a$. The energy minima are shown in the center of **a**-**d** and are associated to the chiral droplet (**a**), the skyrmion bag (**b**), the bag with two inner contours (**c**) and the droplet with an additional tail (**d**). Each configuration is represented by its $m_z = 0$ contours. SPs are drawn in green and energy minimum configurations corresponding to adjacent states are shown in red. Each state is drawn within a colored circle according to its topological charge $Q$ (see legend). For the SPs describing a transformation where the topological charge is not conserved, the location of maximum scalar spin chirality [cf. Eq. (38)] is marked by a small transparent red circle. See Fig. 8 in Paper IV for a visualization of the global exploration of the energy surface represented by a network combining such graphs.

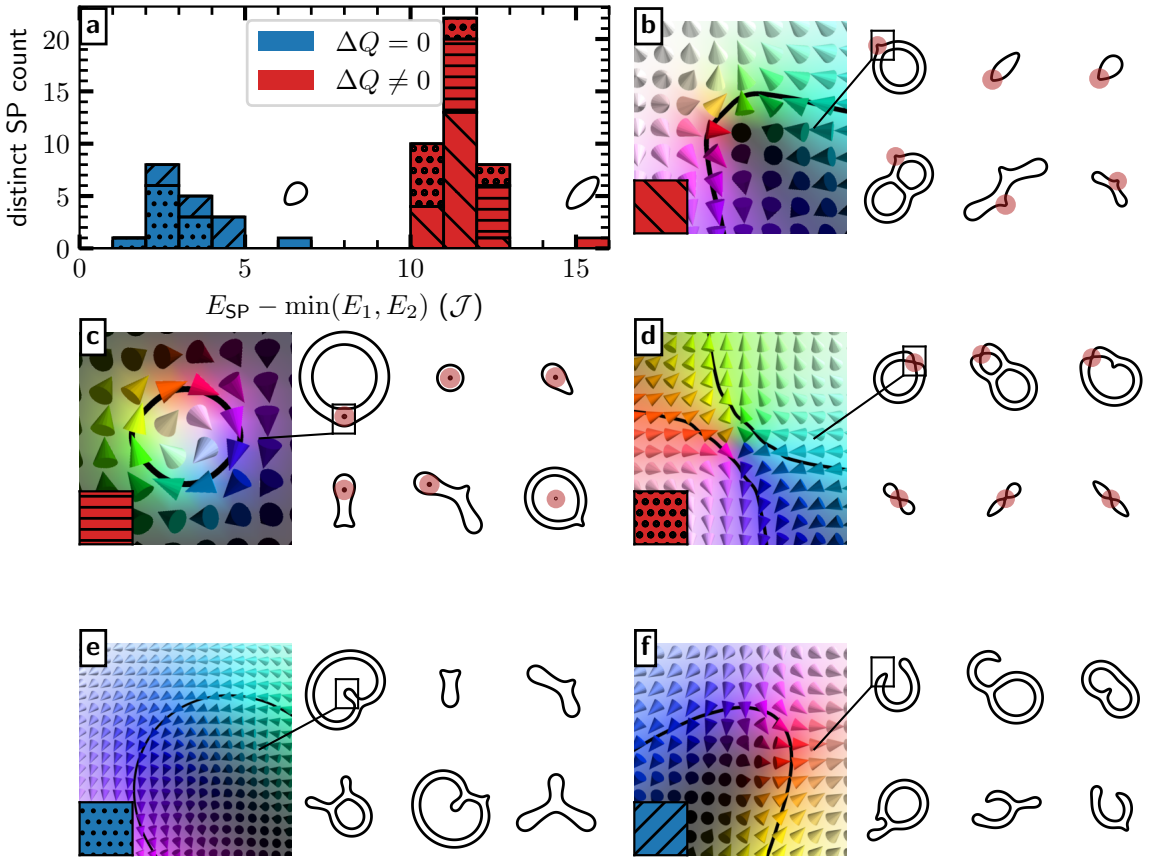


**Figure 3.2.** **a**: Histogram of all SPs identified by the SPSF in Paper IV, sorted by their associated energy barriers, defined with respect to the lower-energy endpoint of each transition, $\min(E_1, E_2)$, and expressed in units of the continuous-theory exchange parameter $\mathcal{J}$. Homotopies are shown in blue and transformations where the topological charge is changing are shown in red. The shading indicates the specific subcategory of the transition (see text): chiral kink nucleation (**b**), closed contour formation via Bloch point-like defect (**c**), merging of two contours (**d**), formation of a tail (**e**), and contour merging accompanied by the nucleation of a chiral kink (**f**). For each subcategory, six representative SPs are displayed. The SPs corresponding to the annihilation of the droplet (antiskyrmion) into the ferromagnetic state are shown in **a** above the respective bars in the histogram. A similar figure is presented in Paper IV.

In contrast to chiral kink nucleation, the formation of an additional closed contour through the injection of a Bloch point–like defect (see Fig. 3.2c) can either increase or decrease the topological charge, $\Delta Q = \pm 1$, depending on the winding of the newly created contour. The winding depends on the background magnetization at the formation site. Specifically, contour formation in the FM vacuum ($+\hat{z}$) reduces $Q$ by one, while nucleation inside the skyrmion perimeter ($-\hat{z}$) increases $Q$ by one.

Contour-merging SPs describe transitions in which two closed contours – either disjoint or nested – combine into a single contour (see Fig. 3.2d). The corresponding change in $Q$ is dictated by their relative arrangement and intrinsic winding. Merging two disjoint contours with positive (negative) winding lowers (raises) $Q$ by one. Conversely, merging a contour with positive (negative) intrinsic winding with an inner contour raises (lowers) $Q$ by one.

Unlike the previous SP types, the last two mechanisms represent homotopies – continuous magnetization transformations that do not modify the topological charge, $\Delta Q = 0$. Tail formation (see Fig. 3.2e) simply reshapes a contour while preserving the rotation sense of the magnetization, and therefore does not affect the topological charge. SPs in the last class describe a second homotopy: two closed contours merge while a chiral kink is nucleated (see Fig. 3.2f), and the latter compensates the former's contribution to the topological charge so that in total the charge is preserved ($\Delta Q = 0$). These transitions occur only for disjoint positively wound contours or for nested contours with an outer contour exhibiting negative intrinsic winding. Examples include the conversion of a skyrmion bag into a chiral droplet, where the merged contour yields $\Delta Q = -1$ and kink nucleation compensates it, and the fusion of two disjoint inner contours into a single inner contour that contains a chiral kink (see Fig. 3.2f).

Two remaining SPs lie outside the identified classes, describing the progressive shrinking of a chiral droplet and an antiskyrmion into the FM background (see Fig. 3.2f).

A histogram of SP energies, measured relative to the lower-energy endpoint of each transition, displays the system's energy-barrier distribution (see Fig. 3.2a). Notably, the energy barriers of the five transformation classes show only minor variation with respect to the host texture. For example, the energy required to nucleate a chiral kink on a skyrmion-bag contour is comparable to that needed to nucleate a second kink on a droplet and thereby create an antiskyrmion. This texture insensitivity highlights the universality of the SP categories.

For the selected $L_D$, homotopies exhibit comparatively low barriers, while topological charge-changing transformations require significantly higher ones – a consequence of the large exchange cost of forming discontinuities such as Bloch point-like defects. Yet, it remains to be determined whether this hierarchy is universal. To explore this further, a minimal and generic host texture is considered: an isolated stripe composed of two closed contours (see Fig. 3.3a), effectively representing a portion of an infinitely extended skyrmion bag. Figs. 3.3i–vi illustrate the adjacent energy-minimum configurations of this stripe, each of which constitutes the final state of one of the universally defined transition mechanisms.

Fig. 3.3b presents the energy barriers versus $L_D$, from regimes of strong canting between adjacent magnetic moments at small $L_D$ to negligible canting at large $L_D$, where the

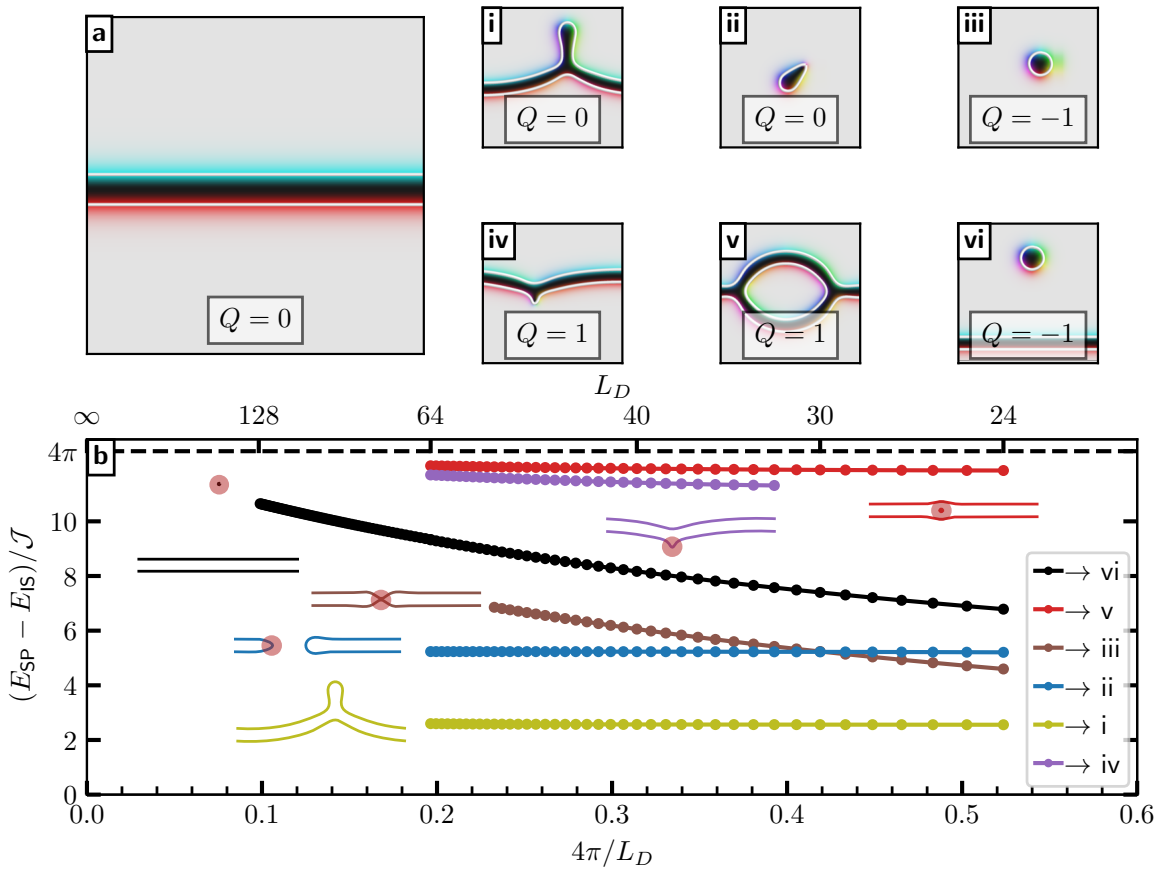


**Figure 3.3.** Energy $E_{\mathrm{SP}}$ of the SPs associated with transitions of the isolated stripe state (**a**) as a function of $L_D$ for $h = 0.623$, shown relative to the energy of the stripe $E_{\mathrm{is}}$ and expressed in units of the continuum exchange parameter $\mathcal{J}$. The simulated system size is $4L_D \times 4L_D$. The SPs are represented by their contours in **b** and **c**, with the point of maximum spin chirality [Eq. (38)] marked by a red circle. For the transitions shown in **b**, the corresponding configurations of the adjacent energy minima are displayed in **i**–**vi**. The transitions in **b** include: tail formation (olive), homotopic contour merging (blue), non-homotopic contour merging (brown), kink nucleation (purple), creation of a contour within the stripe (red), and creation of a contour next to the stripe (black). A similar version of this figure can be found in Paper IV.

lattice model nears the continuum limit. In this limit, the energy barrier for nucleating a skyrmion in the ferromagnetic background (Fig. 3.2vi) converges to $4\pi\mathcal{J}$ [119]. The energies of all SPs associated with the isolated stripe remain below this value for the entire range of $L_D$ considered.

There is a clear distinction in how homotopic and non-homotopic transitions respond to variations in $L_D$. The energy barriers of homotopies – tail formation (Fig. 3.2i) and homotopic contour merging (Fig. 3.2ii) – remain nearly independent of $L_D$. In contrast, the barriers associated with non-homotopic mechanisms – non-homotopic contour merging (Fig. 3.2iii), chiral kink nucleation (Fig. 3.2iv), and contour creation (Figs. 3.2v,,vi) – increase with $L_D$ and appear to approach finite values in the continuum limit. A crossover between the homotopic and non-homotopic contour-merging mechanisms occurs at $L_D \approx 30a$, below which the non-homotopic transition becomes energetically preferred.

The observation that the homotopy does not always provide the lowest energy barrier raises the question of whether an MEP corresponding to a homotopy necessarily exists between states of identical topological charge[10]. To examine this, consider three states with zero topological charge: the skyrmion bag, the chiral droplet, and the FM state. Figure 3.4a shows the partial energy-surface graph involving these three states, the skyrmion ($Q = -1$), and their mutual transformations for $L_D = 30a$ and $h = 0.623$. In particular, consider the homotopy–MEP shown in Fig. 3.4a. The transformation begins with homotopic contour merging accompanied by the nucleation of a chiral kink (i), thereby converting the skyrmion bag into a chiral droplet. The droplet subsequently collapses continuously into the FM state without generating singularities (iv). Other collapse pathways exist, but they do not correspond to homotopies. The skyrmion bag may first transform into a skyrmion, either through collapse of the inner contour (ii) or via non-homotopic contour merging (iii). From the skyrmion state, the system can then reach the FM state either directly (vi) or via the intermediate chiral-droplet configuration (vii).

Notably, the homotopy–MEP exists only within the magnetic-field interval $0.6185 \leq h \leq 0.633$. The disappearance of the homotopy–MEP outside this field range can be understood by examining the energy profiles at the critical fields (Figs. 3.4c–d). Near the lower critical field, $h \approx 0.6185$, homotopic contour merging is followed by a contraction of the resulting structure toward the chiral droplet; however, this contraction entails only a weak decrease in energy. Below this field, the contraction becomes energetically disfavored, and the configuration instead elongates into an extended stripe domain.

As the field increases, the skyrmion bag shrinks, promoting inner–contour collapse. While the homotopy–MEP still exists close to $h \approx 0.633$, a slight increase causes the GMMF optimization to converge to the inner–contour–collapse SP (ii), even when initialized from the homotopic contour-merging SP. The resulting MEP therefore passes through the skyrmion state and is a non–homotopy. The corresponding energy variation is given in Fig. 3.4e.

Interestingly, the homotopic contour-merging mechanism never yields the lowest energy barrier for the collapse of the skyrmion bag. The inner-contour collapse (ii), a non-homotopy pathway, corresponds to the lower barrier, whereas the non-homotopic contour-merging mechanism (iii) results in a higher one, as demonstrated in Fig. 3.4b.

[10]Although homotopy is only an approximate concept in the discrete lattice model considered here, it remains a useful framework for analyzing transitions.

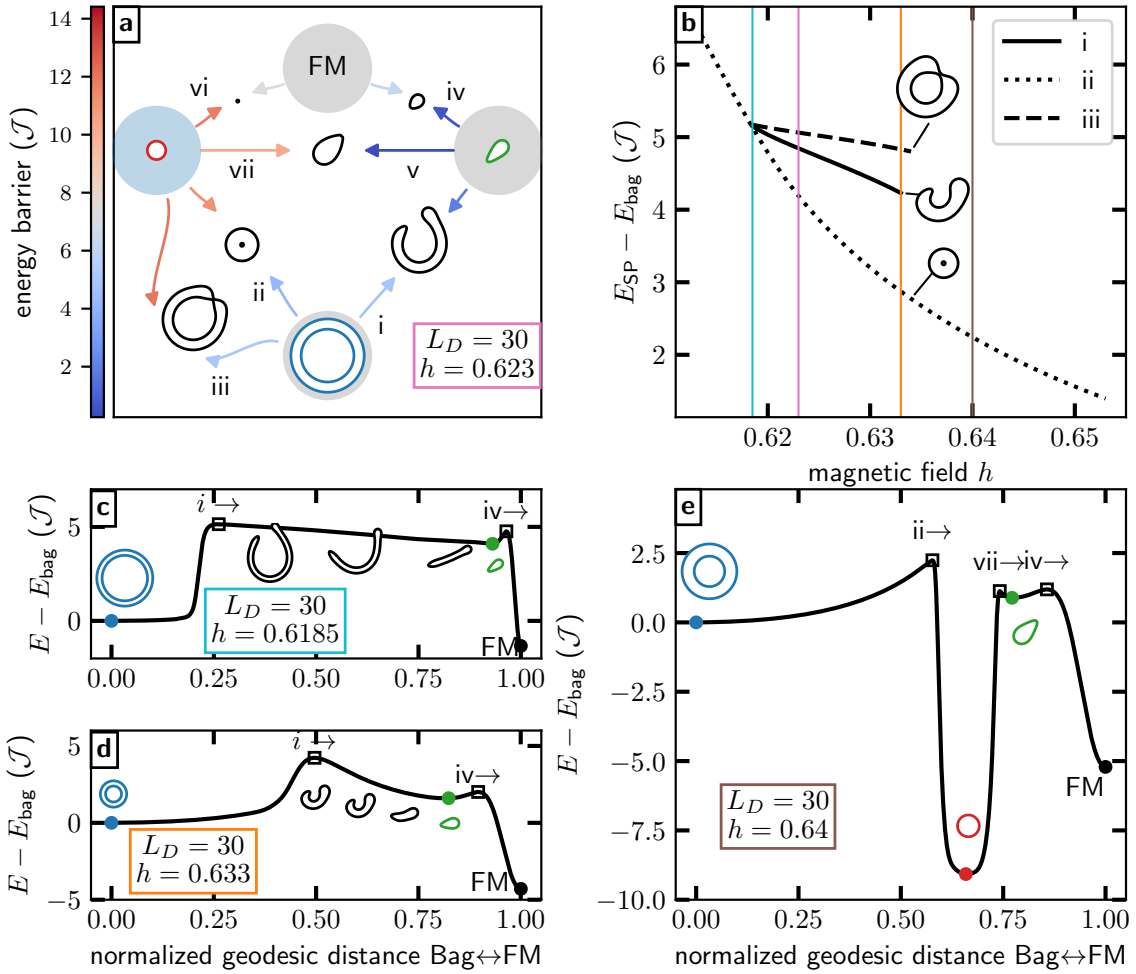


**Figure 3.4.** **a**: Partial graph of the energy surface for $L_D = 30a$ and $h = 0.623$. All magnetic textures are represented by their contours. The metastable configurations are drawn within a colored circle, which indicates the topological charge of either $Q = -1$ for the skyrmion (blue) or $Q = 0$ (gray) for the FM, the droplet and the bag state. The SP configurations associated to the transformations of the states are shown with two arrows pointing from the minima toward them. The color of the arrows corresponds to the respective energy barrier. **b**: Energy of the homotopic contour merging SP (i), the contour annihilation SP (ii) and the non-homotopic contour merging SP (iii) relative to the energy of the bag state as a function of the applied field value $h$. The pink vertical line indicates the parameters for which the graph was obtained, which is displayed in **a**. The other lines indicate the field values $h = 0.6185$ (cyan), $h = 0.633$ (orange) and $h = 0.64$ (brown). **c**,**d**: Energy along the MEPs corresponding to the homotopy connecting the bag with the FM via the droplet state for $h = 0.6185$ (**c**) and $h = 0.633$ (**d**), respectively. **e**: Energy along the MEP corresponding to the non-homotopy connecting the bag with the FM via the skyrmion and the droplet state. The energy is given in reference to the energy of the bag state in units of the continuous-theory exchange parameter $\mathcal{J}$. The MEP is plotted against a normalized geodesic coordinate such that the bag state corresponds to $0$ and the FM state to $1$. A similar version of this figure can be found in Paper IV.

## 3.2 Collapse mechanisms of 3D magnetic states

Beyond the zoo of localized magnetic textures in two-dimensional chiral magnets presented in Sec. 3.1, recently three-dimensional magnetic textures received increased attention – e.g. the localized fully three-dimensional Hopfions with intriguing topology [118, 59]. A skyrmion present in a surface layer can expand into the bulk material forming tube-like textures either terminated by a Bloch point (chiral bobber [174, 34]) or extending through the whole sample (skyrmion tube). If a tube-like texture is terminated by two Bloch points it is referred to as globule [175, 176]. Examples of such textures are visualized in Fig. 3.5. Applying the developed methodology to identify SPs, and thereby minima, in a three-dimensional chiral magnet allows to explore this variety of localized textures and at the same time investigate their mutual transformations.

In Paper II a cubic lattice chiral magnet is considered with lattice constant $a = 3$ Å and $32 \times 32 \times 32$ magnetic moments with open boundaries in the $z$-direction and periodic boundaries in the $xy$-plane. The interactions feature nearest neighbor exchange interactions with $J_1 = 1$ meV and nearest neighbor Bloch-type DMI with $D = 0.45$ meV (see Sec. 1.3.1) within an applied magnetic field $\vec{B} = B\hat{z}$ with $B = 2.8$ T. While the classical dipole-dipole interactions [cf. Eq. (11)] are commonly neglected or taken into account via an effective anisotropy for two-dimensional materials, here these magnetostatic interactions are explicitly included as they become increasingly important in three-dimensional systems with many magnetic moments. This showcases the capabilities of the GMMF algorithm in the convergence stage of the *saddle point search framework* (SPSF) and in particular the RQM method determining the Hessian eigenmodes efficiently, even for systems with such long-range interactions. For comparison also calculations without magnetostatic interactions have been performed. For the above parameters the conical state is the ground state of the system, yet skyrmion tubes and chiral bobbers exist as metastable states [34].

Fig. 3.5 shows how the SPSF is applied to identify SPs and thereby minima on the energy surface corresponding to metastable localized magnetic textures in the system. The system is initialized with a cylindrical region of randomly oriented magnetic moments embedded in the conical phase (see Fig. 3.5a). The diameter of the cylinder is chosen according to the period of the conical modulations, which matches the expected size scale for textures in this material. Such initial configuration corresponds to a point on the energy surface far from an energy minimum and outside a convex region. Therefore, the escape stage becomes unnecessary and the convergence stage of SPSF can directly be applied: 500 GMMF attempts were initialized with such tubes corresponding to different random orientations of the magnetic moments. Figs. 3.5b,c and d exemplarily show three of the obtained SP configurations corresponding to isolated textures visualized by their $m_z = 0$ iso-surface. During the postprocessing stage each SP configuration is slightly displaced in both directions along the unstable mode and a subsequent energy minimization reveals the metastable states that are connected via the identified SPs. Furthermore, calculating the steepest descent path yields the *minimum energy path* (MEP) (cf. Sec. 1.3.5).

Fig. 3.5b shows an SP configuration associated to a skyrmion tube partially withdrawing from the surface and forming an elongated chiral bobber, which is significantly longer than the one originally reported in Ref. [34]. The MEP associated to this col-

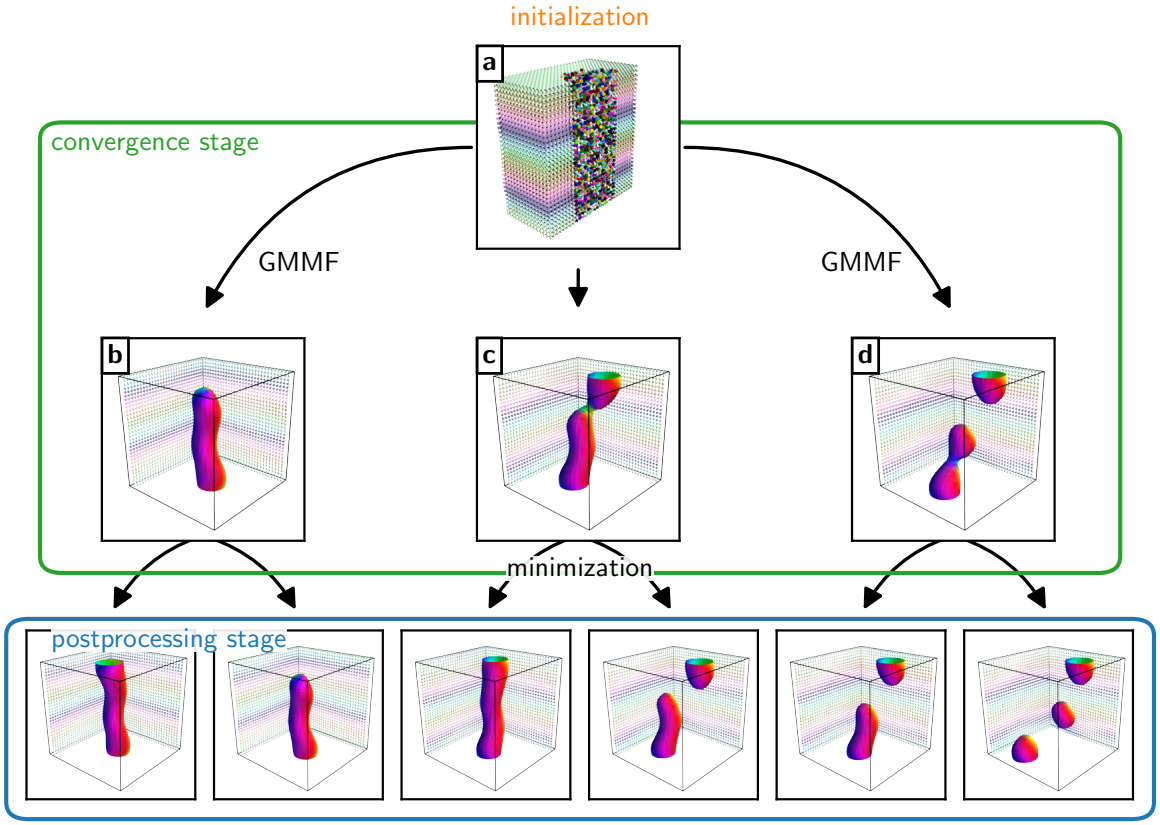


**Figure 3.5.** **a**: Starting configuration for the application of the SPSF represented by a cylindrical region of randomly oriented magnetic moments embedded in the conical phase. During the convergence stage the GMMF algorithm is applied to such initial configurations to obtain SPs associated to isolated magnetic textures (**b**, **c** and **d**). Below the SPs configurations the associated metastable configurations are shown as obtained during postprocessing. The orientation of magnetic moments is indicated by color, as described in Fig. 1.4 a. For the configurations featuring localized magnetic textures the isosurfaces of $m_z = 0$ are shown.

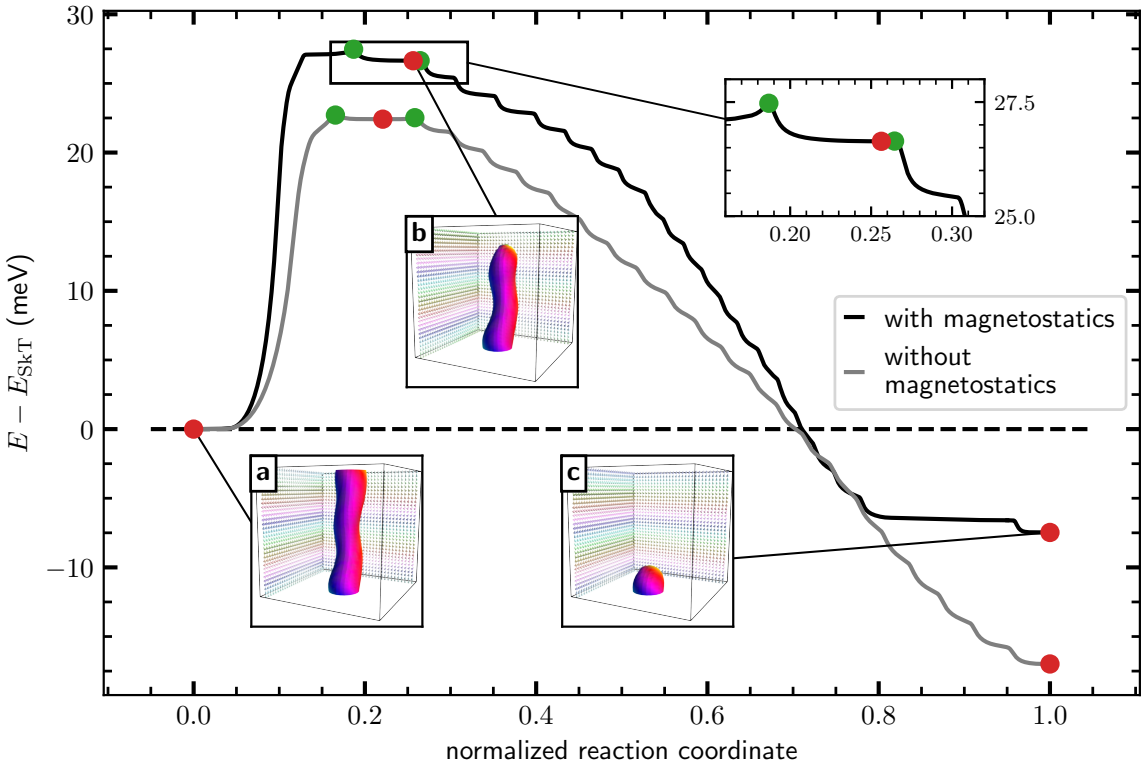


**Figure 3.6.** Energy minima (red) corresponding to the Skyrmion tube (**a**), the elongated chiral bobber (**b**) and the chiral bobber (**c**), calculated via the identification of two SPs (green) associated to two processes: The skyrmion tube detachment from a surface forming an elongated bobber and contraction of the elongated chiral bobber to the chiral bobber. The textures are visualized by the isosurfaces of $m_z = 0$ and the dashed black line corresponds to the energy of the skyrmion tube $E_{\mathrm{SkT}}$. The solid curves represent the energy variation along the calculated MEPs for two cases: with (black) and without (gray) explicit magnetostatic interactions. The dashed line indicates the energy of the skyrmion tube and for each transition, the displacement along the MEP is normalized separately to align the positions of the skyrmion tube and the chiral bobber.

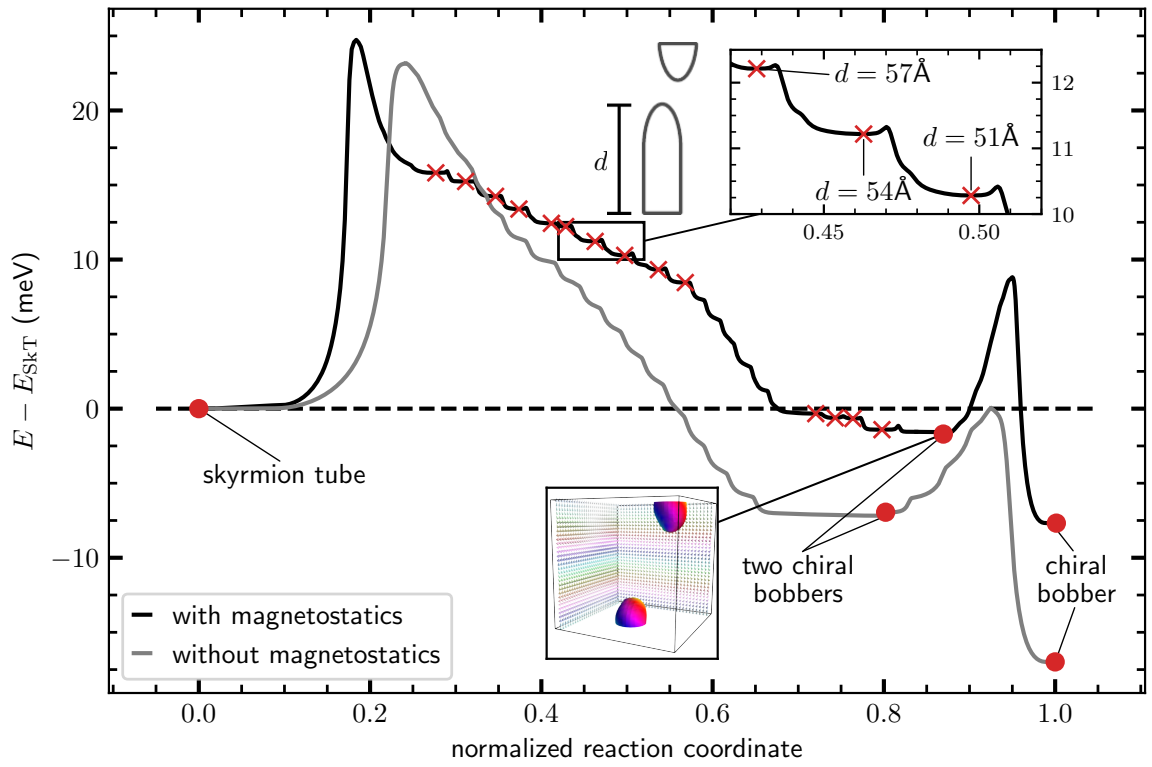


**Figure 3.7.** Energy variation along the MEP corresponding to the rupture of the skyrmion tube into two chiral bobbers of different length, subsequent contraction of the bobbers and collapse of one of the chiral bobbers for two cases: with (black) and without (gray) explicit magnetostatic interactions. The labeled minima are indicated by red circles and the dashed black line corresponds to the energy of the skyrmion tube $E_{\mathrm{SkT}}$. If magnetostatic interactions are included the contraction of the elongated chiral bobber occurs via several intermediate minima (red crosses) and SPs each corresponding to a displacement of the terminating Bloch point toward the base of the bobber (see inset and sketch). The orientation of magnetic moments is indicated by color, as described in Fig. 1.4 a. For the configurations featuring two chiral bobbers the isosurface of $m_z = 0$ is shown.

lapse mechanism is shown in Fig. 3.6. The elongated chiral bobber remains metastable when magnetostatic interactions are neglected (see Fig. 3.6), but the energy barrier corresponding to the skyrmion tube detaching from the surface is roughly 7 meV smaller in this case compared to the case where magnetostatic interactions are explicitly included. Further inspection of the elongated bobber shows that it corresponds to a shallow energy minimum. Displacing the terminating Bloch point of this bobber by one lattice site toward its base and applying the GMMF algorithm yields a nearby SP with slightly larger energy than the corresponding minimum (see inset Fig. 3.6). Following the steepest descent path from this SP reveals an MEP with a step-like energy profile along the path and leads to a shorter chiral bobber (Fig. 3.6c), consistent with the typical length reported in Ref. [34]. The contraction of the chiral bobber yields an energy decrease for each lattice site the terminating Bloch points is moved toward the base of the bobber.

Fig. 3.5c shows an SP configuration corresponding to another collapse mechanism of the skyrmion tube – the rupture of the tube into two chiral bobbers. This collapse yields a smaller energy barrier than the skyrmion tube detachment from one surface. Fig. 3.7 shows the associated MEP connecting the skyrmion tube, the state of two chiral bobbers and the single bobber state as previously reported in Ref. [34] for a system without magnetostatic interactions. Note, that this rupture of the tube can happen in any layer leading to two bobbers of different size. The subsequent contraction of the bobbers is again accompanied by a shoulder in the energy profile along the MEP. However, if magnetostatic interactions are included explicitly (cf. Fig. 3.7) the presence of a second bobber and thus a second Bloch point influences the contraction of the chiral bobber towards its base. Each contraction step of the chiral bobber – each Bloch point displacement by one lattice constant – corresponds to a shallow energy minimum as visualized in the inset of Fig. 3.7.

The contraction of the elongated chiral bobber may also appear via splitting up a globule associated to the SP shown in Fig. 3.5d. For the visualization of the corresponding MEPs for the cases with and without explicit magnetostatics refer to Paper II. It is known that such globules – a droplet shaped state terminated at both ends by a Bloch point – can appear as metastable states in the vicinity of defects or other textures like bobbers. However, they do not correspond to an energy minimum if they appear as isolated textures in a system without magnetostatic interactions [175]. The new result that an isolated globule can represent a metastable states upon inclusion of dipole-dipole interactions in presented in Fig. 3.8. Consider the collapse mechanism of a single chiral bobber (Fig. 3.8a) into the conical state. As reported previously [34] the Bloch point of the chiral bobber can escape through the surface leading to a collapse of the chiral bobber into the conical state (cf. Fig. 3.8). If magnetostatic interactions are included explicitly an alternative collapse mechanism, corresponding to a higher energy barrier, becomes possible: the base of the chiral bobber detaches from the surface and an isolated globule (Fig. 3.8b) forms. After a reorientation which brings the pair of Bloch points closer together (see inset Fig. 3.8) this globule collapses into the conical state through mutual transformation of its Bloch points.

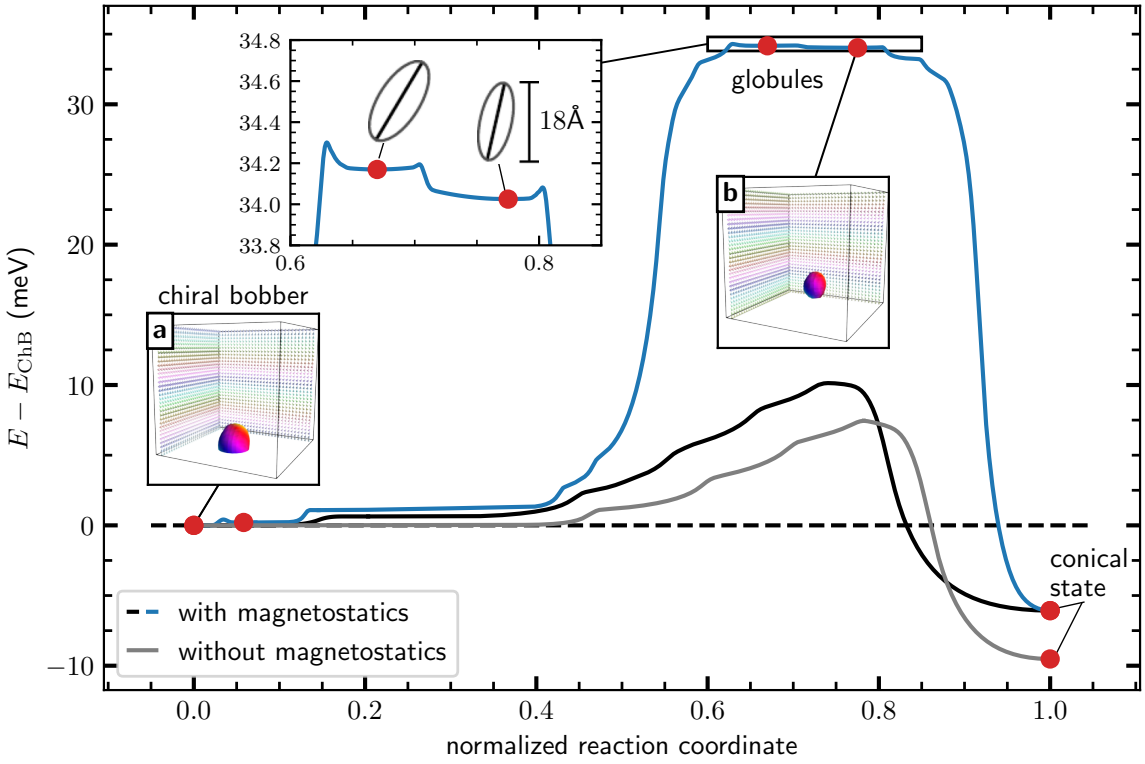


**Figure 3.8.** Energy variation along the MEP corresponding to the collapse of the chiral bobber into the conical state for two cases: with (black) and without (gray) explicit magnetostatic interactions. Another mechanism corresponds to the bobber transforming into a metastable globule which subsequently collapses into the conical state (blue). The inset shows a zoom of the MEP in the region of the two minima corresponding to two metastable globule configurations with different distances between the pair of Bloch points (see sketches). The minima are indicated by red circles and the dashed black line corresponds to the energy of the chiral bobber $E_{\mathrm{ChB}}$. The orientation of magnetic moments is indicated by color, as described in Fig. 1.4 a. For the configurations featuring a chiral bobber (**a**) and a globule (**b**) the isosurface of $m_z = 0$ is shown.

## 3.3 Lifetimes of skyrmions and antiskyrmions in transition-metal films including HOI

From the two- and three-dimensional chiral magnets (cf. Secs. 3.1, 3.2), where competing DMI and exchange interactions govern the formation and collapse of skyrmionic textures, now the focus is shifted to ultrathin transition-metal films. Film systems such as atomic bilayers of Pd/Fe on Ir(111) and Rh(111) are prototypical systems hosting skyrmions and antiskyrmions stabilized by DMI and frustrated exchange interactions [41, 42, 43, 44, 45, 46] (see Fig. 3.9). *Harmonic transition state theory* (HTST)(cf. Sec. 1.3.4) has been widely used to quantitatively predict lifetimes of skyrmionic textures in transition-metal films [55, 177, 69, 10, 46], in good agreement with experiment [56]. Besides determining the energy barrier $\Delta E$ for the collapse of the texture into the ferromagnetic state, HTST requires evaluating the entropic and dynamic contributions encoded in the pre-exponential factor $\nu_0$ of the Arrhenius law [Eq. (47)]. These contributions can strongly influence the lifetime of localized magnetic textures, often by several orders of magnitude [178, 179, 180, 69].

Recently, *higher-order exchange interactions* (HOI) have attracted increasing interest as an additional mechanism impacting skyrmion stability [8, 48, 49, 47]. These interactions couple more than two magnetic moments, and in Paper III three terms of fourth-order terms are considered: the biquadratic, 3-site, and 4-site HOI energies [cf. Eqs. (5),(6),(7)] [103]. Examples of the respective coupling geometries are shown in Figs. 3.9e-g. Prior work demonstrated that especially the 4-site HOI term can significantly enhance the collapse energy barriers in fcc-Pd/Fe/Ir(111) [47]. However, the influence of HOI on the entropic contribution – i.e., on the curvature of the energy surface at the skyrmion, antiskyrmion, and SP configurations – had not been studied before.

In Paper III lifetimes of skyrmions and antiskyrmions are computed in fcc-Pd/Fe/Ir(111) and fcc-Pd/Fe/Rh(111) with the HTST framework including HOI. The magnetic fields are chosen such that the ground state of the system is the *ferromagnetic* (FM) phase ($B > B_C$) [47]. We first obtain SPs associated with the collapse into the FM phase using a combination of the *geodesic nudged elastic band* (GNEB) method and the developed *geodesic minimum mode following* (GMMF) (cf. Sec. 2.3.1) method:

1. Use the GNEB method to obtain a partially converged path for the texture (skyrmion or antiskyrmion) at $B - B_C = 4$ T and define the image with the highest energy of the path as the initial configuration for the next step.
2. Apply the GMMF method and converge onto a first order SP.
3. Define the SP obtained for the current field as the new initial configuration, reduce the field by a small amount of 0.05 T and return to step 2.

As the GMMF method is always initialized with a configuration in the vicinity of an SP, it converges to a first order SP within a few iterations and the SPs are obtained with a high resolution with respect to the values of the magnetic field with negligable computational effort. A subsequent energy minimization during postprocessing yields the adjacent minima – the skyrmion or antiskyrmion and the FM state – and the associated energy barrier for the collapse of the texture.

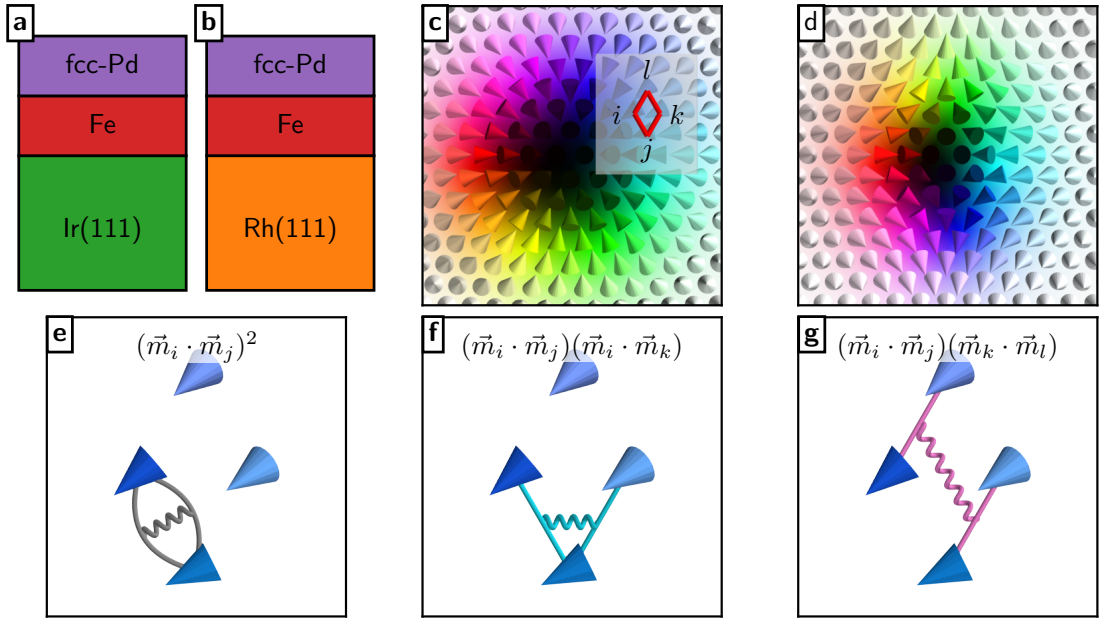


**Figure 3.9.** **a**,**b**: Sketch of atomic bilayers of Pd/Fe on a Ir(111) and Rh(111) substrate, respectively. **c**,**d**: Metastable skyrmion and antiskyrmion at a magnetic field $B - B_C = 3.95$ T in fcc-Pd/Fe/Ir(111), where $B_C$ is the critical field for the onset of the FM phase. In **c** an exemplary placquette of four magnetic moments indexed with $i$, $j$, $k$ and $l$ is highlighted. **e**,**f**,**g**: Examples for couplings of magnetic moments for the biquadratic (**e**), the 3-site (**f**) and the 4-site (**g**) HOI term. The straight lines represent dot-products between magnetic moments while the curved lines correspond to product of such pairs.

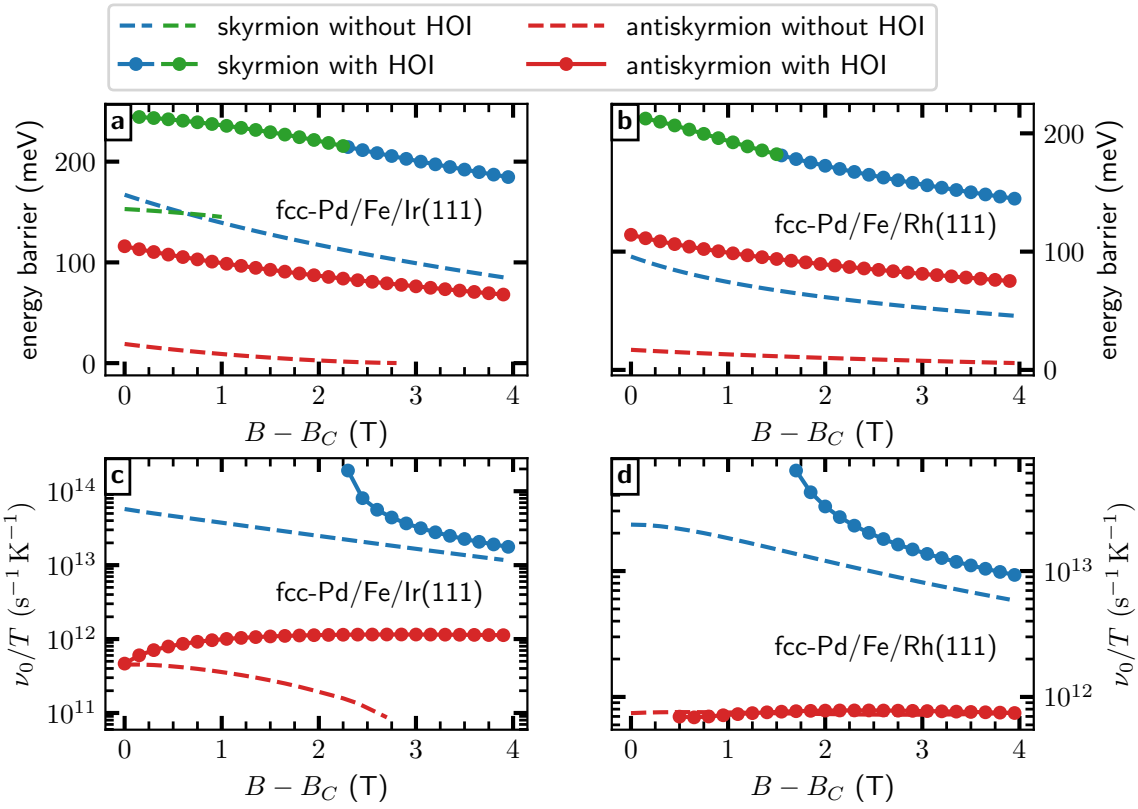


**Figure 3.10.** Energy barriers (**a**,**b**) and pre-exponential factors $\nu_0$ divided by the temperature $T$ (**c**,**d**) for the collapse of skyrmions (blue, green) and antiskyrmions (red) into the field polarized state as a function of the magnetic field in fcc-Pd/Fe/Ir(111) (**a**,**c**) and fcc-Pd/Fe/Rh(111) (**b**,**d**), respectively. The magnetic field $B$ is given relative to the onset $B_C$ of the FM phase (refer to Paper III for values). The energy barriers corresponding to the chimera collapse of the skyrmion are shown in green.

Including HOI increases the skyrmion and antiskyrmion radii slightly but keeps them within the experimentally observed nanometer scale [9, 178, 56]. The energy barriers associated to the collapse of these textures for both systems are shown in Fig 3.10a,b. Explicitly including HOI enhances $\Delta E$ by about 100 meV in both materials, consistent with Ref. [47].

Moreover, for small magnetic fields and HOI the skyrmions collapse into the FM state via the so-called chimera collapse associated to a droplet shaped SP configuration (cf. Fig. 3.10). Note, that for the two-dimensional chiral magnets discussed in Sec. 3.1 a similar configuration corresponded to a metastable state referred to as chiral droplet. Skyrmions at higher magnetic fields and antiskyrmions for all the considered field values collapse in both systems via axially symmetric shrinking and a Bloch point annihilation into the FM state referred to as the radial collapse.

Determining quantitative estimates for the lifetime of skyrmions and antiskyrmion using Eq. (47) requires, beside the energy barrier, the calculation of the entropic contributions encapsulated in the pre-exponential factor $\nu_0$. This term is proportional to the fraction of the product of all eigenvalues $\lambda_i^A$ of the Hessian at the minimum and the eigenvalues $\lambda_i^{\mathrm{SP}}$ at the respective SP [cf. Eq. (48)]. Here $A$ denotes the minimum

corresponding either to the skyrmion or antiskyrmion state. Computing the Hessian, and ultimately its eigenvalues, requires the calculation of the second-order derivatives of the energy with respect to the orientation of the magnetic moments. Specifically, in Paper III the derivation of the second-order derivatives of the HOI energy is shown:

$$\vec{\nabla}_i \vec{\nabla}_j^T E_{\text{4-spin}} = -4 \sum_{kl} \begin{cases} C_{ijkl}\ \vec{m}_k \odot \vec{m}_l & \text{for } (i,j,k,l) \\ C_{ikjl}\ \vec{m}_l \otimes \vec{m}_k & \text{for } (i,k,j,l) \end{cases} , \tag{63}$$

where only the order of indices $i$, $j$, $k$, $l$ has to be considered, including variations with repeating indices which address 3-site and biquadratic HOI terms. The above from uses the following abbreviations:

$$\vec{m}_i \otimes \vec{m}_j = \begin{pmatrix} m_i^x m_j^x & m_i^x m_j^y & m_i^x m_j^z \\ m_i^y m_j^x & m_i^y m_j^y & m_i^y m_j^z \\ m_i^z m_j^x & m_i^z m_j^y & m_i^z m_j^z \end{pmatrix} \tag{64}$$

$$\vec{m}_i \odot \vec{m}_j = \begin{pmatrix} \vec{m}_i \cdot \vec{m}_j & 0 & 0 \\ 0 & \vec{m}_i \cdot \vec{m}_j & 0 \\ 0 & 0 & \vec{m}_i \cdot \vec{m}_j \end{pmatrix} . \tag{65}$$

Finally, the Hessian is computed using Eq. (22).

Including dynamic and zero mode contributions (see Paper III) yields the pre-exponential factors shown in Fig. 3.10c,d divided by the temperature $T$ of skyrmions and antiskyrmions, with and without HOI in fcc-Pd/Fe/Ir(111) and fcc-Pd/Fe/Rh(111), respectively. Note, only the radial skyrmion collapse regime is presented here, while the chimera collapse is discussed in the supplementary material of Paper III. Comparing the skyrmion collapse with and without HOI yields pre-exponential factors slightly increased but of the same of magnitude in both systems if HOI are included. Analyzing the effect of the HOI on the curvature of the energy surface at the critical points, reflected by the respective eigenvalues, reveals a reduced curvature of the energy surface at the SP while the curvature at the minimum remains mostly unchanged if HOI are included (Paper III). Furthermore, mainly the low eigenvalues associated to localized excitations of the SP are effected by HOI. These curvatures are directly linked to the entropic contributions to the pre-exponential factor (cf. Fig. 1.5) and are able to explain the increased pre-exponential factor of skyrmions upon inclusion of HOI. While in fcc-Pd/Fe/Ir(111) the pre-exponential factors of the antiskyrmion collapse are approximately one order of magnitude larger if HOI are included (Fig. 3.10c), in fcc-Pd/Fe/Rh(111) the factors are almost the same with and without HOI (Fig. 3.10d).

Using both $\Delta E$ and $\nu_0$ in the Arrhenius law, lifetimes $\tau$ are computed across a wide range of fields and temperatures (Fig. 3.11). Comparing the results with the one-hour isolifetime line from a model without HOI highlights the strong stabilizing role of HOI. When HOI are included, skyrmions remain stable for at least one hour at temperatures up to 50 K; without HOI, comparable stability requires lowering the temperature below 30 K.

Furthermore, while the antiskyrmions are only stable up to fields of $B_\perp - B_C \approx 2.7$ T without HOI, explicit consideration of HOI yields antiskyrmion lifetimes of at least one hour for temperatures $T \leq 20$ K in the field range of $B_\perp - B_C \approx 3$ T to $B_\perp - B_C \approx$

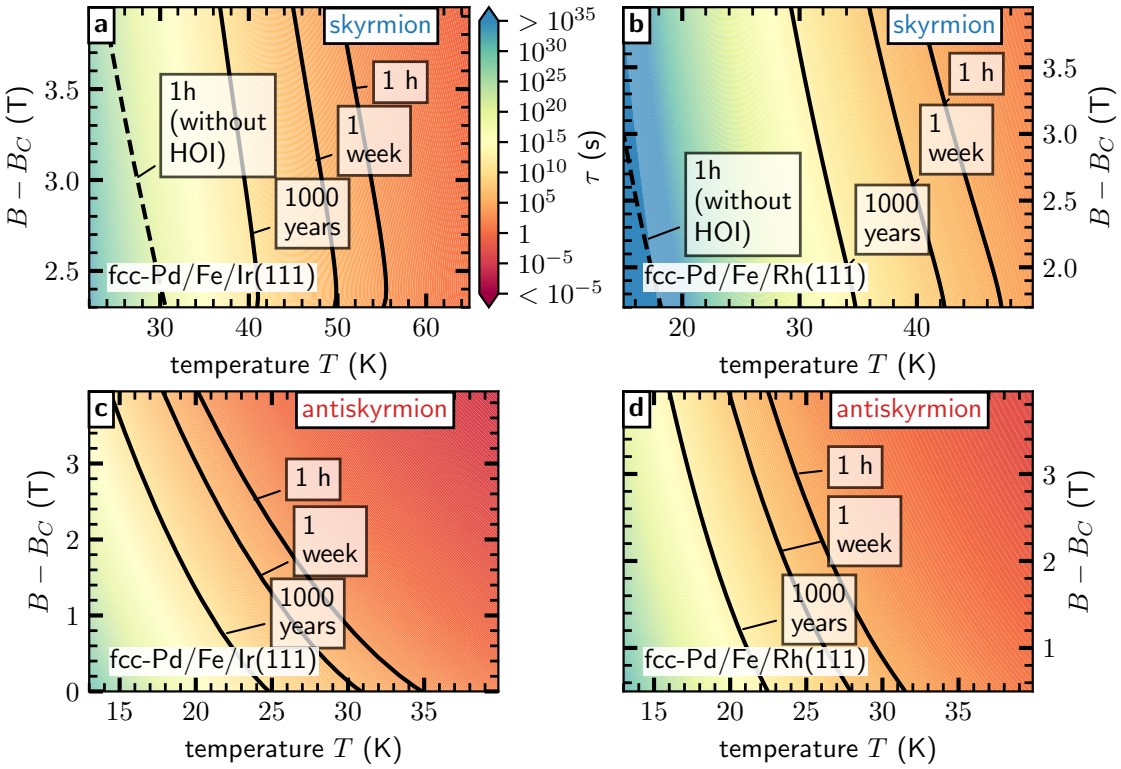


**Figure 3.11.** Mean lifetime $\tau$ for skyrmions (**a**,**b**) and antiskyrmions (**c**,**d**) for different temperatures $T$ and magnetic fields $B - B_C$ in fcc-Pd/Fe/Ir(111) (**a**,**c**) and fcc-Pd/Fe/Rh(111) (**b**,**d**), respectively. HOI are taken into account for each subplot and the iso-lifetime line of one hour for the model without HOI is shown in **a**,**b** for comparison.

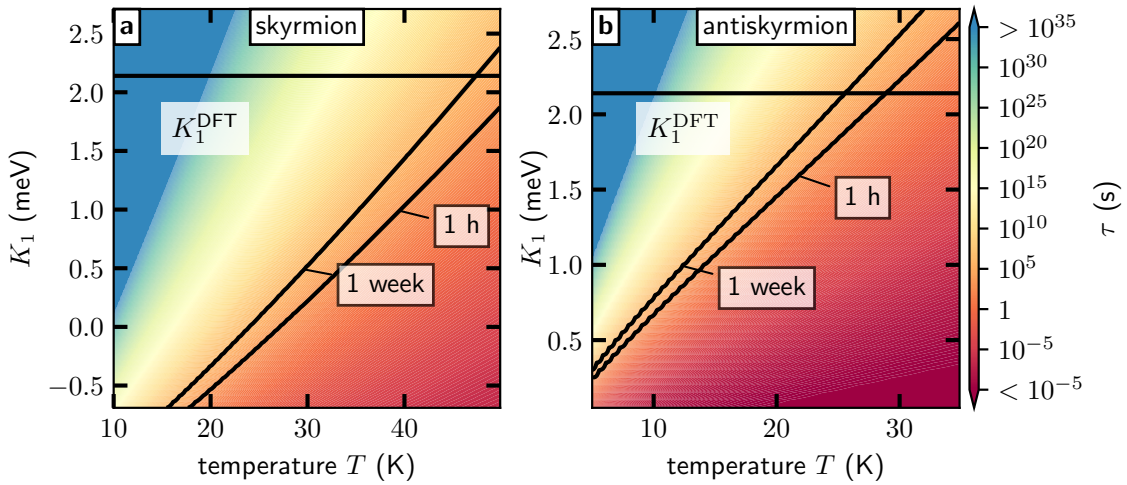


**Figure 3.12.** Lifetime $\tau$ of skyrmions (**a**) and antiskyrmions (**b**) as a function of the 4-site HOI parameter $K_1$ and for various temperatures $T$ in fcc-Pd/Fe/Ir(111). The value of the 4-site HOI parameter that was determined in DFT calculations [47] and is used in the remainder of the section is denoted $K_1^{\mathrm{DFT}}$.

4 T. Overall, inclusion of HOI leads to substantially enhanced stability of metastable magnetic textures in both materials.

Next, the sensitivity of lifetimes to the strength of the 4-site HOI parameter $K_1$ is examined (Fig. 3.12). Because spin-spiral energies do not depend on $K_1$, the bilinear exchange parameters determined from DFT remain valid for arbitrary variations of this term [47]. Consistent with Ref. [47], the energy barriers of both skyrmions and antiskyrmions vary linearly with $K_1$. While skyrmions remain metastable even for slightly negative $K_1$, the antiskyrmion barrier vanishes as $K_1 \to 0$. The pre-exponential factors exhibit a contrasting behavior: for antiskyrmions they remain nearly constant across the considered range, whereas for skyrmions they decrease by about three orders of magnitude as $K_1$ is reduced. The change of pre-exponential factor and energy barrier with strength of the 4-site HOI leads to opposite effects on the thermal stability of skyrmions. While the increase of the energy barrier with $K_1$ also leads to an enhanced lifetime, the increase of the pre-exponential factor results in a decrease of the lifetime as seen from the Arrhenius law [cf. Eq. (47)]. The lifetime of skyrmions (Fig. 3.12a) and antiskyrmions (Fig. 3.12b) changes drastically upon variation of $K_1$. For instance, at $T = 40$ K a skyrmion with $K_1 = 1.0$ meV has a lifetime of about 45 minutes; increasing the 4-site parameter by only 0.5 meV boosts the lifetime to roughly 18 days. For antiskyrmions, a similar trend is observed, however, at overall shorter lifetimes at a given temperature due to the lower energy barriers. The considered range $K_1 \in [-0.75, 2.7]$ meV corresponds to realistic values for ultrathin transition-metal films [47, 181, 81, 106].

## 3.4 Effects of interlayer exchange coupling of the stability of skyrmions

In Paper I it was investigated how the strength of the interlayer exchange coupling affects the mechanisms and energy barriers of skyrmion collapse in multilayer systems. Models with two and more magnetic layers are constructed, such as that the interaction parameters mimic the well-established fcc-Pd/Fe/Ir(111) system that was also discussed in the previous section. Two distinct stacking geometries were considered – $\alpha\alpha$ stacking, where magnetic moments in different layers sit vertically on top of each other, and $\alpha\beta$ stacking, where a horizontal displacement exists between the magnetic layers. By systematically varying the nearest neighbor interlayer exchange $J^{\perp}$ over a wide range, a comprehensive picture is obtained of how multilayer skyrmions collapse and how their thermal stability is modified through interlayer coupling. The analysis combined the *geodesic nudged elastic band* (GNEB) method to calculate *minimum energy path*s (MEPs) and thereby first-order SPs corresponding to skyrmion collapse mechanisms, and *harmonic transition state theory* (HTST) to determine the lifetimes of skyrmions in magnetic bilayers.

To begin, zero-temperature magnetic phase diagrams were obtained for both stacking types. In the $\alpha\beta$ stacking, it is observed that increasing $J^{\perp}$ shifts the critical fields delimiting the spin-spiral, skyrmion-lattice, and *ferromagnetic* (FM) phases to lower values. This shift results from the horizontal displacement of the magnetic layers, which makes non-collinear alignments of magnetic moments in different layers energetically costly under FM interlayer exchange. In contrast, in the $\alpha\alpha$ stacking, the phase boundaries remain essentially unchanged for all values of $J^{\perp}$, because all spins couple vertically to aligned neighbors, so each magnetic phase is shifted by the same amount of energy. Importantly, in both stackings, isolated skyrmions remain metastable at the chosen magnetic field of 4 T across the full range of coupling strengths $J^{\perp}$ considered.

A central outcome of the study is the discovery of a rich variety of skyrmion collapse mechanisms that arise as a direct consequence of tuning the interlayer exchange. For very weak coupling, each layer collapses independently through a monolayer-type radial shrinking, resulting in what is referred to as a successive radial–radial collapse. In this regime, the MEP contains two SPs, each similar to the SP of the skyrmion in the respective magnetic monolayer. Increasing the interlayer exchange slightly, a qualitatively different mechanism emerged: the first layer collapses via a Chimera SP, characterized by a localized tilting at the skyrmion boundary, while the second layer still collapses radially (cf. Fig. 1.7b). This successive chimera–radial collapse arises because the interlayer exchange penalizes non-collinear alignment between magnetic moments of different layers. The chimera-type SP configuration corresponds mostly to the configuration of the energy minimum skyrmion except a small region hosting the chiral kink. Thereby, the non-collinear alignment between magnetic moments of the two layers – one hosting the chimera SP configuration and one with a skyrmion – is confined to small region lowering the interlayer exchange energy costs compared to the successive radial-radial collapse.

At intermediate coupling strengths, the bilayer skyrmion collapse becomes partially simultaneous. In this semisuccessive chimera–radial regime, the first layer still goes

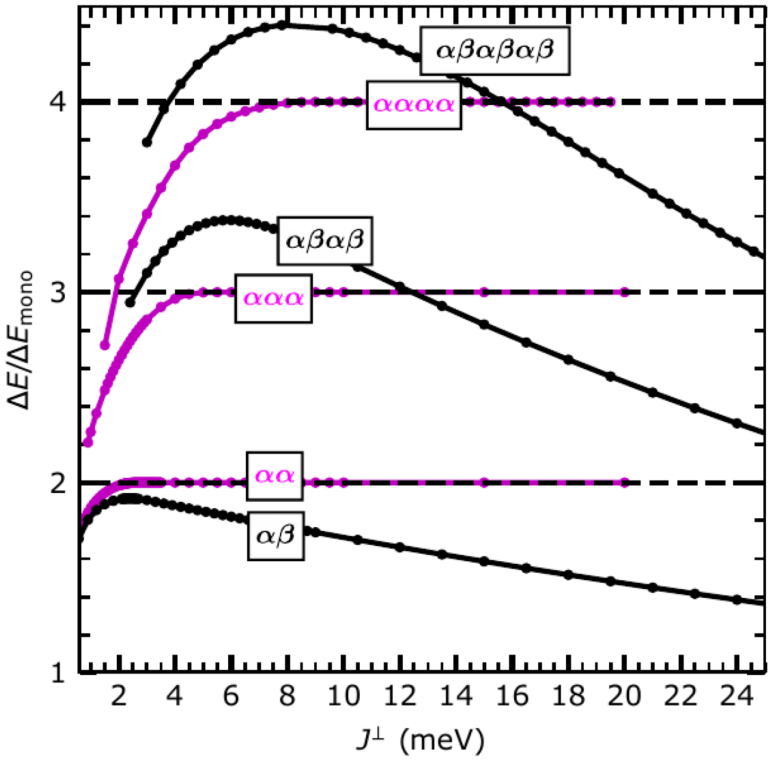


**Figure 3.13.** Energy barriers of skyrmions in magnetic multilayer systems as a function of the interlayer exchange couplings $J^{\perp}$ relative to the energy barrier of the skyrmion in the magnetic monolayer fcc-Pd/Fe/Ir(111). The effective nearest neighbor parametrization was used for the intralayer interactions. The energy barriers for the skyrmions in the two-, three- and four-layer systems obeying an $\alpha\alpha$-stacking sequence are shown in magenta. The barriers for the two-, four-, and sixlayer systems with $\alpha\beta$-stacking are shown in black. Figure modified from Paper I with permission from APS.

through a chimera SP, but the second layer has already begun shrinking by that stage. A further increase in $J^{\perp}$ leads to a semisuccessive radial–radial collapse: both skyrmions shrink nearly in sync, but with slight delays between the collapsing skyrmions in the different layers close to the SP. Only at strong interlayer exchange coupling does the collapse become fully simultaneous in both layers, passing through a single radial SP (cf. Fig. 1.7a). In the $\alpha\alpha$ stacking, this fully simultaneous collapse produces an energy barrier equal to exactly twice the monolayer value, as one would expect for two tightly locked layers evolving identically. In the $\alpha\beta$ stacking, however, a fundamentally different behavior is found. Even though the collapse becomes simultaneous at strong coupling, the corresponding energy barrier does not reach twice the energy barrier of the skyrmion collapse in the respective monolayer system.

Calculating the energy barriers of multilayer skyrmions as a function of the interlayer exchange coupling yields a different behavior for the $\alpha\alpha$- and $\alpha\beta$-stacked systems. The energy barrier of a skyrmion in an $\alpha\beta$-stacked multilayer increases initially with increasing interlayer exchange coupling, then reaches a maximum and then decreases as $J^{\perp}$ is raised further. In contrast, the corresponding energy barriers in the $\alpha\alpha$-stacked systems converge for large interlayer exchange coupling to a maximal value of $n$ times

the energy barrier of the skyrmion collapse in the respective monolayer, where $n$ is the number of layers of the stack. This different result for skyrmions in the two systems with distinct stacking sequences of the layers is a direct consequence of the horizontal displacement between layers. For the $\alpha\beta$-stacked system $J^{\perp}$ favors collinear magnetic configurations in both layers over non-collinear arrangements in terms of interlayer exchange energy. For the SP configuration more magnetic moments a aligned collinear than for the skyrmion configuration, and therefore the interlayer exchange energetically favors the SP as coupling increases. Thereby, the barrier to collapse is reduced at strong interlayer exchange coupling for $\alpha\beta$-stacked systems.

The transitions between collapse regimes are more closely investigated by analyzing the Hessian eigenmodes of the SP. A key observation is the softening of a specific eigenmode, which is referred to as the layer-aligning mode. This mode approaches zero at the transition from semi-successive to fully simultaneous collapse, marking the critical interlayer exchange strength at which the layers begin to behave as a single, rigid unit. For the full model taking into account intralayer exchange frustration, critical values are reported of approximately 10 meV for $\alpha\alpha$ stacking and about 12 meV for $\alpha\beta$ stacking.

To verify that these results do not depend sensitively on exchange frustration, the analysis was repeated using a simplified nearest-neighbor effective model for the intralayer interactions. The same qualitative behavior appears, although the critical coupling strengths are lower, demonstrating that the different collapse regimes are robust features of interlayer-coupled skyrmions. Fig. 3.13 shows the energy barriers of skyrmions in $\alpha\alpha$- and $\alpha\beta$-stacked systems with up to six layers as a function of $J^{\perp}$. It is noteworthy that the more layers are included within the $\alpha\beta$-stacked system, the more pronounced is the decrease of the collapse energy barrier in the large interlayer exchange coupling regime.

To quantify the practical impact on skyrmion robustness, skyrmion lifetimes are computed within *harmonic transition state theory* (HTST) for a magnetic bilayer skyrmion using the effective nearest neighbor model for the intralayer interactions. The lifetimes depend not only on energy barriers but also on entropic contributions encoded in the pre-exponential factor [cf. Eq. (47)], that are visualized as a function of $J^{\perp}$ in Fig. 3.14a for bilayer skyrmions. Interestingly, the pre-exponential factor depends only weakly on the stacking sequence of the magnetic layers. A sharp decline of $\nu_0^{-1}$ occurs around $J^{\perp} = 3.0$ meV followed by an increase towards the pre-exponential factor of the magnetic monolayer system, which is indicated by the dashed line. This narrow sink is produced by the softening of the layer-aligning SP mode which approaches zero in this regime. In this region the applicability of the harmonic approximation is questionable. Nevertheless, it is remarkable that the prefactor reduces the stability of the bilayer skyrmions for both stackings compared to the prefactor of the skyrmion in the magnetic monolayer system (dashed line in Fig. 3.14). This is attributed to an increased entropic difference between the transition state and the skyrmion state for intermediate interlayer exchange couplings as the number of possible transition mechanisms reduces with increased ex- change couplings between the layers.

In Fig. 3.14b, the lifetime $\tau$ is calculated for the exemplary temperature $T = 30$ K. For the shown parameter range of $J_{\perp}$ the stability of the bilayer skyrmion is always

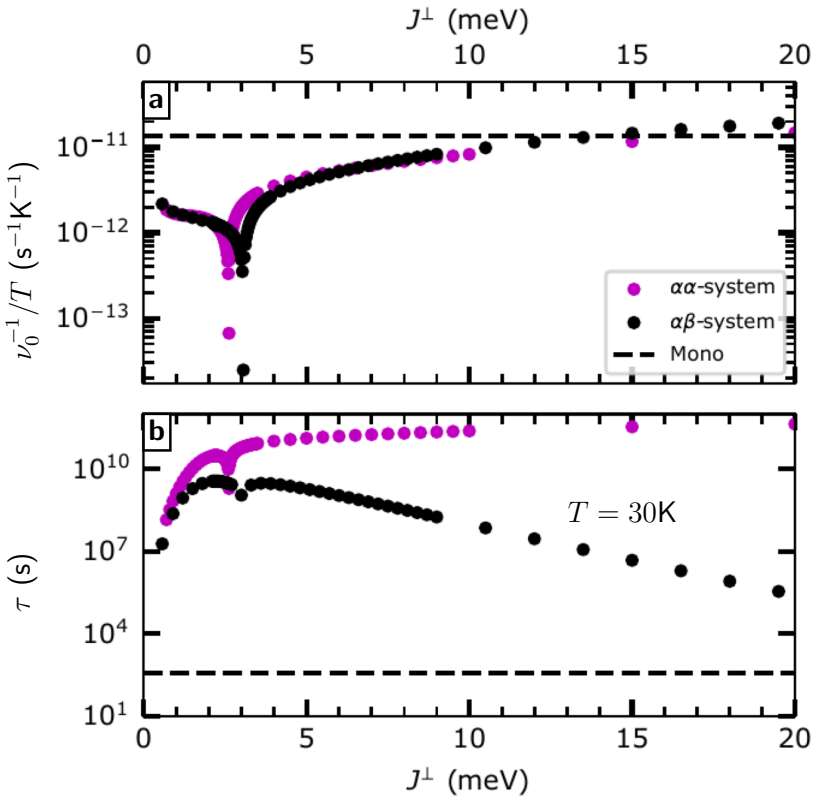


**Figure 3.14.** **a**: Inverse of the pre-exponential factor $\nu_0$ divided by the temperature $T$ [cf. Eq. (48)] for skyrmions in magnetic bilayer systems based on the magnetic monolayer system fcc-Pd/Fe/Ir(111) in $\alpha\alpha$- and $\alpha\beta$-stacking as a function of the interlayer exchange couplings $J^\perp$. The dashed line indicates pre-exponential factor for skyrmions within the magnetic monolayer system fcc-Pd/Fe/Ir(111) [69] for $B = 4.0$ T. **b**: Skyrmion lifetime $\tau$ for $T = 30$ K calculated with the Arrhenius law [cf. Eq. (47)] using the energy barriers from Fig. 3.13 and the pre-exponential factor displayed in part **a** of this figure. Figure reprinted from Paper I with permission from APS.

enhanced compared to the skyrmion in the magnetic monolayer system. Thereby, the thermal stability can in this case be associated to the increased energy barriers of bilayer skyrmions compared to a monolayer skyrmion. It is observed that in the strong interlayer exchange regime the stacking order of the magnetic layers has significant impact on the overall lifetime. The lifetimes drops several orders of magnitude for increasing $J^\perp$ in the $\alpha\beta$-stacked system, while it approaches lifetimes more than seven orders of magnitude larger compared to the lifetime of the respective monolayer skyrmions in the $\alpha\alpha$-stacked system.

# 4 Conclusion and Outlook

The interactions between magnetic moments – such as pairwise Heisenberg exchange, *Dzyaloshinskii-Moriya interaction* (DMI), and *higher-order exchange interactions* (HOI) – define the high-dimensional energy surface of a magnetic system, on which local minima correspond to metastable states, as schematically shown in Fig. 4.1 for a two-dimensional energy surface. This work develops, implements, and applies a methodology for the systematic identification of *saddle point*s (SPs) that surround a local energy minimum on the energy surface. Within *harmonic transition state theory* (HTST), the long-timescale dynamic behavior of a magnetic system is determined by thermally activated transitions between metastable states, represented by local minima of the energy surface. Each such transition is characterized by the point of highest energy along the so-called *minimum energy path* (MEP) between two minima: a first-order SP (see Fig. 4.1). Its identification enables the calculation of transition rates considering the energy barrier and the entropic and dynamic contributions of the process. The present study places particular emphasis on systems that host a rich spectrum of localized magnetic textures, extending beyond the skyrmion state.

The method developed in Sec. 2 extends existing SP search algorithms for magnetic systems [57, 58] by introducing a structured multi-stage design – comprising preprocessing, escape, convergence, and postprocessing stages (Paper IV). A key methodological advance, compared to previous attempts, lies in the escape stage, which strategically samples displacements of the minimum configuration along low-energy excitations. These displacements are applied within subsystems whose centers are distributed across the fundamental domain – the smallest region containing all unique physical information of the texture, identified via automatic symmetry detection during preprocessing. Sampling excitations along several minimal eigenmodes of each subsystem's Hessian then yields a systematic set of escape attempts. Each escape attempt introduces a deformation of the configuration corresponding to a tendency toward an SP, which is associated to breaking locally the symmetry of a metastable localized magnetic texture. Thereby successfull escape attempts mark the entry points for the subsequent convergence onto a first-order SP.

During the convergence stage, the developed *geodesic minimum mode following* (GMMF) method guides the system toward an SP by inverting the force along a characteristic degree of freedom, the inversion mode (Paper II). The repeated calculation of this mode, which represents the bottleneck of the method, is efficiently solved using the *Rayleigh quotient minimization* (RQM) algorithm. making the method applicable to large systems with many magnetic moments (Paper II).

Finally, during postprocessing, redundancy is removed from the set of identified SPs, and the adjacent energy minima are revealed. In this way, additional metastable states are uncovered, which serve as new initial configurations for subsequent applications of

the framework.

In this work, the developed SP search methodology is applied to identify the mechanisms by which metastable localized magnetic textures transform and to determine which neighboring energy minima on the surface are accessible via thermally activated transitions. Furthermore, we quantitatively assess how magnetic interactions influence the transition rates, determined by the energy and entropy difference between SP and minimum. This enables a characterization of the stabilization and transition mechanisms of localized magnetic textures.

In particular, it is demonstrated that the transition mechanisms between the diverse metastable magnetic textures found in two-dimensional chiral magnets [36, 68] can be classified into distinct transformation categories governing the nucleation, annihilation, and rearrangement of the fundamental building blocks of localized magnetic textures. Isolated magnetic textures can be classified by their topology, represented by a distinct topological charge and each of these mechanisms falls into one of two categories: homotopies, which conserve the total topological charge, and transitions that change it. Paper IV shows that two metastable textures belonging to the same topological class are not necessarily connected by a MEP that corresponds to a homotopy; moreover, even when such a path exists, it is not always the energetically preferred transition route. These findings advance the understanding of how topology affects the stability of localized magnetic textures. The computational efficiency of the framework enabled the investigation of a three-dimensional chiral magnet in Paper II, including long-range magnetostatic interactions, and led to the discovery of a complex network of transitions between metastable chiral bobbers of different lengths [34], skyrmion tubes, and globules [175]. Incorporating dipole–dipole interactions explicitly increases the number of local minima on the energy landscape, giving rise, for example, to isolated globules and to pairs of chiral bobbers with distinct lengths. As a consequence, the number of possible transition mechanisms also increases, as confirmed by comparison with a model that omits magnetostatic interactions. In the prototypical ultrathin transition-metal films fcc-Pd/Fe/Ir(111) and fcc-Pd/Fe/Rh(111), significantly enhanced skyrmion and antiskyrmion lifetimes are obtained when *higher-order exchange interactions* (HOI) are included in the model, even in the absence of *Dzyaloshinskii-Moriya interaction* (DMI) (Paper III). Beyond increasing the energy barrier [47], HOI also reshape the curvature of the energy surface, thereby stabilizing or destabilizing skyrmionic textures through entropic contributions to the pre-exponential factor in the Arrhenius law. This effect is particularly relevant in systems where conventional stabilizing interactions such as the DMI are weak or absent, including the rapidly growing class of two-dimensional van-der-Waals magnets. Finally, Paper IV demonstrates that interlayer exchange coupling profoundly influences the collapse pathways and stability of skyrmions in multilayer systems. The interplay between stacking geometry and coupling strength gives rise to multiple distinct collapse regimes, non-monotonic energy-barrier behavior, and even reduced stability at sufficiently strong interlayer coupling.

In summary, these applications highlight both the versatility of the developed methodology and its predictive power. In contrast to approaches based on the construction of MEP, it does not require prior knowledge of the final state of a transition in order to identify the relevant SPs. This feature is particularly valuable in view of the increasing number of two- and three-dimensional systems that host co-existing localized magnetic

textures [32]. A recursive application of the framework to metastable states in such systems enables the discovery of previously unknown metastable configurations and their transition pathways. When this global exploration of the energy landscape is further combined with on-the-fly evaluations of transition rates, the long-time dynamics can be efficiently captured using adaptive kinetic Monte Carlo [61, 62]. Furthermore, the developed methods show considerable potential when combined with other techniques. In particular, GMMF can be used to accelerate convergence to an SP by initializing with the highest-energy image of a partially converged *geodesic nudged elastic band* (GNEB) calculation [182]. The method can also be generalized to locate higher-order SPs, which has proven to be an efficient strategy for computing excited electronic states [183]. The diversity and efficiency of sampling initial displacements during the escape stage could be enhanced even further by incorporating information from previous SP searches [60], for example through multi-objective genetic algorithms [184]. It is therefore foreseeable that the methodology presented here will stimulate further technical developments and applications.

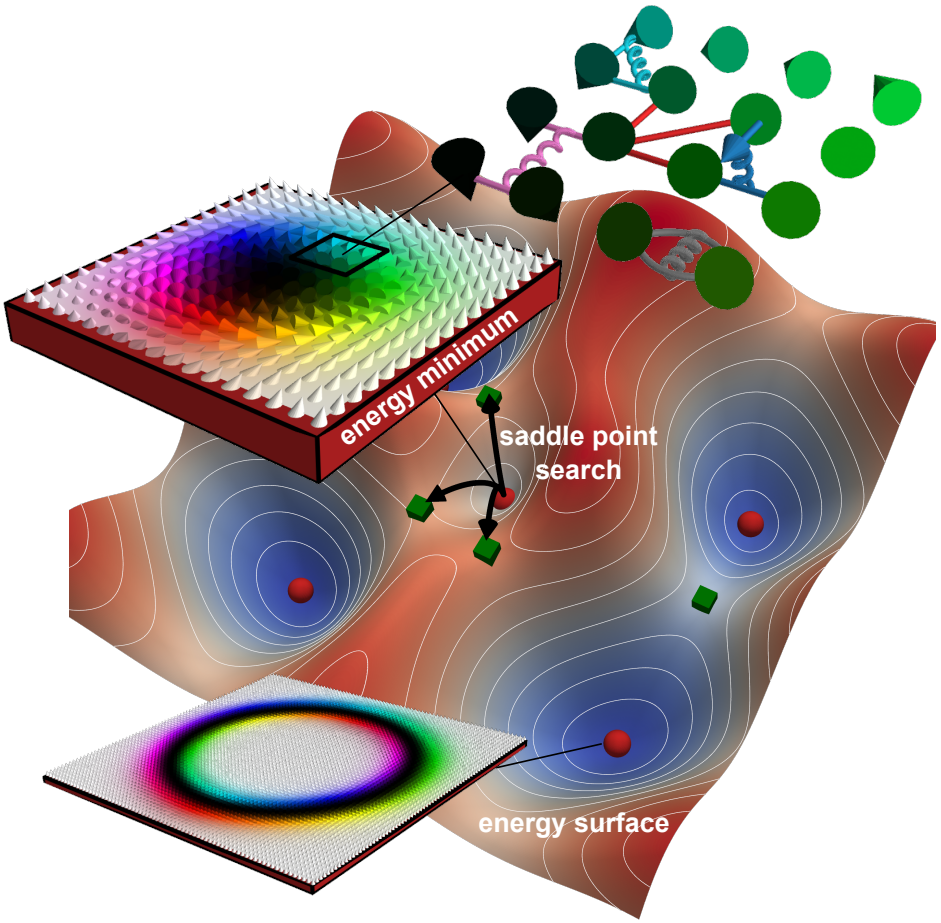


**Figure 4.1.** Schematic illustration of the central theme of this work. The interactions between atomic magnetic moments define a high-dimensional energy surface, with local minima (red dots) corresponding to metastable localized magnetic textures such as skyrmions. Thermally activated transitions to neighboring minima – for instance, to the illustrated skyrmion bag – are governed by first-order *saddle point*s (SPs) (green dots) on the energy surface. This work introduces a framework for the automated identification of these SPs, enabling a systematic characterization of transition mechanisms associated with metastable magnetic states.

# References


[1] M Mitchell Waldrop. "The chips are down for Moore's law." In: *Nature News* 530.7589 (2016), p. 144.

[2] S. A. Wolf, D. D. Awschalom, R. A. Buhrman, J. M. Daughton, S. von Molnár, M. L. Roukes, A. Y. Chtchelkanova, and D. M. Treger. "Spintronics: A Spin-Based Electronics Vision for the Future." In: *Science* 294.5546 (2001), pp. 1488–1495. DOI: 10.1126/science.1065389.

[3] Igor Žuti ć, Jaroslav Fabian, and S. Das Sarma. "Spintronics: Fundamentals and applications." In: *Rev. Mod. Phys.* 76 (2 Apr. 2004), pp. 323–410. DOI: 10.1103/RevModPhys.76.323.

[4] R.R. Schaller. *Moore's law: past, present and future*. 1997. DOI: 10.1109/6.591665.

[5] Wang Kang, Yangqi Huang, Xichao Zhang, Yan Zhou, and Weisheng Zhao. "Skyrmion-Electronics: An Overview and Outlook." In: *Proceedings of the IEEE* 104.10 (2016), pp. 2040–2061. DOI: 10.1109/JPROC.2016.2591578.

[6] S. Mühlbauer, B. Binz, F. Jonietz, C. Pfleiderer, A. Rosch, A. Neubauer, R. Georgii, and P. Böni. "Skyrmion Lattice in a Chiral Magnet." In: *Science* 323.5916 (2009), pp. 915–919. DOI: 10.1126/science.1166767.

[7] X. Z. Yu, Y. Onose, N. Kanazawa, J. H. Park, J. H. Han, Y. Matsui, N. Nagaosa, and Y. Tokura. "Real-space observation of a two-dimensional skyrmion crystal." In: *Nature* 465.7300 (June 2010), pp. 901–904. DOI: 10.1038/nature09124.

[8] Stefan Heinze, Kirsten von Bergmann, Matthias Menzel, Jens Brede, André Kubetzka, Roland Wiesendanger, Gustav Bihlmayer, and Stefan Blügel. "Spontaneous atomic-scale magnetic skyrmion lattice in two dimensions." In: *Nature Physics* 7.9 (Sept. 2011), pp. 713–718. DOI: 10.1038/nphys2045.

[9] Niklas Romming, Christian Hanneken, Matthias Menzel, Jessica E. Bickel, Boris Wolter, Kirsten von Bergmann, André Kubetzka, and Roland Wiesendanger. "Writing and Deleting Single Magnetic Skyrmions." In: *Science* 341.6146 (2013), pp. 636–639. DOI: 10.1126/science.1240573. eprint: https://www.science.org/doi/pdf/10.1126/science.1240573.

[10] Sebastian Meyer, Marco Perini, Stephan von Malottki, André Kubetzka, Roland Wiesendanger, Kirsten von Bergmann, and Stefan Heinze. "Isolated zero field sub-10 nm skyrmions in ultrathin Co films." In: *Nature Communications* 10.1 (Aug. 2019), p. 3823. DOI: 10.1038/s41467-019-11831-4.

[11] Myung-Geun Han, Joseph A. Garlow, Yu Liu, Huiqin Zhang, Jun Li, Donald DiMarzio, Mark W. Knight, Cedomir Petrovic, Deep Jariwala, and Yimei Zhu. "Topological Magnetic-Spin Textures in Two-Dimensional van der Waals Cr2Ge2Te6." In: *Nano Letters* 19.11 (Nov. 2019), pp. 7859–7865. DOI: 10.1021/acs.nanolett.9b02849.

[12] Bei Ding, Zefang Li, Guizhou Xu, Hang Li, Zhipeng Hou, Enke Liu, Xuekui Xi, Feng Xu, Yuan Yao, and Wenhong Wang. "Observation of Magnetic Skyrmion Bubbles in a van der Waals Ferromagnet Fe3GeTe2." In: *Nano Letters* 20.2 (Feb. 2020), pp. 868–873. DOI: 10.1021/acs.nanolett.9b03453.

[13] Yingying Wu, Senfu Zhang, Junwei Zhang, Wei Wang, Yang Lin Zhu, Jin Hu, Gen Yin, Kin Wong, Chi Fang, Caihua Wan, Xiufeng Han, Qiming Shao, Takashi Taniguchi, Kenji Watanabe, Jiadong Zang, Zhiqiang Mao, Xixiang Zhang, and Kang L. Wang. "Néel-type skyrmion in WTe2/Fe3GeTe2 van der Waals heterostructure." In: *Nature Communications* 11.1 (July 2020), p. 3860. DOI: 10.1038/s41467-020-17566-x.

[14] C Back, V Cros, H Ebert, K Everschor-Sitte, A Fert, M Garst, Tianping Ma, S Mankovsky, T L Monchesky, M Mostovoy, N Nagaosa, S S P Parkin, C Pfleiderer, N Reyren, A Rosch, Y Taguchi, Y Tokura, K von Bergmann, and Jiadong Zang. "The 2020 skyrmionics roadmap." In: *Journal of Physics D: Applied Physics* 53.36 (June 2020), p. 363001. DOI: 10.1088/1361-6463/ab8418.

[15] R. Tomasello, E. Martinez, R. Zivieri, L. Torres, M. Carpentieri, and G. Finocchio. "A strategy for the design of skyrmion racetrack memories." In: *Scientific Reports* 4.1 (Oct. 2014), p. 6784. DOI: 10.1038/srep06784.

[16] Xichao Zhang, Yan Zhou, Motohiko Ezawa, G. P. Zhao, and Weisheng Zhao. "Magnetic skyrmion transistor: skyrmion motion in a voltage-gated nanotrack." In: *Scientific Reports* 5.1 (June 2015), p. 11369. DOI: 10.1038/srep11369.

[17] Ik-Sun Hong and Kyung-Jin Lee. "Magnetic skyrmion field-effect transistors." In: *Applied Physics Letters* 115.7 (Aug. 2019), p. 072406. DOI: 10.1063/1.5110752.

[18] Li Zhao, Xue Liang, Jing Xia, Guoping Zhao, and Yan Zhou. "A ferromagnetic skyrmion-based diode with a voltage-controlled potential barrier." In: *Nanoscale* 12 (17 2020), pp. 9507–9516. DOI: 10.1039/C9NR10528J.

[19] Dae-Han Jung, Hee-Sung Han, Namkyu Kim, Ganghwi Kim, Suyeong Jeong, Sooseok Lee, Myeonghwan Kang, Mi-Young Im, and Ki-Suk Lee. "Magnetic skyrmion diode: Unidirectional skyrmion motion via symmetry breaking of potential energy barriers." In: *Phys. Rev. B* 104 (6 Aug. 2021), p. L060408. DOI: 10.1103/PhysRevB.104.L060408.

[20] Xichao Zhang, Motohiko Ezawa, and Yan Zhou. "Magnetic skyrmion logic gates: conversion, duplication and merging of skyrmions." In: *Scientific Reports* 5.1 (Mar. 2015), p. 9400. DOI: 10.1038/srep09400.

[21] Shijiang Luo, Min Song, Xin Li, Yue Zhang, Jeongmin Hong, Xiaofei Yang, Xuecheng Zou, Nuo Xu, and Long You. "Reconfigurable Skyrmion Logic Gates." In: *Nano Letters* 18.2 (Feb. 2018), pp. 1180–1184. DOI: 10.1021/acs.nanolett.7b04722.

[22] Zhizhong Zhang, Yuanzhi Zhu, Yue Zhang, Kun Zhang, Jiang Nan, Zhenyi Zheng, Youguang Zhang, and Weisheng Zhao. "Skyrmion-Based Ultra-Low Power Electric-Field-Controlled Reconfigurable (SUPER) Logic Gate." In: *IEEE Electron Device Letters* 40.12 (2019), pp. 1984–1987. DOI: 10.1109/LED.2019.2946863.

[23] Dongxing Yu, Hongxin Yang, Mairbek Chshiev, and Albert Fert. "Skyrmions-based logic gates in one single nanotrack completely reconstructed via chirality barrier." In: *National Science Review* 9.12 (Feb. 2022), nwac021. DOI: 10.1093/nsr/nwac021.

[24] Z.R. Yan, Y.Z. Liu, Y. Guang, K. Yue, J.F. Feng, R.K. Lake, G.Q. Yu, and X.F. Han. "Skyrmion-Based Programmable Logic Device with Complete Boolean Logic Functions." In: *Phys. Rev. Appl.* 15 (6 June 2021), p. 064004. DOI: 10.1103/PhysRevApplied.15.064004.

[25] Yun Shu, Qianrui Li, Jing Xia, Ping Lai, Yonghong Zhao, Yan Zhou, Xiaoxi Liu, and Guoping Zhao. "Skyrmion-based reconfigurable logic gates and diodes in a racetrack with hard magnetic material and a notch." In: *Journal of Magnetism and Magnetic Materials* 568 (2023), p. 170387. DOI: https://doi.org/10.1016/j.jmmm.2023.170387.

[26] Sai Li, Wang Kang, Yangqi Huang, Xichao Zhang, Yan Zhou, and Weisheng Zhao. "Magnetic skyrmion-based artificial neuron device." In: *Nanotechnology* 28.31 (July 2017), 31LT01. DOI: 10.1088/1361-6528/aa7af5.

[27] Xue Liang, Xichao Zhang, Jing Xia, Motohiko Ezawa, Yuelei Zhao, Guoping Zhao, and Yan Zhou. "A spiking neuron constructed by the skyrmion-based spin torque nano-oscillator." In: *Applied Physics Letters* 116.12 (Mar. 2020), p. 122402. DOI: 10.1063/5.0001557.

[28] Wencong Jiang, Lina Chen, Kaiyuan Zhou, Liyuan Li, Qingwei Fu, Youwei Du, and R. H. Liu. "Physical reservoir computing using magnetic skyrmion memristor and spin torque nano-oscillator." In: *Applied Physics Letters* 115.19 (Nov. 2019), p. 192403. DOI: 10.1063/1.5115183.

[29] Christina Psaroudaki and Christos Panagopoulos. "Skyrmion Qubits: A New Class of Quantum Logic Elements Based on Nanoscale Magnetization." In: *Phys. Rev. Lett.* 127 (6 Aug. 2021), p. 067201. DOI: 10.1103/PhysRevLett.127.067201.

[30] Christina Psaroudaki, Elias Peraticos, and Christos Panagopoulos. "Skyrmion qubits: Challenges for future quantum computing applications." In: *Applied Physics Letters* 123.26 (Dec. 2023), p. 260501. DOI: 10.1063/5.0177864.

[31] Jing Xia, Xichao Zhang, Xiaoxi Liu, Yan Zhou, and Motohiko Ezawa. "Universal Quantum Computation Based on Nanoscale Skyrmion Helicity Qubits in Frustrated Magnets." In: *Phys. Rev. Lett.* 130 (10 Mar. 2023), p. 106701. DOI: 10.1103/PhysRevLett.130.106701.

[32] Börge Göbel, Ingrid Mertig, and Oleg A. Tretiakov. "Beyond skyrmions: Review and perspectives of alternative magnetic quasiparticles." In: *Physics Reports* 895 (2021). Beyond skyrmions: Review and perspectives of alternative magnetic quasiparticles, pp. 1–28. DOI: https://doi.org/10.1016/j.physrep.2020.10.001.

[33] Levente Rózsa, Krisztián Palotás, András Deák, Eszter Simon, Rocio Yanes, László Udvardi, László Szunyogh, and Ulrich Nowak. "Formation and stability of metastable skyrmionic spin structures with various topologies in an ultrathin film." In: *Phys. Rev. B* 95 (9 Mar. 2017), p. 094423. DOI: 10.1103/PhysRevB.95.094423.

[34] Filipp N. Rybakov, Aleksandr B. Borisov, Stefan Blügel, and Nikolai S. Kiselev. "New Type of Stable Particlelike States in Chiral Magnets." In: *Phys. Rev. Lett.* 115 (11 Sept. 2015), p. 117201. DOI: 10.1103/PhysRevLett.115.117201.

[35] Filipp N. Rybakov and Nikolai S. Kiselev. "Chiral magnetic skyrmions with arbitrary topological charge." In: *Phys. Rev. B* 99 (6 Feb. 2019), p. 064437. DOI: 10.1103/PhysRevB.99.064437.

[36] Vladyslav M. Kuchkin, Bruno Barton-Singer, Filipp N. Rybakov, Stefan Blügel, Bernd J. Schroers, and Nikolai S. Kiselev. "Magnetic skyrmions, chiral kinks, and holomorphic functions." In: *Phys. Rev. B* 102 (14 Oct. 2020), p. 144422. DOI: 10.1103/PhysRevB.102.144422.

[37] V. M. Kuchkin and N. S. Kiselev. "Homotopy transitions and 3D magnetic solitons." In: *APL Materials* 10.7 (July 2022), p. 071102. DOI: 10.1063/5.0097559.

[38] I. Dzyaloshinsky. "A thermodynamic theory of "weak" ferromagnetism of antiferromagnetics." In: *J. Phys. Chem. Solids* 4.4 (1958), pp. 241–255. DOI: https://doi.org/10.1016/0022-3697(58)90076-3.

[39] Tôru Moriya. "Anisotropic Superexchange Interaction and Weak Ferromagnetism." In: *Phys. Rev.* 120 (1 Oct. 1960), pp. 91–98. DOI: 10.1103/PhysRev.120.91.

[40] M. Bode, M. Heide, K. von Bergmann, P. Ferriani, S. Heinze, G. Bihlmayer, A. Kubetzka, O. Pietzsch, S. Blügel, and R. Wiesendanger. "Chiral magnetic order at surfaces driven by inversion asymmetry." In: *Nature* 447.7141 (May 2007), pp. 190–193. DOI: 10.1038/nature05802.

[41] A. O. Leonov and M. Mostovoy. "Multiply periodic states and isolated skyrmions in an anisotropic frustrated magnet." In: *Nature Communications* 6.1 (Sept. 2015), p. 8275. DOI: 10.1038/ncomms9275.

[42] Shi-Zeng Lin and Satoru Hayami. "Ginzburg-Landau theory for skyrmions in inversion-symmetric magnets with competing interactions." In: *Phys. Rev. B* 93 (6 Feb. 2016), p. 064430. DOI: 10.1103/PhysRevB.93.064430.

[43] S. von Malottki, B. Dupé, P. F. Bessarab, A. Delin, and S. Heinze. "Enhanced skyrmion stability due to exchange frustration." In: *Scientific Reports* 7.1 (Sept. 2017), p. 12299. DOI: 10.1038/s41598-017-12525-x.

[44] Xichao Zhang, Jing Xia, Yan Zhou, Xiaoxi Liu, Han Zhang, and Motohiko Ezawa. "Skyrmion dynamics in a frustrated ferromagnetic film and current-induced helicity locking-unlocking transition." In: *Nature Communications* 8.1 (Nov. 2017), p. 1717. DOI: 10.1038/s41467-017-01785-w.

[45] L. Desplat, J.-V. Kim, and R. L. Stamps. "Paths to annihilation of first- and second-order (anti)skyrmions via (anti)meron nucleation on the frustrated square lattice." In: *Phys. Rev. B* 99 (17 May 2019), p. 174409. DOI: 10.1103/PhysRevB.99.174409.

[46] Moritz A. Goerzen, Stephan von Malottki, Sebastian Meyer, Pavel F. Bessarab, and Stefan Heinze. "Lifetime of coexisting sub-10 nm zero-field skyrmions and antiskyrmions." In: *npj Quantum Materials* 8.1 (Oct. 2023), p. 54. DOI: 10.1038/s41535-023-00586-3.

[47] Souvik Paul, Soumyajyoti Haldar, Stephan von Malottki, and Stefan Heinze. "Role of higher-order exchange interactions for skyrmion stability." In: *Nature Communications* 11.1 (Sept. 2020), p. 4756. DOI: 10.1038/s41467-020-18473-x.

[48] Changsong Xu, Xueyang Li, Peng Chen, Yun Zhang, Hongjun Xiang, and Laurent Bellaiche. "Assembling Diverse Skyrmionic Phases in $Fe_3GeTe_2$ Monolayers." In: *Advanced Materials* 34.12 (2022), p. 2107779. DOI: https://doi.org/10.1002/adma.202107779.

[49] Peng Li, Dongxing Yu, Jinghua Liang, Yonglong Ga, and Hongxin Yang. "Topological spin textures in 1$T$-phase Janus magnets: Interplay between Dzyaloshinskii-Moriya interaction, magnetic frustration, and isotropic higher-order interactions." In: *Phys. Rev. B* 107 (5 Feb. 2023), p. 054408. DOI: 10.1103/PhysRevB.107.054408.

[50] E. Wigner. "The transition state method." In: *Trans. Faraday Soc.* 34 (0 1938), pp. 29–41. DOI: 10.1039/TF9383400029.

[51] George H. Vineyard. "Frequency factors and isotope effects in solid state rate processes." In: *J. Phys. Chem. Solids* 3.1 (1957), pp. 121–127. DOI: https://doi.org/10.1016/0022-3697(57)90059-8.

[52] H. A. Kramers. "Brownian Motion in a Field of Force and the Diffusion Model of Chemical Reactions." In: *Physica* 7.4 (Apr. 1940), pp. 284–304. DOI: 10.1016/S0031-8914(40)90098-2.

[53] J.S. Langer. "Statistical theory of the decay of metastable states." In: *Ann. Phys.* 54.2 (1969), pp. 258–275. DOI: https://doi.org/10.1016/0003-4916(69)90153-5.

[54] Pavel F. Bessarab, Valery M. Uzdin, and Hannes Jónsson. "Method for finding mechanism and activation energy of magnetic transitions, applied to skyrmion and antivortex annihilation." In: *Computer Physics Communications* 196 (2015), pp. 335–347. DOI: https://doi.org/10.1016/j.cpc.2015.07.001.

[55] Pavel F. Bessarab, Gideon P. Müller, Igor S. Lobanov, Filipp N. Rybakov, Nikolai S. Kiselev, Hannes Jónsson, Valery M. Uzdin, Stefan Blügel, Lars Bergqvist, and Anna Delin. "Lifetime of racetrack skyrmions." In: *Scientific Reports* 8.1 (Feb. 2018), p. 3433. DOI: 10.1038/s41598-018-21623-3.

[56] Florian Muckel, Stephan von Malottki, Christian Holl, Benjamin Pestka, Marco Pratzer, Pavel F. Bessarab, Stefan Heinze, and Markus Morgenstern. "Experimental identification of two distinct skyrmion collapse mechanisms." In: *Nature Physics* 17.3 (Mar. 2021), pp. 395–402. DOI: 10.1038/s41567-020-01101-2.

[57] Gideon P. Müller, Pavel F. Bessarab, Sergei M. Vlasov, Fabian Lux, Nikolai S. Kiselev, Stefan Blügel, Valery M. Uzdin, and Hannes Jónsson. "Duplication, Collapse, and Escape of Magnetic Skyrmions Revealed Using a Systematic Saddle Point Search Method." In: *Phys. Rev. Lett.* 121 (19 Nov. 2018), p. 197202. DOI: 10.1103/PhysRevLett.121.197202.

[58] H. Bocquet and P. M. Derlet. "Searching for activated transitions in complex magnetic systems." In: *Phys. Rev. B* 108 (17 Nov. 2023), p. 174419. DOI: 10.1103/PhysRevB.108.174419.

[59] Moritz Sallermann, Hannes Jónsson, and Stefan Blügel. "Stability of hopfions in bulk magnets with competing exchange interactions." In: *Phys. Rev. B* 107 (10 Mar. 2023), p. 104404. DOI: 10.1103/PhysRevB.107.104404.

[60] Qichen Xu and Anna Delin. *A general optimization framework for mapping local transition-state networks*. 2025. arXiv: 2509.26269 [physics.comp-ph].

[61] Graeme Henkelman and Hannes Jónsson. "Long Time Scale Kinetic Monte Carlo Simulations without Lattice Approximation and Predefined Event Table." In: *J. Chem. Phys.* 115.21 (Dec. 2001), pp. 9657–9666. DOI: 10.1063/1.1415500.

[62] Hannes Jónsson. "Simulation of Surface Processes." In: *Proc. Natl. Acad. Sci.* 108.3 (Jan. 2011), pp. 944–949. DOI: 10.1073/pnas.1006670108.

[63] Manuel Plasencia, Andreas Pedersen, Andri Arnaldsson, Jean-Claude Berthet, and Hannes Jónsson. "Geothermal model calibration using a global minimization algorithm based on finding saddle points and minima of the objective function." In: *Comput. Geosci.* 65 (2014), pp. 110–117. DOI: https://doi.org/10.1016/j.cageo.2013.09.007.

[64] Dóróthea M. Einarsdóttir, Andri Arnaldsson, Finnbogi Óskarsson, and Hannes Jónsson. "Path Optimization with Application to Tunneling." In: *Applied Parallel and Scientific Computing*. Ed. by Kristján Jónasson. Berlin, Heidelberg: Springer Berlin Heidelberg, 2012, pp. 45–55. DOI: 10.1007/978-3-642-28145-7_5.

[65] Vilhjálmur Ásgeirsson, Andri Arnaldsson, and Hannes Jónsson. "Efficient evaluation of atom tunneling combined with electronic structure calculations." In: *J. Chem. Phys.* 148.10 (Jan. 2018), p. 102334. DOI: 10.1063/1.5007180.

[66] Sergei M Vlasov, Pavel F Bessarab, Igor S Lobanov, Mariia N Potkina, Valery M Uzdin, and Hannes Jónsson. "Magnetic skyrmion annihilation by quantum mechanical tunneling." In: *New Journal of Physics* 22.8 (Aug. 2020), p. 083013. DOI: 10.1088/1367-2630/ab9f6d.

[67] Igor A. Nosikov, Maxim V. Klimenko, Gennady A. Zhbankov, Aleksey V. Podlesnyi, Vera A. Ivanova, and Pavel F. Bessarab. "Generalized Force Approach to Point-to-Point Ionospheric Ray Tracing and Systematic Identification of High and Low Rays." In: *IEEE Trans. Antennas Propag.* 68.1 (2020), pp. 455–467. DOI: 10.1109/TAP.2019.2938817.

[68] Vladyslav M. Kuchkin, Nikolai S. Kiselev, Filipp N. Rybakov, and Pavel F. Bessarab. "Tailed skyrmions—An obscure branch of magnetic solitons." In: *Frontiers in Physics* 11 (2023). DOI: 10.3389/fphy.2023.1171079.

[69] Stephan von Malottki, Pavel F. Bessarab, Soumyajyoti Haldar, Anna Delin, and Stefan Heinze. "Skyrmion lifetime in ultrathin films." In: *Phys. Rev. B* 99 (6 Feb. 2019), p. 060409. DOI: 10.1103/PhysRevB.99.060409.

[70] Manuel Plasencia Gutiérrez, Carlos Argáez, and Hannes Jónsson. "Improved Minimum Mode Following Method for Finding First Order Saddle Points." In: *J. Chem. Theory Comput.* 13.1 (Jan. 2017), pp. 125–134. DOI: 10.1021/acs.jctc.5b01216.

[71] M. Gunde, A. Jay, M. Poberžnik, N. Salles, N. Richard, G. Landa, N. Mousseau, L. Martin-Samos, and A. Hemeryck. "Exploring potential energy surfaces to reach saddle points above convex regions." In: *J. Chem. Phys.* 160.23 (June 2024), p. 232501. DOI: 10.1063/5.0210097.

[72] U. Köbler, R. Mueller, L. Smardz, D. Maier, K. Fischer, B. Olefs, and W. Zinn. "Biquadratic exchange interactions in the Europium monochalcogenides." In: *Zeitschrift für Physik B Condensed Matter* 100.4 (Dec. 1996), pp. 497–506. DOI: 10.1007/s002570050153.

[73] Ulrich Köbler, A. Hoser, J. Englich, A. Snezhko, M. Kawakami, M. Beyss, and K. Fischer. "On the Failure of the Bloch–Kubo–Dyson Spin Wave Theory." In: *Journal of the Physical Society of Japan* 70.10 (2001), pp. 3089–3097. DOI: 10.1143/JPSJ.70.3089.

[74] O. N. Mryasov, A. J. Freeman, and A. I. Liechtenstein. "Theory of non-Heisenberg exchange: Results for localized and itinerant magnets." In: *Journal of Applied Physics* 79.8 (Apr. 1996), pp. 4805–4807. DOI: 10.1063/1.361678.

[75] Ph. Kurz, G. Bihlmayer, K. Hirai, and S. Blügel. "Three-Dimensional Spin Structure on a Two-Dimensional Lattice: Mn/Cu(111)." In: *Phys. Rev. Lett.* 86 (6 Feb. 2001), pp. 1106–1109. DOI: 10.1103/PhysRevLett.86.1106.

[76] Samir Lounis and Peter H. Dederichs. "Mapping the magnetic exchange interactions from first principles: Anisotropy anomaly and application to Fe, Ni, and Co." In: *Phys. Rev. B* 82 (18 Nov. 2010), p. 180404. DOI: 10.1103/PhysRevB.82.180404.

[77] Y. Yoshida, S. Schröder, P. Ferriani, D. Serrate, A. Kubetzka, K. von Bergmann, S. Heinze, and R. Wiesendanger. "Conical Spin-Spiral State in an Ultrathin Film Driven by Higher-Order Spin Interactions." In: *Phys. Rev. Lett.* 108 (8 Feb. 2012), p. 087205. DOI: 10.1103/PhysRevLett.108.087205.

[78] Andreas Krönlein, Martin Schmitt, Markus Hoffmann, Jeannette Kemmer, Nicolai Seubert, Matthias Vogt, Julia Küspert, Markus Böhme, Bandar Alonazi, Jens Kügel, Hamad A. Albrithen, Matthias Bode, Gustav Bihlmayer, and Stefan Blügel. "Magnetic Ground State Stabilized by Three-Site Interactions: Fe/Rh(111)." In: *Phys. Rev. Lett.* 120 (20 May 2018), p. 207202. DOI: **10.1103/PhysRevLett.120.207202**.

[79] Niklas Romming, Henning Pralow, André Kubetzka, Markus Hoffmann, Stephan von Malottki, Sebastian Meyer, Bertrand Dupé, Roland Wiesendanger, Kirsten von Bergmann, and Stefan Heinze. "Competition of Dzyaloshinskii-Moriya and Higher-Order Exchange Interactions in Rh/Fe Atomic Bilayers on Ir(111)." In: *Phys. Rev. Lett.* 120 (20 May 2018), p. 207201. DOI: **10.1103/PhysRevLett.120.207201**.

[80] Jonas Spethmann, Sebastian Meyer, Kirsten von Bergmann, Roland Wiesendanger, Stefan Heinze, and André Kubetzka. "Discovery of Magnetic Single- and Triple-**q** States in Mn/Re(0001)." In: *Phys. Rev. Lett.* 124 (22 June 2020), p. 227203. DOI: **10.1103/PhysRevLett.124.227203**.

[81] Mara Gutzeit, André Kubetzka, Soumyajyoti Haldar, Henning Pralow, Moritz A. Goerzen, Roland Wiesendanger, Stefan Heinze, and Kirsten von Bergmann. "Nano-scale collinear multi-Q states driven by higher-order interactions." In: *Nature Communications* 13.1 (Sept. 2022), p. 5764. DOI: **10.1038/s41467-022-33383-w**.

[82] X. Z. Yu, N. Kanazawa, Y. Onose, K. Kimoto, W. Z. Zhang, S. Ishiwata, Y. Matsui, and Y. Tokura. "Near room-temperature formation of a skyrmion crystal in thin-films of the helimagnet FeGe." In: *Nature Materials* 10.2 (Feb. 2011), pp. 106–109. DOI: **10.1038/nmat2916**.

[83] P. Milde, D. Köhler, J. Seidel, L. M. Eng, A. Bauer, A. Chacon, J. Kindervater, S. Mühlbauer, C. Pfleiderer, S. Buhrandt, C. Schütte, and A. Rosch. "Unwinding of a Skyrmion Lattice by Magnetic Monopoles." In: *Science* 340.6136 (2013), pp. 1076–1080. DOI: **10.1126/science.1234657**.

[84] Xiuzhen Yu, Akiko Kikkawa, Daisuke Morikawa, Kiyou Shibata, Yusuke Tokunaga, Yasujiro Taguchi, and Yoshinori Tokura. "Variation of skyrmion forms and their stability in MnSi thin plates." In: *Phys. Rev. B* 91 (5 Feb. 2015), p. 054411. DOI: **10.1103/PhysRevB.91.054411**.

[85] I. Kézsmárki, S. Bordács, P. Milde, E. Neuber, L. M. Eng, J. S. White, H. M. Rønnow, C. D. Dewhurst, M. Mochizuki, K. Yanai, H. Nakamura, D. Ehlers, V. Tsurkan, and A. Loidl. "Néel-type skyrmion lattice with confined orientation in the polar magnetic semiconductor $GaV_4S_8$." In: *Nature Materials* 14.11 (Nov. 2015), pp. 1116–1122. DOI: **10.1038/nmat4402**.

[86] Fumitaka Kagawa, Hiroshi Oike, Wataru Koshibae, Akiko Kikkawa, Yoshihiro Okamura, Yasujiro Taguchi, Naoto Nagaosa, and Yoshinori Tokura. "Current-induced viscoelastic topological unwinding of metastable skyrmion strings." In: *Nature Communications* 8.1 (Nov. 2017), p. 1332. DOI: **10.1038/s41467-017-01353-2**.

[87] Haifeng Du, Xuebing Zhao, Filipp N. Rybakov, Aleksandr B. Borisov, Shasha Wang, Jin Tang, Chiming Jin, Chao Wang, Wensheng Wei, Nikolai S. Kiselev, Yuheng Zhang, Renchao Che, Stefan Blügel, and Mingliang Tian. "Interaction of Individual Skyrmions in a Nanostructured Cubic Chiral Magnet." In: *Phys. Rev. Lett.* 120 (19 May 2018), p. 197203. DOI: 10.1103/PhysRevLett.120.197203.

[88] Naoto Nagaosa and Yoshinori Tokura. "Topological properties and dynamics of magnetic skyrmions." In: *Nature Nanotechnology* 8.12 (Dec. 2013), pp. 899–911. DOI: 10.1038/nnano.2013.243.

[89] David Foster, Charles Kind, Paul J. Ackerman, Jung-Shen B. Tai, Mark R. Dennis, and Ivan I. Smalyukh. "Two-dimensional skyrmion bags in liquid crystals and ferromagnets." In: *Nature Physics* 15.7 (July 2019), pp. 655–659. DOI: 10.1038/s41567-019-0476-x.

[90] Charles Kind, Sven Friedemann, and Dan Read. "Existence and stability of skyrmion bags in thin magnetic films." In: *Applied Physics Letters* 116.2 (Jan. 2020), p. 022413. DOI: 10.1063/1.5127173.

[91] Max T Birch, Lukas Powalla, Kai Litzius, Vanessa Nehruji, Ondrej Hovorka, Sebastian Wintz, Frank Schulz, Daniel A Mayoh, Geetha Balakrishnan, Markus Weigand, Marko Burghard, and Gisela Schütz. "Control of stripe, skyrmion and skyrmionium formation in the 2D magnet $Fe_{3-x}GeTe_2$ by varying composition." In: *2D Materials* 11.2 (Jan. 2024), p. 025008. DOI: 10.1088/2053-1583/ad1a6b.

[92] V. P. Antropov, M. I. Katsnelson, B. N. Harmon, M. van Schilfgaarde, and D. Kusnezov. "Spin dynamics in magnets: Equation of motion and finite temperature effects." In: *Phys. Rev. B* 54 (2 July 1996), pp. 1019–1035. DOI: 10.1103/PhysRevB.54.1019.

[93] Wolfgang Nolting and Anupuru Ramakanth. *Quantum theory of magnetism*. Springer Science & Business Media, 2009.

[94] Ph. Kurz, F. Förster, L. Nordström, G. Bihlmayer, and S. Blügel. "Ab initio treatment of noncollinear magnets with the full-potential linearized augmented plane wave method." In: *Phys. Rev. B* 69 (2 Jan. 2004), p. 024415. DOI: 10.1103/PhysRevB.69.024415.

[95] Olle Eriksson, Anders Bergman, Lars Bergqvist, and Johan Hellsvik. *Atomistic spin dynamics: foundations and applications*. Oxford university press, 2017.

[96] W. Heisenberg. "Zur Theorie des Ferromagnetismus." In: *Zeitschrift für Physik* 49.9 (Sept. 1928), pp. 619–636. DOI: 10.1007/BF01328601.

[97] M. A. Ruderman and C. Kittel. "Indirect Exchange Coupling of Nuclear Magnetic Moments by Conduction Electrons." In: *Phys. Rev.* 96 (1 Oct. 1954), pp. 99–102. DOI: 10.1103/PhysRev.96.99.

[98] Tadao Kasuya. "A Theory of Metallic Ferro- and Antiferromagnetism on Zener's Model." In: *Progress of Theoretical Physics* 16.1 (July 1956), pp. 45–57. DOI: 10.1143/PTP.16.45.

[99] Kei Yosida. "Magnetic Properties of Cu-Mn Alloys." In: *Phys. Rev.* 106 (5 June 1957), pp. 893–898. DOI: 10.1103/PhysRev.106.893.

[100] P. W. Anderson. "Antiferromagnetism. Theory of Superexchange Interaction." In: *Phys. Rev.* 79 (2 July 1950), pp. 350–356. DOI: 10.1103/PhysRev.79.350.

[101] M Takahashi. "Half-filled Hubbard model at low temperature." In: *Journal of Physics C: Solid State Physics* 10.8 (Apr. 1977), p. 1289. DOI: 10.1088/0022-3719/10/8/031.

[102] A. H. MacDonald, S. M. Girvin, and D. Yoshioka. "$\frac{t}{U}$ expansion for the Hubbard model." In: *Phys. Rev. B* 37 (16 June 1988), pp. 9753–9756. DOI: 10.1103/PhysRevB.37.9753.

[103] Markus Hoffmann and Stefan Blügel. "Systematic derivation of realistic spin models for beyond-Heisenberg solids." In: *Phys. Rev. B* 101 (2 Jan. 2020), p. 024418. DOI: 10.1103/PhysRevB.101.024418.

[104] C. Kittel. "Model of Exchange-Inversion Magnetization." In: *Phys. Rev.* 120 (2 Oct. 1960), pp. 335–342. DOI: 10.1103/PhysRev.120.335.

[105] M.E. Lines. "Exchange striction in magnetic cluster complexes." In: *Solid State Communications* 11.12 (1972), pp. 1615–1618. DOI: https://doi.org/10.1016/0038-1098(72)90755-7.

[106] Bjarne Beyer, Mara Gutzeit, Tim Drevelow, Isabel Schwermer, Soumyajyoti Haldar, and Stefan Heinze. "Bilayer triple-Q state driven by interlayer higher-order exchange interactions." In: *Phys. Rev. B* 112 (9 Sept. 2025), p. 094430. DOI: 10.1103/ys1g-8597.

[107] Albert Fert, Vincent Cros, and João Sampaio. "Skyrmions on the track." In: *Nature Nanotechnology* 8.3 (Mar. 2013), pp. 152–156. DOI: 10.1038/nnano.2013.29.

[108] A. Fert and Peter M. Levy. "Role of Anisotropic Exchange Interactions in Determining the Properties of Spin-Glasses." In: *Phys. Rev. Lett.* 44 (23 June 1980), pp. 1538–1541. DOI: 10.1103/PhysRevLett.44.1538.

[109] Niklas Romming, André Kubetzka, Christian Hanneken, Kirsten von Bergmann, and Roland Wiesendanger. "Field-Dependent Size and Shape of Single Magnetic Skyrmions." In: *Phys. Rev. Lett.* 114 (17 May 2015), p. 177203. DOI: 10.1103/PhysRevLett.114.177203.

[110] Patrick Bruno. "Tight-binding approach to the orbital magnetic moment and magnetocrystalline anisotropy of transition-metal monolayers." In: *Phys. Rev. B* 39 (1 Jan. 1989), pp. 865–868. DOI: 10.1103/PhysRevB.39.865.

[111] G. H. O. Daalderop, P. J. Kelly, and M. F. H. Schuurmans. "First-principles calculation of the magnetocrystalline anisotropy energy of iron, cobalt, and nickel." In: *Phys. Rev. B* 41 (17 June 1990), pp. 11919–11937. DOI: 10.1103/PhysRevB.41.11919.

[112] H. J. G. Draaisma and W. J. M. de Jonge. "Surface and volume anisotropy from dipole-dipole interactions in ultrathin ferromagnetic films." In: *Journal of Applied Physics* 64.7 (Oct. 1988), pp. 3610–3613. DOI: 10.1063/1.341397.

[113] Igor S. Lobanov, Hannes Jónsson, and Valery M. Uzdin. "Mechanism and activation energy of magnetic skyrmion annihilation obtained from minimum energy path calculations." In: *Phys. Rev. B* 94 (17 Nov. 2016), p. 174418. DOI: 10.1103/PhysRevB.94.174418.

[114] James W. Cooley and John W. Tukey. "An Algorithm for the Machine Calculation of Complex Fourier Series." In: *Mathematics of Computation* 19.90 (1965), pp. 297–301.

[115] Nobuo Hayashi, Koji Saito, and Yoshinobu Nakatani. "Calculation of Demagnetizing Field Distribution Based on Fast Fourier Transform of Convolution." In: *Japanese Journal of Applied Physics* 35.12R (Dec. 1996), p. 6065. DOI: 10.1143/JJAP.35.6065.

[116] Geoffrey S. D. Beach, Corneliu Nistor, Carl Knutson, Maxim Tsoi, and James L. Erskine. "Dynamics of field-driven domain-wall propagation in ferromagnetic nanowires." In: *Nature Materials* 4.10 (Oct. 2005), pp. 741–744. DOI: 10.1038/nmat1477.

[117] Moritz A. Goerzen. "Thermal equilibrium and stability of complementary topological solitons in two-dimensional magnets." PhD thesis. University of Kiel, 2024.

[118] Filipp N. Rybakov, Nikolai S. Kiselev, Aleksandr B. Borisov, Lukas Döring, Christof Melcher, and Stefan Blügel. "Magnetic hopfions in solids." In: *APL Materials* 10.11 (Nov. 2022), p. 111113. DOI: 10.1063/5.0099942.

[119] Benjamin Heil, Achim Rosch, and Jan Masell. "Universality of annihilation barriers of large magnetic skyrmions in chiral and frustrated magnets." In: *Phys. Rev. B* 100 (13 Oct. 2019), p. 134424. DOI: 10.1103/PhysRevB.100.134424.

[120] Amel Derras-Chouk, Eugene M. Chudnovsky, and Dmitry A. Garanin. "Thermal collapse of a skyrmion." In: *J. Appl. Phys.* 126.8 (Aug. 2019), p. 083901. DOI: 10.1063/1.5109728.

[121] Alan Edelman, Tomás A. Arias, and Steven T. Smith. "The Geometry of Algorithms with Orthogonality Constraints." In: *SIAM Journal on Matrix Analysis and Applications* 20.2 (1998), pp. 303–353. DOI: 10.1137/S0895479895290954.

[122] Anastasiia S. Varentcova, Stephan von Malottki, Maria N. Potkina, Grzegorz Kwiatkowski, Stefan Heinze, and Pavel F. Bessarab. "Toward room-temperature nanoscale skyrmions in ultrathin films." In: *npj Computational Materials* 6.1 (Dec. 2020), p. 193. DOI: 10.1038/s41524-020-00453-w.

[123] P-A Absil, Robert Mahony, and Jochen Trumpf. "An extrinsic look at the Riemannian Hessian." In: *International conference on geometric science of information*. Springer. 2013, pp. 361–368.

[124] P-A Absil, Robert Mahony, and Rodolphe Sepulchre. "Optimization algorithms on matrix manifolds." In: *Optimization Algorithms on Matrix Manifolds*. Princeton University Press, 2009. DOI: https://doi.org/10.1515/9781400830244.

[125] Olinde Rodrigues. “Des lois géométriques qui régissent les déplacements d’un système solide dans l’espace, et de la variation des coordonnées provenant de ces déplacements considérés indépendamment des causes qui peuvent les produire.” In: *Journal de mathématiques pures et appliquées* 5 (1840), pp. 380–440.

[126] Han Wang, Yingying Dai, Gan-Moog Chow, and Jingsheng Chen. “Topological hall transport: Materials, mechanisms and potential applications.” In: *Progress in Materials Science* 130 (2022), p. 100971. DOI: https://doi.org/10.1016/j.pmatsci.2022.100971.

[127] Sheng Yang, Yuelei Zhao, Xichao Zhang, Xiangjun Xing, Haifeng Du, Xiaoguang Li, Masahito Mochizuki, Xiaohong Xu, Johan Åkerman, and Yan Zhou. “Fundamentals and applications of the skyrmion Hall effect.” In: *Applied Physics Reviews* 11.4 (Dec. 2024), p. 041335. DOI: 10.1063/5.0218280.

[128] B. Berg and M. Lüscher. “Definition and statistical distributions of a topological number in the lattice O(3) -model.” In: *Nuclear Physics B* 190.2 (1981), pp. 412–424. DOI: https://doi.org/10.1016/0550-3213(81)90568-X.

[129] Manuel dos Santos Dias, Juba Bouaziz, Mohammed Bouhassoune, Stefan Blügel, and Samir Lounis. “Chirality-driven orbital magnetic moments as a new probe for topological magnetic structures.” In: *Nature Communications* 7.1 (Dec. 2016), p. 13613. DOI: 10.1038/ncomms13613.

[130] S. Grytsiuk, J.-P. Hanke, M. Hoffmann, J. Bouaziz, O. Gomonay, G. Bihlmayer, S. Lounis, Y. Mokrousov, and S. Blügel. “Topological–chiral magnetic interactions driven by emergent orbital magnetism.” In: *Nature Communications* 11.1 (Jan. 2020), p. 511. DOI: 10.1038/s41467-019-14030-3.

[131] Vladyslav M. Kuchkin, Bruno Barton-Singer, Pavel F. Bessarab, and Nikolai S. Kiselev. “Symmetry-governed dynamics of magnetic skyrmions under field pulses.” In: *Comm. Phys.* 8.1 (Jan. 2025), p. 26. DOI: 10.1038/s42005-024-01913-1.

[132] B. A. Ivanov and D. D. Sheka. “Local magnon modes and the dynamics of a small-radius two-dimensional magnetic soliton in an easy-axis ferromagnet.” In: *Journal of Experimental and Theoretical Physics Letters* 82.7 (Oct. 2005), pp. 436–440. DOI: 10.1134/1.2142872.

[133] D. D. Sheka, C. Schuster, B. A. Ivanov, and F. G. Mertens. “Dynamics of topological solitons in two-dimensional ferromagnets.” In: *The European Physical Journal B - Condensed Matter and Complex Systems* 50.3 (Apr. 2006), pp. 393–402. DOI: 10.1140/epjb/e2006-00153-6.

[134] C. Moutafis, S. Komineas, and J. A. C. Bland. “Dynamics and switching processes for magnetic bubbles in nanoelements.” In: *Phys. Rev. B* 79 (22 June 2009), p. 224429. DOI: 10.1103/PhysRevB.79.224429.

[135] Imam Makhfudz, Benjamin Krüger, and Oleg Tchernyshyov. “Inertia and Chiral Edge Modes of a Skyrmion Magnetic Bubble.” In: *Phys. Rev. Lett.* 109 (21 Nov. 2012), p. 217201. DOI: 10.1103/PhysRevLett.109.217201.

[136] D. B. Litvin. “Spin point groups.” In: *Acta Crystallographica Section A* 33.2 (Mar. 1977), pp. 279–287. DOI: 10.1107/S0567739477000709.

[137] Pengfei Liu, Jiayu Li, Jingzhi Han, Xiangang Wan, and Qihang Liu. "Spin-Group Symmetry in Magnetic Materials with Negligible Spin-Orbit Coupling." In: *Phys. Rev. X* 12 (2 Apr. 2022), p. 021016. DOI: 10.1103/PhysRevX.12.021016.

[138] Zhenyu Xiao, Jianzhou Zhao, Yanqi Li, Ryuichi Shindou, and Zhi-Da Song. "Spin Space Groups: Full Classification and Applications." In: *Phys. Rev. X* 14 (3 Aug. 2024), p. 031037. DOI: 10.1103/PhysRevX.14.031037.

[139] Hana Schiff, Alberto Corticelli, Afonso Guerreiro, Judit Romhányi, and Paul McClarty. "The crystallographic spin point groups and their representations." In: *SciPost Phys.* 18 (2025), p. 109. DOI: 10.21468/SciPostPhys.18.3.109.

[140] Bruno Barton-Singer, Calum Ross, and Bernd J. Schroers. "Magnetic Skyrmions at Critical Coupling." In: *Commun. Math. Phys.* 375.3 (May 2020), pp. 2259–2280. DOI: 10.1007/s00220-019-03676-1.

[141] Vladyslav M. Kuchkin, Ksenia Chichay, Bruno Barton-Singer, Filipp N. Rybakov, Stefan Blügel, Bernd J. Schroers, and Nikolai S. Kiselev. "Geometry and symmetry in skyrmion dynamics." In: *Phys. Rev. B* 104 (16 Oct. 2021), p. 165116. DOI: 10.1103/PhysRevB.104.165116.

[142] Albert Fert, Nicolas Reyren, and Vincent Cros. "Magnetic skyrmions: advances in physics and potential applications." In: *Nature Reviews Materials* 2.7 (June 2017), p. 17031. DOI: 10.1038/natrevmats.2017.31.

[143] Pavel F. Bessarab, Valery M. Uzdin, and Hannes Jónsson. "Harmonic transition-state theory of thermal spin transitions." In: *Phys. Rev. B* 85 (18 May 2012), p. 184409. DOI: 10.1103/PhysRevB.85.184409.

[144] Baron Peters. "Chapter 10 - Transition state theory." In: *Reaction Rate Theory and Rare Events Simulations*. Ed. by Baron Peters. Amsterdam: Elsevier, 2017, pp. 227–271. DOI: https://doi.org/10.1016/B978-0-44-456349-1.00010-6.

[145] Stephan von Malottki. "Stability of magnetic skyrmions in ultrathin films." en. PhD thesis. Kiel, 2021.

[146] Moritz Alexander Goerzen. "Thermal equilibrium and stability of complementary topological solitons in two-dimensional magnets." en. PhD thesis. Kiel, 2024.

[147] James C. Keck. "Variational Theory of Chemical Reaction Rates Applied to Three-Body Recombinations." In: *The Journal of Chemical Physics* 32.4 (Apr. 1960), pp. 1035–1050. DOI: 10.1063/1.1730846.

[148] LALE Landau, Evgeny Lifshitz, et al. "On the theory of the dispersion of magnetic permeability in ferromagnetic bodies." In: *Phys. Z. Sowjetunion* 8.153 (1935), pp. 101–114.

[149] Thomas L Gilbert. "A phenomenological theory of damping in ferromagnetic materials." In: *IEEE transactions on magnetics* 40.6 (2004), pp. 3443–3449.

[150] Moritz A. Goerzen, Tim Drevelow, Soumyajyoti Haldar, Hendrik Schrautzer, Stefan Heinze, and Dongzhe Li. *Lifetime of bimerons and antibimerons in two-dimensional magnets*. 2025. arXiv: 2509.09344 [cond-mat.mes-hall].

[151] Josep Maria Anglada, Emili Besalú, Josep Maria Bofill, and Ramon Crehuet. "On the quadratic reaction path evaluated in a reduced potential energy surface model and the problem to locate transition states." In: *Journal of Computational Chemistry* 22.4 (2001), pp. 387–406. DOI: https://doi.org/10.1002/1096-987X(200103)22:4<387::AID-JCC1010>3.0.CO;2-R.

[152] Daniel Sheppard, Rye Terrell, and Graeme Henkelman. "Optimization methods for finding minimum energy paths." In: *The Journal of Chemical Physics* 128.13 (Apr. 2008), p. 134106. DOI: 10.1063/1.2841941.

[153] Daniel Sheppard and Graeme Henkelman. "Paths to which the nudged elastic band converges." In: *Journal of Computational Chemistry* 32.8 (2011), pp. 1769–1771. DOI: https://doi.org/10.1002/jcc.21748.

[154] David K. Hoffman, Ross S. Nord, and Klaus Ruedenberg. "Gradient extremals." In: *Theoretica chimica acta* 69.4 (May 1986), pp. 265–279. DOI: 10.1007/BF00527704.

[155] Horia Metiu, John Ross, Robert Silbey, and Thomas F. George. "On symmetry properties of reaction coordinates." In: *The Journal of Chemical Physics* 61.8 (Oct. 1974), pp. 3200–3209. DOI: 10.1063/1.1682477.

[156] Petros Valtazanos and Klaus Ruedenberg. "Bifurcations and transition states." In: *Theoretica chimica acta* 69.4 (May 1986), pp. 281–307. DOI: 10.1007/BF00527705.

[157] Víctor J. García-Garrido and Stephen Wiggins. "The dynamical significance of valley-ridge inflection points." In: *Chemical Physics Letters* 781 (2021), p. 138970. DOI: https://doi.org/10.1016/j.cplett.2021.138970.

[158] Wolfgang Quapp, Michael Hirsch, and Dietmar Heidrich. "Bifurcation of reaction pathways: the set of valley ridge inflection points of a simple three-dimensional potential energy surface." In: *Theoretical Chemistry Accounts* 100.5 (Dec. 1998), pp. 285–299. DOI: 10.1007/s002140050389.

[159] Wolfgang Quapp, Michael Hirsch, and Dietmar Heidrich. "An approach to reaction path branching using valley–ridge inflection points of potential-energy surfaces." In: *Theoretical Chemistry Accounts* 112.1 (Apr. 2004), pp. 40–51. DOI: 10.1007/s00214-003-0558-8.

[160] Wolfgang Quapp and Benjamin Schmidt. "An empirical, variational method of approach to unsymmetric valley-ridge inflection points." In: *Theoretical Chemistry Accounts* 128.1 (Jan. 2011), pp. 47–61. DOI: 10.1007/s00214-010-0749-z.

[161] Graeme Henkelman and Hannes Jónsson. "Improved tangent estimate in the nudged elastic band method for finding minimum energy paths and saddle points." In: *The Journal of Chemical Physics* 113.22 (Dec. 2000), pp. 9978–9985. DOI: 10.1063/1.1323224.

[162] Normand Mousseau, Laurent Karim Béland, Peter Brommer, Jean-François Joly, Fedwa El-Mellouhi, Eduardo Machado-Charry, Mihai-Cosmin Marinica, and Pascal Pochet. "The Activation-Relaxation Technique: ART Nouveau and Kinetic ART." In: *Journal of Atomic and Molecular Physics* 2012.1 (2012), p. 925278. DOI: https://doi.org/10.1155/2012/925278.

[163] Martin Ester, Hans-Peter Kriegel, Jörg Sander, and Xiaowei Xu. "A density-based algorithm for discovering clusters in large spatial databases with noise." In: *Proceedings of the Second International Conference on Knowledge Discovery and Data Mining*. KDD'96. Portland, Oregon: AAAI Press, 1996, pp. 226–231.

[164] Erich Schubert, Jörg Sander, Martin Ester, Hans Peter Kriegel, and Xiaowei Xu. "DBSCAN Revisited, Revisited: Why and How You Should (Still) Use DBSCAN." In: *ACM Trans. Database Syst.* 42.3 (July 2017), pp. 1–21.

[165] A.V. Ivanov, V.M. Uzdin, and H. Jónsson. "Fast and robust algorithm for energy minimization of spin systems applied in an analysis of high temperature spin configurations in terms of skyrmion density." In: *Computer Physics Communications* 260 (2021), p. 107749. DOI: https://doi.org/10.1016/j.cpc.2020.107749.

[166] Suk-Geun Hwang. "Cauchy's Interlace Theorem for Eigenvalues of Hermitian Matrices." In: *The American Mathematical Monthly* 111.2 (2004), pp. 157–159. DOI: 10.1080/00029890.2004.11920060.

[167] Dong C. Liu and Jorge Nocedal. "On the limited memory BFGS method for large scale optimization." In: *Mathematical Programming* 45.1 (Aug. 1989), pp. 503–528. DOI: 10.1007/BF01589116.

[168] Brendan J. Frey and Delbert Dueck. "Clustering by Passing Messages Between Data Points." In: *Science* 315.5814 (2007), pp. 972–976. DOI: 10.1126/science.1136800.

[169] Danny Matthew SAPUTRA, Daniel SAPUTRA, and Liniyanti D. OSWARI. "Effect of Distance Metrics in Determining K-Value in K-Means Clustering Using Elbow and Silhouette Method." In: *Proceedings of the Sriwijaya International Conference on Information Technology and Its Applications (SICONIAN 2019)*. Atlantis Press, 2020, pp. 341–346. DOI: 10.2991/aisr.k.200424.051.

[170] Fabian Pedregosa, Gaël Varoquaux, Alexandre Gramfort, Vincent Michel, Bertrand Thirion, Olivier Grisel, Mathieu Blondel, Peter Prettenhofer, Ron Weiss, Vincent Dubourg, Jake Vanderplas, Alexandre Passos, David Cournapeau, Matthieu Brucher, Matthieu Perrot, and Édouard Duchesnay. "Scikit-learn: Machine Learning in Python." In: *JMLR* 12.85 (2011), pp. 2825–2830.

[171] M.J. Donahue and R.D. McMichael. "Exchange energy representations in computational micromagnetics." In: *Physica B: Condensed Matter* 233.4 (1997). Hysteresis Modeling and Micromagnetism, pp. 272–278. DOI: https://doi.org/10.1016/S0921-4526(97)00310-4.

[172] Stefan Buhrandt and Lars Fritz. "Skyrmion lattice phase in three-dimensional chiral magnets from Monte Carlo simulations." In: *Phys. Rev. B* 88 (19 Nov. 2013), p. 195137. DOI: 10.1103/PhysRevB.88.195137.

[173] Vladyslav Kuchkin, Bernd Schroers, and Stefan Blügel. *Diversity of chiral magnetic solitons*. RWTH-2022-10481. Fachgruppe Physik, 2022. DOI: 10.18154/RWTH-2022-10481.

[174] F. N. Rybakov, A. B. Borisov, and A. N. Bogdanov. "Three-dimensional skyrmion states in thin films of cubic helimagnets." In: *Phys. Rev. B* 87 (9 Mar. 2013), p. 094424. DOI: 10.1103/PhysRevB.87.094424.

[175] Gideon P. Müller, Filipp N. Rybakov, Hannes Jónsson, Stefan Blügel, and Nikolai S. Kiselev. "Coupled quasimonopoles in chiral magnets." In: *Phys. Rev. B* 101 (18 May 2020), p. 184405. DOI: 10.1103/PhysRevB.101.184405.

[176] Shuang Li, Jing Xia, Laichuan Shen, Xichao Zhang, Motohiko Ezawa, and Yan Zhou. "Mutual conversion between a magnetic Néel hopfion and a Néel toron." In: *Phys. Rev. B* 105 (17 May 2022), p. 174407. DOI: 10.1103/PhysRevB.105.174407.

[177] Soumyajyoti Haldar, Stephan von Malottki, Sebastian Meyer, Pavel F. Bessarab, and Stefan Heinze. "First-principles prediction of sub-10-nm skyrmions in Pd/Fe bilayers on Rh(111)." In: *Phys. Rev. B* 98 (6 Aug. 2018), p. 060413. DOI: 10.1103/PhysRevB.98.060413.

[178] J. Hagemeister, N. Romming, K. von Bergmann, E. Y. Vedmedenko, and R. Wiesendanger. "Stability of single skyrmionic bits." In: *Nature Communications* 6.1 (Oct. 2015), p. 8455. DOI: 10.1038/ncomms9455.

[179] Johannes Wild, Thomas N. G. Meier, Simon Pöllath, Matthias Kronseder, Andreas Bauer, Alfonso Chacon, Marco Halder, Marco Schowalter, Andreas Rosenauer, Josef Zweck, Jan Müller, Achim Rosch, Christian Pfleiderer, and Christian H. Back. "Entropy-limited topological protection of skyrmions." In: *Science Advances* 3.9 (2017), e1701704. DOI: 10.1126/sciadv.1701704.

[180] L. Desplat, D. Suess, J-V. Kim, and R. L. Stamps. "Thermal stability of metastable magnetic skyrmions: Entropic narrowing and significance of internal eigenmodes." In: *Phys. Rev. B* 98 (13 Oct. 2018), p. 134407. DOI: 10.1103/PhysRevB.98.134407.

[181] Mara Gutzeit, Soumyajyoti Haldar, Sebastian Meyer, and Stefan Heinze. "Trends of higher-order exchange interactions in transition metal trilayers." In: *Phys. Rev. B* 104 (2 July 2021), p. 024420. DOI: 10.1103/PhysRevB.104.024420.

[182] Vilhjálmur Ásgeirsson, Benedikt Orri Birgisson, Ragnar Bjornsson, Ute Becker, Frank Neese, Christoph Riplinger, and Hannes Jónsson. "Nudged Elastic Band Method for Molecular Reactions Using Energy-Weighted Springs Combined with Eigenvector Following." In: *Journal of Chemical Theory and Computation* 17.8 (Aug. 2021), pp. 4929–4945. DOI: 10.1021/acs.jctc.1c00462.

[183] Yorick L. A. Schmerwitz, Gianluca Levi, and Hannes Jónsson. "Calculations of Excited Electronic States by Converging on Saddle Points Using Generalized Mode Following." In: *Journal of Chemical Theory and Computation* 19.12 (2023), pp. 3634–3651. DOI: 10.1021/acs.jctc.3c00178.

[184] K. Deb, A. Pratap, S. Agarwal, and T. Meyarivan. "A fast and elitist multiobjective genetic algorithm: NSGA-II." In: *IEEE Transactions on Evolutionary Computation* 6.2 (2002), pp. 182–197. DOI: 10.1109/4235.996017.

[185] Aaron Meurer, Christopher P. Smith, Mateusz Paprocki, Ondřej Čertík, Sergey B. Kirpichev, Matthew Rocklin, AMiT Kumar, Sergiu Ivanov, Jason K. Moore, Sartaj Singh, Thilina Rathnayake, Sean Vig, Brian E. Granger, Richard P. Muller, Francesco Bonazzi, Harsh Gupta, Shivam Vats, Fredrik Johansson, Fabian Pedregosa, Matthew J. Curry, Andy R. Terrel, Štěpán Roučka, Ashutosh Saboo, Isuru Fernando, Sumith Kulal, Robert Cimrman, and Anthony Scopatz. "SymPy: symbolic computing in Python." In: *PeerJ Computer Science* 3 (Jan. 2017), e103. DOI: **10.7717/peerj-cs.103**.

# Appendix A: Software Design

## A.1: Modeling exemplary two-dimensional surfaces

During the development of optimization methods like GMMF operating in spaces with many dimensions, visualizing the corresponding concepts for simple two-dimensional systems has proven helpful. Furthermore, in this thesis the developed methods are also sketched for exemplary two-dimensional systems. A simple **Python** tool providing a class **CEnergyLandscape** has been implemented allowing the user to define a function of two variables, which represents the energy. Using the symbolic computations of the package **sympy** [185] the gradient and Hessian can be evaluated. Simplified versions of the GMMF, GNEB and steepest descent algorithms are included within the tool. The corresponding **Python** class can be accessed in a public GitLab repository (**https://gitlab.com/h.schrautzer/optsurface2d**), where also further examples for its usage are provided. Below an example of usage is provided generating the data for the visualization shown in Fig. 4.2.

```python
from CEnergyLandscape import CEnergyLandscape
import matplotlib.pyplot as plt
import sympy as sp
import numpy as np

# Create the two variables as sympy Symbols and an energy function of these variables as a sympy expression.
x,y = sp.Symbol("x"), sp.Symbol("y")
E = sp.cos(4*x)+sp.cos(4*y)+2
# Define the instance of the Energy landscape
surface = CEnergyLandscape(expression=E,symbols=[x,y])

# Create grid
x,y = np.linspace(-1,1,100), np.linspace(-1,1,100)
X, Y = np.meshgrid(x,y)
# Evaluate the above function at the grid points
E = surface.evaluate(x=X,y=Y)

# Use scipy optimize to identify local energy minima on this surface. Within the provided limits the Nx * Ny
# minimizations are initialized with a grid of starting points in the intervals xlims, ylims.
minima = surface.local_minima_2d(xlims=(-1,1),ylims=(-1,1),Nx=10,Ny=10)
```

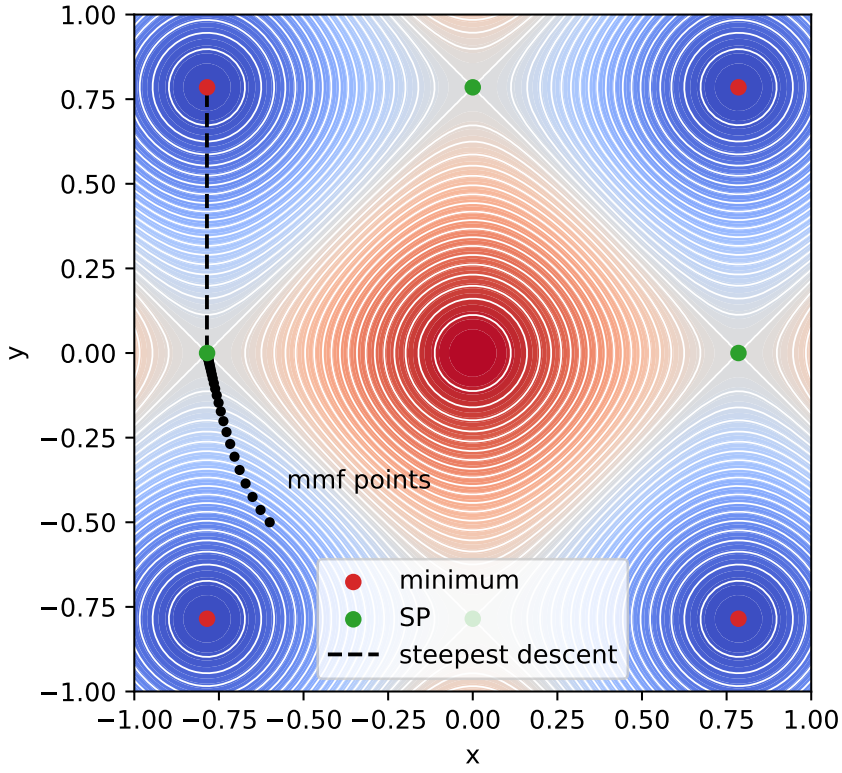


**Figure 4.2.** Two-dimensional energy surface with minima (red) and SPs (green). An GMMF calculation is initialized (black points) converging onto a first-order SP followed by a subsequent steepest descent toward the adjacent energy minimum.

```
# Similar as the above function for minima but identifying
↪ first-order SPs. A custom gradient, which inverts the
# gradient along the minimum mode, is used in scipy optimize.
sps =
↪ surface.saddle_points_2d(xlims=(-1,1),ylims=(-1,1),Nx=10,Ny=10)

# Choose a starting point:
start = np.array([-0.6,-0.5])
# Apply mmf
mmf_points, modgrads =
↪ surface.mmf_2d(startpoint=start,initial_stepscale=0.01)
# Apply steepest descent
sp = sps[0] + np.asarray([0.0,0.01])
sd, grads = surface.steepest_descent_2d(startpoint=sp,
↪ initial_stepscale=0.05)

# Visualization ...
```

## A.2: Symmetries of localized magnetic textures

Given the magnetic moments $\boldsymbol{m} = (\vec{m}_1, \ldots, \vec{m}_T)$ at lattice sites $\boldsymbol{r} = (\vec{r}_1, \ldots, \vec{r}_T)$ of a texture with $T$ moments, the preprocessing state of the SPSF determine the rotational and reflection operations under which the texture stays invariant. The algorithm implemented detecting symmetries for a given texture is presented in Paper IV. The corresponding **Python** code is publicly available at a GitLab repository (**https://gitlab.com/h.schrautzer/magtexturesymmetry**). Below a minimal example is given for the texture shown in Fig. 2.2. Several plotting utilities are provided in the plotting module. The below code snippet, executed in the root of the GitLab repository generates Fig. 4.3.

```python
from spintext.texture import SpinTexture
from spintext.symmetry import TextureSymmetry
from spintext.plotting import *
from pathlib import Path
import numpy as np

# Load texture
texture = SpinTexture(path_texture=Path.cwd() / "scripts" / "texture.dat")
# Define DMI vector angle (has influence on the reflection operation)
beta = 30*np.pi / 180

# Initialize symmetry object
sym = TextureSymmetry(texture=texture,beta=beta)
sym.detect_rotation_symmetries(prime_rotations=(2,3,5,7), geodesic_crit=0.01)
sym.detect_mirror_symmetries(geodesic_crit=0.01)
plot_symmetry_axes(texture=texture,tsym=sym,show=False)

plt.savefig("symmetry_example.pdf")
```

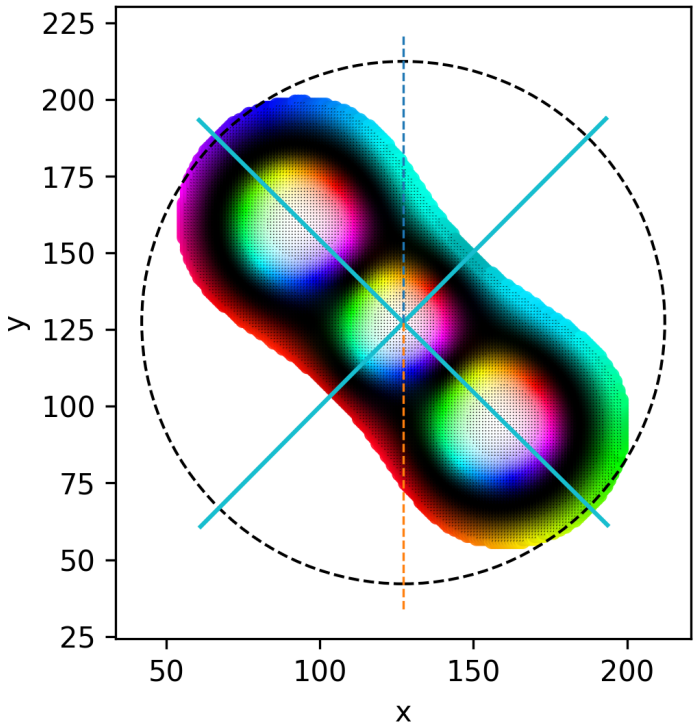


**Figure 4.3.** Magnetic texture corresponding two the group $\mathrm{D}_2$ (cf. Sec. 2.1). The two reflection axes are drawn in cyan. The visualization was obtained using the implemented python library available at (`https://gitlab.com/h.schrautzer/magtexturesymmetry`).

# Appendix B: Mapping between the discrete and continuous energy model for a square lattice.

The starting point are the exchange and DMI term of the lattice Hamiltonian

$$E = -\sum_n \frac{J_n}{2} \sum_{\langle ij \rangle_n} \vec{m}_i \cdot \vec{m}_j - \sum_n \frac{D_n}{2} \sum_{\langle ij \rangle_n} \vec{d}_{ij} \cdot (\vec{m}_i \times \vec{m}_j) \ , \tag{66}$$

where for simplicity Bloch-type DMI is assumed with $\vec{d}_{ij} = \vec{r}_{ij}/|\vec{r}_{ij}|$ for the connection vector $\vec{r}_{ij}$ between the sites $i$ and $j$. The other types of DMI in Eq. (8) can be obtained by applying a rotation $R_\beta$ to the final Lifshitz invariant which will be obtained in the following. On a regular two dimensional lattice the discrete Fourier transform of the magnetization is used

$$\vec{m}_i = \frac{1}{\sqrt{N}} \sum_{\vec{q}} \tilde{\vec{m}}_{\vec{q}} e^{i\vec{q}\cdot\vec{r}_i} \tag{67}$$

and inserted into the lattice Hamiltonian:

$$E = -\sum_n \frac{J_n}{2N} \sum_{\langle ij \rangle_n} \sum_{\vec{q},\vec{p}} \tilde{\vec{m}}_{\vec{q}} \cdot \tilde{\vec{m}}_{\vec{p}} \mathrm{e}^{i\vec{q}\cdot\vec{r}_i} \mathrm{e}^{i\vec{p}\cdot\vec{r}_j} - \sum_n \frac{D_n}{2N} \sum_{\langle ij \rangle_n} \frac{\vec{r}_{ij}}{|\vec{r}_{ij}|} \cdot \sum_{\vec{q},\vec{p}} (\tilde{\vec{m}}_{\vec{q}} \times \tilde{\vec{m}}_{\vec{p}}) \mathrm{e}^{i\vec{q}\cdot\vec{r}_i} \mathrm{e}^{i\vec{p}\cdot\vec{r}_j} \ . \tag{68}$$

For each $i$, the sum over $j$ includes all neighbors with respect to displacement vectors $\vec{a}_n$ corresponding to the $n$-th nearest neighbor shell such that $\vec{r}_j = \vec{r}_i + \vec{a}_n$ while the summation over $j$ changes to a summation over the $\vec{a}_n$:

$$E = -\sum_n \frac{J_n}{2N} \sum_i \sum_{\vec{a}_n} \sum_{\vec{q},\vec{p}} \tilde{\vec{m}}_{\vec{q}} \cdot \tilde{\vec{m}}_{\vec{p}} \mathrm{e}^{i(\vec{q}+\vec{p})\cdot\vec{r}_i} \mathrm{e}^{i\vec{p}\cdot\vec{a}_n} \tag{69}$$

$$- \sum_n \frac{D_n}{2N} \sum_i \sum_{\vec{a}_n} \frac{\vec{a}_n}{|\vec{a}_n|} \cdot \sum_{\vec{q},\vec{p}} (\tilde{\vec{m}}_{\vec{q}} \times \tilde{\vec{m}}_{\vec{p}}) \mathrm{e}^{i(\vec{q}+\vec{p})\cdot\vec{r}_i} \mathrm{e}^{i\vec{p}\cdot\vec{a}_n} \ . \tag{70}$$

The summation over $\vec{p}$ can be transformed into a summation over $-\vec{q}$ using

$$\sum_i e^{i(\vec{q}+\vec{p})\cdot\vec{r}_i} = N\delta_{\vec{q}+\vec{p},0} \ , \tag{71}$$

where $N$ is the number of magnetic moments. This leads to:

$$E = -\sum_n \frac{J_n}{2} \sum_{\vec{a}_n} \sum_{\vec{q}} \tilde{\vec{m}}_{\vec{q}} \cdot \tilde{\vec{m}}_{-\vec{q}} \mathrm{e}^{-i\vec{q}\cdot\vec{a}_n} - \sum_n \frac{D_n}{2} \sum_{\vec{a}_n} \frac{\vec{a}_n}{|\vec{a}_n|} \cdot \sum_{\vec{q}} (\tilde{\vec{m}}_{\vec{q}} \times \tilde{\vec{m}}_{-\vec{q}}) \mathrm{e}^{-i\vec{q}\cdot\vec{a}_n} \ . \tag{72}$$

The neighbor shells are isotropic such that for $\vec{a}_n$ also $-\vec{a}_n$ is part of this shell. Thus, the summation over all vectors of a shell can be changed into a summation over pairs $\vec{a}_n$, $-\vec{a}_n$. Then insert

$$\mathrm{e}^{i\vec{q}\cdot\vec{a}_n} + \mathrm{e}^{-i\vec{q}\cdot\vec{a}_n} = 2\cos(\vec{q}\cdot\vec{a}_n) \tag{73}$$

$$\frac{\vec{a}_n}{|\vec{a}_n|}\mathrm{e}^{i\vec{q}\cdot\vec{a}_n} - \frac{\vec{a}_n}{|\vec{a}_n|}\mathrm{e}^{-i\vec{q}\cdot\vec{a}_n} = 2i\frac{\vec{a}_n}{|\vec{a}_n|}\sin(\vec{q}\cdot\vec{a}_n) \tag{74}$$

into the above sum the prime of the sum over $\vec{a}_n$ denotes the summation over the pairs of antiparallel vectors of a shell:

$$E = -\sum_n J_n \sum_{\vec{a}_n}{}' \sum_{\vec{q}} \vec{\tilde{m}}_{\vec{q}}\cdot\vec{\tilde{m}}_{-\vec{q}}\cos(\vec{q}\cdot\vec{a}_n) \tag{75}$$

$$-\sum_n D_n \sum_{\vec{a}_n}{}' \frac{\vec{a}_n}{|\vec{a}_n|}\cdot\sum_{\vec{q}}(\vec{\tilde{m}}_{\vec{q}}\times\vec{\tilde{m}}_{-\vec{q}})i\sin(\vec{q}\cdot\vec{a}_n)\ . \tag{76}$$

On a square lattice with $J_1$, $D_1$, $J_2 = D_2 = 0$, $J_3$ and $D_3$ the discrete displacements to the neighbors in units of the nearest neighbor distance $a$ are $\vec{a}_1 \in \{a\hat{x}, a\hat{y}\}$ and $\vec{a}_3 \in \{2a\hat{x}, 2a\hat{y}\}$, respectively. This yields:

$$E = -\sum_{\vec{q}} \vec{\tilde{m}}_{\vec{q}}\cdot\vec{\tilde{m}}_{-\vec{q}}\left[J_1(\cos(aq_x)+\cos(aq_y)) + J_3(\cos(2aq_x)+\cos(2aq_y))\right] \tag{77}$$

$$-\sum_{\vec{q}} i(\vec{\tilde{m}}_{\vec{q}}\times\vec{\tilde{m}}_{-\vec{q}})\left[D_1(\hat{x}\sin(aq_x)+\hat{y}\sin(aq_y)) + D_3(\hat{x}\sin(2aq_x)+\hat{y}\sin(2aq_y))\right]\ . \tag{78}$$

Now expand the sine and cosine for small $qa \ll 1$ into a series:

$$\cos(nq_\mu a) \approx 1 - \frac{1}{2}(nq_\mu a)^2 + \frac{1}{24}(nq_\mu a)^4 \tag{79}$$

$$\sin(nq_\mu a) \approx nq_\mu a - \frac{1}{6}(nq_\mu a)^3 \tag{80}$$

for $n = 1, 2$ and $\mu = x, y$. Note that terms up to the order of four are taken into account for rapid changes of the magnetization e.g. in the vicinity of Bloch-like points [119, 120]. With $q^2 = q_x^2 + q_y^2$ the energy reads:

$$E = \sum_{\vec{q}} \vec{\tilde{m}}_{\vec{q}}\cdot\vec{\tilde{m}}_{-\vec{q}}\left[J_1\left(\frac{a^2q^2}{2} - \frac{a^4(q_x^4+q_y^4)}{24}\right) + J_3\left(\frac{4a^2q^2}{2} - \frac{16a^4(q_x^4+q_y^4)}{24}\right)\right] \tag{81}$$

$$-\sum_{\vec{q}} \vec{\tilde{m}}_{\vec{q}}\cdot\vec{\tilde{m}}_{-\vec{q}}\left[2J_1 + 2J_3\right] \tag{82}$$

$$-\sum_{\vec{q}} i(\vec{\tilde{m}}_{\vec{q}}\times\vec{\tilde{m}}_{-\vec{q}})\left[D_1\left(a\vec{q} - \frac{a^3}{6}(\hat{x}q_x^3+\hat{y}q_y^3)\right) + D_3\left(2a\vec{q} - \frac{4a^3}{3}(\hat{x}q_x^3+\hat{y}q_y^3)\right)\right]\ . \tag{83}$$

Rearranging the terms yields:

$$E = \sum_{\vec{q}} \vec{\tilde{m}}_{\vec{q}} \cdot \vec{\tilde{m}}_{-\vec{q}} \left[ \frac{a^2 q^2}{2}(J_1 + 4J_3) - \frac{a^4(q_x^4 + q_y^4)}{24}(J_1 + 16J_3) - 2J_1 - 2J_3 \right] \tag{84}$$

$$- \sum_{\vec{q}} i(\vec{\tilde{m}}_{\vec{q}} \times \vec{\tilde{m}}_{-\vec{q}}) \left[ (D_1 + 2D_3) a\vec{q} - (D_1 + 8D_3) \frac{a^3(\hat{x} q_x^3 + \hat{y} q_y^3)}{6} \right] . \tag{85}$$

In the continuum limit $\sum_{\vec{q}} \to \frac{V_q}{(2\pi)^2} \int \mathrm{dq}^2$, where $V_q = (2\pi/a)^2$ is the volume of the Brillouin zone, in total five terms are obtained

$$\mathcal{E} = \mathcal{E}_{\mathrm{ex}}^{(2)} + \mathcal{E}_{\mathrm{ex}}^{(4)} + \mathcal{E}_{\mathrm{ex}}^{\mathrm{FM}} + \mathcal{E}_{\mathrm{DM}}^{(1)} + \mathcal{E}_{\mathrm{DM}}^{(3)} , \tag{86}$$

where the exchange energy of the ferromagnetic state $\mathcal{E}_{\mathrm{ex}}^{\mathrm{FM}}$ is obtained via inverse Fourier transform and considering the constraint $\vec{m}(\vec{r})^2 = 1$:

$$\mathcal{E}_{\mathrm{ex}}^{\mathrm{FM}} = -\frac{2(J_1 + J_3)}{a^2} \int \mathrm{d}r^2 \ . \tag{87}$$

The remaining exchange terms read

$$\mathcal{E}_{\mathrm{ex}}^{(2)} = \frac{J_1 + 4J_3}{2} \int i q \vec{\tilde{m}}(\vec{q}) \cdot (-i q \vec{\tilde{m}}(-\vec{q}))\, \mathrm{d}q^2 \tag{88}$$

$$\mathcal{E}_{\mathrm{ex}}^{(4)} = -\, a^2 \frac{J_1 + 16J_3}{24} \int \left[ q_x^2 \vec{\tilde{m}}(\vec{q}) \cdot (q_x^2 \vec{\tilde{m}}(-\vec{q})) + q_y^2 \vec{\tilde{m}}(\vec{q}) \cdot (q_y^2 \vec{\tilde{m}}(-\vec{q})) \right] \mathrm{d}q^2 \ , \tag{89}$$

where a factor of $-i^2$ was introduced in Eq. 88. Using $(\vec{\tilde{m}}(\vec{q}) \times \vec{\tilde{m}}(-\vec{q})) \cdot \vec{q} = \vec{\tilde{m}}(\vec{q}) \cdot (\vec{q} \times \vec{\tilde{m}}(-\vec{q}))$ the linear DMI term can be written

$$\mathcal{E}_{\mathrm{DM}}^{(1)} = \frac{D_1 + 2D_3}{a} \int \vec{\tilde{m}}(\vec{q}) \cdot (-i\vec{q} \times \vec{\tilde{m}}(-\vec{q}))\, \mathrm{d}q^2 \ . \tag{90}$$

The cubic DMI term can be similarly rewritten:

$$\mathcal{E}_{\mathrm{DM}}^{(3)} = a \frac{D_1 + 8D_3}{6} \int \vec{\tilde{m}}(\vec{q}) \cdot \left[ \left( (-iq_x)^3 \hat{x} + (-iq_y)^3 \hat{y} \right) \times \vec{\tilde{m}}(-\vec{q}) \right] \mathrm{d}q^2 \ . \tag{91}$$

From $\vec{m}(\vec{r}) \in \mathbb{R}^3$ it follows that $\vec{\tilde{m}}(-\vec{q}) = \vec{\tilde{m}}^*(\vec{q})$ and the following properties of the Fourier transform can be exploited

$$\mathcal{F}[\vec{\nabla} \vec{m}(\vec{r})] = i\vec{q} \vec{\tilde{m}}(\vec{q}) \tag{92}$$

$$\mathcal{F}[\partial_\mu^2 \vec{m}(\vec{r})] = -q_\mu^2 \vec{\tilde{m}}(\vec{q}) \tag{93}$$

$$\mathcal{F}[\partial_\mu^3 \vec{m}(\vec{r})] = (iq_\mu)^3 \vec{\tilde{m}}(\vec{q}) \tag{94}$$

$$\mathcal{F}[\vec{\nabla} \times \vec{m}(\vec{r})] = i\vec{q} \times \vec{\tilde{m}}(\vec{q}) \tag{95}$$

to apply Parseval's theorem and finally denote:

$$\mathcal{E} = \int \frac{J_1 + 4J_3}{2} (\vec{\nabla} \vec{m}(\vec{r}))^2 \, \mathrm{d}r^2 - \int a^2 \frac{J_1 + 16J_3}{24} \left[ (\partial_x^2 \vec{m}(\vec{r})^2 + (\partial_y^2 \vec{m}(\vec{r})^2 \right] \mathrm{d}r^2 \tag{96}$$

$$+ \mathcal{E}_{\mathrm{ex}}^{\mathrm{FM}} + \int \frac{D_1 + 2D_3}{a} R_\beta \vec{m}(\vec{r}) \cdot (\vec{\nabla} \times R_\beta \vec{m}(\vec{r}))\, \mathrm{d}r^2 \tag{97}$$

$$+ \int \frac{a(D_1 + 8D_3)}{6} R_\beta \vec{m}(\vec{r}) \cdot \left[ \sum_{\alpha \in \{x,y\}} \partial_a^3 \hat{\alpha} \times R_\beta \vec{m}(\vec{r}) \right] \mathrm{d}r^2 \ , \tag{98}$$

where the rotation matrix $R_\beta$ was reintroduced. The parameters of the lattice Hamiltonian can be chosen such that Eq. 2 and Eq. 17 are equivalent in the continuum-limit and that the higher-order spatial derivatives in Eqs. (96),(97),(98) vanish. This can be accomplished by:

$$J_1 = \frac{4}{3}\mathcal{J} \tag{99}$$

$$J_3 = -\frac{1}{12}\mathcal{J} \tag{100}$$

$$D_1 = \frac{4}{3}\mathcal{D}a \tag{101}$$

$$D_3 = -\frac{1}{6}\mathcal{D}a \ . \tag{102}$$

# Appendix C: Publications

# Paper I

**Effects of interlayer exchange on collapse mechanisms and stability of magnetic skyrmions**

H. Schrautzer, S. von Malottki, P.F. Bessarab, S. Heinze

Physical Review B **105**, 014414 (2022)



Hendrik performed the calculations, analyzed the data, prepared the figures and wrote the article together with all authors.

Editors' Suggestion

# Effects of interlayer exchange on collapse mechanisms and stability of magnetic skyrmions

Hendrik Schrautzer,[1,2,*] Stephan von Malottki,[1,2] Pavel F. Bessarab,[2,3] and Stefan Heinze[1]
[1]*Institut für Theoretische Physik und Astrophysik, Christian-Albrechts-Universität zu Kiel, D-24098 Kiel, Germany*
[2]*Science Institute, University of Iceland, 107 Reykjavik, Iceland*
[3]*Department of Physics and Engineering, ITMO University, 197101 St. Petersburg, Russia*

(Received 29 July 2021; accepted 14 December 2021; published 11 January 2022)

Theoretical calculations of thermally activated decay of skyrmions in systems comprising several magnetic monolayers are presented, with a special focus on bilayer systems. Mechanisms of skyrmion collapse are identified and corresponding energy barriers and thermal collapse rates are evaluated as functions of the interlayer exchange coupling and mutual stacking of the monolayers using transition state theory and an atomistic spin Hamiltonian. In order to contrast the results to monolayer systems, the magnetic interactions within each layer are chosen so as to mimic the well-established Pd/Fe/Ir(111) system. Even bilayer systems demonstrate a rich diversity of skyrmion collapse mechanisms that sometimes coexist. For very weakly coupled layers, the skyrmions in each layer decay successively via radially symmetric shrinking. Slightly larger coupling leads to an asymmetric chimera collapse stabilized by the interlayer exchange. When the interlayer exchange coupling reaches a certain critical value, the skyrmions collapse simultaneously. Interestingly, the overall energy barrier for the skyrmion collapse does not always converge to a multiple of that for a monolayer system in the strongly coupled regime. For a certain stacking of the magnetic layers, the energy barrier as a function of the interlayer exchange coupling features a maximum and then decreases with the coupling strength in the strong coupling regime. Calculated mechanisms of skyrmion collapse are used to ultimately predict the skyrmion lifetime. Our results reveal a comprehensive picture of the thermal stability of skyrmions in magnetic multilayers and provide a perspective for realizing skyrmions with controlled properties.

DOI: 10.1103/PhysRevB.105.014414

## I. INTRODUCTION

Over the past decade, topological spin textures such as magnetic skyrmions have been in the focus of many experimental and theoretical studies due to their intriguing properties [1–3]. After being predicted theoretically [4], the first experimental evidence of a skyrmion lattice was obtained in cubic B20 compounds [5,6]. The broken inversion symmetry in these crystals induces the Dzyaloshinskii-Moriya interaction (DMI) [7,8] favoring noncollinear magnetic structures [9,10]. Interfaces or surfaces naturally break the inversion symmetry, too, leading to interfacial DMI in ultrathin transition-metal films on substrates with significant spin-orbit coupling [11,12]. This class of skyrmionic systems was established by the discovery of a nanoscale skyrmion lattice in monolayer Fe films on Ir(111) [13], and later enriched by experimental observation of isolated skyrmions in ultrathin film systems such as Pd/Fe/Ir(111) [14,15], Pd/Pd/Fe/Ir(111) [16], 3Fe/Ir(111) [17], Co/Ru(0001) [18], and Rh/Co/Ir(111) [19].

In ultrathin films, the magnetic interactions such as magnetic exchange, DMI and magnetocrystalline anisotropy can be tuned over a wide range via various mechanisms [19–27], making these systems a convenient platform for realizing skyrmions with controlled properties [28]. Moreover, due to their pseudomorphic growth and the possibility of direct observation of their magnetic structures by surface-sensitive measurement techniques, ultrathin films became well-established model systems for the understanding of skyrmion properties [13–15,18,19,29].

One major issue for the technological application of magnetic skyrmions is the thermal stability, which is especially limited in ultrathin-films. Previous theoretical calculations applied to magnetic monolayers have predicted that a skyrmion state in the system coupled to the heat bath could decay into the topologically trivial state via radially symmetric shrinking [30–32] or asymmetric collapse involving local rotation of magnetization at an excentric point of the skyrmion–so called chimera mode [19,33]. Both collapse modes have subsequently been discovered by means of spin-polarized scanning tunneling microscopy in the Pd/Fe/Ir(111) system subject to an oblique external magnetic field [34]. Additionally, skyrmions are expected to be able to escape through the system's boundaries [35] or even duplicate [36]. The decay processes ultimately define the skyrmion lifetime, a quantitative measure of the skyrmion stability, which is usually described by an Arrhenius law [35,37,38]

$$\tau = \tau_0 \exp\left(\frac{\Delta E}{k_B T}\right), \tag{1}$$

where $\tau$ is the mean skyrmion lifetime, $\tau_0$ the pre-exponential factor, $\Delta E$ the energy barrier and $k_B T$ the thermal energy.

*hes93@hi.is

 

Recent atomistic spin simulations, either parameterized by first-principles density functional theory (DFT) calculations or as systematic parameter studies, revealed, that a large DMI, strong exchange frustration [31], the occurrence of higher order exchange interaction [13,39] or tuning of the skyrmion shape [40] can enhance skyrmion stability drastically. Furthermore, a decisive entropic stabilization effect has been found, increasing the prefactor of the Arrhenius law and thus, the skyrmion lifetime [33,37,40–42].

Another theoretically predicted [43] design strategy for improved skyrmion stability is the repeated stacking of additional magnetic layers, increasing the amount of magnetic material in the system. By sandwiching the magnetic layers between two different heavy metals, an additional enhancement of the effective DMI can be achieved as a result of additive interfacial chiral interactions, which additionally favors the stability of magnetic skyrmions [44]. Indeed, by following the idea of multilayer systems, room-temperature stability of skyrmion has been achieved in different materials [44–47]. In contrast to skyrmions in ultrathin film systems, however, skyrmions in multilayers have been found to be larger in size, ranging from 30 nm to several 100 nm [44–47]. More recently, room-temperature skyrmions with sizes down to 20 nm have been accomplished by using a compensated ferrimagnetic material [48]. An additional advantage of multilayers compared to monolayer systems is the suppressed skyrmion Hall effect [49] in antiferromagnetically coupled layers, as it has been demonstrated by Legrand *et al.* at room-temperature conditions and without external magnetic fields [50]. Recently Rana *et al.* also succeeded in stabilizing skyrmions at zero field at room temperature using the exchange-bias effect [51].

In contrast to the great success of its experimental realization, very little is understood about the thermal stability of skyrmions in multilayer systems. In 2017, Stosic *et al.* [52] investigated the stability and collapse mechanisms of skyrmions in trilayers, focusing on the variation of DMI in the different layers. They showed that magnetic interactions differ significantly in a multilayer structure with varying thickness of the magnetic material due to the different interfaces the individual magnetic layers experience. The layer resolved and thus reduced DMI led to more realistic but less stable skyrmions than previously considered. More recently, Hoffmann *et al.* found an increasing skyrmion stability for an increasing number of magnetic layers. They assumed similar magnetic properties in each layer, a strong interlayer exchange coupling and a simultaneous radial symmetric collapse of skyrmions in all layers [53]. Consistent with these general assumptions, Heil *et al.* suggested in 2019 that the energy barrier for skyrmions in such systems is a multiple of the energy barrier of skyrmion collapse in the corresponding monolayer system [54], which reads

$$\Delta E = L\,\Delta E_{\mathrm{mono}}, \tag{2}$$

where $L$ is the number of stacked layers and $\Delta E_{\mathrm{mono}}$ the energy barrier of the skyrmion in the monolayer system.

In this work, we systematically study the role of the interlayer exchange for skyrmion stability and the different regimes and effects it induces. For this purpose, we investigate bilayer and multilayer systems consisting of an artificial repetition of the famous Pd/Fe/Ir(111) [14,15,24,31,37,55–60] monolayer system. Since Dupé *et al.* [43] showed based on DFT calculations that the magnetic interactions are primarily affected by the interfaces of the magnetic material, one can expect the properties of the magnetic layers in such a stacking to be comparable to the monolayer system. In order to obtain a broader view of the emerging effects, we vary the strength of the interlayer exchange coupling per unit cell, $J^{\perp}$ systematically from zero to 20 meV, covering indirectly and weakly coupled to directly and strongly coupled systems. Further, we explore two different crystal structures of the multilayer stackings, revealing effects in systems with magnetic layers horizontally offset from each other, strongly affecting skyrmion stability.

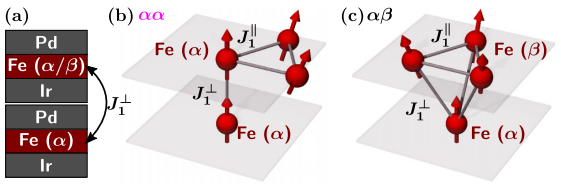


FIG. 1. (a) Magnetic bilayer systems built from two units of the system Pd/Fe/Ir(111). Two different stackings ($\alpha\alpha$ and $\alpha\beta$) are considered which correspond to atoms of the two hexagonal Fe layers being on top of each other or shifted with respect to each other. [(b) and (c)] Schematic representation of the nearest-neighbor intralayer ($J_1^{\parallel}$) and interlayer ($J_1^{\perp}$) exchange bounds for the $\alpha\alpha$-stacked and $\alpha\beta$-stacked magnetic bilayers, respectively. The bonds are indicated through the connections of the red magnetic moments.

The paper is structured as follows. Section II describes the model and Sec. III the method and computational details of our calculations. The presentation of our results in Sec. IV starts with a brief discussion of the phase diagram (Sec. IV A) for magnetic bilayer systems under the influence of interlayer exchange. In Sec. IV B, we discuss collapse mechanisms of skyrmions in magnetic bilayers into the field-polarized state, increasing the interlayer exchange stepwise and analyzing the occurring changes of the collapse mechanism. These results are subsequently condensed in Sec. IV C by studying the corresponding energy barriers. In Sec. IV D, we explain a crossover between two collapse mechanisms for critical interlayer exchange couplings. To understand these critical parameters in more detail, we then vary the DMI and hence the energy barrier of skyrmions in the underlying monolayer system in Sec. IV E. Afterwards we demonstrate that our results transfer to systems with more than two magnetic layers in Sec. IV F. Finally, in Sec. IV G, we discuss calculations of the lifetime of bilayer skyrmions for a generic example. Conclusions and discussion are presented in Sec. V.

## II. MODEL

The model for our spin simulations is shown in Fig. 1. We treat different stacking possibilities of the magnetic monolayer system Pd/Fe/Ir. Note that only the hexagonal Fe layers of the system are included in our atomistic spin model. The effect of the nonmagnetic Pd and Ir layers is included within the framework of the first-principles parametrization of the

magnetic interactions given in Ref. [31] for the magnetic monolayer system (cf. Sec. II A). Two different bilayers were studied. The system in which the magnetic moments in both Fe layers occupy the same lattice sites is called $\alpha\alpha$ system in the following [Fig. 1(b)]. In contrast, the magnetic moments of the different layers in the $\alpha\beta$ system are horizontally offset from each other in such a way that each atomic site of the bottom layer is located right below the interstitial site of the top layer [Fig. 1(c)].

We systematically vary the strength of the interlayer exchange between the Fe layers in our simulations. Therefore the obtained results can be applied to systems in the strong interlayer exchange coupling regime such as directly adjacent Fe layers, e.g., in the system Rh/Pd/2Fe/2Ir [43], as well as in the weak or intermediate regime such as magnetic layers in which the interlayer exchange is mediated by a number of spacer layers.

### A. Extended Heisenberg model

The magnetic bilayer systems are built based on the magnetic interactions of the monolayer system Pd/Fe/Ir(111) and described through normalized magnetic moments $\mathbf{m}_i$ localized in each Fe layer at the sites of a hexagonal lattice. The energy of the $N$-spin system is derived within the extended Heisenberg model and the Hamiltonian can be written as

$$\begin{aligned} H &= E_{\text{ex}} + E_{\text{DMI}} + E_{\text{Ani}} + E_{\text{Zee}} \\ &= -\sum_{\substack{i,j=1 \\ i\neq j}}^{N} J_{ij}(\mathbf{m}_i \cdot \mathbf{m}_j) - \sum_{\substack{i,j=1 \\ i\neq j}}^{N} \mathbf{D}_{ij} \cdot (\mathbf{m}_i \times \mathbf{m}_j) \\ &\quad - \sum_{i=1}^{N} K\left(m_i^z\right)^2 - \sum_{i=1}^{N} \mu_i(\mathbf{m}_i \cdot \mathbf{B}_{\text{ext}}), \end{aligned} \tag{3}$$

which are in the order of appearance the Heisenberg exchange, the DMI, the uniaxial magnetocrystalline anisotropy and the Zeeman interaction. The interaction constants $J_{ij}$ and $\mathbf{D}_{ij}$ and the anisotropy constant $K$ are defined per atom. Therefore each pair of magnetic moments appears twice in the calculation of the exchange and DMI energy. Note that we consider intralayer DMI here, but not interlayer DMI [61,62].

The exchange term can be split into intralayer exchange $J_{ij}^{\parallel}$ and interlayer exchange $J_{ij}^{\perp}$ for pairs of magnetic moments from the same layer and from different layers, respectively.

$$\begin{aligned} E_{\text{ex}} &= E_{\text{ex}}^{\parallel} + E_{\text{ex}}^{\perp} \\ &= -\sum_{l=1}^{2} \sum_{\substack{i,j=1 \\ i\neq j}}^{N_l} J_{ij}^{\parallel}\left(\mathbf{m}_i^l \cdot \mathbf{m}_j^l\right) - \sum_{\substack{k,l=1 \\ k\neq l}}^{2} \sum_{i,j=1}^{N_l,N_k} J_{ij}^{\perp}\left(\mathbf{m}_i^l \cdot \mathbf{m}_j^k\right) \end{aligned} \tag{4}$$

Here $N_l$ denotes the number of spins in the layer $l$.

Motivated by the finding of Dupé *et al.* [43] that the magnetic interactions in multilayers built from Pd/Fe/Ir stacks are very similar to those of the film system Pd/Fe/Ir(111) all intralayer interaction constants, i.e. within a single Fe layer, and the magnetic moments $\mu_i$ were taken from Pd/Fe/Ir(111) [31] as obtained via DFT calculations using the FLEUR code [24,63–65]. In Ref. [31], two different models were used to illustrate the influence of intralayer exchange frustration. On one hand, exchange constants were determined from DFT up to the interaction of ninth neighbors ($J_1^{\parallel}, \ldots, J_9^{\parallel}$). We will refer to this set of parameters as the neighbor resolved exchange (NRE) model. On the other hand, the magnetic interactions of the system were parameterized with only the nearest-neighbor exchange interaction, which resembles a micromagnetic description of the interactions. The resulting parameter set is referred to as the effective model. The values of all parameters used in this work are listed in Table I.

We treat the interlayer exchange coupling in our magnetic Fe bilayers in nearest-neighbor approximation and systematically vary its strength, $J_1^{\perp}$. As visible in Fig. 1, the magnetic unit cell of the $\alpha\beta$ system contains three interlayer bonds while in the unit cell of the $\alpha\alpha$ system only one bond appears. We define the interlayer exchange per unit cell $J^{\perp}$ for better comparability of the different systems as the following:

$$J^{\perp} = \begin{cases} J_1^{\perp}, & \alpha\alpha \text{ system} \\ 3 \cdot J_1^{\perp}, & \alpha\beta \text{ system} \end{cases}. \tag{5}$$

## III. COMPUTATIONAL DETAILS

We use atomistic spin dynamics simulations to solve the Landau-Lifshitz-equations for the spin model introduced in the previous section numerically and to relax spin structures such as bilayer skyrmions into local energy minima. The knowledge of the separating energy barrier $\Delta E$ between metastable spin structures on the energy surface is crucial for the description of the thermal stability of these states following an Arrhenius law for the skyrmion lifetime $\tau$ [Eq. (1)]. The geodesic nudged elastic band method [32] (GNEB) provides a possibility to calculate the energy barrier and the first-order saddle point of skyrmions regarding a transition to the topologically trivial ferromagnetic state. We use the harmonic approximation of the transition-state theory (HTST) for determining the Arrhenius pre-exponential factors and the lifetimes of magnetic states [66]. While the phase diagrams presented in Sec. IV A are calculated with simulation boxes of 100 × 100 magnetic atoms per layer, all other results of this work are obtained with boxes of 50 × 50 magnetic atoms per layer. We applied periodic boundary conditions in in-plane direction, while open boundaries are assumed in out-of-plane direction. Consistency tests for 70 × 70 and 100 × 100 magnetic moments per layer demonstrated that the shown results are not dependent on the system size.

### A. Minimum energy path calculations

The GNEB method is a valuable approach [31,32,35,37,52,67] to calculate the minimum energy path (MEP) between magnetic configurations corresponding to local energy minima. As schematically illustrated in Fig. 2(a), we consider the collapse of an initial magnetic state (A), which is a bilayer skyrmion, to the final magnetic state (B), which is the ferromagnetic or field polarized state. In Sec. IV, we discuss the occurrence of different collapse mechanisms and the associated MEPs caused by the variation of the interlayer exchange. For weak interlayer exchange, paths with additional local minima between the initial and final states occur [cf. Fig. 2(a)]. These intermediate minima (M) are associated with a successive collapse of the skyrmion in the

TABLE I. Value of the $i$th nearest-neighbor intralayer exchange $J_i^{\parallel}$ (meV), the Dzyaloshinskii-Moriya interaction constants $D_i$ (meV) and the magnetocrystalline anisotropy (MAE) $K$ (meV/Fe-atom) for the magnetic monolayer system fcc-Pd/Fe/Ir(111). These values originate from first-principles calculations from Ref. [31]. The positive $K > 0$ parameters represent an out-of-plane easy axis for the anisotropy.

| model | $J_1^{\parallel}$ | $J_2^{\parallel}$ | $J_3^{\parallel}$ | $J_4^{\parallel}$ | $J_5^{\parallel}$ | $J_6^{\parallel}$ | $J_7^{\parallel}$ | $J_8^{\parallel}$ | $J_9^{\parallel}$ | $D_1$ | $K$ |
|---|---|---|---|---|---|---|---|---|---|---|---|
| NRE model | 14.40 | −2.48 | −2.69 | 0.52 | 0.74 | 0.28 | 0.16 | −0.57 | −0.21 | 1.0 | 0.7 |
| eff. model | 3.68 | - | - | - | - | - | - | - | - | 1.39 | 0.7 |

different layers. We split up the paths at the states M after short GNEB calculations (500 iterations), as suggested in Ref. [32]. The energies of these partially relaxed paths are visualized on the example of bilayer skyrmions in the $\alpha\alpha$ system in Fig. 2(b). After the splitting, the M configuration is relaxed into its local energy minimum via spin dynamics. Afterwards, we calculate the MEPs for $A \to M$ and $M \to B$ transitions separately with the GNEB method and finally connect them to create the complete paths $A \to B$. Consequently, there are paths with two first-order saddle points (Sp) ($\mathrm{Sp}_1$, $\mathrm{Sp}_2$) for low values of the interlayer exchange couplings and paths with one saddle point for strong interlayer exchange couplings. These saddle points are determined with the climbing-image GNEB method (CI-GNEB) [32]. A calculation is considered converged when the force on each magnetic moment has dropped below $10^{-8}$ eV/rad.

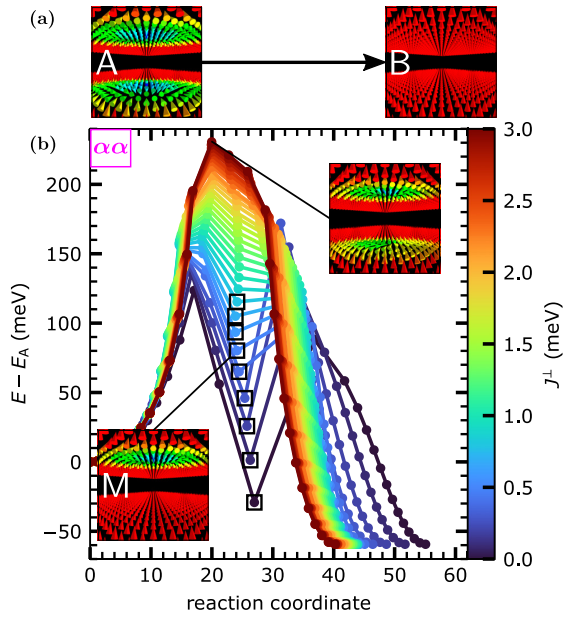


FIG. 2. (a) Representation of a bilayer skyrmion (initial state, A) collapsing into the field polarized state (final state, B). (b) Partially relaxed energy paths for the collapse mechanism of a bilayer skyrmion (A) for the $\alpha\alpha$ system for various interlayer exchange couplings $J^{\perp}$ (visualized by the color code). The shown paths are the results of 500 iterations of a GNEB calculation an do not display the converged minimum energy path. They are the starting point for treating paths with an intermediate energy minimum (M), which are marked with the empty squares. The insets show spin configurations for two interlayer exchange couplings. For $J^{\perp} = 3.0$ meV, the configuration with the highest energy is shown while for $J^{\perp} = 0.5$ meV, the spin configuration of the intermediate minimum is displayed.

### B. Harmonic transition-state theory

We determine the pre-exponential factor $\tau_0$ within the harmonic approximation of the TST. This implies the description of the curvature of the multidimensional energy surface of the spin configuration room via the eigenvalues $\epsilon_{\mathrm{A},i}$ and $\epsilon_{\mathrm{Sp},i}$ of the Hessian matrices $H_{\mathrm{A}}$ and $H_{\mathrm{Sp}}$ for the bilayer skyrmion configuration (A) and the saddle point configuration (Sp), respectively. In the general form, the pre-exponential factor is given by [35,66,68]

$$\tau_0^{-1} = \frac{\lambda}{2\pi}(2\pi k_B T)^{(P_{\mathrm{A}}-P_{\mathrm{Sp}})/2}\frac{V_{\mathrm{Sp}}}{V_{\mathrm{A}}}\sqrt{\frac{\det H_{\mathrm{A}}}{\det' H_{\mathrm{Sp}}}}. \tag{6}$$

The determinants of the Hessian matrices at the bilayer skyrmion and the saddle point state are computed as the product of the corresponding nonzero eigenvalues, while the prime indicates that the negative eigenvalue for the saddle point is omitted. The information about the velocity of the system at the transition state is contained by the dynamical factor $\lambda$ (see Ref. [40] for details). Not all eigenmodes are suited for a description in harmonic approximation. Alternatively, Goldstone modes can be defined and calculated as in Ref. [35], yielding the Goldstone mode volumes $V_{\mathrm{A}}$, $V_{\mathrm{Sp}}$, while the corresponding eigenvalues are omitted in the determinants of Eq. (6) as well. The number of Goldstone modes for the initial state (saddle point) is given by $P_{\mathrm{A}}$ ($P_{\mathrm{Sp}}$). In the case of skyrmion annihilation in bilayers, this applies to the two skyrmion translation modes in in-plane direction as the movement of skyrmions over the lattice does not change their energy, similar to the translation of skyrmions in monolayer systems [37,40]. Throughout this work, we investigate the skyrmion lifetime only in cases, in which the simultaneous radial symmetric collapse mechanism [31,35,36,53] is dominant for the annihilation process. The corresponding saddle point structures contain three neighboring magnetic moments pointing almost towards each other, creating a Bloch-like defect. For low temperatures, this Bloch-like point cannot be moved without noticeable energy costs over the atomic lattice. For elevated temperatures, the eigenmodes corresponding to this movement are potential Goldstone modes in the spectrum of the saddle point state, as discussed in Refs. [33,40]. For the sake of clarity, however, here we treat all eigenmodes of the saddle point structures in harmonic approximation and thereby exclude the high temperature regime.

The unequal number of Goldstone modes found for the skyrmion and saddle point states leads to a linear temperature

dependence for the inverse of the pre-exponential factor [37]:

$$\tau_0^{-1} = \frac{2\lambda k_B T}{V_A}\sqrt{\frac{\det H_A}{\det' H_{Sp}}}. \quad (7)$$

The factor of two arises from the two possible realizations of the Bloch-like point per unit cell, as discussed in Ref. [37].

## IV. RESULTS

### A. Zero-temperature phase diagrams

To study the metastability of skyrmions in the field-polarized phase, first we have to determine the critical fields which correspond to the phase transition between the skyrmion lattice and the field-polarized phase.

Therefore obtaining the zero temperature magnetic phase diagrams [24,31,55] of the $\alpha\alpha$ and $\alpha\beta$ systems as a function of interlayer exchange coupling is the starting point for our investigations. In the following, we present the phase diagrams calculated within the NRE model of intralayer exchange interaction. In Figs. 3(a) and 3(b), the energies of relaxed bilayer spin spirals (SS), bilayer skyrmion lattices (SkX) and the field polarized phase (FM) are shown over varying magnetic field strength. Figure 3(a) shows the phase diagram for the $\alpha\beta$ system with $J^\perp = 15.0$ meV and Fig. 3(b) visualizes the corresponding phase diagram in the case without interlayer exchange coupling ($J^\perp = 0$ meV).

Similar to Ref. [31] we chose the energy reference as the minimum energy of the dispersion of homogeneous spin spirals, $E_{\text{hom, SS}}$, calculated in a 100 × 100 simulation box. Further, we consider the SkX state with the energetically most favorable skyrmion density on the 100 × 100 lattice. The critical magnetic field values $B_{C_1}$ and $B_{C_2}$ mark the phase transitions from the SS state to the SkX state and from the SkX state to the FM state, respectively. As the energy is defined per unit cell and the interlayer exchange is switched off, these critical fields exactly coincide with the fields reported in Ref. [31] for the magnetic monolayer system Pd/Fe/Ir(111).

When we increase the interlayer exchange to $J^\perp = 15$ meV for the $\alpha\beta$ system [see Fig. 3(a)] the critical fields $B_{C_1}$ and $B_{C_2}$ shift to lower values and thereby introduce a shift of the SkX phase. The origin of these energy shifts can be understood by considering the horizontal displacements between the layers [see Fig. 1(c)]. A parallel alignment of two magnetic moments in different layers leads to a minimal exchange energy for ferromagnetic interlayer exchange. Therefore, the FM state gains more energy than the SS state, in which small angles between the magnetic moments of adjacent Fe atoms in the two layers occur that are unfavorable with respect to the interlayer exchange. These angles arise due to the horizontal displacement of the magnetic layers in the $\alpha\beta$ system. The SkX phase lies between those two extremes as there are collinear aligned regions between the skyrmions in the two layers and therefore its energy shift is smaller than for the FM state but greater than for the SS state which leads to a decrease of both $B_{C_1}$ and $B_{C_2}$. Figure 3(c) underlines this behavior as it displays the decrease of the critical fields with increasing interlayer exchange $J^\perp$. In addition, it is noteworthy that the skyrmion density of the SkX phase is slightly reduced for high interlayer exchange couplings. In contrast, for $\alpha\alpha$ systems

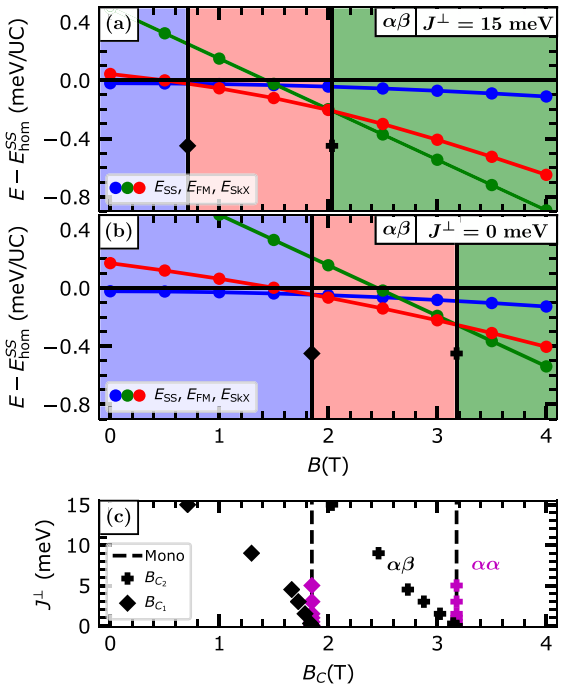


FIG. 3. (a) Zero-temperature phase diagram for the $\alpha\beta$ system for $J^\perp = 15.0$ meV. The critical fields $B_{C_1}$ and $B_{C_2}$ define the phase transitions between the spin spiral phase (SS, blue), the skyrmion lattice phase (SkX, red) and the field polarized phase (FM, green), respectively. The energy is defined per unit cell and displayed relative to the energy of the minimum of the dispersion of homogeneous spin spirals. The background color represents the phases in a certain magnetic field range. (b) Analog visualization of the phase diagram for the $\alpha\beta$ system for $J^\perp = 0$ meV. (c) Critical magnetic fields $B_{C_1}$ or $B_{C_2}$ for different values of $J^\perp$ for the $\alpha\alpha$ and $\alpha\beta$ system. The reference of the magnetic monolayer system Pd/Fe/Ir(111) is plotted as a dashed line.

for each magnetic moment, the next neighbor regarding the interlayer exchange coupling is directly above or below the corresponding moment. Therefore, the magnetic moment and its neighbor are aligned parallel for each magnetic structure considered in the phase diagram and the shifts in the energy are equal when varying the interlayer exchange. Figure 3(c) presents these results by visualizing the critical fields $B_{C_1}$ and $B_{C_2}$. The dashed lines indicate the corresponding fields as determined for the magnetic monolayer system Pd/Fe/Ir(111) [31]. Therefore, the phase diagram remains unchanged for $\alpha\alpha$ systems when varying the interlayer exchange and this will also hold true for systems with more magnetic layers if the atoms of each layer occupy the same lattice sites.

### B. Skyrmion collapse mechanisms in magnetic bilayers

For a detailed understanding of the thermal stability of magnetic bilayer skyrmions (A) in the field polarized phase the MEP regarding a collapse to the ferromagnetic aligned structure (B) is crucial (Fig. 2). To be consistent with the

calculations of the underlying monolayer system [31] we chose an out-of-plane magnetic field of $B = 4.0\,\mathrm{T}$. It has be shown that the skyrmion sizes for the effective and the NRE model are similar for $B = 4.0$ T [31], which allows a reasonable comparison between the NRE and the effective model. Our phase diagram calculations in the previous sections demonstrated that $B_C(J^\perp) < B$ holds true for all interlayer exchange couplings for both stackings of the system [cf. Fig. 3(c)]. Therefore, we expect isolated bilayer skyrmions to be meta-stable in both systems at $B = 4.0\,\mathrm{T}$. Note that in the case of the $\alpha\beta$ system the distance $B - B_C(J^\perp)$ increases with increasing interlayer exchange. A decreased stability of skyrmions in the $\alpha\beta$ system with increasing interlayer exchange can be expected, as elucidated in Sec. IV C in more detail. In that context, it is worth mentioning that the skyrmion radius of the bilayer skyrmions in the $\alpha\beta$ system is marginally reduced when increasing $J^\perp$, which follows the relation between skyrmion size and stability [69]. For the highest values of $J^\perp$ in our work the reduction in the skyrmion size is less than one in-plane lattice constant. However, the radius of the bilayer skyrmions in the $\alpha\alpha$ system agrees for all values of $J^\perp$ with the radius reported for monolayer skyrmions in Pd/Fe/Ir(111) [31].

This section demonstrates how the interlayer exchange affects the collapse mechanisms of bilayer skyrmions in the $\alpha\alpha$ and $\alpha\beta$ system. We use the NRE model throughout this section. Figure 4 presents an overview over the variety of collapse mechanisms of bilayer skyrmions in the $\alpha\alpha$ system for different interlayer exchange couplings. The MEPs are shown in the top row with the spin configurations of the saddle point below. In the high interlayer exchange regime [$J^\perp = 15$ meV, Figs. 4(m)–4(p)], we predict a bilayer skyrmion collapse with a single saddle point configuration which corresponds to twice the energy barrier of a skyrmion in the magnetic monolayer Pd/Fe/Ir(111) [31]. The spin configuration obeys a radial collapse mechanism in both layers where three spins point towards each other. This collapse mechanism is widely investigated for magnetic monolayer skyrmions [31,35,36,54] and agrees with the assumption in Eq. (2).

The other limit of the uncoupled system is displayed in Figs. 4(a)–4(d). Here the collapse of the bilayer skyrmion consists of two independent collapses of the skyrmions in the different layers each of them resembling the radial collapse of a skyrmion in the monolayer system. The energy barriers of both decays coincide with the energy barrier reported for the skyrmion in Pd/Fe/Ir(111) [31].

Collapse mechanisms for the intermediate coupling regime as displayed in Figs. 4(e)–4(h) for $J^\perp = 0.15$ meV and in Figs. 4(i)–4(l) for $J^\perp = 2.5$ meV already demonstrate the increased complexity as opposed to monolayer skyrmions. This regime yields saddle point configurations following the chimera collapse mechanism predicted recently [19,33,54]. During this collapse process the radial symmetric magnetic structure of the skyrmion changes through tilting the spins in one part of the edge [Fig. 4(h)]. Meyer *et al.* found meta-stable skyrmions at zero external magnetic field in the magnetic monolayer system Rh/Co/Ir(111) and predicted them to collapse via the chimera transition mechanism [19]. Very recently the chimera collapse of a skyrmion in a ultrathin magnetic film system was identified experimentally [34]. Here, we observe the chimera transition as part of a successive decay of skyrmions in different layers for $J^\perp = 0.15$ meV where the first transition presents a chimera saddle point configuration while the second skyrmion follows the radial mechanism.

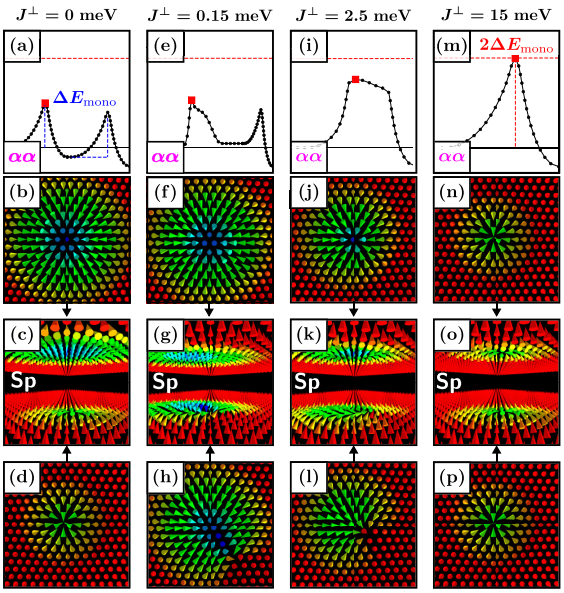


FIG. 4. Representation of collapse mechanisms for bilayer skyrmions in the $\alpha\alpha$ system for different interlayer exchange couplings $J^\perp$. The top row shows the total energy along the minimum energy path, while the first occurring saddle point is marked in red. The blue (red) dashed line represents the energy barrier (twice the energy barrier) of a skyrmion in the magnetic monolayer system Pd/Fe/Ir(111) [31]. Below the spin configuration of the corresponding saddle point is visualized. [(a)–(d)] Successive radial-radial collapses of the bilayer skyrmion for $J^\perp = 0$ meV. [(e)–(h)] Successive chimera-radial collapse for $J^\perp = 0.15$ meV. [(i)–(l)] Chimera type collapse in one layer with shrunken skyrmion in the other layer for $J^\perp = 2.5$ meV. This collapse is called semisuccessive chimera-radial collapse. [(m)–(p)] Simultaneous radial collapse for $J^\perp = 15$ meV.

For slightly higher interlayer exchange $J^\perp = 2.5$ meV, the MEP of the bilayer skyrmion collapse exhibits a single saddle point. The corresponding spin configuration shows a chimera-type configuration in one layer while a skyrmion of reduced size compared to the initial state is obtained for the other layer [Figs. 4(j)–4(l)].

In the following, we analyze the MEPs for the bilayer skyrmions shown in Fig. 4 in detail to achieve understanding of the origin of the variety of the collapses. Although we discuss bilayer skyrmions in the $\alpha\alpha$ system these are representative for the corresponding skyrmions in the $\alpha\beta$ system as we find analog collapse mechanisms for the same interlayer exchange parameters there. Furthermore, it is worth mentioning that we always find two MEPs for collapse mechanisms which include changing first the magnetization in one layer followed by a change in the other layer as the order of the collapses is exchangeable. Starting with the uncoupled bilayer

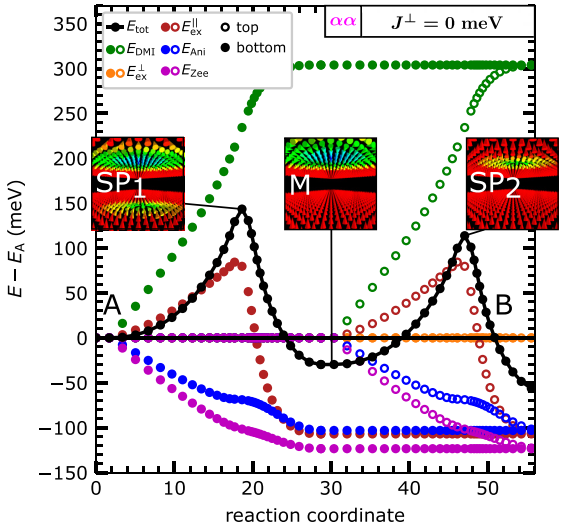


FIG. 5. Minimum energy path for a bilayer skyrmion in the $\alpha\alpha$ system without interlayer exchange coupling ($J^\perp = 0$ meV). The total energy is plotted in black. The energy contributions of the different interactions are represented by the color code (see legend). Open circles represent the top Fe layer while filled circles symbolize the bottom Fe layer. The spin configuration of the saddle points ($SP_1$ and $SP_2$) is shown as well as the spin configuration of the intermediate minimum (M). For the configuration of the initial bilayer skyrmion *A* and the final field polarized state *B* see the insets in Fig. 2.

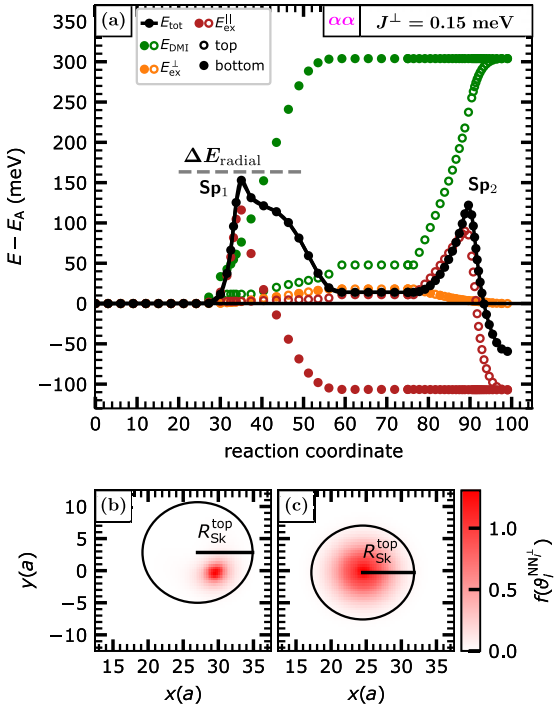


FIG. 6. (a) Minimum energy path for a bilayer skyrmion in the $\alpha\alpha$ system with interlayer exchange coupling ($J^\perp = 0.15$ meV). The energy contributions of the different interactions are represented by the color code (see legend). Open circles represent the top Fe layer while filled circles symbolize the bottom Fe layer. The first saddle point corresponds to a chimera collapse [cf. Figs. 4(e)–4(h)]. The energy barrier corresponding to the meta-stable radial saddle point configuration is visualized by the dashed gray line. [(b) and (c)] The interlayer exchange energy costs $f(\vartheta_i^{NN_i^\perp})$ are presented by the color code versus the in-plane directions, where $a$ is the in-plane lattice constant. The skyrmion radius $R_{Sk}^{top}$ and the position of the unchanged layer (top layer in this example) during the first part of the collapse is represented by a circle. While (b) belongs to the chimera collapse saddle point configuration (c) represents the saddle point of the meta-stable sRR collapse for $J^\perp = 0.15$ meV.

($J^\perp = 0$ meV) we decompose the total energy of the MEP into the different energy contributions of Eq. (3) (Fig. 5). As highlighted in Sec. III A the MEP of a bilayer skyrmion in this system contains an intermediate minimum (M). This minimum is associated with a skyrmion in one Fe layer, which is unchanged concerning the corresponding layer for the A state, and one collinear aligned Fe layer. This indicates that the skyrmions in the different layers collapse independently from each other for the uncoupled Fe layers. Hence, we find two saddle point configurations with energies $E_{Sp_1}$ and $E_{Sp_2}$, respectively. These energies correspond to energy barriers equal to the barrier of the skyrmion in the magnetic monolayer Pd/Fe/Ir(111) [Fig. 4(a)].

Both the anisotropy and the Zeeman term favor a parallel out-of-plane alignment of the spins in both layers. For the sake of completeness we show all energy contributions to the total energy of the MEP in Fig. 5. In the following figures we restrict the decomposition to the intralayer exchange energy $E_{ex}^{\parallel}$ and the DMI energy $E_{DMI}$ since they dominate the energy of the saddle points $E_{Sp_{1/2}}$ and therefore the energy barriers (cf. Fig. 5). Further the interlayer exchange energy $E_{ex}^{\perp}$ is included. Note that the large contribution of $E_{ex}^{\parallel}$ to $E_{Sp_{1/2}}$ originates from the intralayer exchange frustration within the NRE model (Tab. I), as reported in Ref. [31]. Below we will call this mechanism the successive radial-radial (sRR) collapse. We predict the sRR collapse only for very low values of the interlayer exchange coupling. Figure 6(a) shows the MEP when one increases the interlayer exchange to $J^\perp = 0.15$ meV. Now the intermediate configuration M becomes less favorable due to the increasing interlayer energy costs. One can also recognize that the shape of the total energy of the MEP changes for the first collapsing layer with respect to that observed in Fig. 5. This can be attributed to the appearance of the chimera collapse. The first part of the collapse (reaction coordinate $< 25$) corresponds to a side wards movement of the initial skyrmion, which does not lead to an increase in the energy. This movement can be explained as a consequence of the initial geodesic path as described in Ref. [68]. The energy barrier of the chimera collapse is dominated by the intralayer exchange, while the amount of the DMI energy at the saddle point is relatively low compared to the radial collapse mechanism. This is due to the fact that the noncollinear alignment is preserved for the most part of the skyrmion and only the spins in one part of the margin of the skyrmion are tilted as visible

in Fig. 4(h). After the skyrmion in one layer has collapsed to a parallel alignment the second skyrmion follows a radial mechanism with the corresponding saddle point $Sp_2$.

Although the interlayer exchange energy does not contribute to the saddle point corresponding to the chimera collapse in one layer ($Sp_1$) it can explain the appearance of this collapse mechanism. If $N_1$ is the number of magnetic moments in layer 1 the energy costs due to interlayer exchange can be written as:

$$\begin{aligned} E^{\perp}_{\text{costs}} &= 2J^{\perp}_1 \sum_{i=1}^{N_1} \sum_{\text{NN}^{\perp}_i} \left(1 - \mathbf{m}_i \cdot \mathbf{m}_{\text{NN}^{\perp}_i}\right) \\ &= 2J^{\perp}_1 \sum_{i=1}^{N_1} \sum_{\text{NN}^{\perp}_i} \left(1 - \cos \vartheta_i^{\text{NN}^{\perp}_i}\right) \\ &= 2J^{\perp}_1 \sum_{i=1}^{N_1} \sum_{\text{NN}^{\perp}_i} f\left(\vartheta_i^{\text{NN}^{\perp}_i}\right), \end{aligned} \tag{8}$$

while $i$ represents the magnetic moments of one layer, $\text{NN}^{\perp}_i$ numerates the next interlayer neighbors of the magnetic moment $i$. The angle between a magnetic moment $i$ and its neighbor $\text{NN}^{\perp}_i$ is expressed by $\vartheta_i^{\text{NN}^{\perp}_i}$ and the factor of two arises due to the definition of the exchange constant as per atom. The interlayer exchange costs are proportional to the introduced function $f(\vartheta_i^{\text{NN}^{\perp}_i})$. In this formulation it becomes visible that increased angles between the magnetic configurations of the different layers lead to increased interlayer exchange costs. Therefore the intermediate minimum M becomes less favorable, when the interlayer exchange increases.

In Fig. 6(b), we visualize $f(\vartheta_i^{\text{NN}^{\perp}_i})$ for the saddle point configuration $Sp_1$ across the in-plane directions of the system, which is a direct measure for the interlayer exchange energy costs. These costs concentrate mainly on one point of the edge of the skyrmion where the spins are tilting as described above. The rest of the skyrmion is still parallel aligned to the nearly unchanged skyrmion in the other layer, which reduces the interlayer exchange costs. In Fig. 6, the nearly unchanged skyrmion during the first part of the collapse corresponds to the top layer and is represented by its radius $R^{\text{top}}_{\text{Sk}}$. The radius was determined through applying the definition of Bogdanov and Hubert [4] onto the skyrmion profile [69] gained through a fit to the magnetization of the top layer.

The role of the interlayer exchange favoring the chimera saddle point can be underlined by a comparison with the sRR collapse mechanism. For $J^{\perp} = 0.15$ meV, it is still possible within the simulation to meta-stabilize the sRR collapse mechanism. As indicated by the dashed gray line in Fig. 6(a) the corresponding energy barrier of the sRR collapse is slightly larger than the energy barrier of the chimera collapse. Figure 6(c) shows the interlayer exchange costs of the sRR collapse mechanism for $J^{\perp} = 0.15$ meV and one can identify the increased energy costs due to the symmetric shrinking of the skyrmion in one layer compared to the asymmetric chimera collapse [Fig. 6(b)]. Comparing the radius of the skyrmion in the top layer ($R^{\text{top, chim}}_{\text{Sk}} = 7.84a$) for the chimera collapse with the radius for the sRR mechanism ($R^{\text{top, rad}}_{\text{Sk}} = 7.32a$) the skyrmion in the top layer is slightly smaller for the sRR collapse. Here, $a$ is the in-plane lattice constant. This indicates that the radial collapse mechanism already involves a small part of simultaneous shrinking of both skyrmions in the first part of the collapse, which is also related to reducing interlayer exchange costs.

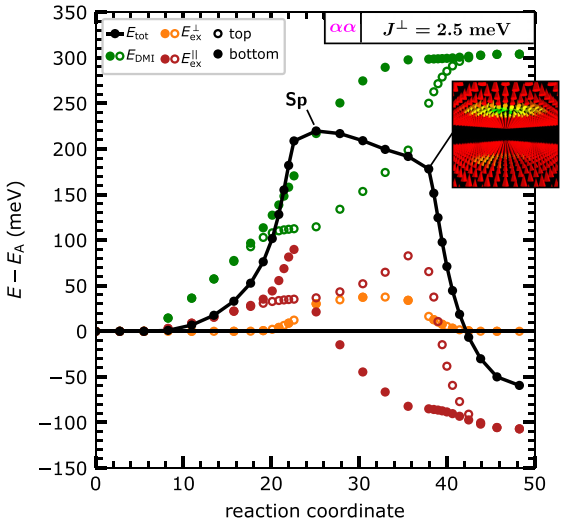


FIG. 7. Minimum energy path for a bilayer skyrmion in the $\alpha\alpha$ system with interlayer exchange coupling ($J^{\perp} = 2.5$ meV). The energy contributions of the different interactions are represented by the color code (see legend). Open circles represent the top Fe layer while filled circles symbolize the bottom Fe layer. An exemplary spin configuration in the region of the collapse of the second skyrmion is shown as an inset. For the spin configuration of the actual saddle point see Figs. 4(i)–4(l).

It is noteworthy that the chimera collapse also occurs in the monolayer system but at lower magnetic fields [68]. Therefore the interlayer exchange interaction shifts the transition of the radial to the chimera collapse so that it can occur also at higher fields. In the following, we assign the name successive chimera-radial (sCR) collapse to transitions which show a chimera collapse for the first layer followed by a radial collapse for the skyrmion in the other layer. Increasing the interlayer exchange to $J^{\perp} = 2.5$ meV (Fig. 7), we enter the regime of intermediate interlayer coupling. The initial GNEB calculations as described in Sec. III A do not show any intermediate minimum and the path has only one saddle point configuration (Sp). This saddle point configuration includes a chimera saddle point [cf. Fig. 4(l)] for one layer, while the other layer has a radial structure of reduced radius compared to the initial configuration [cf. Fig. 4(j)]. Thus the part of the collapse, which reduces the size of the skyrmion, occurs simultaneously in both Fe layers. The region of the saddle point describes a successive chimera collapse of the skyrmion in one layer followed by a radial collapse of the skyrmion in the other layer. This is underlined by the inset in Fig. 7. Although this is not the saddle point configuration the second skyrmion collapse appears to be radial symmetric. To emphasize the fact that this collapse mechanism is partly simultaneous and partly

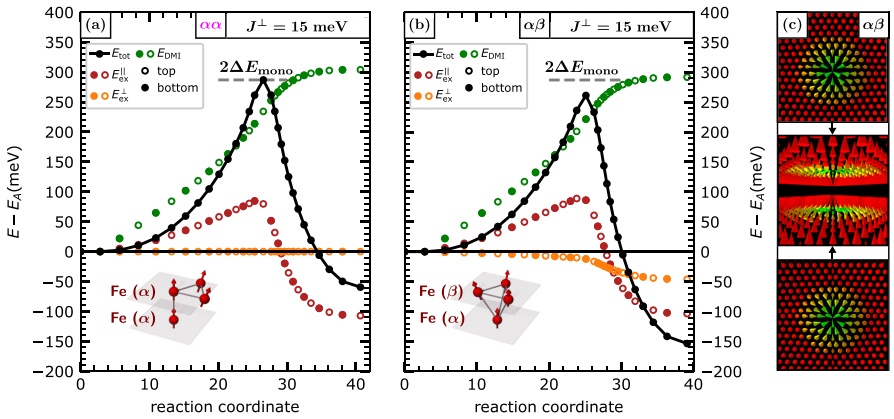


FIG. 8. (a) Minimum energy path for a bilayer skyrmion in the $\alpha\alpha$ system with interlayer exchange coupling ($J^\perp = 15.0$ meV). The energy contributions of the different interactions are represented by the color code (see legend). Open circles represent the top Fe layer while filled circles symbolize the bottom Fe layer. Twice the energy barrier of a skyrmion in the corresponding monolayer system Pd/Fe/Ir(111) is shown as dashed gray line. The inset displays schematically the stacking of the Fe layers. (b) Analog visualization of the minimum energy path for the $\alpha\beta$ system for $J^\perp = 15$ meV. (c) The spin configuration of the saddle point for the collapse of the bilayer skyrmion in the $\alpha\beta$ system is shown. For the corresponding configuration of the $\alpha\alpha$ system see Figs. 4(m)–4(p).

successive we call this mechanism semisuccessive chimera-radial (ssCR) collapse.

Comparing the interlayer exchange energy for the path for $J^\perp = 2.5$ meV with the one for $J = 0.15$ meV it is striking that it varies only slightly. The lifting of the intermediate minimum M occurs rather due to the more concurrent DMI energy curves for the two layers. The difference between the DMI energy of the bottom and top layer along the reaction coordinate could thus be used as a quantity to define how simultaneous a collapse proceeds in the bilayer.

The ssCR collapse mechanism changes to a different semisuccessive mechanism for $J^\perp = 4.9$ meV, where the transition of the bilayer skyrmion is simultaneous for most parts of the collapse but the region of the saddle point reveals two successive radial mechanisms. Due to the similarity of this transition to the ssCR collapse, we do not discuss this mechanism in detail here, but as it becomes important for the effective model later we assign the name semisuccessive radial-radial (ssRR) collapse. Finally increasing the interlayer exchange coupling to $J^\perp = 15$ meV, we end up in the high interlayer coupling regime for both the $\alpha\alpha$ and the $\alpha\beta$ system. The MEPs of the bilayer skyrmions in both systems are presented in Figs. 8(a) and 8(b). In this regime, significant differences occur in the MEP between the $\alpha\alpha$ system and the $\alpha\beta$ system. We start with the description of the bilayer skyrmion in the $\alpha\alpha$ system in Fig. 8(a). The difference between the DMI energy of the bottom and top layers disappears, indicating a simultaneous collapse of both layers. The simultaneous change of both layers during the skyrmion collapse avoids interlayer exchange costs, which can be seen through the vanishing energy contribution $E_{ex}^{\perp}$. The consequence of this simultaneous collapse is that the energy barrier is equal to twice the energy barrier of a skyrmion in the monolayer system ($2\Delta E_{mono}$). Moreover, the mechanism in both layers corresponds to the radial collapse of the monolayer skyrmion.

If we compare this with the collapse of the bilayer skyrmion in the $\alpha\beta$ system [Fig. 8(b)], we also find that the DMI energy contributions of both layers to the MEP are identical. Again, the collapse is simultaneous in both Fe layers. However, if we look at the energy barrier, we find a slight reduction compared to $2\Delta E_{mono}$, which is explained by the interlayer exchange. If we analyze the contribution of $E_{ex}^{\perp}$ to the MEP in Fig. 8(b), we find that the saddle point is energetically favored over the initial state. Furthermore, the field-polarized state is clearly favored with respect to the interlayer exchange. The explanation for this is analogous to the cause of the shift of the critical fields in the magnetic phase diagram discussed in Sec. IV A.

The insets in Figs. 8(a) and 8(b) contrast the horizontal shift of the Fe layers in the case of the $\alpha\beta$ system with the directly superimposed layers of the $\alpha\alpha$ system. This shift causes noncollinear regions of magnetization within one layer to be slightly tilted with respect to the same structure in the other layer. Collinear regions are therefore favored in terms of interlayer exchange and in this sense the bilayer skyrmion is unfavorable relative to the field polarized state. Since the saddle point state has a smaller noncollinear fraction than the skyrmion, the energetic order with respect to interlayer exchange in the $\alpha\beta$ system results in $E_{ex}^{\perp}(\mathrm{A}) > E_{ex}^{\perp}(\mathrm{Sp}) > E_{ex}^{\perp}(\mathrm{B})$. The collapse mechanism, on the other hand, is very similar for the bilayer skyrmions in the $\alpha\alpha$ [Figs. 4(m)–4(p)] and $\alpha\beta$ systems [Fig. 8(c)]. Only the three central spins of the radial saddle point for the skyrmion in the $\alpha\beta$ system have a slightly larger out-of-plane fraction (see Appendix A). We will call this collapse mechanism for high interlayer exchange simultaneous collapse in the following.

### C. Energy barriers for bilayer skyrmions

To understand the role of interlayer exchange for the stability of bilayer skyrmions, a detailed discussion of the corresponding energy barriers is inevitable [cf. Eq. (1)]. We therefore systematically varied the interlayer exchange ($J^\perp \in [0, 30]$ meV) for bilayer skyrmions (A) in the $\alpha\alpha$ and $\alpha\beta$

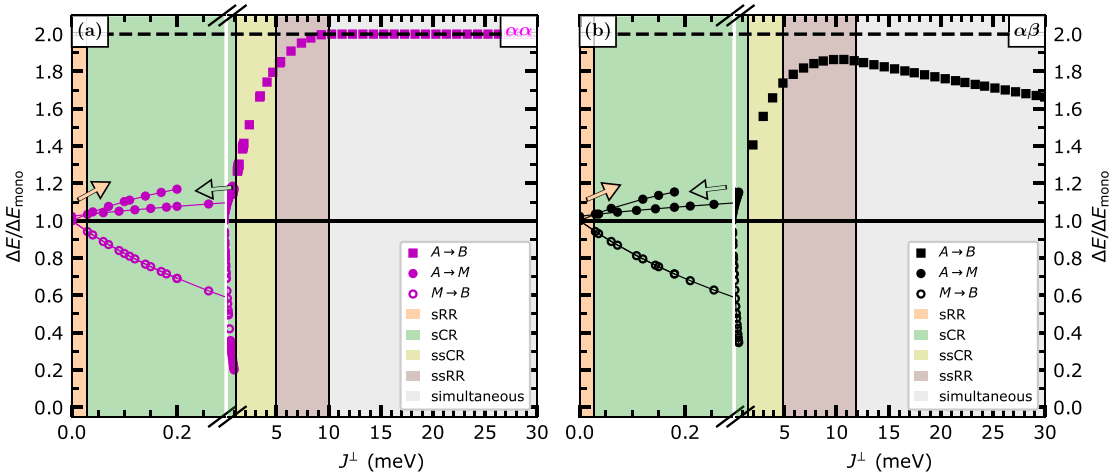


FIG. 9. (a) Energy barriers $\Delta E$ of bilayer skyrmions in the $\alpha\alpha$ system relative to the energy barrier of a skyrmion in the magnetic monolayer system Pd/Fe/Ir(111) for various interlayer exchange couplings $J^\perp$. For clarity the shown data point density is reduced and the $J^\perp$ axis has an enlarged scale for small values. We used the NRE model for these calculations (cf. Table I). The background color represents the type of the collapse mechanism as described in Appendix A and Fig. 17. For collapse mechanisms with two saddle point configurations the corresponding energy barriers of the first (second) collapse are labeled with filled (open) circles, while the energy barriers corresponding to a collapse mechanism with a single saddle point configuration are symbolized with squares. The solid (dashed) black line represents the energy barrier (twice the energy barrier) of a skyrmion in the magnetic monolayer system Pd/Fe/Ir(111). The arrows indicate the directions of the piecewise GNEB calculations as described in detail in the text. (b) Analog visualization to (a) for bilayer skyrmions in the $\alpha\beta$ system.

systems and calculated the energy barriers for the collapse to the field-polarized state (B). As described in Sec. IV B, MEPs with an intermediate minimum occur in the low interlayer exchange coupling region. These MEPs are associated with two energy barriers. While the first barrier describes the transition of the skyrmion in one layer ($A \to M$), the second barrier is associated with the collapse of the skyrmion in the other layer ($M \to B$). In contrast, for high interlayer exchange, we find transitions of the bilayer skyrmion to the field polarized state of the bilayer with just one energy barrier ($A \to B$). Our goal is to study the energy barriers $\Delta E$ of bilayer skyrmions relative to the energy barrier of a skyrmion $\Delta E_{\text{mono}}$ in the magnetic monolayer system Pd/Fe/Ir(111) [31]. Figure 9 displays the ratio $\Delta E/\Delta E_{\text{mono}}$ as a function of $J^\perp$ for the $\alpha\alpha$ and $\alpha\beta$ system. To provide increased resolution for low $J^\perp$ in Fig. 9, the corresponding axis was provided with two different scales. The collapse mechanisms introduced in Sec. IV B are illustrated by the background color in Fig. 9. In the following, we will discuss the determination of these areas and the behavior of the energy barrier with increasing $J^\perp$.

For very low interlayer exchange, the sRR collapse is preferred. This mechanism is associated with large interlayer exchange costs, as discussed in the context of Fig. 6. The sCR collapse minimizes these costs and is therefore preferred for increasing interlayer exchange. However, it is possible to meta-stabilize the sRR mechanism up to $J^\perp = 0.2\,\text{meV}$ as shown in Fig. 9. This was calculated using the following methodology. Since the GNEB method calculates the local MEP closest to the initial path, it is possible to increase (decrease) the interlayer exchange piecewise and always use the result of the previous GNEB calculation as the initial path for calculating the collapse for the next larger (lower) interlayer exchange. The orange arrows in Fig. 9 symbolize such calculations for the sRR collapse starting from $J^\perp = 0\,\text{meV}$. The steps were chosen to be $\Delta J^\perp = 0.01\,\text{meV}$ but for better visibility only a few data points are presented in Fig. 9. Similarly, a calculation of the sCR collapse starting from $J^\perp = 0.3\,\text{meV}$ was performed for piecewise smaller interlayer exchange. This is indicated by the green arrows in Fig. 9. From the intersection of the curve for the sRR collapse and the curve for the sCR collapse, the change of mechanism for $J^\perp = (0.03 \pm 0.01)\,\text{meV}$ for the $\alpha\alpha$- and for $J^\perp = (0.027 \pm 0.009)\,\text{meV}$ for the $\alpha\beta$ system is obtained, where the error results from the distance of the data points in the $J^\perp$ direction.

The further one increases the interlayer exchange, the more energetically unfavorable the intermediate minimum becomes. This leads to the fact that above a certain $J^\perp$ only MEPs with a single saddle point exist. This transition defines the change of the sCR collapse to the ssCR mechanism. For the $\alpha\alpha$ system, this happens at $J^\perp = (1.1 \pm 0.2)\,\text{meV}$ and for the $\alpha\beta$ system at $J^\perp = (1.5 \pm 0.6)\,\text{meV}$, as indicated by the change of the background colors in Fig. 8.

As discussed in Sec. IV B, a chimera-like saddle point is energetically favorable for successive collapsing skyrmions. Considering the ssCR collapse mechanism for increasing interlayer exchange, we find that the magnetization changes in both layers become more and more similar during the collapse, except for the region of the saddle point (see Fig. 7). However, as the shrinkage of the skyrmion proceeds simultaneously in both layers, the noncollinear part of the magnetization for the saddle point becomes smaller. Above a certain interlayer exchange, the saddle point size is small enough that the tilting of the spins at the edge discussed in

the context of Figs. 6(b) and 6(c) for the chimera-like saddle point means only small savings of the interlayer exchange costs. From this point on, the ssRR collapse is preferred. The corresponding limit of the regimes in Fig. 9 is indicated by renewed change of background color. However, the position of this transition cannot be inferred from the behavior of the energy barrier, because the curve in Fig. 9 is continuous. Instead, the central spins of the saddle point configurations are analyzed. This approach is described in Appendix A and Fig. 17. For the $\alpha\alpha$ system as well as for the $\alpha\beta$ system the change of the regimes happens for $J^{\perp} = (4.9 \pm 0.05)\,\mathrm{meV}$.

It is remarkable how closely the collapse mechanisms in the $\alpha\alpha$ and $\alpha\beta$ system match in the regimes discussed so far. Let us now consider the regime of ssRR collapse. Here the energy barrier of the bilayer skyrmion reaches a maximum and the first differences between the $\alpha\alpha$ system and $\alpha\beta$ system appear. While the energy barrier for the bilayer skyrmions in the $\alpha\alpha$ system converges towards twice the value of the energy barrier of the skyrmion in the monolayer system, the curve for the $\alpha\beta$ system only reaches a maximum of about $\max(\Delta E_{\alpha\beta}) \approx 1.86\Delta E_{\mathrm{mono}}$ with a decrease afterwards. Increasing the interlayer exchange further finally leads to the simultaneous collapse regime. The determination of the border is again described in Appendix A and we observe the change for $J^{\perp} = (10.0 \pm 0.05)\,\mathrm{meV}$ for the $\alpha\alpha$ and for $J^{\perp} = (11.9 \pm 0.05)\,\mathrm{meV}$ for the $\alpha\beta$ system.

The decrease in the energy barrier for skyrmions in the $\alpha\beta$ system occurs already before the transition to the completely simultaneous collapse mechanism happens. As the interlayer exchange is increased within the simultaneous regime for the $\alpha\beta$ system the difference between the saddle point configuration and the bilayer skyrmion in terms of interlayer exchange energy increases favoring the saddle point. This leads to a linear decline of the energy barrier as the spin configurations along the MEP do not change anymore in this regime. This is in sharp contrast to the behavior of the bilayer skyrmions in the $\alpha\alpha$ system. Here, the interlayer exchange energy contribution to the MEP reduces to zero when the collapse is simultaneous in both layers as all neighbors coupled via interlayer exchange are aligned parallel. Therefore the energy barrier of the bilayer skyrmion equals twice the monolayer skyrmion energy barrier and is not affected by further changes in $J^{\perp}$.

From the decrease of the energy barrier of the skyrmion in the $\alpha\beta$ system for high interlayer exchange couplings we can draw the conclusion that stability of bilayer skyrmions not inevitably enlarges for increased interlayer exchange. Based on these results, it is important to understand for which interlayer exchange coupling $J_C^{\perp}$ a fully simultaneous collapse of the bilayer skyrmion occurs. The detailed investigation of these critical interlayer exchange parameters is given in Sec. IV D.

### D. Critical interlayer exchange couplings

During the preceding section the question arose for which interlayer exchange $J^{\perp}$ the collapse of bilayer skyrmions becomes fully simultaneous and which underlying physical properties determine this transition. To answer these questions, we reduced the complexity of the system by turning to the more simple representation of the intralayer interaction in effective nearest-neighbor approximation, with a value of $J_1^{||} = 3.68\,\mathrm{meV}$, as reported in Ref. [31]. This excludes the effect of exchange frustration on the energy barrier which is now solely dominated by the DMI, with $D_1 = 1.39\,\mathrm{meV}$ (see Table I). With these parameters, we performed calculations of the magnetic bilayer system analog to the preceding section, yielding the energy barriers, $\Delta E$, over varying interlayer exchange coupling, $J^{\perp}$, for both the $\alpha\alpha$ and the $\alpha\beta$ stacking as displayed in Figs. 10(a) and 10(c), respectively. Similar to the case of frustrated intralayer exchange interaction, we observe an initially strong increase and a subsequent convergence of the energy barrier to twice the value of the corresponding monolayer system for the $\alpha\alpha$-stacked bilayer. This value is again not reached by the skyrmion annihilation in the $\alpha\beta$ stacking, as the barrier starts to decrease with $J^{\perp}$ after a maximum has been reached around $J^{\perp} \approx 2\,\mathrm{meV}$.

Note that within nearest-neighbor approximation no chimera collapse mechanism occurs in the low and intermediate interlayer exchange regimes, highlighting the crucial role of the intralayer exchange frustration for the formation of the chimera saddle point state [19,34,68]. Without this additional stabilization, the energy difference between the radial symmetric and chimera saddle point structures in the monolayer system is larger than the potential energy gain of an occurring chimera saddle point in the bilayer skyrmion collapse. This demonstrates that frustration effects of the intralayer interactions can increase the complexity and variety of transitions in magnetic bilayer systems.

In the following, we focus on the eigenspectra of saddle point states in the interlayer exchange interval $J^{\perp} \in [2.0, 3.5]\,\mathrm{meV}$, in which the transition of the ssRR collapse to the completely simultaneous radial collapse takes place.

The eigenvalues of the Hessian $\mathcal{H}_{\mathrm{Sp}}$ correspond to the curvature of the energy landscape in the vicinity of the saddle point in the basis of the eigenvectors. In Fig. 10(b), the spectra of the eigenvalues, $\epsilon_{\mathrm{Sp},i} \in \{\epsilon_{\mathrm{Sp},1}, \ldots, \epsilon_{\mathrm{Sp},N}\}$, are shown for the saddle points of the $\alpha\alpha$-stacked bilayer versus $J^{\perp}$. The eigenvalues of the monolayer system are added as a reference and agree with the eigenvalues published in Refs. [37,68].

Both transition mechanisms exhibit a first order saddle point as they have exactly one negative eigenvalue shown in the lower part of the panel. The negative eigenvalue of the ssRR mechanism increases with $J^{\perp}$ until it reaches the value of the monolayer close to the critical interlayer exchange of $J_C^{\perp} \approx 2.6\,\mathrm{meV}$. In the regime of simultaneous collapse, the eigenvalue of the unstable mode lies exactly on the value of the monolayer, which can be expected since the magnetic structures of both layers are identical with the monolayer saddle point structure.

In comparison to the monolayer system, a new saddle point eigenmode appears in the bilayer system, which connects the ssRR and the simultaneous collapse mechanisms and is therefore coined layer-aligning mode [Fig. 10(b)]. For increasing $J^{\perp}$, its eigenvalue approaches zero at $J_C^{\perp}$ before it steeply rises again in the simultaneous collapse regime. This mode softening around $J_C^{\perp}$ is responsible for the transition between the ssRR and the simultaneous collapse mechanisms in both the $\alpha\alpha$ and the $\alpha\beta$-stacking. The spectrum of the latter is shown in Fig. 10(d). It resembles the spectrum of the

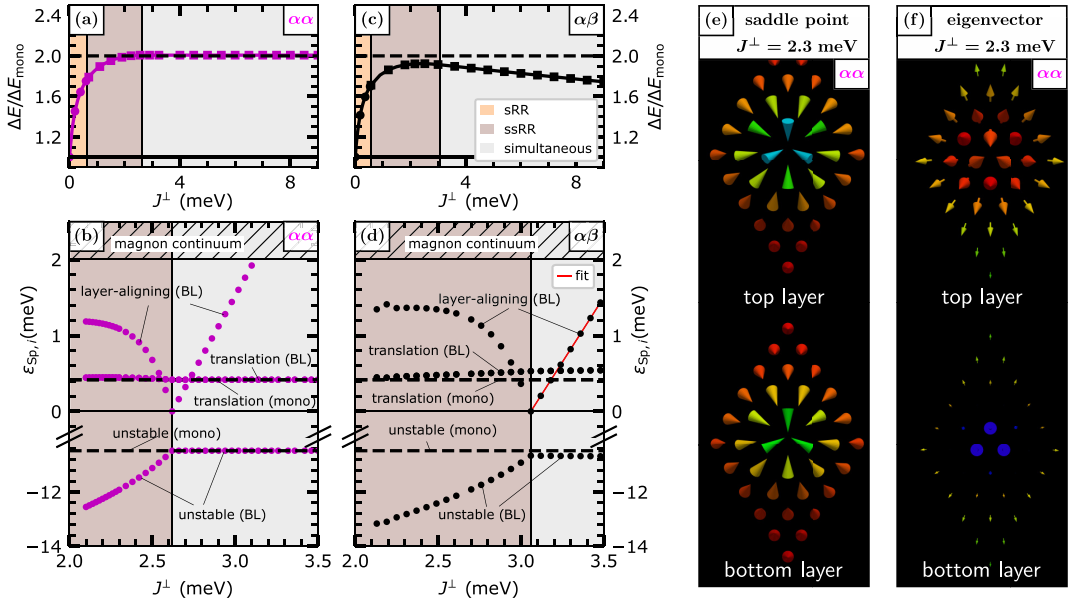


FIG. 10. [(a)–(c)] Energy barriers of bilayer skyrmions in the $\alpha\alpha$ and the $\alpha\beta$ system relative to the energy barrier of skyrmions within the magnetic monolayer system Pd/Fe/Ir(111) for various interlayer exchange constants $J^\perp$. The effective parameter set (cf. Table I) is used and the background colors follow the definition of the collapse mechanisms as defined in Fig. 9 for the NRE model. For better visibility, every third data point is displayed. [(b) and (d)] Visualization for the $\alpha\alpha$ and $\alpha\beta$ system, respectively, of the lowest eigenvalues of the Hessian of the saddle point configuration which belong to the energy barriers displayed in (a) and (b) for various $J^\perp$. The identified eigenmodes calculated for the bilayer system are labeled with BL. For a detailed description see the text. The dashed lines indicate the eigenvalues for a skyrmion in the monolayer system at $B = 4.0\,\mathrm{T}$ described with the effective model [37]. In (d), a fit following Eq. (13) is presented by a red line. (e) Representation of the saddle point configuration for the bilayer skyrmion in the $\alpha\alpha$ system for $J^\perp = 2.3\,\mathrm{meV}$. (f) Visualization of the eigenvector for the layer-aligning mode of the saddle point presented in (e). The color code represents the z-component of the orientation of the vectors.

$\alpha\alpha$-stacking except for a larger critical interlayer exchange of $J_C^\perp \approx 3.0\,\mathrm{meV}$ and eigenvalues that slightly deviate from their monolayer counterparts with increasing $J^\perp$.

In order to deepen the understanding of the layer-aligning mode, we display the spin structure of the ssRR saddle point for a value of $J^\perp = 2.3\,\mathrm{meV}$ in Fig. 10(e). The spin structure of both layers is quite similar, but shows small deviations especially in the three central spins, which are slightly rotated downward in the top layer, but point almost toward each other in the bottom layer, implying that the radial collapse is more advanced in the bottom layer than in the top layer as it is expected for the ssRR collapse mechanism.

By looking at the corresponding eigenvector [Fig. 10(f)], one can already guess that its application to the top layer would push the magnetic structure in this layer further in the direction of the radial collapse. In contrast, the application of the eigenvector to the bottom layer would rotate the central moments in the opposite direction, resulting in more similar saddle points and thus a more simultaneous collapse in both layers.

However, the visual examination of the eigenvector is limited and we apply the mode following method as proposed in Ref. [68]. Each mode following step consists of the calculation of the desired eigenvector by partial diagonalization of the Hessian matrix and the subsequent rotation of the magnetic structure in the direction of this eigenvector. The resulting magnetic state is then the starting point for the next mode following step. A mode tracking algorithm which compares the previous eigenvector with the newly calculated ones ensures that always the eigenvector that is the most similar to the followed eigenmode is chosen. With this technique, the energy landscape in the direction of the eigenmode can be determined. See movies in Ref. [70] for a visualization of this technique.

Figure 11(a) shows the energy over the coordinate $q$, which determines the displacement of the magnetic structure along the layer-aligning mode, where a value of $q = 0$ corresponds to the simultaneous collapse. The color encodes the geodesic distance between the magnetic structures in the top and bottom layer. Thus the more blue (red) the color is, the more simultaneous (successive) the collapse mechanism is. The mode following calculations are performed for varying values of the interlayer exchange, $J^\perp$, resulting in one line per calculation. As starting points, the relaxed saddle point structures as obtained by CI-GNEB have been used.

For small values of $J^\perp$, the energy profiles show two degenerate minima for both possible realizations of the ssRR collapse mechanism. By following the layer-aligning mode from one minimum to the other, the saddle point of the simultaneous collapse is passed as an intermediate local energy maximum. With increasing $J^\perp$, the two degenerate energy minima become more shallow until they vanish at

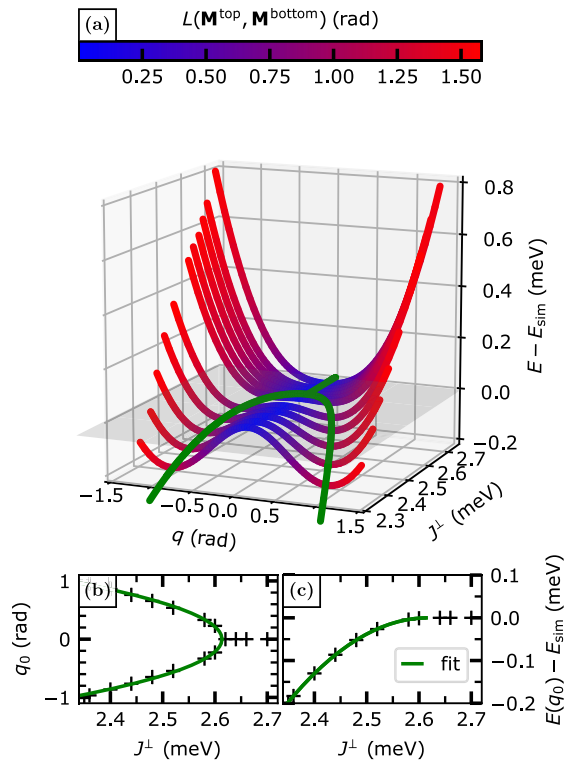


FIG. 11. (a) Local energy landscape along the layer-aligning mode for different $J^\perp$ around the saddle point configurations of bilayer skyrmions in the $\alpha\alpha$ system. An example for a corresponding eigenvector is shown in Fig. 10(f). The energy is displayed relative to the energy of the simultaneous saddle point configuration $E_{\text{sim}}$ and visualized over the displacement $q$ along the mode. The color code represents the geodesic distance between the magnetizations of the top layer $\vec{M}^{\text{top}}$ and the bottom layer $\vec{M}^{\text{bottom}}$. [(b) and (c)] Position and value of the local energy minima from (a) recorded over $J^\perp$. The green lines indicate fits of Eqs. (10) and (11), respectively.

$J_C^\perp \approx 2.6\,\text{meV}$ and a single minimum at $q = 0$ emerges for even larger $J^\perp$.

This behavior can be discussed analog to Landau's theory for continuous phase transitions by modeling the energy to the fourth power along the mode:

$$E(q, J^\perp) - E_{\text{sim}} = a(J^\perp) \cdot q^2 + \frac{b(J^\perp)}{2} q^4, \tag{9}$$

where the displacement along the mode $q$ takes the role of the ordering parameter, $E(q, J^\perp)$ is the energy along this ordering parameter for some value $J^\perp$ of the parameter provoking the phase transition, and $E_{\text{sim}}$ is the zero point of this energy, which will be defined below. In order to prohibit indefinite negative energies for indefinite order parameters $b(J^\perp) > 0$ has to hold and it will be further assumed that $b(J^\perp) = b_0$ is valid near $J^\perp$. Calculating the stationary points $q_0$ of Eq. (9) yields

$$q_0^2 = -\frac{a}{b_0}.$$

We obtain one local minimum ($q_0 = 0$) for $a > 0$ and two local minima for $a < 0$, which mimics exactly the behavior of the energy landscape of the layer-aligning mode near $J_C^\perp$. Therefore one can model $a(J^\perp) \approx a_0(J^\perp - J_C^\perp)$ for $a_0 > 0$ and $J^\perp$ close to $J_C^\perp$ and the positions of the minima follow

$$q_{0,\pm} = \pm \frac{a_0}{b_0} |J^\perp - J_C^\perp|^{\frac{1}{2}}. \tag{10}$$

Further, the energy of the local minima can be determined through

$$E(q_{0,\pm}) = -\frac{a_0^2}{2b_0}(J^\perp - J_C^\perp)^2. \tag{11}$$

Fitting Eqs. (10) and (11) to the data obtained by the mode-following method yields $a_0 = (2.98 \pm 0.04)\,\text{meV/rad}^2$, $b_0 = (1.61 \pm 0.03)\,\text{meV/rad}^4$ and $J_C^\perp = (2.613 \pm 0.003)\,\text{meV}$ [see Figs. 11(b) and 11(c)]. A phase transition implies a symmetric configuration above $J_C^\perp$ which splits up into two configurations with lower symmetry below $J_C^\perp$. The nature of this symmetry can be revealed through visualizing the geodesic distance [32] between the magnetization of the top Fe layer $\vec{M}^{\text{top}}$ to the magnetization of the bottom Fe layer $\vec{M}^{\text{bot}}$:

$$L(\vec{M}^{\text{top}}, \vec{M}^{\text{bot}}) = \sqrt{\left(l_1^{\text{top,bot}}\right)^2 + \left(l_2^{\text{top,bot}}\right)^2 + \cdots + \left(l_{N/2}^{\text{top,bot}}\right)^2}, \tag{12}$$

where $N/2$ is the number of spins per layer and the $l_i^{\text{top, bot}}$ are geodesic distances between the points of the unit sphere, which correspond to the spins in the top and bottom layer, respectively. This quantity is represented by the color code in Fig. 11(a). While blue represents parallel aligned layers, red indicates a net angle between the magnetization of the different layers. Therefore one can conclude that indeed the simultaneous collapse mechanism matches with the high symmetry configuration for interlayer exchange couplings above $J_C^\perp$. Below $J_C^\perp$ two collapse mechanisms are possible with saddle point configurations obeying a successive transgression of the Bloch-like points in each layer and thus representing a lower symmetry. Note that the energy for each slice (each $J^\perp$) in Fig. 11(a) is meant relative to the simultaneous configuration $E_{\text{sim}}$. This simultaneous configuration is a local minimum for $J^\perp > J_C^\perp$ and a local maximum for $J^\perp < J_C^\perp$. The displacement along the mode $q$ is also expressed relative to this simultaneous configuration. All these consideration were done for the bilayer skyrmion collapse within the $\alpha\alpha$ system. For the purpose of substantiating the same mechanism in the $\alpha\beta$ system, we show that $a_0$ and $J^\perp$ can already be derived from the eigenvalue spectrum in Fig. 10(c). The second derivative of Eq. (9) yields the curvature at the minimum along the energy reach along the layer-aligning mode $c$ and thus the corresponding eigenvalue

$$\epsilon_{\text{Sp},c} = \begin{cases} 2a_0|J^\perp - J_C^\perp|, & J^\perp > J_C^\perp \\ -4a_0|J^\perp - J_C^\perp|, & J^\perp < J_C^\perp \end{cases} \tag{13}$$

for $J^\perp$ close to $J_C^\perp$. A fit of Eq. (13) to the layer-aligning mode for $J^\perp > J_C^\perp$ results $a_0 = 1.71\,\text{meV/rad}^2$ and $J_C^\perp = 3.06\,\text{meV}$ for the $\alpha\beta$ system. This fit is displayed by a line in Fig. 10(d).

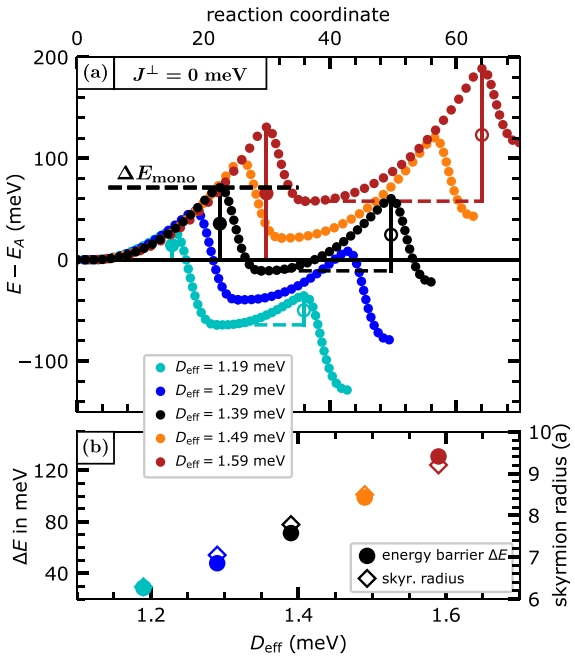


FIG. 12. (a) Minimum energy paths of bilayer skyrmions in the $\alpha\alpha$ system based on the effective parameters from the monolayer system Pd/Fe/Ir(111) for different values of the DMI (see color code in legend). The interlayer exchange constant is set to zero ($J^\perp = 0$ meV). For comparison the energy barrier of the skyrmion in the magnetic monolayer for $D_{\text{eff}} = 1.39$ meV [31] is indicated as dashed line. (b) Energy barriers and radius of the bilayer skyrmions in the magnetic monolayer systems for different values of the DMI. The radius of the relaxed bilayer skyrmion is given in units of the lattice constant $a$.

### E. Varying the monolayer barrier

Addressing the issue of designing a magnetic bilayer system which yields maximum skyrmion stability an estimate of the critical interlayer exchange strength $J_C^\perp$ from the properties of the underlying monolayer system is important. We assume that the energy barrier of the skyrmion in the magnetic monolayer system may influence $J_C^\perp$ of the bilayer system. Therefore we varied the barrier of each skyrmion in the bilayer by systematically varying the DMI within the effective model ($D_{\text{eff}} \in [1.19, 1.59]$ meV). Figure 12(a) shows the obtained MEPs for five values of the DMI for $J^\perp = 0$ meV. The collapses are similar to the MEP of the skyrmion in the underlying monolayer system as discussed in Fig. 5. Figure 12(b) presents the energy barrier of the first collapse and the radius of bilayer skyrmions for switched off interlayer exchange depending on the corresponding value of the DMI. In agreement with Ref. [69] the radius and the energy barrier increase with the DMI strength. Since $J^\perp = 0$ meV this energy barrier corresponds to the energy barrier of the underlying magnetic monolayer system $\Delta E_{\text{mono}}$. Therefore the variation of the DMI parameter yields a variation of the energy barrier of the magnetic monolayer skyrmion in the interval $\Delta E_{\text{mono}} \in [25, 130]$ meV.

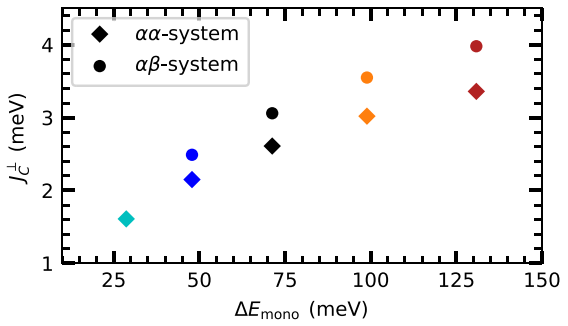


FIG. 13. Critical interlayer exchange $J_C^\perp$ for skyrmions in magnetic bilayer systems based on the effective parameter set (Table I) for different values of the DMI. The color code indicates the different values of the DMI which define the energy barrier of a skyrmion in the corresponding magnetic monolayer system (cf. Fig. 12). Circles denote the $\alpha\alpha$ system and diamonds represent the values of $J_C^\perp$ for the $\alpha\beta$ system. See Fig. 18 for the corresponding visualization of the energy barriers of the bilayer skyrmions.

After defining $\alpha\alpha$- and $\alpha\beta$-stacked systems for these DMI values, we vary the interlayer exchange coupling and calculate the energy barriers of the bilayer skyrmions analog to Sec. IV C. We have to mention that during this variation no chimera type saddle points appear, which we attribute to the lack of intralayer frustration for the effective parameter set. In Appendix B in Fig. 18, we present, similar to Figs. 10(a) and 10(c), the energy barriers of the bilayer skyrmions relative to the energy barrier of the skyrmion in the corresponding monolayer system for the $\alpha\alpha$- and $\alpha\beta$-stacks, respectively. Further we determined the critical interlayer exchange parameters $J_C^\perp$ by calculating the eigenvalue spectrum and applying a fit following Eq. (13) for $J^\perp > J_C^\perp$ as presented in Fig. 10(c). The obtained values of $J_C^\perp$ are displayed for the $\alpha\alpha$ and $\alpha\beta$ system in Fig. 13 as a function of the energy barrier of a skyrmion in the corresponding monolayer system $\Delta E_{\text{mono}}$. Note that the determination of $J_C^\perp$ for $D_{\text{eff}} = 1.19$ meV was not possible for the $\alpha\beta$ system as the divergence of the layer-aligning mode is overlapping in the eigenvalue spectrum with another collapse mechanism of the low interlayer exchange regime here.

Although the critical parameter $J_C^\perp$ is always a bit larger for skyrmions in the $\alpha\beta$-stacked system than for the skyrmions in the $\alpha\alpha$ system both follow the same trend. As the monolayer barrier increases a higher interlayer exchange coupling is needed to force the system into a simultaneous collapse, which is indicated by the increase of $J_C^\perp$ in Fig. 13. For comparison we observed $J_C^\perp = 10.0$ meV for the $\alpha\alpha$ and $J_C^\perp = 11.9$ meV for the $\alpha\beta$ system treated with the NRE-parameter set in Sec. IV C. This corresponded to an energy barrier $\Delta E_{\text{mono}} \approx 143$ meV of the underlying monolayer system.

It is striking that for systems examined with the effective parameter set the critical interlayer exchange parameters are significantly smaller than for the systems treated with the NRE model. This is an indication that in real systems with exchange frustration a much larger interlayer exchange is needed to force a simultaneous collapse of the skyrmions in the different layers. Therefore, if one aims to design a magnetic bilayer system with maximum skyrmion stability two aspects have

to be considered. On the one hand, a higher energy barrier of a skyrmion in the underlying monolayer system provides a higher energy barrier for the simultaneously collapsing bilayer skyrmion. On the other hand, one needs higher interlayer couplings to realize this simultaneous transition.

### F. Energy barriers for multilayer skyrmions

Our previous results for skyrmions in bilayers carry over to systems with more layers. For this purpose, we again use the effective parameter set to exclude exchange frustration effects within the layers. Energy barriers for skyrmions were obtained in three layer and four layer systems, with the magnetic atoms of the different layers all occupying the same lattice sites. Following our notation, these system are of the $\alpha\alpha$ type. We also studied a system with four layers and six layers with an $\alpha\beta$ stacking. For weak interlayer exchange, we calculated increased multiplicity of collapse mechanisms, in agreement with the bilayer results. Presenting this complexity is beyond the aim of this paper. We therefore present here only the regime of large interlayer exchange coupling. The energy barriers depending on the interlayer exchange $J^\perp$ of the skyrmions in the multilayer systems studied are shown in Fig. 14(a) relative to the energy barrier of the skyrmion of the monolayer system.

As expected, the energy barriers for the three layer (four layer) skyrmions in the $\alpha\alpha$ system converge to three (four) times the energy barrier of the skyrmion in the monolayer system. However, it can be observed in Fig. 14(a) that a larger interlayer exchange coupling $J_C^\perp$ is needed in the case of the three and four layer system to force a simultaneous collapse of the skyrmions than in the bilayer. If we extrapolate the results obtained here for the skyrmions in the $\alpha\alpha$ systems [Fig 14(b)] to a system with $L$ layers in which the atoms of all layers occupy the same lattice sites, we confirm the conjecture $\Delta E = L\Delta E_{\text{mono}}$ for the skyrmion in the multilayer system as long as $J^\perp > J_C^\perp$ holds and we only consider nearest-neighbor interlayer exchange interactions. This is in agreement with the prediction in Ref. [54].

It is the general view that an increase in magnetic material leads to an increase in the stability of skyrmions in magnetic multilayers. To ensure simultaneous behavior of these skyrmions, it is often concluded that the largest possible interlayer exchange is desirable. Our calculations for the $\alpha\alpha$ systems confirm this. If we move to the $\alpha\beta$ systems, which are relevant for real layered materials, we also find that increasing the number of layers increases the energy barrier of the skyrmions [Fig. 14(a)] consistent with the studies of Hoffmann *et al.* [53].

However, the situation is more complicated. What can be deduced from the data shown in Fig. 14(a) is that the maximum stability for skyrmions in multilayers is achieved for a certain value of interlayer exchange. The maximum of the energy barrier for the skyrmion in the four layer $\alpha\beta$ system is below 3.5 times the energy barrier of the skyrmion in the monolayer system and is obtained for $J^\perp \approx 6$ meV. The maximum achievable energy barrier for the skyrmion in the six layer $\alpha\beta$ system is even below five times the energy barrier in the monolayer system. This is in contrast to the common belief that interlayer exchange coupling does not affect the stability

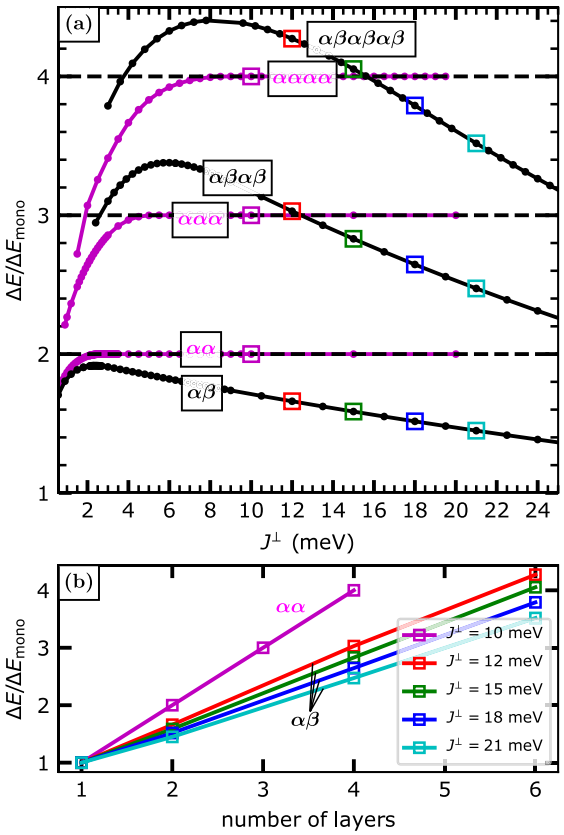


FIG. 14. (a) Energy barriers of skyrmions in magnetic multilayer systems for various interlayer exchange couplings $J^\perp$ relative to the energy barrier of the skyrmion in the magnetic monolayer Pd/Fe/Ir(111). The effective parameter set is used for these calculations. The energy barriers for the skyrmions in the two-, three- and four-layer systems obeying a $\alpha\alpha$-stacking sequence are shown in magenta. The barriers for the two-, four-, and sixlayer systems with $\alpha\beta$-stacking are shown in black. (b) Energy barriers from (a) as a function of the number of layers for fixed values of $J^\perp$. The corresponding data points are indicated by empty squares in (a). For the $\alpha\alpha$ systems the layer-dependent energy barrier is presented for $J^\perp = 10$ meV, while it is shown for the $\alpha\beta$ systems for $J^\perp = 12$, 15, 18, and 21 meV.

of multilayer skyrmions as long as it is strong enough to allow simultaneous behavior of the skyrmion.

Comparing the different $\alpha\beta$ systems also indicates that the decrease of the energy barrier for high interlayer exchange couplings occurs with a more negative slope the more layers are involved. This leads to the fact that the energy gain in terms of skyrmion stability by adding another layer decreases with increasing interlayer exchange coupling [Fig. 14(b)]. We propose that the energy barrier of skyrmions in $\alpha\beta$-stacked multilayer systems with $L$ layers is thus given by $\Delta E = g(J^\perp)L\Delta E_{\text{mono}}$. Where the function $g(J^\perp) < 1$ attributes to the fact that optimizing the skyrmion stability through adding more layers relies on the choice of the optimal interlayer

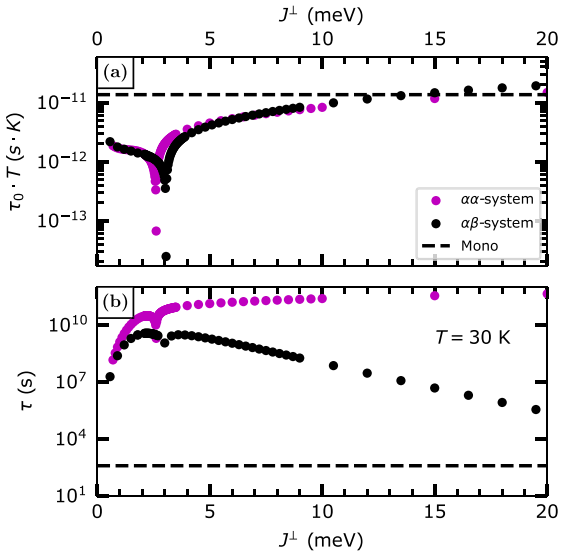


FIG. 15. (a) Temperature independent pre-exponential factor $\tau_0 T$ [Eq. (6)] for skyrmions in magnetic bilayer systems based on the magnetic monolayer system Pd/Fe/Ir(111) in $\alpha\alpha$ and $\alpha\beta$ stacking for various interlayer exchange couplings $J^\perp$. The dashed line indicates pre-exponential factor for skyrmions within the magnetic monolayer system Pd/Fe/Ir(111) [37] for $B = 4.0$ T. (b) Skyrmion lifetime $\tau$ for $T = 30$ K calculated with the Arrhenius law [Eq. (1)] using the energy barriers $\Delta E$ from Fig. 10(a) and the prefactor $\tau_0$ displayed in part (a) of this figure.

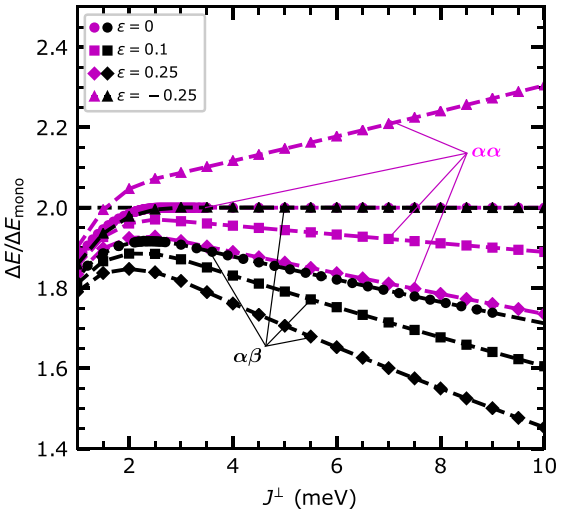


FIG. 16. Energy barriers of bilayer skyrmions in $\alpha\alpha$ (magenta) and $\alpha\beta$ systems (black) relative to the energy barrier of the skyrmion in the magnetic monolayer Pd/Fe/Ir(111) depending on the interlayer exchange per unit cell $J^\perp$. The effective model was used to describe the intralayer exchange coupling. The different values of $\epsilon$ encode different distributions of the interlayer exchange to the first neighbor and second neighbor shell [see Eqs. (14) and (15)]. A value $\epsilon < 0$ indicates a frustrated system in terms of interlayer exchange coupling.

exchange. This counterintuitive result provides an important contribution to the understanding of skyrmion stability in magnetic multilayers and is visualized in Fig. 14(b). Here we extracted the energy barriers for fixed values of $J^\perp$ from Fig. 14(a) and plotted versus the number of layers.

### G. Lifetime of bilayer skyrmions

In the preceding sections we discussed the dependence of the energy barrier on the interlayer exchange in magnetic bilayer systems, which is the dominant contribution to the lifetime at low temperatures due to the exponential term in Eq. (1). However, as reported in Refs. [37,40], the effect of the change of the pre-exponential factor should not be underestimated. Therefore we present the calculation of the pre-exponential factor $\tau_0$ for the generic example of the bilayer stacks based on the effective parameter set as discussed in Sec. IV D. For the purpose of underlining our results concerning the stability of skyrmions in the strong interlayer exchange coupling regime we only discuss here collapse paths passing through a single saddle point on the energy surface. Collapses involving intermediate metastable states can be described using the Master equation and are beyond the scope of this article. The diagonalization of the Hessian matrix for the bilayer skyrmion and the saddle point configuration gives us the eigenvalues of the initial bilayer skyrmion $\epsilon_{A,i}$ and the saddle point configuration $\epsilon_{\text{Sp},i}$. The determined eigenvalues allow the calculation of the prefactors following Eq. (7). Note that in the case of a bilayer system, the Hessian matrix of a spin configuration has twice as many eigenvalues as the corresponding matrix of the monolayer system. However, the pre-exponential factors are still comparable, since only the ratio of the eigenvalues of the initial configuration and the saddle configuration enters into Eq. (7).

Figure 15(a) shows a highly similar behavior for the $\alpha\alpha$ and $\alpha\beta$ stack regarding the pre-exponential factor $\tau_0$. A sharp decline of $\tau_0$ occurs around $J^\perp = 3.0$ meV followed by an increase towards the prefactor of the magnetic monolayer system, which is indicated by the dashed line. This narrow sink is produced by the softening of the layer-aligning saddle point mode which approaches zero in this regime (see Fig. 10). The softening leads to a division by zero in Eq. (7) and therefore $\tau_0$ approaches zero for $J^\perp \approx J_C^\perp$. In this region the applicability of the harmonic approximation is questionable. Nevertheless, it is remarkable that the prefactor reduces the stability of the bilayer skyrmions for both stackings compared to the prefactor of the skyrmion in the magnetic monolayer system (dashed line in Fig. 15). We attribute this to an increased entropic difference between the transition state and the skyrmion state for intermediate interlayer exchange couplings as the number of possible transition mechanisms reduces with increased exchange couplings between the layers.

In 2017, Wild *et al.* [42] investigated the lifetime of skyrmions in B20 compounds. Changes in the magnetic field which lead to an increased energy barrier were counterbalanced by changes in the pre-exponential factor by 30 orders of magnitude leading to a substantial reduction of the lifetime

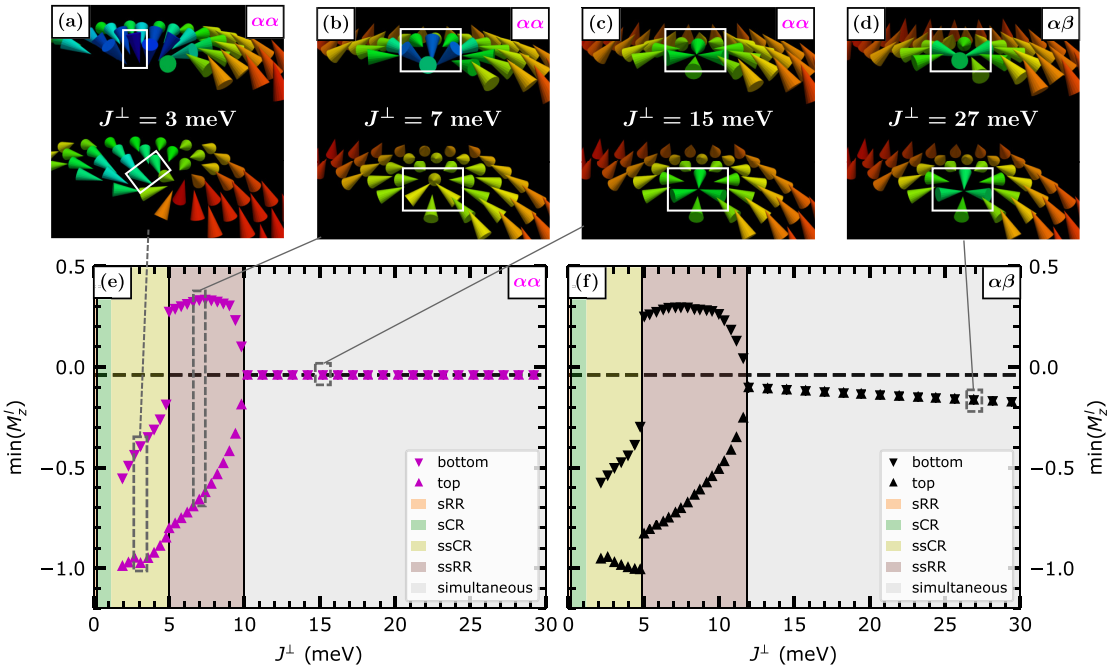


FIG. 17. [(a)–(c)] Representation of the saddle point configuration of the bilayer skyrmion collapse in the $\alpha\alpha$ system for $J^\perp = 3$, 7, and 15 meV. The $m_i^z$-component of the magnetic moments $i$ is emphasized by the color code. In each layer, the magnetic moments $i$ with the minimum $m_i^z$ component are highlighted with a white box. (d) Analog representation for the saddle point configuration of a collapse in the $\alpha\beta$ system for $J^\perp = 27$ meV. (e) Visualization of the minimum component of the magnetization in the $z$ direction for collapses of bilayer skyrmions in the $\alpha\alpha$ system for various $J^\perp$ for both layers $l = 1$ and 2. The background color indicates the regime of the collapse types as introduced in Sec. IV B. (f) Analog visualization to (e) for the $\alpha\beta$ system. For comparison the corresponding value for the monolayer skyrmion collapse in Pd/Fe/Ir(111) is indicated as dashed black line in (e) and (f). All calculations where done with the NRE parameter set and only each third data point is shown for better visibility in (e),(f).

of skyrmions by entropic effects [42]. However we expect that the increase in the energy barrier for skyrmions in systems with multiple magnetic layers always goes along with such a entropic induced decrease of the pre-exponential-factor $\tau_0$ for low $J^\perp$. As the interlayer exchange coupling increases above $J^\perp \approx 15$ meV the prefactor of the bilayer systems reaches the prefactor for skyrmions in the monolayer system [Fig. 15(a)]. Note that the visualization in Fig. 15(a) is valid for all temperatures $T$ since the linear dependance in Eq. (7) allows to display $\tau_0 T$. Since there are two minimum energy paths describing independent but equivalent realizations of the ssRR collapse for $J^\perp < J_C^\perp$, we multiplied $\tau_0^{-1}$ by a further factor of two in this regime. These two realizations can be obtained from one another by swapping the magnetic configurations of the layers.

In Fig. 15(b), we calculated the lifetime $\tau$ for the exemplary temperature $T = 30$ K. For the shown parameter range of $J^\perp$, the stability of the bilayer skyrmion is always enhanced compared to the skyrmion in the magnetic monolayer system. The results of this section exemplify that the effects of changing the pre-exponential factor are relatively small when varying the interlayer exchange compared to the influence of the energy barrier on the lifetime of the bilayer skyrmions discussed here. Therefore one can associate the results of the previous sections regarding the energy barriers of bilayer skyrmions directly with the stability of these skyrmions.

## V. CONCLUSIONS AND DISCUSSION

In this work, we investigated fundamental properties of skyrmion stability in magnetic multilayer systems. We considered multilayers built from single Fe layers with the magnetic properties taken from the well-studied film system Pd/Fe/Ir(111) and coupled by interlayer exchange of variable strength $J^\perp$. The layers are either stacked in $\alpha\alpha$ order, in which the magnetic atoms are placed on top of each other, or in $\alpha\beta$ order, with magnetic layers horizontally offset from each other. This shift describes the relative position of the magnetic layers with respect to each other and is therefore characteristic for directly adjacent magnetic layers in fcc- or hcp-stacked thicker magnetic layers as well as for various multilayer systems consisting of magnetic layers sandwiched between nonmagnetic layers.

For both stacking orders of magnetic bilayers, we found the expected simultaneous collapse of skyrmions in both Fe layers when $J^\perp$ exceeds a critical interlayer exchange, $J_C^\perp$. The collapse splits into the successive annihilation of skyrmions in individual layers for small $J^\perp$, which can be seen as the

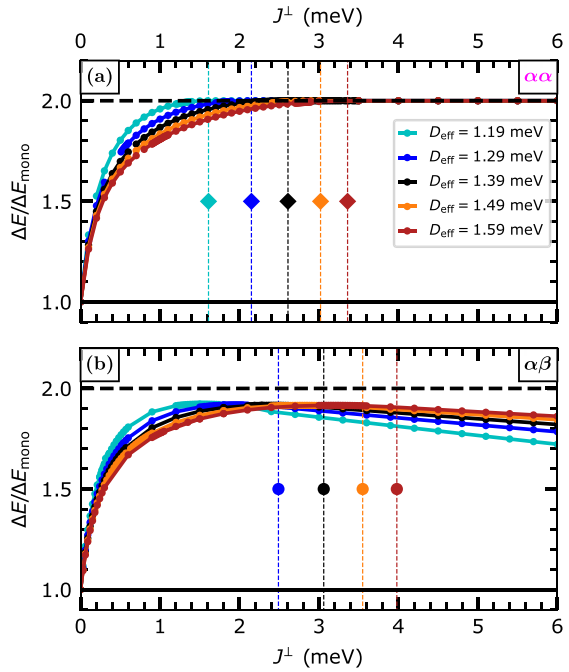


FIG. 18. [(a) and (b)] Energy barrier $\Delta E$ of bilayer skyrmions in the $\alpha\alpha$ and $\alpha\beta$ system for various interlayer exchange couplings $J^\perp$ relative to the energy barrier of a skyrmion in the underlying monolayer system $\Delta E_{\text{mono}}$. The variation of the DMI is indicated through the color code in the legend. (a) displays the $\alpha\alpha$ and (b) presents the $\alpha\beta$ system. The vertical dashed lines indicate the positions of $J_C^\perp$ (see Fig. 10). These critical interlayer exchange couplings $J_C^\perp$ are displayed in dependence of $\Delta E_{\text{mono}}$ in Fig. 13.

bilayer analog to the occurrence of chiral magnetic bobbers in bulk systems [67]. For intermediate strengths of $J^\perp$, a rich phase space of collapse mechanisms arises, in which the interlayer exchange interaction can favor a mix of semisuccessive chimera and radial symmetric mechanisms.

Our analysis of the eigenvalue spectrum of the bilayer system revealed the layer-aligning eigenmode, which is responsible for the transition from the ssRR collapse to the simultaneous collapse. We found, that this transition can be described accurately by Landau's theory for continuous phase transitions, which provides a stable definition of the critical interlayer exchange $J_C^\perp$. This can help to design multilayer systems in the simultaneous collapse regime, which is desirable for most applications since the annihilation processes become more complex and thus harder to control for less strongly coupled systems.

Harmonic transition state theory calculations show a small dependence of the prefactor on the interlayer exchange constant and the number of magnetic layers which indicates only a minor role of entropic effects in the investigated parameter space. However, the situation could be different for couplings below $J_C^\perp$ where the role of additional multilayer eigenmodes is more complex.

Considering nearest-neighbor interlayer exchange, the energy barrier protecting skyrmions in the $\alpha\alpha$-stacked systems equals the energy barrier for the corresponding skyrmion in the magnetic monolayer multiplied by the number of magnetic layers $L$ as long as $J^\perp > J_C^\perp$. The critical value $J_C^\perp$, on the other hand, is increasing with $L$ as well and is thus limiting the number of layers in the simultaneous collapse regime for a given $J^\perp$. These results are consistent with the notion that a strong interlayer exchange is desirable for increasing skyrmion stability.

However, for an $\alpha\beta$ stacking, collinear structures are favored by the nearest-neighbor interlayer exchange interaction. This leads to the existence of a sweet spot for the strength of $J^\perp$, at which the increase of the total energy barrier due to the increased number of layers and the reduction of the energy barrier caused by strong interlayer coupling is optimized.

It turns out, that the optimal choice of $J^\perp$ changes drastically with the number of coupled magnetic layers, the other interaction parameters, and the crystal structure of the multilayer. These results occur systematically and consistent for our model systems with and without intralayer exchange frustration and over a large interval of nearest-neighbor interlayer exchange parameters.

Our motivation was to obtain general trends for exchange-coupled monolayers with a single-parameter study and at the same time to be consistent with a well-established Pd/Fe/Ir(111) system in the case of vanishing interlayer exchange. However, as contributions of second nearest-neighbor interlayer exchange bonds introduce horizontal components of the interlayer exchange interaction for both the $\alpha\alpha$ and $\alpha\beta$ stackings, it is important to discuss their influence in the context of the presented results. To address this aspect, we performed calculations where we model the interlayer exchange according to the following formulas:

$$J_1^\perp = \frac{1-\epsilon}{n_1^x} J^\perp, \tag{14}$$

$$J_2^\perp = \frac{\epsilon}{n_2^x} J^\perp, \tag{15}$$

where $J_1^\perp$ and $J_2^\perp$ are the interlayer exchange constants per atom for the first and second neighbor shells, respectively; $n_1^x$, $n_2^x$ are the number of neighbors in the corresponding shells for stacking $x$. For $\alpha\alpha$ and $\alpha\beta$ stacking, we particularly have $n_1^{\alpha\alpha} = 1$, $n_2^{\alpha\alpha} = 6$ and $n_1^{\alpha\beta} = 3$, $n_2^{\alpha\beta} = 3$. The value of $\epsilon$ describes the contribution of the first and second neighbors into the total interlayer exchange per unit cell. We have investigated the case of $\epsilon = 0.1$ and 0.25 for a bilayer system and calculated the skyrmion collapse energy barrier as a function of $J^\perp$. The intralayer exchange was modeled according to the effective model.

The corresponding results are presented in Fig. 16. We found that for a given $J^\perp > J_C^\perp$ the skyrmion collapse barrier $\Delta E$ decreases with $\epsilon$ for both stackings of the magnetic layers. Nevertheless, adding interlayer exchange beyond nearest-neighbors does not lead to qualitative changes in the $J^\perp$ dependence of the collapse energy barrier for the $\alpha\beta$ stacking. In contrast, the behavior of $\Delta E$ for the $\alpha\alpha$ stacking changes sharply and becomes similar to that for the $\alpha\beta$ stacking thanks to the presence of the horizontal components of the interlayer

exchange. As a consequence, $\Delta E$ does not converge to twice the value of the energy barrier for a monolayer system $\Delta E_{\text{mono}}$ in the strong coupling regime even for the $\alpha\alpha$ stacking. Quantitatively, for the same value of $\epsilon$, the energy barriers of the skyrmions in the $\alpha\alpha$-stackings are always larger than in the corresponding $\alpha\beta$ system in the strong interlayer exchange regime. Noteworthy, one can achieve a barrier larger than $2\Delta E_{\text{mono}}$ by engineering the interlayer exchange frustration modeled here by negative $\epsilon$ values (see Fig. 16).

Note that these calculations cannot be considered an exhaustive study of the effect of the shell-resolved interlayer exchange on the skyrmion stability. However, they demonstrate that the energy barrier of multilayer skyrmions is hardly ever a simple multiple of the energy barrier for the corresponding monolayer skyrmion $\Delta E_{\text{mono}}$, as in-plane components of the interlayer exchange couplings are likely present in real systems. In the case of nonfrustrated interlayer exchange, this simple scaling relation $\Delta E = L\Delta E_{\text{mono}}$ can be regarded as an upper limit for the achievable energy barriers of skyrmions in multilayer systems. The actual energy barrier can be significantly smaller than this value.

## ACKNOWLEDGMENTS

We gratefully acknowledge financial support from the Deutsche Forschungsgemeinschaft (DFG, German Research Foundation) via project Nos. 414321830 (HE3292/11-1) and 418425860 (HE3292/13-1), the Icelandic Research Fund (Grant No. 217750 and 184949), the University of Iceland Research Fund and the Russian Science Foundation (Grant No. 19-72-10138).

## APPENDIX A: IDENTIFICATION OF COLLAPSE MECHANISMS

The examination of bilayer skyrmion collapses as a function of interlayer exchange coupling $J^{\perp}$ in Sec. IV B revealed several mechanisms. In Fig. 9 in Sec. IV C, an overview of the parameter range of $J^{\perp}$ for the respective collapse mechanisms is indicated by the background color. While the boundaries between the mechanisms in the low interlayer exchange region are determined from the corresponding energy barriers in Fig. 9, this section shows how the boundaries between the regimes in the intermediate and high coupling regions were determined.

In Figs. 17(a)–17(d), saddle point configurations are shown for different values of $J^{\perp}$ for the $\alpha\alpha$- and $\alpha\beta$ systems. While Fig. 17(a) shows a saddle point of ssCR collapse, Fig. 17(b) illustrates the ssRR collapse, and Fig. 17(c) demonstrates the saddle point for the simultaneous collapse in the $\alpha\alpha$ system.

An example of a saddle point for large $J^{\perp}$ for the $\alpha\beta$ system is given in Fig. 17(d). If one searches for the magnetic moment with the minimum magnetization in the $z$ direction for each layer [see white boxes in Figs. 17(a)–17(d)] and plots this value above $J^{\perp}$, a systematic classification of the mechanisms can be made. For the $\alpha\alpha$ system this representation can be found in Fig. 17(e) and for the $\alpha\beta$ system in Fig. 17(f). At this point, it is important to mention that the indexing of the layers is arbitrary, since the order of the skyrmion transitions in the different layers is not fixed. We now define the transition between the ssCR regime to the ssRR collapse mechanism by the jump visible in Figs. 17(e) and 17(f) for $J^{\perp} \approx 5$ meV. The transition from the ssRR regime to the region of simultaneous collapse can again be defined by the point at which the minimum magnetization in the $z$ direction coincides in both layers.

## APPENDIX B: VARYING THE MONOLAYER SKYRMION BARRIER

Similar to Figs. 10(a) and 10(c), we varied the interlayer exchange coupling and calculated the energy barriers of bilayer skyrmions. In addition, we varied the energy barrier of the skyrmions in each layer by changing the value of the DMI ($D_{\text{eff}}$). This is described in Sec. IV E. The results of these calculations are shown in Fig. 18(a) for the $\alpha\alpha$ systems and in Fig. 18(b) for the $\alpha\beta$ systems. We calculated the critical interlayer exchange parameters $J_C^{\perp}$, which mark the onset of the regime of the simultaneous skyrmion collapse, by calculating the eigenvalue spectrum as presented in Figs. 10(b) and 10(d) and fitting of Eq. (13) to the eigenvalues of the layer-aligning mode above $J_C^{\perp}$.

[1] C. Back, V. Cros, H. Ebert, K. Everschor-Sitte, A. Fert, M. Garst, T. Ma, S. Mankovsky, T. L. Monchesky, M. Mostovoy *et al.*, J. Phys. D: Appl. Phys. **53**, 363001 (2020).
[2] A. Fert, N. Reyren, and V. Cros, Nat. Rev. Mater. **2**, 17031 (2017).
[3] R. Wiesendanger, Nat. Rev. Mater. **1**, 16044 (2016).
[4] A. Bogdanov and A. Hubert, Phys. Stat. Sol. (b) **186**, 527 (1994).
[5] S. Mühlbauer, B. Binz, F. Jonietz, C. Pfleiderer, A. Rosch, A. Neubauer, R. Georgii, and P. Böni, Science **323**, 915 (2009).
[6] X. Z. Yu, Y. Onose, N. Kanazawa, J. H. Park, J. H. Han, Y. Matsui, N. Nagaosa, and Y. Tokura, Nature (London) **465**, 901 (2010).
[7] I. Dzyaloshinsky, J. Phys. Chem. Solids **4**, 241 (1958).
[8] T. Moriya, Phys. Rev. **120**, 91 (1960).
[9] M. Heide, G. Bihlmayer, and S. Blügel, Phys. Rev. B **78**, 140403(R) (2008).
[10] M. Perini, S. Meyer, B. Dupé, S. von Malottki, A. Kubetzka, K. von Bergmann, R. Wiesendanger, and S. Heinze, Phys. Rev. B **97**, 184425 (2018).
[11] M. Bode, M. Heide, K. von Bergmann, P. Ferriani, S. Heinze, G. Bihlmayer, A. Kubetzka, O. Pietzsch, S. Blügel, and R. Wiesendanger, Nature (London) **447**, 190 (2007).
[12] P. Ferriani, K. von Bergmann, E. Y. Vedmedenko, S. Heinze, M. Bode, M. Heide, G. Bihlmayer, S. Blügel, and R. Wiesendanger, Phys. Rev. Lett. **101**, 027201 (2008).
[13] S. Heinze, K. von Bergmann, M. Menzel, J. Brede, A. Kubetzka, R. Wiesendanger, G. Bihlmayer, and S. Blügel, Nat. Phys. **7**, 713 (2011).

[14] N. Romming, C. Hanneken, M. Menzel, J. E. Bickel, B. Wolter, K. von Bergmann, A. Kubetzka, and R. Wiesendanger, Science **341**, 636 (2013).

[15] N. Romming, A. Kubetzka, C. Hanneken, K. von Bergmann, and R. Wiesendanger, Phys. Rev. Lett. **114**, 177203 (2015).

[16] D. Cortés-Ortuño, N. Romming, M. Beg, K. von Bergmann, A. Kubetzka, O. Hovorka, H. Fangohr, and R. Wiesendanger, Phys. Rev. B **99**, 214408 (2019).

[17] P.-J. Hsu, A. Kubetzka, A. Finco, N. Romming, K. von Bergmann, and R. Wiesendanger, Nat. Nanotechnol. **12**, 123 (2017).

[18] M. Hervé, B. Dupé, R. Lopes, M. Böttcher, M. D. Martins, T. Balashov, L. Gerhard, J. Sinova, and W. Wulfhekel, Nat. Commun. **9**, 1015 (2018).

[19] S. Meyer, M. Perini, S. von Malottki, A. Kubetzka, R. Wiesendanger, K. von Bergmann, and S. Heinze, Nat. Commun. **10**, 3823 (2019).

[20] S. S. P. Parkin, Phys. Rev. Lett. **67**, 3598 (1991).

[21] P. Ferriani, I. Turek, S. Heinze, G. Bihlmayer, and S. Blügel, Phys. Rev. Lett. **99**, 187203 (2007).

[22] B. Hardrat, A. Al-Zubi, P. Ferriani, S. Blügel, G. Bihlmayer, and S. Heinze, Phys. Rev. B **79**, 094411 (2009).

[23] S. Blizak, G. Bihlmayer, and S. Blügel, Phys. Rev. B **86**, 094436 (2012).

[24] B. Dupé, M. Hoffmann, C. Paillard, and S. Heinze, Nat. Commun. **5**, 4030 (2014).

[25] H. Yang, A. Thiaville, S. Rohart, A. Fert, and M. Chshiev, Phys. Rev. Lett. **115**, 267210 (2015).

[26] A. Belabbes, G. Bihlmayer, F. Bechstedt, S. Blügel, and A. Manchon, Phys. Rev. Lett. **117**, 247202 (2016).

[27] G. Beutier, S. P. Collins, O. V. Dimitrova, V. E. Dmitrienko, M. I. Katsnelson, Y. O. Kvashnin, A. I. Lichtenstein, V. V. Mazurenko, A. G. A. Nisbet, E. N. Ovchinnikova, and D. Pincini, Phys. Rev. Lett. **119**, 167201 (2017).

[28] R. Juge, S.-G. Je, D. S. Chaves, L. D. Buda-Prejbeanu, J. Peña-Garcia, J. Nath, I. M. Miron, K. G. Rana, L. Aballe, M. Foerster, F. Genuzio, T. O. Mentes, A. Locatelli, F. Maccherozzi, S. S. Dhesi, M. Belmeguenai, Y. Roussigné, S. Auffret, S. Pizzini, G. Gaudin *et al.*, Phys. Rev. Appl. **12**, 044007 (2019).

[29] J. Grenz, A. Köhler, A. Schwarz, and R. Wiesendanger, Phys. Rev. Lett. **119**, 047205 (2017).

[30] I. S. Lobanov, H. Jónsson, and V. M. Uzdin, Phys. Rev. B **94**, 174418 (2016).

[31] S. Malottki, B. Dupé, P. F. Bessarab, A. Delin, and S. Heinze, Sci. Rep. **7**, 12299 (2017).

[32] P. Bessarab, V. Uzdin, and H. Jónsson, Comput. Phys. Commun. **196**, 335 (2015).

[33] L. Desplat, J.-V. Kim, and R. L. Stamps, Phys. Rev. B **99**, 174409 (2019).

[34] F. Muckel, S. von Malottki, C. Holl, B. Pestka, M. Pratzer, P. F. Bessarab, S. Heinze, and M. Morgenstern, Nat. Phys. **17**, 395 (2021).

[35] P. F. Bessarab, G. P. Müller, I. S. Lobanov, F. N. Rybakov, N. S. Kiselev, H. Jónsson, V. M. Uzdin, S. Blügel, L. Bergqvist, and A. Delin, Sci. Rep. **8**, 3433 (2018).

[36] G. P. Müller, P. F. Bessarab, S. M. Vlasov, F. Lux, N. S. Kiselev, S. Blügel, V. M. Uzdin, and H. Jónsson, Phys. Rev. Lett. **121**, 197202 (2018).

[37] S. von Malottki, P. F. Bessarab, S. Haldar, A. Delin, and S. Heinze, Phys. Rev. B **99**, 060409(R) (2019).

[38] L. Desplat, D. Suess, J.-V. Kim, and R. L. Stamps, Phys. Rev. B **98**, 134407(R) (2018).

[39] S. Paul, S. Haldar, S. von Malottki, and S. Heinze, Nat. Commun. **11**, 4756 (2020).

[40] A. S. Varentcova, S. von Malottki, M. N. Potkina, G. Kwiatkowski, S. Heinze, and P. F. Bessarab, npj Comput. Mater. **6**, 193 (2020).

[41] U. Ritzmann, S. von Malottki, J.-V. Kim, S. Heinze, J. Sinova, and B. Dupé, Nat. Electron. **1**, 451 (2018).

[42] J. Wild, T. N. G. Meier, S. Pöllath, M. Kronseder, A. Bauer, A. Chacon, M. Halder, M. Schowalter, A. Rosenauer, J. Zweck, J. Müller, A. Rosch, C. Pfleiderer, and C. H. Back, Sci. Adv. **3**, e1701704 (2017).

[43] B. Dupé, G. Bihlmayer, M. Böttcher, S. Blügel, and S. Heinze, Nat. Commun. **7**, 11779 (2016).

[44] C. Moreau-Luchaire, C. Moutafis, N. Reyren, J. Sampaio, C. A. F. Vaz, N. Van Horne, K. Bouzehouane, K. Garcia, C. Deranlot, P. Warnicke, P. Wohlhüter, J.-M. George, M. Weigand, J. Raabe, V. Cros, and A. Fert, Nat. Nanotechnol. **11**, 444 (2016).

[45] S. Woo, K. Litzius, B. Krüger, M.-Y. Im, L. Caretta, K. Richter, M. Mann, A. Krone, R. M. Reeve, M. Weigand *et al.*, Nat. Mater. **15**, 501 (2016).

[46] O. Boulle, J. Vogel, H. Yang, S. Pizzini, D. de Souza Chaves, A. Locatelli, T. O. Menteş, A. Sala, L. D. Buda-Prejbeanu, O. Klein *et al.*, Nat. Nanotechnol. **11**, 449 (2016).

[47] A. Soumyanarayanan, M. Raju, A. L. G. Oyarce, A. K. C. Tan, M.-Y. Im, A. P. Petrović, P. Ho, K. H. Khoo, M. Tran, C. K. Gan *et al.*, Nat. Mater. **16**, 898 (2017).

[48] L. Caretta, M. Mann, F. Büttner, K. Ueda, B. Pfau, C. M. Günther, P. Hessing, A. Churikova, C. Klose, M. Schneider *et al.*, Nat. Nanotechnol. **13**, 1154 (2018).

[49] N. Nagaosa and Y. Tokura, Nat. Nanotechnol. **8**, 899 (2013).

[50] W. Legrand, D. Maccariello, F. Ajejas, S. Collin, A. Vecchiola, K. Bouzehouane, N. Reyren, V. Cros, and A. Fert, Nat. Mater. **19**, 34 (2020).

[51] K. G. Rana, R. L. Seeger, S. Ruiz-Gómez, R. Juge, Q. Zhang, V. T. Pham, M. Belmeguenai, S. Auffret, M. Foerster, L. Aballe *et al.*, Appl. Phys. Lett. **119**, 192407 (2021).

[52] D. Stosic, J. Mulkers, B. Van Waeyenberge, T. B. Ludermir, and M. V. Milosevic, Phys. Rev. B **95**, 214418 (2017).

[53] M. Hoffmann, G. P. Müller, and S. Blügel, Phys. Rev. Lett. **124**, 247201 (2020).

[54] B. Heil, A. Rosch, and J. Masell, Phys. Rev. B **100**, 134424 (2019).

[55] M. Böttcher, S. Heinze, S. Egorov, J. Sinova, and B. Dupé, New J. Phys. **20**, 103014 (2018).

[56] J. Hagemeister, N. Romming, K. von Bergmann, E. Vedmedenko, and R. Wiesendanger, Nat. Commun. **6**, 8455 (2015).

[57] C. Hanneken, F. Otte, A. Kubetzka, B. Dupé, N. Romming, K. von Bergmann, R. Wiesendanger, and S. Heinze, Nat. Nanotechnol. **10**, 1039 (2015).

[58] A. O. Leonov, T. L. Monchesky, N. Romming, A. Kubetzka, A. N. Bogdanov, and R. Wiesendanger, New J. Phys. **18**, 065003 (2016).

[59] L. Rózsa, E. Simon, K. Palotás, L. Udvardi, and L. Szunyogh, Phys. Rev. B **93**, 024417 (2016).
[60] E. Simon, K. Palotás, L. Rózsa, L. Udvardi, and L. Szunyogh, Phys. Rev. B **90**, 094410 (2014).
[61] E. Y. Vedmedenko, P. Riego, J. A. Arregi, and A. Berger, Phys. Rev. Lett. **122**, 257202 (2019).
[62] D.-S. Han, K. Lee, J.-P. Hanke, Y. Mokrousov, K.-W. Kim, W. Yoo, Y. L. Van Hees, T.-W. Kim, R. Lavrijsen, C.-Y. You *et al.*, Nat. Mater. **18**, 703 (2019).
[63] P. Kurz, F. Förster, L. Nordström, G. Bihlmayer, and S. Blügel, Phys. Rev. B **69**, 024415 (2004).
[64] M. Heide, G. Bihlmayer, and S. Blügel, Phys. B: Condens. Matter **404**, 2678 (2009).
[65] B. Zimmermann, M. Heide, G. Bihlmayer, and S. Blügel, Phys. Rev. B **90**, 115427 (2014).
[66] P. F. Bessarab, V. M. Uzdin, and H. Jónsson, Phys. Rev. B **85**, 184409 (2012).
[67] F. N. Rybakov, A. B. Borisov, S. Blügel, and N. S. Kiselev, Phys. Rev. Lett. **115**, 117201 (2015).
[68] S. von Malottki, Ph.D. thesis, Christian-Albrechts-Universität zu Kiel, 2021.
[69] A. Varentsova, M. N. Potkina, S. von Malottki, S. Heinze, and P. Bessarab, Nanosystems: Phys. Chem. Math. **9**, 356 (2018).
[70] See Supplemental Material at http://link.aps.org/supplemental/10.1103/PhysRevB.105.014414 for movies visualizing the application of mode following technique for the layer-aligning mode.

# Paper II

**Identification of mechanisms of magnetic transitions using an efficient method for converging on first-order saddle points**

H. Schrautzer, M. Sallermann, P.F. Bessarab, H. Jónsson

Physical Review B **112**, 104433 (2025)



Hendrik developed the method together with M. Sallermann, implemented and tested the method, performed the simulations and prepared the figures and wrote the article together with all authors.

# Identification of mechanisms of magnetic transitions using an efficient method for converging on first-order saddle points

Hendrik Schrautzer,[1,*] Moritz Sallermann,[1,2,3,*] Pavel F. Bessarab,[1,4,†] and Hannes Jónsson[1]

[1]*Science Institute and Faculty of Physical Sciences, University of Iceland, VR-III, 107 Reykjavík, Iceland*

[2]*Peter Grünberg Institut and Institute for Advanced Simulation, Forschungszentrum Jülich and JARA, 52425 Jülich, Germany*

[3]*Department of Physics, RWTH Aachen University, 52056 Aachen, Germany*

[4]*Department of Physics and Electrical Engineering, Linnaeus University, SE-39231 Kalmar, Sweden*

(Received 23 December 2024; revised 1 July 2025; accepted 22 August 2025; published 24 September 2025)

An efficient and scalable implementation of a method for locating first-order saddle points on the energy surface of a magnetic system is presented, along with several applications in which the mechanisms of various magnetic transitions are identified. The starting point for the iterative search algorithm can be anywhere, even close to a local energy minimum representing an initial state of the system, and the final state need not be specified. Convergence on a saddle point is obtained by inverting the component of the gradient along the minimum mode, thereby effectively transforming the neighborhood of the saddle point to that of a local minimum. The method requires only the lowest two eigenvalues and corresponding eigenvectors of the Hessian of the system's energy and they are found using a quasi-Newton limited-memory Broyden-Fletcher-Goldfarb-Shanno solver for the minimization of the Rayleigh quotient without explicit evaluation of the Hessian. The method is applicable to large systems, as it does not introduce additional scaling overhead to the computational complexity determined by the interactions present in the system. Applications are presented to transitions in systems that reveal significant complexity of coexisting magnetic states, such as skyrmions, skyrmion bags, skyrmion tubes, chiral bobbers, and globules. The identification of new metastable three-dimensional (3D) textures, such as magnetic bobbers with extended equilibrium distance between the base and the terminating Bloch point, and magnetic globules appearing as isolated states in 3D due to magnetostatic interactions, demonstrates the usefulness of the method for the characterization of complex energy surfaces of magnetic systems. When combined with rate theory within the harmonic approximation, the method can be used for simulations of the long timescale dynamics of complex magnetic systems characterized by multiple metastable states.

DOI: 10.1103/z673-hhnp

## I. INTRODUCTION

The task of identifying the mechanism of possible transitions and estimating the corresponding rate within harmonic transition state theory (HTST) [1,2] or Kramers/Langer theory [3,4] involves finding low-lying first-order saddle points (SPs) on the energy surface that specifies how the energy of the system varies as a function of the various degrees of freedom. A first-order SP is an extremal point, i.e., of zero gradient, where one and only one eigenvalue of the Hessian of the energy of the system is negative. It is challenging to locate an SP because of the need to maximize the energy with respect to one degree of freedom while it is minimized with respect to all others, as it is not known *a priori* which degree of freedom to treat separately [5]. If, in addition to the initial state, the final state of the transition is known, the minimum energy path (MEP) between the two corresponding minima on the energy surface can be found [6,7], and the relevant SP located as the point of highest energy along the path. However, various applications, such as a simulation of long timescale dynamics using the adaptive kinetic Monte Carlo algorithm [8,9], necessitate the identification of likely transitions without any prior assumptions about final states. This is a more challenging task than the calculation of a minimum energy path for given initial and final states and can lead to the discovery of transition mechanisms into unexpected final states. SP searches can also be used as the basis for global optimization of an objective function in a broader context [10], as well as for path optimization [11], e.g., in calculations of tunneling within instanton theory [12,13] and radio wave propagation [14]. An efficient algorithm for locating SPs can, therefore, have wide applicability.

The development of SP search methods that do not require knowledge of the final state has, primarily, been in the context of atomic rearrangements, such as diffusion and chemical reactions [15]. There, an SP search typically starts near the local energy minimum representing an initial state of the system and is carried out in two stages. First, the system is

*These authors contributed equally to this work.
†Contact author: pavel.bessarab@lnu.se

driven out of the convex region where all eigenvalues of the Hessian of the energy are positive. Second, after the lowest eigenvalue turns negative, an algorithm for converging on the nearest SP is used. The first phase can be done in several different ways. In eigenvector following methods that are often used in studies of atomic rearrangements in small systems, the Hessian is evaluated and the eigenvalue problem solved to determine the eigenvectors. Various search paths are then generated starting from the minimum by following each one of the eigenvectors uphill until the convex region has been exited [15]. A more efficient approach, especially for large systems, is to generate several starting points by displacing the system in some random way from the minimum and then moving uphill along the eigenvector corresponding to the lowest eigenvalue, the so-called minimum mode, until the lowest eigenvalue turns negative [16]. Alternatively, the system can be pushed further along the direction defined by the difference between the starting configuration and the minimum while the energy is minimized in orthogonal directions [17]. Several ways have been introduced for generating the starting configurations, for example, Gaussian distributed displacements of the atoms from the minimum in some subregion of the system [18] or evenly distributed points on the surface of a hypersphere with radius pushed out to the edge of the convex region [19].

In the second stage, after escaping the convex region, the force acting on the atoms, i.e., the negative gradient of the energy with respect to atom coordinates, is modified by inverting the component along the minimum mode and the atoms displaced so as to zero this modified force. This ensures energy maximization along only the minimum mode and minimization along all other directions. Such a path eventually convergences on an SP. This technique is referred to as minimum mode following (MMF) method. Thus, the search path is guided by the uphill direction of the minimum mode, while the energy is minimized with respect to all perpendicular directions. The minimum mode can be found by using, for example, the dimer [16], Lanczos [17,20], or Davidson [19,21] methods without even evaluating the Hessian matrix.

Since the starting point of an SP search can be anywhere on the energy surface, MMF can also be used to converge on an SP starting from an approximate estimate, coming, for example, from a partially converged nudged elastic band calculation [6]. Such a combination of an MEP finding method that is only partially converged followed by an SP search method starting from the point of highest energy along the obtained path, provides the most efficient way of converging on an SP corresponding to a transition to a given final state [12].

The rate of magnetic transitions, i.e., transitions where magnetic moments rotate, can in a similar manner be estimated by identifying SPs on the energy surface of a magnetic system [22–24]. When both initial and final states are specified, the minimum energy path can be found using the geodesic nudged elastic band method (GNEB) or the climbing image version CI-GNEB, where the highest-energy image is pushed up to the maximum along the path [7]. This method has been used, for example, to study the collapse of localized magnetic structures such as skyrmions [25–32] as well as textures beyond skyrmions [33–36] including three-dimensional (3D) states such as hopfions or skyrmion tubes [37–42].

When investigating transitions between topological magnetic textures using the GNEB method, generating appropriate initial paths can be challenging and often requires intuition. For example, a linear interpolation between the initial and final states is often not sufficient for the identification of transitions involving translations of a magnetic texture.

Similarly to atomic rearrangements, the search for SPs without specifying a final state or generating an initial path can be carried out for magnetic transitions. There, however, the curvature of the configuration space poses additional challenges as compared to the atomic rearrangements. The convergence on an SP involves rotating the magnetic moments using the force modified by an inversion along the minimum mode and projected onto the local tangent space of the current configuration. We refer to this as the geodesic minimum mode following (GMMF) method.

Analogous to the MMF method for atomic rearrangements, the GMMF method can be used to identify possible magnetic transitions from a given initial state without specifying a final state, thereby possibly discovering new and unexpected mechanisms and final states. Also, analogous to the atomic rearrangements, GMMF can be used in combination with a GNEB calculation that is not carried to completion, so as to converge on an SP corresponding to a transition to a known final state. The method can, furthermore, be generalized to find higher-order saddle points, and this has been shown to be an efficient way to calculate excited electronic states [43].

A straightforward implementation of the GMMF method would involve the evaluation of the Hessian and calculation of at least the lowest eigenvalue and corresponding eigenvector, as was done by Müller *et al.* [44]. However, the computational effort then increases rapidly with system size. The number of magnetic moments in relevant model systems can be large, often on the order of $10^5$ to $10^7$. Henceforth, even the mere evaluation of the full Hessian can require substantial effort. In particular, the explicit inclusion of long-range magnetostatic effects, as is frequently necessary in large three-dimensional systems, may not be feasible with such an approach. The reason is that the Hessian matrix then becomes dense and storing it can exceed the working memory capacity of a typical compute node, even for systems of moderate size. In addition, models that go beyond a simple Heisenberg approach, such as the noncollinear extension of the Alexander-Anderson model [45,46] and density functional theory calculations, make the computation of second-order derivatives a significant task.

After the introduction of the GMMF method by Müller *et al.* [44], it has been successfully used to identify mechanisms of magnetic transitions in several systems including the duplication of magnetic skyrmions [44], transformation of defects in skyrmion lattices [47], annihilation of three-dimensional hopfions [41], and transitions in a two-dimensional dipolar spin glass [47]. However, previous implementations of GMMF have been less than optimal in several respects, in that the full Hessian is explicitly evaluated and this limits the applicability of the method to rather small systems. Since the GMMF method strictly requires only the eigenvector corresponding to the lowest eigenvalue of the Hessian, the evaluation of the full Hessian is, in fact, not

needed. A more efficient implementation of GMMF is, therefore, possible and is described in detail in this article.

We report, in particular, an efficient way of computing the modified force in the GMMF method, using an iterative approach that does not require the evaluation of the Hessian. It is, thereby, applicable to large systems and more complex Hamiltonians than the Heisenberg form. Knowledge of the second lowest eigenvalue can also be useful to guide GMMF calculations, especially at mode crossings, as will be demonstrated below, and the method presented here is noteworthy in that the lowest two eigenvalues and corresponding eigenvectors are found simultaneously, using the generalized Rayleigh quotient and an L-BFGS optimizer on the Grassmann manifold.

The article is organized as follows. The method is described in Sec. II. This is followed by Sec. III, where the application systems are described. Results of several GMMF calculations are presented Sec. IV featuring various magnetic structures in two- and three-dimensional systems and the performance is compared to that of a partial eigenvalue calculation with the Intel Math Kernel Library [48]. The final section summarizes the main findings and discusses their implications. Six Appendices provide additional details: (A) description of the four-spin system used to illustrate mode crossings; (B) pseudocode for the Rayleigh quotient optimization; (C) full Hessian expressions for reference; (D) summary of numerical parameters used in the calculations; (E) results for a 3D system without magnetostatics; and (F) analysis of the method's scaling behavior.

## II. METHOD

One important aspect of the GMMF method is the correct consideration of the configuration space $\mathcal{R}$ of magnetic systems which is a Riemannian manifold. Typically, the magnitude of the magnetic vectors is either assumed to be independent of orientation or treated as a fast variable within the adiabatic approximation. In the latter case, the magnitude is calculated for fixed orientations of the magnetic moments, which are considered to be slow variables [49]. In either case, the configuration space of a system with $N$ magnetic moments is a direct product of two-dimensional spheres $S_2$ associated with each magnetic moment vector:

$$\mathcal{R} = \bigotimes_N S_2 \subset \mathbb{R}^{3N}, \tag{1}$$

giving rise to $2N$ degrees of freedom. Displacements in the configuration space correspond to rotations of the magnetic moments. It is computationally advantageous to work in the embedding space $\mathbb{R}^{3N}$ and to eliminate the $N$ superfluous degrees of freedom by applying the projection operator approach [44,47,50,51].

The iterative optimization procedure used in the SP search typically starts near a local energy minimum representing the initial state of the magnetic system. The climb up to the SP involves two stages: (i) Escape from the convex region around the minimum, and (ii) convergence on a first-order SP using the GMMF technique. This two-stage procedure is to be repeated multiple times so as to identify, with some degree of confidence, all relevant SPs surrounding the given energy minimum. Convergence on various SPs is achieved by generating several different starting points near the energy minimum and/or by following different scenarios in the escape stage. For example, the convex region can be escaped by displacing the system from the initial state minimum along various eigenmodes of the system [44]. However, following the eigenmodes in the escape stage is not a requirement, as other strategies may also be used. In studies of atomic rearrangements, a method based on even distribution of points on a hypersphere in the configuration space has been used to sample different directions away from the initial state minimum [19,52,53]. Clearly, the choice of the escape strategy affects the efficiency of the method in finding as many distinct SPs as possible while keeping the number of the SP searches to a minimum. Choosing the optimal escape strategy is an important task which, however, goes beyond the scope of this study.

At a certain point during the escape stage, the minimum eigenvalue of the Hessian becomes negative, indicating that a basin of attraction for an SP [16] has been reached and that the convergence stage can be started. An efficient implementation of the GMMF method, used in the SP convergence stage, is the focus of this study. The steps involved in the GMMF calculations are summarized in the flowchart in Fig. 1(a).

In contrast to the escape stage, which can be organized in many different ways, the strategy for advancing the system during the convergence stage once the system is outside the convex region is more straightforward. The corresponding rotations of the magnetic moments are guided by a modified magnetic force designed so as to carry out a maximization of the energy along a certain direction, the inversion mode, and minimization along all orthogonal directions. Near an SP, the inversion mode necessarily is the minimum mode, i.e., the eigenvector of the Hessian corresponding to the lowest eigenvalue. However, near the boundary of the convex region, it can be advantageous to choose the inversion mode to be the Hessian's eigenvector corresponding to the second lowest eigenvalue or even higher eigenvalue. Such a formulation eventually results in a convergence on a first-order SP rather than a minimum. Specifically, the GMMF force on the $i$th magnetic moment in the system is defined as

$$\vec{f}_i = \vec{b}_i - (\vec{b}_i \cdot \vec{s}_i)\vec{s}_i, \tag{2}$$

where $\vec{s}_i$ is the unit vector in the direction of the $i$th magnetic moment and $\vec{b}_i$ is the effective field whose component along the inversion mode is reversed. The modified effective field $\vec{b}_i$ is defined by the following equation:

$$\vec{b}_i = -\vec{\nabla}_i E + 2(\nabla E \cdot \boldsymbol{q})\vec{q}_i. \tag{3}$$

Here, $E = E(\boldsymbol{s})$ is the energy as a function of the magnetic configuration defined by vector $\boldsymbol{s} = (\vec{s}_1, \vec{s}_2, \ldots, \vec{s}_N)$, $\boldsymbol{q} = (\vec{q}_1, \vec{q}_2, \ldots, \vec{q}_N)$ is the unit vector representing the inversion mode, and $\boldsymbol{\nabla} = (\vec{\nabla}_1, \vec{\nabla}_2, \ldots, \vec{\nabla}_N)$, with $\vec{\nabla}_i \equiv \partial/\partial\vec{s}_i$. By construction, the GMMF force $\boldsymbol{f} = (\vec{f}_1, \vec{f}_2, \ldots, \vec{f}_N)$ is orthogonal to the magnetic moments, i.e., lies in the tangent space of $\mathcal{R}$ for a given magnetic configuration $\boldsymbol{s}$: $\boldsymbol{f} \in T_{\boldsymbol{s}}$ (see Fig. 2 for an illustration of the tangent space for a single magnetic moment).

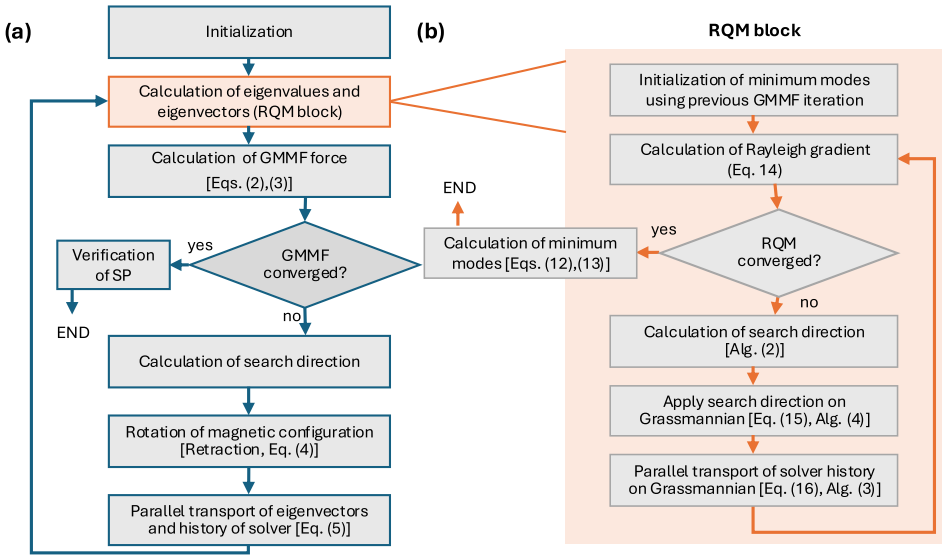


FIG. 1. Flowchart for the algorithm of the GMMF method (a) and for the Rayleigh quotient minimization (RQM) eigensolver method (b) as presented in Sec. II. In each GMMF iteration, the RQM block is executed to calculate the eigenvalues and eigenvectors of the Hessian for the current magnetic configuration. The pseudocode for the algorithms describing the RQM method is given in Appendix B.

The inversion along the minimum mode makes the effective field correspond to the neighborhood of a minimum of $E(\boldsymbol{s})$ rather than that of an SP. This is the basic idea of the method: a transformation of the problem of locating a first-order SP into the much simpler task of gradient-based minimization. In particular, the GMMF force is used to guide an iterative advancement of the magnetic structure toward an SP using some numerical optimization method, preferably one that accounts for the curvature of the configuration space $\mathcal{R}$ via retraction and parallel transport [54]. The concepts of retraction (movement on a manifold in a certain direction without leaving the manifold) and parallel transport (translation of geometrical data on a manifold) are implemented

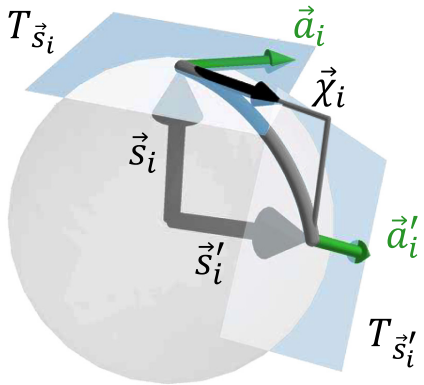


FIG. 2. Visualization of rotating a single magnetic moment $\vec{s}_i$ in the direction $\vec{\chi}_i \in T_{\vec{s}_i}$ (retraction). Also, the parallel transport of an exemplary vector $\vec{a}_i \in T_{\vec{s}_i}$ (green) towards the tangent space of the retracted magnetic moment $T_{\vec{s}'_i}$ is shown.

for magnetic systems via rotations and illustrated for a single magnetic moment in Fig. 2. Specifically, retracting a magnetic moment $\vec{s}_i$ in the direction $\vec{\chi}_i \in T_{\vec{s}_i}$, with $T_{\vec{s}_i}$ being the corresponding tangent space, to the updated position $\vec{s}_i'$ characterized by the tangent space $T_{\vec{s}_i'}$, as well as the parallel transport of a vector $\vec{a}_i$ (e.g., the gradient or search direction from previous iterations in optimization methods with memory) from $T_{\vec{s}_i}$ to $T_{\vec{s}_i'}$ can be computed using

$$\vec{s}_i' = D_{\vec{\chi}_i}(\varphi)\vec{s}_i, \tag{4}$$

$$\vec{a}_i' = D_{\vec{\chi}_i}(\varphi)\vec{a}_i. \tag{5}$$

Here, the $3\times3$ rotation matrix $D_{\vec{\chi}_i}(\varphi)$ is given by the Rodriguez rotation formula

$$D_{\vec{\chi}_i}(\varphi) = I + \sin\varphi_i K_{\vec{\chi}_i} + (1-\cos\varphi_i)K^2_{\vec{\chi}_i}, \tag{6}$$

where $I$ is a $3\times3$ identity matrix and $\varphi_i = \varphi|\vec{\chi}_i|$ is the angle between $\vec{s}_i'$ and $\vec{s}_i$. The matrix $K_{\vec{\chi}_i}$ is given by

$$K_{\vec{\chi}_i} = \begin{pmatrix} 0 & -k_i^z & k_i^y \\ k_i^z & 0 & -k_i^x \\ -k_i^y & k_i^x & 0 \end{pmatrix}, \tag{7}$$

with $k_i^x, k_i^y, k_i^z$ being the Cartesian components of the rotation axis $\vec{k}_i$:

$$\vec{k}_i = \vec{s}_i \times \frac{\vec{\chi}_i}{|\vec{\chi}_i|}. \tag{8}$$

The retraction and parallel transport on the configuration space $\mathcal{R}$ can be described by the direct sum of the $3\times3$

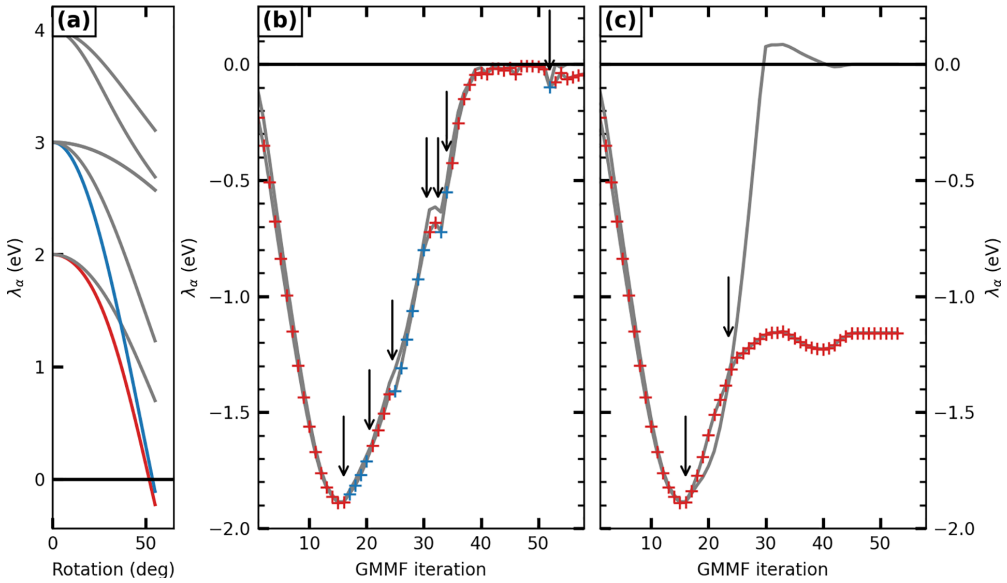


FIG. 3. SP search applied to the system of four magnetic moments described in Appendix A. (a) The lowest eigenvalues of the Hessian as functions of the angle of rotation of two moments with respect to the initial parallel-aligned state during the escape stage. The red and blue curves correspond to the modes that experience mode crossings during the convergence stage. The maximum rotation angle corresponds to the starting configuration used in the GMMF calculation during the convergence stage. The lowest eigenvalues are nearly equal at the maximum rotation angle. (b), (c) Evolution of the two lowest eigenvalues during the GMMF calculation, following two different strategies. The mode-crossing events are marked with black arrows. The color of the crosses codes the inversion mode. In (b), the inversion mode is always chosen to be the minimum mode. In (c), the definition of the inversion mode changes when a mode crossing occurs. In particular, the inversion mode corresponds to the Hessian's eigenvector associated with the second lowest eigenvalue between the mode-crossing events.

rotation matrices for the individual magnetic moments:

$$\mathcal{D}_{\boldsymbol{\chi}}(\varphi) = \begin{pmatrix} D_{\vec{\chi}_1}(\varphi) & 0 & \dots & 0 \\ 0 & D_{\vec{\chi}_2}(\varphi) & \dots & 0 \\ \vdots & \vdots & \ddots & \vdots \\ 0 & 0 & \dots & D_{\vec{\chi}_N}(\varphi) \end{pmatrix}. \quad (9)$$

While many different optimization algorithms can be used, we employ here a limited-memory Broyden-Fletcher-Goldfarb-Shanno (L-BFGS) solver [55] adapted to magnetic systems [56]. Typically, the calculation is considered to be converged when the magnitude of the GMMF force has dropped below some threshold value [see Fig. 1(a)]. After that, the candidate SP is verified by ensuring that one and only one eigenvalue of the Hessian is negative. Occasionally, following the GMMF force can lead back into the convex region around a minimum. This happens if the inversion mode becomes nearly orthogonal to the energy gradient. In this case, the GMMF optimization is essentially just an energy minimization with a displacement along the negative energy gradient. Such reentrance into the convex region can be detected when the lowest eigenvalue of the Hessian becomes positive, indicating the need to restart the SP search.

Calculating the GMMF force involves reversing the component of the effective field along the inversion mode. Typically, and always towards the end of the convergence stage, the inversion along the minimum mode is carried out. However, during GMMF optimization, a crossing of the two lowest eigenvalues and corresponding modes may occur. Such a situation is depicted in Fig. 3. The corresponding calculations were performed for a system with four magnetic moments described in Appendix A. In such a case, the use of only the minimum mode for the inversion at each iteration step leads to an abrupt change in the GMMF force. Most of the times, this does not cause problems and the method converges on an SP after the mode-crossing event. However, there are some situations where the two lowest modes are close to being degenerate and yet describe completely different changes in the magnetic structure. Then the use of only the minimum mode for the inversion may lead to repetitive mode-crossing events [see Fig. 3(b)]. In this case, the consistency between iteration steps is lost due to multiple abrupt changes in the GMMF force, preventing the optimization procedure from converging. By selecting the eigenvector corresponding to the second-lowest eigenvalue as the direction of inversion for several iterations after the mode-crossing event can help prevent this unwanted behavior [see Fig. 3(c)]. Inversion along several different modes can also increase the likelihood of identifying distinct SPs. It is, therefore, useful to calculate the two lowest modes, not just the minimum mode. Furthermore, it is necessary to calculate the second lowest eigenvalue in order to verify that the candidate SP is of first order, i.e., only the lowest eigenvalue of the Hessian is negative.

The evaluation of the Hessian eigenvectors corresponding to the two lowest eigenvalues needs to be carried out efficiently as it tends to be a computational bottleneck of

the GMMF method. Commonly used algorithms for finding the lowest few eigenvalues and corresponding eigenvectors include the Lanczos method [20] and extensions thereof, such as the Davidson method [21] and other even more sophisticated Krylov subspace algorithms [57]. In this work, we present an alternative approach where the lowest eigenpairs of the Hessian are obtained via the direct minimization of the generalized Rayleigh quotient. The high efficiency of the method is achieved by avoiding the evaluation of the full Hessian explicitly and by using the L-BFGS solver, adapted to account for the curvature of the Grassmann manifold on which the objective function is defined. A detailed description of the method is provided in the following subsections and the corresponding pseudocode presented in Appendix B.

### A. Calculation of the two lowest modes using generalized Rayleigh quotient minimization

The two lowest modes, i.e., the eigenvectors corresponding to the two lowest eigenvalues of the Hessian, can be identified using the following Rayleigh quotient:

$$R(X) = \mathrm{tr}(X^T H X), \tag{10}$$

where $H$ is the $2N\times 2N$ Hessian matrix and $X$ is a $2N\times 2$ matrix whose columns are orthonormal vectors parametrizing all possible two-dimensional subspaces of the local tangent space of $\mathcal{R}$. The subspace containing the two lowest modes is spanned by the columns of $X_{\mathrm{min}}$ corresponding to a minimum of $R(X)$ [50]:

$$X_{\mathrm{min}} : R(X_{\mathrm{min}}) \rightarrow \mathrm{min}\,. \tag{11}$$

The representation of the two lowest modes $\boldsymbol{v}_\alpha$, $\alpha = 1, 2$, in the embedding $3N$-dimensional Euclidean space can be obtained from $X_{\mathrm{min}}$ using

$$\boldsymbol{v}_\alpha = U X_{\mathrm{min}} \tilde{\boldsymbol{v}}_\alpha, \tag{12}$$

where $U$ is the projector onto the local tangent space of $\mathcal{R}$ and $\tilde{\boldsymbol{v}}_\alpha$ are the eigenvectors of the following $2\times 2$ eigenvalue problem:

$$\left(X_{\mathrm{min}}^T H X_{\mathrm{min}}\right)\tilde{\boldsymbol{v}}_\alpha = \lambda_\alpha \tilde{\boldsymbol{v}}_\alpha, \quad \alpha \in \{1, 2\}. \tag{13}$$

The Rayleigh quotient minimization (RQM) needs to be performed at every iteration of the GMMF procedure. To achieve this, we have implemented an efficient method based on the L-BFGS solver equipped with the gradient of $R(X)$ on the Grassmann manifold [50]:

$$\nabla R(X) = 2[HX - X(X^T H X)]. \tag{14}$$

The pseudocode for the GMMF/RQM algorithm is presented in Appendix B. The RQM calculations are highly efficient and typically converge to $X_{\mathrm{min}}$ in just a few L-BFGS iterations, especially when the initial guess for $X_{\mathrm{min}}$ is taken from the solution of a previous GMMF iteration. In Sec. IV A, the performance of the GMMF/RQM approach is compared with that of an implementation of GMMF equipped with a state of the art extremal eigensolver based on a Krylov-Schur (KS) [58] method as implemented in the Intel Math Kernel Library [48] (GMMF/KS).

It is important to realize that the domain of $R(X)$ represents a curved, Grassmann manifold $G_{2N,2}$. Therefore, an efficient RQM requires implementation of retraction and parallel transport that adhere to the geometric constraints of $G_{2N,2}$. Given a search direction $\Lambda$ for the current iteration $X$, the retraction to the next iteration $X'$ on $G_{2N,2}$ must ensure orthonormality of the columns of $X'$. Here, we make use of the exponential map, which is a special kind of retraction following geodesics. On the Grassmann manifold, the action of the exponential map can be found by the compact singular value decomposition $\Lambda = P\Sigma V^T$ of the tangent vector $\Lambda$ [50] (see Appendix B, Algorithm 4):

$$X' = XV\,\cos(\Sigma)V^T + P\,\sin(\Sigma)V^T. \tag{15}$$

The L-BFGS algorithm that we use for finding $X_{\mathrm{min}}$ approximates the second derivative of the Rayleigh quotient and combines information of the gradients and the search directions from the past few iterations. These history vectors are anchored in the tangent spaces of their point of calculation on the curved manifold. Thus, in each iteration of the RQM a history vector $A$ has to be transported from the tangent space of $X$ to the tangent space of $X'$ using $A' = TA$ with [50]

$$T = (XV \quad P)\begin{pmatrix} -\sin\Sigma \\ \cos\Sigma \end{pmatrix} P^T + (I - PP^T), \tag{16}$$

where $I$ is the $2N\times 2N$ identity matrix. A computationally efficient multiplication with this parallel transport matrix is given in Appendix B, Algorithm 3.

Finally, the global minimum of the Rayleigh quotient is given by $X_{\mathrm{min}}$ which spans the same subspace as the sought-for two eigenvectors of the Hessian. Note that all $2N\times 2$ matrices whose orthonormal columns span the same subspace represent the same point on $G_{2N,2}$. Thus, the eigenvectors corresponding to the two lowest eigenvalues of the Hessian are linear combinations of the columns of $X_{\mathrm{min}}$, and are determined by solving Eq. (13).

A method for computing the Hessian for magnetic systems is described in Refs. [44,51] and is also summarized in Appendix C. Explicit evaluation of the Hessian is feasible for systems of moderate size and/or systems with only short-range interactions as the Hessian matrix then becomes sparse. The explicit Hessian is used in the KS implementation of the GMMF method.

The evaluation of the gradient of the Rayleigh quotient does not, however, require the explicit evaluation of the Hessian; only its action on $X$ is needed [see Eq. (14)]. The action of the Hessian on $X$ can be obtained through separate matrix-vector multiplications. These can be calculated using a finite-difference scheme for the energy gradient, as described in the following subsection. This approach avoids the explicit evaluation of the Hessian, providing a significant speedup in the GMMF calculations.

### B. Action of the Hessian matrix

Calculation of the matrix-vector multiplication $H\boldsymbol{x}$, where $\boldsymbol{x}$ is a column of $X$, is needed for the gradient-based minimization of the Rayleigh quotient [see Eq. (14) for $\nabla R(X)$]. It can be performed without the explicit evaluation of the Hessian $H$ using a finite-difference scheme for the energy gradient. In such a scheme, one needs to take into account the curvature of the configuration space. In particular, energy

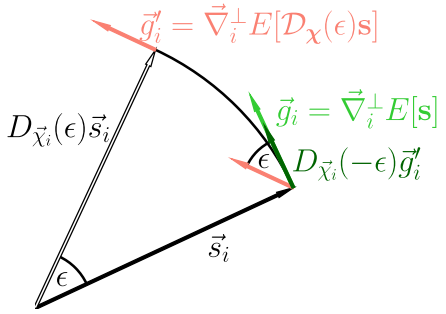


FIG. 4. Illustration of the quantities involved in calculating the action of the Hessian by forward finite-difference approximation with a displacement parameter $\epsilon$ for a single magnetic moment $\vec{s}_i$. To calculate the finite difference of the gradient $\vec{g}_i$ along a given direction, the magnetic moment is first retracted (rotated) along this direction and the gradient $\vec{g}_i'$ is calculated for the rotated magnetic moment $D_{\vec{\chi}_i}(\epsilon)\vec{s}_i$. Parallel transport $[D_{\vec{\chi}_i}(-\epsilon)\vec{g}_i']$ is then applied towards the tangent space of the initial magnetic moment $\vec{s}_i$ to ensure that both gradients are defined within the same tangent space for the calculation of the finite difference.

gradients for retracted magnetic configurations must be parallel transported to the location of the current magnetic configuration so as to be anchored in the same tangent space (see Fig. 4). The retraction and parallel transport are implemented through rotations [see Eqs. (4) and (5)] in the direction of $\boldsymbol{x}$, which can be expressed in terms of the vector $\boldsymbol{\chi}$ in the embedding $3N$-dimensional Euclidean space, thereby avoiding basis changes:

$$\boldsymbol{\chi} = U\boldsymbol{x}. \tag{17}$$

The forward finite-difference scheme for computing $H\boldsymbol{x}$ is used:

$$H\boldsymbol{x} \approx U^T \frac{\mathcal{D}_{\boldsymbol{\chi}}(-\epsilon)\nabla^{\perp}E[\mathcal{D}_{\boldsymbol{\chi}}(\epsilon)\boldsymbol{s}] - \nabla^{\perp}E[\boldsymbol{s}]}{\epsilon}. \tag{18}$$

Here, $\nabla^{\perp} = (\vec{\nabla}_1^{\perp}, \ldots, \vec{\nabla}_N^{\perp})$, with $\vec{\nabla}_i^{\perp} = \vec{\nabla}_i - \vec{s}_i(\vec{s}_i \cdot \vec{\nabla}_i)$, $\epsilon > 0$ is the displacement parameter, and projector $U^T$ yields the $2N$-dimensional representation of the action of the Hessian matrix as required in the context of the RQM algorithm. Note that the angle of rotation is not uniform across the entire system. Instead, it is defined individually for each magnetic moment based on the components of $\boldsymbol{\chi}$ [see Eqs. (6)–(9)]. The optimal value of the displacement parameter $\epsilon$ yielding the minimum error of the finite difference was determined using the Richardson extrapolation scheme [59–61] with the initial $\epsilon$ value of $10^{-6}$. If necessary, the finite-difference scheme can be extended to incorporate additional stencil points. However, this increases computational cost, as each additional point requires extra parallel transport and retraction operations. We find that the forward (or, equivalently, backward) finite-difference scheme, in which these operations are performed only once, combined with Richardson extrapolation, provides a good balance between accuracy and computational efficiency of the RQM calculations.

### C. Further analysis

The GMMF/RQM method offers various synergies with other approaches, as listed below. On the one hand, it is straightforward to generate the MEP once a first-order SP and the corresponding unstable mode have been determined. To achieve this, a steepest descent path is generated from the SP on both sides toward the stable states. During the minimization, the cumulative geodesic distance can be used to control how many points are generated to provide a good discrete representation of the MEP, similar to the path that would be obtained by the GNEB method if both initial and final state minima were known beforehand.

On the other hand, the highest-energy image of a partially converged GNEB calculation can be used as a starting point for a GMMF calculation. In this way, the fast convergence of the GMMF method on a first-order SP is used instead of the larger computational effort of converging all images in a GNEB simulation.

Once an SP has been found, the preexponential factor in the rate constant for the corresponding transition can be obtained within the harmonic transition state theory (HTST) approximation [23]. By identifying all relevant, low-energy SPs connecting to a given initial state, a Monte Carlo procedure can be used to select which transition will occur next in a long timescale evolution of the system, as has been done for atomic systems in the adaptive kinetic Monte Carlo method [8] where the system recursively traverses from one energy minimum to another *via* the identified SPs. Such a long timescale simulation at a finite temperature, combined with systematic coarse graining of the energy landscape [62,63], can be the basis for simulated annealing search for the global energy minimum representing the most stable state of the system.

## III. MODEL

The GMMF/RQM method described in Sec. II can be applied to any system where the energy depends on the orientation of magnetic moments $\boldsymbol{s}$, such as atomistic spin models [64]. One example is the extended Heisenberg model which has been extensively used to describe various topological spin textures such as magnetic skyrmions and other even more complicated magnetic states [35,65], including those containing Bloch points [37,38,66].

To demonstrate the GMMF/RQM method, we use the following Hamiltonian on square (see Sec. IV A) and cubic lattice (see Sec. IV B, Appendix E) models:

$$\begin{aligned} E = &-J\sum_{i,j}\vec{s}_i\cdot\vec{s}_j - D\sum_{i,j}\hat{d}_{ij}\cdot(\vec{s}_i\times\vec{s}_j) \\ &- \mu\sum_i \vec{B}\cdot\vec{s}_i + \eta E_{\mathrm{mag}}. \end{aligned} \tag{19}$$

Nearest-neighbor exchange ($J$) is included as well as nearest-neighbor Bloch-type Dzyaloshinskii-Moriya interaction (DMI) ($D$), with the unit DMI vector $\hat{d}_{ij}$ oriented along the connection line of the interacting magnetic moments $i$ and $j$. The magnitude of the magnetic moments is set to $\mu = 1\,\mu_B$, with $\mu_B$ being the Bohr magneton. An external magnetic field $\vec{B}$ is applied in the $z$ direction. The last term in Eq. (19)

TABLE I. Parameters of the extended Heisenberg model [Eq. (19)] used in the calculations. The size refers to the number of magnetic moments in the $x$, $y$, and $z$ directions, respectively. For the first application, a range in parameter values was explored. The magnetic moment is $\mu = 1\mu_B$ and the exchange parameter is $J = 1$ meV for all calculations. The explicit calculation of magnetostatics using a lattice constant of 3 Å is controlled by the parameter $\eta$ in Eq. (19). The 3D system employs periodic boundary conditions along the $x$ and $y$ directions and open boundaries in the $z$ direction. For the monolayer system, open boundary conditions are applied along all spatial directions.

| System size | Section | Explicit magnetostatics | $D$ (meV) | $B$ (T) |
|---|---|---|---|---|
| 50×50×1 | IV A | no | 0.2–0.8 | 2.0–5.0 |
| 32×32×32 | IV B | yes | 0.45 | 2.8 |
| 32×32×32 | Appendix E | no | 0.45 | 2.8 |

represents the magnetostatic interaction whose energy $E_{\mathrm{mag}}$ is computed using the fast Fourier transform [67,68]. The parameter $\eta = 0, 1$ is used to either activate ($\eta = 1$) or deactivate ($\eta = 0$) explicit treatment of magnetostatics. The values of all parameters are listed in Table I.

Magnetostatic interaction is not explicitly considered in the monolayer system studied in Sec. IV A, both for consistency with the study by Müller *et al.* [44] and because magnetostatics can effectively be reduced to a local anisotropy in this case [69]. In contrast, magnetostatics is explicitly included in the 3D system analyzed in Sec. IV B. In that case, the values of $J$, $D$, and $B$ are chosen to match those in Ref. [37] and a lattice constant of 3 Å is used. The size of the monolayer system is 50×50×1 magnetic moments, while the 3D system has a size of 32×32×32 moments. The 3D system employs periodic boundary conditions along the $x$ and $y$ directions and open boundary conditions along the $z$ direction. Open boundary conditions are applied along all spatial directions for the monolayer system. For comparison, we also consider in Appendix E a 3D system without magnetostatics, identical to the one studied in Ref. [37].

## IV. RESULTS

### A. Skyrmion collapse mechanisms

In this section, the application of the GMMF method to systems hosting skyrmions is demonstrated. The energy-minimum skyrmion state [see Fig. 5(a)] serves as a starting configuration for the SP searches. For $J = 1$ meV, $D = 0.55$ meV, and $B = 3.1$ T, four distinct SPs corresponding to different skyrmion collapse mechanisms can be identified using the GMMF method:

(1) $\mathrm{SP_{rad}}$ corresponding to a Bloch pointlike configuration [Fig. 6(c)] on the path that connects the skyrmion state with the FM state via radially symmetric shrinking of the skyrmion.

(2) $\mathrm{SP_{esc}}$ characterizing the collapse of the skyrmion via an escape through the boundary of the system [Fig. 6(d)]. The SP configuration is a dropletlike deformed skyrmion attached to the system's boundary.

(3) $\mathrm{SP_{dup}}$ corresponding to the splitting of a single skyrmion into two skyrmions (skyrmion duplication). The SP configuration is an eight-shaped deformed skyrmion [Fig. 6(b)].

(4) $\mathrm{SP_{bag}}$ characterizing the transformation of the skyrmion state into the skyrmion bag state [Fig. 6(a)].

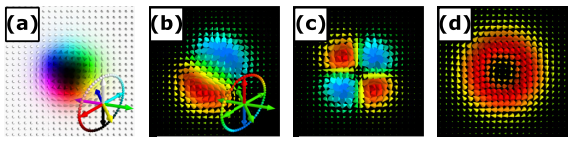


FIG. 5. (a) Skyrmion corresponding to a local energy minimum on a square lattice with $J = 1$ meV, $B = 3.1$ T, and $D = 0.55$ meV [see Eq. (19)]. The inset explains the hue-saturation-lightness color scheme. While the azimuthal angle of the magnetic moments is represented by the hue, the lightness encodes the polar angle of the magnetic moments for a fixed saturation of 1.0. (b)–(d) Vector field representation of the Hessian eigenvectors corresponding to the translation (a), elongation (b), and breathing (c) modes. The color codes the polar angle of the eigenvector components [see inset in (b)].

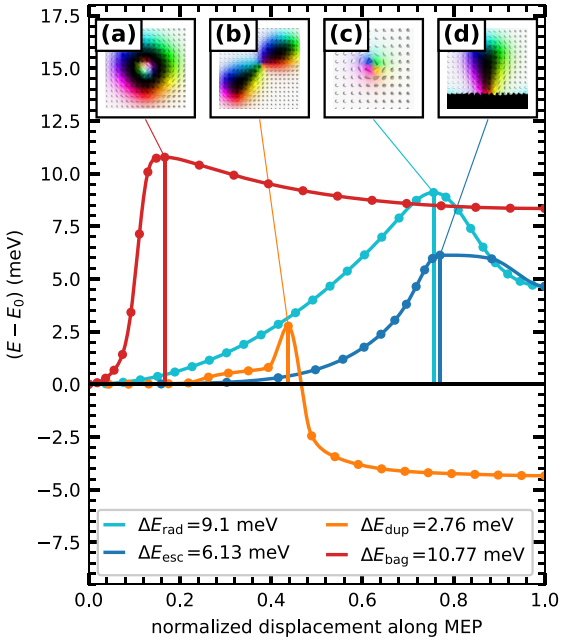


FIG. 6. Energy variation along MEPs for skyrmion collapse, shown relative to the skyrmion energy $E_0$, as obtained by CI-GNEB calculations for the monolayer system with $J = 1$ meV, $B = 3.1$ T and $D = 0.55$ meV [see Eq. (19)]. The initial paths were generated using the SP configurations obtained with the GMMF algorithm (see Sec. II C). The insets show the first-order SP configurations for the transition of the skyrmion into the skyrmion bag (a), the duplication of a skyrmion (b), the radially symmetric skyrmion collapse (c), and the escape of the skyrmion through the system boundary (d). The energy barriers defined as the energy difference between the SP state and the skyrmion state are represented by vertical lines, with their values provided in the legend.

The SP configuration is a skyrmion with strongly canted magnetic moments at the skyrmion center.

Each of these SPs corresponds to the configuration of highest energy of the MEP connecting the skyrmion state with the FM state, the skyrmion bag state, or the state of two skyrmions. The MEPs are shown in Fig. 6. They were obtained from CI-GNEB calculations where an initial path was generated by sliding down the energy surface from the SP on both sides toward the stable states (see Sec. II C). For the selected values of the Hamiltonian parameters, the energy of the ferromagnetic state is higher than the energy of the isolated skyrmion, and the energy of two skyrmions is the lowest.

To locate the four SPs, the convex region of the skyrmion energy minimum is escaped using four different strategies. Each strategy corresponds to a specific deformation of the magnetic configuration, thereby introducing tendencies that reflect the shape of the SP configurations. Three of the four deformations are generated using eigenvectors from the low-curvature part of the skyrmion state's eigenvalue spectrum. In this case, the sparsity of the Hessian and the moderate system size make it feasible to explicitly construct the Hessian matrix and compute the eigenvectors using standard methods. Specifically, we used the Krylov-Schur solver as implemented in the Intel Math Kernel Library [48] to perform the eigenvector computations. The results are shown in Figs. 5(b)–5(d), and the corresponding modes have been discussed in several previous publications [44,51,70–72]. While $SP_{bag}$ should, in principle, be reachable by combining several modes, here a simple rotation of the magnetic moments at the skyrmion center is used instead to generate the appropriate deformation. At the end of the escape stage, a suitable configuration for initiating the subsequent GMMF stage is obtained, characterized not only by at least one negative eigenvalue, but also by the corresponding eigenvector used for inversion with a significant component along the force direction, which reduces the likelihood of the system returning to the convex region. To test the sensitivity of the GMMF method to the choice of the starting point, six such initial configurations $\mathcal{I}_1$–$\mathcal{I}_6$ were selected for each collapse mechanism [see black diamonds in Figs. 7, 8(a), and 9(a)]. These configurations differ in their distance from the convex region around the skyrmion-state minimum, yet all converge to the same SP associated with the respective mechanism, as described below.

Iteratively displacing the skyrmion configuration along the eigenvector of the breathing mode [see Fig. 5(d)] shrinks or expands the skyrmion. Figure 7(a) shows how several of the lowest eigenvalues change as the skyrmion shrinks. At some point, one of the eigenvalues rapidly decreases and turns negative indicating that the convex region around the skyrmion-state minimum has been escaped. A subsequent application of GMMF leads to $SP_{rad}$. A similar displacement along one of the two skyrmion translational modes [see Fig. 5(b)] induces a tendency for the skyrmion escape through the edge of the system. As the skyrmion approaches the edge, the open boundaries lift the degeneracy between the translational modes. The eigenvalue associated with the mode corresponding to motion orthogonal to the one being followed becomes negative earlier. Still, it is appropriate to continue following the initially selected mode to bring the skyrmion

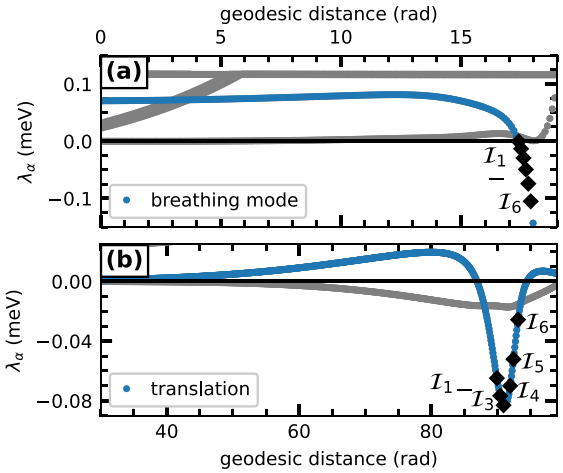


FIG. 7. Evolution of the lowest eigenvalues of the Hessian during iterative displacement along the breathing mode (a) and the translation mode (b) starting from the skyrmion state. The cumulated geodesic distance along this displacement is shown on the $x$ axis. The black diamonds $\mathcal{I}_1$–$\mathcal{I}_6$, corresponding to six different starting configurations for the GMMF method, indicate the eigenvalues associated with the inversion mode. The parameters of the Hamiltonian are $J = 1$ meV, $B = 3.1$ T, and $D = 0.55$ meV.

closer to the edge of the system and steer the magnetic configuration toward $SP_{esc}$. Eventually, this mode becomes the minimum mode [see Fig. 7(b)]. The corresponding configurations mark suitable initial points for finding $SP_{esc}$ using GMMF.

To induce a tendency toward $SP_{dup}$, the escape stage begins by following one of the two skyrmion elongation modes [see Fig. 5(c)]. However, elongation alone is insufficient to produce a suitable starting point for convergence to $SP_{dup}$. Additional local narrowing of the elongated skyrmion is required during the escape stage. This deformation can be induced by switching to a corresponding mode that emerges in the low-curvature part of the spectrum while the elongation mode is being followed. From that point onward [Fig. 8(a)], following the narrowing mode causes the eigenvalue associated with another mode to decrease rapidly, eventually making that mode the minimum mode. Once this occurs, a configuration is selected as the starting point for the GMMF simulation, which then converges to $SP_{dup}$. Note that in this case, the inversion mode does not coincide with any of the modes used during the escape stage.

The escape strategy for $SP_{bag}$ is not based on the displacement along eigenmodes of the skyrmion, which is in contrast to other SPs. Instead, the magnetic moments at the skyrmion center are rotated toward the direction of the applied magnetic field. This is schematically shown in the inset in Fig. 9(a). During this deformation, one of the eigenvalues begins to decrease rapidly and eventually becomes the lowest eigenvalue. At this point, the application of the GMMF method leads to the identification of $SP_{bag}$.

Realization of various additional deformations during the escape stage did not lead to the identification of any further

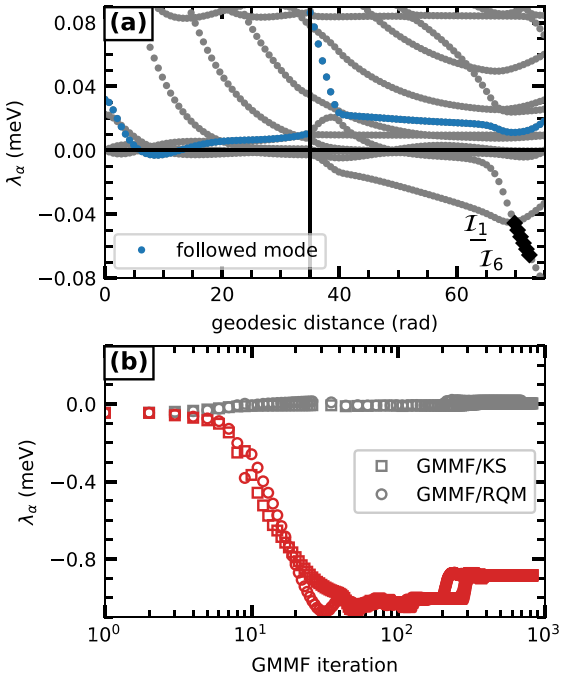


FIG. 8. (a) The evolution of the lowest eigenvalues of the Hessian during the escape stage corresponding to iterative displacement of the system along the skyrmion elongation mode (before the black vertical line) and the mode describing a narrowing of the central part of the elongated skyrmion (after the black vertical line). The black diamonds $\mathcal{I}_1$–$\mathcal{I}_6$, corresponding to six different starting configurations for the GMMF method, indicate the eigenvalues associated with the inversion mode. (b) The evolution of the two lowest eigenvalues during the application of the GMMF/RQM and GMMF/KS methods for the starting point $\mathcal{I}_1$. The final configuration of the GMMF algorithm corresponds to $\mathrm{SP}_{\mathrm{dup}}$. The parameters of the Hamiltonian are $J = 1$ meV, $B = 3.1$ T, and $D = 0.55$ meV.

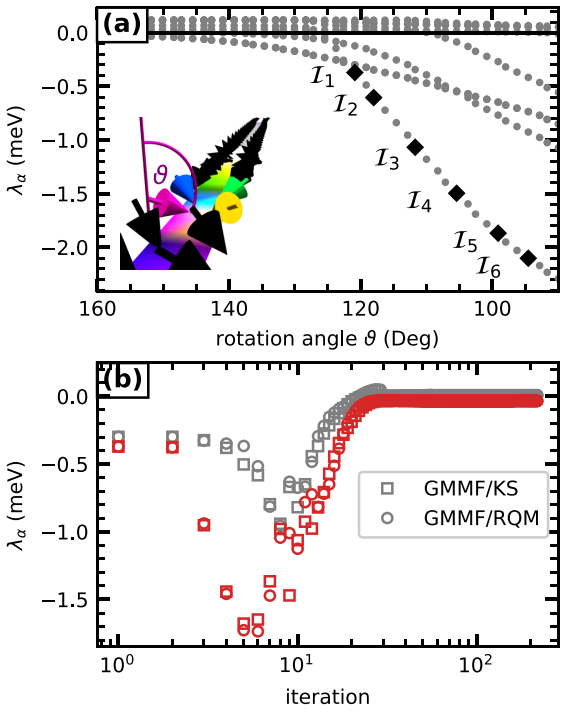


FIG. 9. (a) The evolution of the lowest eigenvalues of the Hessian during the uniform rotation of the four magnetic moments in the core of the skyrmion. The angle between the magnetic moment and the $z$ axis is $\vartheta$, while the in-plane component of the magnetic moments always points towards the center of the skyrmion. The black diamonds $\mathcal{I}_1$–$\mathcal{I}_6$, corresponding to six different starting configurations for the GMMF method, indicate the eigenvalues associated with the inversion mode. (b) The evolution of the two lowest eigenvalues during the application of the GMMF/RQM and GMMF/KS methods for the starting point $\mathcal{I}_1$. The final configuration of the GMMF algorithm corresponds to $\mathrm{SP}_{\mathrm{bag}}$. The values of the Hamiltonian parameters are $J = 1$ meV, $B = 3.1$ T, and $D = 0.55$ meV.

SPs. In particular, following the skyrmion triangular deformation mode, which induces a tendency toward skyrmion "triplication," causes the GMMF procedure to return to the convex region of the energy surface and the corresponding "triplication" SP is not identified. Physical arguments also suggest that the "triplication" SP, or other SPs associated with transitions involving a change in the system's topological charge by more than one, are either improbable or inaccessible due to their likely very high energy. In skyrmionic systems, the magnetic transitions reported so far involve no change in topological charge or a change by one, with the latter mediated by SPs involving high-energy Bloch pointlike defects. Changing the topological charge by an amount greater than one would likely require an even higher-energy configuration with either several such defects or a new type of defect capable of inducing such a change in the topological number, both of which seem unlikely.

The evolution of the two lowest eigenvalues during the application of the GMMF method equipped with the RQM eigensolver (GMMF/RQM) is shown in Fig. 8(b) for $\mathrm{SP}_{\mathrm{dup}}$ and in Fig. 9(b) for $\mathrm{SP}_{\mathrm{bag}}$. For comparison, the same results are depicted for a GMMF method using the Krylov-Schur eigensolver. One can identify slight differences between the eigenvalues obtained in GMMF/RQM and GMMF/KS. This is expected due to the qualitative difference between the RQM and KS eigensolvers leading to slightly different search directions on the energy landscape. Accordingly, the eigenspectrum is not determined at exactly the same point in configuration space in the following iteration. Therefore, the GMMF method is stable against a slight variation of the optimization path, which is underlined by the behavior shown in Figs. 8(b) and 9(b) as both methods converge reliably on the same SP.

Figure 9(b) illustrates that the lowest and second-lowest eigenvalues can approach each other closely during GMMF calculations. This places a requirement on the eigensolver to be able to resolve spectra that are nearly degenerate, and the RQM method successfully meets this requirement in all situations encountered here.

TABLE II. The mean wall time $\tau$ and the number of iterations $\kappa$ required to find SPs describing skyrmion transformations using the GMMF/RQM method, as ratios of those required using the GMMF/KS method.

| | $SP_{rad}$ | | $SP_{esc}$ | | $SP_{dup}$ | | $SP_{bag}$ | |
|---|---|---|---|---|---|---|---|---|
| Initial point | $\tau$ | $\kappa$ | $\tau$ | $\kappa$ | $\tau$ | $\kappa$ | $\tau$ | $\kappa$ |
| $\mathcal{I}_1$ | $0.14 \pm 0.04$ | 1.18 | $0.08 \pm 0.05$ | 1.50 | $0.05 \pm 0.02$ | 0.83 | $0.12 \pm 0.04$ | 1.73 |
| $\mathcal{I}_2$ | $0.14 \pm 0.04$ | 1.07 | $0.10 \pm 0.05$ | 2.05 | $0.06 \pm 0.03$ | 1.02 | $0.13 \pm 0.04$ | 1.84 |
| $\mathcal{I}_3$ | $0.14 \pm 0.05$ | 1.10 | $0.10 \pm 0.04$ | 1.93 | $0.04 \pm 0.02$ | 0.80 | $0.14 \pm 0.04$ | 1.89 |
| $\mathcal{I}_4$ | $0.14 \pm 0.05$ | 1.09 | $0.11 \pm 0.04$ | 2.09 | $0.05 \pm 0.03$ | 0.92 | $0.10 \pm 0.04$ | 1.22 |
| $\mathcal{I}_5$ | $0.14 \pm 0.04$ | 1.14 | $0.10 \pm 0.04$ | 1.97 | $0.06 \pm 0.04$ | 1.02 | $0.11 \pm 0.05$ | 1.45 |
| $\mathcal{I}_6$ | $0.13 \pm 0.05$ | 1.06 | $0.06 \pm 0.04$ | 1.09 | $0.04 \pm 0.03$ | 0.82 | $0.11 \pm 0.04$ | 1.42 |

In order to get an impression of how the performance of the GMMF/RQM method compares to a straightforward implementation of the GMMF method equipped with a state-of-the-art eigensolver from the widely used Intel Math Kernel Library, we compare the wall times required by each implementation of the GMMF to achieve convergence on the four targeted SPs. The wall time (averaged over 50 runs) and the number of iterations until convergence of the GMMF/RQM and GMMF/KS methods for each starting configuration and SP are provided in Table II. The GMMF/RQM is on average 10 times faster, although a slightly longer path is followed on the energy surface resulting in a small increase in the number of iterations. Comparison of the computational efficiency of the RQM and KS eigensolvers is not straightforward. The RQM method benefits significantly from using finite differences of the gradients instead of explicitly calculating the Hessian, even when the Hessian is sparse. Furthermore, it is not clear how the convergence behavior of an L-BFGS optimization of the Rayleigh quotient compares to the KS method. A detailed analysis of this will be done in the future.

Note also that we do not restrict the application of the GMMF algorithm to regions of the configuration space where one and only one eigenvalue is negative. Such points can be hard to find especially in high-dimensional systems. Therefore, we allow for starting points where multiple eigenvalues are negative. As the energy is minimized along all directions orthogonal to the inversion mode, only one eigenvalue becomes negative at some point.

The efficiency of the GMMF/RQM method in locating SPs enables the straightforward identification of the domains in the parameter space where particular transition mechanisms exist, analogous to how magnetic phase diagrams are constructed by energy minimization. The domains of existence for $SP_{rad}$, $SP_{esc}$, $SP_{dup}$, $SP_{bag}$, along with those for the corresponding energy minima, are shown in Fig. 10. They were obtained by varying the $B$ and $D$ parameters and performing GMMF/RQM calculations for each point in the parameter space. Each calculation was initialized using the SPs determined for $B = 3.1$ T and $D = 0.55$ meV. For parameter values outside the domains shown in Fig. 10, all GMMF calculations either converge to SPs unrelated to the corresponding domain or return to the convex region near a local minimum.

$SP_{rad}$ is present as long as the skyrmion state and the FM state coexist [see Figs. 10(a) and 10(b)]. Interestingly, the domains of existence for SPs do not always coincide with those of the adjacent energy minima. For example, the escape mechanism is not always available as the domain for $SP_{esc}$ is smaller than that for $SP_{rad}$ [see Figs. 10(b) and 10(c)]. At large $D$ values, where the isolated skyrmion remains metastable and its radial collapse is still possible, the skyrmion tends to elongate as it approaches the system boundary, forming an intermediate metastable state rather than escaping directly through the boundary [73]. Similarly, $SP_{dup}$ is only present in the part of the skyrmion domain with large DMI [see Figs. 10(a) and 10(d)], although duplication of a skyrmion is always possible through the emergence of a second skyrmion from the FM background via $SP_{rad}$. Finally, $SP_{bag}$ is limited to a very narrow region in the parameter space [see Fig. 10(e)].

The energy barrier for each skyrmion transformation can be obtained from the energy difference between the skyrmion state and the corresponding SP. Figure 10(f) shows how the energy barriers for each transition mechanism depend on the external magnetic field for a fixed DMI strength, $D = 0.5$ meV.

### B. Collapse mechanisms of 3D magnetic states

The advantage of using the finite-difference scheme in the GMMF method becomes particularly evident for large systems with long-range interactions, where building the full Hessian would be prohibitively expensive in terms of time and memory. This is demonstrated through the application of the GMMF/RQM method to a system of $32\times32\times32$ magnetic moments, where the magnetostatic interaction is explicitly included. For the chosen interaction parameters (see Table I), the conical phase is the ground state of the system. However, skyrmion tubes and chiral bobbers [37], skyrmion tubelike spin textures that extend from the surface into the bulk and terminate at a Bloch point, can also exist as metastable states. Here, we demonstrate how the GMMF/RQM method can locate SPs in this system, providing insight into the mechanisms of transitions between different magnetic configurations and even revealing previously unknown metastable textures. Notably, significant results can be obtained without performing an escape stage, as demonstrated in the following.

Specifically, we initialize the system with a cylindrical region of randomly oriented magnetic moments embedded in the conical phase [see Fig. 11(a)]. The cylinder's diameter is set to be roughly the modulation period of the conical phase, an expected size scale for magnetic textures in this material. Since the initial state lies far from any energy minimum, it is outside the convex region of the energy landscape, and the escape stage becomes unnecessary. Thus, the GMMF optimization can start directly from this state. An example of

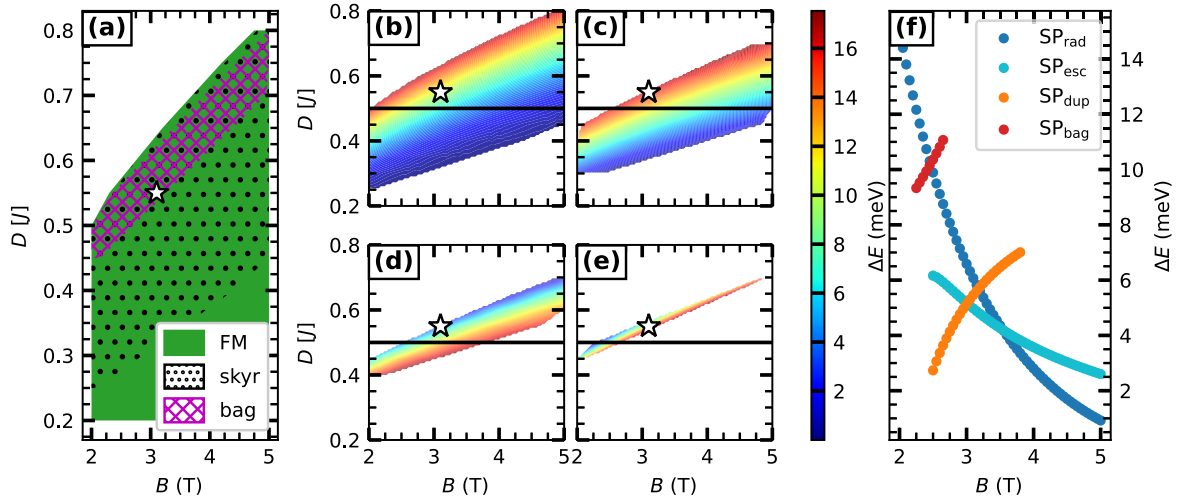


FIG. 10. (a) Parameter domains of metastability of the ferromagnetic state (FM), the skyrmion (skyr), and the skyrmion bag (bag) obtained by energy minimization initiated with the corresponding states for the parameters $B = 3.1$ T and $D = 0.55$ meV (star symbol). The white area corresponds to the domain where all minimizations yield the spin spiral state. (b)–(e) Existence diagrams for the SPs $SP_{rad}$, $SP_{esc}$, $SP_{dup}$, and $SP_{bag}$ obtained via the GMMF/RQM method initialized with the corresponding SP at $B = 3.1$ T and $D = 0.55$ meV (star symbol). The color map represents the energy barrier $\Delta E$ which is the difference of the energy of the SP and the energy of the skyrmion. (f) The energy barriers $\Delta E$ as functions of the applied magnetic field for a constant DMI parameter $D = 0.55$ meV [horizontal lines in (b)–(e)].

such a GMMF calculation is illustrated in Fig. 11. Although multiple negative eigenvalues of the Hessian are present at the beginning of the optimization, the GMMF method brings the system to a valley characterized by a single negative eigenvalue and eventually converges on a first-order SP corresponding to the magnetic configuration shown in Fig. 11(b). Multiple mode-crossing events occur during the optimization process. These crossings appear as cusps in Fig. 11(c), which shows the evolution of the two lowest eigenvalues during the GMMF calculation. In each mode-crossing event, the minimum mode is consistently chosen as the inversion direction.

A small displacement from the SP along the unstable mode, followed by energy minimization, reveals two adjacent energy minima corresponding to the skyrmion tube and the chiral bobber [see Figs. 11(d) and 11(e)]. This illustrates a mechanism for skyrmion tube collapse via detachment of its end from the surface and the formation of a single chiral bobber.

Interestingly, the chiral bobber shown in Fig. 11 and inset i of Fig. 12 is significantly longer than the one originally reported in Ref. [37]. The elongated bobber remains a metastable state even when magnetostatic interactions are excluded (see Appendix E). Further analysis shows that the elongated chiral bobber corresponds to a relatively shallow energy minimum. Displacing the Bloch point by one lattice constant toward the base of the bobber and applying the GMMF method reveals a nearby SP only slightly higher in energy. Following the steepest descent path from this SP yields an MEP corresponding to the contraction of the bobber. The MEP terminates at a shorter chiral bobber, consistent with the typical length reported in Ref. [37] (see inset v in Fig. 12). The energy profile along this MEP exhibits a steplike structure, with each step associated with a reduction of the bobber length by one lattice constant (see Fig. 12). However, no intermediate energy minima are formed during this process.

Performing around 500 GMMF simulations from different initial states similar to that shown in Fig. 11(a) yields a variety of SPs, although different simulations often converge to the same configuration. For each SP, we construct an MEP by following steepest descent paths in both directions. Interestingly, MEPs originating from different SPs sometimes terminate at the same energy minima, thereby revealing connections between distinct metastable configurations. In this way, the set of identified SPs, minima, and corresponding MEPs maps out the network of transitions between metastable states. The resulting network describes various mechanisms for the decay of a skyrmion tube into the conical phase, as illustrated in Fig. 12. This transformation may proceed through various intermediate states, including combinations of chiral bobbers and coupled Bloch point pairs known as chiral globules [38].

In addition to the detachment of the skyrmion tube from the surface, GMMF calculations reveal another collapse mechanism that corresponds to a lower-energy barrier: the rupture of the skyrmion tube, followed by the formation of two chiral bobbers at opposite surfaces of the system. This second mechanism was also identified by Rybakov *et al.* [37] using the GNEB method. In our case, however, depending on the rupture point, either both bobbers or only one may appear elongated; the latter scenario is shown in Fig. 12, inset ii. From this state, the transition to the conical phase can follow several pathways. One involves the detachment of a chiral globule from an elongated bobber, forming a metastable complex consisting of two chiral bobbers and a globule (see inset iii in Fig. 12). The system eventually reaches the conical phase through the sequential collapse of the individual com-

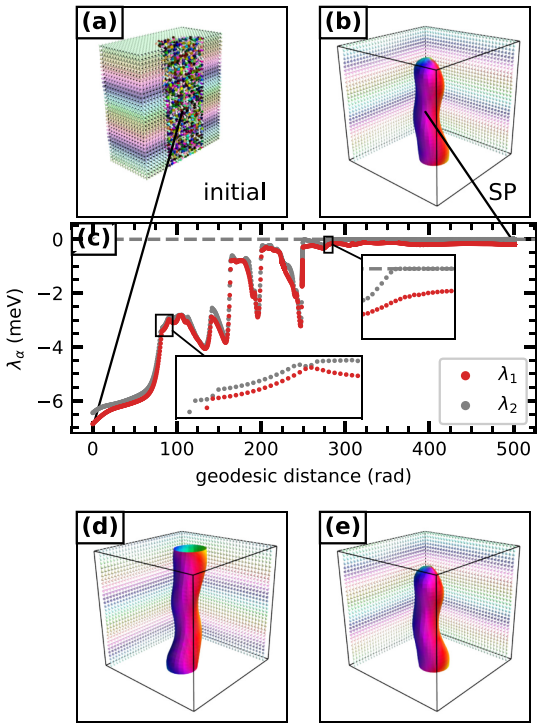


FIG. 11. An example of GMMF calculations applied to a 3D system. (a) Starting configuration represented by a cylindrical region of randomly oriented magnetic moments embedded in the conical phase. (b) The SP configuration to which the GMMF method converges. (c) The lowest ($\lambda_1$, red) and the second-lowest ($\lambda_2$, gray) eigenvalues of the Hessian of the energy as functions of the cumulative displacement of the system in the configuration space during the GMMF optimization. The left bottom inset shows a mode-crossing event. The right top inset highlights that one and only one eigenvalue is negative at the end of the optimization and thus the final state represents a first-order SP. (d), (e) Metastable configurations adjacent to the SP shown in (b). The orientation of magnetic moments is indicated by color, as described in Fig. 5(a). For (b), (d), and (e), the isosurfaces of $s_z = 0$ are shown.

ponents of this complex (not shown in Fig. 12). Alternatively, the system can reach the conical state via stepwise bobber contraction. The presence of a second bobber influences this process: each contraction by one lattice constant corresponds to a metastable state, producing a sequence of shallow intermediate minima along the corresponding MEP [see the black line in Fig. 12(b)]. This contrasts with the case of a single bobber, where the energy profile exhibits shoulders instead [see the cyan line in Fig. 12(b)]. Eventually, the system relaxes into a configuration with two chiral bobbers whose sizes agree with the predictions of Ref. [37] (inset iv in Fig. 12). Afterward, one of the bobbers collapses, and the system reaches the same state as in the process involving the contraction of a single elongated bobber. From here, the system can either proceed directly to the conical phase via the escape of the bobber's Bloch point through the surface, or follow a higher-energy pathway in which a second Bloch point nucleates at the surface, forming an isolated globule state (see inset vi in Fig. 12) that reorients and then collapses through mutual annihilation of its Bloch points [see Fig. 12(c)].

Previous studies have reported chiral globules as stabilized through confinement or interaction with defects [38]. Recent work [74] suggests that globule states can also exist as true 3D solitons in certain parameter regimes without magnetostatics. Our results provide an alternative mechanism for the localization and stabilization of globule states via magnetostatic interactions. Without these interactions, the isolated globule is no longer metastable for the chosen set of parameters (see Appendix E).

Despite the complexity of metastable states and transition mechanisms revealed in this study, the picture summarized in Fig. 12 is likely incomplete. A more systematic exploration based on recursively connecting metastable states via saddle-point searches is expected to uncover additional transitions. This approach requires a method for escaping the convex region associated with each metastable state. One possibility is to follow specific low-lying modes of the system, which can be efficiently computed using a finite-difference scheme within an extended Rayleigh quotient framework. Other escape strategies may also be employed. Developing an optimal escape procedure for 3D magnetic systems remains an important direction for future research.

For comparison, we repeated the GMMF calculations for a system with the same interaction parameters but without magnetostatics, identical to the one studied by Rybakov *et al.* [37]. The results, which exhibit fewer metastable states overall, are summarized in Appendix E. As expected, including magnetostatic interactions increases the computational cost. However, the implemented GMMF method does not introduce additional scaling overhead beyond the computational complexity determined by the interactions present in the system (see Appendix F), making it well suited for large-scale simulations.

## V. CONCLUSIONS AND DISCUSSION

In the GMMF/RQM method, convergence to SPs is achieved by maximizing the energy along one of the two lowest modes, defined by the eigenvectors corresponding to the two lowest eigenvalues of the Hessian, and minimizing it along all other directions. Instead of the computationally demanding task of repeatedly evaluating the Hessian and solving the eigenvalue problem, we introduce an efficient methodology based on the direct minimization of the generalized Rayleigh quotient using only the energy gradients. This becomes particularly important for large systems and/or systems with dense Hessians.

An important aspect of our methodology is the correct treatment of the geometry of the manifolds on which the optimization of the magnetic structure and minimization of the Rayleigh quotient are performed. In particular, optimization algorithms used in our method take into account the curvature of the corresponding manifolds via retraction and parallel transport. The GMMF/RQM method exhibits a high degree of computational efficiency and stability which we demonstrate in applications to 2D and 3D magnetic systems.

We show consistency with previously published results by identifying the three SPs corresponding to the mechanisms

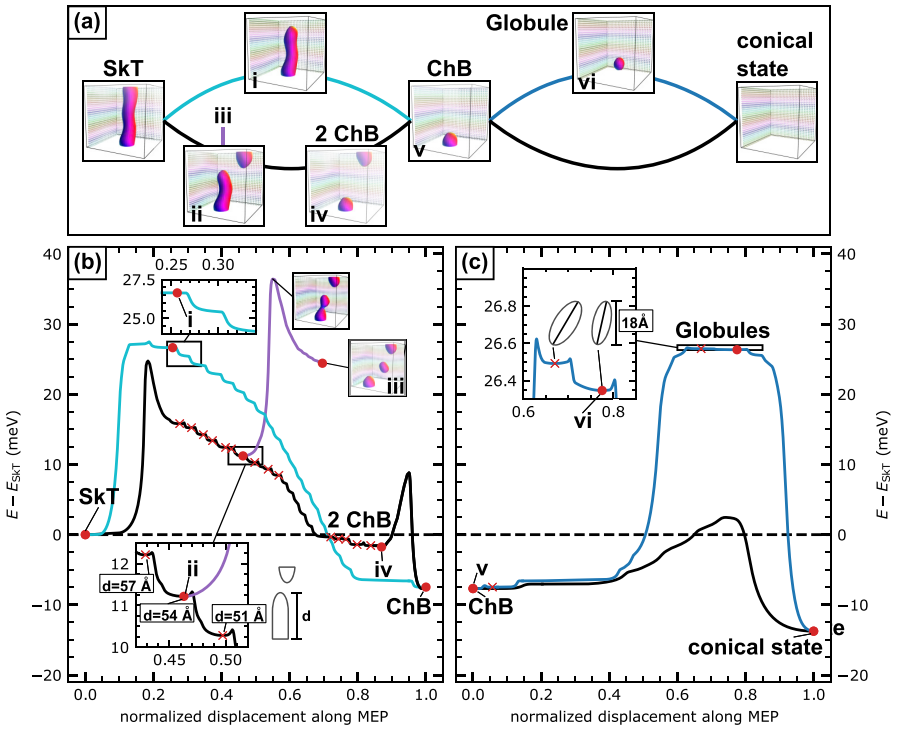


FIG. 12. (a) Graph showing metastable configurations (insets) and possible transitions between them in the 3D system with magnetostatic interactions, as obtained with the GMMF method. The magnetic configurations are visualized by the isosurfaces of $s_z = 0$ where the color code is described in Fig. 5(a). (b) Energy variation along the calculated MEPs: from the skyrmion tube (SkT) state to the chiral bobber (ChB) state via the elongated bobber (cyan line) and two ChB (black line) states, and from the state corresponding to two bobbers of different lengths to the metastable state involving a globule between two chiral bobbers (magenta line). The insets show zoomed-in views of the plots, magnetic configurations at specific points along the MEPs, and a sketch of the two-bobber state. (c) Energy variation along calculated MEPs connecting the ChB state to the conical state directly (black line) and via the isolated globule state (blue line). The insets show a zoomed-in view of the plot and sketches of the globule states. The red crosses mark position of the energy minima. The energy minima corresponding to metastable configurations shown in (a) are indicated with red dots. For each transition, the displacement along the MEP is normalized separately to align the positions of energy minima corresponding to the same magnetic configurations. The dashed line shows the zero-energy level corresponding to the relaxed skyrmion tube configuration.

of skyrmion transformation reported by Müller *et al.* [44]. In addition, we identify the fourth mechanism corresponding to the transformation of the skyrmion into a skyrmion bag.

An efficient computational scheme requiring only the evaluation of the gradient of the energy to compute the action of the Hessian has enabled the application of the GMMF method to a 3D system with magnetostatic interactions, and the discovery of a complex network of transitions between metastable chiral bobbers, skyrmion tubes, and globules. We obtain a mechanism for the collapse of a skyrmion tube via rupture followed by formation of metastable chiral bobbers, analogous to what has been reported by Rybakov *et al.* [37]. In addition, we identify a mechanism corresponding to detachment of the end of a skyrmion tube from the surface [75] and the formation of a new chiral bobber state where the equilibrium distance between the base and the terminating Bloch point is extended. Moreover, we report metastable magnetic globules appearing as isolated states due to magnetostatic interactions. It is important to realize that these results are obtained via straightforward application of the GMMF/RQM method without relying on subjective assumptions about the system.

While the GMMF/RQM method can be used independently to study transitions in various magnetic systems, it shows great promise when combined with other techniques such as the GNEB method or the CI-GNEB method where a climbing image is included to better converge on the SP [7]. Instead of converging all images representing the path to a low tolerance, the calculation can be terminated at an earlier stage and the highest-energy image used as a starting point for an efficient GMMF/RQM convergence on the SP. This is found to be the optimal strategy for magnetic systems, analogous to what has been found for atomic rearrangements [76].

The GMMF/RQM method can be integrated into a global optimization framework for magnetic textures by recursively traversing between local energy minima through first-order SPs [10]. Within this framework, calculating transition rates on the fly, using, for example, harmonic transition state theory, would enable the simulation of long timescale dynamics through the adaptive kinetic Monte Carlo algorithm [8,9].

To summarize, the GMMF/RQM method represents a valuable tool for studying transitions in various magnetic systems. This becomes particularly important in the context of topological magnetism where various 2D and 3D states have recently been discovered.

While the focus of this work is on locating first-order SPs, which are directly associated with transition mechanisms and energy barriers within HTST [1,2,23] and Kramers-Langer theory [3,4,77], the method can, in principle, be extended to identify higher-order SPs: stationary points characterized by more than one unstable mode. This would require inverting the magnetic force components along several modes simultaneously, using a generalized Rayleigh quotient to compute multiple eigenpairs of the Hessian. A second-order saddle point, for example, represents a maximum in energy along an energy ridge, and can be used to assess the accuracy of the harmonic approximation to TST. A generalization of our method to higher-order saddle points can be useful for other applications and remains a possible direction for future work.

The first phase of the SP search, the escape from the convex region, remains a challenging task. In our study of skyrmion collapse mechanisms in the 2D system, following various Hessian eigenvectors during the escape stage provided a straightforward means of introducing deformations that reflect the shape of the SP configurations. Thanks to the sparsity of the Hessian and the moderate system size, it was feasible, though not optimal, to construct the Hessian explicitly and compute the eigenvectors using standard techniques. A natural improvement is to obtain the relevant eigenvectors without constructing the full Hessian, for instance, via finite-difference evaluation of its action within an extended Rayleigh quotient framework. Further optimization is possible given that the precise determination of the escape direction is not critical: even crude approximations to the eigenvectors may suffice, or it may be possible to escape the convex region without explicitly following them at all. These considerations suggest substantial room for improving the escape stage. One promising direction is to exploit the symmetries of magnetic textures. Optimization of the escape stage remains a subject of future research.

## ACKNOWLEDGMENTS

M.S. is grateful to A. Goswami and G. P. Müller for fruitful discussions. H.S. is grateful to M. Görzen and S. Heinze for fruitful discussions. This work received financial support from the Icelandic Research Fund (Grants No. 239435 and No. 217750), the University of Iceland Research Fund (Grants No. 15673 and No. 15661), the Swedish Research Council (Grant No. 2020-05110), and the Crafoord Foundation (Grant No. 20231063). The calculations were carried out at the high-performance computing resources available at the Kiel University Computing Centre and at the Icelandic Research e-Infrastructure facility supported by the Icelandic Infrastructure Fund.

## DATA AVAILABILITY

The data that support the findings of this article are not publicly available upon publication because it is not technically feasible and/or the cost of preparing, depositing, and hosting the data would be prohibitive within the terms of this research project. The data are available from the authors upon reasonable request.

## APPENDIX A: SYSTEM OF FOUR MAGNETIC MOMENTS ILLUSTRATING MODE CROSSING

To illustrate the mode crossings in Fig. 3, a system of four magnetic moments placed in the corners of a square is considered. Only the nearest-neighbor moments are coupled via the exchange $J$ and a magnetic field in the negative $z$ direction is applied. Furthermore, the uniaxial anisotropy favors alignment along the $\pm z$ direction. The Hamiltonian of the system reads as

$$\tilde{E} = -J(\vec{s}_1 \cdot \vec{s}_2 + \vec{s}_1 \cdot \vec{s}_3 + \vec{s}_2 \cdot \vec{s}_4 + \vec{s}_3 \cdot \vec{s}_4) - \mu \sum_{i=1}^{4} \vec{B} \cdot \vec{s}_i - \sum_{i=1}^{4} K(\vec{s}_i \cdot \vec{e}_z)^2 \tag{A1}$$

with $J = 0.5$ eV, K $= 1.0$ eV, and $\vec{B}_{\text{ext}} = -1.0\hat{e}_z$ T as well as $\mu = 1\,\mu_B$. For these parameters, the parallel alignment of the magnetic moments in the $+z$ direction is a local energy minimum configuration. From this minimum configuration, a suitable start configuration for the application of the GMMF method is obtained by rotating two magnetic moments sitting on opposite corners of the square. The lowest eigenvalue spectrum of the system during this rotation is visualized in Fig. 3(a).

## APPENDIX B: PSEUDOCODE FOR OPTIMIZATION OF THE RAYLEIGH QUOTIENT

The optimization is represented by the four algorithms. The main routine is given in Algorithm 1. To compute the search direction, we use the well-known "two loop recursion," listed in Algorithm 2. Algorithm 1, in combination with Algorithm 2, constitutes a fairly standard L-BFGS method with some exceptions: A minor one is that the algorithm is being applied to matrices instead of, as perhaps more commonly seen, vectors. The other, much more important, is the use of the `Parallel transport` and `Retraction` functions to move across the Grassmann manifold, in a way that respects its inherent geometry. These two are implemented in Algorithms 3 and 4, respectively, and make use of equations given by Edelmann *et al.* [50].

## APPENDIX C: EVALUATION OF THE HESSIAN MATRIX

The Hessian matrix for a magnetic system characterized by $N$ constraints on the length of the magnetic moments can be computed as follows. First, the $3N \times 3N$ matrix $H^{3N}$ of the second-order derivatives of the energy with respect to the Cartesian components of the magnetic moments is calculated. After that, the shape operator $\mathcal{L}$ is subtracted from $H^{3N}$. The shape operator is a diagonal matrix of the form

$$\mathcal{L} = \begin{pmatrix} L_1 & \dots & 0 \\ \vdots & \ddots & \vdots \\ 0 & \dots & L_N \end{pmatrix}, \tag{C1}$$

ALGORITHM 1. L-BFGS optimizer for the generalized Rayleigh quotient.

**Require:** Initial point $X$ on the Grassmann manifold $G_{2,2N}$, Hessian matrix $H$, tolerance $\epsilon$, maximum memory $m$
**Ensure:** Solution $X$ that spans the minimal invariant subspace of $H$
  Initialize $k \leftarrow 0$
  Initialize $X_0 \leftarrow X$
  Initialize the history $S \leftarrow [], Y \leftarrow [], \rho \leftarrow []$
  **while** $k <$ maxIterations **do**
    // Here, we denote the action of the Hessian as $HX$
    // In practice, we use the finite-difference scheme
    // described in Sec. II B
    $G_k \leftarrow 2X_k[HX_k - X_k(X_k^T HX_k)]$
    **if** $\|G_k\|_F < \epsilon$ **then**
      **break**
    **end if**
    // Transport the history to the current tangent frame
    **if** len$(S) > 0$ **then**
      $S_i \leftarrow$ `Transport`$(X_{k-1}, S_i, P, \Sigma, V) \quad \forall\, S_i \in S$
      $Y_i \leftarrow$ `Transport`$(X_{k-1}, Y_i, P, \Sigma, V) \quad \forall\, Y_i \in Y$
    **end if**
    **if** k $> 1$ **then**
      // Append to the history
      Append $\Lambda$ to $S$
      Append $G_k -$ `Transport`$(X_{k-1}, G_{k-1}, P, \Sigma, V)$ to $Y$
      Append $\mathrm{tr}[(X_k - X_{k-1})^T (G_k - G_{k-1})]^{-1}$ to $\rho$
      **if** len$(S) > m$ **then**
        Delete oldest entry of $S, Y$, and $\rho$
      **end if**
      // Curvature rejection condition
      **if** $\rho_{-1} < 0$ **then**
        // Reset the history
        $S \leftarrow [], Y \leftarrow [], \rho \leftarrow []$
      **end if**
    **end if**
    // Compute the search direction via two-loop recursion
    $\Lambda \leftarrow$ `TwoLoopRecursion`$(S, Y, \rho, G_k)$
    // Perform compact singular value
    // decomposition of $\Lambda$ such that $\Lambda = P\Sigma V^T$
    $P, \Sigma, V \leftarrow$ `SVD`$(\Lambda)$
    // Update $X$ via retraction
    $X_{k+1} \leftarrow$ `Retraction`$(X_k, P, \Sigma, V)$
    $k \leftarrow k + 1$
  **end while**

with

$$L_i = \begin{pmatrix} \vec{s}_i \cdot \vec{\nabla}_i E & 0 & 0 \\ 0 & \vec{s}_i \cdot \vec{\nabla}_i E & 0 \\ 0 & 0 & \vec{s}_i \cdot \vec{\nabla}_i E \end{pmatrix}. \tag{C2}$$

Finally, the matrix $U \in \mathbb{R}^{3N \times 2N}$ is applied, that projects the embedding space vectors into the tangent space of the current configuration $\boldsymbol{s}$ (see Refs. [44,51]):

$$H = U^T (H^{3N} - \mathcal{L}) U. \tag{C3}$$

ALGORITHM 2. Two-loop recursion.

**function** `TwoLoopRecursion`$(S, Y, \rho, G)$
  $\Lambda \leftarrow G$
  $s \leftarrow$ len$(S)$
  **for** $i = s$ down to 1 **do**
    $\alpha_i \leftarrow \rho_i \mathrm{tr}(S_i^T \Lambda)$
    $\Lambda \leftarrow \Lambda - \alpha_i Y_i$
  **end for**
  **if** $s > 0$ **then**
    // Initial diagonal approximation
    // for the inverse Hessian
    $H^{s-1} \leftarrow \rho_i^{-1} \sqrt{\mathrm{tr}(Y_{s-1}{}^T Y_{s-1})}$
    $\Lambda \leftarrow H^{s-1} \Lambda$
  **end if**
  **for** $i = 1$ to $s$ **do**
    $\beta \leftarrow \rho_i \mathrm{tr}(Y_i^T \Lambda)$
    $\Lambda \leftarrow \Lambda + (\alpha_i - \beta) S_i$
  **end for**
  // Minus sign for minimization
  **return** $-\Lambda$
**end function**

## APPENDIX D: NUMERICAL PARAMETERS FOR GMMF CALCULATIONS

The GMMF calculations are considered converged if the maximum norm of the effective field components drops below a value of $10^{-12}$ eV:

$$\max_{i \in \{1,\ldots,N\}} |\vec{b}_i| < 10^{-12} \text{ eV}. \tag{D1}$$

The L-BFGS based GMMF algorithm is used without a line search procedure. As described in Ref. [56] we restrict the maximum step length with a parameter $\vartheta_{\max}$. The number of memory quantities taken into account is $m = 3$ for all calculations in this publication. For the GMMF calculations presented in Sec. IV A we always chose $\vartheta_{\max}^{\mathrm{GMMF}} = 0.5$. Also the L-BFGS solver of the RQM method was set to $\vartheta_{\max}^{\mathrm{RQM}} = 0.5$. The calculation of the two lowest modes within the RQM method is considered converged if the Frobenius norm of the Rayleigh gradient drops below $10^{-8}$ eV.

## APPENDIX E: EFFECT OF EXCLUDING MAGNETOSTATICS ON THE COLLAPSE MECHANISMS OF 3D MAGNETIC STATES

Following the approach described in Sec. IV A, we compute the SPs, energy minima, and MEPs for the system

ALGORITHM 3. Parallel transport.

**function** Transport$(X, A, P, \Sigma, V)$
  // The parentheses are necessary to ensure a
  // computationally efficient order of evaluation
  $T_1 A \leftarrow -XV \ \sin(\Sigma)(P^T A)$
  $T_2 A \leftarrow P \cos(\Sigma)(P^T A)$
  $T_3 A \leftarrow A - P(P^T A)$
  **return** $T_1 A + T_2 A + T_3 A$
**end function**

ALGORITHM 4. Retraction.

**function** `Retraction`($X$, $P$, $\Sigma$, $V$)
  $X' \leftarrow XV\ \cos(\Sigma)V^T + P\ \sin(\Sigma)V^T$
  // Prevent accumulation of numerical errors
  Orthonormalize columns of $X'$ with QR algorithm
  **return** $X'$
**end function**

without magnetostatic interactions. Additionally, we test whether SPs identified in the system with magnetostatics persist by using the corresponding configurations as starting points for GMMF optimization in the system without magnetostatics. The results of these calculations are summarized in Fig. 13.

Overall, excluding magnetostatics results in fewer metastable states and possible transitions. Nevertheless, rupture of the skyrmion tube and detachment of its end from the surface are still present. In the absence of magnetostatics, however, these two mechanisms of the skyrmion tube collapse exhibit nearly equal energy barriers. Consistent with Ref. [37], the rupture of the tube results directly in the formation of two short chiral bobbers. No intermediate states appear along this transition, which is in contrast to the case with magnetostatic interactions. Interestingly, the metastable elongated bobber still forms following detachment of the end of the tube from the surface.

As in the case with magnetostatics, both collapse mechanisms eventually lead to a single bobber state. From there, the system proceeds directly to the conical phase via the escape of the bobber's Bloch point through the surface. No alternative collapse mechanism for the bobber was found. In particular, no pathway involving the formation of globules was obtained. Moreover, globules do not form metastable isolated

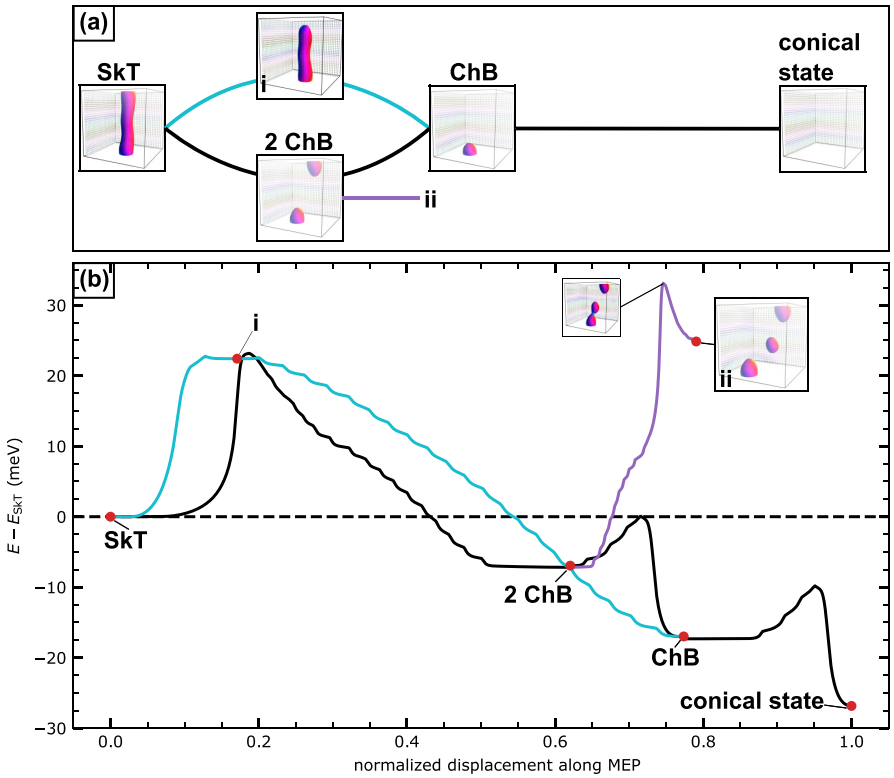


FIG. 13. (a) Graph showing metastable configurations (insets) and possible transitions between them in the 3D system without magnetostatic interactions, as obtained with the GMMF method. The magnetic configurations are visualized by the isosurfaces of $s_z = 0$ where the color code is described in Fig. 5(a). (b) Energy variation along the calculated MEPs: from the skyrmion tube (SkT) state to the conical state via the two-bobber state (black line), from the SkT state to the chiral bobber (ChB) state via the elongated bobber state (cyan line), and from the two ChB state to the state involving a globule between two chiral bobbers (magenta line). The insets show magnetic configurations at specific points along the MEPs. The red dots mark position of the energy minima. For each transition, the displacement along the MEP is normalized separately to align the positions of energy minima corresponding to the same magnetic configurations. The dashed line shows the zero-energy level corresponding to the relaxed skyrmion tube configuration.

configurations in the absence of magnetostatics for the chosen set of parameter values. However, they can still become metastable near defects [38]. In particular, the state involving a globule positioned between two bobbers is metastable even without magnetostatics and is connected to the two-bobber configuration.

## APPENDIX F: SCALING OF THE COMPUTATIONAL EFFORT

To assess the computational performance of the GMMF method, we examine its scaling with the number of magnetic moments $N$ in the system. A key computational step in the method is the evaluation of the gradient of the Rayleigh quotient, $\nabla R(X)$ [see Eq. (14)], which dominates the cost per iteration during saddle-point searches. We therefore use the mean CPU time required for a single gradient evaluation as a representative benchmark.

Figure 14 shows the CPU time as a function of $N$ for cubic systems with and without magnetostatic interactions, where magnetic moments are oriented randomly. The observed scaling reflects the complexity determined by the underlying interactions: for systems without magnetostatics, the scaling is linear, $O(N)$. When magnetostatic interactions are included, the scaling follows $O(N \log N)$ due to the use of fast Fourier transform-based methods. While the distinction between linear and $O(N \log N)$ scaling is subtle in the current system size range, the data remain consistent with the expected behavior.

Crucially, the GMMF algorithm itself introduces no additional scaling overhead beyond what is required to compute the system energy and its gradient. This makes it well suited for application to large systems, including those with long-range interactions.

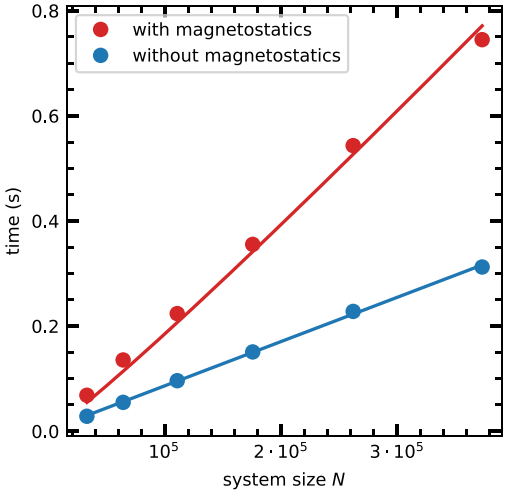


FIG. 14. Mean CPU time required for a single evaluation of the Rayleigh quotient gradient $\nabla R(X)$ [see Eq. (14)] as a function of the number of magnetic moments $N$ in a cubic system with and without magnetostatic interactions, as indicated in the legend. The blue (red) line shows the linear ($N \log N$) fit.


[1] E. Wigner, The transition state method, Trans. Faraday Soc. **34**, 29 (1938).

[2] G. H. Vineyard, Frequency factors and isotope effects in solid state rate processes, J. Phys. Chem. Solids **3**, 121 (1957).

[3] H. A. Kramers, Brownian motion in a field of force and the diffusion model of chemical reactions, Physica (Amsterdam) **7**, 284 (1940).

[4] J. Langer, Statistical theory of the decay of metastable states, Ann. Phys. **54**, 258 (1969).

[5] D. V. Berkov, Magnetization dynamics including thermal fluctuations: Basic phenomenology, fast remagnetization processes and transitions over high-energy barriers, in *Handbook of Magnetism and Advanced Magnetic Materials* (Wiley, Hoboken, NJ, 2007), Vol. 2, pp. 795–823.

[6] H. Jónsson, G. Mills, and K. W. Jacobsen, Nudged elastic band method for finding minimum energy paths of transitions, in *Classical and Quantum Dynamics in Condensed Phase Simulations*, edited by B. J. Berne, G. Ciccotti, and D. F. Coker (World Scientific, Singapore, 1998), pp. 385–404.

[7] P. F. Bessarab, V. M. Uzdin, and H. Jónsson, Method for finding mechanism and activation energy of magnetic transitions, applied to skyrmion and antivortex annihilation, Comput. Phys. Commun. **196**, 335 (2015).

[8] G. Henkelman and H. Jónsson, Long time scale kinetic Monte Carlo simulations without lattice approximation and predefined event table, J. Chem. Phys. **115**, 9657 (2001).

[9] H. Jónsson, Simulation of surface processes, Proc. Natl. Acad. Sci. USA **108**, 944 (2011).

[10] M. Plasencia, A. Pedersen, A. Arnaldsson, J.-C. Berthet, and H. Jónsson, Geothermal model calibration using a global minimization algorithm based on finding saddle points and minima of the objective function, Comput. Geosci. **65**, 110 (2014).

[11] D. M. Einarsdóttir, A. Arnaldsson, F. Óskarsson, and H. Jónsson, Path optimization with application to tunneling, in *Applied Parallel and Scientific Computing*, edited by K. Jónasson (Springer, Berlin, 2012), pp. 45–55.

[12] V. Ásgeirsson, A. Arnaldsson, and H. Jónsson, Efficient evaluation of atom tunneling combined with electronic structure calculations, J. Chem. Phys. **148**, 102334 (2018).

[13] S. M. Vlasov, P. F. Bessarab, I. S. Lobanov, M. N. Potkina, V. M. Uzdin, and H. Jónsson, Magnetic skyrmion annihilation by quantum mechanical tunneling, New J. Phys. **22**, 083013 (2020).

[14] I. A. Nosikov, M. V. Klimenko, G. A. Zhbankov, A. V. Podlesnyi, V. A. Ivanova, and P. F. Bessarab, Generalized force approach to point-to-point ionospheric ray tracing and systematic identification of high and low rays, IEEE Trans. Antennas Propag. **68**, 455 (2020).

[15] B. Peters, *Reaction Rate Theory and Rare Events* (Elsevier, Amsterdam, 2017).

[16] G. Henkelman and H. Jónsson, A dimer method for finding saddle points on high dimensional potential surfaces using only first derivatives, J. Chem. Phys. **111**, 7010 (1999).
[17] R. Malek and N. Mousseau, Dynamics of Lennard-Jones clusters: A characterization of the activation-relaxation technique, Phys. Rev. E **62**, 7723 (2000).
[18] A. Pedersen, S. F. Hafstein, and H. Jónsson, Efficient sampling of saddle points with the minimum-mode following method, SIAM J. Sci. Comput. **33**, 633 (2011).
[19] M. P. Gutiérrez, C. Argáez, and H. Jónsson, Improved minimum mode following method for finding first order saddle points, J. Chem. Theory Comput. **13**, 125 (2017).
[20] C. Lanczos, An iteration method for the solution of the eigenvalue problem of linear differential and integral operators, J. Res. Natl. Bureau Stand. **45**, 255 (1950).
[21] E. R. Davidson, The iterative calculation of a few of the lowest eigenvalues and corresponding eigenvectors of large real-symmetric matrices, J. Comput. Phys. **17**, 87 (1975).
[22] W. T. Coffey, D. A. Garanin, and D. J. Mccarthy, Crossover formulas in the kramers theory of thermally activated escape rates–application to spin systems, in *Advances in Chemical Physics* (Wiley, Hoboken, NJ, 2001), pp. 483–765.
[23] P. F. Bessarab, V. M. Uzdin, and H. Jónsson, Harmonic transition-state theory of thermal spin transitions, Phys. Rev. B **85**, 184409 (2012).
[24] P. F. Bessarab, V. M. Uzdin, and H. Jónsson, Potential energy surfaces and rates of spin transitions, Z. Phys. Chem. **227**, 1543 (2013).
[25] I. S. Lobanov, H. Jónsson, and V. M. Uzdin, Mechanism and activation energy of magnetic skyrmion annihilation obtained from minimum energy path calculations, Phys. Rev. B **94**, 174418 (2016).
[26] D. Cortés-Ortuño, W. Wang, M. Beg, R. A. Pepper, M.-A. Bisotti, R. Carey, M. Vousden, T. Kluyver, O. Hovorka, and H. Fangohr, Thermal stability and topological protection of skyrmions in nanotracks, Sci. Rep. **7**, 4060 (2017).
[27] S. von Malottki, B. Dupé, P. F. Bessarab, A. Delin, and S. Heinze, Enhanced skyrmion stability due to exchange frustration, Sci. Rep. **7**, 12299 (2017).
[28] P. F. Bessarab, G. P. Müller, I. S. Lobanov, F. N. Rybakov, N. S. Kiselev, H. Jónsson, V. M. Uzdin, S. Blügel, L. Bergqvist, and A. Delin, Lifetime of racetrack skyrmions, Sci. Rep. **8**, 3433 (2018).
[29] B. Heil, A. Rosch, and J. Masell, Universality of annihilation barriers of large magnetic skyrmions in chiral and frustrated magnets, Phys. Rev. B **100**, 134424 (2019).
[30] D. Cortés-Ortuño, N. Romming, M. Beg, K. von Bergmann, A. Kubetzka, O. Hovorka, H. Fangohr, and R. Wiesendanger, Nanoscale magnetic skyrmions and target states in confined geometries, Phys. Rev. B **99**, 214408 (2019).
[31] H. Schrautzer, S. von Malottki, P. F. Bessarab, and S. Heinze, Effects of interlayer exchange on collapse mechanisms and stability of magnetic skyrmions, Phys. Rev. B **105**, 014414 (2022).
[32] M. A. Goerzen, S. von Malottki, S. Meyer, P. F. Bessarab, and S. Heinze, Lifetime of coexisting sub-10 nm zero-field skyrmions and antiskyrmions, npj Quantum Mater. **8**, 54 (2023).
[33] J. Hagemeister, A. Siemens, L. Rózsa, E. Y. Vedmedenko, and R. Wiesendanger, Controlled creation and stability of $k\pi$ skyrmions on a discrete lattice, Phys. Rev. B **97**, 174436 (2018).
[34] L. Desplat, J.-V. Kim, and R. L. Stamps, Paths to annihilation of first- and second-order (anti)skyrmions via (anti)meron nucleation on the frustrated square lattice, Phys. Rev. B **99**, 174409 (2019).
[35] V. M. Kuchkin, B. Barton-Singer, F. N. Rybakov, S. Blügel, B. J. Schroers, and N. S. Kiselev, Magnetic skyrmions, chiral kinks, and holomorphic functions, Phys. Rev. B **102**, 144422 (2020).
[36] V. M. Kuchkin, N. S. Kiselev, F. N. Rybakov, and P. F. Bessarab, Tailed skyrmions—An obscure branch of magnetic solitons, Front. Phys. **11**, 1171079 (2023).
[37] F. N. Rybakov, A. B. Borisov, S. Blügel, and N. S. Kiselev, New type of stable particlelike states in chiral magnets, Phys. Rev. Lett. **115**, 117201 (2015).
[38] G. P. Müller, F. N. Rybakov, H. Jónsson, S. Blügel, and N. S. Kiselev, Coupled quasimonopoles in chiral magnets, Phys. Rev. B **101**, 184405 (2020).
[39] V. M. Kuchkin and N. S. Kiselev, Homotopy transitions and 3D magnetic solitons, APL Mater. **10**, 071102 (2022).
[40] I. S. Lobanov and V. M. Uzdin, Lifetime, collapse, and escape paths for hopfions in bulk magnets with competing exchange interactions, Phys. Rev. B **107**, 104405 (2023).
[41] M. Sallermann, H. Jónsson, and S. Blügel, Stability of hopfions in bulk magnets with competing exchange interactions, Phys. Rev. B **107**, 104404 (2023).
[42] Y. Li, Y. Zang, R. Chen, and C. Moutafis, Tailoring energy barriers of bloch-point-mediated transitions between topological spin textures, Phys. Rev. B **109**, 024418 (2024).
[43] Y. L. A. Schmerwitz, G. Levi, and H. Jónsson, Calculations of excited electronic states by converging on saddle points using generalized mode following, J. Chem. Theory Comput. **19**, 3634 (2023).
[44] G. P. Müller, P. F. Bessarab, S. M. Vlasov, F. Lux, N. S. Kiselev, S. Blügel, V. M. Uzdin, and H. Jónsson, Duplication, collapse, and escape of magnetic skyrmions revealed using a systematic saddle point search method, Phys. Rev. Lett. **121**, 197202 (2018).
[45] P. F. Bessarab, V. M. Uzdin, and H. Jónsson, Calculations of magnetic states and minimum energy paths of transitions using a noncollinear extension of the alexander-anderson model and a magnetic force theorem, Phys. Rev. B **89**, 214424 (2014).
[46] A. V. Ivanov, D. Dagbartsson, J. Tranchida, V. M. Uzdin, and H. Jónsson, Efficient optimization method for finding minimum energy paths of magnetic transitions, J. Phys.: Condens. Matter **32**, 345901 (2020).
[47] H. Bocquet and P. M. Derlet, Searching for activated transitions in complex magnetic systems, Phys. Rev. B **108**, 174419 (2023).
[48] Intel math kernel library (2024.2.2) (2024).
[49] V. P. Antropov, M. I. Katsnelson, B. N. Harmon, M. van Schilfgaarde, and D. Kusnezov, Spin dynamics in magnets: Equation of motion and finite temperature effects, Phys. Rev. B **54**, 1019 (1996).
[50] A. Edelman, T. A. Arias, and S. T. Smith, The geometry of algorithms with orthogonality constraints, SIAM J. Matrix Anal. Appl. **20**, 303 (1998).
[51] A. S. Varentcova, S. von Malottki, M. N. Potkina, G. Kwiatkowski, S. Heinze, and P. F. Bessarab, Toward room-temperature nanoscale skyrmions in ultrathin films, npj Comput. Mater. **6**, 193 (2020).

[52] K. Ohno and S. Maeda, A scaled hypersphere search method for the topography of reaction pathways on the potential energy surface, Chem. Phys. Lett. **384**, 277 (2004).

[53] S. Maeda, Y. Watanabe, and K. Ohno, A scaled hypersphere interpolation technique for efficient construction of multidimensional potential energy surfaces, Chem. Phys. Lett. **414**, 265 (2005).

[54] P.-A. Absil, R. Mahony, and R. Sepulchre, *Optimization Algorithms on Matrix Manifolds* (Princeton University Press, Princeton, NJ, 2008).

[55] D. C. Liu and J. Nocedal, On the limited memory BFGS method for large scale optimization, Math. Program. **45**, 503 (1989).

[56] A. V. Ivanov, V. M. Uzdin, and H. Jónsson, Fast and robust algorithm for energy minimization of spin systems applied in an analysis of high temperature spin configurations in terms of skyrmion density, Comput. Phys. Commun. **260**, 107749 (2021).

[57] G. L. G. Sleijpen and H. A. Van der Vorst, A Jacobi–Davidson iteration method for linear eigenvalue problems, SIAM Rev. **42**, 267 (2000).

[58] G. W. Stewart, A Krylov–Schur algorithm for large eigenproblems, SIAM J. Matrix Anal. Appl. **23**, 601 (2002).

[59] C. Brezinski, Some pioneers of extrapolation methods, in *The Birth of Numerical Analysis* (World Scientific, Singapoire, 2010), pp. 1–22.

[60] L. F. Richardson, IX. The approximate arithmetical solution by finite differences of physical problems involving differential equations, with an application to the stresses in a masonry dam, Philos. Trans. R. Soc. London, Ser. A **210**, 307 (1911).

[61] L. F. Richardson and J. A. Gaunt, VIII. The deferred approach to the limit, Philos. Trans. R. Soc. London, Ser. A **226**, 299 (1927).

[62] A. Pedersen, J.-C. Berthet, and H. Jónsson, Simulated annealing with coarse graining and distributed computing, in *Applied Parallel and Scientific Computing*, edited by K. Jónasson (Springer, Berlin, 2012), pp. 34–44.

[63] S. T. Chill, M. Welborn, R. Terrell, L. Zhang, J.-C. Berthet, A. Pedersen, H. Jónsson, and G. Henkelman, Eon: Software for long time simulations of atomic scale systems, Modell. Simul. Mater. Sci. Eng. **22**, 055002 (2014).

[64] O. Eriksson, A. Bergman, L. Bergqvist, and J. Hellsvik, *Atomistic Spin Dynamics: Foundations and Applications* (Oxford University Press, Oxford, 2017).

[65] Q. Xu, I. P. Miranda, M. Pereiro, F. N. Rybakov, D. Thonig, E. Sjöqvist, P. F. Bessarab, A. Bergman, O. Eriksson, P. Herman, and A. Delin, Metaheuristic conditional neural network for harvesting skyrmionic metastable states, Phys. Rev. Res. **5**, 043199 (2023).

[66] F. Zheng, F. N. Rybakov, A. B. Borisov, D. Song, S. Wang, Z.-A. Li, H. Du, N. S. Kiselev, J. Caron, A. Kovács, M. Tian, Y. Zhang, S. Blügel, and R. E. Dunin-Borkowski, Experimental observation of chiral magnetic bobbers in b20-type fege, Nat. Nanotechnol. **13**, 451 (2018).

[67] J. W. Cooley and J. W. Tukey, An algorithm for the machine calculation of complex fourier series, Math. Comput. **19**, 297 (1965).

[68] N. Hayashi, K. Saito, and Y. Nakatani, Calculation of demagnetizing field distribution based on fast fourier transform of convolution, Jpn. J. Appl. Phys. **35**, 6065 (1996).

[69] H. J. G. Draaisma and W. J. M. de Jonge, Surface and volume anisotropy from dipole-dipole interactions in ultrathin ferromagnetic films, J. Appl. Phys. **64**, 3610 (1988).

[70] V. L. Zhang, C. G. Hou, K. Di, H. S. Lim, S. C. Ng, S. D. Pollard, H. Yang, and M. H. Kuok, Eigenmodes of néel skyrmions in ultrathin magnetic films, AIP Adv. **7**, 055212 (2017).

[71] L. Desplat, D. Suess, J.-V. Kim, and R. L. Stamps, Thermal stability of metastable magnetic skyrmions: Entropic narrowing and significance of internal eigenmodes, Phys. Rev. B **98**, 134407 (2018).

[72] S. von Malottki, P. F. Bessarab, S. Haldar, A. Delin, and S. Heinze, Skyrmion lifetime in ultrathin films, Phys. Rev. B **99**, 060409(R) (2019).

[73] See Supplemental Material at http://link.aps.org/supplemental/10.1103/z673-hhnp for details of the calculations illustrating the breakdown of the skyrmion escape mechanism.

[74] V. M. Kuchkin, N. S. Kiselev, A. Haller, I. C. V. Liščák, A. Michels, and T. L. Schmidt, Stability and nucleation of dipole strings in uniaxial chiral magnets, Phys. Rev. B **111**, 174410 (2025).

[75] G. P. Müller, M. Hoffmann, C. Dißelkamp, D. Schürhoff, S. Mavros, M. Sallermann, N. S. Kiselev, H. Jónsson, and S. Blügel, Spirit: Multifunctional framework for atomistic spin simulations, Phys. Rev. B **99**, 224414 (2019).

[76] V. Ásgeirsson, B. O. Birgisson, R. Bjornsson, U. Becker, F. Neese, C. Riplinger, and H. Jónsson, Nudged elastic band method for molecular reactions using energy-weighted springs combined with eigenvector following, J. Chem. Theory Comput. **17**, 4929 (2021).

[77] G. Fiedler, J. Fidler, J. Lee, T. Schrefl, R. L. Stamps, H. B. Braun, and D. Suess, Direct calculation of the attempt frequency of magnetic structures using the finite element method, J. Appl. Phys. **111**, 093917 (2012).

# Supplemental Material: Identification of mechanisms of magnetic transitions using an efficient method for converging on first order saddle points

Hendrik Schrautzer,[1,*] Moritz Sallermann,[1,2,3,*] Pavel F. Bessarab,[1,4,†] and Hannes Jónsson[1]

[1] *Science Institute and Faculty of Physical Sciences, University of Iceland, VR-III, 107 Reykjavík, Iceland*
[2] *Peter Grünberg Institut and Institute for Advanced Simulation, Forschungszentrum Jülich and JARA, 52425 Jülich, Germany*
[3] *Department of Physics, RWTH Aachen University, 52056 Aachen, Germany*
[4] *Department of Physics and Electrical Engineering, Linnaeus University, SE-39231 Kalmar, Sweden*

Figure S1 shows the magnetic configurations corresponding to saddle points (SPs) and their adjacent energy minima for two sets of magnetic interaction parameters, obtained using the geodesic minimum mode following (GMMF) method. For $B = 3.1$ T and $D = 0.55$ meV, the GMMF method converges to $\mathrm{SP_{esc}}$, which corresponds to a droplet-like deformed skyrmion attached to the system boundary [see Fig. S1(a)]. The adjacent energy minima correspond to the isolated skyrmion [see Fig. S1(b)] and the ferromagnetic (FM) state [see Fig. S1(c)], confirming the presence of the skyrmion escape mechanism.

For $B = 3.1$ T and $D = 0.6$ meV, which lies outside of the domain for $\mathrm{SP_{esc}}$ [see Fig. 10(c) of the main text], the GMMF method initialized with the SP found for $D = 0.55$ meV converges to an SP which is significantly different from $\mathrm{SP_{esc}}$ [see Fig. S1(d)]. This SP does not represent skyrmion escape as the adjacent local minima do not correspond to either an isolated skyrmion or the FM state [see Figs. S1(e)-S1(f)].

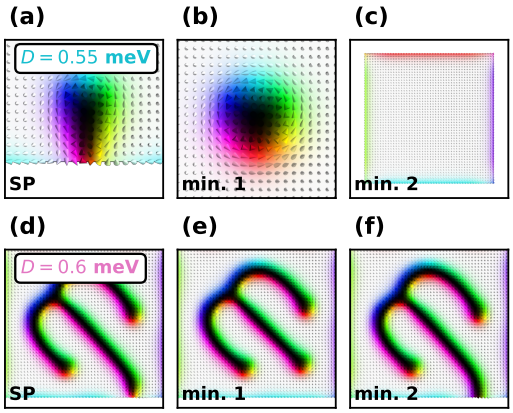


FIG. S1. (a)-(c): $\mathrm{SP_{esc}}$ and adjacent energy minima configurations for $B = 3.1$ T and $D = 0.55$ meV, obtained using the GMMF method. (d)-(f): Saddle point and adjacent energy minima configurations for $B = 3.1$ T and $D = 0.6$ meV, obtained using the GMMF method initialized with the $\mathrm{SP_{esc}}$ found at $D = 0.55$ meV.

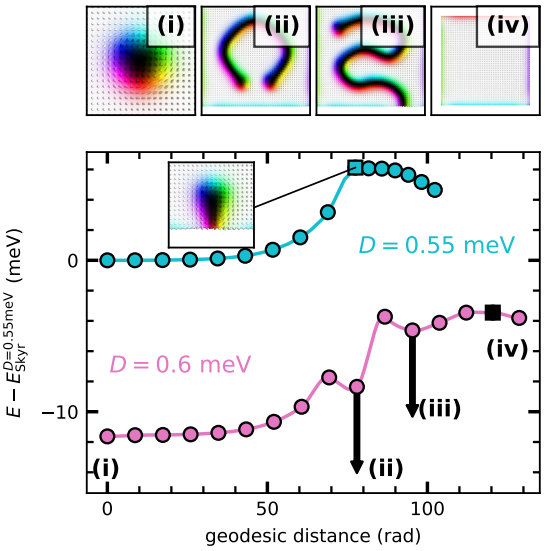


FIG. S2. Results of GNEB calculations for skyrmion escape through the system boundary. The energy variation along the converged MEP for $B = 3.1$ T and $D = 0.55$ meV, and along the partially converged MEP for $B = 3.1$ T and $D = 0.6$ meV, is shown by the cyan and pink lines, respectively. The insets show the isolated skyrmion state (i), the ferromagnetic state (iv), and two metastable configurations obtained by minimizing the energy of configurations near the intermediate minima along the partially converged MEP (ii), (iii).

The breakdown of the escape mechanism with increasing Dzyaloshinskii-Moriya interaction is further illustrated by additional minimum energy path (MEP) calculations using the geodesic nudged elastic band (GNEB) method. For $B = 3.1$ T and $D = 0.55$ meV, the GNEB method yields the MEP for skyrmion escape [see the cyan curve in Fig. S2]. The energy maximum, obtained using the climbing image technique, corresponds to an SP configuration [see the inset in Fig. S2] that matches the one

* These authors contributed equally to this work.
† Corresponding author: pavel.bessarab@lnu.se

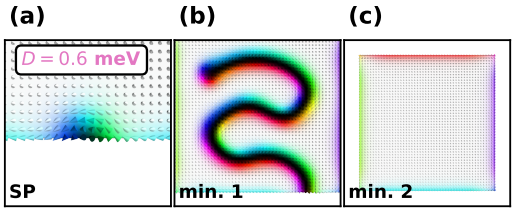


FIG. S3. (a)-(c): Saddle point and adjacent energy minima configurations for $B = 3.1$ T and $D = 0.6$ meV, obtained using the GMMF method initialized with the highest energy configuration along the partially converged MEP in Fig. S2.

obtained using the GMMF method [see Fig. S1(a)].

When this MEP is used as the initial path for the GNEB method for $B = 3.1$ T and $D = 0.6$ meV, the calculation does not converge to an MEP describing a direct transition between the skyrmion and FM states via the escape mechanism. Instead, intermediate minima form along the path during the calculation [see the pink curve in Fig. S2]. Energy minimization of the images near these minima yields metastable elongated skyrmionic textures influenced by the system boundaries [see insets (ii) and (iii) in Fig. S2]. Notably, the isolated skyrmion in the interior of the system [inset (i)] remains metastable at $D = 0.6$ meV, and its radial collapse is still possible. However, direct escape is no longer accessible; Instead, the skyrmion elongates as it approaches the system boundary.

An SP configuration resembling that of skyrmion escape is nevertheless present for $D = 0.6$ meV [see Fig. S3(a)]. It can be obtained using the GMMF method initialized with the highest-energy image along the partially converged MEP [see the black square on the pink curve in Fig. S2]. However, this SP does not connect the FM state with the skyrmion state directly, but rather via the intermediate metastable state shown in inset (iii) of Fig. S2, as confirmed by computing adjacent energy minima [see Figs. S3(b)-S3(c)].

# Paper III

**Impact of higher-order exchange on the lifetime of skyrmions and antiskyrmions**

H. Schrautzer, M. A. Goerzen, B. Beyer, S. Haldar, P.F. Bessarab, S. Heinze

npj Computational Materials (submitted), preprint: arXiv:2511.05278

Hendrik performed the calculations, prepared the figures, implemented the method together with M. Goerzen and B. Beyer and wrote the article together with all authors.

# Impact of higher-order exchange on the lifetime of skyrmions and antiskyrmions

Hendrik Schrautzer,[1,*] Moritz A. Goerzen,[2,3,*] Bjarne Beyer,[3]
Soumyajyoti Haldar,[3] Pavel F. Bessarab,[1,4] and Stefan Heinze[3,5,†]

[1] *Science Institute and Faculty of Physical Sciences, University of Iceland, VR-III, 107 Reykjavík, Iceland*
[2] *CEMES, Université de Toulouse, CNRS, 29 rue Jeanne Marvig, F-31055 Toulouse, France*
[3] *Institut für Theoretische Physik und Astrophysik, Christian-Albrechts-Universität zu Kiel, D-24098 Kiel, Germany*
[4] *Department of Physics and Electrical Engineering, Linnaeus University, SE-39231 Kalmar, Sweden*
[5] *Kiel Nano, Surface, and Interface Science (KiNSIS), University of Kiel, Germany*

(Dated: November 10, 2025)

Reliable control of skyrmion lifetime is essential for realizing spintronic devices, yet the role of higher-order exchange – which can lead to skyrmion stabilization – remains largely unexplored. Here we calculate lifetimes of isolated skyrmions and antiskyrmions at transition-metal interfaces based on an atomistic spin model that includes all fourth-order exchange terms. Within harmonic transition-state theory, we evaluate both energetic and entropic contributions and find substantially enhanced lifetimes when higher-order exchange is included. The four-spin four-site interaction raises the energy barrier and lowers the curvature of the energy landscape at the collapse saddle point, increasing the pre-exponential factor. We show that skyrmions and antiskyrmions can remain thermally stable even without Dzyaloshinskii–Moriya interaction (DMI), and that tuning the four-spin term by a small amount modulates the prefactor over orders of magnitude. Our results identify higher-order exchange as a promising route to stabilize topological magnetic textures – in particular in systems lacking DMI – and to engineer their thermally activated decay.

## Introduction

Magnetic skyrmions [1] and antiskyrmions [2] are nanoscale, topologically non-trivial magnetic textures [3] that have garnered intense interest for their potential use in future spintronic technologies. Their small size, metastability, and efficient current-driven motion [4–8] make them attractive candidates for information storage [9], logic devices, and neuromorphic computing architectures [10–12]. These magnetic textures have been observed in various systems, including non-centrosymmetric bulk magnets [13, 14], ultrathin transition-metal films [15–18], multilayers [19–21], and two-dimensional (2D) van der Waals magnets [22–31]. A key mechanism enabling their stabilization is the Dzyaloshinskii-Moriya interaction (DMI) [32, 33], which emerges from spin-orbit coupling in systems with broken inversion symmetry such as surfaces [34]. In addition to DMI, frustrated Heisenberg exchange interactions – arising from competing ferromagnetic and antiferromagnetic couplings beyond nearest neighbors – have been shown to stabilize isolated skyrmions [35–39] and antiskyrmions [40] even in the absence of DMI.

Recently, higher-order exchange interactions (HOI) have come into focus as another interaction influencing skyrmion stability [15, 30, 31, 41]. These exchange interactions, which couple more than two spins, can affect the magnetic ground-state of the system [42]. They can be important for magnetic insulators [43, 44] but also for itinerant magnets [42, 45, 46] and can lead to complex spin structures as observed experimentally [15, 47–51]. Extending the pairwise Heisenberg model within perturbation theory [52–54] gives rise to higher-order energy contributions. In this work, we focus on the fourth-order HOI term:

$$E_{\text{4-spin}} = -\sum_{ijkl} C_{ijkl}(\mathbf{m}_i \cdot \mathbf{m}_j)(\mathbf{m}_k \cdot \mathbf{m}_l) \ , \qquad (1)$$

including up to four different magnetic moments $\mathbf{m}_i$ (4-spin) of the system. However, if $i = k$ and $j = l$, effectively only two lattice sites (2-site) are contributing to the so called biquadratic or 4-spin-2-site interaction. Similar 4-spin-3-site and 4-spin-4-site terms have been discussed [54]. In this work these are referred to as the biquadratic, the 3-site and the 4-site HOI terms.

A critical challenge in information technologies based on magnetic textures is ensuring the stability of these nanoscale bits against thermal fluctuations and thus maximizing their lifetime $\tau$ given by the Arrhenius law [55–57]:

$$\tau^{-1} = \nu_0 \mathrm{e}^{-\beta \Delta E} \ , \qquad (2)$$

where $\beta = 1/(k_{\mathrm{B}}T)$ with the temperature $T$. This does not only include maximizing the corresponding energy barrier $\Delta E$. It has been shown that entropic and dynamic contributions – incorporated in the pre-exponential factor $\nu_0$ – can significantly affect the lifetime, leading to differences of several orders of magnitude even for systems with similar energy barriers [55, 58–60].

The role of HOI in stabilizing skyrmions and antiskyrmions has only recently been appreciated. In particular, it has been demonstrated that the 4-site interaction can significantly alter the energy landscape enhanc-

* These authors contributed equally to this work.
† Corresponding author: heinze@physik.uni-kiel.de

ing the energy barrier of topological spin structures [41]. However, despite the importance of the entropic and dynamic contributions to lifetimes of magnetic textures, the effect of HOI on the pre-exponential factor – essential to quantify the stability of metastable spin states via their lifetime – has not been investigated yet.

In this work, we present the development of a general computational framework for lifetime calculations of topological spin states based on transition-state theory including higher-order exchange interactions and we use it to study lifetimes of skyrmions and antiskyrmions in ultrathin films. An efficient implementation of HOI enables us to investigate how it modifies the curvature of the energy landscape and thereby affects entropic contribution to the stability of magnetic textures. We apply our approach to study topological spin states in the famous ultrathin film system Pd/Fe/Ir(111), in which isolated skyrmions have been experimentally first observed [16, 18, 58], and the related system Pd/Fe/Rh(111), in which nanoscale skyrmions have been predicted based on first-principles calculations [61].

Using harmonic transition-state theory and an atomistic spin model parameterized via density functional theory (DFT), we quantify the impact of HOI on the lifetimes of isolated skyrmions and antiskyrmions. We show that the pre-exponential factor in the Arrhenius law can be modified by orders of magnitude for small changes of the four-site four spin interaction within the range of typical values. Our findings highlight the potential role of HOI in determining the thermal robustness of topological spin textures and provide key insights for designing stable, nanoscale magnetic bits for device applications. This is especially interesting in light of the advent of defect-free 2D van-der-Waals magnets, which often exhibit inversion symmetry in their structure and therefore lack DMI but may exhibit significant HOI.

## Results

**Atomistic spin simulations.** We investigate the stability of skyrmions (Fig. 1a) and antiskyrmions (inset of Fig. 1d) in fcc-Pd/Fe/Ir(111) and fcc-Pd/Fe/Rh(111) using an atomistic spin model parameterized via DFT calculations (see Supplementary Note 1). Note, that fcc indicates the stacking order of the Pd overlayer. In this spin model, the magnetic moments are represented as classical unit vectors $\mathbf{m}_i$ located on each site $i$ of a 2D hexagonal lattice. The total energy of a magnetic configuration is given by the Hamiltonian

$$\begin{aligned} H = &- \sum_{i,j} J_{ij}(\mathbf{m}_i \cdot \mathbf{m}_j) - \sum_{i,j} \mathbf{D}_{ij} \cdot (\mathbf{m}_i \times \mathbf{m}_j) - K_\mathrm{u} \sum_i (\mathbf{m}_i \cdot \hat{\mathbf{e}}_z)^2 - \mu \sum_i \mathbf{m}_i \cdot \mathbf{B}_\mathrm{ext} - \sum_{ij} B_{ij}(\mathbf{m}_i \cdot \mathbf{m}_j)^2 \\ &- 2 \sum_{ijk} Y_{ijk}(\mathbf{m}_i \cdot \mathbf{m}_j)(\mathbf{m}_i \cdot \mathbf{m}_k) - \sum_{ijkl} K_{ijkl} \big[ (\mathbf{m}_i \cdot \mathbf{m}_j)(\mathbf{m}_k \cdot \mathbf{m}_l) + (\mathbf{m}_i \cdot \mathbf{m}_l)(\mathbf{m}_j \cdot \mathbf{m}_k) - (\mathbf{m}_i \cdot \mathbf{m}_k)(\mathbf{m}_j \cdot \mathbf{m}_l) \big] \end{aligned} \tag{3}$$

including Heisenberg exchange, DMI, uniaxial magnetic anisotropy, Zeeman interaction as well as biquadratic, 3-site and 4-site HOI. The interaction strengths are given by $J_{ij}$, $\mathbf{D}_{ij}$, $K_u$, $\mathbf{B}_\mathrm{ext}$, $B_{ij}$, $Y_{ijk}$ and $K_{ijkl}$ respectively. The vector $\mathbf{D}_{ij}$ is aligned perpendicular to the connection line of the sites $i$ and $j$ within the plane of the magnetic film. Together with the isotropic $J_{ij}$ the shell resolved interactions strengths have been included for up to 11 shells of neighbors. The magnetic anisotropy is treated in uniaxial approximation with the easy axis perpendicular to the film surface ($\hat{\mathbf{e}}_z$). The external magnetic field is denoted by the component perpendicular to the film surface $\mathbf{B}_\mathrm{ext} = B_\perp \hat{\mathbf{e}}_z$.

The summation of the HOI (Eq. (1)) covers double counting of indices $i, j, k, l$, respectively leading to three distinguished terms – the biquadratic, 3-site and 4-site exchange – restricted to shortest distances between magnetic moments on the hexagonal lattice, which is why we refer to the constants as $B_1$, $Y_1$, $K_1$ in the following, i.e. using the same notation as in Ref. [41]. For a plaquette of four magnetic moments $\mathbf{m}_i, \mathbf{m}_j, \mathbf{m}_k, \mathbf{m}_l$ these interactions are illustrated in Fig. 1a. Here, a straight line between two magnetic moments $\mathbf{m}_i$ and $\mathbf{m}_j$ symbolizes a direct dot-product $\mathbf{m}_i \cdot \mathbf{m}_j$, while a curved connection between two of such pairs represents a product of these pairs. See for example the top sketch for the 4-site HOI in Fig. 1b representing the term $(\mathbf{m}_i \cdot \mathbf{m}_j)(\mathbf{m}_l \cdot \mathbf{m}_k)$ and refer also to Ref. [54]. General fourth-order HOI (Eq. (1)) include up to four different atomic sites $i$,$j$,$k$,$l$. Thus, any specific HOI term can be uniquely identified through an array of six distances between the four sites:

$$d = [d_{ij}, d_{ik}, d_{il}, d_{jk}, d_{jl}, d_{kl}] \,, \tag{4}$$

where the distances are encoded in units of the $n$-th nearest neighbor distance. The unique identifier of the 4-site HOI term is for example given by $d = [1, 1, 1, 1, 2, 1]$ meaning that all sites are in nearest neighbor distance to each other except the sites $j$ and $l$, which are in second nearest neighbor distance (cf. Fig. 1b). We imple-

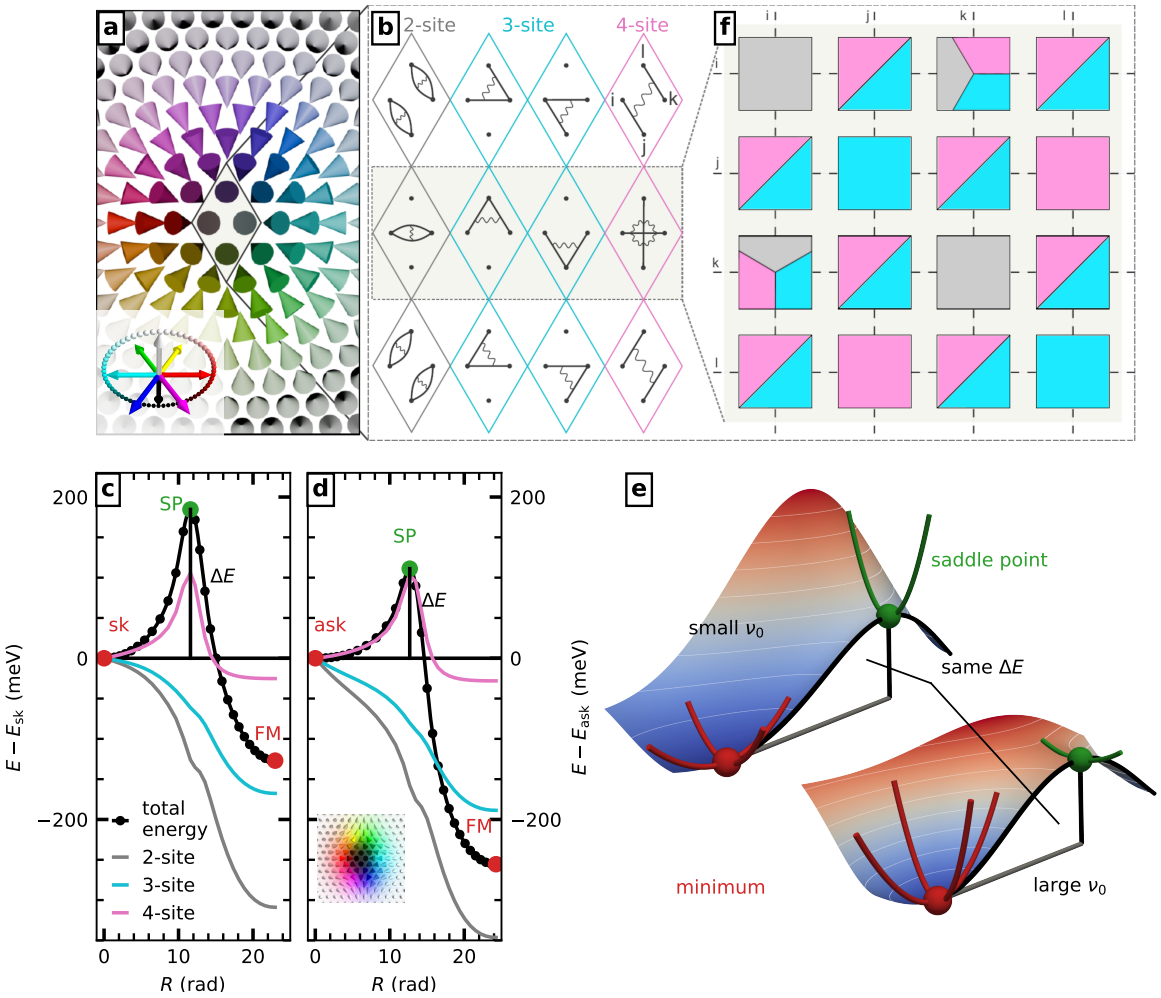


Figure 1. **Higher-order exchange interactions and harmonic transition state theory**. **a** Meta-stable skyrmion at $B_\perp - B_C = 3.95$ T in fcc-Pd/Fe/Ir(111) including higher-order exchange interactions (HOI). The color-code for the orientation of magnetic moments used in this work is shown in the lower-left corner. **b** The interactions of magnetic moments due to the biquadratic (2-site, gray), the 3-site (cyan) and the 4-site (pink) HOI are schematically depicted by straight lines (products $\mathbf{m}_i \cdot \mathbf{m}_j$) and curved lines (combinations of products) (see Eq. (3)). **c,d** Total energy including all terms in Eq. (3) (black) and HOI energy contributions (gray, cyan, pink) to the total energy as a function of the geodesic distance $R$ along the minimum energy path (MEP) of a skyrmion (**c**) and antiskyrmion annihilation (**d**) at $B_\perp - B_C = 3.95$ T. The minima (saddle points (SPs)) are visualized by red (green) circles and the energy barrier is depicted by a vertical black line. **e** Schematic two-dimensional energy landscapes with low curvature at the minimum (red) and large curvature at the SP (green) in the upper left corner and vice versa in the lower right corner. **f** Schematic adjacency pattern for a sub-matrix of the matrix of second-order derivatives for four magnetic moments ($\mathbf{m}_i$, $\mathbf{m}_j$, $\mathbf{m}_k$, $\mathbf{m}_l$) in nearest neighbor distance of each other. For the mid row of panel **b** chosen as an example, each block is colored according to the specific HOI term contributing to its values.

mented an efficient and general pre-processing routine automatically finding the contributing sites for a given HOI identifier (see "Methods"). The identifiers for the biquadratic, 3-site and 4-site HOI discussed in this work contain mostly nearest neighbor distances. However, the implementations are valid for any combination and distance of four magnetic moments and apply to any lattice model, even three-dimensional ones [62].

To quantify the role of HOI, we compare two models previously used in Ref. [41]: one including HOI and one

neglecting HOI. The interaction parameters for the latter model were obtained by DFT total energy calculations conducted in Ref. [63] for the ultrathin film system fcc-Pd/Fe/Ir(111) and in Ref. [61] for fcc-Pd/Fe/Rh(111). The HOI parameters ($B_1$, $Y_1$, $K_1$) were calculated in Ref. [41]. Note, that the extension of HOI modifies the first three Heisenberg exchange parameters $J_1, J_2$ and $J_3$.

Above the critical magnetic field, $B_C$, the ferromagnetic (FM) alignment of magnetic moments corresponds to the ground state of the system. For fcc-Pd/Fe/Ir(111) these values are $B_C = 2.75$ T [41] for the model considering HOI explicitly and $B_C = 3.17$ T [37] for the model neglecting HOI (see Supplementary Note 2 for values of fcc-Pd/Fe/Rh(111)). We focus on the field regime $B_\perp \geq B_C$, where isolated skyrmions and antiskyrmions are meta-stable with respect to the FM state. Such a skyrmion (antiskyrmion) at a field of $B_\perp - B_C = 3.95$ T is visualized in Fig. 1a (inset of Fig. 1d).

**Higher order exchange interactions in lifetime calculations.** Harmonic transition-state theory (HTST) provides a framework for definite calculations of average lifetime (Eq. (2)) of meta-stable magnetic configurations subject to thermal fluctuations. The Hamiltonian given in Eq. (3) defines the material-specific energy surface for magnetic textures – such as skyrmions, antiskyrmions, and the FM state – and allows for the computation of minimum energy paths (MEP) between them. Such a path exhibits a first-order saddle point (SP), which is the configuration with the highest energy along the MEP and yields the energy barrier for a particular transition:

$$\Delta E = E_{\mathrm{SP}} - E_{\mathrm{min}} \tag{5}$$

such as the annihilation of a skyrmion or antiskyrmion into the FM state. Fig. 1c (Fig. 1d) shows the total energy – composed of all terms of Eq. (3) – along the MEP of the skyrmion (antiskyrmion) annihilation at $B_\perp - B_C = 3.95$ T when explicitly considering HOI. The contribution of the biquadratic, 3-site and 4-site HOI to the total energy along the MEP is also shown in Fig. 1c,d. It can be seen that the 4-site HOI term plays a prominent role in increasing the barrier for both skyrmions and antiskyrmions.

Until now, studies on the role of HOI in the metastability of skyrmions and antiskyrmions have focused on their effect on the energy barrier alone [41, 64] while neglecting entropic stabilization or destabilization effects included in the pre-exponential factor of the Arrhenius law (Eq. (2)). This term reads [55–57, 65]:

$$\nu_0 = \frac{\lambda}{\sqrt{2\pi\beta}} \mathrm{e}^{\Delta\mathcal{S}/k_{\mathrm{B}}} \ , \tag{6}$$

where $\lambda$ describes the dynamical contribution [56], and $\Delta\mathcal{S} = \mathcal{S}^{\mathrm{SP}} - \mathcal{S}^{\mathrm{min}}$ is the relevant entropy difference between the transition state and the minimum. The $2N$ degrees of freedom of the system with $N$ magnetic moments are treated within harmonic approximation except the unstable mode at the SP and the contribution of possible zero modes:

$$\frac{\Delta\mathcal{S}}{k_{\mathrm{B}}} = \ln\left[\frac{V^{\mathrm{SP}}}{V^{\mathrm{min}}}\left(\frac{2\pi}{\beta}\right)^{\frac{\Delta Z}{2}} \frac{\prod_{k=1+Z^{\mathrm{min}}}^{2N}\sqrt{\epsilon_k^{\mathrm{min}}}}{\prod_{k=2+Z^{\mathrm{SP}}}^{2N}\sqrt{\epsilon_k^{\mathrm{SP}}}}\right] \ , \tag{7}$$

where $\epsilon_k^{\mathrm{min/SP}}$ are the eigenvalues of the Hessian of the energy reflecting the curvature of the energy surface at the critical points. An unequal number of zero modes at the minimum ($Z^{\mathrm{min}}$) and the SP ($Z^{\mathrm{SP}}$), with volumes $V^{\mathrm{min}}$ and $V^{\mathrm{SP}}$, yields an explicit temperature dependence with $\Delta Z = Z^{\mathrm{min}} - Z^{\mathrm{SP}} - 1$ for the pre-exponential factor of skyrmions and antiskyrmions (see "Methods"). Note, that the true entropy difference $\Delta\mathcal{S}'$, which arises from free energy $\mathcal{F}$ of a canonical ensemble by $\mathcal{S}' = -\partial\mathcal{F}/\partial T$, relates to the numerically relevant entropy by $\Delta\mathcal{S}' = \Delta\mathcal{S} + k_{\mathrm{B}}\Delta Z/2$.

The effect of the curvatures $\epsilon_k^{\mathrm{min/SP}}$ on the lifetime of a metastable state is schematically illustrated in Fig. 1d, where two-dimensional energy landscapes are shown with identical energy differences between a minimum and an SP, but different shape of the energy surface around them. A flat minimum combined with a sharply curved energy landscape at the SP corresponds to a large entropy barrier and yields a small $\nu_0$, leading to a longer lifetime in such a situation. Conversely, a sharply curved energy landscape at the minimum and a less curved energy landscape at the SP increase $\nu_0$, reducing the lifetime. Despite its importance, the influence of HOI on the curvature of the energy landscape – and thus on entropy – has not yet been systematically explored.

Similar to bilinear exchange being mediated by isotropic tensors $\underline{\mathrm{J}}_{ij} \in \mathbb{R}^{3\times3}$ the HOI in Eq. (1) can be expressed by isotropic tensors of fourth order $\underline{\mathrm{C}}_{ijkl} \in \mathbb{R}^{3\times3\times3\times3}$, which correspond to an interaction between lattice sites with indices $i, j, k, l$. Due to the multilinearity of HOI the calculation of the second-order derivatives with respect to the components of the magnetic moments comes down to sums of quadratic forms of $\underline{\mathrm{C}}_{ijkl}$ (see "Methods"). Fig. 1f schematically shows a part of the matrix of second-order derivatives associated with the four sites $i$, $j$, $k$ and $l$ depicted in Fig. 1b. Each block in Fig. 1f corresponds to a $(3 \times 3)$-block for the derivatives $\nabla_{ij} E_{4\text{-spin}}$ with respect to the $m_x$, $m_y$ and $m_z$-components of the magnetic moments, respectively. The block colors indicate the contributing HOI terms in Fig. 1b. Note, that only the contributions from the interactions presented in the mid row of Fig. 1b are shown, which already yields a complex pattern of contributions to the displayed sub-matrix. In comparison, bilinear interactions produce a relatively simple off-diagonal pattern of the matrix of second derivatives.

**Lifetime of skyrmions and antiskyrmions.** In this section we discuss numerically obtained observables, including the radius (Fig. 2d), the energy barrier (Fig. 2e), the pre-exponential factor (Fig. 2f) and

the lifetimes (Fig. 2g,h) of skyrmions and antiskyrmions in Pd/Fe/Ir(111) as a function of the magnetic field for two cases: with and without explicit HOI. The radius – obtained through a fit of a theoretical profile [66] to the magnetic texture – increases upon the explicit inclusion of HOI (Fig. 2d) but still the skyrmions and antiskyrmions are of the size of few nanometers agreeing well with experimental data [16, 18, 58].

For the energy barrier, pre-exponential factor, and lifetimes, identifying the relevant first-order SP – characteristic of the respective collapse mechanism – is crucial. We compute SPs for annihilations of metastable states for various magnetic fields in the FM phase ($B_\perp > B_C$) using the GMMF method [67] (see "Methods"). When HOI are taken into account explicitly, the skyrmion annihilation proceeds via a Chimera collapse [17, 18] for magnetic fields satisfying $B_\perp - B_C < 2.25$ T. The corresponding SP at a field of $B_\perp - B_C = 1.25$ T is shown in Fig. 2a. At higher magnetic fields, the more commonly observed radial collapse mechanism [37, 60, 68, 69] occurs, as illustrated in Fig. 2b for $B_\perp - B_C = 3.25$ T. This SP can be characterized by four magnetic moments forming a Bloch point-like defect.

Within the explored parameter range, the collapse mechanism of the antiskyrmion corresponds to a radial shrinking of the configuration from the energy minimum (Fig. 2c). The energy barriers for the collapse of the skyrmions and antiskyrmions are shown in Fig. 2e. For comparison, the corresponding barriers obtained in the model neglecting HOI are also included. In agreement with Ref. [41], explicitly considering HOI increases the energy barriers by approximately 100 meV for fcc-Pd/Fe/Ir(111).

To quantify the thermal stability of skyrmions and antiskyrmions at a given temperature $T$ the mean-lifetime $\tau$ is computed using Eq. (2) [69, 70] (see "Methods"). In magnetic systems, the entropic contribution – contained in the pre-exponential factor $\nu_0$ – can vary by several orders of magnitude as a function of the magnetic field [55, 59]. Thus, it is essential to consider this factor explicitly. Fig. 2f shows the pre-exponential factor divided by the temperature as a function of the magnetic field $B_\perp - B_C$. Explicitly including HOI yields pre-exponential factors slightly increased but of the same order of magnitude for skyrmions, and approximately one order of magnitude larger for antiskyrmions, compared to the model neglecting HOI. This consequently has to be related to effects on the curvature of the energy surface, as discussed in the next section. It should be noted that the pre-exponential factor is only shown in the regime $B_\perp - B_C \geq 2.25$ T, where the radial collapse mechanism of the skyrmion is favored (Fig. 2f).

Using HTST considering both the effect of the energy barrier and the entropic contributions contained in the pre-exponential factor in Eq. (2), the mean lifetime of skyrmions (Fig. 2g) and antiskyrmions (Fig. 2h) is evaluated across a range of temperatures and for varying $B_\perp - B_C$. Comparison with the iso-lifetime line corresponding to one-hour in the model where we neglect HOI demonstrates that the explicit consideration of HOI leads to substantially increased thermal stability for both skyrmions and antiskyrmions. While skyrmions remain stable for at least one hour at $T = 50$ K within the considered field range when HOI are included, the temperature must be reduced to $T < 30$ K to achieve comparable stability in the model neglecting HOI. Furthermore, while the antiskyrmions are only stable up to fields of $B_\perp - B_C \approx 2.7$ T without HOI, explicit consideration of HOI yields antiskyrmion lifetimes of at least one hour for temperatures $T \leq 20$ K in the field range of $B_\perp - B_C \approx 3$ T to $B_\perp - B_C \approx 4$ T. Thus, we record a beneficial effect of HOI on the lifetime and robustness of metastable magnetic states in this material. We have performed similar calculations for fcc-Pd/Fe/Rh(111) leading to qualitatively similar results presented in Supplementary Note 2.

**Curvature of the energy surface.** The curvature of the energy surface in the vicinity of stationary points determines the entropic contributions to the lifetime of meta-stable configurations (Eq. (2)) as sketched in Fig. 1d. Here, we explain the increased pre-exponential factor $\nu_0$ when HOI are explicitly included (cf. Fig. 2f), compared to the case in which HOI are neglected. Figs. 3a,b present the eigenvalues of the Hessian of the energy (see Eq. (15)) as functions of the magnetic field $B_\perp - B_C$ for the skyrmion (Fig. 3a) and for the SP (Fig. 3b) associated with skyrmion collapse in the fcc-Pd/Fe/Ir(111) system. For each stationary point, we divide the eigenspectrum into eigenmodes with eigenvalues below and above the boundary of the magnon gap. For the Hamiltonian in Eq. (3) this gap reads:

$$\epsilon_{\mathrm{mag}} = \mu B_\perp + 2K_u \ . \tag{8}$$

Eigenvalues below $\epsilon_{\mathrm{mag}}$ correspond to excitations of the localized magnetic texture in the FM background and are referred to as local part of the eigenspectrum. For the skyrmion, this local spectrum includes two zero modes (translations), a breathing mode, two degenerate elongation modes, and a helicity mode (see "Methods") The eigenvalue spectrum of the skyrmion including HOI closely resembles that of the skyrmion in the model without HOI [55], depicted as dashed gray lines in Fig. 3a. Quantitatively, the eigenvalues of the rotation and elongation modes of the skyrmion shift to lower values when HOI are explicitly included.

Considering HOI explicitly favors the Chimera collapse as the dominant skyrmion annihilation mechanism for $B - B_C \leq 2.25$ T, as shown in Fig. 2e. The Chimera SP features a rotation mode (a zero mode) and a low-curvature seesaw mode. This name was chosen since following this mode leads to a 180°-rotated Chimera SP via a configuration which is very similar to the radial SP and in fact constitutes a second-order SP on the energy landscape. Since HTST requires a clear separation between first- and second-order SPs, calculating the prefactor in

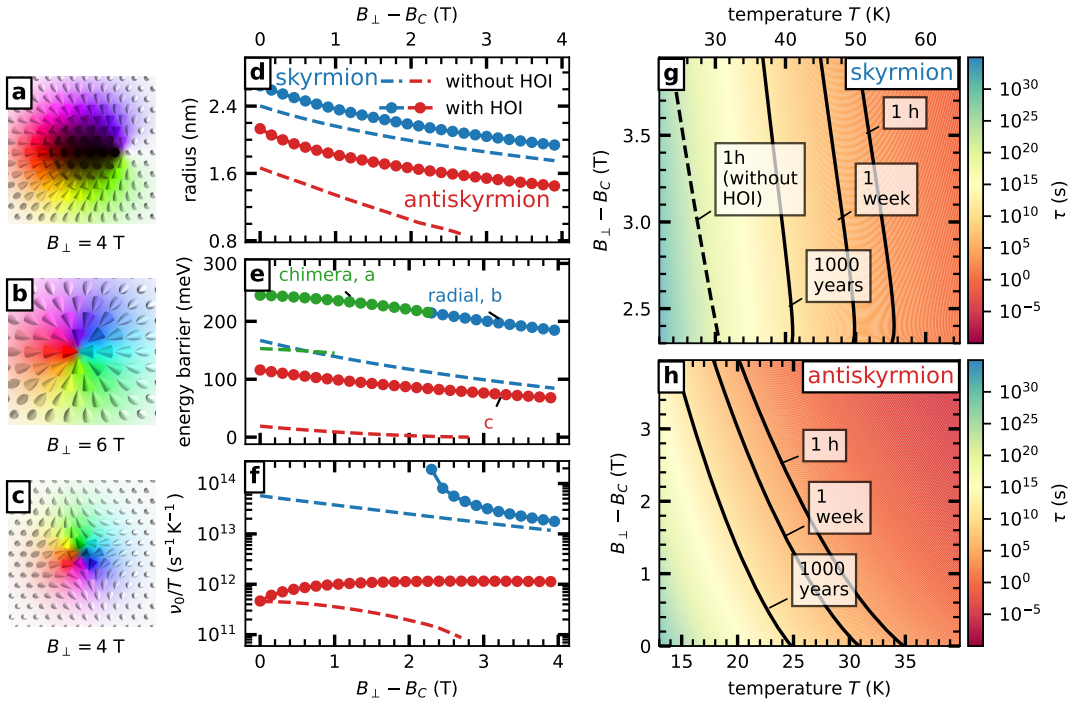


Figure 2. **Effect of higher-order exchange interactions on skyrmion and antiskyrmion lifetime. a,b,c** Saddle point configuration for the collapse of the isolated skyrmion at $B_\perp - B_C = 1.25$ T (**a**) and $B_\perp - B_C = 3.25$ T (**b**) and antiskyrmion at $B_\perp - B_C = 3.25$ T (**c**). **d** Radius of skyrmions (blue) and antiskyrmions (red) in fcc-Pd/Fe/Ir(111) with (solid lines and circles) and without (dashed line) explicitly considering HOI as a function of the magnetic field. The magnetic field is given relative to the field $B_C$ for the onset of the field polarized phase for the respective energy model. **e** Energy barriers associated with the skyrmion and antiskyrmion collapse as a function of the magnetic field with and without (see Ref. [41, 55]) explicitly considering HOI. The field regime where the Chimera collapse of the skyrmion is favoured is colored green. **f** Pre-exponential factor $\nu_0$ in units of temperature $T$ plotted over $B_\perp - B_C$ for skyrmions (blue) in the regime of the radial collapse and antiskyrmions (red) for the energy model considering HOI (circles) and not explicitly taking HOI into account (dashed lines) **g** Mean lifetime $\tau$ (see colorbar) for different magnetic fields and different temperatures for the regime of radial skyrmion collapse. As a reference, the contour line for a lifetime of 1 h for skyrmions without considering HOI explicitly is also given (see Ref. [55]). **h** Mean lifetime of antiskyrmions taking HOI into account.

this regime is technically challenging. We present results for the pre-exponential factor of the Chimera collapse for the case of an applied in-plane magnetic field in Supplementary Note 3, since the main focus of this paper is the effect of HOI on lifetimes and the Chimera collapse has been discussed elsewhere [18].

However, the seesaw mode is also relevant for the radial collapse regime. At $B_\perp - B_C = 2.25$ T, its eigenvalue approaches zero, signaling a flat energy landscape between the Chimera and radial SPs, reminiscent of a second-order phase transition [71]. For higher fields, the radial SP becomes a first-order SP with two non-degenerate seesaw eigenvalues (Fig. 3b). This SP (Fig. 3f) can be characterized by four magnetic moments, placed at the four vertices of a diamond, pointing toward each other. The seesaw eigenmodes act as a deformation of the diamond-like SP configuration (Fig. 3f) into asymmetric states along the diagonals of the diamond (Fig. 3g). Since eigenvalues are directly associated with the curvature of the energy landscape the situation can be visualized by the parabolic energy dependence along the eigenvectors of the two seesaw eigenmodes which is shown in Fig. 3d in blue.

In contrast, neglecting HOI yields degenerate and larger seesaw eigenvalues (Fig. 3b, dashed), consistent with the triangular SP configuration (Fig. 3h) that preserves lattice symmetry and explains the degeneracy (Fig. 3h, gray). Overall, explicit HOI reduce the curvature of the seesaw modes, and also lower the helicity and breathing eigenvalues of the SP associated to the radial collapse, similar to the shifts observed for the skyrmion elongation and helicity modes upon consideration of ex-

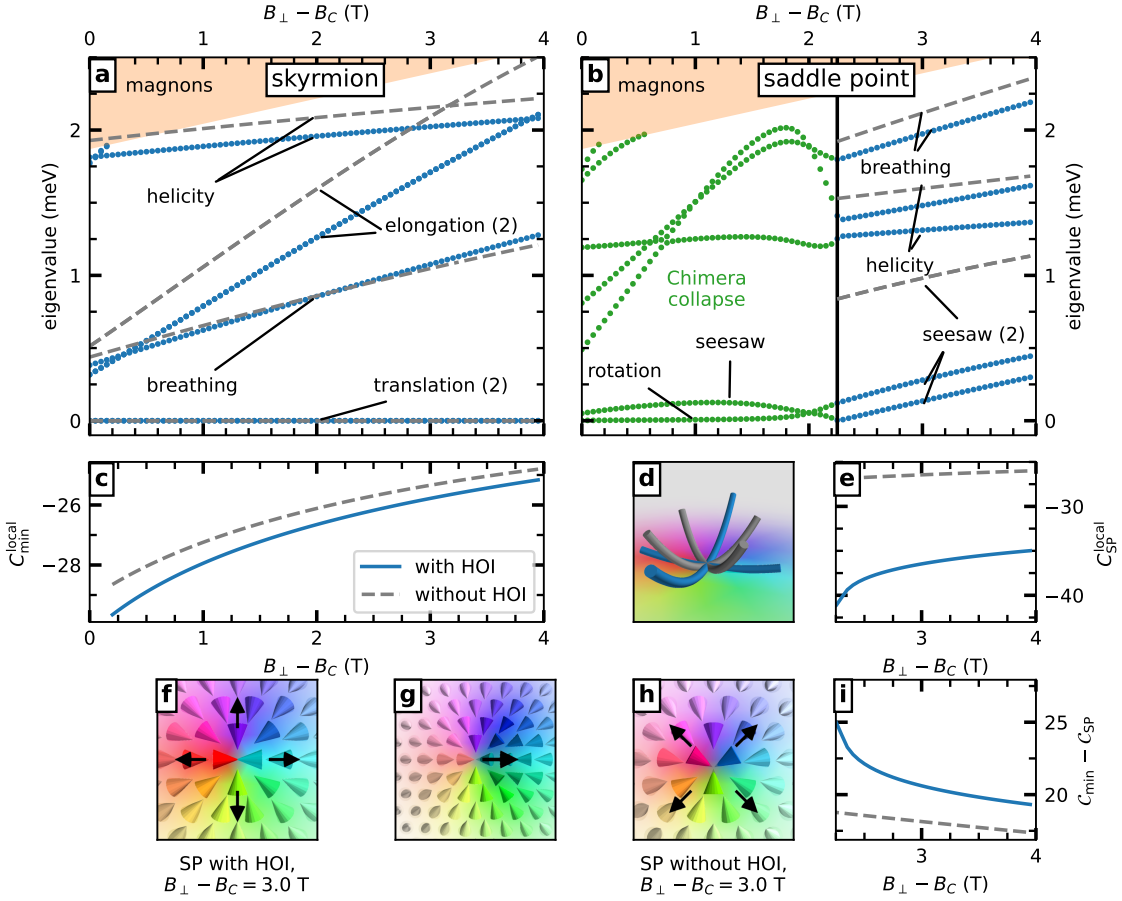


Figure 3. **HOI and curvature of the energy surface for the skyrmion. a,b** Local part of the eigenvalue spectrum of the Hessian matrix of the skyrmion (**a**, blue) and the skyrmion saddle point (SP) (**b**, green and blue) in fcc-Pd/Fe/Ir(111) including HOI as a function of the magnetic field $B_\perp - B_C$. Eigenvalues above the magnon gap are indicated by the orange painted area. For reference the corresponding local eigenvalue spectra in the model without considering HOI explicitly are shown as gray dashed lines. Selected eigenmodes are labeled while the number in brakets gives their multiplicity (see surrounding text). **c,e** Curvature associated with the local eigenvalue spectrum (see Eq. 10)) for the skyrmion (blue, **c**) and the corresponding SP (green and blue, **e**) for the energy model including HOI (solid line). The local curvatures of the SP for the model neglecting HOI are drawn with dashed gray lines. In **e** only the regime of the radial collapse is shown. **d** Energy along the seesaw eigenmodes of the SP including HOI (blue, SP in **f**) and of the SP excluding HOI (gray, SP in **h**). **g** Configuration obtained after displacing the SP in **f** along the indicated direction (black arrow) using the corresponding eigenvector of the seesaw mode. **i** Total curvature difference of the minimum and the SP for the regime of the radial collapse mechanism.

plicit HOI.

We define a measure $\mathcal{C}$ for curvature of the energy landscape at the minimum ($\mathcal{C} = \mathcal{C}_{\mathrm{min}}$) and the SP ($\mathcal{C} = \mathcal{C}_{\mathrm{SP}}$) excluding zero-modes, which are identified below the threshold $\delta_{\mathrm{zero}} = 10^{-12}$ eV, and the unstable mode of the SP with $\epsilon_1^{\mathrm{SP}} < 0$. Further, in order to identify thermodynamically relevant parts of the spectrum, we distinguish into local and magnon contribution, separated by $\epsilon_{\mathrm{mag}}$ from Eq. (8):

$$\mathcal{C} = \mathcal{C}^{\mathrm{local}} + \mathcal{C}^{\mathrm{magnon}} \tag{9}$$

$$\mathcal{C} = \sum_{\delta_{\mathrm{zero}} < \epsilon_k < \epsilon_{\mathrm{mag}}} \ln \frac{\epsilon_k}{\epsilon_0} + \sum_{\epsilon_k \geq \epsilon_{\mathrm{mag}}} \ln \frac{\epsilon_k}{\epsilon_0}\,, \tag{10}$$

where an energy scale $\epsilon_0 = 1$ eV was introduced to ensure dimensionless expressions in the logarithms. This establishes an intuitive connection between curvatures and the

entropy from Eq. (7), which explicitly reads:

$$\frac{\Delta\mathcal{S}}{k_\mathrm{B}} = \frac{\mathcal{C}_\mathrm{min} - \mathcal{C}_\mathrm{SP}}{2} + \ln\left[\frac{V^\mathrm{SP}}{V^\mathrm{min}}\left(\frac{2\pi}{\beta\epsilon_0}\right)^{\frac{\Delta Z}{2}}\right] . \qquad (11)$$

As shown in Fig. 3c,e, the curvature of the local part of the spectrum at the minimum is nearly unaffected by HOI, whereas the local curvature at the SP is strongly reduced due to shift of the seesaw eigenmodes. Since SP curvature enters Eq. (11) with a negative sign, this reduction, caused by HOI, enhances the annihilation rate. Including contributions above the magnon gap (Fig. 3i) reproduces the field dependence of the pre-exponential factor (Fig. 2f). However, it can be seen that the difference between both models is smaller in Fig. 3i than in Fig. 3e. This implies that the curvature contribution of the eigenspectrum above the magnon gap counteracts – but not compensates – the entropic destabilization by the eigenvalues of the local spectrum that are reduced upon explicit consideration of HOI. In Supplementary Note 4 we present a similar discussion for the curvature of the energy surface for the antiskyrmion collapse.

**Tuning the 4-site HOI interaction.** Now we turn to the influence of variations in the 4-site HOI parameter $K_1$ (see Eq. (3)) on the lifetimes of skyrmions (Fig. 4b) and antiskyrmions (Fig. 4d) with respect to thermally activated annihilation into the FM state. Since spin spiral energies are degenerate with respect to the 4-site HOI parameter, the parametrization of the bilinear interaction constants obtained in DFT remains valid even if $K_1$ is varied [41]. This allows us to analyze the role of the 4-site HOI in stabilizing topological magnetic textures. In Ref. [41], a linear dependence of the energy barriers on $K_1$ was reported for both skyrmions and antiskyrmions. Our calculations reproduce this behavior (Fig. 4a,c). While skyrmions remain metastable even for negative $K_1$, the energy barrier for antiskyrmions vanishes as $K_1 \to 0$ meV.

Here, we also compute the pre-exponential factor for skyrmions and antiskyrmions as a function of $K_1$. We find that the pre-exponential factor for antiskyrmions (Fig. 4c) remains nearly constant across the considered range, whereas for skyrmions it decreases by about three orders of magnitude upon reducing $K_1$ (Fig. 4a). The change of pre-exponential factor and energy barrier with strength of the 4-site HOI, leads to opposite effects on the thermal stability of skyrmions. While the increase of the energy barrier with $K_1$ also leads to an enhanced lifetime, the increase of the pre-exponential factor results in a decrease of the lifetime as seen from the Arrhenius law (cf. Eq. (2)). Note that the variation of $K_1$ within the considered range $K_1 \in [-0.75, 2.7]$ meV represents realistic values for the 4-site HOI in transition-metal thin film systems [41, 51, 62, 72].

The lifetime of skyrmions (Fig. 4b) and antiskyrmions (Fig. 4d) changes drastically upon variation of $K_1$. For instance, at $T = 40$ K the predicted lifetime of a skyrmion with $K_1 = 1.0$ meV is about 45 minutes. Increasing $K_1$ by only 0.5 meV extends the lifetime to roughly 18 days. The effect of HOI on the stability is also visible from the increase of the temperature for a given lifetime. For example, a mean lifetime of above one hour is obtained below a temperature of about 30 K for $K_1 = 0$ and increases to above 40 K for a small 4-site four spin term of $K_1 = 1$ meV. For antiskyrmions, we observe a similar trend, however, at overall shorter lifetimes at a given temperature due to the lower energy barriers (Fig. 4c).

**Skyrmions and antiskyrmions without DMI**. Designing systems hosting isolated skyrmions with maximum thermal stability typically requires large DMI constants and/or exchange frustration. In Ref. [41], it was predicted that both skyrmions and antiskyrmions are metastable when HOI are explicitly included, even in the absence of DMI, based on calculations of the energy barriers for their collapse into the FM state. However, thermal stability cannot be deduced from the barrier height alone. In this section, we present the calculated pre-exponential factor in the Arrhenius law and the corresponding mean lifetime for fcc-Pd/Fe/Ir(111), including HOI but neglecting DMI (see Fig. 5). The isolated skyrmion and its topological counterpart, the antiskyrmion, exhibit significant and identical energy barriers for their collapse into the FM state (Fig. 5a) consistent with previous work [41]. The origin of the energy barrier is nearly entirely due to the effect of the 4-site HOI while the exchange frustration contributes only little.

In addition, we quantify the pre-exponential factors and demonstrate that they are also degenerate when DMI is neglected (Fig. 5a). The values obtained for the pre-exponential factor are basically independent of the applied magnetic field and of a similar order of magnitude as previously reported for skyrmions in ultrathin films including DMI [55]. This independence can be related to the skyrmion and antiskyrmion radius (Fig. 5b), which is only changing little upon variation of the applied field. Neglecting DMI leads to a smaller values of the radius of skyrmions and antiskyrmions and to a weaker field-dependence of the size compared to the radius of these textures including DMI (cf. Fig. 2d). Furthermore, the SP configurations corresponding to the annihilation of these textures into the FM state consist of only few magnetic moments forming the Bloch point-like defect and consequently their size also does not change upon variation of the applied field. Since the size and the shape of the configurations of the minima and the SPs change only little, the curvature values of the energy landscape at the stationary points, expressed by the respective eigenvalues of the Hessian, and consequently also the pre-exponential factors show a minor dependence to the applied magnetic field. The corresponding eigenvalue spectra for the skyrmion and antiskyrmion – again degenerate – and the SP when neglecting DMI but explicitly considering HOI are presented in Supplementary Note 5.

Since the pre-exponential factors are the same for skyrmions and antiskyrmions, their mean lifetimes – as obtained from HTST – are also identical (Fig. 5c). Note,

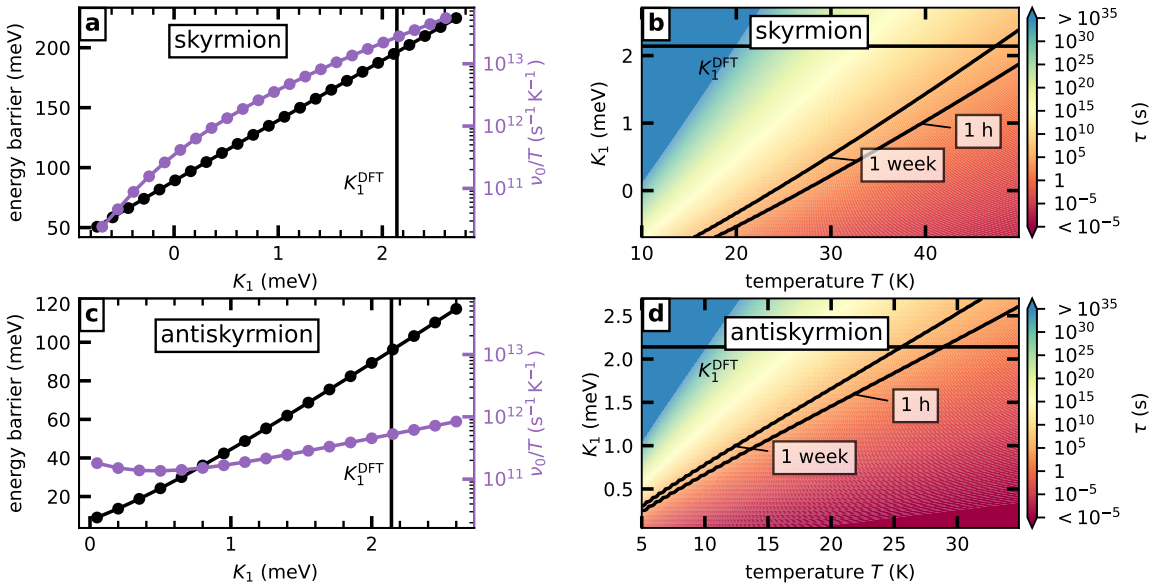


Figure 4. **Lifetimes of skyrmions and antiskyrmions as a function of the 4-site HOI. a**,**b** Energy barrier (black) and pre-exponential factor $\nu_0/T$ (purple) for the skyrmion (**a**) and the antiskyrmion (**b**) annihilation in fcc-Pd/Fe/Ir(111) for a magnetic field of $B_\perp = 6$ T (skyrmions) and $B_\perp = 4$ T (antiskyrmions) as a function of the 4-site HOI $K_1$. The value $K_1^{\mathrm{DFT}}$ corresponds to the one determined in DFT calculations [41]. **b**,**d** Mean lifetime $\tau$ for isolated skyrmions (**b**) and antiskyrmions (**d**) for various temperatures $T$ and values of $K_1$ calculated within HTST. The one-week- and one-hour-isoline of $\tau$ are given as black lines.

that in the case of skyrmions in a Hamiltonian without DMI the helicity mode of the minimum and the SP configuration becomes a zero mode [36, 40] ("Methods"). The results in Fig. 5c indicate that skyrmions and antiskyrmions remain metastable over a broad range of magnetic fields $B_\perp - B_C$, at timescales and temperatures relevant to low temperature STM experiments, even in the absence of DMI.

## Discussion

In this work, we have investigated the effect of higher-order exchange interactions (HOI) on the lifetimes of isolated skyrmions and antiskyrmions in fcc-Pd/Fe/Ir(111) and fcc-Pd/Fe/Rh(111), focusing on their thermally activated annihilation into the FM state. By implementing general fourth-order HOI terms for the energy, gradient and Hessian of the system into our atomistic spin simulations code, we are able to provide a comprehensive, quantitative description of these lifetimes within the framework of HTST. This enables a quantitative description of lifetimes in systems with HOI that goes well beyond simple energy-barrier arguments for the stability of skyrmions and antiskyrmions. Since HOI can play a key role in many materials such as transition-metal interfaces [15, 41, 47, 48, 50, 51, 62] and 2D van der Waals magnets and heterostructures [28–31, 64] our results represent an important step towards realistic stability predictions for topological magnetic textures in these systems.

The enhanced energy barriers observed upon explicitly considering HOI lead to markedly increased lifetimes of skyrmions and antiskyrmion (see Fig. 2e,g,h), which has important implications for the design of robust topological magnetic bits. Furthermore, we report a slight reduction of the stability of skyrmions and antiskyrmions due to changed entropic contributions when including HOI in materials that are subject to our investigation (Fig 2f). We were able to identify the origin of the increased pre-exponential factor for the skyrmion collapse as a reduced curvature of the energy landscape due to the local Hessian eigenvalue spectrum at the SP (see Fig. 3c,e,i). The dynamic contributions to the pre-exponential factor change only little upon considering HOI explicitly.

For both cases – the skyrmion and the antiskyrmion collapse – the HOI terms affect the curvature in the direction of the localized excitations at the SP significantly more than the corresponding curvatures at the minimum. These SP configurations exhibit larger canting angles between adjacent magnetic moments than the minima. Since the contribution of the HOI terms to the energy is strongly affected by strong canting of the mag-

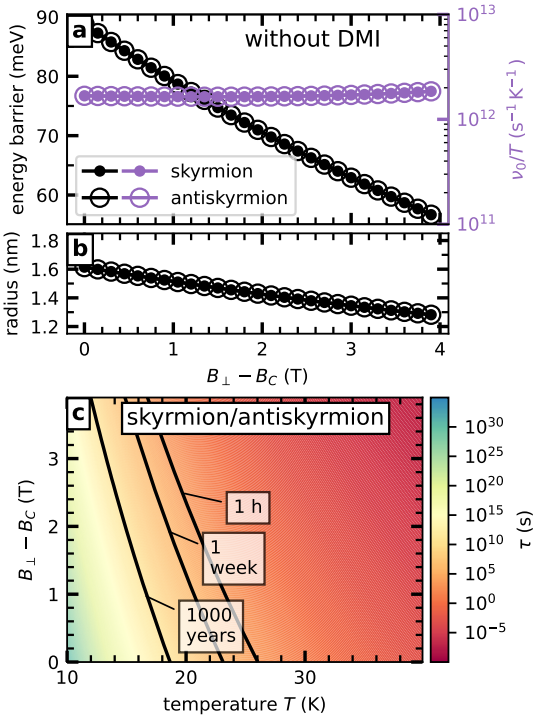


Figure 5. **Skyrmion and antiskyrmion lifetime including HOI and neglecting DMI. a** Energy barriers (black) and pre-exponential factors $\nu_0$ (purple) of skyrmions (filled circles) and antiskyrmions (open circles) in fcc-Pd/Fe/Ir(111) considering HOI and vanishing DMI for varying the magnetic field relative to the critical field $B_\perp - B_C$. **b** Radius of skyrmions and antiskyrmions as a function of the magnetic field. **c**: Mean lifetime $\tau$ (see colorbar) of the above mentioned isolated magnetic textures as a function of the temperature $T$ and the external magnetic field $B_\perp - B_C$.

netization this is likely to be the origin of the pronounced effect of HOI on the energy landscape at the SP. This makes entropic stabilization by HOI, due to increased (decreased) curvature of the energy surface at the SP (minimum), a promising route to engineer skyrmion and antiskyrmion stability. A particularly striking result is the sensitivity of lifetimes to the 4-site interaction parameter $K_1$, which underlines the critical role of HOI in determining skyrmion and antiskyrmion stability. It also suggests that targeted manipulation of $K_1$, for example by material choice or interface engineering, could provide a powerful strategy to design skyrmions with lifetimes tailored for specific experimental or technological applications. Remarkably, our study reveals a strong dependence of the pre-exponential factor on the strength of the 4-site interaction for skyrmions. This suggests that accurate lifetime predictions require full entropic modeling rather than assuming a constant prefactor.

Finally, we also predict that both skyrmions and antiskyrmions remain metastable in the complete absence of DMI – stabilized almost entirely by HOI – at timescales and temperatures relevant to experiments. While switching off the DMI in fcc-Pd/Fe/Ir(111) represents a toy model, our results highlight the potential of HOI as a promising route for designing systems that host topological magnetic textures in materials with inversion symmetry or without heavy transition-metals required for large spin-orbit coupling. These findings are timely, given the recent progress in 2D van der Waals magnets where DMI is often weak or even absent, positioning HOI as a promising stabilization mechanism in future material systems.

## Methods

**Calculation of the pre-exponential factor.** The mean-lifetime $\tau$ for thermally activated annihilation of skyrmions and antiskyrmions into the FM state are computed in this work using the Arrhenius law (Eq. (2)) within the framework of harmonic transition state theory (HTST) [70]. In HTST the transition state for a particular reaction mechanism described by an MEP connecting two minima (skyrmion/antiskyrmion and FM state) is chosen as the hyperplane through a first order SP perpendicular to its unstable mode. This SP is the configuration of highest energy along the MEP. The contributions to the Arrhenius law are, on the one hand, the energy barrier $\Delta E$, which is given as the energy difference of the SP and the energy minimum configuration (see Eq. (5)). On the other hand, the pre-exponential factor $\nu_0$ is given by the entropic and the dynamic contribution $\lambda$ to the transition [56] (Eq. (6)).

Note, that while several formulations exist for the pre-exponential factor [55, 60, 70], Eq. (6) is particularly useful to discuss entropic effects (Eq. (7)). While almost all degrees of freedom are treated in harmonic approximation, translations, rotations or modes changing the helicity of the localized magnetic texture are often better treated in Goldstone mode approximation [40, 55, 69] and their contribution to the entropy then corresponds to the zero mode volume $V$. Additionally, a factor $\rho$ for the multiplicity of identical SP per unit cell [55] is required. In this work, it is either $\rho = 1$ or $\rho = 2$. Supplementary Note 6 presents the values of $\rho$ of the pre-exponential factor calculations of this work. Note, that the helicity degree of freedom of the skyrmion in the HO model neglecting DMI, for which the pre-exponential factor is shown in Fig. 5a, is also a zero mode with volume [40]

$$V_{\text{hel}} = 2\pi \sum_{n=1}^{N} \left[1 - (m_n^z)^2\right] \ . \tag{12}$$

The respective degree of freedom describes the continuous deformation between Néel- and Bloch-type skyrmions, which comes down to a collective rotation of

all spins in the $m_x - m_y$ plane.

**Identification of first order saddle points.** It is essential to identify the corresponding SP in order to calculate the energy barrier and the pre-exponential factor of the skyrmion and antiskyrmion collapse into the FM state. In this work, these SPs are determined by combining the geodesic nudged elastic band method (GNEB) [73] with the recently developed geodesic minimum mode following method (GMMF) [67]. The GNEB method was used to determine the skyrmion or antiskyrmion collapse mechanism and the SP for the maximum magnetic field considered for the specific parameter set ($B_\perp - B_C = 4$ T). Subsequently, the GMMF method was initialized using this SP and the magnetic field was reduced by a small amount of $\Delta B = 0.05$ T.

In contrast to the GNEB method, in which the GNEB force for a series of replicas of the system (path) is minimized, the GMMF method operates on a single magnetic configuration. The GMMF force corresponds to the negative energy gradient where the direction of the gradient is inverted along the direction of the minimum mode of the Hessian of the energy:

$$\mathbf{F}_{\mathrm{GMMF}} = -\nabla E - 2(\nabla E \cdot \mathbf{v}_1)\mathbf{v}_1 \ . \tag{13}$$

This yields a minimization of the energy along all degrees of freedom except one, while the energy is maximized along the direction of the eigenvector $\mathbf{v}_1$ of the minimum mode. If the GMMF method is initialized with a configuration in the vicinity of an SP, it converges to a first order SP within a few iterations. The computational bottleneck is the repeated calculation of the eigenvector of the lowest eigenvalue of the Hessian matrix of the energy of the system.

Recently, we introduced Rayleigh Quotient minimization [67], a method that makes an efficient calculation of the minimum mode feasible and is based on finite difference calculations of the energy gradient without the need for the explicit calculation of the Hessian matrix. The efficient combination of these methods allowed us to calculate the activation energies with a high resolution with respect to the values of the magnetic field with almost negligible computational effort.

**Hessian matrix including HOI.** This section describes the calculation of the Hessian matrix for general fourth-order HOI, which is required to determine the pre-exponential factors of the skyrmion and antiskyrmion collapse. We approximate the energy surface $E(\mathbf{m})$ on the $2N$-dimensional configuration space $\mathbf{m} \in \bigotimes_n^N \mathbb{S}^2$ up to second order in the vicinity of critical points $\mathbf{m}_0$. Since first order terms vanish in these points the series expansions in terms of tangential deflections $\delta\mathbf{m}$ reads

$$E(\mathbf{m}_0, \delta\mathbf{m}) = E(\mathbf{m}_0) + \frac{1}{2}\delta\mathbf{m}^{\mathrm{T}}\mathrm{H}\delta\mathbf{m} + \mathcal{O}(\delta\mathbf{m}^3) \ . \tag{14}$$

Due to the constraint of magnetic moments having fixed length the Hessian $\mathrm{H} \in \mathbb{R}^{2N\times 2N}$ is constrained to the tangent space of the magnetic configuration:

$$\mathrm{H}_{ij} = \mathrm{P}_i(\nabla_{ij}\mathcal{L})\mathrm{P}_j^T \ , \quad \mathcal{L} = E - \sum_{i=1}^{N}(\mathbf{m}_i^2 - 1)\omega_i \tag{15}$$

with the Lagrange function $\mathcal{L}$ and Lagrange multipliers $\omega_i = \mathbf{m}\cdot\nabla_i E/2$. Here $\nabla_i = \frac{\partial}{\partial \mathbf{m}_i}$ is the partial derivative with respect to the coordinates of the magnetic moment $\mathbf{m}_i$ and $\mathrm{P}_i \in \mathbb{R}^{2\times 3}$ is the projection on the tangent space of $\mathbf{m}_i$ [56, 68]. In our setup derivatives of the Lagrange multiplier $\omega_i$ can be omitted, because they describe changes of the energy under variation of the spin length. Thus, they are perpendicular to the manifold associated with configuration space and vanish in the quadratic form of Eq. (14), since they are perpendicular to tangential deflections $\delta\mathbf{m}$.

While bilinear interactions between magnetic moments have been considered extensively in the framework of HTST [40, 55, 56, 60, 69], the novelty of this work is the consideration of HOI (cf. Eq. (1)). Gradients with respect to coordinates of magnetic moments are computed as

$$\nabla_i E_{\text{4-spin}} = -4\sum_{jkl} C_{ijkl}\left(\mathbf{m}_k \cdot \mathbf{m}_l\right)\mathbf{m}_j \ . \tag{16}$$

Similar to bilinear exchange $E_{\mathrm{exc}} \propto \mathbf{m}_i^{\mathrm{T}}\underline{\mathrm{J}}_{ij}\mathbf{m}_j$ being mediated by a tensor $\underline{\mathrm{J}}_{ij} \in \mathbb{R}^{3\times 3}$, HOI are mediated by a tensor $\underline{\mathrm{C}}_{ijkl} \in \mathbb{R}^{3\times 3\times 3\times 3}$. Since both the bilinear exchange as well as HOI are invariant under global rotation of all magnetic moments, and therefore isotropic in configuration space, the HOI tensor can be expressed in the basis of isotropic tensors of fourth-order, which are usually denoted as products of Kronecker $\delta$ symbols

$$\underline{\mathrm{C}}_{ijkl} = C_{ijkl}\delta_{ij}\delta_{kl} \tag{17}$$

with interaction constant $C_{ijkl}$. It is commonly known that this basis contains only two more linearly independent elements, $\delta_{ik}\delta_{jl}$ and $\delta_{il}\delta_{kj}$, which in our case correspond to certain permutations of indices $(i, j, k, l)$. In

matrix form these tensors can be constructed as

$$\delta_{ij}\delta_{kl} = \left[\begin{bmatrix}1&0&0\\0&1&0\\0&0&1\end{bmatrix}\begin{bmatrix}0&0&0\\0&0&0\\0&0&0\end{bmatrix}\begin{bmatrix}0&0&0\\0&0&0\\0&0&0\end{bmatrix}\right.$$
$$\begin{bmatrix}0&0&0\\0&0&0\\0&0&0\end{bmatrix}\begin{bmatrix}1&0&0\\0&1&0\\0&0&1\end{bmatrix}\begin{bmatrix}0&0&0\\0&0&0\\0&0&0\end{bmatrix}$$
$$\left.\begin{bmatrix}0&0&0\\0&0&0\\0&0&0\end{bmatrix}\begin{bmatrix}0&0&0\\0&0&0\\0&0&0\end{bmatrix}\begin{bmatrix}1&0&0\\0&1&0\\0&0&1\end{bmatrix}\right]$$

$$\delta_{ik}\delta_{jl} = \left[\begin{bmatrix}1&0&0\\0&0&0\\0&0&0\end{bmatrix}\begin{bmatrix}0&1&0\\0&0&0\\0&0&0\end{bmatrix}\begin{bmatrix}0&0&1\\0&0&0\\0&0&0\end{bmatrix}\right.$$
$$\begin{bmatrix}0&0&0\\1&0&0\\0&0&0\end{bmatrix}\begin{bmatrix}0&0&0\\0&1&0\\0&0&0\end{bmatrix}\begin{bmatrix}0&0&0\\0&0&1\\0&0&0\end{bmatrix}$$
$$\left.\begin{bmatrix}0&0&0\\0&0&0\\1&0&0\end{bmatrix}\begin{bmatrix}0&0&0\\0&0&0\\0&1&0\end{bmatrix}\begin{bmatrix}0&0&0\\0&0&0\\0&0&1\end{bmatrix}\right] \tag{18}$$

$$\delta_{il}\delta_{kj} = \left[\begin{bmatrix}1&0&0\\0&0&0\\0&0&0\end{bmatrix}\begin{bmatrix}0&0&0\\1&0&0\\0&0&0\end{bmatrix}\begin{bmatrix}0&0&0\\0&0&0\\1&0&0\end{bmatrix}\right.$$
$$\begin{bmatrix}0&1&0\\0&0&0\\0&0&0\end{bmatrix}\begin{bmatrix}0&0&0\\0&1&0\\0&0&0\end{bmatrix}\begin{bmatrix}0&0&0\\0&0&0\\0&1&0\end{bmatrix}$$
$$\left.\begin{bmatrix}0&0&1\\0&0&0\\0&0&0\end{bmatrix}\begin{bmatrix}0&0&0\\0&0&1\\0&0&0\end{bmatrix}\begin{bmatrix}0&0&0\\0&0&0\\0&0&1\end{bmatrix}\right]$$

In this notation the indices $i, j$ address the position of each $3 \times 3$-matrix within the tensors above. The indices $k, j$ address the position of 1 or 0 within these submatrices. Note, that other representations of this basis exist as well. Intuitively, the linearly independent basis elements reflect that some permutations of lattice sites in fourth-order HOI lead to different energies

$$\begin{aligned}(\mathbf{m}_i \cdot \mathbf{m}_j)(\mathbf{m}_k \cdot \mathbf{m}_l) &\neq (\mathbf{m}_i \cdot \mathbf{m}_k)(\mathbf{m}_j \cdot \mathbf{m}_l) \\ &\neq (\mathbf{m}_i \cdot \mathbf{m}_l)(\mathbf{m}_k \cdot \mathbf{m}_j)\end{aligned} \tag{19}$$

while linear dependent permutations leave the energy invariant

$$\begin{aligned}(\mathbf{m}_i \cdot \mathbf{m}_j)(\mathbf{m}_k \cdot \mathbf{m}_l) &= (\mathbf{m}_k \cdot \mathbf{m}_l)(\mathbf{m}_i \cdot \mathbf{m}_j) \\ &= (\mathbf{m}_l \cdot \mathbf{m}_k)(\mathbf{m}_j \cdot \mathbf{m}_i)\ .\end{aligned} \tag{20}$$

In order to find the most general form of second derivatives of the fourth-order HOI energy with respect to $\mathbf{m}_i$ and $\mathbf{m}_j$ all linearly independent permutations have to be considered

$$\begin{aligned}\nabla_{ij} E_{\text{4-spin}} &= \sum_{kl} \mathbf{m}_k^{\mathrm{T}} \big(C_{ijkl}\delta_{ij}\delta_{kl} + C_{ikjl}\delta_{ik}\delta_{jl} \\ &\qquad + C_{ilkj}\delta_{il}\delta_{kj}\big)\mathbf{m}_l \qquad (21) \\ &= \sum_{kl} \big(C_{ijkl}\,\mathbf{m}_k \odot \mathbf{m}_l + C_{ikjl}\,\mathbf{m}_l \otimes \mathbf{m}_k \\ &\qquad + C_{ilkj}\,\mathbf{m}_k \otimes \mathbf{m}_l\big) \qquad (22)\end{aligned}$$

where we used the abbreviations

$$\mathbf{m}_i \otimes \mathbf{m}_j = \begin{pmatrix} m_i^x m_j^x & m_i^x m_j^y & m_i^x m_j^z \\ m_i^y m_j^x & m_i^y m_j^y & m_i^y m_j^z \\ m_i^z m_j^x & m_i^z m_j^y & m_i^z m_j^z \end{pmatrix} \tag{23}$$

$$\mathbf{m}_i \odot \mathbf{m}_j = \begin{pmatrix} \mathbf{m}_i \cdot \mathbf{m}_j & 0 & 0 \\ 0 & \mathbf{m}_i \cdot \mathbf{m}_j & 0 \\ 0 & 0 & \mathbf{m}_i \cdot \mathbf{m}_j \end{pmatrix} \tag{24}$$

The step between Eq. (21) and Eq. (22) involves quadratic forms of spins with every $3 \times 3$-submatrix denoted within the tensors of Eq. (18) [57]. Since the last two terms in Eq. (22) are related by $\mathbf{m}_k \otimes \mathbf{m}_l = (\mathbf{m}_l \otimes \mathbf{m}_k)^T$ (transposing inverts order of magnetic moments) the construction of Hessian blocks comes down to the two cases:

$$\nabla_{ij} E_{\text{4-spin}} = -4 \sum_{kl} \begin{cases} C_{ijkl}\ \mathbf{m}_k \odot \mathbf{m}_l & \text{for } (i,j,k,l) \\ C_{ikjl}\ \mathbf{m}_l \otimes \mathbf{m}_k & \text{for } (i,k,j,l) \end{cases}, \tag{25}$$

where only the order of indices has to be considered, including variations with repeating indices which address 3-site and biquadratic HOI terms. Fig. 6 shows exemplarily contributions of HOI to the Hessian blocks of four magnetic moments within nearest neighbor distance to each other. It is noteworthy that $\nabla_{ij} E_{\text{4-spin}} = (\nabla_{ji} E_{\text{4-spin}})^T$, so that the Hessian itself is symmetric, as required on torsion-free configuration spaces.

**Implementation of the HOI.** General fourth-order HOI (Eq. (1)) were implemented in our atomistic simulation package SPINAKER for arbitrary lattice models, including three-dimensional ones. The code is capable of an efficient computation of the energy, gradients and Hessians of user-input fourth-order HOI over arbitrary distances of the lattice. Each term contributing to the general form of the fourth-order HOI, e.g. the biquadratic, 3-site or 4-site term, can be uniquely identified through an array of six distances (Eq. (4)). These distances are given in units of $n$-th nearest neighbor distances between the atomic sites of the respective lattice model. Based on this adjacency information the neighbor relations of a specific HOI are derived in a pre-processing step through the "Pairfinder"-algorithm explained below. A pseudocode representation of the core of the Pairfinder algorithm is given in Alg. 1.

The lattice of atoms is constructed by repetitions of the chemical unit cell containing one or more atomic species. Consider a central atomic site with index $i$. Figs. 7a,b illustrate small 3 by 3 segments of a hexag-

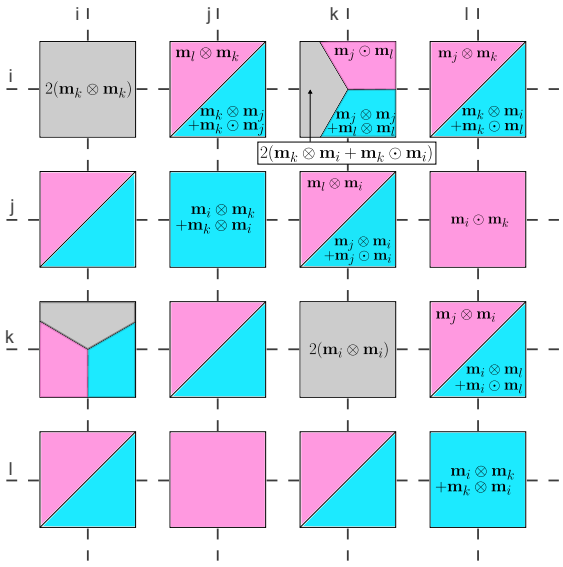


Figure 6. Schematic adjacency pattern for sub-matrix of the Hessian for four magnetic moments ($\mathbf{m}_i$, $\mathbf{m}_j$, $\mathbf{m}_k$, $\mathbf{m}_l$) in nearest neighbor distance of each other (see Fig. 1a). Each block $ij$ corresponds to the $3 \times 3$ cartesian components of the second derivatives of the energy in Eq. (1) with respect to the magnetic moments. The blocks colors refer to the specific HOI term contributing (biquadratic (gray), 3-site (cyan) and 4-site (pink) HOI.

onal lattice with an exemplary central atomic site $i$ and an integer index assigned to each site of these nine unit cells (Fig. 7b). In Fig. 7a the Pairfinder is illustrated for the 4-site HOI (denoted by the interaction strength $K$ in Eq. (3). In this case, the array of distances is $[d_{ij}, d_{ik}, d_{il}, d_{jk}, d_{jl}, d_{kl}] = [1, 1, 1, 1, 2, 1]$, involving only nearest neighbors except for the connection of $j$ and $l$: $d_{jl} = 2$.

The outermost loop in Alg. 1 iterates over the neighbors of the atomic site $i$ satisfying the constraint $d_{ij}$. For the 4-site HOI $j$ corresponds to a site in nearest neighbor distance to $i$ and for the specific system in Fig. 7b we have e.g. $j = 8$ for $i = 5$. Subsequently the index shift $n_{ij} = j - i$ is stored, which is here $n_{ij} = 3$. Ascending one level in the nested loops in Alg. 1, the next loop iterates over the neighbors with the distance constraint $d_{ik}$ and the index shift $n_{ik}$ is stored. For the 4-site HOI term these are again the sites in nearest neighbor distance to $i$ ($d_{ik} = 1$). Consider e.g. the atomic site with index $k = 9$ to be selected at this stage (see Fig. 7b) with $n_{ik} = 4$. Now it has to be checked whether the selected neighbors $j$ and $k$ of $i$ fulfill also the distance constraint $d_{jk}$, which is in this case again $d_{jk} = 1$. For this purpose the neighbors $k'$ in distance $d_{jk}$ of $j$ are iterated. For each candidate $k'$ it is tested if the index shifts of the candidate sites correspond to a closed path via $n_{ij} + n_{jk'} - n_{ik} = 0$. If this equation is satisfied, as for the site $k'$ marked on the right in Fig. 7a, we set $k = k'$ and continue. The sites marked with blue triangles are candidates for $k, k'$ satisfying the equation above. However, if this condition is not satisfied $k'$ is discarded and the loop over the neighbors of $j$ in distance $d_{jk}$ continues with the next candidate $k'$. The next embedded loop iterates over the neighbors of $i$ within distance $d_{il}$ to the site $i$ to produce candidates for the fourth site $l$. For the 4-site HOI these are again the nearest neighbors of $i$. For each candidate $l$ we now have to test whether it also fulfills the distance constraints $d_{jl}$ and $d_{kl}$, which are $d_{jl} = 2$ and $d_{kl} = 1$ here. Similar to the procedure above this is achieved by iterating the neighbors $l'$ of $j$ in distance $d_{jl}$ and iterating the neighbors $l''$ of $k$ in distance $d_{kl}$. For each $l'$ and $l''$ it is checked whether $n_{ij} + n_{jl'} - n_{il} = 0$ and $n_{ik} + n_{kl''} - n_{il} = 0$, respectively. Only if both conditions are satisfied the candidate $l$ completes the set of the four magnetic moments searched for the specific HOI term and the six index shifts are stored.

Note, that for each specific HOI term several sets fulfilling the above conditions exist. Consider again the 4-site HOI, where the site $l$ has to be in second nearest neighbor distance to $j$ and in nearest neighbor distance to $k$. In Fig. 7a this is only satisfied by the lattice site marked with the green diamond if $j$ and $k$ are chosen as schematically depicted in Fig. 7. However, also the lattice sites $j = 4$ and $k = 1$ satisfy the conditions for the first three magnetic moments participating in the 4-site HOI term. This leaves the site $l = 2$ as the only option to complete this set. Iterating over lattice sites corresponding to the array of distances recursively and evaluating conditions of closed paths ensures, finding all the sets of interacting lattice sites for a specific HOI, 12 for the case of the 4-site HOI.

Given the translational symmetry of the lattice it is sufficient to calculate these relative index shifts only once for a representative atomic site $i$. Thus, the computational complexity of this pre-processing step is negligible with respect to the thousands of energy and energy gradient calculations employed in a typical simulation, e.g. an iterative energy minimization algorithm.

Note, that the above representation uses single integer indices to address atomic sites and represent relative positions of sites for the sake of clarity. However, in practice SPINAKER stores multi-indices $(i_{\mathbf{a}_1}, i_{\mathbf{a}_2}, i_{\mathbf{a}_3}, i_{\text{species}})$ addressing a site via the coefficients of the linear combination of lattice vectors to reach its unit cell together with a unique index of the atomic species within this cell. This allows to detect neighbors connected via periodic boundaries. These are handled with a precomputed lookup mask storing for each site whether a neighbor is present or not, which allows also to simulate defects and missing atoms.

The Pairfinder algorithm explained above provides the necessary adjacency information used in the calculation of derivatives of the HOI energy with respect to the components of the magnetic moments – gradient and the ma-

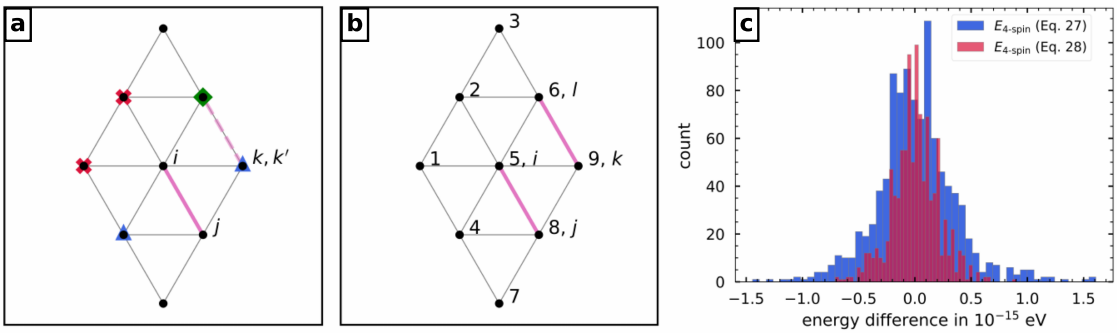


Figure 7. **Pairfinder illustrations and energy derivative consistency test. a,b** Schematic illustration of the Pairfinder algorithm utilized to calculate the neighbor relations for a specific HOI term for a 3 by 3 segment of the hexagonal lattice. Exemplary the derivation of the 4-site HOI term is shown. The moments $i$ and $j$ participate in the first scalar product and $k$, $l$ in the latter. The sites marked by blue triangles satisfy the adjacency to $i$ and $j$ during the generation of the neighbor $k, k'$. For $k, k'$ on the right only the site marked by the green diamond satisfies the adjacency of the fourth moment $l$ to the others. **b** The final set of four moments with pink lines as the scalar products is illustrated in addition to the indices of the atomic sites. **c** Histogram of via Euler's theorem numerically calculated 4-spin energy differences within the atomistic spin simulation code SPINAKER. The difference between the energy and the energy via the gradient in Eq. (27) (red) and the energy via the matrix of second-order derivatives in Eq. (28) (blue) of 1000 states with random magnetization is compared.

trix of second-order derivatives (Eqs. (16),(25)). On the one hand, the implementations are verified through comparing the results with analytical solutions, e.g. comparing the energy of magnetic structures with literature [74]. On the other hand, the consistency between the energy calculation and derivation of the first- and second-order derivatives with respect to the magnetization is checked via Euler's theorem for homogeneous functions. The fourth-order HOI term is a homogeneous function with order four of $3N$ variables $m_i^\alpha$ for $i = 1, \ldots, N$ and $\alpha \in \{x, y, z\}$:

$$E_{4\text{-spin}}(s\mathbf{m}_1, \ldots, s\mathbf{m}_N) = s^4 E_{4\text{-spin}}(\mathbf{m}_1, \ldots, \mathbf{m}_N) \quad (26)$$

with $s \neq 0$. Differentiating both sides of this equation with respect to $s$ and taking the limit of the results with $s \to 1$ yields:

$$4E_{4\text{-spin}} = \sum_i \mathbf{m}_i \cdot (\nabla_i E_{4\text{-spin}}) \ . \quad (27)$$

Therefore the energy is expressed in terms of the gradient. Similarly, the energy can be restored from the matrix of second derivatives via

$$12E_{4\text{-spin}} = \sum_{i,j} \mathbf{m}_i^T \cdot (\nabla_{ij} E_{4\text{-spin}}) \cdot \mathbf{m}_j \ . \quad (28)$$

Fig. 7c shows the energy difference of the left sides of Eqs. (27) and (28) computed with the HOI energy routine and the respective right sides, computed using the gradient and second-order derivative routines, respectively. The fluctuations are on the order of machine precision. The histogram for errors in the computation via the Hessian shows a broader distribution of numerical fluctuations, due to a quadratically increased amount of floating point operations.

## Data availability.

The data presented in this paper are available from the authors upon reasonable request.

## Code availability.

The atomistic spin simulation code is available from the authors upon reasonable request.


### ACKNOWLEDGEMENT

H. S. acknowledges financial support from the Icelandic Research Fund (grant No. 239435). P F. B. acknowledges financial support from the Icelandic Research Fund (Grants No. 2410333 and No. 217750), the University of Iceland Research Fund (Grant No. 15673), the Swedish Research Council (Grant No. 2020-05110), and the Crafoord Foundation (Grant No. 20231063). S. Ha and S. He. gratefully acknowledge financial support from the Deutsche Forschungsgemeinschaft (DFG, German Research Foundation) through SPP2137 "Skyrmionics" (project no. 462602351) and project no. 418425860. This work was performed using HPC resources available at the Kiel University Computing Centre. H. S. thanks S. Paul and S. von Malottki for valuable discussions.

**Algorithm 1** Pairfinder

```
// declare i as the central atomic site
// reset the set-counter for the specific HOI term
N ← 0
// iterates the neighbors j of i
for j in neighbors(d_ij) do
    // store the index shift between i and j
    n_ij ← indexshift(d_ij, j)
    for k in neighbors(d_ik) do
        n_ik ← indexshift(d_ik, k)
        for k' in neighbors(d_jk) do
            n_jk' ← indexshift(d_jk, k')
            if n_ij + n_jk' − n_ik ≠ 0 then
                cycle
            end if
            // now k = k', proceed with l, l' and l''
            for l in neighbors(d_il) do
                n_il ← indexshift(d_il, l)
                for l' in neighbors(d_jl) do
                    n_jl' ← indexshift(d_jl, l')
                    if n_ij + n_jl' − n_il ≠ 0 then
                        cycle
                    end if
                    for l'' in neighbors(d_kl) do
                        n_kl'' ← indexshift(d_kl, l'')
                        if n_ik + n_kl'' − n_il ≠ 0 then
                            cycle
                        end if
                        // set of 4 moments found
                        N ← N + 1
                        // store index shifts
                        n[N] ← [n_ij, n_ik, n_il, n_jk, n_jl, n_kl]
                    end for
                end for
            end for
        end for
    end for
end for
```

## Additional information

**Supplementary Information** accompanies this paper.

**Competing interests:** The authors declare that there are no non-financial or financial competing interests.

## Author contributions

H.S. performed the calculations and prepared the figures. B.B. implemented and tested higher-order interactions in the code supported by M.A.G. and H.S. All authors discussed the results. H.S. and M.A.G. wrote the first version of the manuscript, and all authors contributed to the final version.

## References


[1] Bogdanov, A. N. & Yablonskii, D. Thermodynamically stable "vortices" in magnetically ordered crystals. the mixed state of magnets. *Zh. Eksp. Teor. Fiz* **95**, 178 (1989).

[2] Nayak, A. K. *et al.* Magnetic antiskyrmions above room temperature in tetragonal heusler materials. *Nature* **548**, 561–566 (2017).

[3] Nagaosa, N. & Tokura, Y. Topological properties and dynamics of magnetic skyrmions. *Nature Nanotechnology* **8**, 899–911 (2013).

[4] Iwasaki, J., Mochizuki, M. & Nagaosa, N. Universal current-velocity relation of skyrmion motion in chiral magnets. *Nature Communications* **4**, 1463 (2013).

[5] Sampaio, J., Cros, V., Rohart, S., Thiaville, A. & Fert, A. Nucleation, stability and current-induced motion of isolated magnetic skyrmions in nanostructures. *Nature Nanotechnology* **8**, 839–844 (2013).

[6] Zhou, Y. & Ezawa, M. A reversible conversion between a skyrmion and a domain-wall pair in a junction geometry. *Nature Communications* **5**, 4652 (2014).

[7] Woo, S. *et al.* Observation of room-temperature magnetic skyrmions and their current-driven dynamics in ultrathin metallic ferromagnets. *Nature Materials* **15**, 501–506 (2016).

[8] Fert, A., Reyren, N. & Cros, V. Magnetic skyrmions: advances in physics and potential applications. *Nature Reviews Materials* **2**, 17031 (2017).

[9] Fert, A., Cros, V. & Sampaio, J. Skyrmions on the track. *Nature Nanotechnology* **8**, 152–156 (2013).

[10] Pinna, D. *et al.* Skyrmion gas manipulation for probabilistic computing. *Phys. Rev. Appl.* **9**, 064018 (2018).

[11] Song, K. M. *et al.* Skyrmion-based artificial synapses for neuromorphic computing. *Nature Electronics* **3**, 148–155 (2020).

[12] Grollier, J. *et al.* Neuromorphic spintronics. *Nature Electronics* **3**, 360–370 (2020).

[13] Mühlbauer, S. *et al.* Skyrmion lattice in a chiral magnet. *Science* **323**, 915–919 (2009).

[14] Yu, X. Z. *et al.* Real-space observation of a two-dimensional skyrmion crystal. *Nature* **465**, 901–904 (2010).

[15] Heinze, S. *et al.* Spontaneous atomic-scale magnetic skyrmion lattice in two dimensions. *Nature Physics* **7**, 713–718 (2011).

[16] Romming, N. *et al.* Writing and deleting single magnetic skyrmions. *Science* **341**, 636–639 (2013).

[17] Meyer, S. *et al.* Isolated zero field sub-10 nm skyrmions in ultrathin Co films. *Nature Communications* **10**, 3823 (2019).

[18] Muckel, F. *et al.* Experimental identification of two distinct skyrmion collapse mechanisms. *Nature Physics* **17**, 395–402 (2021).

[19] Moreau-Luchaire, C. *et al.* Additive interfacial chiral interaction in multilayers for stabilization of small individual skyrmions at room temperature. *Nature Nanotechnology* **11**, 444–448 (2016).

[20] Boulle, O. *et al.* Room-temperature chiral magnetic skyrmions in ultrathin magnetic nanostructures. *Nature Nanotechnology* **11**, 449–454 (2016).

[21] Soumyanarayanan, A. *et al.* Tunable room-temperature magnetic skyrmions in Ir/Fe/Co/Pt multilayers. *Nature Materials* **16**, 898–904 (2017).

[22] Han, M.-G. *et al.* Topological magnetic-spin textures in two-dimensional van der Waals $Cr_2Ge_2Te_6$. *Nano Letters* **19**, 7859–7865 (2019).

[23] Ding, B. *et al.* Observation of magnetic skyrmion bubbles in a van der Waals ferromagnet $Fe_3GeTe_2$. *Nano Letters* **20**, 868–873 (2020).

[24] Wu, Y. *et al.* Néel-type skyrmion in $WTe_2/Fe_3GeTe_2$ van der Waals heterostructure. *Nature Communications* **11**, 3860 (2020).

[25] Yang, M. *et al.* Creation of skyrmions in van der Waals ferromagnet $Fe_3GeTe_2$ on $(Co/Pd)_n$ superlattice. *Science Advances* **6**, eabb5157 (2020).

[26] Wu, Y. *et al.* A van der Waals interface hosting two groups of magnetic skyrmions. *Advanced Materials* **34**, 2110583 (2022).

[27] Liu, C. *et al.* Magnetic skyrmions above room temperature in a van der Waals ferromagnet $Fe_3GaTe_2$. *Advanced Materials* **36**, 2311022 (2024).

[28] Kartsev, A., Augustin, M., Evans, R. F. L., Novoselov, K. S. & Santos, E. J. G. Biquadratic exchange interactions in two-dimensional magnets. *npj Computational Materials* **6**, 150 (2020).

[29] Ni, J. Y. *et al.* Giant biquadratic exchange in 2D magnets and its role in stabilizing ferromagnetism of $NiCl_2$ monolayers. *Phys. Rev. Lett.* **127**, 247204 (2021).

[30] Xu, C. *et al.* Assembling diverse skyrmionic phases in $Fe_3GeTe_2$ monolayers. *Advanced Materials* **34**, 2107779 (2022).

[31] Li, P., Yu, D., Liang, J., Ga, Y. & Yang, H. Topological spin textures in 1$T$-phase Janus magnets: Interplay between Dzyaloshinskii-Moriya interaction, magnetic frustration, and isotropic higher-order interactions. *Phys. Rev. B* **107**, 054408 (2023).

[32] Dzyaloshinskii, I. *et al.* Thermodynamic theory of weak ferromagnetism in antiferromagnetic substances. *Sov. Phys. JETP* **5**, 1259–1272 (1957).

[33] Moriya, T. New mechanism of anisotropic superexchange interaction. *Phys. Rev. Lett.* **4**, 228–230 (1960).

[34] Bode, M. *et al.* Chiral magnetic order at surfaces driven by inversion asymmetry. *Nature* **447**, 190–193 (2007).

[35] Leonov, A. O. & Mostovoy, M. Multiply periodic states and isolated skyrmions in an anisotropic frustrated magnet. *Nature Communications* **6**, 8275 (2015).

[36] Lin, S.-Z. & Hayami, S. Ginzburg-Landau theory for skyrmions in inversion-symmetric magnets with competing interactions. *Phys. Rev. B* **93**, 064430 (2016).

[37] von Malottki, S., Dupé, B., Bessarab, P. F., Delin, A. & Heinze, S. Enhanced skyrmion stability due to exchange frustration. *Scientific Reports* **7**, 12299 (2017).

[38] Zhang, X. *et al.* Skyrmion dynamics in a frustrated ferromagnetic film and current-induced helicity locking-unlocking transition. *Nature Communications* **8**, 1717 (2017).

[39] Desplat, L., Kim, J.-V. & Stamps, R. L. Paths to annihilation of first- and second-order (anti)skyrmions via (anti)meron nucleation on the frustrated square lattice. *Phys. Rev. B* **99**, 174409 (2019).

[40] Goerzen, M. A., von Malottki, S., Meyer, S., Bessarab, P. F. & Heinze, S. Lifetime of coexisting sub-10 nm zero-field skyrmions and antiskyrmions. *npj Quantum Materials* **8**, 54 (2023).

[41] Paul, S., Haldar, S., von Malottki, S. & Heinze, S. Role of higher-order exchange interactions for skyrmion stability. *Nature Communications* **11**, 4756 (2020).

[42] Kurz, P., Bihlmayer, G., Hirai, K. & Blügel, S. Three-dimensional spin structure on a two-dimensional lattice: Mn/Cu(111). *Phys. Rev. Lett.* **86**, 1106–1109 (2001).

[43] Köbler, U. *et al.* Biquadratic exchange interactions in the europium monochalcogenides. *Zeitschrift für Physik B Condensed Matter* **100**, 497–506 (1996).

[44] Köbler, U. *et al.* On the failure of the bloch–kubo–dyson spin wave theory. *Journal of the Physical Society of Japan* **70**, 3089–3097 (2001).

[45] Mryasov, O. N., Freeman, A. J. & Liechtenstein, A. I. Theory of non-heisenberg exchange: Results for localized and itinerant magnets. *Journal of Applied Physics* **79**, 4805–4807 (1996).

[46] Lounis, S. & Dederichs, P. H. Mapping the magnetic exchange interactions from first principles: Anisotropy anomaly and application to Fe, Ni, and Co. *Phys. Rev. B* **82**, 180404 (2010).

[47] Yoshida, Y. *et al.* Conical spin-spiral state in an ultrathin film driven by higher-order spin interactions. *Phys. Rev. Lett.* **108**, 087205 (2012).

[48] Krönlein, A. *et al.* Magnetic Ground State Stabilized by Three-Site Interactions: Fe/Rh(111). *Phys. Rev. Lett.* **120**, 207202 (2018).

[49] Romming, N. *et al.* Competition of Dzyaloshinskii-Moriya and Higher-Order Exchange Interactions in Rh/Fe Atomic Bilayers on Ir(111). *Phys. Rev. Lett.* **120**, 207201 (2018).

[50] Spethmann, J. *et al.* Discovery of magnetic single- and triple-**q** states in Mn/Re(0001). *Phys. Rev. Lett.* **124**, 227203 (2020).

[51] Gutzeit, M. *et al.* Nano-scale collinear multi-q states driven by higher-order interactions. *Nature Communications* **13**, 5764 (2022).

[52] Takahashi, M. Half-filled Hubbard model at low temperature. *Journal of Physics C: Solid State Physics* **10**, 1289 (1977).

[53] MacDonald, A. H., Girvin, S. M. & Yoshioka, D. $\frac{t}{U}$ expansion for the Hubbard model. *Phys. Rev. B* **37**, 9753–9756 (1988).

[54] Hoffmann, M. & Blügel, S. Systematic derivation of realistic spin models for beyond-Heisenberg solids. *Phys. Rev. B* **101**, 024418 (2020).

[55] von Malottki, S., Bessarab, P. F., Haldar, S., Delin, A. & Heinze, S. Skyrmion lifetime in ultrathin films. *Phys. Rev. B* **99**, 060409 (2019).

[56] Varentcova, A. S. *et al.* Toward room-temperature nanoscale skyrmions in ultrathin films. *npj Computational Materials* **6**, 193 (2020).

[57] Goerzen, M. A. *Thermal equilibrium and stability of complementary topological solitons in two-dimensional magnets*. Ph.D. thesis, University of Kiel (2024).

[58] Hagemeister, J., Romming, N., von Bergmann, K., Vedmedenko, E. Y. & Wiesendanger, R. Stability of single skyrmionic bits. *Nature Communications* **6**, 8455 (2015).

[59] Wild, J. *et al.* Entropy-limited topological protection of skyrmions. *Science Advances* **3**, e1701704 (2017). https://www.science.org/doi/pdf/10.1126/sciadv.1701704.

[60] Desplat, L., Suess, D., Kim, J.-V. & Stamps, R. L. Thermal stability of metastable magnetic skyrmions: Entropic narrowing and significance of internal eigenmodes. *Phys. Rev. B* **98**, 134407 (2018).

[61] Haldar, S., von Malottki, S., Meyer, S., Bessarab, P. F. & Heinze, S. First-principles prediction of sub-10-nm skyrmions in Pd/Fe bilayers on Rh(111). *Phys. Rev. B* **98**, 060413 (2018).

[62] Beyer, B. *et al.* Bilayer triple-q state driven by interlayer higher-order exchange interactions. *Phys. Rev. B* **112**, 094430 (2025).

[63] Dupé, B., Hoffmann, M., Paillard, C. & Heinze, S. Tailoring magnetic skyrmions in ultra-thin transition metal films. *Nature Communications* **5**, 4030 (2014).

[64] Arya, M. *et al.* A new skyrmion topological transition driven by higher-order exchange interactions in Janus MnSeTe. *arXiv preprint arXiv:2509.10661* (2025).

[65] von Malottki, S., Goerzen, M. A., Schrautzer, H., Bessarab, P. F. & Heinze, S. Eigenmode following for direct entropy calculation and characterization of magnetic systems (2025).

[66] Bocdanov, A. & Hubert, A. The properties of isolated magnetic vortices. *physica status solidi (b)* **186**, 527–543 (1994).

[67] Schrautzer, H., Sallermann, M., Bessarab, P. F. & Jónsson, H. Identification of mechanisms of magnetic transitions using an efficient method for converging on first-order saddle points. *Phys. Rev. B* **112**, 104433 (2025).

[68] Müller, G. P. *et al.* Duplication, collapse, and escape of magnetic skyrmions revealed using a systematic saddle point search method. *Phys. Rev. Lett.* **121**, 197202 (2018).

[69] Bessarab, P. F. *et al.* Lifetime of racetrack skyrmions. *Scientific Reports* **8**, 3433 (2018).

[70] Bessarab, P. F., Uzdin, V. M. & Jónsson, H. Harmonic transition-state theory of thermal spin transitions. *Phys. Rev. B* **85**, 184409 (2012).

[71] Schrautzer, H., von Malottki, S., Bessarab, P. F. & Heinze, S. Effects of interlayer exchange on collapse mechanisms and stability of magnetic skyrmions. *Phys. Rev. B* **105**, 014414 (2022).

[72] Gutzeit, M., Haldar, S., Meyer, S. & Heinze, S. Trends of higher-order exchange interactions in transition metal trilayers. *Phys. Rev. B* **104**, 024420 (2021).

[73] Bessarab, P. F., Uzdin, V. M. & Jónsson, H. Method for finding mechanism and activation energy of magnetic transitions, applied to skyrmion and antivortex annihilation. *Computer Physics Communications* **196**, 335–347 (2015).

[74] Kurz, P. *Non-Collinear Magnetism at Surfaces and in Ultrathin Films*. Ph.D. thesis, Rheinisch-Westfälische Technische Hochschule Aachen (2000).

# Supplementary Information for: Impact of higher-order exchange on the lifetime of skyrmions and antiskyrmions

Hendrik Schrautzer,[1,*] Moritz Goerzen,[2,3,*] Bjarne Beyer,[2] Soumyajyoti Haldar,[2] Pavel F. Bessarab,[1,4] and Stefan Heinze[2,5,†]

[1] *Science Institute and Faculty of Physical Sciences, University of Iceland, VR-III, 107 Reykjavík, Iceland*
[2] *Institut für Theoretische Physik und Astrophysik, Christian-Albrechts-Universität zu Kiel, D-24098 Kiel, Germany*
[3] *CEMES, Université de Toulouse, CNRS, 29 rue Jeanne Marvig, F-31055 Toulouse, France*
[4] *Department of Physics and Electrical Engineering, Linnaeus University, SE-39231 Kalmar, Sweden*
[5] *Kiel Nano, Surface, and Interface Science (KiNSIS), University of Kiel, Germany*

(Dated: November 28, 2025)

**Supplementary Note S1: Interaction parameters of the Hamiltonian.**

We consider the ultrathin film systems fcc-Pd/Fe/Ir(111) and fcc-Pd/Fe/Rh(111) and use the same parameters as used in Ref. [1] for Eq. (3) in the main text. Those are listed in Tab. **S1** and Tab. **S2**. The pairwise Heisenberg exchange, the DMI and the biquadratic HOI parameters are given per pair of magnetic moment and are therefore twice as large as the parameters given in Ref. [1], where they were given per magnetic moment. If HOI is considered explicitly the first three bilinear exchange constants are modified as described in Ref. [1]. The parameters without considering HOI explicitly were originally calculated in Ref. [2] for fcc-Pd/Fe/Ir(111) and in Ref. [3] for fcc-Pd/Fe/Rh(111).

| Systems | $J_1/J_1'$ | $J_2/J_2'$ | $J_3/J_3'$ | $J_4/J_4'$ | $J_5/J_5'$ | $J_6/J_6'$ | $J_7/J_7'$ | $J_8/J_8'$ | $J_9/J_9'$ | $J_{10}/J_{10}'$ | $J_{11}/J_{11}'$ | $B_1$ | $Y_1$ | $K_1$ |
|---|---|---|---|---|---|---|---|---|---|---|---|---|---|---|
| fcc-Pd/Fe/Ir(111) | 28.81 | −4.96 | −5.37 | 1.04 | 1.48 | 0.56 | 0.32 | −1.15 | 0.43 | – | – | – | – | – |
| | 27.21 | −6.56 | −8.33 | 1.04 | 1.48 | 0.56 | 0.32 | −1.15 | 0.43 | – | – | 5.92 | 0.80 | 2.14 |
| fcc-Pd/Fe/Rh(111) | 26.70 | −5.37 | −5.68 | 1.24 | 0.93 | −0.20 | −0.61 | −0.22 | 0.05 | 0.33 | −0.13 | – | – | – |
| | 23.46 | −8.61 | −8.42 | 1.24 | 0.93 | −0.20 | −0.61 | −0.22 | 0.05 | 0.33 | −0.13 | 5.48 | 1.62 | 2.61 |

**Supplementary Table S1**. **Exchange interaction parameters for the atomistic spin model.** Interaction constants of the neighbor shell-resolved bilinear exchange ($J_n$) and the HOI terms corresponding to shortest distances ($B_1$, $Y_1$, $K_1$). The pairwise exchange and the biquadratic exchange constants are given in meV per pair of Fe-atoms and $Y_1$ and $K_1$ are given in meV per atom. The upper line for each system shows the exchange constants without explicit consideration of HOI. The lower line shows the modified exchange constants $J_n'$ when HOI is explicitly taken into account [1]. For the exchange parameters without HOI also refer to Ref. [2, 4] for fcc-Pd/Fe/Ir(111) and to Ref. [3] for fcc-Pd/Fe/Rh(111).

| Systems | $D_1$ | $D_2$ | $D_3$ | $D_4$ | $D_5$ | $K_\mathrm{u}$ | $\mu$ |
|---|---|---|---|---|---|---|---|
| fcc-Pd/Fe/Ir(111) | 2.0 | – | – | – | – | 0.7 | 3.0 |
| fcc-Pd/Fe/Rh(111) | 1.25 | −0.09 | 0.07 | 0.01 | 0.1 | 0.17 | 3.2 |

**Supplementary Table S2**. **Dzyaloshinskii-Moriya interaction constants, magnetic anisotropy and total magnetic moments.** Interaction constants of the neighbor shell-resolved Dzyaloshinskii-Moriya interaction (DMI, $D_n$), the anisotropy constant $K_\mathrm{u}$ and the total magnetic moment $\mu$. Note a positive (negative) value of $K_\mathrm{u}$ indicates an out-of-plane (in-plane) easy-axis direction. The pairwise DMI constants are given in meV per pair of Fe-atoms and the anisotropy constant is given in meV per atom. The magnetic moment is given in units of $\mu_B$. The parameters were taken from Ref. [1] and originally calculated in Ref. [2] for fcc-Pd/Fe/Ir(111) and Ref. [3] for fcc-Pd/Fe/Rh(111).

**Supplementary Note S2: Lifetime of skyrmions and antiskyrmions in fcc-Pd/Fe/Rh(111).**

Complementing the calculation of the energy barriers, the pre-exponential factors and the lifetimes for skyrmions and antiskyrmions in fcc-Pd/Fe/Ir(111) in the main text, we present here analogue derivations for the fcc-Pd/Fe/Rh(111) system. In this system the critical fields for the onset of the FM phase are given as $B_C = 2.25$ T for the model where HOI are taken explicitly into account and as $B_C = 2.75$ T if HOI are neglected [1]. Fig. **S1**d shows the energy barriers of the annihilation of skyrmions and antiskyrmions into FM state. For low $B_\perp - B_C$ the collapse mechanism of skyrmions is associated with the Chimera type SP (Fig. **S1**a). For large values of the applied field the preferred skyrmion annihilation mechanism corresponds to the radial collapse (Fig. **S1**b). A representative SP configuration for the decay of antiskyrmions is shown in Fig. **S1**c. Fig. **S1**e shows the

* These authors contributed equally to this work.
† Corresponding author: heinze@physik.uni-kiel.de

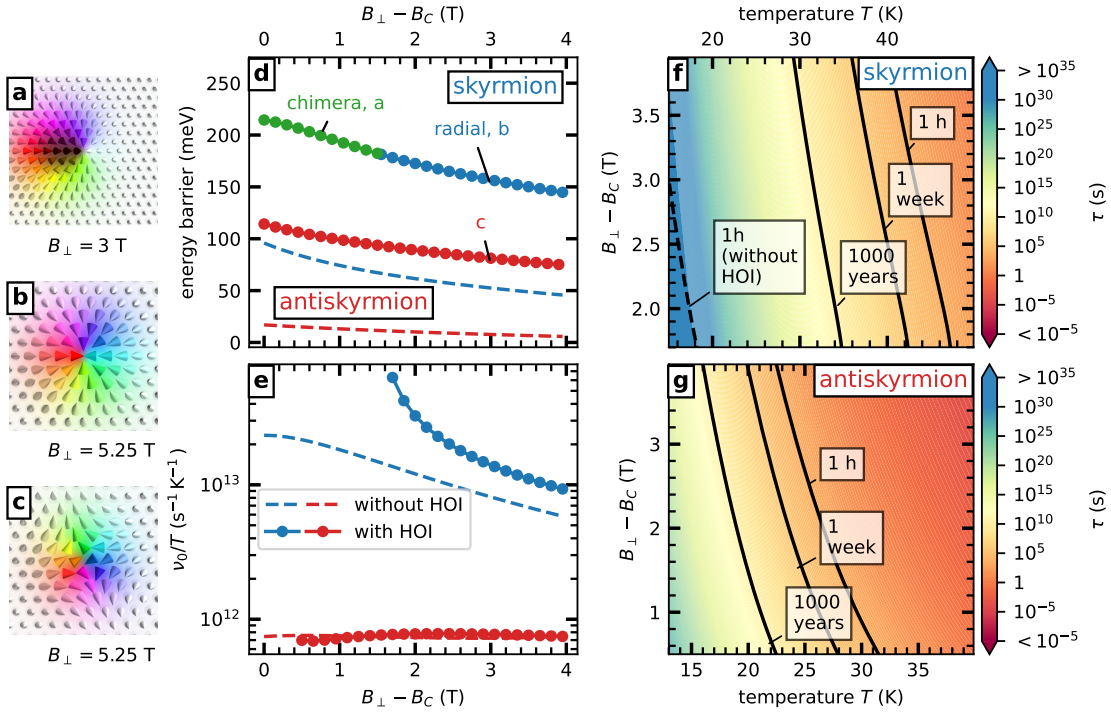


**Supplementary Figure S1**. **Effect of higher-order exchange interactions on skyrmion and antiskyrmion lifetime in fcc-Pd/Fe/Rh(111). a,b,c** Saddle point (SP) configuration for the collapse of the isolated skyrmion at $B_\perp - B_C = 0.75$ T(**a**) and $B_\perp - B_C = 3.0$ T (**b**) and antiskyrmion at $B_\perp - B_C = 3.0$ T (**c**). **d** Energy barriers of skyrmions (blue) and antiskyrmions (red) in fcc-Pd/Fe/Rh(111) plotted as a function of the magnetic field. The energy barriers for an energy model without HOI are shown by dashed lines (see Ref. [1, 5]). The magnetic field is given relative to the field $B_C$ for the onset of the field polarized phase for the respective energy model. **e** Pre-exponential factor $\nu_0$ in units of temperature $T$ plotted over $B_\perp - B_C$ for skyrmions (blue) in the regime of the radial collapse and antiskyrmions (red). **f** Mean lifetime $\tau$ (see colorbar) for different magnetic fields and different temperatures for the region of radial skyrmion collapse. As a reference, the contour line for a lifetime of 1 h for skyrmions in the energy model without HOI is also given (see Ref. [5]). **g** Mean lifetime for antiskyrmions taking HOI into account.

pre-exponential factor as a function of the magnetic field for both cases: explicitly considering HOI and neglecting HOI. Similar to the results in the main text for the fcc-Pd/Fe/Ir(111) system we observe a slight entropic destabilization of skyrmions visible in an increased pre-exponential factor upon the explicit consideration of HOI. Interestingly, we see that including HOI explicitly does not affect the pre-exponential factors of the antiskyrmion collapse in this system. Overall, drastically enhanced lifetimes are observed for both textures when considering HOI (Fig. **S1**f,g).

**Supplementary Note S3: Breaking the symmetry of the chimera collapse.**

For $B_\perp - B_C \leq 2.25$ T skyrmions annihilate via the Chimera collapse in fcc-Pd/Fe/Ir(111) when including HOI explicitly. The low curvature eigenmodes of the corresponding SP complicate the application of HTST for the computation of the pre-exponential factor for this mechanism. Focusing on the effect of HOI on the pre-exponential factor in the main text, we decided to present the discussion of the transition rate of the skyrmion via the Chimera collapse for the case of an applied in-plane magnetic field for the interested reader here.

The theoretically predicted Chimera collapse of skyrmions [6] was recently observed experimentally in fcc-Pd/Fe/Ir(111) under an applied magnetic field with components both perpendicular and parallel to the film surface, showing excellent agreement between experiment and theory [7]. However, the theoretical analysis in that study was based on the energy model neglecting HOI. Here, we apply an external magnetic field $\mathbf{B}_{\text{ext}} = B_{||}\hat{e}_x + B_\perp\,\hat{e}_z$ using an in-plane field value of $B_{||} = 1.5$ T, similar as in Ref. [7], but explicitly including HOI. Fig. **S2**a shows the MEP of the Chimera collapse for $B_\perp = 3.0$ T for the case of switched off and switched on in-plane magnetic field. Although the two paths are qualitatively similar, the barrier is approximately 25 meV lower in the presence of the in-plane field. The energy barrier $\Delta E = E_{\text{SP}} - E_{\text{sk}}$ associated with the annihilation of skyrmions as a function of $B_\perp$ while keeping $B_{||} = 1.5$ T constant are shown in Fig. **S2**b. For all considered values of $B_\perp$,

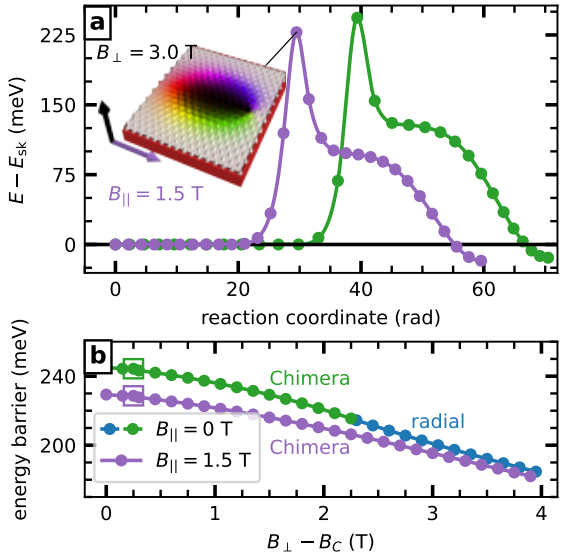


**Supplementary Figure S2**. **Minimum energy path and energy barriers for the Chimera collapse for an in-plane magnetic field. a** Energy $E$ over the geodesic distance along the minimum energy path (MEP) for a skyrmion ($E_{\text{sk}}$) collapsing into the FM state in fcc-Pd/Fe/Ir(111) for an applied magnetic field $B_\perp = 3.0$ T perpendicular to the film surface. The in-plane field contribution is set to $B_{||} = 1.5$ T (purple) and to $B_{||} = 0$ T (green). The SP configuration for the purple drawn MEP is shown in the inset and for both cases HOI are explicitly considered. **b** Energy barriers for the skyrmion annihilation as a function of the perpendicular magnetic field $B_\perp - B_C$ with an in-plane field $B_{||} = 1.5$ T (purple) and without an in-plane magnetic field (green for Chimera, blue for radial collapse). The energy barriers of the in part **a** shown MEPs are marked via empty squares.

the skyrmion collapse corresponds to an asymmetric, Chimera-like process. To assess the skyrmion's thermal stability quantitatively, the pre-exponential factor must be considered. This requires a detailed analysis of the low-curvature eigenmodes $\epsilon_i^{\text{SP}}$ of the Chimera SP, as shown in Fig. **S3**a. To this end, we explore the energy landscape perpendicular to the unstable mode ($i = 1$, not shown in Fig. **S3**a) of the SP along the rotational ($i = 2$) and the seesaw ($i = 3$) modes (Fig. **S3**b), using an eigenmode following algorithm [8]. In this algorithm, the magnetic texture is displaced stepwise along the direction of the eigenvector of the corresponding mode, while updating the followed eigenmode at each step.

First, consider the case with no in-plane magnetic field ($B_{||} = 0$ T, $B_\perp = 3.0$ T). The in-plane rotation $\varphi$ (see Fig. **S3**d) of the Chimera SP around the Bloch point-like defect corresponds to a zero mode with a very small eigenvalue. The energy dependence along this mode is shown by the green circle in Fig. **S3**b, where $q$ is the cumulated geodesic distance traveled along the rotation eigenmode. The seesaw mode, which involves transitioning between mirror-symmetric representations of the Chimera SP (with respect to the $\hat{e}_y$ axis), contributes with another low-curvature direction. The local energy maximum along this path corresponds to the radial collapse SP (see Fig. **S3**c), which, in this case, is of second order.

HTST requires a significant separation between the energy of the first- and second-order SPs. Since a reliable quantitative evaluation of the pre-exponential factor for the Chimera collapse under these conditions falls outside the scope of this work, we restrict our analysis to the radial collapse regime for $B_{||} = 0$ T (Fig. 2b,c of the main text). Nonetheless, it is worth noting that the eigenvalue of the seesaw mode approaches zero at the change between chimera and radial collapse mechanism (indicated in Fig. **S3**a by the dashed line for $B_{||} = 0.$ T). This behavior can be interpreted analogously to Landau's theory of phase transitions, as discussed in Ref. [9] for a mode mediating the collapse of coupled skyrmions in a bilayer. In contrast, applying an in-plane field of $B_{||} = 1.5$ T and an out-of-plane field of $B_\perp = 3.0$ T breaks the rotational symmetry of the Chimera SP. This is evidenced by the increased energy variation along the rotational mode which is no longer a zero mode (Fig. **S3**b). Additionally, the two local energy minima along the seesaw direction are no longer degenerate, and the energy of the radial collapse configuration is significantly elevated compared to the case of $B_{||} = 0$ T. The increased curvature of the energy surface along the rotational and seesaw modes when applying an in-plane field is also reflected in their respective eigenvalues in Fig. **S3**a. These changes, consistent with the analysis in Ref. [7], make the harmonic treatment of the seesaw and rotational mode viable in the presence

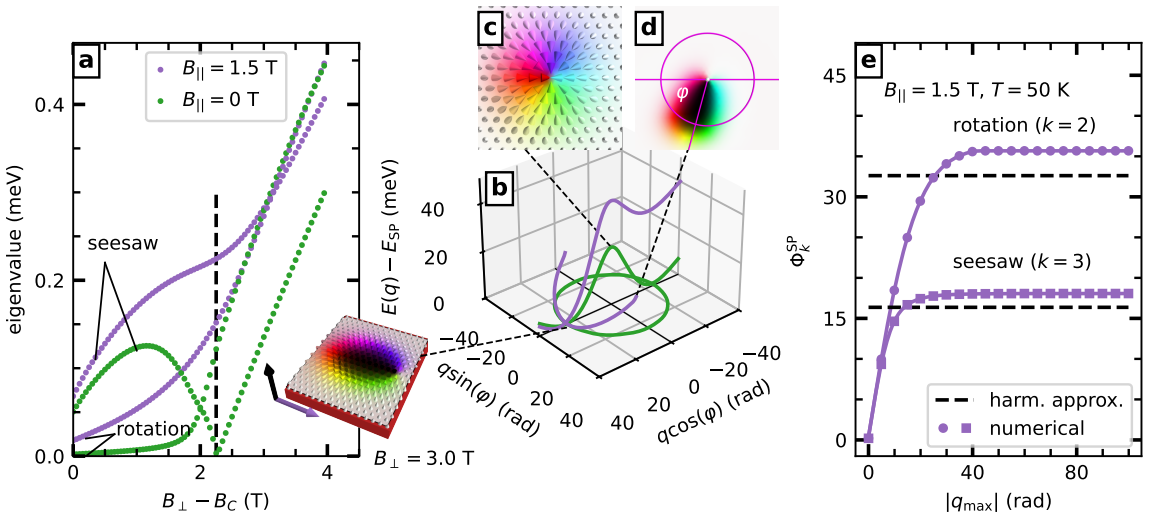


**Supplementary Figure S3**. **Low curvature eigenspace of the Chimera SP of the skyrmion collapse.** **a** Eigenvalues of the rotation and seesaw eigenmode of the Hessian of the Chimera SP plotted over the perpendicular component $B_\perp - B_C$ of the external magnetic field in fcc-Pd/Fe/Ir(111) with (purple, $B_{||} = 1.5$ T) and without (green) an in-plane magnetic field (see inset). **b** Energy as a function of the displacement $q$ of the chimera SP configuration along the seesaw and rotation relative to the energy of the SP ($E_{SP}$) for $B_{||} = 1.5$ T (purple). For the rotation mode the angle $\varphi$ of the longitudinal chimera axis with respect to $\hat{e}_x$ is displayed (**d**). For the seesaw mode the configuration corresponding to the maximum of the energy is shown in **c**. For reference, an analogue visualization is given for $B_{||} = 0$ T (green). **e** Comparison of numerical calculation of the partition function $\Phi_k^{SP}$ of the rotation and seesaw mode with harmonic approximation (dashed black line).

of an in-plane field. To validate this, we numerically integrate the contributions to the partition function

$$\Phi_k^{SP} = \sum_{j=1}^{N_{EMF}} e^{-\beta\left[E\left(q_k^j\right) - E_{SP}\right]} \Delta q \,, \tag{1}$$

where $N_{EMF}$, $\Delta q$ and $E_{SP}$ are the number of iterations of the EMF algorithm, the geodesic displacement along the mode per iteration and the energy of the stationary point at which we explore the energy surface. The displacement parameter for each step was set to $\Delta q = 0.1$ rad.

In Fig. **S3**e these numerical results for the rotation mode ($k = 2$) and for the seesaw mode ($k = 3$) are compared with the prediction of the harmonic approximation at $T = 50$ K for $B_\perp = 3.0$ T. A deviation of less than $10\%$ between the harmonic approximation and the numerical result for the partition function is reported and thus we conclude that the harmonic treatment of the rotation and seesaw eigenmodes is justified for the case of an applied in-plane field at a temperature of $T = 50$ K. Since the integrand grows exponentially with temperature, we further conclude that the harmonic approximation is valid in this case for temperatures $T \leq 50$ K at least. In this temperature regime Fig. **S4**b presents the mean lifetime $\tau$ of skyrmions in fcc-Pd/Fe/Ir(111) as a function of $B_\perp - B_C$ for $B_{||} = 1.5$ T, while the corresponding pre-exponential factors are shown in Fig. **S4**a. Notably, the difference in mean lifetime $\tau$ predicted is minimal compared to the radial collapse regime for $B_{||} = 0$ T and $B_\perp - B_C \geq 2.25$ T. In principle it is possible to calculate the pre-exponential factor also in the regime of $B_{||}$ by numerically integrating the seesaw and rotation eigenmodes of the Chimera SP. However, to do this for every value of the perpendicular field $B_\perp$ is a large numerical effort and beyond the scope of this paper investigating the effect of HOI on the lifetimes of skyrmions and antiskyrmions.

**Supplementary Note S4: Curvature of the energy surface for the antiskyrmion.**

In Fig. **S5**a,b the eigenvalues of the antiskyrmion and of the respective SP for its annihilation into the FM state are shown upon explicitly considering HOI in fcc-Pd/Fe/Ir(111). For reference the eigenvalues for the model without HOI are also shown. When HOI is neglected the antiskyrmion is only meta stable up to fields of $B_\perp - B_C \leq 2.75$ T and the eigenvalues are only presented for this regime. Comparing the summed curvature values of all eigenmodes corresponding to eigenvalues below the magnon gap yields the values of $\mathcal{C}_{\text{min}}^{\text{local}}$ ($\mathcal{C}_{\text{SP}}^{\text{local}}$) shown in Fig. **S5**c (Fig. **S5**d). Complementary to the results for the skyrmion in Fig. 3 of the main text a stronger effect on the curvature at the SP is observed than on the minimum upon inclusion of HOI. Different to the SP of the skyrmion the curvature of the local part of the spectrum increases for the SP of the antiskyrmion if HOI is included.

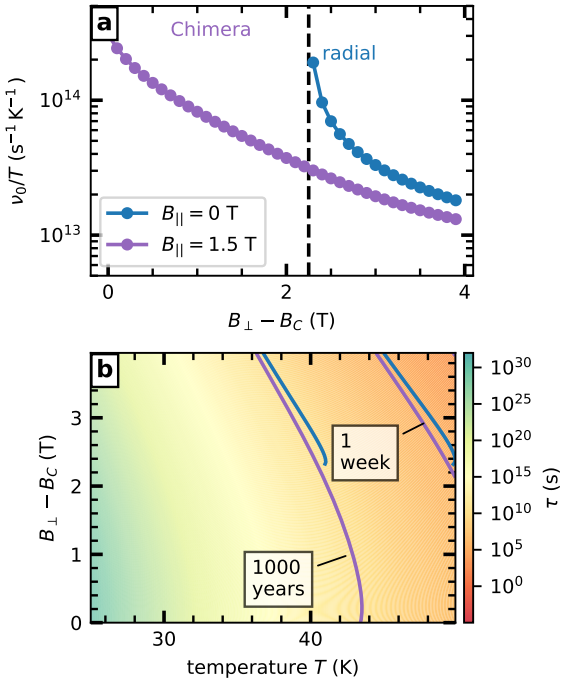


**Supplementary Figure S4**. **a** Pre-exponential factor $\nu_0$ divided by the temperature $T$ for the skyrmion annihilation in fcc-Pd/Fe/Ir(111) including HOI for $B_{||} = 1.5$ T (purple) and for the radial collapse regime of the case $B_{||} = 0$ T (cf. Fig. **S2**b). **b** Skyrmion lifetime as a function of $B_\perp - B_C$ and temperature $T$ for $B_{||} = 1.5$ T. The iso-lines for a lifetime of 1000 years and 1 week are drawn in purple. For reference the respective iso-lines at $B_{||} = 0$ T are shown in blue.

This corresponds to reducing the pre-exponential factor if HOI is considered (see Eq. (11) of the main text). However, this effect is compensated by the difference of the magnon contributions to the curvature at the minimum and the SP visualized in Fig. **S5**e, which is larger if HOI is considered explicitly. Fig. **S5**f presents the difference of the curvature at the antiskyrmion with the curvature of the respective SP, showing the same qualitative behavior as the corresponding pre-exponential factors displayed in Fig. 2f of the main text.

**Supplementary Note S5: Eigenvalues of skyrmions and antiskyrmions without DMI.**

Fig. **S6** shows the Hessian eigenvalues of the skyrmion and the antiskyrmion and their respective SPs in fcc-Pd/Fe/Ir(111) when explicitly considering HOI but neglecting DMI as a function of the magnetic field. Comparing these spectra with the respective eigenvalues when including DMI and HOI (Fig. 3 in the main text for the skyrmion, and Fig. **S5** for the antiskyrmion), here a less complicated functional dependence of the local part of the eigenvalue spectrum is observed. For all stationary points the eigenvalues show a simple linear dependence on the value of the applied field.

**Supplementary Note S6: Multiplicity of SP configurations per unit cell.**

For the derivation of the pre-exponential factor for collapses via Bloch point-like defects a factor $\varrho$, indicating the multiplicity of SPs configurations per unit cell, has to be considered (see "Methods"). Fig. **S7** shows representative SP configurations and the corresponding values of $\varrho$ occurring in the calculations of this work. The transitions investigated are associated with a change of the topological charge $Q$ from $-1$ for the skyrmion (1 for the antiskyrmion) to $Q = 0$ for the FM state. This topological charge can be calculated as the sum of the topological density $q(\mathbf{r}^*)$ over the sites $\mathbf{r}^*$ of the dual lattice defined by a triangulation of the lattice [10]. Inevitable strongly canted magnetic moments forming a Bloch point-like defect occur during these transitions changing the topology. For the lattice sites corresponding to the magnetic moments in the vicinity of these Bloch point like configurations in Fig. **S7** the edges of the triangulation are shown and the value of topological density is given for each triangle with magnetic moments $\mathbf{m}_i$, $\mathbf{m}_j$ and $\mathbf{m}_k$: [10]:

$$q(\mathbf{r}^*) = \frac{1}{4\pi}(\mathcal{A}(\mathbf{m}_i, \mathbf{m}_j, \mathbf{m}_k)) \,, \tag{2}$$

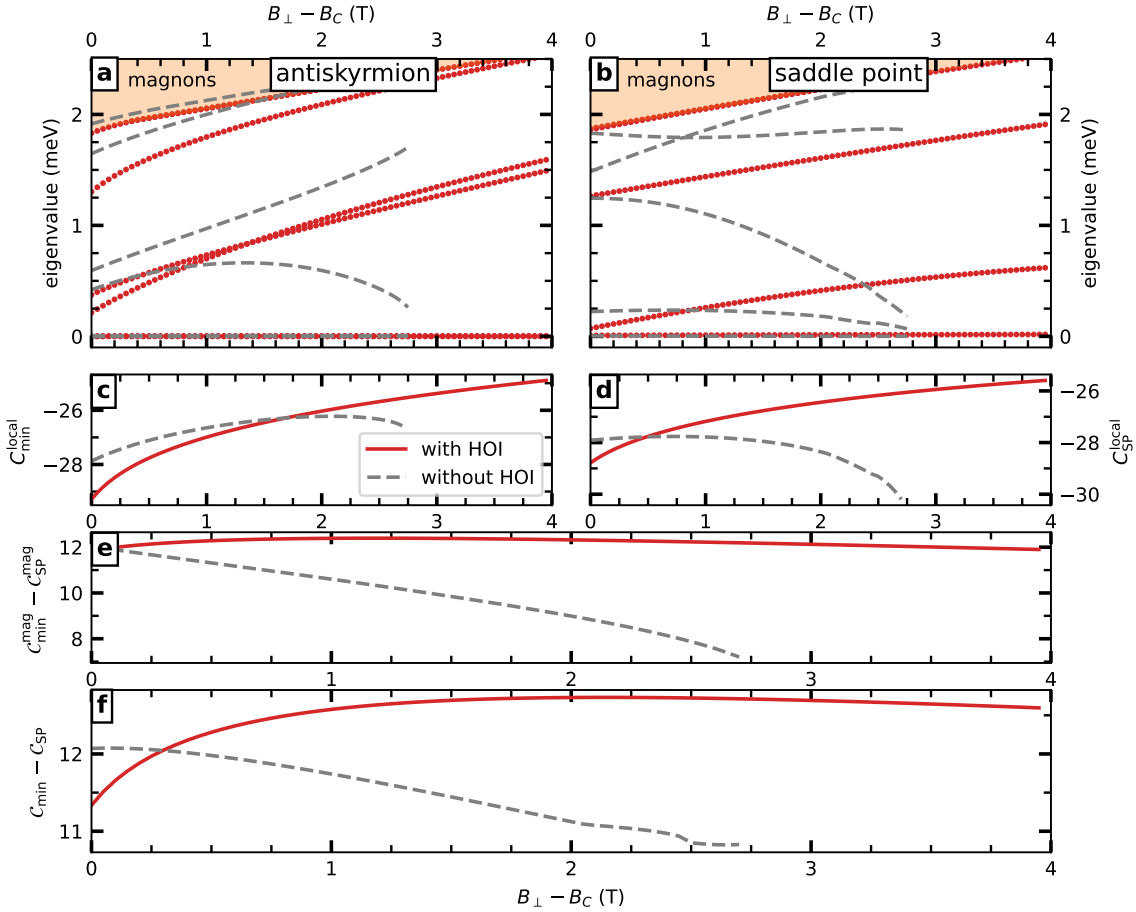


**Supplementary Figure S5**. **HOI and curvature of the energy surface for the antiskyrmion. a,b** Local part of the eigenvalue spectrum of the Hessian matrix of the antiskyrmion (**a**, red) and the skyrmion saddle point (SP) (**b**, red) in fcc-Pd/Fe/Ir(111) including HOI as a function of the magnetic field $B_\perp - B_C$. Eigenvalues above the magnon gap are indicated by the orange painted area. For reference the corresponding local eigenvalue spectra in the model without considering HOI explicitly are shown as gray dashed lines. **c,d** Curvature associated with the local eigenvalue spectrum (see Eq. (10)) for the antiskyrmion (red, **c**) and the corresponding SP (red, **d**) for the energy model including HOI (solid line). The local curvatures of the SP for the model neglecting HOI are drawn with dashed gray lines. **e** Curvature difference of the minimum and the SP using only the spectrum above the magnon gap for the model explicitly considering HOI (red line) and without HOI (dashed gray line). **i**: Total curvature difference of the minimum and the SP.

where $\mathcal{A}$ is the area of the spherical triangle spanned by the three magnetic moments. See for example the SP of the radial skyrmion collapse in fcc-Pd/Fe/Ir(111) without considering HOI visualized in Fig. **S7**a. The unit cell of the hexagonal lattice is visualized by the red edges forming a diamond. The central magnetic moments pointing toward each other occupy three of the four vertices of this diamond with an assigned topological density of $-0.4$. Note, since these three magnetic moments have a small out-of-plane component ($m_z \neq 0$) the topological density is well-defined in this case. This SP configuration can also be realized placing the three magnetic moments forming the defect at the upper triangle within the unit cell. Thus, in total we have two equivalent representations of the same SP per unit cell yielding $\varrho = 2$ in this case. The collapse of the skyrmions in fcc-Pd/Fe/Rh(111) without considering HOI explicitly are also associated to this SP type. However, if HOI is explicitly considered for skyrmions in fcc-Pd/Fe/Ir(111) (fcc-Pd/Fe/Rh(111)) the SP configuration of the radial collapse corresponds to the one visualized in Fig. **S7**b. Here four magnetic moments are involved in forming the Bloch point like defect of the magnetization occupying all the four lattice sites of the diamond corresponding to the unit cell of the lattice. The topological density is equal for the two triangles forming the diamond of the unit cell ($q = -0.25$) leaving a single exemplar of this SP. Thus, we have $\varrho = 1$

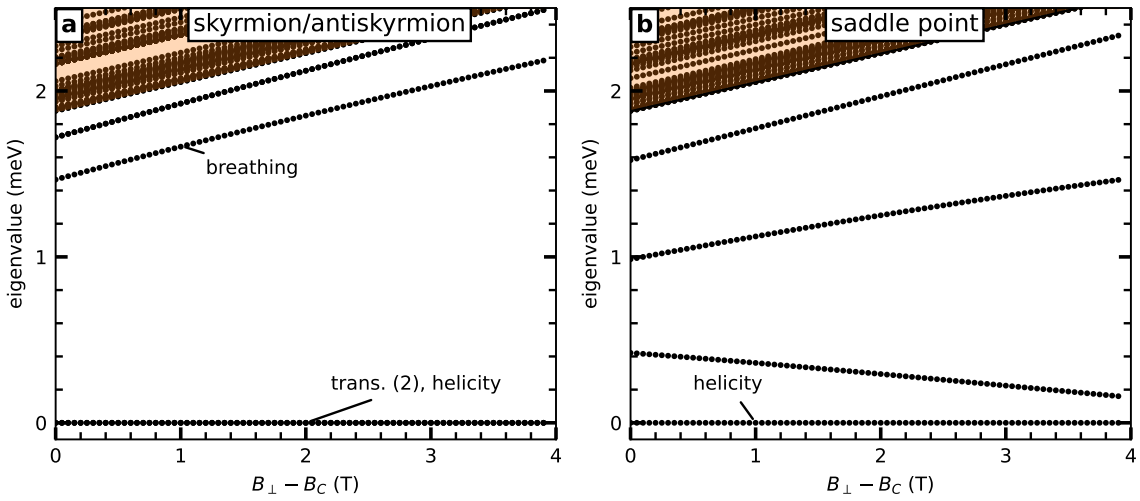


**Supplementary Figure S6**. **Hessian eigenvalues of magnetic textures including HOI and neglecting HOI.** Eigenvalues of the Hessian of the energy of skyrmions and antiskyrmions (**a**) and the SPs associated with a collapse into the FM state (**b**) as a function of the magnetic field in fcc-Pd/Fe/Ir(111). The orange colored part represents the eigenvalues above the magnon gap. For the description of the eigenmodes of the labeled eigenvalues refer to the main text.

in this case. For low magnetic fields and including HOI the skyrmions collapse via the Chimera mechanism. Here, again four magnetic moments form the defect leading to $\varrho = 1$ as visualized in Fig. **S7**c. Note, also the Chimera SP calculated for varying $B_\perp - B_C$ and $B_{||} = 1.5$ T in fcc-Pd/Fe/Ir(111) corresponds to a similar structure as the one shown in Fig. **S7**c.

The SP associated to the antiskyrmion collapse into the FM in fcc-Pd/Fe/Ir(111) without considering HOI is shown in Fig. **S7**d. A single SP representation per unit cell is possible in this case ($\varrho = 1$). However, in fcc-Pd/Fe/Rh(111) without HOI the antiskyrmion SP corresponds to the structure shown in Fig. **S7**e. Here, the topological density of the two facets forming the unit cell is not equal indicating again two SPs per unit cell ($\varrho = 2$). Finally, introducing HOI for the antiskyrmion annihilation in fcc-Pd/Fe/Ir(111) and fcc-Pd/Fe/Rh(111) leads to a slightly rotated SP configuration beeing favoured (Fig. **S7**f), leaving the relative orientation of the central magnetic moments unchanged compared to Fig. **S7**d and thus also giving $\varrho = 1$. A tabular overview over the multiplicity factors $\varrho$ used for the pre-exponential factor calculated in this work is provided in Tab. **S3**.


[1] S. Paul, S. Haldar, S. von Malottki, and S. Heinze, Role of higher-order exchange interactions for skyrmion stability, Nature Communications **11**, 4756 (2020).

[2] B. Dupé, M. Hoffmann, C. Paillard, and S. Heinze, Tailoring magnetic skyrmions in ultra-thin transition metal films, Nature Communications **5**, 4030 (2014).

[3] S. Haldar, S. von Malottki, S. Meyer, P. F. Bessarab, and S. Heinze, First-principles prediction of sub-10-nm skyrmions in Pd/Fe bilayers on Rh(111), Phys. Rev. B **98**, 060413 (2018).

[4] S. von Malottki, B. Dupé, P. F. Bessarab, A. Delin, and S. Heinze, Enhanced skyrmion stability due to exchange frustration, Scientific Reports **7**, 12299 (2017).

[5] S. von Malottki, P. F. Bessarab, S. Haldar, A. Delin, and S. Heinze, Skyrmion lifetime in ultrathin films, Phys. Rev. B **99**, 060409 (2019).

[6] S. Meyer, M. Perini, S. von Malottki, A. Kubetzka, R. Wiesendanger, K. von Bergmann, and S. Heinze, Isolated zero field sub-10 nm skyrmions in ultrathin Co films, Nature Communications **10**, 3823 (2019).

[7] F. Muckel, S. von Malottki, C. Holl, B. Pestka, M. Pratzer, P. F. Bessarab, S. Heinze, and M. Morgenstern, Experimental identification of two distinct skyrmion collapse mechanisms, Nature Physics **17**, 395 (2021).

[8] S. von Malottki, M. A. Goerzen, H. Schrautzer, P. F. Bessarab, and S. Heinze, Eigenmode following for direct entropy calculation and characterization of magnetic systems (2025).

[9] H. Schrautzer, S. von Malottki, P. F. Bessarab, and S. Heinze, Effects of interlayer exchange on collapse mechanisms and stability of magnetic skyrmions, Phys. Rev. B **105**, 014414 (2022).

[10] B. Berg and M. Lüscher, Definition and statistical distributions of a topological number in the lattice o(3) $\sigma$-model, Nuclear Physics B **190**, 412 (1981).

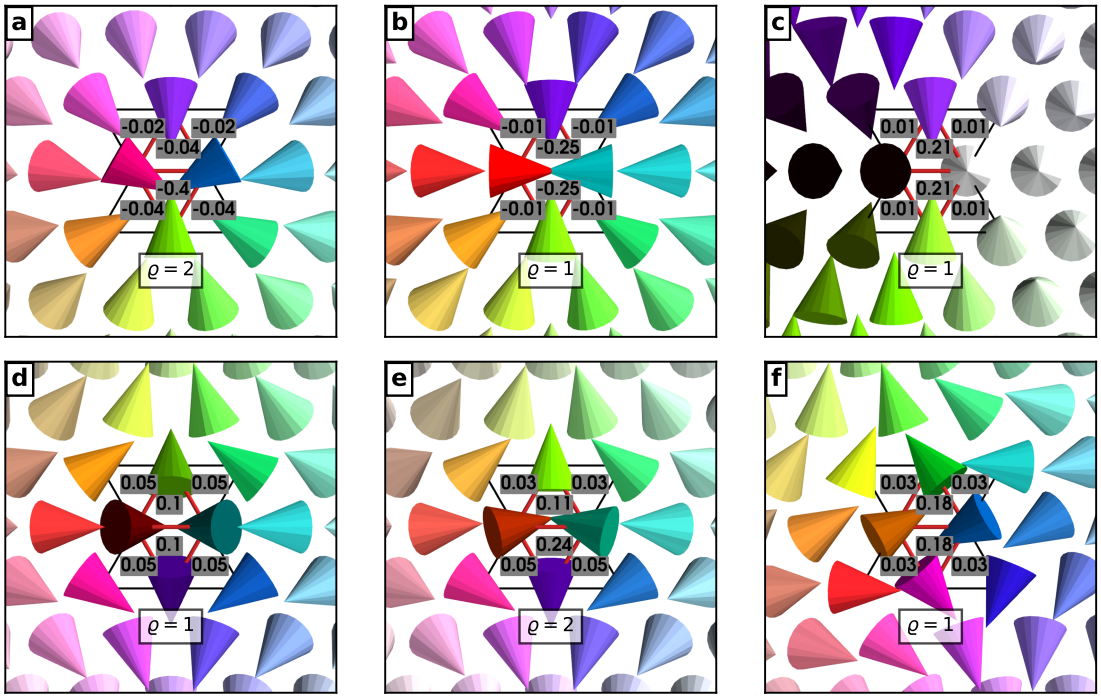


**Supplementary Figure S7**. **Number of saddle point configurations per unit cell.** Saddle point (SP) configurations associated to skyrmion (**a**,**b**,**c**) and antiskyrmion (**d**,**e**,**f**) collapse into the FM state in fcc-Pd/Fe/Ir(111) (**a-d**,**f**) and fcc-Pd/Fe/Rh(111) (**e**). The triangulation of the hexagonal lattice is indicated by black and red lines in the vicinity of the strong canted magnetic moments forming the Bloch point-like defect. The red diamond in the center represents the unit cell. For each triangle the topological density $q(\mathbf{r}^*)$ is given. The multiplicity is denoted as $\varrho$. **a** SP for $B_\perp = 6.02$ T for the model neglecting HOI. **b** SP for $B_\perp = 6.0$ T (with HOI). **c** SP for $B_\perp = 4.0$ T (with HOI). **d** SP for $B_\perp = 4.87$ T (without HOI). **e** SP for $B_\perp = 6.0$ T (without HOI in fcc-Pd/Fe/Rh(111)). **f** SP for $B_\perp = 6.0$ T (with HOI).

| System | Texture | interaction model | $B_\perp - B_C$ (T) | pre-exponential factor | mechanism | $\varrho$ |
|---|---|---|---|---|---|---|
| fcc-Pd/Fe/Ir(111) | skyrmion | without HOI | [0,4] | Fig. 2e | radial (Fig. **S7**a) | 2 |
| fcc-Pd/Fe/Ir(111) | skyrmion | with HOI | [2.25,4] | Fig. 2e | radial (Fig. **S7**b) | 1 |
| fcc-Pd/Fe/Ir(111) | antiskyrmion | without HOI | [0,2.75] | Fig. 2e | radial (Fig. **S7**d) | 1 |
| fcc-Pd/Fe/Ir(111) | antiskyrmion | with HOI | [0,4] | Fig. 2e | radial (Fig. **S7**f) | 1 |
| fcc-Pd/Fe/Ir(111) | skyrmion | with HOI, $B^{\vert\vert} = 1.5$ T | [0,4] | Fig. **S4**a | chimera (Fig. **S7**c) | 1 |
| fcc-Pd/Fe/Ir(111) | skyrmion | with HOI, without DMI | [0,4] | Fig. 5a | radial (Fig. **S7**b) | 1 |
| fcc-Pd/Fe/Ir(111) | antiskyrmion | with HOI, without DMI | [0,4] | Fig. 5a | radial (Fig. **S7**d) | 1 |
| fcc-Pd/Fe/Ir(111) | skyrmion | variation of 4-site HOI | [0,4] | Fig. 4c | radial (Fig. **S7**b) | 1 |
| fcc-Pd/Fe/Ir(111) | antiskyrmion | variation of 4-site HOI | [0,4] | Fig. 4c | radial (Fig. **S7**d) | 1 |
| fcc-Pd/Fe/Rh(111) | skyrmion | without HOI | [0,4] | Fig. **S1**e | radial (Fig. **S7**a) | 2 |
| fcc-Pd/Fe/Rh(111) | skyrmion | with HOI | [1.5,4] | Fig. **S1**e | radial (Fig. **S7**b) | 1 |
| fcc-Pd/Fe/Rh(111) | antiskyrmion | without HOI | [0,4] | Fig. **S1**e | radial (Fig. **S7**e) | 2 |
| fcc-Pd/Fe/Rh(111) | antiskyrmion | with HOI | [0.5,4] | Fig. **S1**e | radial (Fig. **S7**f) | 1 |

**Supplementary Table S3**. **Multiplicities of saddle point configurations.** Overview of the figures where the pre-exponential factors of the skyrmion and antiskyrmion collapse into the FM state in fcc-Pd/Fe/Ir(111) and fcc-Pd/Fe/Rh(111) are presented in this work. Calculations where done with and without considering HOI explicitly, applying an in-plane magnetic field $B_{||}$, neglecting DMI and tuning the 4-site HOI term. The range of magnetic fields $B_\perp - B_C$ simulated is given relative to the critical field $B_C$. Six different types of SPs occur which are presented in Fig. **S7**. The multiplicity of the SP is given by $\varrho$.

# Paper IV

**Network of localized magnetic textures revealed using a saddle-point search framework**

**H. Schrautzer**, T. Drevelow, H. Jónsson, P.F. Bessarab

preprint: arXiv:2512.07663

Hendrik developed and implemented the methodology, performed the calculations, analyzed the data together with P.F. Bessarab and wrote the article together with all authors.

# Network of localized magnetic textures revealed using a saddle-point search framework

Hendrik Schrautzer,[1] Tim Drevelow,[2] Hannes Jónsson,[1] and Pavel F. Bessarab[1,3,*]

[1] *Science Institute and Faculty of Physical Sciences, University of Iceland, VR-III, 107 Reykjavík, Iceland*
[2] *Institute of Theoretical Physics and Astrophysics, Christian-Albrechts-University, 24118 Kiel, Germany*
[3] *Department of Physics and Electrical Engineering, Linnaeus University, SE-39231 Kalmar, Sweden*

A computational framework is presented for the structured sampling of the energy surface of magnetic systems via the systematic identification of first-order saddle points that determine connectivity of metastable states and define the mechanisms and rates of transitions between them within harmonic transition state theory or Kramers/Langer theory. The framework combines four stages: first, the symmetry of a given minimum-energy configuration is identified and used to define subsystems whose eigenmodes provide relevant deformation directions; the subsystem eigenmodes are then used to guide the system toward the vicinity of different saddle points surrounding the energy minimum; next, the geodesic minimum mode following method is employed to efficiently converge onto the saddle points; and finally, the identified saddle points are embedded into the state network. The efficient implementation of the method makes it applicable to large systems and/or systems characterized by long-range interactions. Applied to metastable textures in two-dimensional chiral magnets described by a lattice Hamiltonian, the method reveals a hierarchy of transition mechanisms governing the nucleation, annihilation, and rearrangement of the fundamental components of localized magnetic textures. Knowledge of the identified saddle points enables the construction of the network of metastable states, where energy minima correspond to vertices and saddle points define the connectivity between them, providing a comprehensive map of accessible transitions and their associated energy barriers. Transitions corresponding to both homotopies that preserve the topological charge and transformations that change it are identified through their associated saddle points. By scaling the interaction parameters, the distinct behavior of these two classes is obtained as the continuum limit is approached. Finally, it is demonstrated that textures with the same topological charge are not necessarily connected by a homotopy corresponding to a minimum-energy path: in specific parameter regimes, the total topological charge necessarily increases and then decreases (or vice versa) during the transition, returning to its initial value at the final state.

## I. INTRODUCTION

In recent years, the field of topological magnetism has advanced significantly with the discovery of various magnetic textures localized in 2D and 3D, extending beyond magnetic skyrmions [1]. Magnetic systems capable of hosting multiple structures simultaneously [2–6] are of particular interest, as they hold great promise for technological applications and offer a potential for interesting phenomena driven by the interactions and transformations between different magnetic textures.

The system's ability to accommodate several stable states signifies the presence of multiple minima on its energy surface. How the system traverses between these minima due to thermal activation can be studied using harmonic transition state theory (HTST) [7, 8] or Kramers/Langer theory [9, 10]. The identification of first-order saddle points (SPs) on the energy surface is the key part of this analysis, with each SP defining the mechanism and the rate of possible transitions between minima.

In the context of topological magnetism these minima correspond to localized magnetic textures that can be sorted into classes, characterized by the topological charge [11]

$$Q = \frac{1}{4\pi}\int [\vec{m}\cdot(\partial_x\vec{m}\times\partial_y\vec{m})]\,\mathrm{d}r^2 \ , \tag{1}$$

where $\vec{m}\,(\vec{r}\,)$ denotes the magnetization. Mathematically it is always possible to define continuous transformation of the magnetization between two textures of the same class, which is called a homotopy [6] – in fact there is an infinite number of such homotopies. A continuous transformation between magnetic textures with a different topological charge $Q$ is not possible as it inevitable leads to the formation of discontinuities of the magnetization [4]. However, magnetism arises due to magnetic moments $\vec{m}_i$ at discrete lattice sites and both homotopies and non-homotopies between magnetic textures correspond to overcoming finite energy barriers [12].

The variety of unknown metastable configurations and possible transitions between minima in such systems motivates the search for SPs connected to a given initial-state minimum, without prior knowledge of the final states. This so-called single-ended problem differs from double-ended problems, where both the initial and final states are known and the SP can be located by finding the minimum energy path (MEP) connecting them [13–16].

Algorithms designed for single-ended problems [17–20] typically involve two stages. In the first, or escape stage, the system is displaced away from the convex region of the initial state minimum. In the second, or con-

* Corresponding author: pavel.bessarab@lnu.se

vergence stage, the system is iteratively driven toward a first-order SP. Implementations of the convergence stage rely on the observation that first-order SPs are located at the ends of ascending valleys of the energy surface, with the ascent direction parallel to the eigenvector of the Hessian corresponding to the lowest eigenvalue – the minimum mode. Maximizing the energy along the minimum mode, while minimizing it along all other directions, ultimately leads to convergence to an SP.

Single-ended SP search algorithms have been extended to magnetic systems, where special care must be taken to account for the curvature of the configuration space arising from the constraint on the lengths of the magnetic moments. These developments have mostly focused on the convergence stage [21–24], where the main challenge lies in the evaluation of the minimum mode. In particular, recent implementation of the geodesic minimum mode following (GMMF) method enables an efficient determination of the minimum mode without explicit evaluation of the Hessian, making it applicable to large magnetic systems, including those with long-range interactions [24].

An energy minimum can be connected to multiple SPs, each representing a particular transition mechanism. To sample these properly, several SP searches must be performed, with the convergence stage in each search starting from sufficiently distinct configurations to ensure that different valleys of the energy surface are explored and different SPs are reached. These entry points for the convergence stage are generated during the escape stage. Therefore, the escape stage is a crucial part of the SP search, directly affecting the completeness of sampling of SPs surrounding a given minimum. An effective strategy for the escape stage should yield a diverse and unbiased ensemble of entry configurations, ultimately enabling systematic identification of distinct SPs.

Previous implementations of the escape stage typically pursue an eigenmode following strategy [21, 22, 24]. The energy minimum configuration is iteratively displaced along selected eigenvectors of the Hessian recomputed at each step until an escape criterion is met. Combining this approach with initial random displacements distributed on a hypersphere was reported to increase the number of different SPs identified in the convergence stage while the overall number of attempts is reduced [25]. Recently, multi-objective genetic algorithms [26] were applied [27] to learn from previous SP search attempts and improve the diversity and quality of initial displacements. Exiting low-energy eigenmodes is a natural approach, but there are limitations. First, there is no one-to-one mapping between specific eigenmodes and particular SPs. Second, many important SPs – e.g. localized symmetry breaking transformations – may involve deformations of only a small subsystem of the configuration. Introducing a tendency to such SPs during the escape stage may require following several eigenmodes sequentially [24], making the approach less systematic. Moreover, recomputing the Hessian eigenmodes for the full system is computationally expensive.

Most likely there is no universal best strategy for the realization of the escape stage. In this paper we address these challenges by proposing a subsystem-based escape stage suitable for localized magnetic textures. The key idea is to restrict excitations to subsystems – symmetry informed regions of the texture varying in size and shape. Such localized excitations break the symmetry of the configuration and introduce a directed bias toward SPs involving spatially confined deformations. Furthermore, sampling such subsystems allows a systematical search for these SPs. The approach draws inspiration from displacing only specific atoms in the context of chemical reactions [28–31].

This paper presents a systematic approach to realize such an escape stage for localized magnetic textures in two-dimensional magnets. Furthermore, we complement the escape and convergence stage with a preprocessing stage, where the symmetries of a given texture are identified, and a postprocessing stage, where unique SPs are identified and embedded into the state network. The method is then applied to understand the systematics of transformations between localized magnetic textures in two-dimensional chiral magnets known to simultaneously host a large variety of topological solitons [5].

The paper is organized as follows. Sec. II introduces the magnetic model and the properties of localized magnetic textures. Sec. III presents the method, detailing the preprocessing, escape, convergence, and postprocessing stages. In Sec. IV, we use the framework to explore the energy surface of two-dimensional chiral magnets and obtain a network of energy minima and SPs representing transition mechanisms of localized magnetic textures. Sec. V concludes the paper with a summary of the main findings.

## II. MODEL

### A. Hamiltonian

In this study, the isolated textures in 2D magnets [4, 5, 32] (see Fig. 1 for examples) are modeled on a square lattice, where the magnetic configuration $\boldsymbol{m} = (\vec{m}_1, \ldots, \vec{m}_N)$ is described by $N$ unit vectors $\vec{m}_i$ specifying the directions of the magnetic moments at the lattice sites, each of magnitude $\mu$. The corresponding lattice Hamiltonian includes contributions from the Heisenberg exchange, the Dzyaloshinskii-Moriya (DM) interaction, and the Zeeman interaction:

$$\begin{aligned} E = &- \sum_n \frac{J_n}{2} \sum_{\langle ij \rangle_n} \vec{m}_i \cdot \vec{m}_j \\ &- \sum_n \frac{D_n}{2} \sum_{\langle ij \rangle_n} \vec{d}_{ij} \cdot (\vec{m}_i \times \vec{m}_j) \\ &- \mu \sum_i \vec{B} \cdot \vec{m}_i \,. \end{aligned} \tag{2}$$

Here, the outer sum in the first two terms runs over the neighbor shells $n = 1, 2, \ldots$, and the inner sum includes all sites $i, j$ separated by the distance corresponding to the $n$-th neighbor shell, with the strengths of the Heisenberg exchange and DMI characterized by $J_n$ and $D_n$, respectively. The unit DM vector $\vec{d}_{ij}$ is given by the following formula:

$$\vec{d}_{ij} = R_\beta \vec{r}_{ij} / |\vec{r}_{ij}|, \tag{3}$$

where $\vec{r}_{ij}$ connects sites $i$ and $j$ and $R_\beta \in \mathbb{R}^{3\times3}$ describes the right-handed rotation around the normal to the system plane by angle $\beta$.For $\beta = 0$, this corresponds to Bloch DM interaction [33–35], while $\beta = \pi/2$ describes Néel-type chiral modulations [36–38]. The external magnetic field $\vec{B}$ is perpendicular to the system plane and periodic boundary conditions within the system plane are used.

A 2D chiral magnet can also be described within the continuous magnetization framework, where the energy of the system is given by the following functional

$$\mathcal{E} = \int \left[ \frac{\mathcal{J}}{2} |\vec{\nabla}\, \vec{m}\,|^2 + \mathcal{D}\left( R_\beta \vec{m} \cdot \vec{\nabla} \times R_\beta \vec{m} \right) - M_S(\vec{B} \cdot \vec{m} - B) \right] \mathrm{d}r^2 + \mathcal{E}^{\mathrm{FM}}. \tag{4}$$

Here $\vec{m} = \vec{m}(\vec{r})$ is the unit vector field describing distribution of the magnetization in the two-dimensional film. $M_S$ is the saturation magnetization, and $\mathcal{J}$ and $\mathcal{D}$ continuous-theory exchange and DM interaction parameter, respectively. The energy of the ferromagnetic state (FM) is denoted by $\mathcal{E}^{\mathrm{FM}}$. By comparing the series expansion of the lattice Hamiltonian [39] with Eq. (4) the parameters $J_n$ and $D_n$ are defined such that Eq. (2) and Eq. (4) are equivalent in continuum limit. To improve the correspondence between the lattice model and continuous-magnetization theory up to fourth-order terms of the series are considered [12, 40]. Furthermore, to maintain this correspondence but avoid higher-order spatial derivatives of $\vec{m}(\vec{r})$ in Eq. (4) the lattice Hamiltonian parameters are chosen such that the higher-order term vanishes [41, 42]. In this work we vary the equilibrium period of chiral modulations at the ground state $L_D = 2\pi\mathcal{J}/\mathcal{D}$ and define the energy in units of $\mathcal{J}$. Within the lattice model, the continuum limit is approached by increasing $L_D$. The magnetic field is varied by the dimensionless parameter $h$ measuring $B = hB_D$ in units the saturation field $B_D = \mathcal{D}^2/(M_S\mathcal{J})$. The model parameter used in this work for the lattice Hamiltonian are given in Tab. I.

TABLE I. Parameters of Eq. (2) chosen such that the fourth-order series expansion of the square lattice Hamiltonian with nearest neighbor distance $a$ and continuous-theory agree. The period of the spin spiral $L_D = 2\pi\mathcal{J}/\mathcal{D}$ defines the length scale of the Hamiltonian and the magnetic field is given in units $h$ of the saturation field $B_D = \mathcal{D}^2/(M_S\mathcal{J})$.

| $J_1$ | $J_2$ | $J_3$ | $D_1$ | $D_2$ | $D_3$ | $B$ | $\mu$ |
|---|---|---|---|---|---|---|---|
| $\frac{4}{3}\mathcal{J}$ | 0 | $-\frac{1}{12}\mathcal{J}$ | $\frac{8\pi}{3L_D}a\mathcal{J}$ | 0 | $-\frac{2\pi}{3L_D}a\mathcal{J}$ | $hB_D$ | $M_S a^2$ |

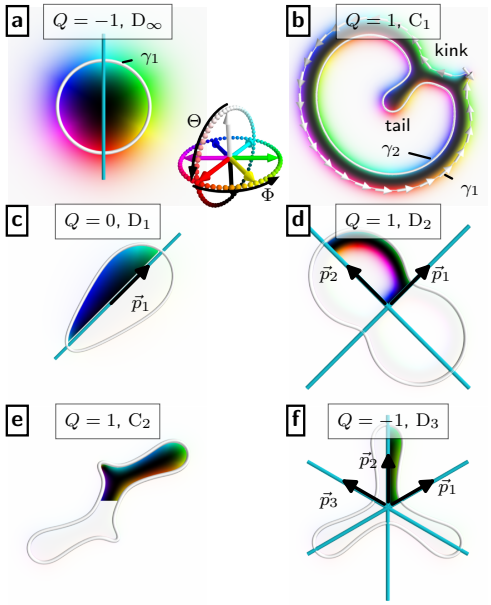


FIG. 1. Examples of magnetic textures with different topological charges $Q$ and symmetries, described by spin point groups $\mathrm{C}_n$ and $\mathrm{D}_n$, for a magnetic field of $h = 0.623$ and $L_D = 40$. The contours ($m_z = 0$) are shown in white. The inset explains the hue-saturation-lightness color scheme encoding the azimuthal angle $\Phi$ of the magnetic moments by the hue, while the lightness represents the polar angle $\Theta$ for a fixed saturation of 1.0. **a**: Skyrmion with axial symmetry ($\mathrm{D}_\infty$). **b**: Texture featuring a chiral kink, a tail and two nested closed contours $\gamma_1$ and $\gamma_2$. The magnetic moments along the outer contour are shown by white arrows. **c**-**f**: Chiral droplet (**c**), skyrmion bag with two inner contours (**d**), two-tailed texture with two chiral kinks (**e**) and three-tailed state (**f**) with mirror axes depicted in cyan. The orientation of the mirror axes is denoted $\vec{p}_j$. The fundamental domain is highlighted while the remaining part of the texture is grayed out.

### B. Isolated magnetic textures

Magnetic textures emerging as metastable states in two-dimensional chiral magnets, whose energy is described by Eqs. (2) and (4), can take a wide variety of forms. Nevertheless, any isolated texture can be described in terms of three fundamental building blocks:

- **Closed contours:** Lines in space separating regions of opposite out-of-plane magnetization. The sense of magnetization rotation along a contour is

determined by the chirality of the system set by the DM interaction. Closed contours can be nested within one another, with the outermost contour defining the boundary of the localized texture.

- **Chiral kinks:** Localized twists of the magnetization along a contour where the sense of rotation reverses relative to the intrinsic chirality of the system.

- **Tails:** Local distortions or extensions of a contour that modify the overall shape of the texture but, unlike kinks, do not alter the sense of magnetization rotation.

By combining these elementary building blocks in various ways, a surprisingly large diversity of configurations can be obtained. Whether a given configuration corresponds to a true energy minimum ultimately depends on the specific parameters of the Hamiltonian. Figure 1(b) shows an exemplary texture involving all types of the constituent elements: two closed contours, a chiral kink, and a tail. This texture corresponds to a minimum of Eq. (2) for a magnetic field of $h = 0.623$ and $L_D = 40a$.

All magnetic textures predicted by the 2D chiral magnet model fall into distinct homotopy classes defined by their topological charge $Q$ [see Eq. (1)], which can be expressed as the sum of the winding numbers of the magnetization along all closed contours [5]:

$$Q = \sum_i \Omega_i, \tag{5}$$

where the winding number $\Omega_i$ associated with contour $\gamma_i$ is defined as

$$\Omega_i = \frac{1}{2\pi} \oint_{\gamma_i} \vec{\nabla}\, \Phi(\vec{r}) \cdot \mathrm{d}\vec{r} \ , \tag{6}$$

with $\Phi(\vec{r})$ being the azimuthal angle of the magnetization. The orientation of each contour is defined such that, when the contour is traversed, the region with $\Theta > \pi/2$ lies on its left.

This representation illustrates how nested contours, chiral kinks, and tails contribute to the total topological charge. Each contour without a kink contributes a winding of $\pm 1$, depending on the sense of magnetization rotation relative to the contour orientation. For the metastable configurations considered here, each chiral kink adds one positive winding to its host contour. Note, models with strong easy-axis anisotropy can also support metastable textures with negative chiral kinks [5]. Tails affect only the geometric shape of the texture and do not modify its topological charge [32]. For example, an isolated skyrmion contains a single contour without kinks, yielding $Q = -1$, while more complex multi-contour, multi-kink configurations can have $Q = 0, \pm 1, \pm 2, \ldots$, depending on the number and arrangement of the constituent elements [see Fig. 1].

The topological charge is a key property that governs many physical phenomena, such as the topological Hall effect [43] and the skyrmion Hall effect [44]. However, $Q$ alone is insufficient to uniquely specify the structure of a texture. Distinct configurations may share the same topological charge yet differ in morphology and symmetry [see Fig. 1(b) and Fig. 1(d)]. Moreover, the symmetry of a texture has a direct impact on its dynamics [45].

To further distinguish localized textures, their symmetry properties can be analyzed. In this work, we identify texture symmetries with respect to $n$-fold rotations ($\mathrm{C}_n$) and $n$-fold rotations combined with reflections ($\mathrm{D}_n$). This analysis is used during the preprocessing stage of the developed framework to define the *fundamental domain* of each magnetic texture – loosely speaking, the smallest region containing all unique physical information about the texture without repetition (Sec. III A). The strategy of the escape stage is based on excitations of various subsystems centered on the points within the fundamental domain, as described in the following. In Fig. 1(c,d), the fundamental domain is highlighted, while the remaining parts of each texture are grayed out.

The wide diversity of localized textures, including distinct states sharing the same topological charge, makes the 2D chiral magnet model an excellent platform for studying physical realizations of homotopies – continuous transformations between textures of the same $Q$. Textures belonging to the same homotopy class can always be continuously transformed into one another, and infinitely many such homotopies exist. In contrast, transformations between textures of different homotopy classes are impossible without forming discontinuities in the magnetization [4]. An important question is whether such homotopies can have physical relevance – for example, whether they can represent dynamical trajectories or minimum energy paths (MEPs). The latter pass through SPs on the energy surface and define the kinetics of transformations between magnetic configurations within the HTST or Kramers/Langer theory. It is of particular interest to determine whether homotopy MEPs always exist and whether their energy barriers are smaller than those involving discontinuous transformations. This question is nontrivial since magnetization discontinuities have finite energy [12, 40], and the discrete nature of the system introduces further complexity. The SP search framework developed here is agnostic to whether a SP corresponds to a continuous or discontinuous transformation, making it ideally suited for addressing this problem.

## III. METHOD

The scope of this work is to present an automated framework for SP searches (SPSF) designed such that it can be executed repeatly for many different meta-stable states, thus enabling an embedding in global optimization methods and methods for calculating long-timescale dynamics. The SPSF consists of different algorithmic

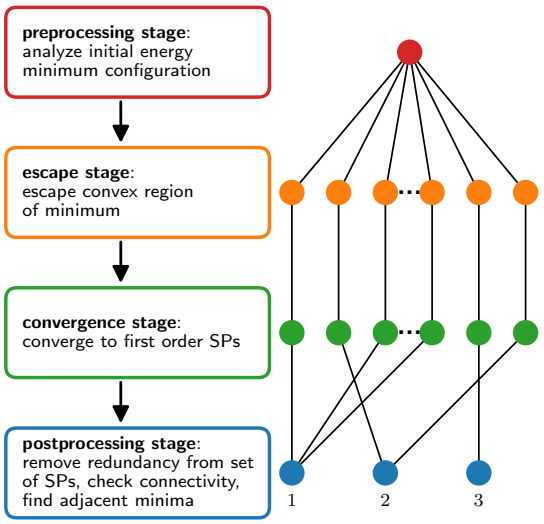


FIG. 2. The SPSF is structured into different stages. During the preprocessing stage, the properties of the local energy minimum configuration are analyzed to define suitable settings for escaping the convex region (escape stage) and then converging onto first order SPs (convergence stage). The tree on the right highlights the fact that the convex region is escaped at multiple points on the high dimensional energy surface resulting into many SP search attempts computed in parallel. Finally, during postprocessing the redundant SPs are filtered, the connectivity of the identified SPs to the initial minimum is tested and the adjacent energy minimum state is revealed.

phases which are referred to as stages in the following (see Fig. 2). The starting point is always a magnetic texture corresponding to a local energy minimum, which is first examined with regard to its size, shape and symmetries (preprocessing stage, see Sec. III A). These properties define the localized deformations of the texture in the subsequent escape stage (Sec. III B) to leave the convex region at as many different points as possible, which is a crucial part designing efficient SP searches [25]. In this stage, many parallel calculations are started which iteratively move the configuration of the minimum close to the boundary of the convex region. Each of these points then serves as the initialization of a calculation in the subsequent convergence stage (Sec. III C) in which convergence to first-order SPs is sought. Finally, the postprocessing stage (Sec. III D) groups the found SPs into clusters of equivalent SPs and checks their connectivity to the initial minimum.

### A. Preprocessing stage

The SPSF is initialized with a local energy minimum associated with one or more isolated magnetic textures – see, for example, a state shown in Fig. 3a. The goal of the preprocessing stage is to calculate the fundamental domain for each of the isolated textures using their symmetry elements. The textures are first separated from one another and extracted from the FM background (see Sec. III A 1). After that, the symmetry elements and fundamental domains of the textures are determined using an algorithm we developed (see Sec. III A 2). Finally, each texture, together with the information about its fundamental domain, are passed to the escape stage. A detailed description of the preprocessing stage is presented in the following.

#### 1. *Recognition of isolated magnetic textures*

Fig. 3a shows a meta-stable configuration including three skyrmions and one texture with three inner contours. The objects can be extracted from the FM background using distribution of the out-of-plane component of the magnetization, $m_z$ In particular, the $m_z = 0$ contour curves are computed (see Fig. 3a) and the lattice sites in the nearest neighbor distance to the contour curves are identified and grouped into clusters using a density-based clustering algorithm [46, 47] with a metric considering periodic boundary conditions (Fig. 3b). Each cluster is associated with a single closed contour and for each contour the convex hull enclosing all points of a cluster is computed [48]. Possible inner contours are detected by testing whether their corresponding convex hulls lie within some other, outer contour. Magnetic textures are isolated by identifying all outermost disjoint contours, with the magnetic moments enclosed by each such contour defining one texture.

A center of mass of a given isolated texture can be computed using the following expression [49–52]:

$$\vec{c} = \frac{\sum_{i\in\mathcal{I}} \vec{r}_i(m_i^z - 1)}{\sum_{i\in\mathcal{I}} m_i^z - 1} \,, \tag{7}$$

where $\mathcal{I}$ is a set of sites associated with the texture, and $\vec{r}_i$ is the position of site $i$.

#### 2. *Symmetries of magnetic textures*

Possible symmetries of two-dimensional magnetic textures correspond to elements $[\mathcal{M}||\mathcal{N}]$ of spin point groups [53–56], where $\mathcal{N}$ is an ordinary point group element acting in real space and $\mathcal{M}$ acts on the space of magnetic moments

$$[\mathcal{M}||\mathcal{N}]\vec{m}\,(\vec{r}_i) = \mathcal{M}\vec{m}\,(\mathcal{N}^{-1}(\vec{r}_i - \vec{c}) + \vec{c}) \,, \tag{8}$$

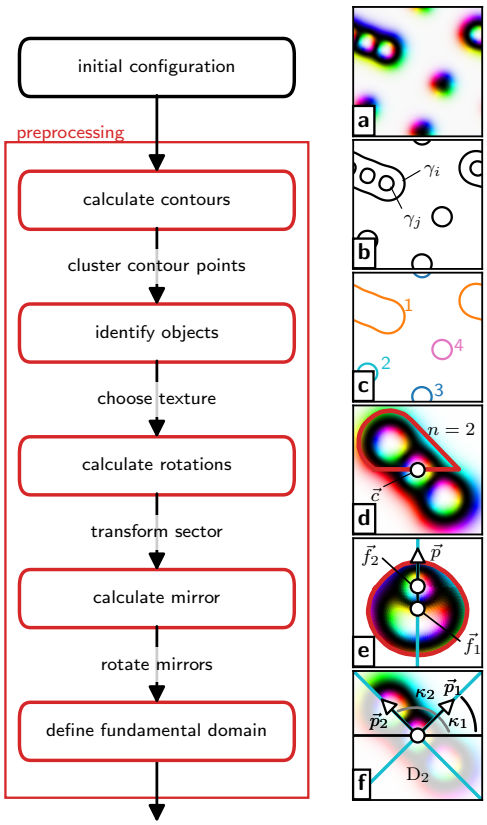


FIG. 3. Flowchart describing the preprocessing of the SPSF for an exemplary magnetic state (**a**) in a chiral magnet for a magnetic field of $h = 0.65$ and model parameters chosen according to $L_D = 64a$ (cf. Tab. I). The DM interaction angle is set to $\beta = 30°$ [cf. Eq. (2)]. **b**: The black lines represent the $m_z = 0$ contours. **c**: Magnetic textures defined by their outer contour ($\gamma_i$) and separated using a density-based spatial clustering. Each color corresponds to one magnetic texture. Inner contours have been excluded ($\gamma_j$). **d**: Texture selected from **a,b** centered at $\vec{c}$. A two-fold rotational symmetry was detected. The red surrounded part of the texture marks one of two equivalent sectors. **e**: Sector transformed using Eqs. (12),(13). The orientation $\vec{p}$ of the mirror axis (cyan) is determined by the connection line between two fixpoints $\vec{f}$ and $\vec{g}$ (see text). For the original texture this yields $n = 2$ mirror axes $\vec{p}_n$ with angles $\kappa_n$ to the $x$-axis depicted in **f**, where the fundamental domain is highlighted and the remaining texture is grayed out.

with $i \in \mathcal{I}$. An element $[\mathcal{M}||\mathcal{N}]$ constitutes a symmetry if it leaves the magnetic configuration invariant such that $\vec{m}\,'(\vec{r}_i) = \vec{m}\,(\vec{r}_i)$ with $\vec{m}\,'(\vec{r}) = [\mathcal{M}||\mathcal{N}]\vec{m}\,(\vec{r}_i)$ for all $i \in \mathcal{I}$. Based on the symmetries of the Hamiltonian [Eq. (4)] [57] we consider $n$-fold rotational elements $[R_{2\pi/n}||R_{2\pi/n}]$ [58]:

$$\vec{m}\,'(\vec{r}_i) = R_{2\pi/n}\vec{m}\,\left(R_{-2\pi/n}(\vec{r}_i - \vec{c}) + \vec{c}\right) \ . \qquad (9)$$

If a texture is invariant under $n$-fold rotations, then its symmetry is described by the spin point group $C_n$. Furthermore, mirror operations corresponding to elements $[R_{\pi-2\beta}P||P]$ [57] are considered:

$$\vec{m}\,'(\vec{r}_i) = R_{\pi-2\beta}P\vec{m}\,(P(\vec{r}_i - \vec{c}) + \vec{c}) \ , \qquad (10)$$

where the reflection matrix $P = 2\vec{p}\cdot\vec{p}^{\,T} - I$ is given by a unit vector $\vec{p}$ corresponding to the direction of the reflection axis in the system plane and the $3 \times 3$ unity matrix $I$. The additional rotation by $\pi - 2\beta$ in the space of the magnetic moments accounts for the helicity of the energy model. If a texture is invariant under $n$-fold rotations combined with $n$ reflections its symmetry is described by $D_n$. Note, that $C_n$ and $D_n$ correspond to spin point groups, they should not be confused with purely spatial crystallographic point groups.

Fig. 1 shows exemplary textures corresponding to different symmetry groups. While the texture in Fig. 1b has no symmetries except the identity ($C_1$), Fig. 1e shows a texture invariant under two-fold rotations ($C_2$). The texture visualized in Fig. 1c exhibits a single reflection axis ($D_1$). The texture in Fig. 1d (Fig. 1f) belongs to $D_2$ ($D_3$) due to its invariance under two-fold (three-fold) rotations with one reflection axis per rotational domain. An axially symmetric object, like a skyrmion (Fig. 1a), will be assigned to the infinite group $D_\infty$.

In practice, by applying a rotation [Eq. (9)] or a reflection operation [Eq. (10)] to a magnetic texture – specified by localized moments $\vec{m}_i = \vec{m}\,(\vec{r}_i)$ at sites $\vec{r}_i$ – yields transformed magnetic moments at transformed sites. However, these transformed sites do only approximately coincide with the positions in the set of sites of the original texture, even if the operation is nominally a symmetry. Therefore, we use a cubic-interpolation to obtain the transformed magnetic moments $\vec{m}\,'_i = \vec{m}\,'(\vec{r}_i)$ at the original sites. The above operation constitutes a symmetry of the magnetic texture if $\vec{m}\,'(\vec{r}_i) \approx \vec{m}\,(\vec{r}_i)$ is approximately satisfied. Numerically the similarity is quantified calculating the geodesic distance [16]:

$$d = \sqrt{\sum_{i\in\mathcal{I}} \left(\arctan2\left(|\vec{m}\,'_i \times \vec{m}_i|, \vec{m}\,'_i \cdot \vec{m}_i\right)\right)^2} \ . \qquad (11)$$

If the geodesic distance per magnetic moment is smaller than a threshold $d/|\mathcal{I}| \leq d_{\mathrm{sym}}$ the operation that generated the $\vec{m}\,'_i$ corresponds to a symmetry.

The following procedure was used to determine the number of rotations and the orientation of reflection axes for a magnetic texture:

1. Since the symmetry under an $n$-fold rotation must revolve around $\vec{c}$, its presence can be determined by performing a rotation of the texture with an angle $2\pi/n$ for each magnetic moment $\vec{m}_i \mapsto R_{2\pi/n}\vec{m}_i$

and each site $\vec{r}_i \mapsto R_{2\pi/n}\vec{r}_i$. An $n$-fold rotation is considered a symmetry if the texture $\vec{m}\,'(\vec{r}_i)$ interpolated at the sites $\vec{r}_i$ of the original texture has a small geodesic distance to the original texture as described above. In the scope of this paper, two- to eleven-fold rotations are tested. If all of these rotations are detected for the given texture, a continuous rotational symmetry is assumed instead. In this case continue with step 3.

2. Introduce $\varphi_i$ as the angle between $\vec{r}_i$ and the $x$-axis. Once we know the texture has $n$-fold rotational symmetry, we can divide it into $n$ identical sectors. Select the magnetic moments $\vec{m}_l$ at lattice sites $\vec{r}_l$ with $\varphi_l \leq 2\pi/n$. This corresponds to a sector of the texture addressed by the indices $l \in \mathcal{L} \subset \mathcal{I}$ (see red sector in Fig. 3d) For each $l \in \mathcal{L}$ apply the following transformation:

$$\vec{m}_l \mapsto \vec{m}_l^{\,s} = R_{(n-1)\varphi_l}\vec{m}_l \tag{12}$$
$$\vec{r}_l \mapsto \vec{r}_l^{\,s} = R_{(n-1)\varphi_l}(\vec{r}_l - \vec{c}) \ , \tag{13}$$

effectively stretching the sector around $\vec{c}$ (Fig. 3e). The transformed sector exhibits either no or exactly one reflection axis and no rotational symmetries. If the sector exhibits mirror symmetry, we can compute a candidate for the reflection axis orientation by

$$\vec{p} = \vec{f}_2 - \vec{f}_1 \ , \tag{14}$$

where $\vec{f}_1$ and $\vec{f}_2$ are two distinct fix-points invariant under reflections [Eq. (10)](cf. Fig. 3e). In this paper we compute $\vec{f}_1$ using Eq. (7) for the magnetic moments $\vec{m}_l^{\,s}$ and positions $\vec{r}_l^{\,s}$ of the sector. Furthermore, $\vec{f}_2$ is chosen as the second moment of the distribution of the $z$-component of the magnetization:

$$\vec{f} = \frac{\sum_{l\in\mathcal{L}} \vec{r}_l^{\,s}(m_l^s \cdot \hat{z})^2}{\sum_{l\in\mathcal{L}} (m_l^s \cdot \hat{z})^2} \ . \tag{15}$$

If $\vec{p}$ constitutes a reflection axis of the sector, the originial texture will have $n$ reflection axes $\vec{p_1}, \ldots, \vec{p}_n$. Each axis corresponds to one rotational domain and is characterized by its angle $\kappa_l$ with respect to the $x$-axis. Their orientation can be calculated using

$$\kappa_l = \frac{l\pi}{n} + \frac{\varphi_{\vec{p}}}{n} \ , \tag{16}$$

where $\varphi_{\vec{p}}$ denotes the angle of $\vec{p}$ with respect to the $x$-axis and $l \in \{1 : n\}$ and.

3. Finally, it has to be tested if the candidate $\vec{p}_l$ really represent reflection axis of the texture. Similar to step 1, this is done by applying the mirror and comparing it to the untransformed structure. If a continuous rotational symmetry was detected in step 1, any direction provides a mirror axis if one is present ($D_\infty$ otherwise $C_\infty$).

The fundamental domain of a texture is then defined using the calculated symmetry elements and the outer contour. For $C_\infty$ and $D_\infty$ we simply choose the fundamental domain as the line connecting the center of the texture with its contour in the $y$-direction (see Fig. 1a). In case the texture is of symmetry $C_n$ (no mirrors) the fundamental domain is defined by the sites $\vec{r}_i$ with $\varphi_i \leq 2\pi/n$ (see Fig. 1e). If the symmetry group is $D_n$ with $n > 1$ the fundamental domain is the part of the texture between the mirror axes $\vec{p}_1$ and $\vec{p}_2$ calculated via $\kappa_2 \geq \varphi_i \geq \kappa_1$ (see Figs. 1d,f). The case $D_1$ is calculated with $\kappa_1 + \pi \geq \varphi_i \geq \kappa_1$.

### B. Escape stage

The GMMF method [21, 24] and related approaches [22] used in the convergence stage of the SP search framework should not be initialized from within the convex region of a local minimum. Suitable starting points for the convergence stage are generated during the escape stage, and this task is nontrivial. The objective is to sample a diverse set of points outside the convex region, where at least one eigenvalue of the Hessian becomes negative. Ideally, these points should lie in different regions containing ascending valleys so as to maximize the likelihood that the subsequent convergence stage, initialized at these points, will reach distinct SPs. Therefore, the escape stage is a crucial part of the SPSF [31, 59], and its strategy must be chosen carefully so as to maximize the completeness of SP sampling.

An escape strategy proposed in this study is based on low-energy excitations of subsystems of a given texture. Each subsystem is defined as an ellipse-shaped region centered within the fundamental domain of the texture. A family of about 50 subsystems is generated by sampling the position of the ellipse center, the length of the semi-axes, and the orientation of the major axis (see Fig. 4a). This sampling ensures that different physically nonequivalent parts of the texture are probed. Note that ellipses may extend beyond the fundamental domain. In particular, at least one subsystem is defined to encompass the entire texture, ensuring that deformations affecting the full texture are properly captured.

Starting from an energy-minimum state, escape trajectories are generated by concerted rotations of the magnetic moments, guided by the low-energy eigenmodes of a subsystem, i.e., the eigenvectors of the corresponding partial Hessian. In practice, each escape trajectory is constructed iteratively. At each iteration, the magnetic moments in the subsystem are displaced by a small distance $\delta$ using a retraction [24, 60], after which the rest of the system is relaxed using the *limited-memory Broyden–Fletcher–Goldfarb–Shanno* (L-BFGS) method [61].

This energy minimization while keeping the subsystem configuration fixed ensures smooth magnetization across the subsystem boundary and prevents formation of artificial boundary effects. After this, the subsystem eigenmode is updated, providing input for the next iteration. The procedure of generating an escape trajectory is summarized in the flowchart in Fig. 4.

An escape attempt is considered successful if the iterative procedure brings the system to a point outside the convex region of the initial minimum while reducing the risk of re-entrance into the convex region during the subsequent convergence stage as explained below. In particular, an attempt is accepted when the following conditions are satisfied:

$$\lambda_1 < 0, \tag{17}$$

$$\frac{|\boldsymbol{v}_1 \cdot \boldsymbol{g}|}{|\boldsymbol{g}|} \geq w_{\text{esc}}, \tag{18}$$

where $\lambda_1$ is the lowest eigenvalue of the Hessian $H$, $\boldsymbol{v}_1$ is the corresponding eigenvector, also referred to as the minimum mode, and $\boldsymbol{g} = (\vec{g}_1, \ldots, \vec{g}_N)$ is the gradient of the energy with respect to the orientation of the magnetic moments given by:

$$\vec{g}_i = \frac{\partial E}{\partial \vec{m}_i} - \left( \frac{\partial E}{\partial \vec{m}_i} \cdot \vec{m}_i \right) \vec{m}_i \, . \tag{19}$$

Note, the Hessian $H \in \mathbb{R}^{2N \times 2N}$ and the gradient adhere to the curvature of the $2N$-dimensional configuration space of magnetic sytems [21, 22, 24, 62]. If only Eq. (17) is enforced, there is a risk of reentering the convex region during the convergence stage. Therefore, Eq. (17) is supplemented by Eq. (18), which requires sufficient alignment between the energy gradient $\boldsymbol{g}$ and the minimum mode $\boldsymbol{v}_1$. Note, this alignment is also a signature of ascending valleys on the energy surface [63–66]. The degree of alignment between $\boldsymbol{g}$ and $\boldsymbol{v}_1$ is controlled by the parameter $w_{\text{esc}} \lesssim 1$. Alternatively, a single escape condition alone may be employed:

$$\lambda_1 \leq \lambda_{\text{esc}}, \tag{20}$$

where the threshold parameter $\lambda_{\text{esc}} < 0$ controls how far the system must move away from the convex region. This escape threshold is particularly important in high-dimensional systems, where configurations can exhibit zero modes, along which an excitation corresponds to overcoming a very small, but different from zero, energy barrier. During the escape process such a mode can acquire a small negative eigenvalue indicating the vicinity to an SP associated to e.g. a skyrmion translation [67, 68]. An escape threshold efficiently filters out these uninteresting SPs.

In practice, it is sufficient to apply Eqs. (17), (18) or Eq. (20) to the subsystem. Consider the partial Hessian $H^s$ constrained to the tangent space of the subsystem that is obtained by the columns and rows of $H$ associated to the magnetic moments of the subsystem. Thus, $H^s$ is a compression of $H$ and Cauchy's interlacing eigenvalue theorem [69] relates the eigenvalues $\lambda^s_\alpha$ of the subsystem Hessian to the eigenvalues $\lambda_\alpha$ of the full system implying:

$$\lambda_1 \leq \lambda^s_1 \, . \tag{21}$$

Hence, checking $\lambda^s_1 \leq \lambda_{\text{esc}}$ and $\lambda^s_1 < 0$ is a conservative and computationally cheap way testing the criteria in Eqs. (17),(20). After a few escape-stage iterations – during which the magnetic texture is deformed only within the chosen subsystem – we find that the minimum mode of the full system becomes strongly localized in this same region. Its components outside the subsystem remain negligible, and the resulting eigenvector closely matches the minimum mode obtained from the subsystem calculation itself. Therefore, in practice $|\boldsymbol{v}^s_1 \cdot \boldsymbol{g}^s|/|\boldsymbol{g}^s| \geq w_{\text{esc}}$ is calculated to evaluate the escape criterion in Eq. (18). Here $\boldsymbol{g}^s$ and $\boldsymbol{v}^s_1$ are the subsystems energy gradient and minimum mode, respectively.

A set of suitable starting points for the convergence stage is obtained by sampling parameters of the subsystems and corresponding low-energy eigenmodes. In practice, it is sufficient to sample deformations along only the lowest five to ten eigenmodes taking into account both signs of the respective eigenvectors. Fig. 4a shows an exemplary sampling of different subsystems centered in the fundamental domain of the double bag state. Figs. 4b-d visualize four subsystem eigenmodes along which may be used in the escape stage.

The proposed escape stage strategy has several advantages. Consider e.g. the SP associated to the duplication mechanism of a skyrmion [21, 24]. There, the skyrmion with symmetry $D_\infty$ transforms via a figure-eight shaped SP configuration exhibiting $D_2$ symmetry. Introducing a tendency toward this SP by following eigenmodes of the full system can require manually switching between several modes subsequently [24]. Sampling spatially confined subsystem excitations during the proposed escape stage offers a degree of control where we want to look for SPs corresponding to transformations locally breaking the symmetry of the minimum texture. Moreover, recomputing the Hessian spectrum for the full system is computationally expensive. The number of magnetic moments within the subsystems is order of magnitude smaller such that many escape attempts can be executed efficiently and in parallel.

### C. Convergence stage

The escape stage yields a set of magnetic configurations outside the convex region of the initial energy minimum. These configurations are then used to initialize the convergence stage, which aims to identify first-order SPs adjacent to that minimum. A detailed description of the *geodesic minimum mode following* (GMMF) method [21] used in the convergence stage as well as its efficient implementation can be found in Ref. [24]. Here, a brief summary is provided for completeness. The GMMF method

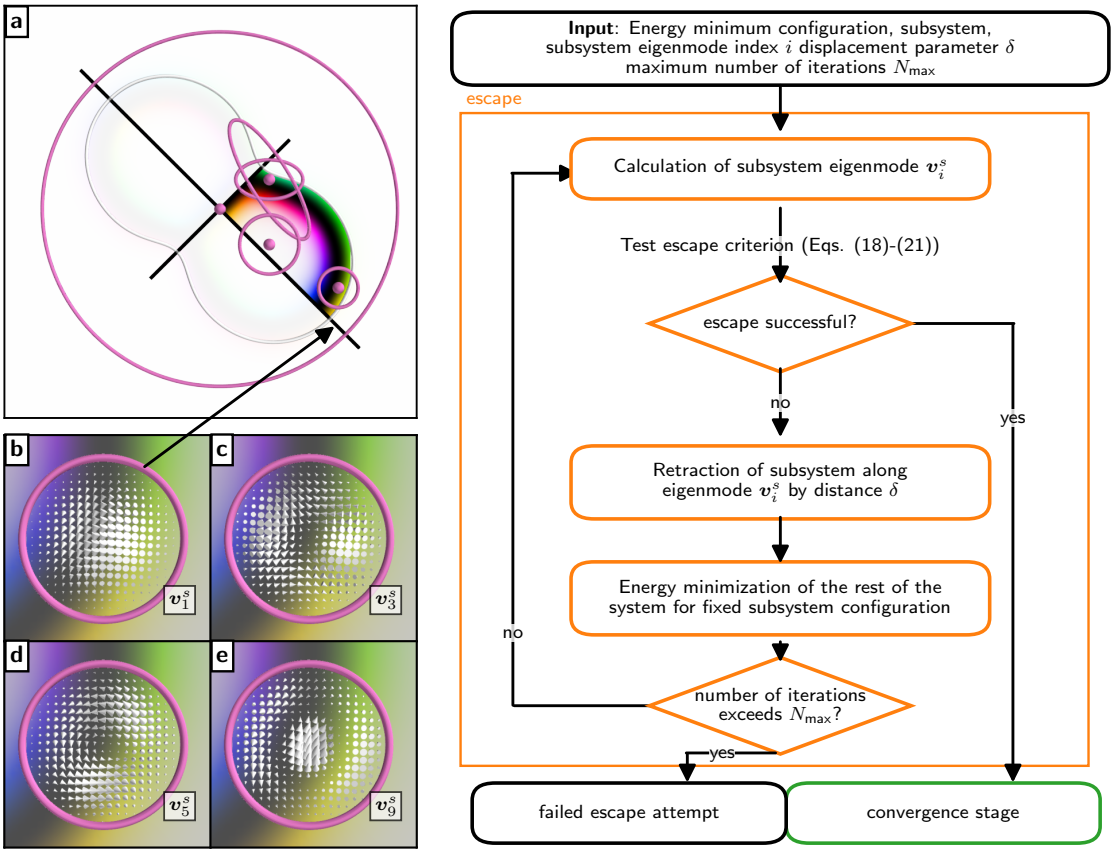


FIG. 4. Illustration of the proposed subsystem-based escape stage of the SPSF. A sampling of elliptical subsystems centered in the fundamental domain is generated (**a**). A set of low-energy subsystem eigenmodes is defined for each subsystem (see **b-e**). Taking into account both signs of the respective eigenvectors each escape attempt iteratively displaces the configuration within the subsystem along a subsystem eigenmodes until the escape criterion is satisfied [Eqs. (17),(18),(20)]. The displacement is guided by a retraction by a distance $\delta$ [24, 60]. In each iteration, after the displacement of the texture, the energy of the rest of the system is minimized while keeping the subsystem fixed. Successful escape attempts mark entry points for the subsequent convergence stage of the SPSF.

iteratively advances the magnetic structure so as to maximize the energy along a certain direction – the inversion mode $\boldsymbol{q}$ – while minimizing the energy along all other directions. In particular, the GMMF force guiding the rotation of the magnetic moments is obtained by reversing the component of the gradient $\boldsymbol{g}$ along the inversion mode:

$$\boldsymbol{f} = -\boldsymbol{g} + 2(\boldsymbol{g}\cdot\boldsymbol{q})\boldsymbol{q}. \tag{22}$$

In the vicinity of an SP, the inversion mode is always the minimum mode, i.e., $\boldsymbol{q} = \boldsymbol{v}_1$. However, near the boundary of the convex region and/or in case of a mode-crossing event, choosing the inversion mode to be the Hessian's eigenvector corresponding to the second lowest eigenvalue or even higher eigenvalue can improve the performance of the GMMF method [24].

The convergence on an SP is achieved using some numerical optimization technique, preferably respecting the curvature of the magnetic configuration space [24, 60], equipped with the GMMF force. We find that an L-BFGS algorithm adapted for magnetic systems [61] yields optimal performance. A GMMF calculation is considered converged on a first order SP if the following conditions are met simultaneously:

$$\max_{i\in\{1,\dots,N\}} |\vec{f}_i| \leq c_{\text{conv}}, \quad \lambda_1 < 0, \quad \text{and} \quad \lambda_2 \geq 0\,. \tag{23}$$

During a calculation, the inversion mode $\boldsymbol{q}$ and the gradient $\boldsymbol{g}$ may become nearly orthogonal, causing the GMMF force to reduce to $-\boldsymbol{g}$. In this case, the GMMF optimization essentially becomes an energy minimization, which may pull the system into a convex region and prevent

convergence on an SP. Such attempts are regarded as failed.

The computational bottleneck of the GMMF algorithm – the repeated calculation of the inversion mode – can be addressed efficiently via direct minimization of the generalized Rayleigh Quotient using the L-BFGS solver [70], adapted to account for the curvature of the Grassmann manifold on which the objective function is defined, while avoiding explicit Hessian evaluations [24]. Efficient evaluation of the inversion mode is significant especially for large systems and/or systems with long-range interactions. For details of the implementation, refer to Ref. [24].

Performance of the convergence stage can be further improved by applying the GMMF method to subsystems defined in the escape stage. In such subsystem-based GMMF (S-GMMF) approach, only magnetic configuration of the subsystem is modified iteratively according to the GMMF algorithm, while the rest of the system is relaxed after each iteration. Computing the inversion mode for a subsystem is much computationally cheaper than for the full system. On the other hand, the subsystem-constrained SP found using the S-GMMF method is often quite close to the true SP of the full system, allowing the subsequent GMMF calculation applied to the full system to converge quickly. This formulation significantly reduces the overall computational cost of the convergence stage compared with applying GMMF to the full system immediately after the escape stage. Another benefit of the S-GMMF approach is that, by constraining the SP search to the same subsystems used in the escape stage, the method improves the correspondence between escape-stage excitations and the identified SPs, making SP sampling more systematic.

Every S-GMMF attempt is followed by a full-system GMMF calculation, initialized with the final configuration of the S-GMMF calculation, even if the S-GMMF does not find a subsystem-constrained SP. S-GMMF may fail to converge if the chosen subsystem is too small. In such cases, the method typically returns to a convex region of the subsystem, indicated by $\lambda_1^s \geq 0$. However, according to Eq. (21), this does not imply that the corresponding configuration lies in the convex region of the full system. As a result, the subsequent full-system GMMF calculation often converges on an SP.

A flowchart summarizing the convergence stage is shown in Fig. 5.

### D. Postprocessing stage

Different SP searches may converge to SPs that represent essentially the same magnetic configuration, differing only by a translation and/or a global rotation of the texture. Consequently, the list of SPs obtained during the convergence stage can contain significant redundancy. The purpose of the postprocessing stage is to eliminate this redundancy, yielding a unique set of saddle points, and to embed them into a state network by identifying the adjacent energy minima.

#### 1. *Filtering of redundant saddle points*

Cluster algorithms used in unsupervised learning are well suited to identify redundant SPs by grouping the corresponding magnetic textures into clusters according to their similarity. Two configurations are considered similar when their feature vectors are close. We find it sufficient to characterize the magnetic textures using compact feature vectors whose components include total energy, individual interaction-resolved contributions to the total energy, the topological charge, and the two lowest eigenvalues of the Hessian. Other choices of features are also possible.

To make the features comparable, each component of the feature vectors is normalized to the unit interval. A subsequent principal component analysis [71, 72] reduces the feature vectors to two dimensions, yielding $\{\boldsymbol{\mathcal{F}}_1, \ldots, \boldsymbol{\mathcal{F}}_{N_{\mathrm{SP}}}\}$ with $\boldsymbol{\mathcal{F}}_j \in \mathbb{R}^2$ and $N_{\mathrm{SP}}$ being the number of SPs found in the convergence stage. These reduced feature vectors form the input to the clustering procedure, where two SPs are assigned to the same cluster if the norm of their feature-vector difference is small. SPs within the same cluster correspond to essentially equivalent magnetic configurations, whereas SPs in different clusters represent significantly different textures.

Because the number of distinct SPs is not known a priori, the number of clusters must be determined from the data. Given the modest number of SP configurations on the scale of machine learning problems, we repeatedly apply k-means clustering [73] for several candidate cluster counts and select the best partition using the silhouette score [74]. This workflow can be implemented straightforwardly using standard machine-learning libraries [75]. Only one representative from each cluster is kept, yielding a set of unique SP configurations.

#### 2. *Connectivity and adjacent minima*

To construct the graph of metastable states, each SP must be linked with the minima it connects. This is done by performing steepest-descent energy minimizations in both directions of the unstable mode, starting from every identified SP. These minimizations confirms whether the SP is connected to the initial minimum used in the SPSF search and, simultaneously, reveals the adjacent minimum, thereby extending the network of states. If neither minimization returns to the initial minimum, the SP is still stored, as it corresponds to a transition between some other metastable states and therefore remains relevant for mapping the global energy landscape.

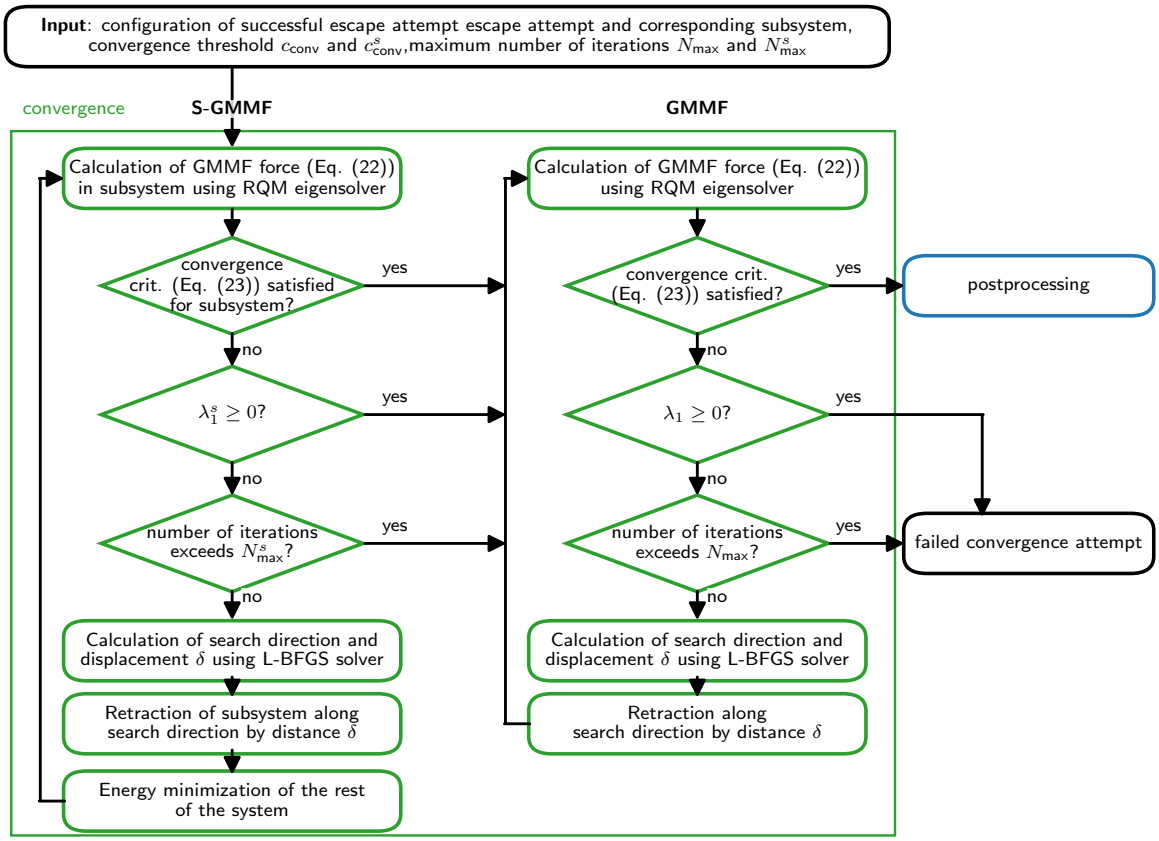


FIG. 5. Flowchart of the convergence stage. For each of the final configurations from the escape stage an S-GMMF calculation is initialized while using the same subsystem as in the corresponding escape attempt. First the GMMF force is computed in the subsystem [Eq. (22)]. If none of the exit criteria for S-GMMF is satisfied (see text) the search direction and the displacement parameter $\delta$ is computed using an L-BFGS solver. The subsystem is subsequently retracted along this search direction and after minimizing the energy of the rest of the system the process repeats until either a subsystem-constrained SP has been identified, a convex region has been entered for the subsystem or the number of iterations exceeds $N^s_{\text{max}}$. In all cases subsequently the full system GMMF algorithm is applied. For details about the GMMF implementation refer to Ref. [24]. The convergence stage yields a set of SPs that is passed to postprocessing.

## IV. RESULTS

In the following, we apply the developed SPSF to the 2D chiral magnet system to investigate transitions between metastable magnetic textures formed by various combinations of closed loops, chiral kinks, and tails. In Sec. IV A, we analyze SPs surrounding the skyrmion state and identify the adjacent textures corresponding to local energy minima. SPSF calculations initiated from each minimum progressively map out the graph of magnetic textures, where the edges correspond to SPs and the nodes correspond to local energy minima. In Sec. IV B we analyze this graph and reveal a hierarchy of energy barriers associated with transformations of the fundamental elements of magnetic textures. In Sec. IV C we examine how these transformations change under variation of the lattice discretization. Finally, Sec. IV D addresses whether an MEP always exists between two magnetic states belonging to the same homotopy class. Unless stated otherwise, the external magnetic field is set to $h = 0.623$, for which all of the fundamental elements – closed contours, chiral kinks, and tails – can be present as components of meta-stable textures [76], and the period of the helical ground-state modulation is set to $L_D = 40a$.

### A. Skyrmion collapse mechanisms and adjacent states

Fig. 6 provides an overview of the SPSF calculations applied to the most prominent 2D topological magnetic texture – axially-symmetric skyrmion with topological charge $Q = -1$. Since the skyrmion exhibits $D_\infty$ symmetry, its fundamental domain is a radius, i.e., a line segment from the skyrmion center to its perimeter contour (Fig 6b). Two points on the skyrmion radius were chosen as centers of the elliptical subsystems used to generate excitations in the escape stage (Fig. 6b). Each ellipse was oriented with one of the axes aligned along the skyrmion radius. For each center position, a set of nine ellipses was defined using the following values of the semiaxes $a_S$ and $b_S$:

$$a_S, b_S \in \{L_D/2, L_D/4, L_D/8\}. \tag{24}$$

Escape attempts are performed for each subsystem using the eigenvectors of the subsystem Hessian corresponding to the five lowest eigenvalues, until the escape criterion [cf. Eqs. (17),(18),(20)] is satisfied. Considering both directions along each eigenvector, this results in a total of 180 escape attempts, all successful. An escape attempt is considered successful if either the criterion in Eq. (20) is satisfied or both Eq. 17 and Eq. 18 are fulfilled. In this work we use $\lambda_{\text{esc}} = -0.2\mathcal{J}$ and $w_{\text{esc}} = 0.25$ for the numerical thresholds in these criteria.

Each escaped configuration was passed to the convergence stage. Among 180 convergence attempts, 73 failed, ending in convex regions, while 107 yielded SPs. Postprocessing grouped them into clusters corresponding to 11 unique SPs. Connectivity tests using steepest-descent calculations showed that three of the identified SPs are not connected with the initial minimum, resulting in eight mechanisms ($SP_1$-$SP_8$) of the skyrmion collapse.

Fig. 6a shows the unique SPs, their occurrence counts in repeated searches, and their energies relative to the skyrmion state minimum.

Fig. 7 illustrates all stages of a successful SP search attempt for a circular subsystem with a radius of $L_D/8$ (Fig. 7a) and an excitation chosen along the subsystem eigenmode corresponding to the fifth lowest eigenvalue of the subsystem Hessian (see inset of Fig. 7a). Following the chosen eigenmode of the subsystem is accompanied by relaxation of the rest of the system, as described in Sec. III B. Note that mode crossings occurred several times during the escape stage, resulting in changes of the index of the eigenmode. Fig. 7b presents several of the lowest eigenvalues $\lambda_i^s$ of the subsystem Hessian during the escape process. After several iterations, the lowest eigenvalue becomes negative, while the gradient maintains a substantial overlap with the minimum mode, indicating a successful escape from the convex region and providing a suitable starting point for the subsequent convergence stage [see Eqs. (17),(18)]. The corresponding deformed configuration with strongly canted magnetic moments is shown in the inset of Fig. 7b.

By the final iteration of the escape stage, the minimum modes of the subsystem and the full system describe nearly identical excitations. This is also reflected in the alignment measures. For the full system, Eq. (18) evaluates to $w \approx 0.29$, while a value of approximately 0.35 is calculated using the subsystem quantities. The vector field representation of the subsystem minimum mode is shown in the inset of Fig. 7b.

The convergence stage, initialized from the escaped configuration, involves an S-GMMF calculation followed by a full-system GMMF refinement (Fig. 7c). The application of the S-GMMF yields a subsystem-constrained SP corresponding to the formation of a chiral kink in the subsystem. Subsequent full-system GMMF calculation converges to the SP illustrated in Fig. 7d. The lowest eigenvalues of the subsystem and full-system Hessians are nearly identical. In contrast, the second-lowest eigenvalues differ qualitatively: in the subsystem, $\lambda_2^s > 0$, while in the full system $\lambda_2 \approx 0$, indicating a mode whose excitation costs almost no energy. This zero mode corresponds to a rotation of the texture shown in Fig. 7d around the chiral kink. Zero modes are absent in the subsystem due to the imposed constraints.

Steepest descent calculations in the postprocessing stage confirm the connection of the identified SP to the initial skyrmion state and reveals the adjacent energy minimum corresponding to a topologically trivial ($Q = 0$) chiral droplet, which can be viewed as a skyrmion with a chiral kink, see Fig. 7d. The identified SP, also referred to as the Chimera SP [77, 78], describes nucleation of the chiral kink at the skyrmion perimeter – a process that changes the topological charge by one.

Other skyrmion collapse mechanisms are discussed in the following in the order of increasing energy barrier. In Fig. 6a, the corresponding SP configurations are visualized by their contours. For each SP configuration connecting states from different homotopy classes, the maximum of the scalar spin chirality [79, 80]

$$\chi_{ijk} = \vec{m}_i \cdot (\vec{m}_j \times \vec{m}_k) \,, \tag{25}$$

is marked with a transparent red circle Fig. 6a. Maxima of $\chi$ correspond to regions of strongest canting of the magnetic moments, thereby indicating the locations of topological charge injection and the regions of highest exchange energy density.

The lowest-barrier mechanism connects the skyrmion with the triangular-shaped texture carrying three tails (Fig. 6i). Here, the skyrmion elongates and can be interpreted as a texture with two tails, while $SP_1$ corresponds to the nucleation of a third tail between the two ends of the elongated skyrmion. The topological charge does not change upon the formation of tails.

The three SPs – $SP_2$, $SP_3$ and $SP_4$ – all connect the skyrmion state to the two-skyrmion state ($Q = -2$) (Fig. 6ii) via three different mechanisms. In particular, $SP_3$ corresponds to the skyrmion-duplication mechanism

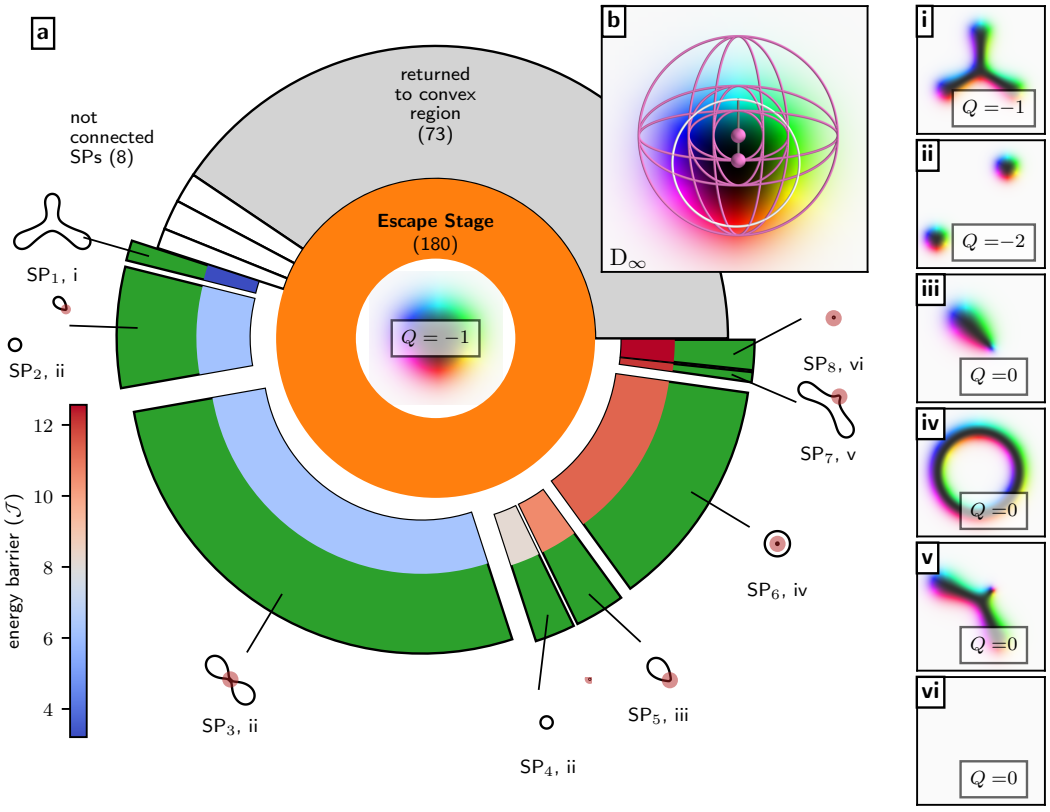


FIG. 6. **a**: SPSF applied to the axial symmetric skyrmion ($D_\infty$) in a chiral magnet using 180 escape stage attempts based on the subsystems shown in **b** for a magnetic field of $h = 0.623$ and exchange and DM interaction parameters according to $L_D = 40a$. The escape criteria are set to $\lambda_{\text{esc}} = -0.2\mathcal{J}$ [cf. Eq. (20)] and $w_{\text{esc}} = 0.25$ [cf. Eq. (18)]. Convergence stage calculations returning to a convex region are shown in gray; green and white wedges represent the converged SPs, grouped into 11 clusters. White wedges indicate three clusters whose SPs do not reconnect back to the initial minimum. The eight green clusters represent SPs connected to the skyrmion state. The SP configurations are depicted by their $m_z = 0$ contours. The respective adjacent energy minimum configurations are labeled **i-vi**. The colorbar gives the energy barrier ($E_{\text{SP}} - E_{\text{Sk}}$) in units of the continuous-theory exchange parameter $\mathcal{J}$.

reported in Ref. [21]. $SP_4$ corresponds to the formation of a second isolated skyrmion in the FM background via a Bloch point-like defect nucleation. $SP_2$ describes the mechanism, where the second skyrmion is formed from an isolated droplet-shaped configuration, similar to that shown in Fig. 7d. In this case, the presence of the second skyrmion destabilizes the droplet, so that the final state is two skyrmions rather than a skyrmion-droplet pair. In contrast, a single skyrmion can transform into a meta-stable droplet (Fig. 6iii), as described earlier in the context of Fig. 7d.

$SP_6$ corresponds to the nucleation of an inner contour within the skyrmion via a Bloch point-like defect, thereby transforming the skyrmion into a skyrmion bag also referred to as skyrmionium. Since the outer contour and inner contour have opposite windings, the skyrmion bag carries zero topological charge $Q = 0$ (Fig. 6iv). The skyrmion can also elongate and form a kink on its perimeter, as described by $SP_7$. The adjacent state ($Q = 0$) (Fig. 6v) can be interpreted either as a chiral droplet with an attached tail or as an elongated skyrmion with a chiral kink. Finally, the skyrmion can disappear via the usual radially-symmetric collapse mechanism described by $SP_8$ (Fig. 6vi).

### B. Network of states in 2D chiral magnets

Recursive application of the SPSF to the metastable states enables the discovery of new metastable configu-

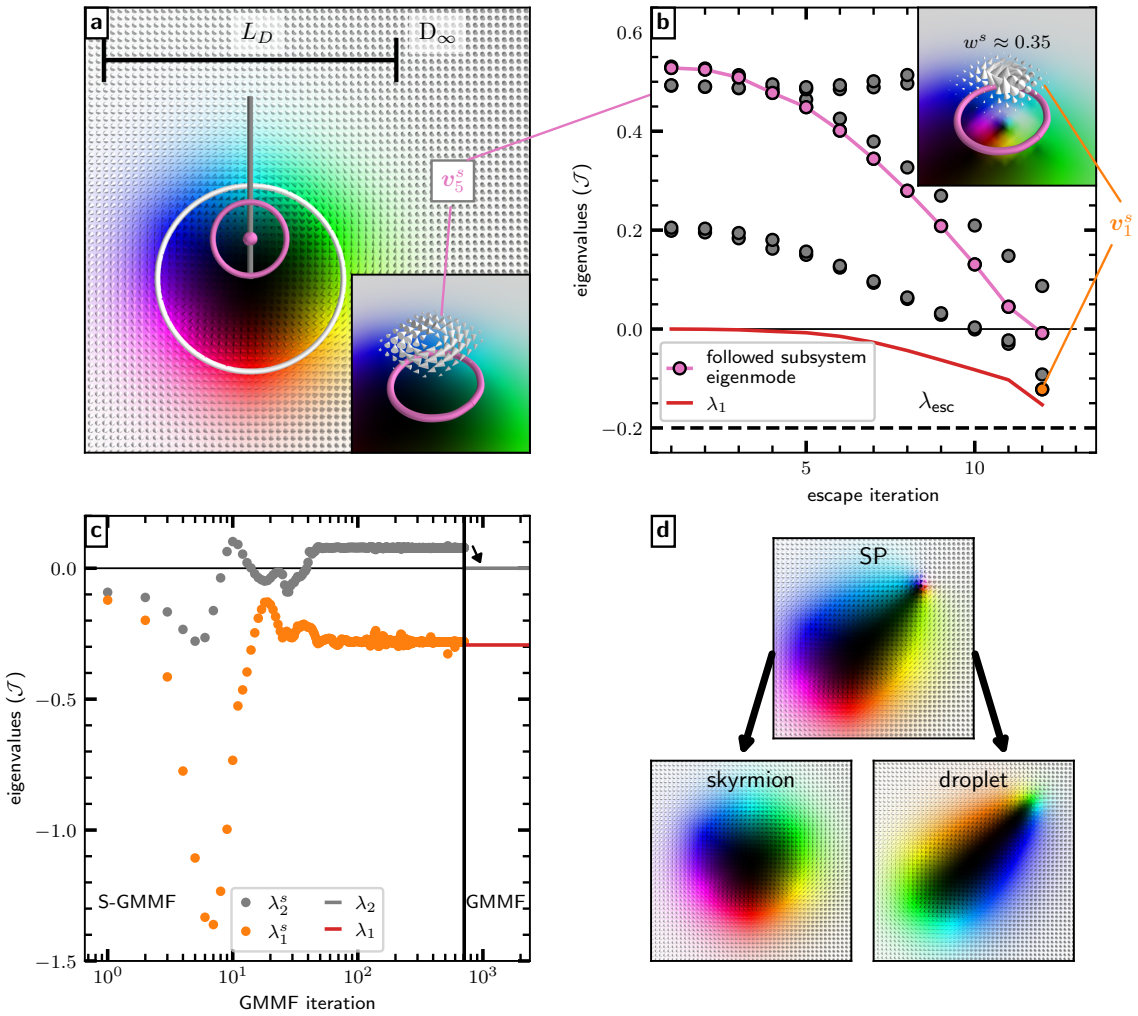


FIG. 7. **a**: Axial symmetric skyrmion ($D_\infty$) in a square lattice chiral magnet with $200 \times 200$ magnetic moments for a magnetic field of $h = 0.623$ and exchange and DM interaction parameters chosen according to $L_D = 40a$. A circular subsystem (pink) is centered within the fundamental domain (gray line segment). The eigenvector $\boldsymbol{v}_5^s$ of the subsystem Hessian is shown in the inset. **b**: Evolution of the subsystem Hessian eigenvalues $\lambda_i^s$ during the escape attempt, initialized with the eigenvector that has initially index five. The eigenvalue of the followed mode is shown in pink; the lowest eigenvalue $\lambda_1$ of the full system is plotted in red and remains below $\lambda_1^s$ as expected from Eq. (21). The escape threshold is set to $\lambda_{esc} = -0.2\mathcal{J}$ [cf. Eq. (20)] and is visualized by a black dashed line. For the alignment measure threshold $w_{esc} = 0.25$ is used [cf. Eq. (18)]. The lowest eigenvalue of the subsystem for the final configuration of the escape attempt is shown in orange (the corresponding eigenvector is shown in the inset). The alignment between the gradient and the minimum mode in the subsystem is given by $w^s \approx 0.35$. **c**: Evolution of the two lowest subsystem Hessian eigenvalues $\lambda_1^s$ (orange dots), $\lambda_2^s$ (gray dots) during the convergence stage. The vertical black line marks the switch to the full system GMMF with the Hessian eigenvalues $\lambda_1$ (red line) and $\lambda_2$ (gray line). **d**: SP reached in the convergence stage corresponding to a skyrmion with a chiral kink. Below the configurations are shown obtained by energy minimization initialized with the slightly displaced SP.

rations and the connections between them, thereby allowing a systematic exploration of the energy surface of the magnetic system. The resulting data can be represented as a directed graph in which energy minima form the vertices and the SPs defining transitions between the minima form the edges.

Figure 8 presents an example of such a graph, obtained after several recursive SPSF applications to the

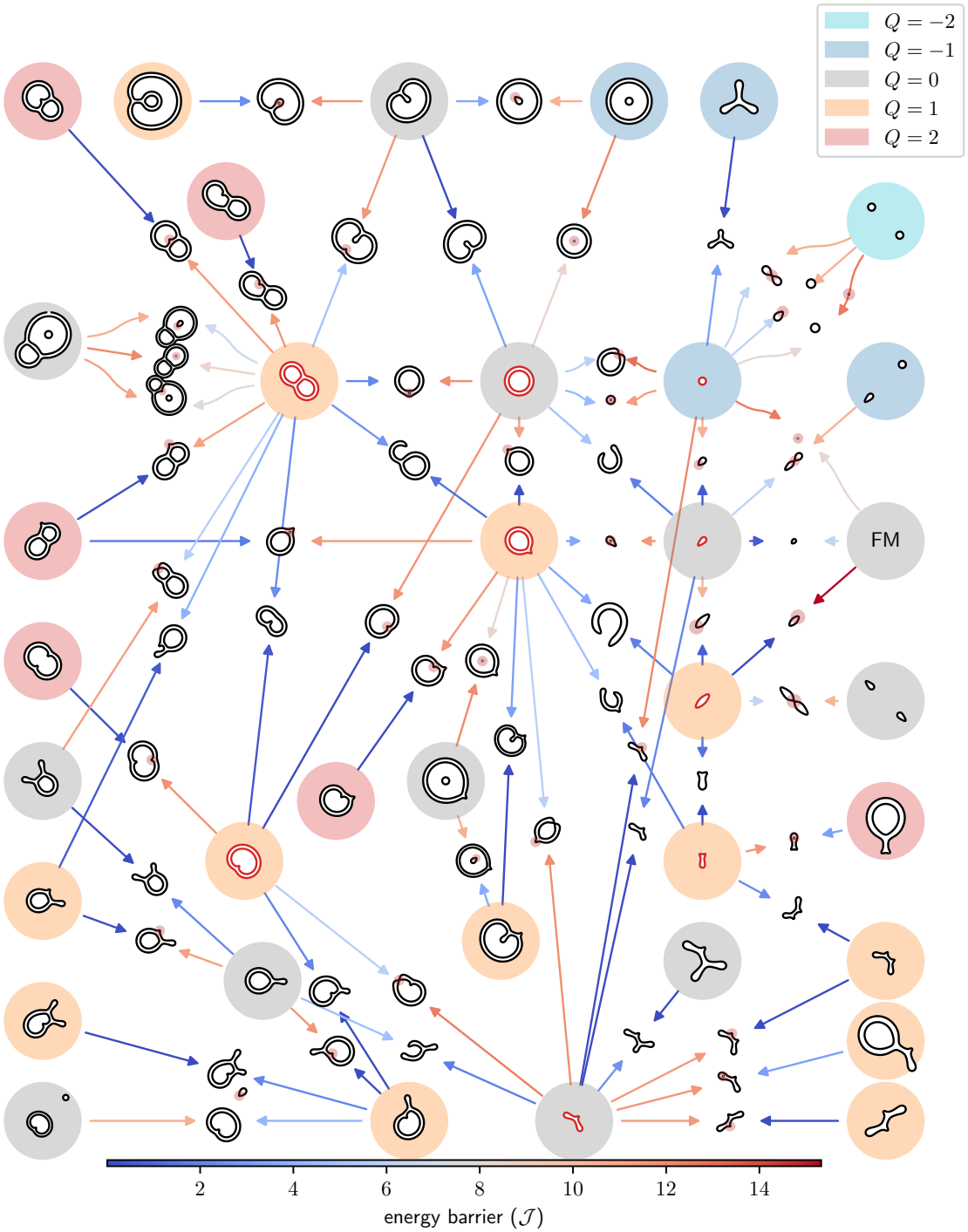


FIG. 8. Graph representation of the minima (vertices) and SPs (edges) revealed by applications of the SPSF to a chiral magnet with $L_D = 40a$ and $h = 0.623$. The $m_z = 0$ contours of the meta-stable states are shown within colored circles according to their topological charge. The initial states of the SPSF are shown by red contours. For each transition the corresponding SP is visualized in the middle of the respective edge. Each arrow – starting at a minimum and ending at an SP – is colored depending on the height of the energy barrier which needs to be climbed to reach this SP (see colorbar). For transitions where the topological charge is changing, the area of maximum spin chirality [Eq. (25)] of the SP marked with a transparent red circle.

system with $L_D = 40a$ and $h = 0.623$ and labeled with the topological charge of each state and the energy barrier of each transition. This graph exposes a rich variety of localized textures and the transitions between them.

Despite the complexity of the network of localized textures, most SPs characterizing transitions in this network can be grouped into five categories based on the transformations of the fundamental building blocks of the textures:

- Nucleation of a chiral kink
- Formation of a closed contour via injection of a Bloch point–like defect
- Merging of two contours
- Formation of a tail
- Merging of two contours accompanied by the nucleation of a chiral kink

Examples of SP configurations from each category are shown in Fig. 9b-f.

The nucleation of a chiral kink (see Fig. 9b) locally changes the winding of the magnetization along a contour and thereby leads to small region where the sense of rotation of the magnetic moments is opposite to the systems's intrinsic chirality. Since anisotropy is not included in this work, only positive chiral kinks, which contribute $+1$ to the winding number of the hosting contour, appear as constituents of metastable textures. Consequently, this SP category corresponds to transformations in which the total topological charge changes by $\Delta Q = +1$.

In contrast to the chiral kink nucleation, formation of an additional closed contour via injection of a Bloch-point–like defect (see Fig. 9c) can either increase or decrease the topological charge, $\Delta Q = \pm 1$, depending on the winding of the newly formed contour. For example, formation of the contour in the FM vacuum decreases $Q$ by one, while nucleation of the contour inside the skyrmion perimeter increases $Q$ by one.

SPs in the contour-merging category capture the mechanism in which two closed contours – nested or disjoint – combine and form one closed contour (see Fig. 9d). Similar to the Bloch-point-like defect injection, such a transformation can either increase or decrease the total topological charge, $\Delta Q = \pm 1$, depending on the hierarchy of the merging contours as well as on their intrinsic winding, i.e. winding of the magnetization along the bare (kink-free) contours. In particular, merging two disjoint contours with positive (negative) intrinsic winding decreases (increases) $Q$ by one, while merging a contour with positive (negative) intrinsic winding with an inner contour increases (decreases) $Q$ by one.

In contrast to chiral kink nucleation, Bloch point-like defect injection, and contour merging, the last two mechanisms correspond to homotopies, i.e. continuous transformations of the magnetization that preserve the topological charge of the system, $\Delta Q = 0$. Indeed, formation of a tail (see Fig. 9e) only deforms a contour without changing sense of rotation of magnetization, thereby leaving the topological charge unchanged.

The SPs from the fifth category describe the second homotopy, where two closed contours merge simultaneously with the nucleation of a chiral kink (see Fig. 9f). This compensation ensures that the total topological charge remains unchanged. Such transformations occur only for disjoint contours with positive intrinsic winding or for nested contours in which the outer contour has negative winding. Examples of this mechanism include the transformation of a skyrmion bag into a chiral droplet, where the merging of two nested contours contributes $-1$ to the topological charge change, which is compensated by the nucleation of a chiral kink, and the transformation of a skyrmion bag with two disjoint inner contours into a skyrmion bag with a single inner contour containing a chiral kink (Fig. 9f).

Finally, two special SPs do not belong to any of the identified categories. They correspond to the progressive shrinking and eventual collapse of a chiral droplet and an antiskyrmion into the FM background (see Fig. 9a).

A histogram of SP energies for all identified transitions, measured relative to the lower-energy endpoint of each transition, shows the distribution of energy barriers in the system (see Fig. 9a). Clearly, the energy barriers associated with the five identified mechanisms exhibit only a weak dependence on the specific host texture and are only marginally influenced by the presence of tails, chiral kinks, or closed contours. For example, nucleating a chiral kink on the outer contour of a skyrmion bag requires nearly the same energy as creating a second kink on a droplet to convert it into an antiskyrmion. This insensitivity to the underlying texture highlights the universal character of the identified SP categories.

A clear separation of energy scales of homotopies and non-homotopies is also observed for the chosen value of $L_D$, with homotopies exhibiting lower energy barriers than transitions that change the topological charge. Motivated by this observation, we next examine the universality of this hierarchy through a scaling analysis presented in the following section.

### C. Scaling analysis of transition mechanisms

To further assess the universality of the identified transition mechanisms, we consider a simple host texture: an isolated stripe formed by two closed contours (Fig. 10a), which can also be seen as a fragment of an infinitely large skyrmion bag. The five SP categories —tail formation, chiral kink nucleation, contour creation, contour merging, and contour merging with chiral kink nucleation — are analyzed in this context.

Figure 10b shows the corresponding energy barriers as a function of $L_D$ ranging from small values, where adjacent magnetic moments exhibit strong canting, to large values, where canting is small and the lattice model

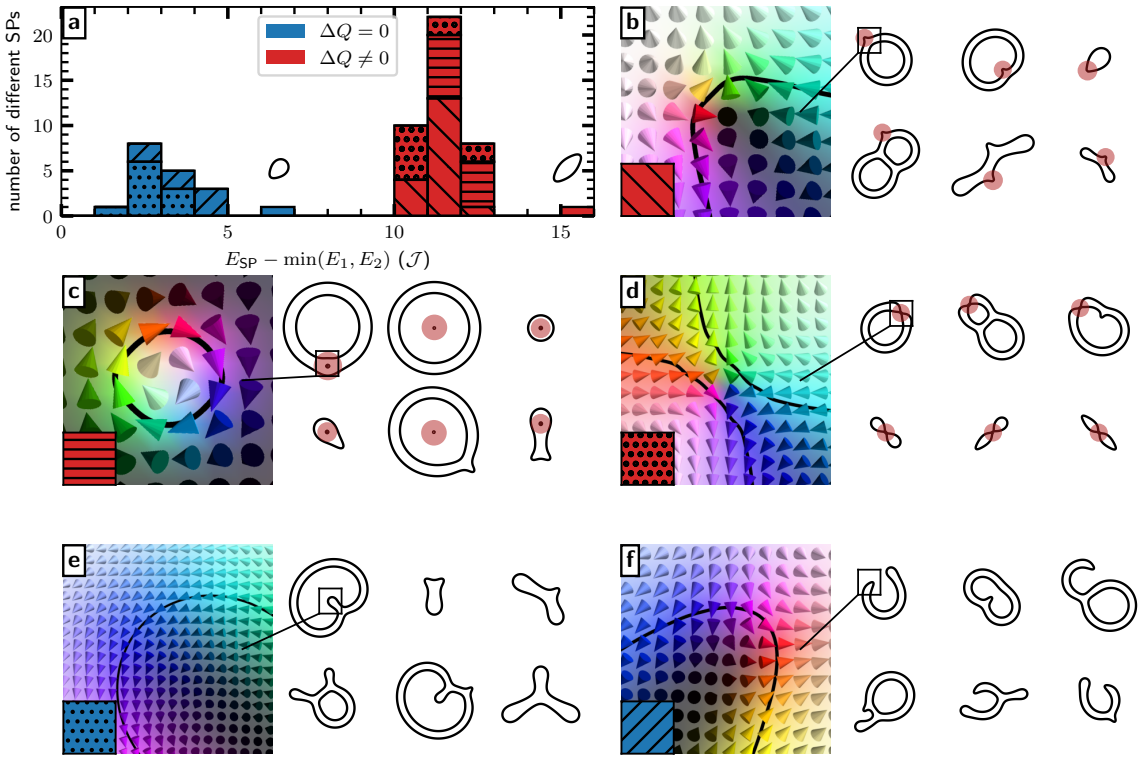


FIG. 9. **a**: The number of different SPs shown in Fig. 8 sorted in a histogram with respect to the associated energy barrier corresponding to the low-energy endpoint ($\min(E_1, E_2)$) of the transition in units of the continuous-theory exchange parameter $\mathcal{J}$. Homotopies (non-homotopies) are colored blue (red). The shading refers to one of five specific types of transitions (see text): chiral kink nucleation (**b**), creation of a closed contour via a Bloch point-like defect (**c**), merging of two contours (**d**), formation of a tail (**e**) and merging of two contours accompanied by the nucleation of a chiral kink (**f**). For each category six exemplary SPs from Fig. 8 are shown. The SP associated to the annihilation of the droplet (antiskyrmion) into the FM state is shown in **a** above the corresponding bar of the histogram.

approaches the continuum limit. In this limit, the energy barrier for nucleating a skyrmion in the ferromagnetic background (Fig. 10vi) converges to $4\pi\mathcal{J}$ [12]. Energies of all considered SPs in the isolated stripe system remain below this limit for all considered values of $L_D$.

There is a clear distinction in how homotopic and non-homotopic transitions behave under variation of $L_D$. The energy barriers associated with homotopies – tail formation (Fig. 10i) and homotopic contour merging (Fig. 10ii) – remain nearly independent of $L_D$. In contrast, the barriers for non-homotopic mechanisms – non-homotopic contour merging (Fig. 10iii), chiral kink nucleation (Fig. 10iv), and contour creation (Figs. 10v,vi) – increase with $L_D$ and appear to approach finite values in the continuum limit.

A crossover between the homotopic and non-homotopic contour-merging mechanisms occurs at $L_D \approx 30a$. For lower $L_D$, the non-homotopic transition becomes energetically favorable. The fact that the homotopy does not always yield the lowest energy barrier raises the question of whether an MEP representing a homotopy always exists between states with the same topological charge. This question is addressed in the following section.

Finally, Fig. 10c shows that the presence of a tail on the isolated stripe has only a minor influence on the energy barriers associated with homotopic contour merging, chiral kink nucleation, and contour creation (Fig. 10c, orange).

### D. Homotopies and MEPs

There exists an infinite number of homotopies between textures with the same topological charge. In this section, we investigate under what conditions a MEP can represent a homotopy. Although homotopy is only an approximate notion in the discrete lattice model considered

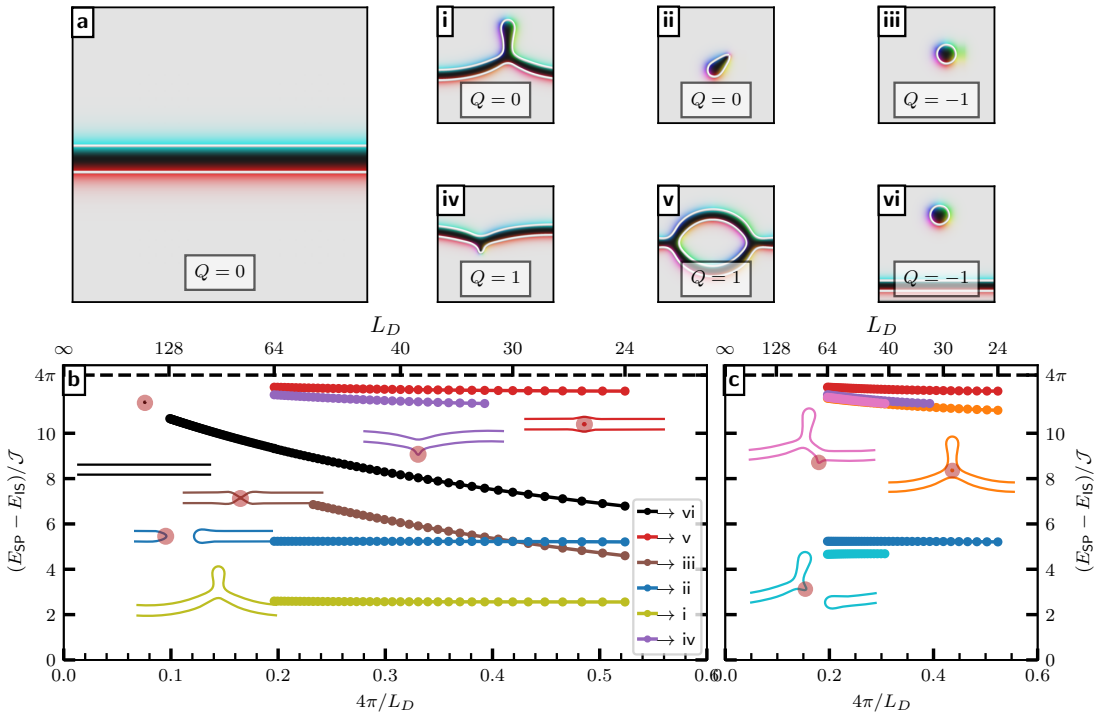


FIG. 10. Energy $E_{\mathrm{SP}}$ of SPs associated to transitions of the isolated stripe state (**a**) as a function of $L_D$ for $h = 0.623$ relative to the energy of the stripe $E_{\mathrm{IS}}$ in units of the continuous-theory exchange parameter $\mathcal{J}$. The simulated system size is $4L_D \times 4L_D$. The SPs are represented by their contours in **b**,**c** and the position of maximum spin chirality [Eq. (25)] is marked with a red circle. The corresponding configurations of the adjacent energy minima for the transitions in **b** are shown in **i**-**vi**. The transitions in **b** are tail forming (olive), contour-merging accompanied by chiral kink nucleation (blue), contour-merging (brown), chiral kink nucleation (purple), contour curve creation via a Bloch point-like defect within the stripe (red) and next to the stripe (black). **c**: Tail forming (cyan), contour curve creation (orange) and chiral kink nucleation (pink) for the isolated stripe with an attached tail.

here, it remains a useful framework for analyzing transitions. We focus on the collapse of the skyrmion bag state ( $Q = 0$) into the FM state for $L_D = 30a$.

A homotopy-MEP is illustrated in Fig. 11a. The transformation begins with homotopic contour merging accompanied by the nucleation of a chiral kink (i), converting the skyrmion bag into a chiral droplet. The droplet then continuously collapses into the FM state without forming singularities (iv).

Other collapse mechanisms are possible, but they do not represent homotopies. The skyrmion bag may first transform into a skyrmion either by collapse of the inner contour (ii) or via non-homotopic contour merging (iii). From the skyrmion state, the system can reach the FM state either directly (vi) or via the chiral droplet state (vii).

The homotopy-MEP, however, exists only for magnetic fields in the range $0.6185 \leq h \leq 0.633$. The disappearance of the homotopy-MEP for the fields outside this range can be understood by analyzing the energy profiles at the critical fields (Figs. 11c–d). Near the lower critical field, $h \approx 0.6185$, the homotopic contour merging is followed by a contraction of the resulting structure toward the chiral droplet; however, this contraction is accompanied by only a weak decrease in energy. Below this field, the contraction becomes energetically unfavorable, and the configuration instead elongates toward an extended stripe domain.

With increasing field, the skyrmion bag becomes progressively more compact, enhancing the tendency toward collapse of the inner contour. Although the homotopy-MEP still exists near the upper critical field, $h \approx 0.633$, a slight increase destabilizes it: the GMMF method converges to the SP corresponding to inner-contour collapse (ii) even when initialized from the homotopic contour-merging SP obtained at $h = 0.633$. As a result, the actual MEP passes through the skyrmion state and does not represent a homotopy. The corresponding energy variation is shown in Fig. 11e.

Interestingly, the homotopic contour-merging mech-

anism never provides the lowest energy barrier for the collapse of the skyrmion bag. The inner-contour collapse (ii), which is a non-homotopy, corresponds to a lower barrier, while the non-homotopic contour merging (iii) yields a larger barrier, as summarized in Fig. 11b.

## V. CONCLUSIONS AND DISCUSSION

The *saddle point search framework* (SPSF) developed in this work offers a systematic method to identify the SPs on the system's energy surface that surround a given initial energy minimum corresponding to a metastable state. The developed SPSF is particularly suitable for magnetic systems capable of hosting various co-existing localized textures. The method extends existing SP search algorithms for magnetic systems [21, 22, 24] by introducing a structured multi-stage design – comprising preprocessing, escape, convergence, and postprocessing stages – that enables a systematic and automated exploration of the energy surface around minima. A key methodological advancement lies in the systematic escape stage, which strategically samples deformations of the minimum-energy configuration following low-energy excitations in symmetry-informed subsystems. Thereby each escape attempt introduces a tendency toward an SP, which is associated to breaking locally the symmetry of the minimum-energy configuration corresponding to a localized magnetic texture. Distributing subsystems with centers within the fundamental domain – the smallest region containing all unique physical information of the texture – and sampling excitations along several low-energy eigenmodes of the subsystem makes this approach systematic and computationally efficient. Combining the escape process, which requires only calculation within a small subset of the system, and the GMMF method for convergence onto SPs that efficiently determines the minimal Hessian eigenmodes via minimization of the Rayleigh Quotient [24] yields a methodology applicable to large systems and systems characterized by long-range interactions.

We apply the SPSF to localized magnetic textures corresponding to metastable states in two-dimensional chiral magnets and explore the energy surface by recursively traversing between energy minima via first-order SPs. A rich set of metastable localized textures is exposed, all of which can be described using just three fundamental building blocks: closed contours, chiral kinks [5], and tails [32].

Importantly, our work provides a systematic analysis of the SP configurations that govern transformations between the metastable states. Five characteristic categories of SPs are identified corresponding to the following transition mechanisms: chiral kink nucleation, contour-merging, contour line creation via injection of a Bloch point-like defect, tail forming and contour-merging accompanied by simultaneous chiral kink nucleation. The last two mechanisms represent homotopies, whereas the others change the topological charge of the system. Remarkably, the energy barriers associated with these transformations depend only weakly on the specific host texture, pointing to a universal character of the identified SP categories and motivating the analysis of a simple, generic host texture: a pair of closed contours forming an isolated stripe. To probe this universality, the energy barriers associated to the five identified mechanisms for the isolated stripe are calculated while scaling the model toward the continuum limit.

During this scaling, all energy barriers remain below the known nucleation barrier of an isolated skyrmion in the FM background in the continuum limit [12]. Moreover, transformations that change the topological charge and homotopies exhibit fundamentally different trends: while the energy barriers associated to the former class of transformations increase as the continuum limit is approached, the barriers corresponding to homotopies remain constant under variation of $L_D$.

Although any two textures with the same topological charge $Q$ can always be continuously transformed into one another without changing the total topological charge of the system, our results show that, under certain conditions, no homotopy between the states corresponds to a *minimum energy path* (MEP) characterized by a first-order SP. In particular, we find that the skyrmion bag ($Q = 0$) and the ferromagnetic state ($Q = 0$) are connected by an MEP associated with a homotopy only within a certain range of magnetic fields. Outside this field range, the transformation between these two textures inevitably involves the nucleation and subsequent annihilation of topological charge, rather than a homotopy. This demonstrates an important point: Two metastable states corresponding to textures that belong to the same homotopy class are not always connected with an MEP that at the same time describes a homotopy. Furthermore, MEPs associated with homotopies do not always correspond to the lowest energy barrier transformations of a system.

The idea of sampling symmetry-informed subsystem excitations can be straightforwardly applied to a broad range of magnetic materials included three-dimensional systems. Furthermore, our work paves the way for further improvements of the SPSF. On the one hand, techniques such as genetic multi-objective algorithms [27] could be used to learn the optimal distributions of subsystems yielding the richest diversity of SPs. On the other hand the number of convergence stage calculations reentering a convex region could be further reduced by implementing re-escaping strategies [31]. Due to its modular structure and efficiency, the SPSF is ideally suited to be used in advanced methods that rely on repeated SP searches. For example, the energy surface can be explored globally by searching for metastable states via recursive traversing from one energy minimum to another over SPs. Combining this with on-the-fly calculation of the transition rates at a given temperature using the rate theory methods yields the adaptive kinetic Monte Carlo

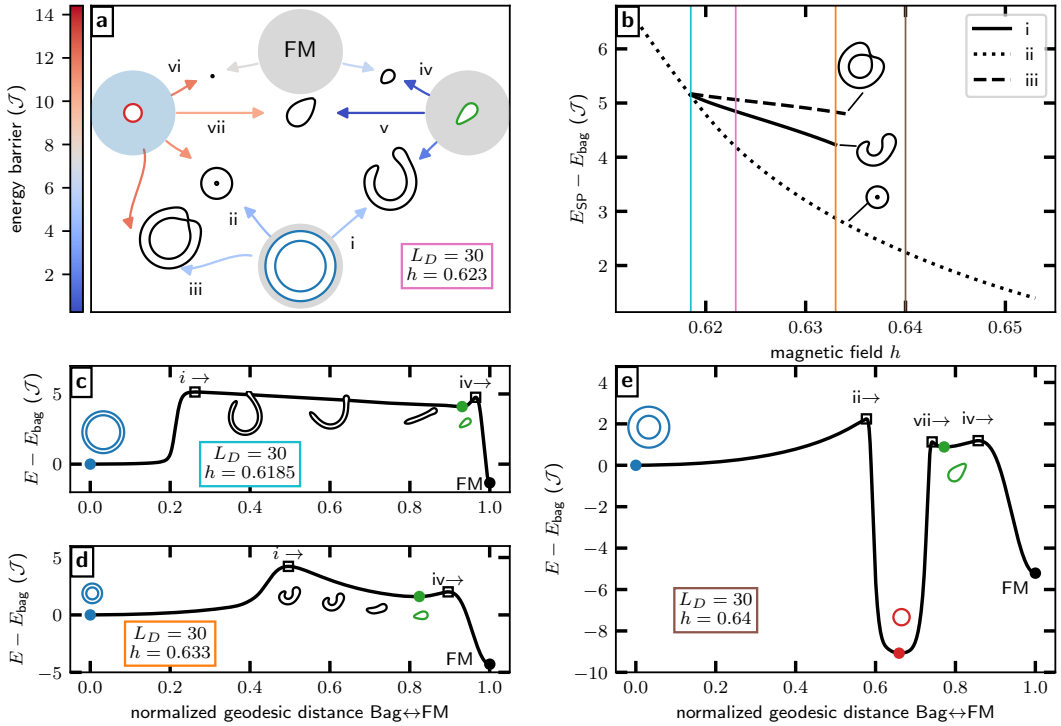


FIG. 11. **a**: Partial graph of the energy surface for a chiral magnet for a magnetic field $h = 0.623$ and $L_D = 30a$. All magnetic textures are represented by their contours. The metastable configurations are drawn within a colored circle, which indicates the topological charge of either $Q = -1$ for the skyrmion (blue) or $Q = 0$ (gray) for the FM, the droplet and the bag state. The SP configurations associated to the mutual transformations of the states are shown with two arrows pointing from the minima toward them. The color of the arrows corresponds to the respective energy barrier. **b**: Energy of the SP corresponding to the contour-merging process accompanied by nucleation of a chiral kink (i), the contour annihilation SP (ii) and the contour-merging SP (iii) with respect to the energy of the bag state as a function of the applied field value $h$. The pink vertical line indicates the parameters for which the graph displayed in **a** was obtained. The other lines indicate the field values $h = 0.6185$ (cyan), $h = 0.633$ (orange) and $h = 0.64$ (brown). **c**,**d**: Energy along the MEPs corresponding to the homotopy connecting the bag with the FM via the droplet state for $h = 0.6185$ (**c**) and $h = 0.633$ (**d**), respectively. **e**: Energy along the MEP corresponding to the a transformation that induces a change of the topological charge connecting the bag with the FM via the skyrmion and the droplet state. The energy is given relative to the energy of the bag state in units of the continuous-theory exchange parameter $\mathcal{J}$. The MEP is plotted against a normalized geodesic coordinate such that the bag state corresponds to 0 and the FM state to 1.

method [81, 82] capable of simulating the long timescale dynamic behavior of a system. SP searches can also serve as a foundation for global optimization of an objective function in a wider context [59], as well as for path optimization [83], such as in the calculation of tunneling within instanton theory [84, 85] and the propagation of radio waves [86]. In summary, the proposed SPSF constitutes a powerful and versatile tool for uncovering transition mechanisms in topological magnetic systems and estimating the associated transition rates.

## ACKNOWLEDGMENTS

H. S. acknowledges financial support from the Icelandic Research Fund (grant No. 239435). The calculations were carried out at the high-performance computing resources available at the Kiel University Computing Centre and at the Icelandic Research e-Infrastructure facility supported by the Icelandic Infrastructure Fund. P. F. B. acknowledges financial support from the Icelandic Research Fund (Grants No. 2410333 and No. 217750), the University of Iceland Research Fund (Grant No. 15673), the Swedish Research Council (Grant No. 2020-05110), and the Crafoord Foundation (Grant No. 20231063).

[1] B. Göbel, I. Mertig, and O. A. Tretiakov, Phys. Rep. **895**, 1 (2021).
[2] L. Rózsa, K. Palotás, A. Deák, E. Simon, R. Yanes, L. Udvardi, L. Szunyogh, and U. Nowak, Phys. Rev. B **95**, 094423 (2017).
[3] F. N. Rybakov, A. B. Borisov, S. Blügel, and N. S. Kiselev, Phys. Rev. Lett. **115**, 117201 (2015).
[4] F. N. Rybakov and N. S. Kiselev, Phys. Rev. B **99**, 064437 (2019).
[5] V. M. Kuchkin, B. Barton-Singer, F. N. Rybakov, S. Blügel, B. J. Schroers, and N. S. Kiselev, Phys. Rev. B **102**, 144422 (2020).
[6] V. M. Kuchkin and N. S. Kiselev, APL Materials **10**, 071102 (2022).
[7] E. Wigner, Trans. Faraday Soc. **34**, 29 (1938).
[8] G. H. Vineyard, J. Phys. Chem. Solids **3**, 121 (1957).
[9] H. A. Kramers, Physica **7**, 284 (1940).
[10] J. Langer, Ann. Phys. **54**, 258 (1969).
[11] N. Nagaosa and Y. Tokura, Nat. Nanotechnol. **8**, 899 (2013).
[12] B. Heil, A. Rosch, and J. Masell, Phys. Rev. B **100**, 134424 (2019).
[13] G. Henkelman, B. P. Uberuaga, and H. Jónsson, J. Chem. Phys. **113**, 9901 (2000).
[14] E. L. Kolsbjerg, M. N. Groves, and B. Hammer, J. Chem. Phys. **145**, 094107 (2016).
[15] N. R. Mathiesen, H. Jónsson, T. Vegge, and J. M. García Lastra, J. Chem. Theory Comput. **15**, 3215 (2019).
[16] P. F. Bessarab, V. M. Uzdin, and H. Jónsson, Comput. Phys. Commun. **196**, 335 (2015).
[17] G. T. Barkema and N. Mousseau, Phys. Rev. Lett. **77**, 4358 (1996).
[18] N. Mousseau and G. T. Barkema, Phys. Rev. E **57**, 2419 (1998).
[19] G. Henkelman and H. Jónsson, J. Chem. Phys. **111**, 7010 (1999).
[20] B. Peters, in *Reaction Rate Theory and Rare Events Simulations*, edited by B. Peters (Elsevier, Amsterdam, 2017) pp. 183–208.
[21] G. P. Müller, P. F. Bessarab, S. M. Vlasov, F. Lux, N. S. Kiselev, S. Blügel, V. M. Uzdin, and H. Jónsson, Phys. Rev. Lett. **121**, 197202 (2018).
[22] H. Bocquet and P. M. Derlet, Phys. Rev. B **108**, 174419 (2023).
[23] M. Sallermann, H. Jónsson, and S. Blügel, Phys. Rev. B **107**, 104404 (2023).
[24] H. Schrautzer, M. Sallermann, P. F. Bessarab, and H. Jónsson, Phys. Rev. B **112**, 104433 (2025).
[25] M. Plasencia Gutiérrez, C. Argáez, and H. Jónsson, J. Chem. Theory Comput. **13**, 125 (2017).
[26] K. Deb, A. Pratap, S. Agarwal, and T. Meyarivan, IEEE Transactions on Evolutionary Computation **6**, 182 (2002).
[27] Q. Xu and A. Delin, A general optimization framework for mapping local transition-state networks (2025), arXiv:2509.26269 [physics.comp-ph].
[28] A. Jay, C. Huet, N. Salles, M. Gunde, L. Martin-Samos, N. Richard, G. Landa, V. Goiffon, S. De Gironcoli, A. Hémeryck, and N. Mousseau, J. Chem. Theory Comput. **16**, 6726 (2020).
[29] N. Mousseau, L. K. Béland, P. Brommer, J.-F. Joly, F. El-Mellouhi, E. Machado-Charry, M.-C. Marinica, and P. Pochet, Journal of Atomic and Molecular Physics **2012**, 925278 (2012).
[30] M.-C. Marinica, F. Willaime, and N. Mousseau, Phys. Rev. B **83**, 094119 (2011).
[31] M. Gunde, A. Jay, M. Poberžnik, N. Salles, N. Richard, G. Landa, N. Mousseau, L. Martin-Samos, and A. Hemeryck, J. Chem. Phys. **160**, 232501 (2024).
[32] V. M. Kuchkin, N. S. Kiselev, F. N. Rybakov, and P. F. Bessarab, Frontiers in Physics **11**, 10.3389/fphy.2023.1171079 (2023).
[33] X. Z. Yu, Y. Onose, N. Kanazawa, J. H. Park, J. H. Han, Y. Matsui, N. Nagaosa, and Y. Tokura, Nature **465**, 901 (2010).
[34] X. Z. Yu, N. Kanazawa, Y. Onose, K. Kimoto, W. Z. Zhang, S. Ishiwata, Y. Matsui, and Y. Tokura, Nature Materials **10**, 106 (2011).
[35] X. Yu, A. Kikkawa, D. Morikawa, K. Shibata, Y. Tokunaga, Y. Taguchi, and Y. Tokura, Phys. Rev. B **91**, 054411 (2015).
[36] N. Romming, C. Hanneken, M. Menzel, J. E. Bickel, B. Wolter, K. von Bergmann, A. Kubetzka, and R. Wiesendanger, Science **341**, 636 (2013).
[37] I. Kézsmárki, S. Bordács, P. Milde, E. Neuber, L. M. Eng, J. S. White, H. M. Rønnow, C. D. Dewhurst, M. Mochizuki, K. Yanai, H. Nakamura, D. Ehlers, V. Tsurkan, and A. Loidl, Nature Materials **14**, 1116 (2015).
[38] N. Romming, A. Kubetzka, C. Hanneken, K. von Bergmann, and R. Wiesendanger, Phys. Rev. Lett. **114**, 177203 (2015).
[39] F. N. Rybakov, N. S. Kiselev, A. B. Borisov, L. Döring, C. Melcher, and S. Blügel, APL Materials **10**, 111113 (2022).
[40] A. Derras-Chouk, E. M. Chudnovsky, and D. A. Garanin, J. Appl. Phys. **126**, 083901 (2019).
[41] M. Donahue and R. McMichael, Physica B: Condensed Matter **233**, 272 (1997), hysteresis Modeling and Micromagnetism.
[42] S. Buhrandt and L. Fritz, Phys. Rev. B **88**, 195137 (2013).
[43] H. Wang, Y. Dai, G.-M. Chow, and J. Chen, Progress in Materials Science **130**, 100971 (2022).
[44] S. Yang, Y. Zhao, X. Zhang, X. Xing, H. Du, X. Li, M. Mochizuki, X. Xu, J. Åkerman, and Y. Zhou, Applied Physics Reviews **11**, 041335 (2024).
[45] V. M. Kuchkin, B. Barton-Singer, P. F. Bessarab, and N. S. Kiselev, Comm. Phys. **8**, 26 (2025).
[46] M. Ester, H.-P. Kriegel, J. Sander, and X. Xu, in *Proceedings of the Second International Conference on Knowledge Discovery and Data Mining*, KDD'96 (AAAI Press, 1996) p. 226–231.
[47] E. Schubert, J. Sander, M. Ester, H. P. Kriegel, and X. Xu, ACM Trans. Database Syst. **42**, 1 (2017).
[48] A. N. Gamby and J. Katajainen, Algorithms **11**, 10.3390/a11120195 (2018).
[49] B. A. Ivanov and D. D. Sheka, Journal of Experimental and Theoretical Physics Letters **82**, 436 (2005).
[50] D. D. Sheka, C. Schuster, B. A. Ivanov, and F. G. Mertens, The European Physical Journal B - Condensed Matter and Complex Systems **50**, 393 (2006).

[51] C. Moutafis, S. Komineas, and J. A. C. Bland, Phys. Rev. B **79**, 224429 (2009).
[52] I. Makhfudz, B. Krüger, and O. Tchernyshyov, Phys. Rev. Lett. **109**, 217201 (2012).
[53] D. B. Litvin, Acta Crystallographica Section A **33**, 279 (1977).
[54] P. Liu, J. Li, J. Han, X. Wan, and Q. Liu, Phys. Rev. X **12**, 021016 (2022).
[55] Z. Xiao, J. Zhao, Y. Li, R. Shindou, and Z.-D. Song, Phys. Rev. X **14**, 031037 (2024).
[56] H. Schiff, A. Corticelli, A. Guerreiro, J. Romhányi, and P. McClarty, SciPost Phys. **18**, 109 (2025).
[57] B. Barton-Singer, C. Ross, and B. J. Schroers, Commun. Math. Phys. **375**, 2259 (2020).
[58] V. M. Kuchkin, K. Chichay, B. Barton-Singer, F. N. Rybakov, S. Blügel, B. J. Schroers, and N. S. Kiselev, Phys. Rev. B **104**, 165116 (2021).
[59] M. Plasencia, A. Pedersen, A. Arnaldsson, J.-C. Berthet, and H. Jónsson, Comput. Geosci. **65**, 110 (2014).
[60] A. Edelman, T. A. Arias, and S. T. Smith, SIMAX **20**, 303 (1998).
[61] A. Ivanov, V. Uzdin, and H. Jónsson, Computer Physics Communications **260**, 107749 (2021).
[62] A. S. Varentcova, S. von Malottki, M. N. Potkina, G. Kwiatkowski, S. Heinze, and P. F. Bessarab, npj Comput. Mater. **6**, 193 (2020).
[63] D. K. Hoffman, R. S. Nord, and K. Ruedenberg, Theoretica chimica acta **69**, 265 (1986).
[64] P. Jørgensen, H. J. A. Jensen, and T. Helgaker, Theor. Chim. Acta **73**, 55 (1988).
[65] H. B. Schlegel, Theor. Chim. Acta **83**, 15 (1992).
[66] J. M. Bofill, W. Quapp, and M. Caballero, J. Chem. Theory Comput. **8**, 927 (2012).
[67] S. von Malottki, P. F. Bessarab, S. Haldar, A. Delin, and S. Heinze, Phys. Rev. B **99**, 060409 (2019).
[68] P. F. Bessarab, G. P. Müller, I. S. Lobanov, F. N. Rybakov, N. S. Kiselev, H. Jónsson, V. M. Uzdin, S. Blügel, L. Bergqvist, and A. Delin, Scientific Reports **8**, 3433 (2018).
[69] S.-G. Hwang, The American Mathematical Monthly **111**, 157 (2004).
[70] D. C. Liu and J. Nocedal, Mathematical Programming **45**, 503 (1989).
[71] K. Pearson, The London, Edinburgh, and Dublin Philosophical Magazine and Journal of Science **2**, 559 (1901).
[72] I. T. Jolliffe, in *Principal Component Analysis* (Springer New York, New York, NY, 1986) pp. 115–128.
[73] H.-H. Bock, Clustering methods: A history of k-means algorithms, in *Selected Contributions in Data Analysis and Classification*, edited by P. Brito, G. Cucumel, P. Bertrand, and F. de Carvalho (Springer Berlin Heidelberg, Berlin, Heidelberg, 2007) pp. 161–172.
[74] D. M. Saputra, D. Saputra, and L. D. Oswari, in *Proceedings of the Sriwijaya International Conference on Information Technology and Its Applications (SICONIAN 2019)* (Atlantis Press, 2020) pp. 341–346.
[75] F. Pedregosa, G. Varoquaux, A. Gramfort, V. Michel, B. Thirion, O. Grisel, M. Blondel, P. Prettenhofer, R. Weiss, V. Dubourg, J. Vanderplas, A. Passos, D. Cournapeau, M. Brucher, M. Perrot, and Édouard Duchesnay, JMLR **12**, 2825 (2011).
[76] V. Kuchkin, B. Schroers, and S. Blügel, *Diversity of chiral magnetic solitons*, RWTH-2022-10481 (Fachgruppe Physik, 2022).
[77] S. Meyer, M. Perini, S. von Malottki, A. Kubetzka, R. Wiesendanger, K. von Bergmann, and S. Heinze, Nature Communications **10**, 3823 (2019).
[78] F. Muckel, S. von Malottki, C. Holl, B. Pestka, M. Pratzer, P. F. Bessarab, S. Heinze, and M. Morgenstern, Nature Physics **17**, 395 (2021).
[79] M. dos Santos Dias, J. Bouaziz, M. Bouhassoune, S. Blügel, and S. Lounis, Nature Communications **7**, 13613 (2016).
[80] S. Grytsiuk, J.-P. Hanke, M. Hoffmann, J. Bouaziz, O. Gomonay, G. Bihlmayer, S. Lounis, Y. Mokrousov, and S. Blügel, Nature Communications **11**, 511 (2020).
[81] G. Henkelman and H. Jónsson, J. Chem. Phys. **115**, 9657 (2001).
[82] H. Jónsson, Proc. Natl. Acad. Sci. **108**, 944 (2011).
[83] D. M. Einarsdóttir, A. Arnaldsson, F. Óskarsson, and H. Jónsson, in *Applied Parallel and Scientific Computing*, edited by K. Jónasson (Springer Berlin Heidelberg, Berlin, Heidelberg, 2012) pp. 45–55.
[84] V. Ásgeirsson, A. Arnaldsson, and H. Jónsson, J. Chem. Phys. **148**, 102334 (2018).
[85] S. M. Vlasov, P. F. Bessarab, I. S. Lobanov, M. N. Potkina, V. M. Uzdin, and H. Jónsson, New Journal of Physics **22**, 083013 (2020).
[86] I. A. Nosikov, M. V. Klimenko, G. A. Zhbankov, A. V. Podlesnyi, V. A. Ivanova, and P. F. Bessarab, IEEE Trans. Antennas Propag. **68**, 455 (2020).